Universität Hamburg
DER FORSCHUNG | DER LEHRE | DER BILDUNG

Search for new long-lived particles with the CMS experiment at $\sqrt{s} = 13\,\text{TeV}$

Dissertation
zur Erlangung des Doktorgrades
an der Fakultät für Mathematik, Informatik und Naturwissenschaften
Fachbereich Physik
der Universität Hamburg

vorgelegt von
Melanie Eich

Hamburg
2022

Gutachter/innen der Dissertation:	Prof. Dr. Gregor Kasieczka Prof. Dr. Peter Schleper
Zusammensetzung der Prüfungskommission:	Prof. Dr. Gregor Kasieczka Prof. Dr. Gudrid Moortgat-Pick Dr. Isabell Melzer-Pellmann Prof. Dr. Arwen Pearson Prof. Dr. Peter Schleper
Vorsitzende/r der Prüfungskommission:	Prof. Dr. Arwen Pearson
Datum der Disputation:	05.09.2022
Vorsitzender Fach-Promotionsausschusses PHYSIK:	Prof. Dr. Wolfgang J. Parak
Leiter des Fachbereichs PHYSIK:	Prof. Dr.Günter H. W. Sigl
Dekan der Fakultät MIN:	Prof. Dr. Heinrich Graener

in memory of

Bruno Eich

(1953-2021)

Who showed me the beauty of nature,
set the basis for my interest in natural sciences
and won't be forgotten.

Abstract

Long-lived particles are an interesting extension of the standard model of particle physics. This thesis presents a search for such new long-lived particles with lifetimes of the order of a few millimetres produced in Higgs boson decays that then themselves decay into b quark pairs. The long-lived particles are predicted by, for example, Twin Higgs models. These theories solve the so-called little hierarchy problem, increasing the validity of the standard model. The search is performed with proton-proton collisions at a centre-of-mass energy of 13 TeV at the LHC corresponding to an integrated luminosity of $\mathcal{L} = 36.3\,\mathrm{fb}^{-1}$ recorded with the CMS experiment.

The search is split into two analyses, depending on the mass of the long-lived particles, because the decay kinematics differ. One analysis is designed for light long-lived particles ($m_{\pi_\nu} = 15\,\mathrm{GeV}$), and the other analysis is for heavier long-lived particles ($m_{\pi_\nu} = 40\,\mathrm{GeV}$ and $m_{\pi_\nu} = 55\,\mathrm{GeV}$). The final state of the signal events is expected to contain up to four b quarks. Therefore, events with at least four jets of which at least three have to be b-tagged jets are selected. Two production modes for the signal are investigated: gluon-gluon fusion and vector-boson fusion Higgs boson production modes. Possible signal events are identified by a requirement on the invariant mass of the signal candidate jets. Signal events are further separated from background events using a neural network based jet tagger. The network is parametrised as a function of the masses and lifetimes of the signal prediction. This makes it possible to train the network only once and simultaneously use it for the analyses of different masses and lifetimes. The main background consists of QCD multijet production and is estimated using a data-driven method. Upper limits on the signal strength modifier are calculated at 95 % CL as a function of the lifetimes for all investigated masses of the long-lived particles. No evidence for such long-lived particles is observed.

Zusammenfassung

Langlebige Teilchen sind eine interessante Erweiterung des Standardmodells der Teilchenphysik. In dieser Doktorarbeit wird eine Suche nach solchen neuen langlebigen Teilchen vorgestellt, für die Lebenszeiten von wenigen Millimetern erwartet werden. Die langlebigen Teilchen werden von verschiedenen Theorien, wie zum Beispiel den "Twin Higgs" Modellen, vorhergesagt und erweitern die Gültigkeit des Standardmodells. Diese langlebigen Teilchen zerfallen bevorzugt in b Quarks und werden bei Higgs-Boson-Zerfällen erzeugt. Für die Suche werden Proton-Proton-Kollisionen verwendet, welche bei einer Schwerpunktsenergie von 13 TeV am LHC entstanden sind, mit dem CMS-Experiment aufgezeichnet wurden und einer integrierten Luminosität von $\mathcal{L} = 36.3\,\mathrm{fb}^{-1}$ entsprechen. Die Suche ist, abhängig von der Masse der langlebigen Teilchen, in zwei Analysen aufgeteilt, da sich die Zerfallskinematiken unterscheiden. Eine Analyse ist auf leichte langlebige Teilchen ausgelegt ($m_{\pi_\nu} = 15\,\mathrm{GeV}$) und die andere Analyse auf schwerere langlebige Teilchen ($m_{\pi_\nu} = 40\,\mathrm{GeV}$ und $m_{\pi_\nu} = 55\,\mathrm{GeV}$). Es werden bis zu vier b Quarks im Endzustand erwartet, weshalb Ereignisse mit mindestens vier Jets, von denen mindestens drei b identifizierten Jets sein müssen, ausgewählt werden. Es werden zwei Higgs-Boson Produktionsmodi für das Signal untersucht: die Gluon-Gluon-Fusion und die Vektor-Boson-Fusion. Mögliche Signalereignisse werden durch eine Forderung an die invariante Masse, der aus den langlebigen Teilchen hervorgehenden Jets identifiziert. Für die weitere Unterscheidung zwischen solchen Jets aus langlebigen Teilchen und solchen aus Untergrundprozessen wurde ein neuronales Netz entwickelt, welches als Funktion der Massen und Lebensdauern der Signalvorhersage parametrisiert ist. Dadurch ist es möglich, das Netzwerk nur einmal zu trainieren und es gleichzeitig für sämtliche untersuchten Massen und Lebensdauern zu verwenden. Der Hauptuntergrund besteht aus QCD-Multijet-Prozessen und wird durch eine datengetriebene Methode abgeschätzt. Für alle untersuchten Massen werden obere Ausschlussgrenzen mit 95 % CL für den Signalstärkemodifikator in Abhängigkeit der Lebensdauer der langlebigen Teilchen berechnet. Es wurden keine Hinweise auf solche neuen langlebigen Teilchen beobachtet.

Contents

1 Introduction

More than two thousand years of theories, experiments and analysis of data have passed between early ideas of indivisible particles in ancient Greece and our understanding of modern particle physics. It took until 1897 to find the first truly elementary particle, the electron [1]. Over a hundred years later, the last missing piece of the standard model (SM) of particle physics was found - the Higgs boson [2, 3]. Its discovery in 2012 was only achievable with the world's most powerful particle collider to date, the Large Hadron Collider (LHC) [4], in combination with the two multi-purpose particle experiments called A Toroidal LHC ApparatuS (ATLAS) [5] and Compact Muon Solenoid (CMS) [6].
The SM of particle physics aims to provide a complete description of fundamental processes in the universe. The SM of particle physics is a quantum field theory (QFT) and able to describe all discovered elementary particles with their interactions mediated by force carrier particles. Three out of the four forces that govern the universe are included in the SM of particle physics. Various experiments provided precise measurements or confirmed predictions of the theoretical model, such as the existence of particles like the top or bottom quark, properties of particles or decay modes. So far, almost all experimental results agree with the SM of particle physics, making it a successful and well-tested theory. There are, however, several shortcomings highlighted by experimental results that do not agree with the SM of particle physics. Furthermore, phenomena exist, which are currently not explainable by the theory.
Observations, for example, have confirmed the existence of Dark Matter, while the SM of particle physics predicts no suitable particle candidate. Furthermore, only the unification of the electromagnetic and the weak forces was possible, while a unification of them together with the strong force is not successful. Gravity, the fourth force in the universe, was so far not successfully included in the SM of particle physics. Another example is that within the SM of particle physics, neutrinos are expected to be massless, contradicting experimental results [7–9]. In addition, it is assumed that the SM of particle physics is valid up to the Planck scale of 10^{19} GeV, where quantum gravitational effects are no longer negligible. If this assumption is valid, large scale differences between the electroweak scale

and the Planck scale must be handled by the theory. This leads to the hierarchy problem, where fine-tuning of radiative corrections is needed to account for the mass of the Higgs boson, measured to be approximately 125 GeV [10].

Various theories beyond the standard model (BSM) have been developed to answer one or several open questions. Many of these new theories have in common that they predict new, so far undiscovered particles. For example, Twin Higgs models [11–13] predict a new gauge group with twin partners of some or all the SM particles. These twin particles do not carry SM quantum numbers and are therefore uncharged under the SM gauge groups. The Higgs boson can interact with the twin sector, and decay into a pair of scalar particles. These scalars could be long-lived and therefore travel a finite distance within our particle experiments without interacting before they decay back into SM particles. The Twin Higgs models can explain why the Higgs boson is so light and solve the so-called little hierarchy problem.

The search presented in this thesis uses a simplified version of the Twin Higgs models as a benchmark. Two Higgs production modes, vector-boson fusion (VBF) and gluon-gluon fusion (ggF), are investigated. The Higgs boson is expected to decay to two long-lived particles (LLPs), where a decay of each LLP to a pair of SM bottom quarks is predicted to be the main decay channel. Mass and lifetime of the LLPs are tunable parameters of the theoretic model, and the search aims for masses between 15-55 GeV and lifetimes of up to 1 mm in the particle's rest frame. The lifetime of the LLPs impacts the displacement of the bottom quark decays, resulting in a slightly displaced bottom quark signature. Additionally, the mass of the LLP has an impact on the distance between the decay products. Light LLP masses lead to bottom quarks that are close together and make a reconstruction within one jet possible, denoted as boosted topology. The heavier the LLP mass is, the further apart are the two bottom quarks, and their jets can be reconstructed separately, denoted as resolved topology. Since this leads to different signatures of the reconstructed signal, the search is split into two analyses, focussing on the boosted and resolved topology, respectively. A search with data recorded by the ATLAS experiment has been previously performed [14], but the studied phase space has not been explored by CMS data so far. Therefore, this thesis presents the first CMS analysis searching for LLPs in this phase space. Analysed are data of proton-proton (pp) collisions produced at the LHC at $\sqrt{s} = 13\,\text{TeV}$ with an integrated luminosity of $\mathcal{L} = 36.3\,\text{fb}^{-1}$ [15], recorded by the CMS detector in 2016. The signature of the benchmark model is similar to SM QCD multijet events, making this search challenging. Commonly used analyses methods, for example, the χ^2 method to select jets of interest, are combined with novel techniques,

for example the parametrisation of a deep neural network (DNN) with the masses and lifetimes of the LLPs. The parametrisation of the DNN has the advantage that one training with a mixture of the different LLP masses and lifetimes is enough to use the same DNN for the boosted and the resolved topology. The DNN is trained to predict a probability that a jet is originated from a LLP decay. Exclusion limits as a function of the LLP masses and lifetimes were set with the presented analysis.

This thesis is structured in four parts. In Part I, an overview of theoretical aspects of particle physics is summarised, focussing on the SM of particle physics in Chapter 2, its open questions in Chapter 3 and theories extending the SM of particle physics in Chapter 4. Furthermore, relevant concepts of the physics of pp collisions are explained in Chapter 5, before some concepts of machine learning (ML), especially those used for this thesis, are introduced in Chapter 6. Part II is dedicated to the measurement and reconstruction steps happening after the pp collisions until the final particle identification. Therefore, Chapter 7 gives an overview of the particle collider LHC and the CMS detector, while Chapter 8 presents details about the event reconstruction and the final particle identification. Part III describes the search for LLPs produced in Higgs boson decays with slightly displaced b quark like signatures. First, fundamental components of the analyses are summarised in Chapter 9, before the analyses with the boosted and the resolved topologies are presented in Chapters 10 and 11, respectively. The first results in this phase space with CMS data are presented in Chapter 12, containing the exclusion limits of both analyses. Finally, the thesis concludes with a summary in Part IV, which also gives an outlook on the future prospects of the presented LLP search.

Part I

Theoretical Aspects of Particle Physics

Particle physics aims to describe all elementary particles and forces with mathematical methods and thus to provide a complete description of nature. The SM of particle physics unifies all elementary particles discovered so far and three out of four known forces. Its mathematical formulation is a QFT, a mathematical construct to describe the fermions and bosons as excitations of quantum fields. These quantum mechanical field equations can be derived by applying the Euler-Lagrange formalism to the Lagrangian density $\mathcal{L}$ [16]. If the quantity of observables do not change under transformation when the Lagrangian density is invariant under that specific transformation, the symmetry is conserved. With Noether's theorem, each differentiable symmetry is related to a conservation law, and each conserved variable is connected to a symmetry. The SM of particle physics is a well known and successful theory, predicting (almost) all experimental results.
An overview of the SM of particle physics is given in Chapter 2 and open questions to the SM are raised in Chapter 3. Theories extending the SM are explained in Chapter 4. Chapter 5 contains some unique details of the physics of pp collisions. The following discussion is based on References [16] and [17] if not indicated otherwise. Some basic concepts of ML, used for this thesis, are summarised in Chapter 6.

2 The Standard Model of Particle Physics

The SM of particle physics unifies three of the four known forces into one theory. Only gravity has not yet been successfully described as a QFT, and is therefore not included. The symmetry group of the SM of particle physics is composed of:

$$U(1)_{\mathrm{Y}} \otimes SU(2)_{\mathrm{L}} \otimes SU(3)_{\mathrm{C}}, \tag{2.1}$$

with the electromagnetic interaction $U(1)_{\mathrm{Y}}$ with the hypercharge Y, the weak interaction $SU(2)_{\mathrm{L}}$, which couples to left-handed particles (and right-handed antiparticles) only, and the strong interaction $SU(3)_{\mathrm{C}}$, where C is the colour charge. The relevant particles, forces, and mechanisms of the SM of particle physics are introduced in the following.

2.1 Particles and Forces of the Standard Model

Depending on the spin of a particle, it belongs either to the group of *fermions* or *bosons*. Fermions carry half-integer spin and are described by the Fermi-Dirac statistics [18, 19]. Therefore, two fermions with the same quantum numbers cannot occupy the same quantum state. In contrast, bosons carry integer spin and are characterised by Bose-Einstein statistics [20]. As a result, bosons with the same quantum numbers can occupy the same quantum state.

Fermions are further separated into leptons and quarks. To each of the electrically charged[1] lepton types electron (e), muon (μ) and tau (τ), an electrically neutral neutrino of this flavour (ν_e, ν_μ, ν_τ) exists. The leptons can be sorted into three generations, where e and ν_e are the first generation. The particles of the second and third generations have the same properties but a higher mass. More recent experiments have shown that

[1] The electrical charge of particles is given in multiples of -1e, the elementary charge carried by one electron.

neutrinos are not massless but very light particles [21,22]. The weak eigenstates ν_e, ν_μ, ν_τ can be described by a coherent linear superposition of the mass eigenstates ν_1, ν_2, ν_3, and therefore, neutrinos can oscillate between the different flavours. The quarks are divided into the up- and down-type quarks. The up-type ones carry $+\frac{2}{3}$e and are the up (u), charm (c) and top (t) quarks, while down-type ones carry $-\frac{1}{3}$e and are the down (d), strange (s) and bottom (b) quarks. Similarly to the leptons, up and down quarks build the first generation, while the other quarks are heavier copies. In addition to the electric charge, quarks also carry colour charge of the types red, green or blue and can therefore interact through the strong interaction. Each fermion has an antiparticle, with the same mass, but opposite charges.

The interactions are mediated by spin-1 particles, the so-called *gauge bosons*. The gauge group theories predict these gauge bosons and the corresponding new vector fields and are constructed in such a way to keep the gauge group invariant under space-dependent phase transformations.

The boson corresponding to the $U(1)$ gauge group is the massless and electrically neutral photon (γ). It is the mediator of the electromagnetic interaction, affecting all electrically charged particles. The corresponding QFT is called quantum electrodynamics (QED). This interaction is, for example, responsible for the cohesion of atoms. The fine-structure constant

$$\alpha_{\text{em}} = \frac{g_{\text{em}}^2}{4\pi}, \tag{2.2}$$

with $g_{\text{em}} = e$ denoting the QED coupling strength. A closer investigation reveals that the fine structure is not a constant value but has a logarithmical dependence on the energy. At low energies, approaching a squared momentum transfer q^2 of zero, the coupling can be estimated as $\alpha_{\text{em}} \approx \frac{1}{137}$, while for higher energies, virtual lepton and quark corrections have an non negligible impact and change the effective coupling strength.

The quantum chromodynamics (QCD) is the QFT of the strong force, which has as quantum numbers the colour charges red, green or blue. Quarks carry colour charge and can interact through QCD. The QCD is mediated by eight massless gluons (g), which carry colour charge[2] themself and can hence interact with each other. A consequence of this self-coupling is the *colour confinement*. This concept describes that the potential of the colour field is proportional to the distance between two quarks, and the potential increases the further the quarks are pulled apart. Therefore, it is more efficient to form new quark-antiquark pairs at a certain distance. Only within a quark-gluon plasma are

[2]Each gluon carries both a color chage and an anticolor charge.

quarks deconfined, as investigated for example in heavy-ion collisions [23]. Due to this confinement, coloured objects are not present in nature as single particles but form colour neutral hadrons. Hadrons can consist of a quark-antiquark pair, or of three quarks. Those bound states of two or three quarks are called mesons or baryons, respectively. In pp collisions, the highly energetic quarks undergo *hadronisation* and produce sprays of particles, which are called *jets* (see Section 8.3). Only the top quark behaves differently because it is so heavy that it decays before the hadronisation process starts. This property can be used to identify the top quark produced in pp collisions and recorded by colliding experiments. The fine-structure constant of QCD depends on the momentum transfer q^2

$$\alpha_{\mathrm{S}}(q^2) = \frac{12\pi}{(11n - 2f)\ln(q^2/\Lambda^2_{\mathrm{QCD}})}, \tag{2.3}$$

with $n = 3$ colours and $f = 6$ quark flavours for the SM of particle physics. The QCD scale denoted by $\Lambda_{\mathrm{QCD}} \approx 200\,\mathrm{MeV}$ was measured experimentally. As can be seen from Equation 2.3, the larger the momentum transfer is, the less are the quarks affected by the strong interaction. This dependency is called asymptotic freedom. For modern pp collider experiments, the energy of the hadrons is high enough, that the distances between interacting quarks become small enough that quarks can be treated nearly as free particles. The QCD is responsible for holding the atomic nucleus together by a potential well.

In contrast to the other two interactions, the weak interaction has massive bosons. These are the electrically neutral Z boson with a mass of $91.1876 \pm 0.0021\,\mathrm{GeV}$ [21] and the two electrically charged bosons W^+ and W^- with a mass of $80.379 \pm 0.012\,\mathrm{GeV}$ [21]. The finite masses of these bosons lead to a small effective range of $\mathcal{O}(10^{-17}\mathrm{m})$ for this interaction. The observation of the radioactive β decay has caused the formulation of this theory [24] and is one crucial example of everyday weak interactions. The W bosons allow transitions within one generation between a charged lepton and the corresponding neutrino, while the interaction between different generations is forbidden. Therefore, in the SM of particle physics, the lepton numbers of all flavours have to be preserved within each interaction. Quarks, on the other hand, behave differently. Predictions of rates of particle decays did not match the experimental results, for example, for the $K^0 \to \mu^+\mu^-$ process. The predictions can only match the experimental results, when transitions between different generations of quarks via a W boson are allowed. A solution was the definition of weak eigenstates instead of mass eigenstates, which couple differently. A relation between the mass eigenstates and the weak eigenstates can be established by the Cabbibo-Kobayashi-Maskawa (CKM) matrix. It is composed of three rotation angles and a complex phase.

Each element squared $|V_{ij}|^2$ represents the probability of transitions between quarks of the type i and j via a W boson. The values are determined from experimental measurements as [21]:

$$\begin{pmatrix} |V_{ud}| & |V_{us}| & |V_{ub}| \\ |V_{cd}| & |V_{cs}| & |V_{cb}| \\ |V_{td}| & |V_{ts}| & |V_{tb}| \end{pmatrix} \approx \begin{pmatrix} 0.974 & 0.227 & 0.004 \\ 0.226 & 0.973 & 0.041 \\ 0.009 & 0.040 & 0.999 \end{pmatrix}, \tag{2.4}$$

and includes assumptions of the unitarity. The CKM matrix shows, that transitions between all quark generations are possible, but the probability of transitions across two generations is suppressed. W bosons couple only to particles that carry the weak isospin T_3. Left-handed fermions or right-handed antifermions can be grouped into isospin doublets:

$$\begin{pmatrix} \nu_e \\ e \end{pmatrix}_{\mathrm{L}}, \begin{pmatrix} \nu_\mu \\ \mu \end{pmatrix}_{\mathrm{L}}, \begin{pmatrix} \nu_\tau \\ \tau \end{pmatrix}_{\mathrm{L}}, \tag{2.5}$$

$$\begin{pmatrix} u \\ d \end{pmatrix}_{\mathrm{L}}, \begin{pmatrix} c \\ s \end{pmatrix}_{\mathrm{L}}, \begin{pmatrix} t \\ b \end{pmatrix}_{\mathrm{L}}. \tag{2.6}$$

Neutrinos and up-type quarks carry weak isospin of $T_3 = +\frac{1}{2}$. Charged leptons and down-type quarks carry weak isospin of $T_3 = -\frac{1}{2}$. Right-handed fermions (and left-handed antifermions) are isospin singlets and carry weak isospin of $T_3 = 0$. Unlike the W bosons, the Z boson couples not only to isospin doublets, but also to isospin singlets. This behaviour can be explained with the unification of electromagnetic and weak interaction, which is described in the next section.

2.2 Electroweak Unification

The unification of the electromagnetic and the weak forces to the electroweak sector $U(1)_{\mathrm{Y}} \otimes SU(2)_{\mathrm{L}}$ was first described by Salam, Glashow and Weinberg in the 1960s [25, 26]. It was experimentally observed that Z bosons couple to the left- and right-handed particles, but with different strengths and before the unification, this was not allowed by the weak theory.

Besides the weak isospin T_3, the weak interaction introduces three gauge fields, W_1, W_2 and W_3. Right-handed fermions carry an isospin of 0 and can not interact with charged currents of the weak interaction, represented by the three new gauge fields. Linear com-

binations between two of the three fields describe the two W bosons:

$$W^{\pm} = \frac{1}{\sqrt{2}}(W_1 \mp W_2). \tag{2.7}$$

The electromagnetic gauge group is introduced together with the hypercharge Y and the gauge field B. The correlation between the electromagnetic charge Q, the hypercharge Y and the weak isospin T_3 is:

$$Q = T_3 + \frac{Y}{2}. \tag{2.8}$$

The connection between the electromagnetic force g_{em} and the weak force g_{S} is:

$$g_{\mathrm{em}} = g_{\mathrm{S}} \sin\theta_{\mathrm{W}}, \tag{2.9}$$

with θ_{W} being the Weinberg angle or weak mixing angle.
The Z boson and the photon γ can be derived by using the Weinberg angle and the two remaining gauge fields, W_3 and B:

$$\begin{pmatrix} Z \\ \gamma \end{pmatrix} = \begin{pmatrix} \cos\theta_{\mathrm{W}} & \sin\theta_{\mathrm{W}} \\ -\sin\theta_{\mathrm{W}} & \cos\theta_{\mathrm{W}} \end{pmatrix} = \begin{pmatrix} B \\ W_3 \end{pmatrix}. \tag{2.10}$$

The mixing of the two gauge fields, W_3 and B, explains why the Z boson allows weak neutral current interactions, with couplings (of different strength) to left and right-handed particles.
Gauge invariance under electroweak transformation is only achieved when all vector fields, and hence fermions as well as W and Z bosons are massless, which is in contrast to all experimental observations.

2.3 Electroweak Symmetry Breaking and Higgs Mechanism

Even though the mathematical constructs of the SM of particle physics can describe many experimental results and precise measurements were performed, it is not a consistent theory. For example, the local gauge symmetry in the U(1) gauge group is only valid because the photon is a massless particle. However, for the electroweak interaction the situation is different, since the W and Z bosons are experimentally found to be massive. The Brout-Englert-Higgs (BEH) mechanism developed independently by Brout, Englert [27],

and Higgs [28] introduces the masses of the electroweak gauge bosons in such a way that the local gauge invariance is preserved. It is based on the so-called spontaneous symmetry breaking. *Spontaneous* indicates that no external interactions are responsible in this context, instead, the theory model itself is the initiator. First, a new complex scalar field in the form of an electroweak isospin doublet is introduced:

$$\Phi = \begin{pmatrix} \Phi^+ \\ \Phi^0 \end{pmatrix} = \frac{1}{\sqrt{2}} \begin{pmatrix} \Phi_1 + i\Phi_2 \\ \Phi_3 + i\Phi_4 \end{pmatrix}. \tag{2.11}$$

It contains one electromagnetically charged and one neutral component and is the only spin-0 field in the SM of particle physics. The BEH mechanism postulates the potential

$$V(\Phi) = \mu^2 \Phi^\dagger \Phi + \lambda (\Phi^\dagger \Phi)^2, \tag{2.12}$$

where the first term can be interpreted as the mass of the particle and the last term describes self-interaction among the scalar field, and λ and μ are two new parameters. Only $\lambda > 0$ gives a stable vacuum, while μ^2 can be either positive or negative. A value of $\mu^2 > 0$ leads to a symmetric, parabolic potential with one minimum and does not help solve the initial problem. Instead, with $\mu^2 < 0$, the shape of the potential is similar to a Mexican hat with an infinite set of minima

$$\Phi^\dagger \Phi = -\frac{\mu^2}{2\lambda} = \frac{v^2}{2}, \tag{2.13}$$

with v being called the vacuum expectation value. This ground state is responsible for symmetry breaking since it is no longer invariant under $SU(2)_L \otimes U(1)_Y$ transformations. Due to the invariance under $U(1)$ transformations, the photon has to be massless, and therefore the minimum of the neutral scalar field is

$$\Phi^0 = \frac{1}{\sqrt{2}} \begin{pmatrix} 0 \\ v \end{pmatrix}. \tag{2.14}$$

Expanding the fields around the minimum introduces a massive scalar boson h

$$\Phi = \frac{1}{\sqrt{2}} \begin{pmatrix} 0 \\ v + h \end{pmatrix}. \tag{2.15}$$

This new boson can be interpreted as the Higgs boson.

After symmetry breaking, the electroweak gauge boson masses are predicted as

$$m_{\mathrm{W}} = \frac{1}{2} g_{\mathrm{W}} v \qquad \text{and} \qquad m_{\mathrm{Z}} = \frac{1}{2} v \sqrt{g_{\mathrm{W}}^2 + \left(\frac{e}{\theta_{\mathrm{W}}}\right)^2}. \tag{2.16}$$

Based on the experimentally measured masses of W and Z bosons, the vacuum expectation value is found to be $v = 246\,\mathrm{GeV}$. The Higgs boson mass itself can be described by the equation:

$$m_{\mathrm{H}}^2 = 2\lambda v^2. \tag{2.17}$$

The theory predicts that the Higgs boson couples only to massive particles. In addition, fermion loops make indirect couplings to massless particles such as photons and gluons possible.

Furthermore, the BEH mechanism can include the masses of the fermions to the SM of particle physics. With the so-called Yukawa coupling y_i, defined as the interaction between fermions with the Higgs field, the masses of each fermion type i can be derived as

$$m_i = \frac{v y_i}{\sqrt{2}}. \tag{2.18}$$

The coupling strength between the Higgs boson and all fermions is proportional to their mass.

2.4 The Higgs Boson

The Higgs boson was predicted since 1964, but the discovery took until 2012. This last missing piece of the SM of particle physics was found by the ATLAS and the CMS experiments at the LHC [2, 3]. These experiments also measured the mass of the Higgs boson to be approximately 125 GeV. Since 2012 the Higgs boson is included in the SM of particle physics and is the only spin-0 particle within the theory.

Different production modes of the Higgs boson are possible. The leading order Feynman diagrams of these processes are shown in Figure 2.1. A focus was set to processes mainly happening at the LHC and are from the top left to the bottom right: ggF, vector boson associated production, VBF and the associated production with heavy quarks[3]. Each production mode has a certain production cross section, depending on the centre-of-mass energy and the mass of the Higgs boson. Figure 2.2 (left) shows the production

[3] top or bottom quarks

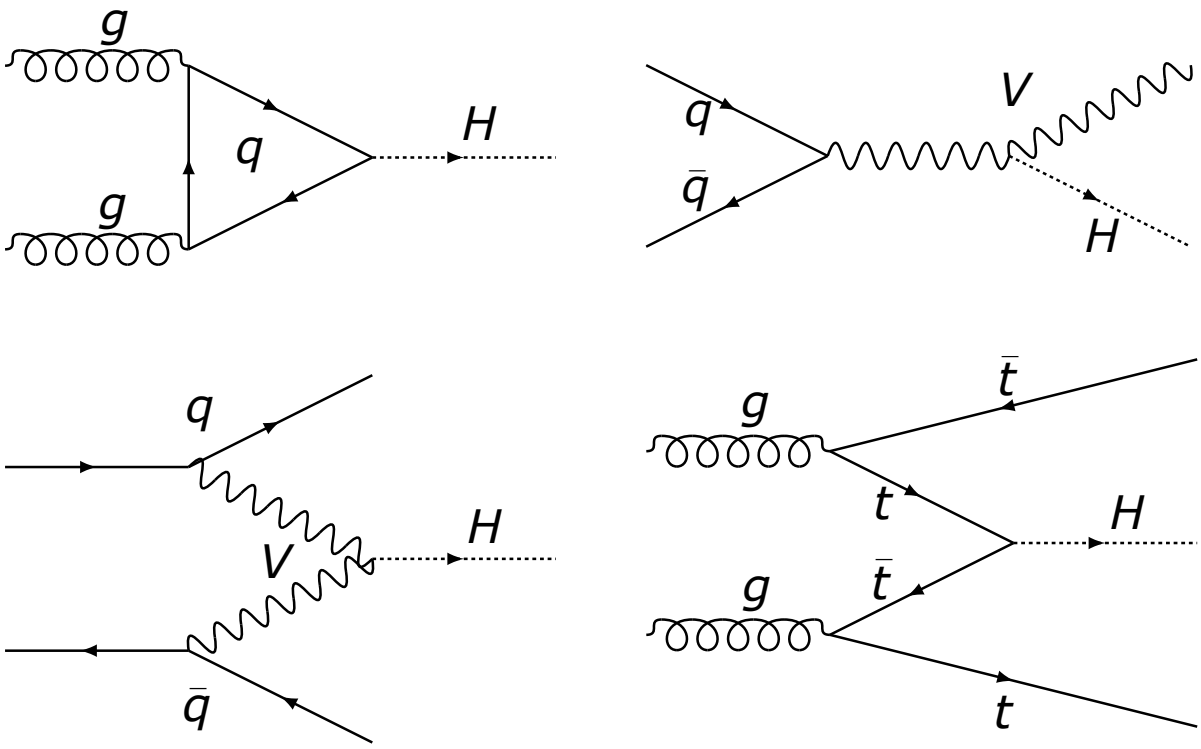

Figure 2.1: Feynman diagrams of different Higgs boson production modes are shown: Gluon-gluon fusion (upper left), vector-boson associated production (upper right), vector-boson fusion (lower left) and the associated production with heavy quarks (lower right). Drawn with [29].

cross sections for $\sqrt{s} = 13\,\text{TeV}$. The ggF, has the highest production cross section. With approximately one order of magnitude lower cross section, it is followed by the VBF production mode and the associated production with a W or Z boson. Higgs bosons produced in association with a W or a Z boson can be easier identified due to the additional particles present in the event. The production modes with heavy quarks allow a measurement of the direct Yukawa couplings of the Higgs boson to the heavy quarks. So far, only the production associated with top quarks was observed [30, 31], while the associated production with bottom quarks is harder to distinguish from other SM background processes.

The branching ratios of the Higgs boson into other particles are determined by the mass of the Higgs boson. Since the Higgs boson couples to all massive particles, decays into various particles are possible. Furthermore, decays via fermion loops make massless particles in the final states possible. An overview is shown in Figure 2.2 (right). Even though the final state with $b\bar{b}$ quarks has the highest branching ratio, it was not the decay channel

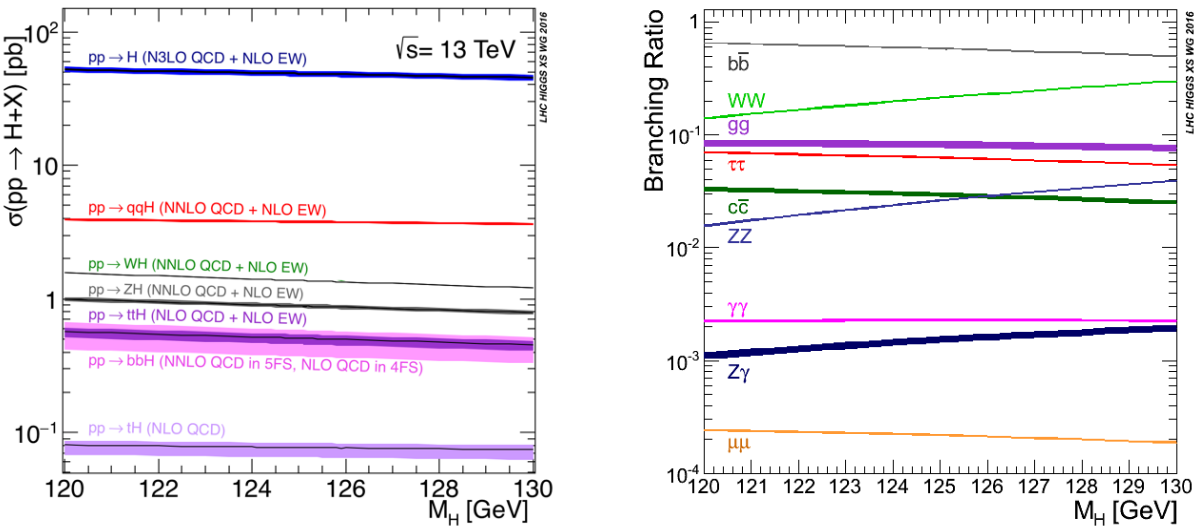

Figure 2.2: The production cross sections (left) and the branching ratios (right) as function of the Higgs boson mass are shown. Taken from [10].

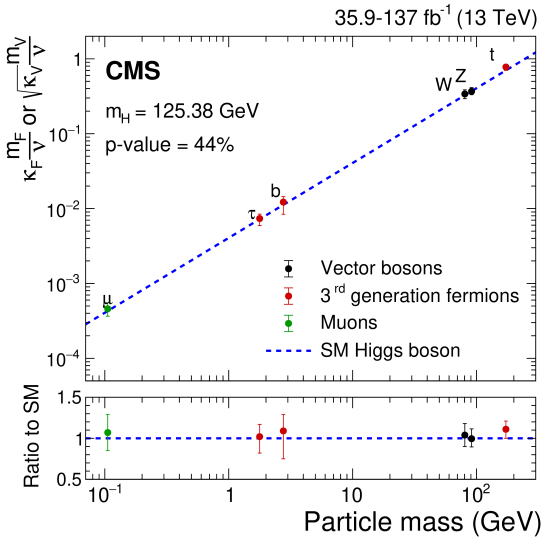

Figure 2.3: Reduced coupling modifiers of fermions (red and green circles) and weak bosons (black circles) as a function of the particle mass compared to their SM prediction (blue dashed line). Taken from [35].

with which the Higgs boson was initially found. Instead, the $\gamma\gamma$ and ZZ channels gave enough discrimination power to observe and measure the Higgs boson [2, 3]. Over time, other decay channels were also observed (e.g. [32–34]) since more data or new analysis techniques with better algorithms increased the sensitivity.

Besides measurements of the production cross sections and branching ratios, other prop-

erties of this neutral scalar particle have been intensively investigated since the discovery. Of immense interest is, for example, the exact mass of the Higgs boson, since this is a free parameter in the BEH mechanism. In addition, the couplings of the Higgs boson to different particles can be derived from experimental results [35]. For each particle a coupling modifier κ includes the production and decay rate of a certain channel. Since the Yukawa coupling between the Higgs boson and any fermion is proportional to the fermion's mass, while the coupling to the gauge bosons of the weak interaction is proportional to the square of their masses, the reduced coupling strength modifier is either expressed as $\kappa_{\mathrm{F}} m_{\mathrm{F}}/v$ or as $\sqrt{\kappa_{\mathrm{V}}} m_{\mathrm{V}}/v$, with v being the vacuum expectation value of the Higgs field. Six of these reduced coupling strength modifiers are derived from experimental measurements so far and presented as a function of the particle mass in Figure 2.3, which all agree well with the prediction from the SM. Additional properties of the Higgs boson, as the decay widths, the spin and CP properties have been investigated, e.g. in References [36–39]. So far, all measured properties of the found Higgs boson agree with the predictions of the SM of particle physics.

3 Open Questions of the Standard Model

Although many experimental results agree well with the theoretical predictions of the SM of particle physics, several open questions remain unanswered. A few of such open questions are introduced in the following, focussing on those relevant to this thesis.

The overview of the SM of particle physics given above shows only a small part of the complex theory. In total, it is a mixture of the Dirac equation of relativistic quantum mechanics motivating the dynamics of fermions, QFTs describing particles and their interactions, and a local gauge principle motivating the interaction behaviour. Furthermore, the Higgs mechanism of electroweak symmetry breaking explaining why particles are massive [16]. Many experimental results confirmed predictions of the SM of particle physics and provided additionally values to free parameters[1] of the theory such as particle masses or the CKM matrix elements (see Equation 2.4).

Like the masses of all particles in the SM of particle physics, the mass of the Higgs boson was not predicted by the theory. When the new particle was found with a mass of around 125 GeV in 2012, it was first unclear whether it was the Higgs boson or not. A higher mass for this new boson was expected, but all other investigated properties are consistent with the predictions for the Higgs boson. A higher mass was predicted since the SM of particle physics can theoretically be valid up to the Planck scale $\Lambda_{\text{Planck}} \approx 10^{19}\,\text{GeV}$. At such high scales gravitational affects can not longer be neglected. Therefore, at some cutoff scale Λ_{cutoff} there should be new physics experimentally observable, which is not explainable by the SM of particle physics. Unfortunately, such a cutoff scale affects the properties of the Higgs boson and is called the *naturalness problem* [40, 41]. The Higgs boson's interaction with different particle types corrects the mass of the Higgs boson. These corrections are

[1] More than 20 free parameters exist in the SM of particle physics, which are not predicted from theory and are independent of other parameters.

in addition dependent on the energy scale Λ:

$$\delta m_{\mathrm{H}}^2 = \frac{3G_{\mathrm{F}}}{4\sqrt{2\pi}}(4m_{\mathrm{t}}^2 - 2m_{\mathrm{W}}^2 - m_{\mathrm{Z}}^2 - m_{\mathrm{H}}^2)\Lambda^2, \tag{3.1}$$

with G_{F} Fermi's constant, m_{t}, m_{W}, m_{Z} and m_{H}, the masses of the top quark, the W, Z and Higgs bosons, respectively. When the SM of particle physics is valid up to the Planck scale, the Higgs boson mass has to be kept constant, which leads to corrections to the Higgs boson mass that are orders of magnitudes larger than the observed mass. This issue is called the *hierarchy problem*. Only when individual contributions to the loop corrections are fine-tuned and cancel out each other is the Higgs boson mass independent of the energy scale. This fine-tuning is required to be of at least 15 orders of magnitude, but this is considered to be unnatural.

Another unexplained fact is the imbalance between matter and anti-matter in our universe. In the Big Bang cosmology, both particle types existed equally often in the early universe, while the universe mainly consists of matter particles today.

Although observations of galaxy velocities or precise measurements of the cosmic microwave background have shown that dark matter exists, no particle can provide the necessary matter density in the SM of particle physics.

No massive particles are allowed in the SM of particle physics without the Higgs mechanism. Even though the Higgs mechanism solves the problem for most of the particles, the neutrinos remain massless in the current state of the theory. This is in contrast to measurements [22, 42], which show that neutrinos have a mass and that differences between the neutrino mass eigenvalues were detectable.

A rather new experimental evidence that the SM of particle physics is not complete was given by the $g-2$ experiment [43] in 2021[2]. The magnetic moment g of muons was measured with high precision. The SM of particle physics predicts g to be very close to two, where exact predictions are provided by theory. Measurements of electrons showed very good agreement with the predictions. However, the $g-2$ experiment measurement showed differences for muons, and recent results increased the difference between theoretical prediction and experimental result to 4.2 standard deviations [44].

The mentioned open questions are just a short overview, while much more exist, e.g., gravity was so far not possible to be described as a QFT, and therefore it is impossible to include it in the SM of particle physics. Therefore, several theories were developed

[2]The collaboration outstandingly improved the experimental and theoretical significance compared to previous results.

to extend the SM of particle physics and address one or more of these open questions. The benchmark model used for the search described in this thesis is one of these possible extensions and is explained in the following chapter.

4 Extending the Standard Model of Particle Physics

Various so-called BSM theories have been proposed to answer one or several open questions of the SM of particle physics. Many of them have in common that they predict new and not yet detected particles. Furthermore, some of these BSM theories predict LLPs that can travel a finite distance within the detector before they decay.
One of the major BSM theories is Supersymmetry (SUSY) [45,46], which connects fermions and bosons via a new symmetry. In that theory, each SM particle has a supersymmetric partner with the same properties but different spin. The supersymmetric partner of the top quark cancels out the quadratic corrections of the top quark to the Higgs boson mass and hence solves the hierarchy problem. Although the theory of SUSY has existed for a long time and searches have been performed at different collider experiments, no evidence for SUSY has yet been found. All these searches provided limits that exclude several regions of phase space.
Instead of searching for new particles that carry colour charge, different kinds of theories requiring new particles without colour charge come more and more into the focus of particle physicists. The Twin Higgs models [11–13] are examples of such theories and try to solve the hierarchy problem of the Higgs boson. The Twin Higgs models are in this thesis the analyses benchmarks, and are presented in the following section. Mainly References [11–13, 47, 48] are used, if not indicated differently.

4.1 Twin Higgs Models

The basic idea behind the Twin Higgs models is to introduce a new SU(4) gauge group with a discrete Z_2 symmetry between the SM and the new group. This new group contains mirror (or twin) partners of the SM particles, which are only charged under the new gauge group, but not under the SM gauge groups, often referred to as Neutral Naturalness. The

twin sector does not carry SM quantum numbers, which is also referred to as *dark* sector. The twin particles are expected to have masses up to a few hundred GeV.

A complex scalar field $\mathcal{H}$ with the potential V is introduced:

$$V = \lambda \left(|\mathcal{H}|^2 - f^2/2 \right)^2 , \tag{4.1}$$

with the vacuum expectation value $\langle \mathcal{H} \rangle = f/\sqrt{2}$ and f being the decay constant of the Higgs boson. The Higgs fields of the SM and the twin sector are invariant under the spontaneously broken global symmetry. The field $\mathcal{H}$ with its potential breaking SU(4)→SU(3), results in the prediction of seven pseudo Nambu-Goldstone bosons [48], where pseudo indicates that they are massive bosons. Six of them can be interpreted as the vector bosons of the SM and the twin gauge groups, and the remaining one is considered to be the Higgs boson. The theory would also explain why the mass of the Higgs boson is so small. The largest contribution to the correction to the Higgs boson mass originates from the top quark. The Z_2 symmetry protects the mass of the Higgs boson from these large correction contributions since the contributions of the top quark of the SM and of its twin partners cancel each other out.

The complex scalar field $\mathcal{H}$ is composed of the two doublets A and B, $\mathcal{H} = (A, B)$, where A is the doublet of the SM Higgs, while B represents the doublet of the twin version. A and B can be exchanged due to the Z_2 symmetry. The vacuum expectation values of the Higgs field $v_\mathrm{A}/\sqrt{2}$ and the twin field $v_\mathrm{B}/\sqrt{2}$ fulfil $f^2 = v_\mathrm{A}^2 + v_\mathrm{B}^2$. The mixing between the Higgs boson and both sectors can be characterised by defining:

$$v_\mathrm{A} := f \sin(v/f) = f \sin(\theta) \quad \text{and} \quad v_\mathrm{B} := f \cos(v/f) = f \cos(\theta), \tag{4.2}$$

with $v_\mathrm{A} = 246\,\mathrm{GeV}$. The Higgs boson is only an equal mixture of the SM and the twin sectors, when $\theta = \pi/4$ [47], which would reduce the coupling of the SM particles to the Higgs boson. This can not be correct since the SM Higgs boson has been observed experimentally, and the couplings have been measured precisely with no significant deviations observed so far. The Higgs boson is mixing more with the SM field when the discrete symmetry Z_2 is softly broken. This modest mixing makes the Higgs boson a perfect candidate to build portals to the twin sector. Furthermore, it introduces masses of the twin fermions m_{F_T}, which are connected to the SM fermion masses in the following a way:

$$m_{\mathrm{F_T}} = m_\mathrm{F} \cot(\theta) \approx m_\mathrm{F} \cdot f/v. \tag{4.3}$$

A similar correlation is also true for the gauge bosons of both sectors.
The twin top partner t_T gives the main contribution, within the twin sector, to the Higgs mass parameter:

$$\delta m_H^2 = \frac{3 y_{t_T} m_{t_T}^2}{4\pi^2} \ln\left(\frac{\Lambda}{m_{t_T}}\right), \tag{4.4}$$

with y_{t_T} and m_{t_T} the Yukawa coupling and mass of the twin top particle, respectively. A cancellation of the twin and the SM top contribution is only the case if the Yukawa couplings of both top quark particles have a similar strength. Λ is the cutoff scale of the model, which is valid up to a few TeV and the tuning is of the form:

$$\left|\frac{\delta m_H^2}{m_H^2}\right|^{-1} \sim \mathcal{O}\left(\frac{v^2}{f^2}\right). \tag{4.5}$$

The model solves the so-called little hierarchy problem, with valid ranges between the weak scale and a cutoff of at the multi-TeV region, where no significant fine-tuning is needed [12, 48].

Fraternal Twin Higgs Model

The baseline model explained above predicts a twin of each of the SM particles. In contrast, the Fraternal Twin Higgs [48] scenario has only twins of the third generation (top, bottom quark, tau lepton and neutrino). This model is similar to the Hidden Valley models [49, 50]. The twin particles of the third generation can decay to twin gluons[1], which can hadronise within the twin sector into so-called glueballs, which can travel a finite distance. There are 12 stable glueball states predicted, but more unstable ones are possible. Within the twin sector, a cascade of decays of massive, metastable and neutral[2] states can happen until the lightest and stable bound state is reached, leading to a travel distance of micrometres to kilometres (depending on the parameters of the theory). Only this lightest twin glueball 0^{++} can mix again with the SM Higgs boson, making a decay back to detectable light SM fields Y possible within the detector via an off-shell Higgs boson $0^{++} \to h^* \to YY$. The decay width of $0^{++} \to YY$ as the dominant decay is:

$$\Gamma_{0^{++}\to \mathrm{YY}} = \left(\frac{\hat{\alpha}_3 v f_0}{6\pi f^2 \left(m_H^2 - m_0^2\right)}\right)^2 \Gamma^{\mathrm{SM}}_{\mathrm{h}\to\mathrm{YY}}(m_0^2), \tag{4.6}$$

[1] Due to the absense of light mirror particles.
[2] Neutral under the SM gauge group, but there might be charge within the twin group.

with $\Gamma^{\mathrm{SM}}_{\mathrm{h}\to\mathrm{YY}}(m_0^2)$ the width of a SM like Higgs boson with the mass m_0, f_0 the 0^{++} decay constant and $4\pi\hat{\alpha_3}f_0 = 3.06m_0^3$ [48]. All other possible decays, such as the decay to twin leptons, are negligible. Expecting that the glueballs are much lighter than the Higgs boson, the following approximation of the decay width becomes possible:

$$\Gamma \sim 1.1 \times 10^{-17}\,\mathrm{GeV} \times \left(\frac{m_0}{10\,\mathrm{GeV}}\right)^7 \left(\frac{750\,\mathrm{GeV}}{f}\right)^4, \tag{4.7}$$

and the corresponding decay length of:

$$c\tau_0 \sim 18\,\mathrm{m} \times \left(\frac{10\,\mathrm{GeV}}{m_0}\right)^7 \left(\frac{f}{750\,\mathrm{GeV}}\right)^4. \tag{4.8}$$

The glueballs are expected to have masses between 10-60 GeV [47], while the higher the predicted glueball mass is, the prompter is the decay back to SM particles. In addition to the glueballs, a light enough twin bottom quark might mix with the SM Higgs boson and enhance the signal detectable at collider experiments.

4.1.1 Signal Properties

A simplified signal model of the Twin Higgs Model is used for this thesis, following Reference [51], where the Higgs boson decays into a pair of hidden scalars π_ν. These new scalars (also called LLPs in the following) are mixing with the Higgs boson, and the dominant decay to pairs of SM particles are bottom quark (85 %), tau leptons (8 %) and charm quarks (5 %) [51]. For searches at colliding experiments, benchmark masses and lifetimes of the LLP are suggested in Reference [10] to be: $m_{\pi_\nu} = [7, 15, 40, 55]\,\mathrm{GeV}$ and $c\tau_0$ between $5 \cdot 10^{-5}$ and 10 m.
The signal benchmark is $H \to \pi_\nu\pi_\nu \to b\bar{b}b\bar{b}$, and the VBF and ggF Higgs boson production modes are taken into account for the analyses in this thesis. The properties of the generator particles of the signal simulation are presented in the following, focussing on those LLP mass-lifetime combinations used in the analyses later on.
In Figure 4.1, the p_{T} of the Higgs boson is shown. The distributions are produced from the signal simulation samples and represent the distributions of the SM Higgs boson production modes, since only the Higgs boson decay is of exotic nature. As expected, a clear difference is visible between the p_{T} distributions of the VBF and the ggF Higgs production mode. The additional radiation in the ggF Higgs production mode is typically hard and leads to a Higgs boson with lower p_{T}, compared to the VBF production mode.

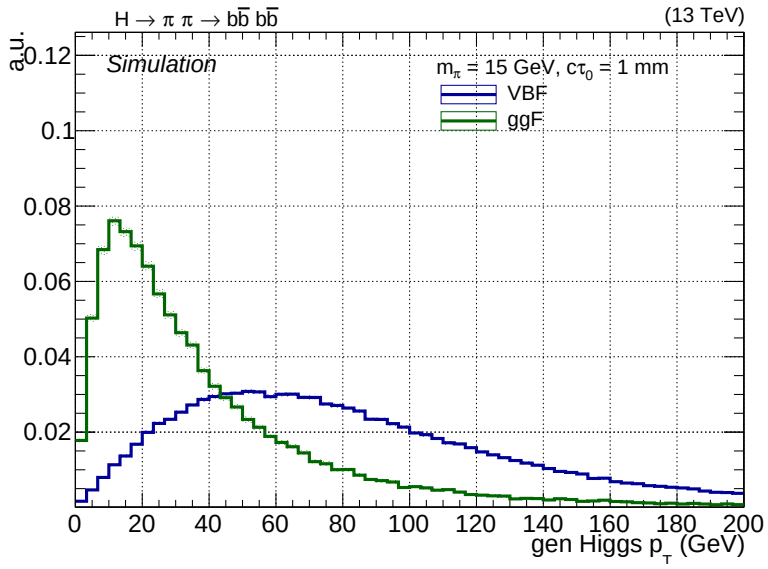

Figure 4.1: The p_{T} of the Higgs boson on generator level of the VBF (blue) and the ggF (green) production modes.

The p_{T} of the LLP for a lifetime of 1 mm and different masses is shown in Figure 4.2. Similar to the Higgs boson, the p_{T} distribution of the LLP is softer in the ggF Higgs boson production mode. A similar difference is visible for both production modes amongst the different masses, where, as expected, the higher the LLP mass is, the softer the p_{T} becomes. Furthermore, a difference between the leading and subleading LLP, sorted via p_{T}, is visible as expected, since p_{T} is not conserved in such a 2-body decay in a collider experiment.

The same comparison as for the LLPs was performed for their direct decay products, the generator b quarks, and the result is presented in Figure 4.3. The maximum and minimum p_{T} amongst the four b quarks is shown in the upper and lower row, respectively. Similar distributions are visible for the two production modes, while the distribution for the VBF Higgs production mode is wider. The b quarks with the minimum p_{T} are much softer. The LLP masses of 15 GeV and 40 GeV have similar distributions, while the mass of 55 GeV shows slightly shifted values. The low transversal momentum of the b quarks, might lead to missing reconstructed objects in the analysis and is discussed in Chapter 11.

The π_ν travel a finite distance within the detector. This 3D flight distance depends highly on the lifetime in the rest frame of the LLPs and their mass. The left plot of Figure 4.4 shows the dependency on the LLP lifetimes for the mass of 15 GeV. The probability that the decay happens with larger displacements rises with longer lifetimes, while shorter flight distances still have a certain probability. The dependency on the LLP mass is

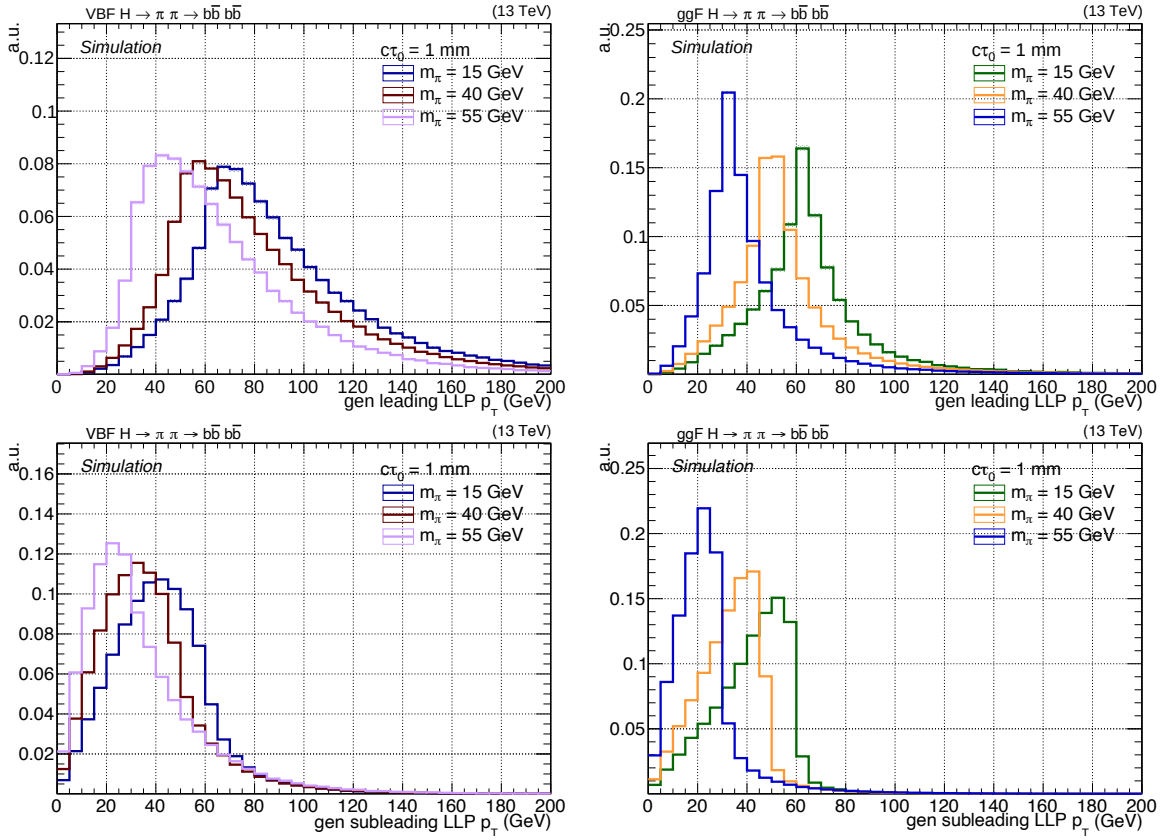

Figure 4.2: The p_{T} of the leading (upper) and subleading (lower) LLP on generator level of the VBF (left) and the ggF (right) Higgs boson production modes. Different masses of the LLP are compared for a lifetime of 1 mm.

visualised on the right plot of Figure 4.4, where the LLP lifetime of 1 mm was used. A clear trend is visible that with higher masses the decay happens closer to the interaction point of the collider experiment, which was mentioned earlier.

The the angular distance between two objects is often referred to as ΔR in particle physics and defined as:

$$\Delta \mathrm{R} = \sqrt{(\Delta\eta)^2 + (\Delta\phi)^2}, \text{ with } \Delta\eta = |\eta_1 - \eta_2| \text{ and } \Delta\phi = |\phi_1 - \phi_2|. \tag{4.9}$$

The ΔR distributions between different generator particles are essential for the kinematic understanding of the signal. Therefore, the ΔR between the two generator LLPs with 1 mm and the two Higgs boson production modes are shown in Figure 4.5. In the left plot, a clear dependency of the mass is visible for the VBF Higgs boson production mode. The lighter the LLPs are, the more back-to-back are the two particles, while higher masses,

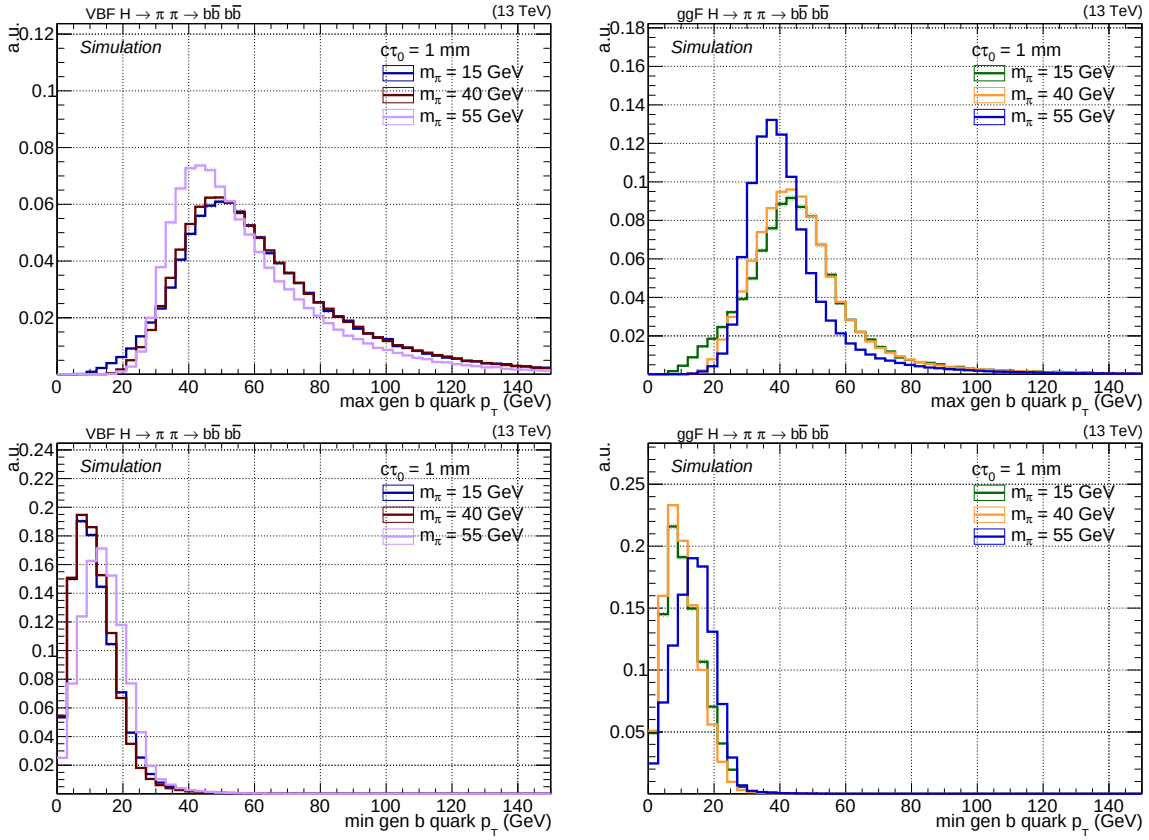

Figure 4.3: The p_{T} of the leading (upper) and fourth (lower) b quark on generator level of the VBF (left) and the ggF (right) Higgs boson production modes. Different masses of the LLP lifetime of 1 mm are compared.

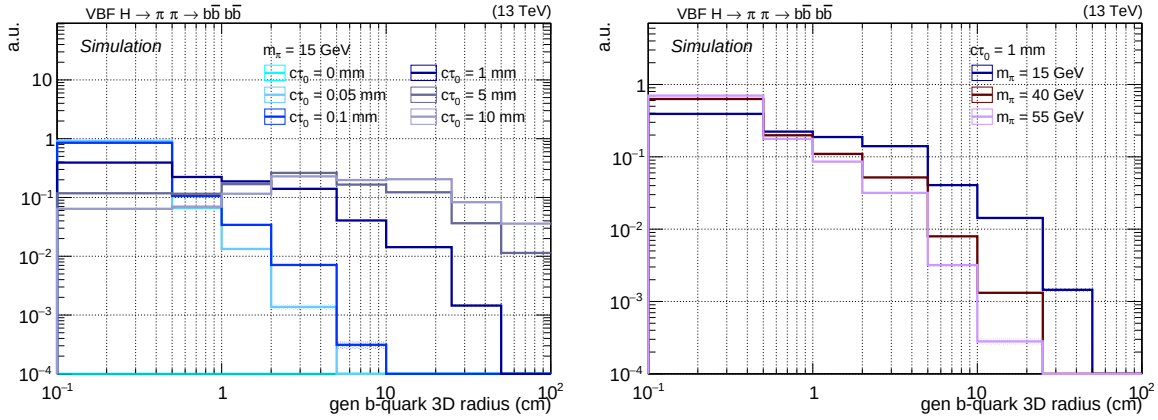

Figure 4.4: 3D flight distance of the LLP in the detector rest frame for different LLP lifetimes and a mass of 15 GeV (left) and for 1 mm lifetime and different masses (right).

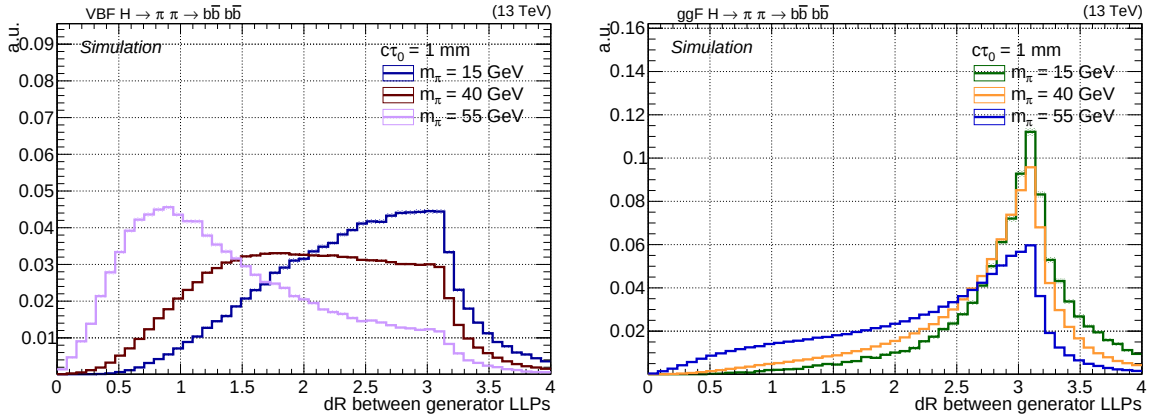

Figure 4.5: The ΔR between the two LLPs with 1 mm lifetime and different masses of the VBF (left) and the ggF (right) Higgs boson production modes.

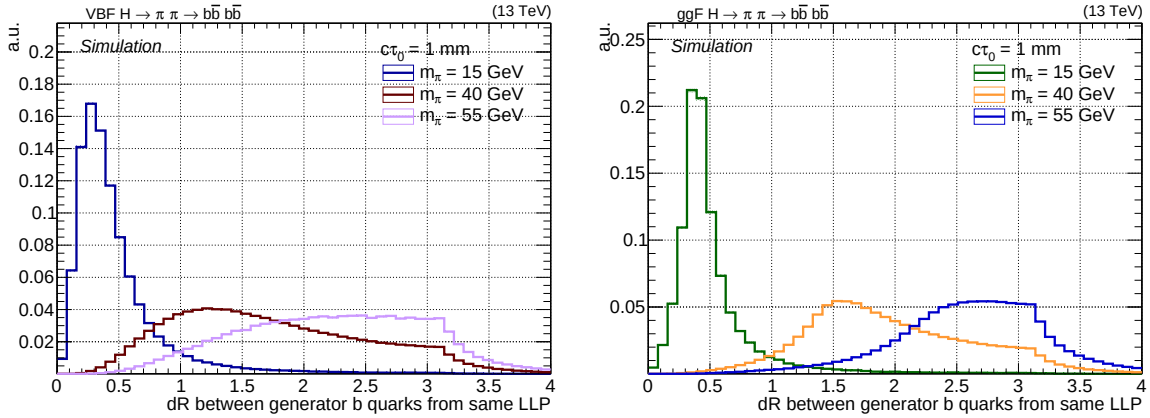

Figure 4.6: The ΔR between the two b quarks decaying from one LLPs with 1 mm lifetime and different masses of the VBF (left) and the ggF (right) Higgs boson production modes.

lead to a closer distance between the two LLPs. This is in contrast to the distributions of the ggF Higgs boson production mode, where for all three masses, the LLPs decay preferably back-to-back.

Three different ΔR between the four b quarks, being the direct decay products of the LLPs, are of interest. First, the ΔR between the two b quarks of one LLP is investigated and shown in Figure 4.6 for both Higgs boson production modes. The distributions are similar between both production modes but different for various LLP the masses. The lighter the LLPs are, the closer are the two b quarks, leading to a *boosted* topology, while for higher masses the b quarks are further apart and their jets can be reconstructed separately or *resolved*. Furthermore, the smallest distance between two b quarks of different

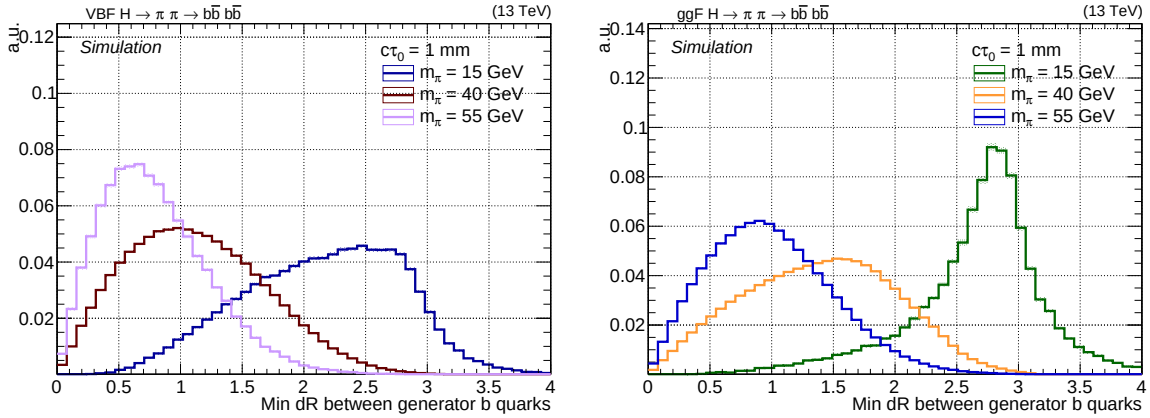

Figure 4.7: The minimum ΔR between two b quarks decaying from different LLPs with 1 mm lifetime and different masses of the VBF (left) and the ggF (right) Higgs boson production modes.

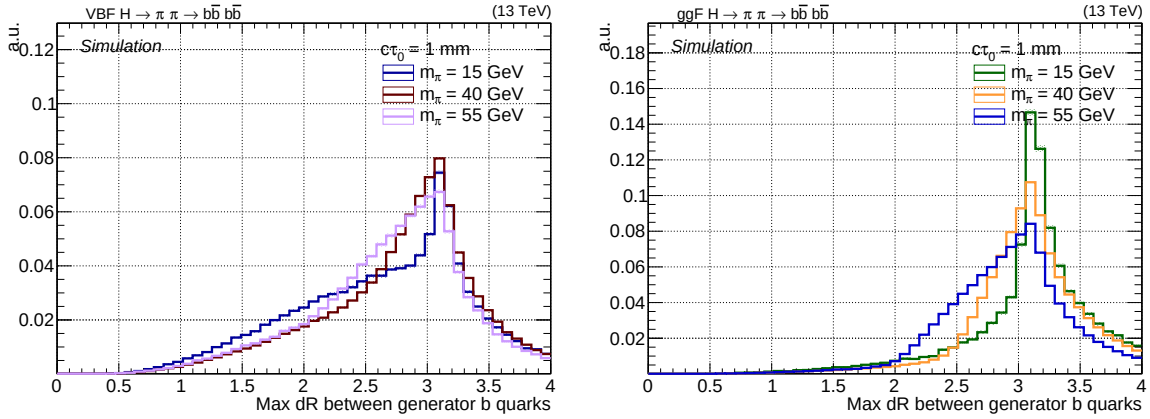

Figure 4.8: The maximum ΔR between two b quarks decaying from different LLPs with 1 mm lifetime and different masses of the VBF (left) and the ggF (right) Higgs boson production modes.

LLPs impacts the reconstructed objects used for the analyses in this thesis. Therefore, in Figures 4.7 and 4.8, the minimum and maximum ΔR amongst those two b quarks are shown, respectively. Again the distributions between the two production modes are similar. For light LLP masses, the ΔR between both LLPs are large, while their decay products are more boosted, and therefore, this results in a large ΔR between the two b quarks of different LLPs. As visible in the figure, the higher the masses, the smaller the ΔR. This is a direct result of the smaller ΔR values between the LLPs and the more separated b quarks of one LLP. These distributions are important since the hadronisation products of the closest b quarks for the 55 GeV mass can end up in one reconstructed

object and therefore impact the results in the analyses. The maximum ΔR is instead similar amongst all masses and shows that the two b quarks are mainly distributed in opposite directions.

4.2 Comparisons to Other Searches

A summary of different LLP analysis results by the CMS and ATLAS experiments is given in Reference [52]. Figure 4.9 provides an overview of the different analyses, showing the observed upper limits with 95 % CL on the cross section normalised to the SM Higgs boson cross section times the branching ratio of the SM Higgs boson decay to two LLPs, as a function of the LLP lifetime. The analyses search for different LLP lifetimes, different decays and investigate different Higgs boson production modes. The different decay modes of the LLP are comparable, since the branching ratios of the LLPs decays are set to BR($b\bar{b}$) $\approx$ 85 %, BR($c\bar{c}$) $\approx$ 5 % and BR($\tau\bar{\tau}$) $\approx$ 8 %, respectively. As visible, for shorter lifetimes, the observed limits become less stringent. Of interest for this thesis is the region

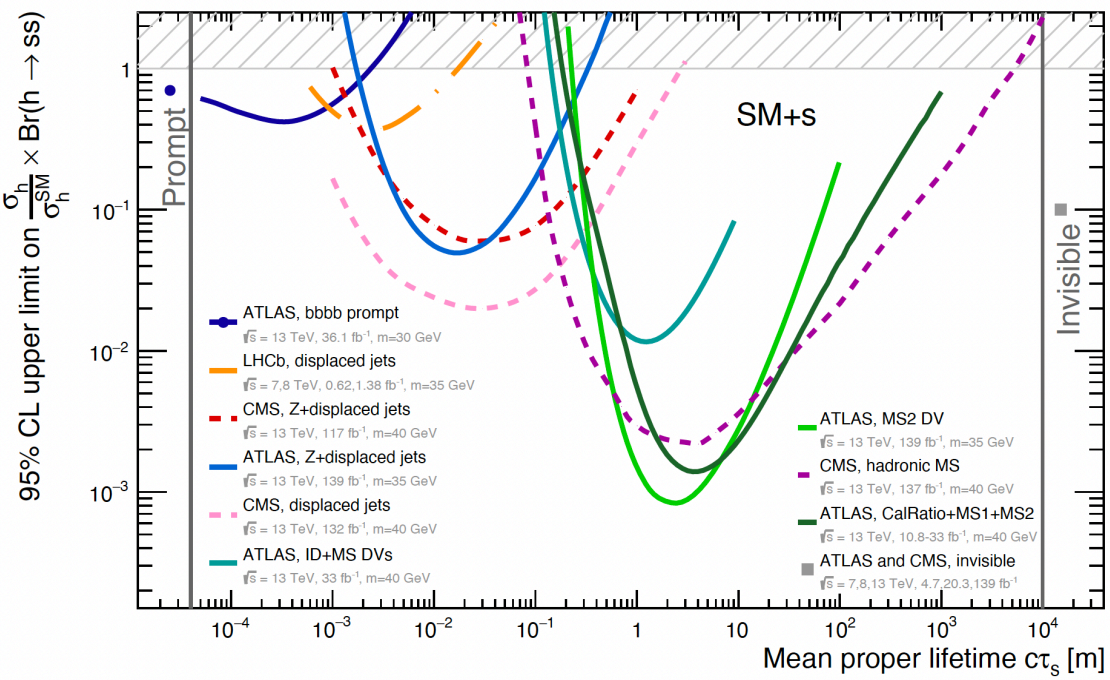

Figure 4.9: Comparison of the results of different searches for new long-lived, neutral scalar particles with hadronic final state. Shown are the observed upper limits with 95 % CL on the cross section times branching ratio normalised to the SM Higgs boson cross section. Taken from Reference [52].

up to 10 mm, which was mainly investigated by one search by the ATLAS experiment (solid blue line) with data recorded in 2015 and 2016 [14]. This search uses the Higgs boson production mode of the associated vector boson fusion and LLP decays to four b quarks. The additional lepton produced by the vector boson decays is used to select events of interest, leading to a clear signal signature and a different SM background composition than of the presented analysis. LLP masses between 20 GeV and 60 GeV are investigated and the lifetime of the LLPs is taken to be very short leading to prompt decays. The results are reinterpreted to cover decay lengths of up to 10 mm. Other searches, such as the displaced jets search of the CMS experiment (dashed rose-coloured line), set limits down to 1 mm with the data collected in 2016 and 2018. This CMS search investigates the ggF Higgs production mode, LLP masses between 15 GeV and 55 GeV and decays to four b or d quarks.

5 Physics of Proton-Proton Collisions

The open questions discussed in Chapter 3 indicate that the SM of particle physics is incomplete. Therefore, precision measurements of SM particles and searches for unknown particles or processes are performed. Several different particle colliders were used in the past, colliding hadrons, leptons or mixtures of both, probing the SM with high precision. Currently, the most powerful circular hadron accelerator and collider, the LHC, is located at the European Organization for Nuclear Research (CERN) in Switzerland. The measurements and searches based on the pp collision data, including the search presented in this thesis, are dependent on the understanding of basic concepts, such as the inner structure of the protons, theory models, for example, the cross section calculations, and the event simulation to which the recorded data are compared. All of them will be briefly explained in the following.

5.1 Proton Structure

Protons are not elementary particles since they have an inner structure and consist of quarks and gluons, the so-called partons. Hence, if inelastic scattering happens in pp collisions, the partons interact with each other. Therefore, the inner structure of the proton is essential to understand pp collisions.

The proton is a bound state of two u quarks and one d quark, and is therefore classified as a hadron. These so-called *valence* quarks interact with each other via the strong force. These interactions are mediated by gluons, which also interact with each other. In addition to the valence quarks and the gluons, also *sea* quarks can be probed within the protons. These quark-antiquark pairs are created and annihilated spontaneously by vacuum fluctuations. The proton structure was probed by deep inelastic scattering of electrons with protons, for example, at the DESY Hadron-Electron Ring Accelerator (HERA) [53]. The transferred momentum q^2 in such a process can be treated as a measure of the resolution of the inner structure of the proton measurement.

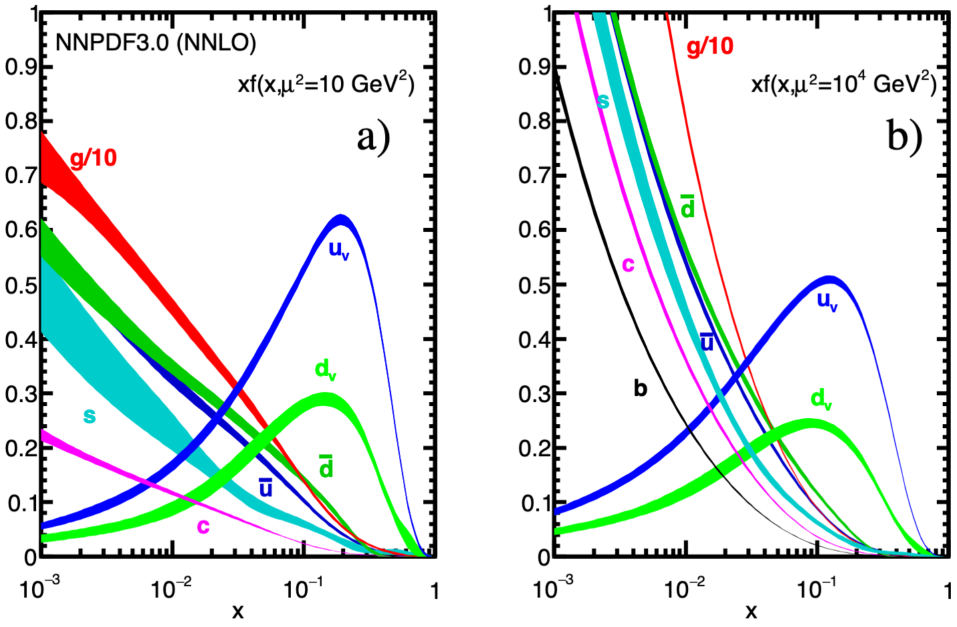

Figure 5.1: The example PDFs at next-to-next-to-leading order (NNLO) for momentum transfers of $q^2 = 10\,\mathrm{GeV}^2$ (left) and $q^2 = 10^4\,\mathrm{GeV}^2$ (right). Taken from Reference [55].

The momentum of the proton is divided among its partons. The variable 'Bjorken'-x describes the fraction of the momentum a specific parton carries. This means that the actual centre-of-mass energy $\sqrt{\hat{s}}$ of two partons depends on the centre-of-mass energy of the pp collision $\sqrt{s}$ and the two momentum fractions x_1 and x_2 of the partons:

$$\sqrt{\hat{s}} = \sqrt{x_1 x_2 s}. \tag{5.1}$$

Each parton has distinct parton distribution functions (PDFs) that describes the probabilities to find a parton of a specific type with a value x for a given momentum transfer q. Different measurements from HERA and LHC experiments are combined to derive the PDFs, depending on x and q^2 and provided, for example, by the NNPDF Collaboration [54]. Figure 5.1 presents two examples of PDFs for momentum transfers of $q^2 = 10\,\mathrm{GeV}^2$ (left) and $q^2 = 10^4\,\mathrm{GeV}^2$ (right). The results indicate that the interactions are dominated by valence quarks for high x values and by sea quarks and gluons, for low x values.

The two interacting partons most likely carry a different momentum fraction, which results in a Lorentz-boost along the beam direction by an unknown amount. The coordinate system of colliding experiments are chosen in such a way that the particles are accelerated along the z-axis. This means the z component of the energy and the momentum is un-

known for the interaction processes. Transverse components, on the other hand, are very close to zero (see also definition of the coordinate system used by CMS in Section 7.2.1). The transverse momentum $p_{\mathrm{T}} = \sqrt{p_{\mathrm{x}}^2 + p_{\mathrm{y}}^2}$ of the pp collision is negligibly small, and due to momentum conservation, the sum of all transverse momenta from the final state objects needs to be close to zero again. Transverse variables are widely used for pp collisions, for example, to calculate missing transverse momentum, as explained in Section 8.8.

5.2 Cross section of Proton Collisions

The total cross section of pp collisions σ_{pp} can be derived with different approaches. One of them is the factorisation approach [56, 57], which uses a convolution of the PDFs f_i and f_j and the cross section of the parton interaction $\hat{\sigma}_{ij}$, where i and j are the parton flavours of the initial state. The integration over the momentum fractions x_1 and x_2 as well as summing over all possible initial state parton flavours completes the calculation of the total cross section:

$$\sigma_{\mathrm{pp}} = \sum_{i,j} \int \int dx_1 dx_2 f_i(x_1, q^2) f_j(x_2, q^2) \hat{\sigma}_{ij}(x_1, x_2, q^2). \tag{5.2}$$

Similarly, the cross section for each possible decay process of the hard scattering process can be derived. Such theoretically calculated predictions can be probed with collision data, as it is done by the CMS experiment at the LHC. The results of some of the tested processes can be found in Figure 5.2. These measurements of the cross section are another way of verifying the SM of particle physics. Measurements confirm theoretical predictions that span several orders of magnitude and different final states.

5.3 Event Simulation

Data recorded with particle collision experiments are typically compared to theoretical predictions. Therefore, Monte-Carlo (MC) event generators are used to generate simulated events, following the SM or BSM predictions. The MC generators randomly sample from different distribution sources and mimic the actual recorded data. Software programs are used for all different simulation steps from pp collision to the interactions of the decay products with detector material and the electronic readout of the detector signals. This is briefly discussed in the following.

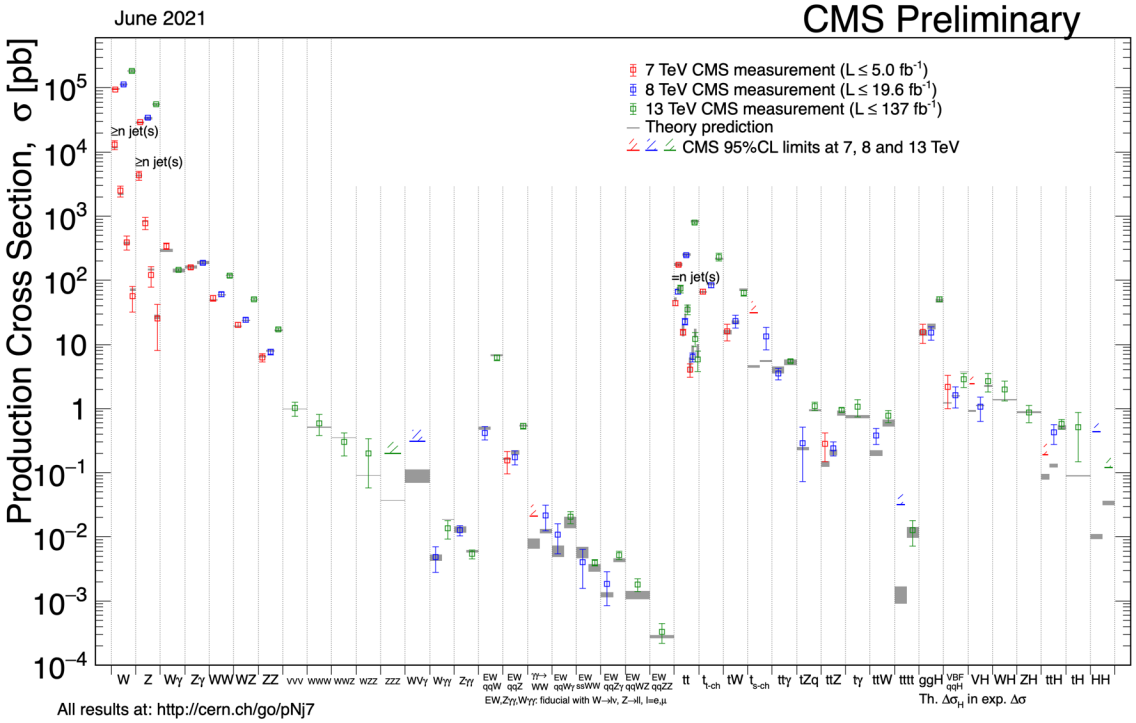

Figure 5.2: Summary plot of theoretical prediction and measurements of cross sections for different SM processes. Taken from Reference [58].

The initial hard pp scattering process is simulated by randomly sampling the PDFs of Equation 5.2, choosing the parton flavours and using the partonic interaction cross section. Depending on the produced process, different event generators and precision settings can be used. For all samples used in this thesis, the initial hard pp scattering process is simulated using POWHEG [59], PYTHIA8 [60], MADGRAPH [61] or MADGRAPH5_aMC@NLO [62].

The showering process of the particles into the final states is performed after the simulation of the scattering process, in this thesis with PYTHIA8. The MLM algorithm [61] is used for some of the simulated samples to match parton showers and final state particles.

Additional processes happening in pp collisions are taken into account. One of these processes is the additional parton interactions of the proton collision, which is called underlying events (UE). The UE are measured in data and settings are 'tuned' in simulations to match the behaviour of the data. Another of these processes is the so-called pileup (PU), which describes the fact that more than one pair of protons can interact at the same time. Both processes can be simulated using PYTHIA8.

As the last step, the interactions of the resulting particles with the detector materials

is simulated using the GEANT4 toolkit [63]. This toolkit includes a model of the CMS detector consisting of the used materials and their positions. In addition, a simulation of the readout electronics is performed. In the end, the simulated events can be analysed in the same way as events recorded in real pp collisions.

6 Machine Learning for High-Energy Physics

Research in the field of machine learning (ML) began already several decades ago. However, its widespread implementation to problems in science or applications in industry to everyday life products significantly increased over the last years. This was required by the increase in big data issues and enabled due to the increases in readily available computing power and reductions in associated costs, mainly driven by improvements in algorithms and advances in highly parallel computing, such as graphics processing units (GPUs).
The basic idea behind ML is to train or optimise an algorithm with data to learn a distinct function in that process. Well-trained algorithms can even solve complex problems where traditional statistical methods might fail or need too much time. In principle, the method is used to construct a complicated, non-linear function whose parameters are *learned* by minimising a loss function over a set of data.
In high-energy physics (HEP), simple ML classifiers based on boosted decision trees or simple neural networks (NNs) have been in use for several years. The ML algorithms are, for example, used to identify objects originated by W, Z or H bosons or to identify *top* quark [64] decays. Furthermore, the identification of jets originated by b quark decays is of enormous interest and several tagging algorithms have been developed and used in CMS [65]. Improvements to these algorithms have made it possible to identify not only jets originating from b, but also from c quark decays [66] and discriminate both from light quark jets. ML algorithms helped, for example, to observe the Higgs boson decay to b quarks [32]. In almost every recent published CMS analysis, one or more ML algorithm were used.
In ML, the word data is used differently than in HEP. While a clear difference between simulated and recorded data is always made in the latter one, the distinction is less strict in ML. Therefore, in this chapter, the term data describes either simulated or recorded data or both, and if needed, a distinction is made.
This chapter gives a basic overview of the terminology and ML algorithms focussing

on those used or mentioned in this thesis. References [67, 68] provide more detailed summaries, which are also used as a basis of this chapter, if not indicated differently.

6.1 Terminology

In HEP, labelled simulated events exist for a wide range of processes, from SM events to the production and decays of new particles. ML algorithms can be trained using these labelled data, in a process called supervised learning, which is widely used for HEP tasks. In contrast, unsupervised learning uses unlabelled data for training, which can be used, for example, to observe anomalies in the recorded data with generative models [69]. The ML algorithms in the thesis use supervised learning methods; hence only this approach is described.

Different ML approaches can be applied depending on the problem to be solved. In this thesis, ML is used to classify, i.e. separate data into categories of *signal* and *background*. This approach is also used, for example, in b tagging algorithms [65, 66]. Other ML approaches do exist, such as the regression approach that can be used to predict a continuous number.

A simple NN architecture has several layers of connected neurons, as shown in Figure 6.1. The layers are separated into the input and output layers, the first and the last layers of the architecture, respectively, and the hidden layers in-between these two. The network is called *deep* when the NN has several hidden layers. Fully connected networks specify that all neurons of one layer are connected to all neurons of the following layer. The strength of the connections is set by a weight w corresponding to their importance, which is adjusted during the network's training. The sum of the weighted inputs x within each neuron produces the output value o which is used as input for the next layer:

$$o = \phi(\Sigma_{i=1}^{N} x_i \cdot w_i + b), \tag{6.1}$$

where b is an added bias. The activation function ϕ introduces a non-linearity to the neurons and therefore directly impacts the output value. Different activation functions are available, and the two activation functions used for this thesis are the rectified linear unit:

$$\mathrm{ReLU}(x) = \max(0, x), \tag{6.2}$$

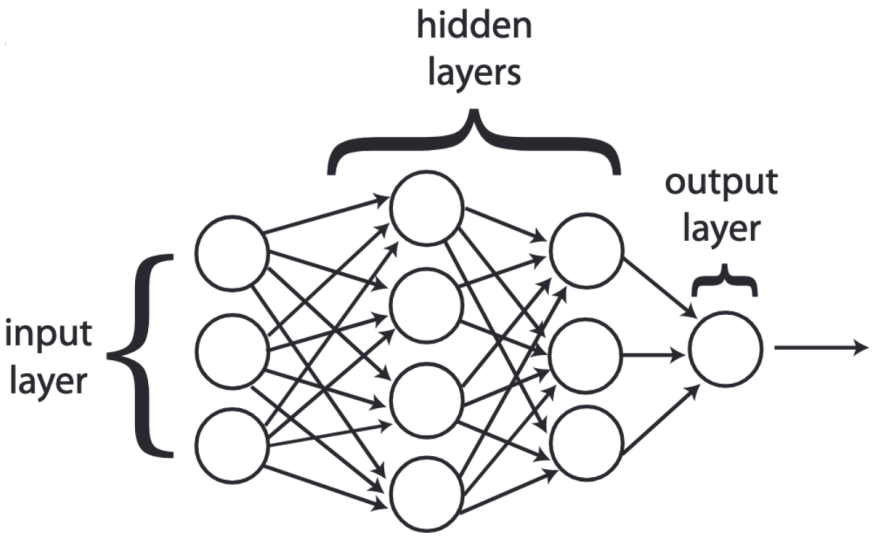

Figure 6.1: Basic architecture of a NN model. With one input layer, two hidden and one output layer. Taken from Reference [68].

which is used for the hidden layers and softmax:

$$\text{softmax}(x_i) = \frac{e^{x_i}}{\Sigma_j e^{x_j}}, \tag{6.3}$$

with j classes of the of the classification problem, used for the output layer.
In addition to the architecture and the activation function, several essential ingredients are needed to set up a ML algorithm.
First of all, the model can be described by a function $f(x, w)$, with $f : x \to y$, that predicts an output y based on the input values x and the weights w. The weights are initialised by randomly chosen values, depending on the type of initialiser. During the training, the weights are adjusted using the data. The model itself depends on the architecture, e.g. if the neurons are fully connected or how many hidden layers are present.
Another important part of NN is the dataset $D(X, y)$ used for training. X indicates a vector or a matrix of variables, called input features, while y is the truth label per entry. The network shall predict the truth label, which is for example a boolean if the entry is signal or not, and this prediction is optimised during the training. It is important to use two independent datasets for training and for the analysis, because otherwise a bias could be introduced, worsening the results of the analysis. For example, the network could learn specific features of some true signal entries, which are again identified in the analysis only because these entries have been used for both cases. The dataset used for the training

is, for example, split in 80:20, where the larger part is used for training. The remaining entries are used for the evaluation of the performance of the network, respectively. The training dataset can further split into so-called batches, where a certain number of entries of the dataset are used to perform a training run and after each batch the weight is updated. In general, training is performed in batches because of two reasons. When the whole dataset is used at once for the training and the minimisation is computed after each entry, it will become extremely computationally expensive. In addition, the batches of the dataset can introduce statistical fluctuation, which can help the model to get out of local minima, since instead the global minima should be found.

Especially, when there are few entries in the training dataset, so-called overfitting can occur. Here the model confuses small, statistical fluctuations in the training dataset for important patterns. While such overfitting effects tend to be less serious for smaller, simpler models, complex models with a large number of trainable parameters are able to optimise the model by taking sufficiently large number of different patterns into account. Therefore, the statistical fluctuations of the training dataset can be falsely identified as relevant patterns and lead to a drop in the performance, when the fluctuations are not identical in different datasets. The impact of overfitting can be minimised by larger training datasets, simpler models or early stopping. The latter one describes an approach that monitors the performance of the model during validation and stops the training once the performance decreases. In addition, the dropout technique [70] can help preventing overfitting and in addition improves the NN performance. The dropout technique switches off a random set of hidden nodes during the different batches while training. Therefore, the training is performed with different combinations of hidden nodes.

The model is optimised by minimising the so-called loss function $\mathcal{L}(f(x, w), y)$ that evaluates the model's performance during the training. The model is optimised by minimising the loss function with the training dataset. The loss function needs to be selected according to the underlying problem. For example to compare predictions to the true value y in a classification problem, one can use the binary cross entropy:

$$\mathcal{L} = -\frac{1}{N}\Sigma_x(y_x \ln(o_x^L)) + (1 - y_x)\ln(1 - o_x^L), \tag{6.4}$$

where N is the number of entries x in the dataset, y_x is the true value of an entry and o_x^L is the output of the final layer of the NN with the input of an entry.

The last missing piece is the optimiser that optimises the weights within the minimisation process of the loss function. This is achieved via gradient descent, an iterative process, that

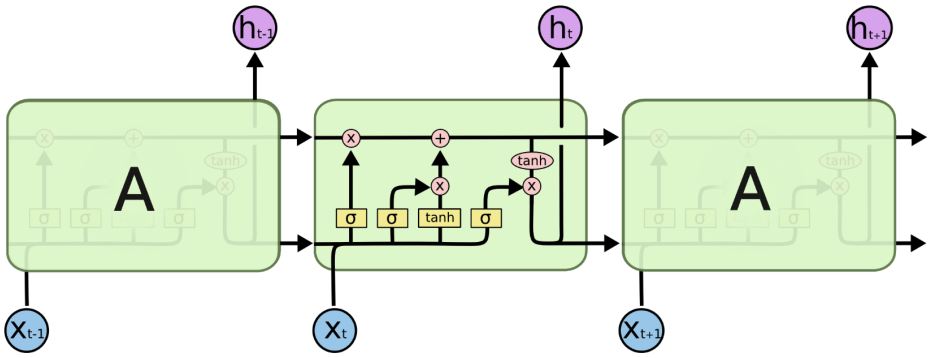

Figure 6.2: Basic example of three LSTM cells with their internal structure. Blue circles are the inputs, purple circles the outputs, yellow boxes indicate NN layers, rose-coloured circles the point wise operation. Taken from Reference [72].

calculates the gradients of the loss functions with regards to every network weight (and bias) and then adjusts the weights to minimise the loss function. These weight updates are performed after every batch. The model converges when a minimum is reached. The learning rate indicates how large the weight adjustments can be, and a balance between finding the global minima and computing intensity needs to be found. The optimiser called ADAM [71] is used in this thesis and is initialised with a learning rate, which is internally changed over the different iteration steps.

Beside the so far explained fully connected networks (FCNs), a specific type of the recurrent neural network (RNN), called a LSTM network [73] is used in this thesis. Instead of using several layers where neurons give their output to the next layer, as in the FCN, RNN reuses basically the same network in loops, and information of the previous step are handed over to the following step. In order to not run into long-term memory problems[1], the LSTM networks have a different setup of the internal network and instead of neurons consist of cells, also called cell states, as visualised in Figure 6.2. These cells are identical copies of each other and the information of the previous cell is used as input to the next one. Each cell has three so-called gates: a forget gate, an input gate, and an output gate. The forget gate decides how much of the information from the previous cells is used (left-hand sigmoid layer), where a value between zero and one define that none or all of the information are let through the cell. The input gate carries information from the previous iteration (second and third layers from left) and updates the information within the actual cell state. This twofold step consists of a sigmoid layer that selects the input

[1]RNN have the advantage, that the information of previous steps are only available, if there are not too many steps in between.

values which will be updated and the tanh layer that produces new candidate values of the cell, and both parts are combined to update the cell state. Finally, the output gate decides how much information leaves the current loop (right sigmoid layer). In that way, information of previous steps are available over a longer timescale ($\mathcal{O}(1000)$ loops).

6.2 Receiver Operating Characteristic

The performance of a NN can be summarised with the area under the curve (AUC) of the ROC curves. The ROC curves presented in this thesis are defined as the background efficiency as a function of the signal efficiency, where the efficiency is defined as the number of objects above a certain threshold, divided by the number of all objects. Only objects matched by $\Delta R < 0.4$ to generator particles are used as true labelled ones for the signal, since only these objects are truly originate from the signal. A basic example is given in Figure 6.3. The performance of two example models is shown and can be compared to the diagonal (dashed orange curve), representing a classifier which is not capable of distinguishing signal and background, such as deciding on random guessing. The NN output, which can be interpreted as a probability of how likely the investigated object is a signal object, is a value between zero and one. The ROC curve is reconstructed by

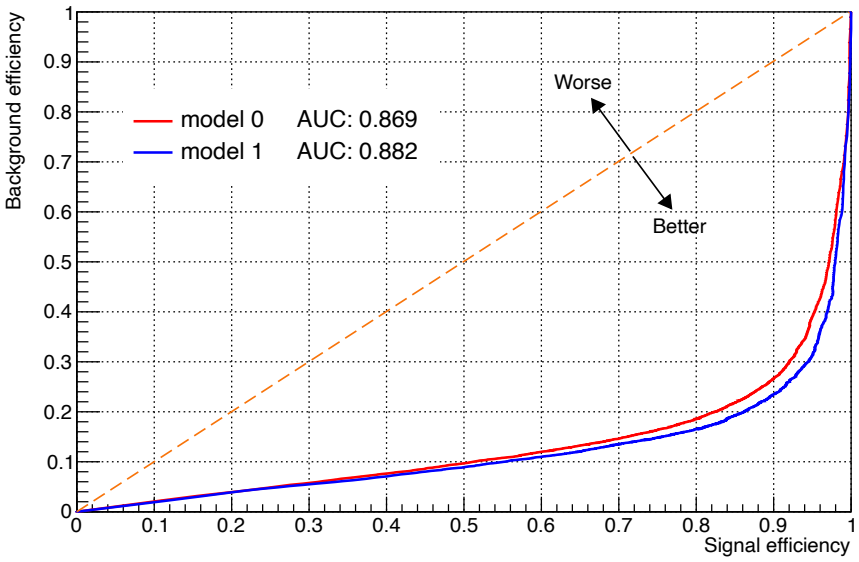

Figure 6.3: Basic example of ROC curves, with background over signal efficiency of two different models (red and blue lines).

scanning over different thresholds of the NN output and calculating the efficiencies of signal and background separately. The AUC is, in this case, one minus the integral of the ROC curve. The diagonal has an AUC score of 0.5. The best performance is reached with high signal efficiency while the background efficiency is as low as possible, leading to an AUC score close to one. Hence, model 1 of Figure 6.3 is performing slightly better, than model 0.

6.3 Software Settings

The software used for the ML algorithms used in this thesis is written in Python with the Keras API [74] and the Tensorflow [75] backend.
The procedure used for the specified supervised ML algorithms in this thesis involves several steps:

1. The set of simulated events is split into those used for training and for the analysis.
2. The training set is further split, and 80 % of it is used for training, while the remaining 20 % are used to evaluate of the architecture.
3. During the final analysis steps, the trained architecture is used to classify the previously set aside simulated events, as well as the recorded data events.

Section 9.5 summarises the information on the different ML settings, the DNN architecture and additional details.

Part II

From the Collider to the Particle Identification

7 Experimental Setup

The data analysed in this thesis come from pp collisions at the LHC [4], recorded with the CMS [6] experiment. The data taking period 2016 is used, where the LHC was operated at centre-of-mass energy of 13 TeV. In the following, first, the LHC is introduced and afterwards, the CMS detector with all its sub-components is described in more detail.

7.1 The Large Hadron Collider

The LHC is the most powerful circular hadron accelerator and collider to date. The 26.7 km circumference ring is located at the CERN close to Geneva and designed to operate and collide protons at a centre-of-mass energy of up to 14 TeV with an instantaneous luminosity of $10^{34}\,\mathrm{s}^{-1}\mathrm{cm}^{-2}$. Furthermore, it is possible to operate the LHC with heavy ions. However, heavy ion physics is not part of this thesis and therefore neglected in the following. The LHC started its operation in 2011 with a centre-of-mass energy of 7 TeV and 8 TeV ('Run1'). After a shutdown where several upgrades were implemented, the centre-of-mass energy was increased to 13 TeV and physics at this energy was pursued between 2015 and 2018 ('Run2'). This time period accumulates to a total integrated luminosity of about $145\,\mathrm{fb}^{-1}$. A currently ongoing shutdown is again used for upgrades of both the accelerator and all experiments and a re-start of the LHC is planned in 2022 ('Run3') with the goal to reach the design centre-of-mass energy of 14 TeV. Beyond this run there are significant upgrades planned to build the High-Luminosity LHC [76].
Protons are extracted from hydrogen molecules by ionisation and pre-accelerated by several linear and circular colliders up to 450 GeV. The protons are separated in bunches and injected into the two opposing pipes of the LHC. The twin-bore magnet design makes it possible to use the magnetic field of one magnet for both beam directions. Depending on the year of operation the proton bunches are accelerated up to an energy of 6.5 TeV each, which results in the centre-of-mass energy of 13 TeV. Along the LHC ring four interaction points are defined, where proton bunches collide every 25 ns, resulting in a 40 MHz event rate. At those interaction points four experiments, also called detectors, are placed to

record the results of the pp collisions. ATLAS [5] and CMS as multi-purpose detectors investigate physics processes and observe possible new physics in proton or heavy ion collisions. Large Hadron Collider beauty (LHCb) [77] with a lower event rate than ATLAS and CMS, is designed to mainly study B hadrons and understand CP violation better. A Large Ion Collider Experiment (ALICE) [78] is specialised for heavy ion collision, with the aim to investigate quark-gluon plasma and therefore the time fraction after the Big Bang, before hadrons and heavier particles got formed.
The designed instantaneous luminosity $\mathcal{L}$ of the LHC was reached in 2018 and can be described with the equation:

$$\mathcal{L} = N_b f_r \frac{n_1 n_2}{4\pi\sigma_x\sigma_y}, \tag{7.1}$$

where the number of proton bunches is N_b, f_r is the revolution frequency, n_1 and n_2 are the numbers of protons per bunch and a Gaussian distribution is used to describe the beam with σ_x and σ_y the spatial width in x- and y- directions. The cross section area of the beam $4\pi\sigma_x\sigma_y$ is frequently measured by so-called Van der Meer scans. Adjusting this parameter of the beam helped to achieve the design luminosity. The high instantaneous luminosity, as well as the high centre-of-mass energy, are used to increase the probability for the production of heavy particles and rare processes. The expected number of a certain event N of interest, within a given time unit, can be calculated by

$$\mathrm{N} = \sigma \int \mathcal{L}\mathrm{dt} \tag{7.2}$$

where σ is the cross section of this specific process.

7.2 The Compact Muon Solenoid

The CMS detector is built in a cylindrical shape around the interaction point, to detect particles moving outwards in all directions. The central cylindrical part of the detector is called 'barrel', while the 'endcaps' or 'forward region' refer to the two symmetric lateral parts. The CMS detector consists of several subdetectors that all measure different quantities of particles as muons, electrons, photons as well as neutral and charged hadrons, pass through the detector. A schematic view can be found in Figure 7.1. The closest part to the interaction point is the tracking system, that measures the trajectory of charged particles. Two different types of calorimeters are located next to the tracking system and absorb electromagnetically and hadronically interacting particles, respectively. As the

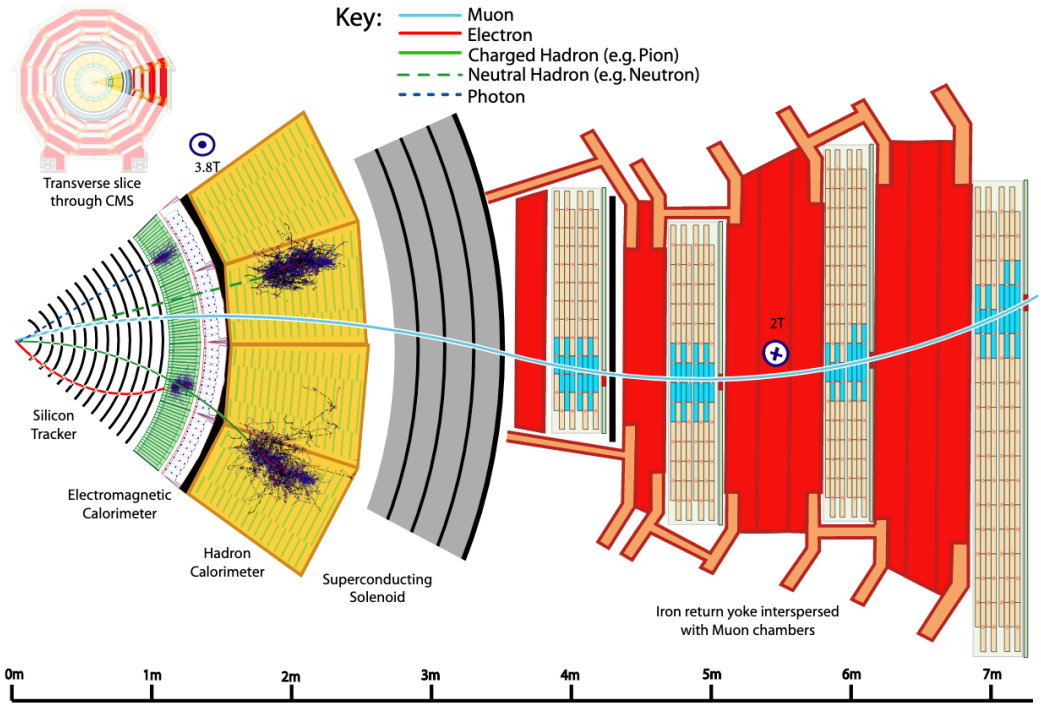

Figure 7.1: Schematic view of the CMS detector and the specific particle signatures. Taken from Ref. [79].

name implies, the CMS detector contains a strong superconducting solenoid providing a magnetic field of 3.8 T which bends particles depending on the electrical charge and the momentum. Therefore, it is possible to determine the sign of the electrical charge and the momentum of charged particles. Muons interact only weakly with the detector material and can not be absorbed. Therefore, the outermost part of the detector is the muon system, where the trajectories of the muons are measured. All this individual information is combined by an algorithm called Particle-Flow (PF) [79], described in more detail in Section 8.2, used to reconstruct the particles. In the following, each sub-detector part is described separately, and mainly reference [6] was used, if not indicated differently.

7.2.1 Coordinate System

Two coordinate systems are set and used for the CMS detector. A Cartesian coordinate system is defined relative to the LHC ring, where the x-axis points radially to the centre, the y-axis points vertically upwards and the z-axis points in the counter-clockwise accelerator direction. Due to the design of the CMS detector, it is in addition useful to use

spherical coordinates. The radial distance r is measured from the interaction point in the centre of the detector. The azimuthal angle ϕ is defined in the (x,y)-plane and the polar angle θ describes the angle between the (x,y)-plane and the z-axis.

In addition, some variables are widely used in particle physics experiments. Those are the pseudorapidity η

$$\eta = -\ln\left(\tan\left(\frac{\theta}{2}\right)\right) \tag{7.3}$$

and the angular distance between two objects ΔR

$$\Delta\mathrm{R} = \sqrt{(\Delta\eta)^2 + (\Delta\phi)^2}, \text{ with } \Delta\eta = |\eta_1 - \eta_2| \text{ and } \Delta\phi = |\phi_1 - \phi_2| \tag{7.4}$$

where both variables are invariant under Lorentz boosts along the z-axis. Furthermore, the transverse component of several quantities are used, which means that only x- and y-components are used for the calculation, while the z-component is neglected.

7.2.2 Tracking System

The innermost part of the detector is the tracking system with a length of 5.6 m and a diameter of 2.6 m. It consists of the segmented silicon sensors of the pixel detector and the silicon strip sensors. Both parts measure the trajectories of charged particles with high precision. Already around 65 % of the energy of hadronic decays can be reconstructed with the tracking system alone [79]. Especially the pixel detector has to resist radiation damage coming from particles passing through its material, which is closest to the interaction point. A reduced hit efficiency of the sensors is induced by too much radiation damage. Therefore, end of 2016 the pixel detector formerly consisting of three layers of pixel modules in the barrel region and two disks in each endcap region covering up to $|\eta| < 2.5$, was replaced by a complete new pixel detector, as indicated in Figure 7.2. It consists of four pixel module layers in the barrel part and three disks each in the endcap region, now covering a region up to $|\eta| < 2.7$ [80]. The innermost layer is now as well closer to the beam pipe. The silicon strip detector surrounds the pixel detector and consists of 10 layers of strip modules in the barrel part complemented by 12 layers in each endcap. Hit position resolutions of charged particles in the barrel part are approximately 10 μm for the pixel sensors and approximately 13-38 μm for the strip detectors and slightly worse in the endcap regions for both parts of the tracking system [81].

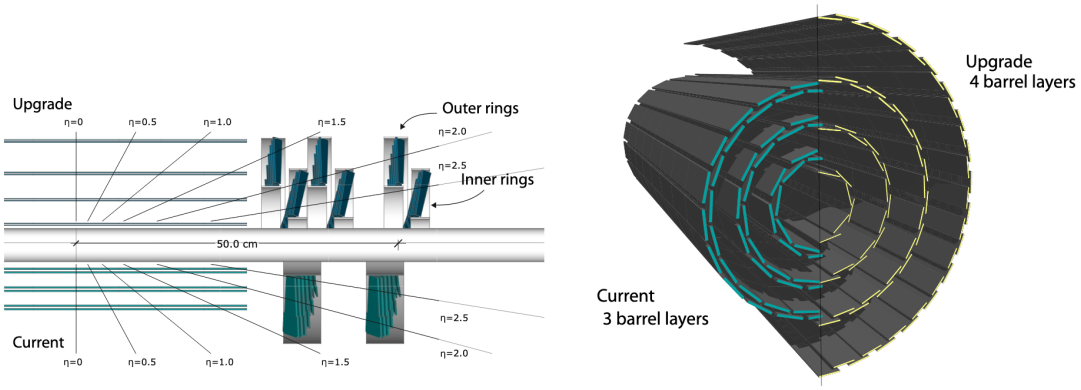

Figure 7.2: Layout of the pixel system used until the end of 2016 compared to the upgrade. The view in the (z,r) plane (left) and the (x,y) plane from the barrel part (right) is shown. Taken from Ref. [80].

7.2.3 Calorimeter

The electromagnetic calorimeter (ECAL) and the hadronic calorimeter (HCAL) are still placed inside the solenoid in order to avoid material in front which would otherwise absorb the energy of the incoming particles. Therefore, the space for the calorimeters is limited and high-density material is used to stop the particles within the material.

The homogeneous lead tungstate crystals of the ECAL stops electrons and photons, so their energy can be measured. For electrons and photons up to 1 TeV more than 98 % of the energy is deposited inside the ECAL. Fine segmentation of the crystals with $2.2 \times 2.2\,\mathrm{cm}^2$ and $2.9 \times 2.9\,\mathrm{cm}^2$ in the barrel and endcap regions respectively allows it to fully resolve energy deposits 5 cm apart from each other. The scintillation light of the crystals is measured by avalanche photodiodes. The relative energy resolution [79] of the ECAL

$$\frac{\sigma_\mathrm{E}}{\mathrm{E}} = \frac{2.8\,\%}{\sqrt{\mathrm{E/GeV}}} \oplus \frac{12\,\%}{\mathrm{E/GeV}} \oplus 0.30\,\% \tag{7.5}$$

is a combination of the stochastic fluctuations of the detector material (first term = stochastic term), electronic, digital and pileup noise (second term = noise term) and inhomogeneities of the calorimeters or calibration errors (third term = constant term). The highly granular ECAL is also able to start the hadronisation process already and around a quarter of the hadronic spray leaves the energy already here.

The remaining part of the hadronic showers is absorbed in the HCAL, which is designed as a sampling calorimeter. Alternating brass radiators for enhancement of the showering and plastic scintillators to measure the energy cover a range in the barrel and forward

region up to $|\eta| < 3$. This setup makes it suitable to have most of the HCAL part be placed inside the solenoid, while one layer measures particles from the hadronic decays, being able to also pass the solenoid. The forward region is equipped with steel absorber and quartz fibre sensors to be able to measure electromagnetic as well as hadronic showers up to $|\eta| < 5$. A combined energy resolution [79] of ECAL and HCAL was measured to be

$$\frac{\sigma_{\mathrm{E}}}{\mathrm{E}} = \frac{110\,\%}{\sqrt{\mathrm{E}/\mathrm{GeV}}} \oplus 9\,\%. \tag{7.6}$$

7.2.4 Solenoid

The superconducting solenoid magnet is 13 m long and has a diameter of 6 m. It produces a uniform magnetic field of 3.8 T inside the solenoid. Such a high magnetic field makes it possible to distinguish between neutral and charged particles with a sufficient momentum and space resolution. Furthermore, the sign of the charge can be distinguished due to the bending direction of the particle. Saturation of the magnetic field towards the outside of the detector is achieved by 10,000 t iron flux return yoke, placed in between the muon system. The direction of the magnetic field in the outer part of the detector is changed and therefore trajectories are bent into the opposite direction. This results in a better resolution of momentum measurements of particles reaching this part of the detector, e.g. muons.

7.2.5 Muon System

In the most outward region of the detector, the muon system is placed. Three different gaseous particle detectors measure all particles reaching this part. In the barrel region up to $|\eta| < 1.2$ drift tubes (DT) are used. Here, the muon rate is rather low, and a high precision measurement is done. In the more forward region, covering $0.9 < |\eta| < 2.4$ cathode strip chambers (CSC) are used. In this part, the magnetic field starts to be non-uniform and both muon rate, as well as background rate, are rather high. In addition resistive plate chambers (RPC) are placed in the barrel part up to $|\eta| < 1.6$. These three detector types can all be used for the trigger system, described in the next section.

7.2.6 Data Acquisition and Trigger System

The LHC provides pp collisions at a 40 MHz rate. The offline computing system is only able to handle around 100 Hz rates and in addition storage space is limited. Therefore,

a trigger system selects in two steps events of interest, which are stored. First, a rough selection with only a few information of some detector parts is done, called the level-1 trigger (L1). It is based on programmable electronics, which decides from hits in the muon system or energy deposits in the calorimeters if an event should be stored. Programmable electronics as the usage of FPGA technology has the opportunity that changes of the L1 triggers over time can be easily adjusted. The L1 trigger reduces the event rate down to 100 kHz. Events passing this L1 step are afterwards processed by the high-level trigger (HLT), which combines the information of all different subdetectors and apply filter selections. Therefore, a variety of complex calculation is done at this step, where the results of those calculations are close to the ones coming from the offline event reconstruction technique. The HLT filter selection reduces the event rate down to the order of 100 Hz. These events are then reconstructed offline as described in Chapter 8.

8 Event Reconstruction and Particle Identification

Various information can be calculated and interpreted from the plain electronic signals recorded with the subdetectors described in Section 7.2. From hits in the tracking system, the trajectory (track) of a charged particle, as well as its origin, the so-called vertex (more in Section 8.1), can be determined. In order to reconstruct the full pp collision, a combination of the different records by the subdetectors is essential. Therefore, not only adequate resolution for hits in the tracking and muon system and energy measurements with the calorimeter system needs to be required by the CMS detector itself, but in addition, all this information needs to be processed and combined by a powerful algorithm. For this purpose the CMS Collaboration uses the PF algorithm [79], further described in Section 8.2. The PF algorithm combines signals from different subdetectors to PF candidates. Since each particle leaves a distinct signature in the detector, it can be used for identification. Hadrons produce showers of particles, which are also called jets (see Section 8.3). Hadrons containing a bottom quark have a specific, longer, lifetime, which makes it possible to distinguish them from other jets (see Section 8.4). Electrons can be identified with their trajectory pointing to an energy cluster in the ECAL, while photons leave all their energy as electromagnetic showers in the ECAL without any trajectory (more in Section 8.5). Muons leave mainly hits in the muon detectors in the outermost part of the detector (see Section 8.6). Antiparticles of charged particles can be identified by the trajectory bending in the opposite direction. Some particles, for example neutrinos, leave the detector without any interaction and can only be reconstructed from the missing transverse momentum (see Section 8.8).

This chapter will mainly focus on objects used in the thesis, while objects which are used to remove events or nor used objects are only mentioned briefly.

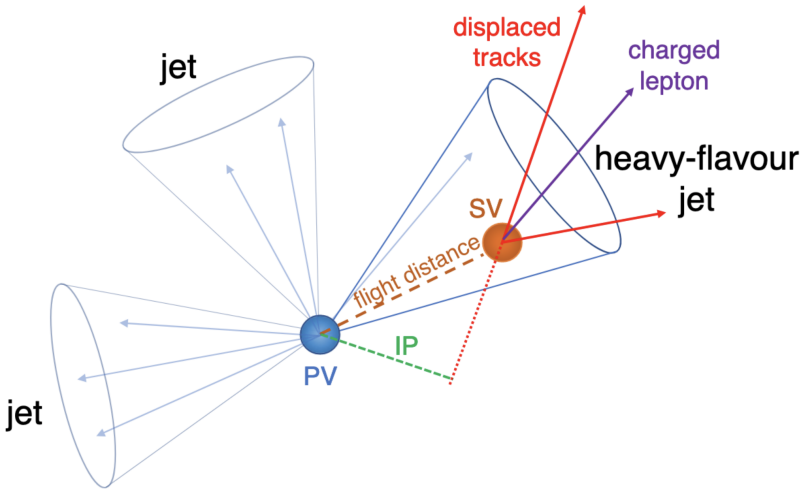

Figure 8.1: Sketch of the difference between jets originated by light quarks or gluons and a heavy-flavour jet including a displaced SV. Displaced tracks produced at the SV position have a bigger IP to the PV, as indicated. Taken from Ref. [65].

8.1 Track and Vertex Reconstruction

Good track reconstruction and resolution are essential for many analyses. Therefore, the whole range between low momentum (order of 100 MeV) and high momentum (up to 1 TeV) tracks must be covered. Furthermore, the closest distance between the trajectory and a reference point (e.g. primary or secondary vertex), the so-called impact parameter (IP) highlighted in green in Figure 8.1, requires to have an excellent resolution [81]. The latter one is not only important for precise measurements of the primary vertices but is, in addition, a key point of identifying jets originated by b quarks and hence also very important for the analysis described in this thesis. On average, about 29 pp interactions occurred simultaneously between the run periods 2016 and 2018 [82], leading to approximately 1000 charged particles passing through the detector at every bunch crossing [81]. This makes track reconstruction a challenging and computationally expensive task. Furthermore, only one pp interaction is of interest in most cases, and all other particles, coming from softer pp interactions so-called PU, need to be removed.

In the following, the reconstruction from hits in the tracking detector to tracks is explained in detail. Furthermore, an overview of how those tracks are selected and combined to reconstruct vertices is given.

8.1.1 Track Reconstruction

Before the track reconstruction algorithm described in the following can be used, first, the hits from the charged particles in the pixel and strip detector sensors need to be identified. A more detailed description of this procedure can be found in [81]. For both subdetectors, only such sensor signals are taken into account, which fulfil a certain threshold to suppress electronic noise. Hits and uncertainties are defined with respect to the plane of each sensor. For the pixel sensors, two algorithms are used to describe the cluster of hits. First, a faster algorithm is performed, which takes either the centre of one hit pixel as the hit position or calculates this position by using two pixels at the end of the found cluster. In both cases, the hit position is corrected for the Lorentz drift due to the magnetic field. This result is used for track seeding and pattern recognition steps. Afterwards, a more accurate algorithm is run, where the results are used for the final track fit. The so-called template-based hit reconstruction compares the found clusters in the pixel sensors with simulated clusters using the PIXELAV program [83]. This procedure makes it possible to compensate for radiation damage of the sensors since it is possible to simulate templates for different states of irradiated sensors. Strip detector clusters are formed by using neighbouring cells, if their signal is above a certain threshold. As done for the pixel clusters, a correction for the Lorentz drift is performed. The hit efficiency in both subdetectors was measured with selected tracks and found to be on average above 99 % [81].
Hits in the tracking system are afterwards combined to trajectories (tracks) with an iterative combinatorial track finder based on Kalman Filtering [84]. Each iteration follows the four stages:

1. seeding track candidates with a certain amount of hits,
2. extrapolation of the seed trajectory to add additional hits to the track,
3. track-fitting to find the best assumption of the trajectory parameters, and
4. a track selection, where each track has to fulfil different criteria.

Tracks are seeded in the first iteration step with at least two hits in successive pixel detector layers and at least eight hits in total. The purity[1] of these tracks is already high enough. Hence no additional quality criteria are needed. With further iterations, the goal is to increase the efficiency, while the misreconstruction rate needs to stay low. This requirement remains stable because additional quality criteria are set and applied to

[1]Purity defines the absence of fake tracks, where no charged particle is associated to.

all remaining hits, not used in previous iterations. Such criteria are different track seed combinations between hits in pixel and tracking detector, the track fit χ^2 and if the track matches the main interaction point (PV) of the pp collisions. With relaxed criteria in later iterations, missing hits in the pixel detector and therefore, inefficiencies of these layers are covered. With this procedure, the CMS experiment reaches track-reconstruction efficiency of 94 % within $|\eta| < 0.9$ and 85 % at higher pseudorapidity regions [81]. The resolution in p_{T} of central region tracks ($|\eta| < 1.4$) with transverse momentum between 1 and 10 GeV is roughly 1.5 %. The resolution of the transverse (longitudinal) IP is between 25 μm (45 μm) for tracks with transverse momentum of 10 GeV and 90 μm (150 μm) for softer tracks with transverse momenta of 1 GeV. Providing a good tracking efficiency is essential for vertex reconstruction and has a significant impact on jet properties. For example, tracking inefficiencies of 20 % would lead to an increased hadron energy fraction in a jet from 10 % to 20 % and therefore raise changes to jet energy and its angular resolution [79].

8.1.2 Primary Vertices and Pileup

Only certain tracks found by the iterative procedure explained above are used to reconstruct PVs. The different selection criteria make sure that only tracks originating from a PV are used. The significance of the transverse impact parameter with respect to the beam position is not allowed to exceed a 4.0[2]. Furthermore, the tracks need to fulfil at least two hits in the pixel and five hits in the strip detectors, and the normalised fit χ^2 needs to be below 10. Since the number of pp interactions can vary with each bunch crossing, the combination of tracks to these vertices needs to be independent. Tracks are combined by comparing their point of closest approach and the centre of the beam spot along the z-axis. For this procedure, the deterministic annealing algorithm is used. A track can either be assigned to only one PV, or the algorithm specifies a probability to which of the vertices the track can be assigned. A combination of possible tracks is found in that way for each PV candidate. Each candidate with at least two tracks assigned is afterwards processed by the adaptive vertex fitter algorithm [85] to determine the vertex position, among other values. Furthermore, each track gets a weight, which indicates the probability that this track originated from this specific vertex by comparing the fitted vertex position to the trajectory. The weight is taken into account to calculate the number of degrees of freedom for each PV candidate. The resolution of the position of a PV can

[2]Values of track selection mentioned here are taken from the framework setup for 2016 data taking area. All numbers can vary over different years of data recording.

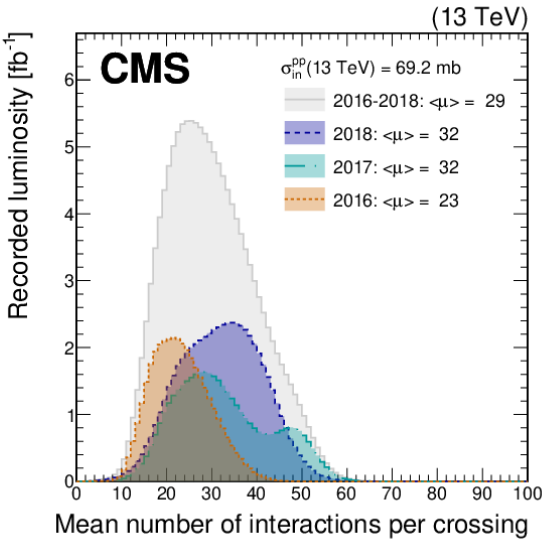

Figure 8.2: Mean number of inelastic pp interactions in collisions of data eras 2016 (dotted orange line), 2017 (dotted dashed green line), 2018 (dashed blue line) and the integrated values for all three run eras (solid grey line). Taken from Ref. [82].

be determined to an accuracy of 10-12 μm in the three dimensions [81]. The resolution decreases the fewer tracks are assigned to a vertex.

Pileup

Typically, more then two protons interact per bunch crossing. The mean number of pp interactions at each bunch crossing can be found in Figure 8.2. On average, in 2016, 23 interactions occurred per bunch crossing, and this value increased to 32 for 2017 and 2018 [82]. Therefore, the PV of interest needs to be selected. All PVs per event are ordered via the summed p_{T}^2 value of all physics objects assigned to each vertex. The leading vertex is the one where most likely the physics of interest happens, while the rest is defined as soft interaction and hence PU. Furthermore, charged particles coming from PU need to be carefully removed from the objects used for analyses. There are two main algorithms available in the CMS Collaboration to mitigate the effect of PU. The pileup per particle identification (PUPPI) algorithm [82] was developed recently. For each neutral and charged particle, a weight is determined, and depending on that value, this specific particle is removed from the event or not. If it is kept, the four-momentum of this particle is scaled accordingly to the weight found in the previous step. The other algorithm is called charged hadron subtraction (CHS) [86] and, as the name indicates, focuses on

charged particles only. The CHS algorithm removes charged particles that are assigned to PU vertices from the event. Comparisons show that the PUPPI algorithm rejects better PU particles and is more robust for higher PU scenarios [82]. Since the PUPPI algorithm is relatively new, not all necessary information for this analysis is currently provided, and therefore the CHS algorithm is applied. Nevertheless, the PUPPI algorithm can be used for the signal investigated in this thesis and follow up analyses might make use of it.

8.1.3 Secondary Vertices

Particles with a specific lifetime, such as new particles investigated in this thesis or SM hadrons including b quarks, leave signatures only after some flight distance from the PV. If the flight distance is up to the order of centimetres, another type of vertices at this decay position can be reconstructed, so-called SV. A sketch is shown in Figure 8.1, where the difference between tracks coming from a direct hadronisation process of light quarks *u, s, d* and the displaced hadronisation of *b, c* hadron decays with a SV is shown. The tracks of the latter have, amongst others, a larger IP and can therefore be identified and combined by the Inclusive Vertex Finder (IVF) algorithm [87, 88] to reconstruct SVs. Tracks with a large IP in 3D are used to seed the algorithm. Tracks are clustered to the seed track when they fulfil criteria on the angle between the two tracks and the distance of the closest approach. Only when the distance between the two tracks is smaller than the distance of the closest approach between the seed track and the PV, both are taken into account for the SV. As for the PVs, the adaptive vertex fitting algorithm determines the vertex position of the clustered tracks. Only SVs found with a minimum value of the flight distance significance are kept. After this fitting step, it is possible that some tracks are removed from the cluster, since they are not any longer suitable to the new vertex position. The SVs are refitted and have to fulfil again a flight distance significance criterion. The probability of finding SVs is much higher for jets originated from hadrons including b quarks, than jets originated from light quarks. Therefore, after jet clustering (Section 8.3), an assignment between SVs and jets is performed by comparing mainly the distance of the SV flight direction to the jet axis. As an example of how this works in data, Figure 8.3 shows an event display of reconstructed data taken in 2016 at 13 TeV. In the (x,y) plane, tracks with $p_{\mathrm{T}} > 0.5\,\mathrm{GeV}$ are shown in green, PVs in yellow dots, yellow areas represent the jet cones, and SVs are shown in black dots, while tracks assigned to these SVs are coloured in black as well.

If SVs are displaced by more than two centimetres, one has to take into account that the

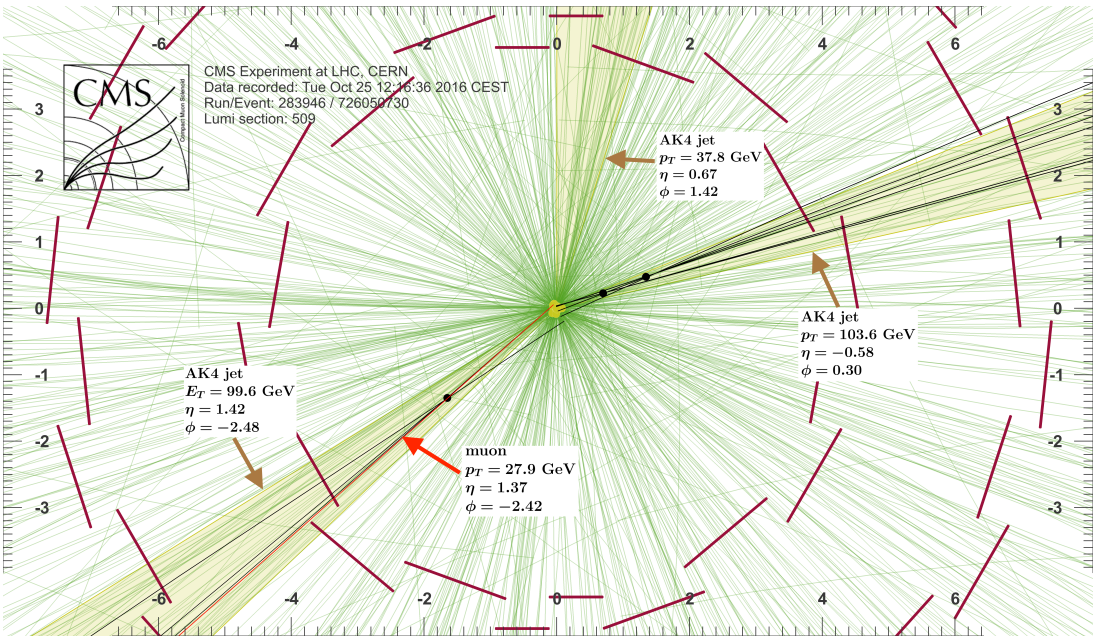

Figure 8.3: Event display in the (x,y) plane of reconstructed data taken in 2016 at 13 TeV. This event is classified as QCD multijet event and contains 53 reconstructed PVs. Tracks with $p_{\mathrm{T}} > 0.5\,\mathrm{GeV}$ are shown as green lines, yellow dots represent the PVs, yellow areas show the jet cones, black dots highlight the SVs, and the black lines are the assigned tracks to the SVs. The position of the pixel detector is indicated by the red bars arranged in a circular geometry. The scale is given in centimetres. The two leading jets are tagged as b jets by the CSVv2 algorithm. Taken from Ref. [89].

material of the detector is present, and nuclear interaction (NI)s of neutral hadrons with the detector material can mimic SVs. A study about the rejection possibility of NIs is presented in Section 8.4.2.

8.2 The Particle-Flow Algorithm

The concept underlying the PF algorithm was already developed in the 1980s [79] and is also planned to be used for future particle physics colliders. The great advantage of the algorithm is to combine all information from the subdetectors and hence providing a more precise determination of the properties of all particles in the event. After reconstruction of tracks and energy clusters (PF elements) in the subdetectors, possible links between them are identified by various fit methods and called PF blocks. In the last step, the PF blocks are identified as particles (PF candidates). In the following, each step is described

more in detail, following mainly [79]. A decent distinction between the different particles requires a good resolution with a fine granularity of the subdetectors, which is valid for the CMS detector tracking, muon and calorimeter system.

Tracks are reconstructed as described in Section 8.1.1. And used for the PF algorithm.

The next step is to find clusters in the calorimeters. This step is done separately in ECAL and HCAL. Cells that exceed a specific energy threshold[3] and have the highest energy of the surrounding cells are used as seeds. Surrounding cells are added to the cluster as long as their energy is higher than twice the noise level. Within the found clusters, an expectation-maximization algorithm based on a Gaussian-mixture model is applied to find substructures. It uses the number of seeding cells as well as the number of cells where energy is deposited.

Particular strategies are applied to identify tracks originated by electrons and muons. Electron reconstruction makes use of two different seeding strategies. ECAL clusters, fulfilling a certain energy threshold, are used and, possible tracking hits produced by either photons or electrons are extrapolated. This method works well when the electrons are isolated, while overlaps with other charged particles lead to inefficiencies. The second strategy uses the fact that electrons often produce bremsstrahlung already in the tracking system, while charged hadrons won't radiate that early in the detector. The first step of the strategy is to start with all tracks found by the iterative approach above. The track fit χ^2 and the number of hits are used as preselections and, in addition, it allows to distinguish between electron and photon hit collections. Tracks matching innermost ECAL clusters are used as electron seeds and fit by a specialised fitting technique, particularly coping with possible energy losses, based on a Gaussian-sum filter. The combination of electron seeds found with the two strategies is afterwards fit with a Gaussian-sum filter, with more components than in the second strategy. With that combined procedure, it is possible to increase the efficiency of electron reconstruction as well for very soft electrons ($p_{\mathrm{T}} \geq 2\,\mathrm{GeV}$), but this also increases the misidentification rate, which is handled at a later step (see more in Section 8.5).

Since muons have a quite clear signature in the muon detectors as the outermost detector part, detecting muons with high purity and efficiency is granted. Furthermore, this clear signature can be augmented by the more accurate momentum measurement of the tracking system. Therefore, an extrapolation between the clusters in muon detectors with the muon tracks in the tracking detector is performed.

[3] This threshold is typically above the noise level.

After the reconstruction of all PF elements, a *link algorithm* combines them into so-called PF blocks. Due to physical decays as well as computing time reasons, only nearest neighbours in the (η, ϕ) plane of PF elements are taken into account for possible link calculation. In that way, track extrapolations to ECAL and HCAL are performed and only linked if the extrapolation overlaps with clusters. Furthermore, calorimeter clusters in ECAL and HCAL are connected when the position of the ECAL cluster is overlapping with the cluster envelope in the HCAL, where only the cluster of closest distance will be linked. Finally, PF blocks are formed by linking tracks from the tracking system and hits in the muon detectors.

Each PF block is afterwards processed, possible PF candidates are identified, and PF elements are removed from the PF block. This order for the identification of PF candidates is always the same. Therefore, isolated muons are first selected by requiring hits in the tracking system and additional energy clusters in the calorimeters along the flight direction. For muons produced inside jets, more stringent requirements for hits and energy clusters are set. Afterwards, electron and isolated photon candidates are processed. For both candidates, only a tiny fraction of the energy is expected to end up in the HCAL. Finally, all remaining PF blocks are used to identify charged or neutral hadrons as well as photons or muons coming from specific particle decays.

Finally, a post-processing algorithm is correcting for possible misreconstruction or misidentification. Especially, events with large missing transverse momentum are again checked and, for example, candidates with high momentum in the event corrected. Afterwards, the missing transverse momentum is calculated again.

8.3 Jet Reconstruction

Quarks and gluons, produced by pp collisions in the LHC, hadronise and create showers of particles due to colour confinement. These showers of charged and neutral hadrons, as well as photons, leave a combination of energy clusters in ECAL and HCAL. Combining all these objects is necessary to describe the properties of the particle which initiated the jet. Furthermore, corrections of the energy and resolution of the jets due to different sources are needed.

8.3.1 Jet Clustering Algorithms

Several jet clustering algorithms were developed for particle physics. Two requirements have to be fulfilled by all of these algorithms. They have to be *infrared* and *collinear safe*, which means that neither additional soft radiation nor an exchange of one particle with two collinear ones, keeping the four-momenta the same, changes the reconstructed jet. Objects found by the PF algorithm are used by these algorithms.
The three most commonly used jet clustering algorithms make use of two variables. These are

$$d_{i,j} = \min(k_{t,i}^{2p}, k_{t,j}^{2p}) \frac{\Delta R_{i,j}^2}{R_{jet}^2}, \tag{8.1}$$

$$d_{i,B} = k_{t,i}^{2p}, \tag{8.2}$$

where $d_{i,j}$ describes the distance between the i-th and j-th entity, which are either particles or pseudo-jets, $\mathrm{k}_{t,i}$ is the transverse momenta of the i-th entity, ΔR the angular distance between two objects (Equation 7.4), R_{jet} is the radius parameter of the jet and $d_{i,B}$ is the distance between the i-th entity and the beam axis. The parameter p can be either -1, 0 or +1 and is different for each of the following jet cluster algorithms. p = 0 is called Cambridge/Aachen [90] algorithm. Only geometrical distances are taken into account for the clustering. The $\mathrm{k_T}$ [91] algorithm uses $p = +1$ and starts with the clustering of soft particles, while $p = -1$ is used by the anti-$\mathrm{k_T}$ jet algorithm [92], which clusters particles with large transverse momenta first. In all cases, each iteration calculates the minimum between $d_{i,j}$, $d_{i,B}$ and $d_{j,B}$. Entities are clustered together when $d_{i,j}$ is smaller, while otherwise, the pseudo-jet is defined as a jet, and all used particles are removed from the list.
For this thesis, jets clustered with the anti-$\mathrm{k_T}$ algorithm are used with the radius parameter R = 0.4, called AK4 from now on.

8.3.2 Jet Corrections

Before the jet clustering is performed, the CHS algorithm removes particles coming from PU (see 8.1.2). Besides cleaning remaining PU energy deposits, jet energy correction (JEC) [93] corrects detector effects, like a non-linear response of modules, which changes the measurement and hence the reconstruction of the jet energy. Each source is investigated in an individual step of the JEC, as indicated in Figure 8.4. The corrected jet four-momenta of each step are used as input for the next step. JEC is applied to data and

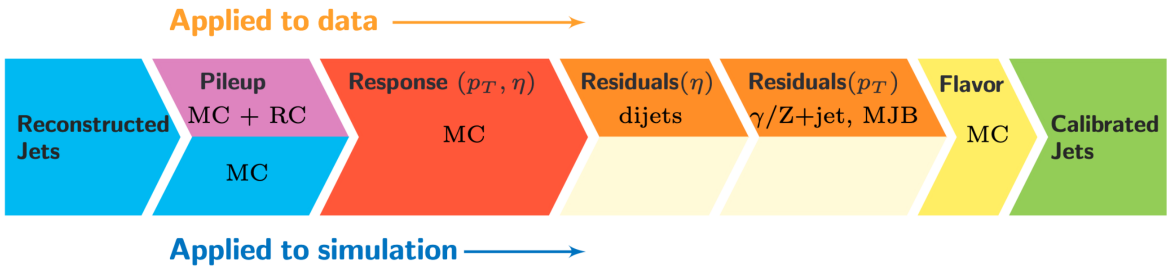

Figure 8.4: JEC procedure applied for data (upper row) and simulation (lower row) from the CMS Collaboration. Taken from Ref. [93].

simulated events. However, not all steps are applied to the latter one. A brief overview is given in the following, using [93] as a primary reference, where more information can be found. The first step of JEC removes additional PU contribution, which adds an offset to the jet energy. The PU offsets are estimated from simulated events and depend on the energy density ρ, as well as the area, pseudorapidity η and transverse momentum p_{T} of the jet. The next step corrects for different detector responses. Simulated multijet events are used to derive differences of jets at generator-level and reconstruction level as factors dependent on η and p_{T}. Information of the detector geometry, alignment and calibration of detector elements, as well as readout electronics imitation, are used in this step. After these two steps, minor differences between data and simulation still exist. Hence, a residual correction is applied to data only. Residual corrections with dependence in η are derived from dijet events, while simulations with γ+ jet or Z+jet events are taken to derive p_{T} dependent correction factors. The final correction for jet flavour, as indicated in Figure 8.4, is optionally and not applied in this thesis.
After the JEC procedure, there are still differences between data and simulation in the jet energy resolution (JER). Typically JER in simulation does not describe the performance of the detector but shows a better one. Therefore, simulated jets on particle-level are used to measure the JER, and different variables are used to derive $|\eta|$ dependent scale factors. This factor is used to smear the jet four-momenta in simulation and mimic the detector resolution better.

8.4 Identification of Jets Originating from *b* Quarks

Properties of jets originating from gluons or light flavour quarks (uds) are very similar and difficult to distinguish. However, jets originating from b or c quarks can be identified.

These b and c quarks have, on average, a lifetime around 1.5 ps and 0.1 ps in their rest frame, respectively [21] and travel a finite distance before they produce particle showers. These lifetimes lead to a travel distance in the detector rest frame between millimetres and centimetres from the PV. Therefore, SVs can be found at the decay vertex (see Figure 8.1), which gives rise to several very unique properties. As already mentioned, tracks produced at SVs have large IPs. Furthermore, masses of hadrons, containing b and c quarks, are around 5 GeV and 2 GeV and much higher than the masses of hadrons without b or c quarks, which are in the order of 100 MeV. Soft electrons or muons are produced at around a fifth of the SV of B hadrons and at around a tenth of SV of hadrons containing c quarks. All these properties can be used within tagging algorithms to identify and flag so-called b and c jets. Since the focus is on slightly more displaced b quark decays in this analysis, a focus on only such techniques are provided for these decays.

8.4.1 *b* Tagging Algorithms

Various b tagging algorithms have been developed for analysing data, collected with the CMS detector. Developments from a multivariate technique based algorithm combining high-level information of displaced tracks and vertices (CSV and CSVv2 [65]) over a combined multivariate analysis (cMVA) tagger to ML based tagger have been used. The DeepCSV [65] tagger uses the same input variables as the CSVv2 tagger but takes the information of six instead of three tracks, and it has more hidden layers and more nodes per layer. Input variables include the number of SVs in the jet, IP and its significance of selected tracks in 2D and 3D space, SV flight distance from PV, and several more [65]. The CSVv2 tagger provides one discriminant value, giving the probability that the jet is produced by a B hadron. Instead, the DeepCSV tagger provides classifier discriminator values for one or two b quarks (b or bb), c quarks or light quark/gluon ($udsg$) decays. The sum of the probabilities $P(b)+P(bb)$ is taken as a discriminating variable, to identify jets as b jets. The latest development by the CMS Collaboration is the DeepJet (sometimes called DeepFlavour) tagging algorithm [66]. Instead of using only high-level tracking variables of selected tracks as input, DeepJet uses more low-level information of up to 25 charged and neutral PF jet constituents each. The information for these PF jet constituents is, for example, relative p_{T} with respect to the jet p_{T}, ΔR between the constituent and the closest SV, χ^2 value of tracks (in case of charged constituent). Furthermore, input features of up to four SVs are fed into the network, as, for example, the invariant mass and p_{T} of the SV, ΔR between the flight direction of the SV and the jet axis, number of tracks

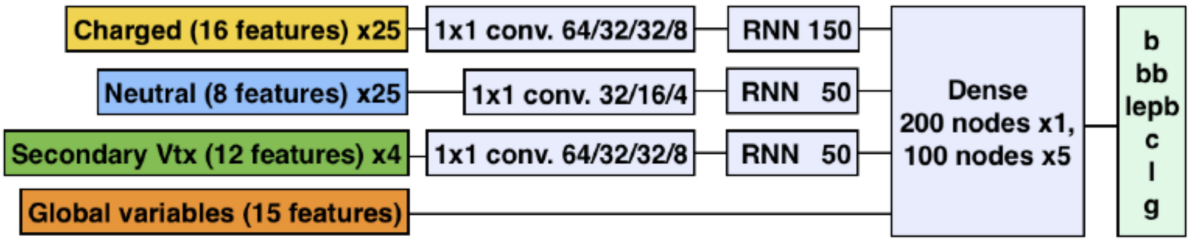

Figure 8.5: DeepJet tagger architecture with different input feature sources. Features for charged and neutral PF constituents and SVs are used to train 1x1 convolutional layers of different depth separately. These outputs are compressed and stored in long short-term memories (indicated as RNN in the schematic). Afterwards, all information is combined fed into one dense layer and several hidden layers. Classifier outputs for different jet flavours are provided. Taken from Ref. [66].

associated with the SV. In addition, global features like numbers of PVs and SVs in the event or jet features as p_{T} and $|\eta|$ as well as a number of reconstructed SVs within the jet cone are used. All this information is fed into the DeepJet architecture, which is shown in Figure 8.5. The input features of the SVs, charged and neutral constituents are used to train three 1x1 convolutional layers with different depth and filter sizes separately. The output of each of these convolutional layers is handed over separately to long short-term memory layers. Finally, all these outputs are combined with the global input features in one dense layer before everything passes several dense layers. In the end, six different discriminator values are provided, and jets can be classified as jets originating from one or two b quarks (b or bb), leptonic b decays ($lep\,b$), one c quarks (c), light quark (uds) or gluon (g) decays. As for the DeepCSV algorithm, for DeepJet the probabilities are added, e.g. $P(b) + P(bb) + P(lep\,b)$ and used as discriminating variables for b tagging.

In addition to using the full discriminator shape of the tagging algorithms, the CMS Collaboration provides three working points, called *loose*, *medium* and *tight*. They are defined as the discriminating values where 10 %, 1 % or 0.1 % misidentification of *light* as b jets happens. Therefore, the specific values vary over the different data-taking periods, especially for the different b tagging algorithms.

In this analysis, the DeepJet discriminants of all jet flavours are used to train a DNN to identify b like jets originating from new physics decays. Furthermore, some of the input features of the tagging algorithm itself are used. A more detailed description about the used DNN can be found in Section 9.5.

b Tagging Corrections

All b tagging algorithms are trained and evaluated on simulated events since truth information about the jet flavour is crucial. However, differences between data and simulation exist, and therefore, it is necessary to correct for these differences. The CMS Collaboration provides scale factors for the full shape of the discriminator distribution. The method for reweighting the discriminator shape is first described in [94] and in more detail in [88]. Each jet introduces a specific weight, depending on p_{T} and η, for the scale factor calculation. Furthermore, the discriminator values D_i of a specific flavour i have an impact on the weight. The flavour dependency is important since the whole discriminating range is used for the analysis and has to be corrected. The correction is calculated taking only jets that pass the analysis's preselection criteria (see Section 9.3). A combined event weight is evaluated by measuring the scale factors for b and *light* flavour jets simultaneously and combined in the equation:

$$\omega_{\text{b tag}}^{\text{shape}} = \prod_{i}^{N_{\text{jets}}} \mathrm{SF}(D_i, p_{\mathrm{T},i}, \eta_i). \tag{8.3}$$

Uncertainties to the b tagging corrections come from different sources as jet energy correction, statistical and uncertainties related to the flavour selection for the scale factor derivation. All are taken into account and evaluated in Section 9.7.

8.4.2 Rejection Studies for Nuclear Interaction

As described in Section 7.2.2, several layers of the tracking system are placed close to the beam pipe. Figure 8.6 left shows the pixel detector material thickness x in units of nuclear interaction lengths λ_0 as a function of the pseudorapidity η of a particle. It can be seen that mainly 'dead' material, namely the surrounding parts (support structure, electronics, cables and cooling) around the pixel modules, raises NI. Mainly pions, but also other hadrons, can scatter inelastically with the nucleons of this material, so-called NI. This process produces several new charged particles. If neutral hadrons interact with the material, no other tracks are recorded before the NI. Therefore, NIs can mimic a vertex displacement and be reconstructed as SVs. This can happen within a reconstructed jet, resulting in a misidentification of *light* as b jets. As indicated in Figure 8.6 right, the probability that pions undergo NIs is dependent on the number of layers of the tracking material it crosses and can be as high as 25 %.

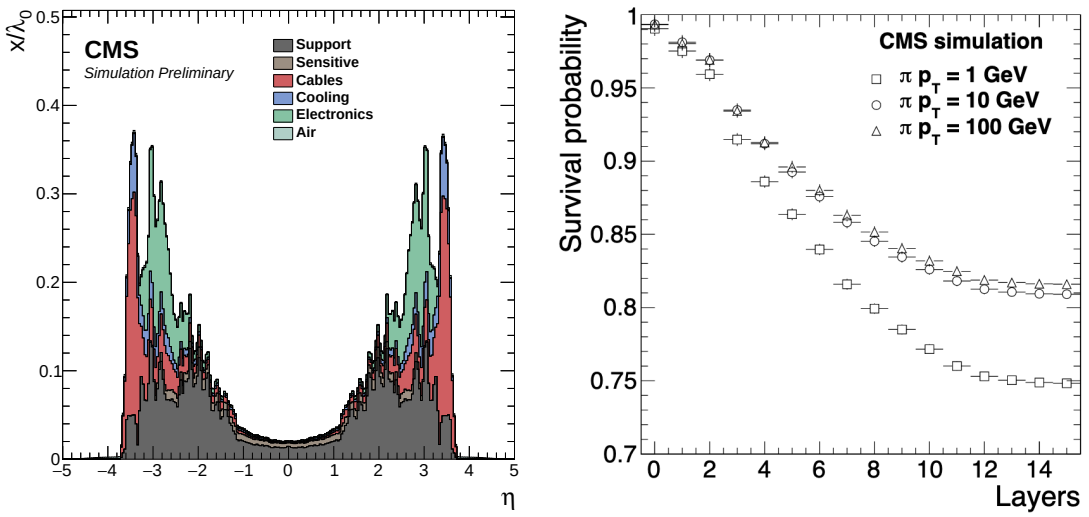

Figure 8.6: Material thickness x in units of nuclear interaction length λ_0 as a function of the pseudorapidity η of the pixel detector (left). Survival probability of pions produced in $|\eta| < 2.5$ not interacting with the material, depending on the number of layers in the tracking system (right). Taken from Refs. [95, 96].

An enlarged study about the impact of NIs on b tagging algorithms on data recorded in 2017 was performed. It previously has been studied with events of the 2012 run period [97]. The goal was to find a set of requirements to reject NIs from the SV collection and therefore improve the input to b tagging algorithms. The performance was evaluated for the b taggers CSVv2 and DeepCSV. The impact of NIs within the SVs collection was visualised with data recorded in 2017 with the CMS detector, while simulated $t\bar{t}$ events are used for the performance study of the b tagging algorithms.

Typically, there are hard requirements set on the flight distances in 2D and 3D and their significances. These are used for the b tagging algorithms to select only certain SVs from all SVs found with the IVF algorithm. The requirements are applied to train the taggers, but as well when the trained taggers calculate discriminants. For example, all SVs with a vertex position, also called decay radius, above 2.5 cm (measured from the PV) are rejected. These requirements make sure that areas with high material density and potentially many NIs are not considered. A visualisation why such hard requirements are needed can be found in Figure 8.7. The distribution of all SVs found with the IVF algorithm of data recorded in 2017 at $\sqrt{s} = 13\,\text{TeV}$ are shown. The upper and lower left plots of Figure 8.7 show the distributions in (x,y) and (z,r) planes, respectively. In both plots, the interaction point of the pp collisions is at (0,0). Around that point, the decay of hadrons containing b or c quarks are expected, and therefore a lot of SVs are

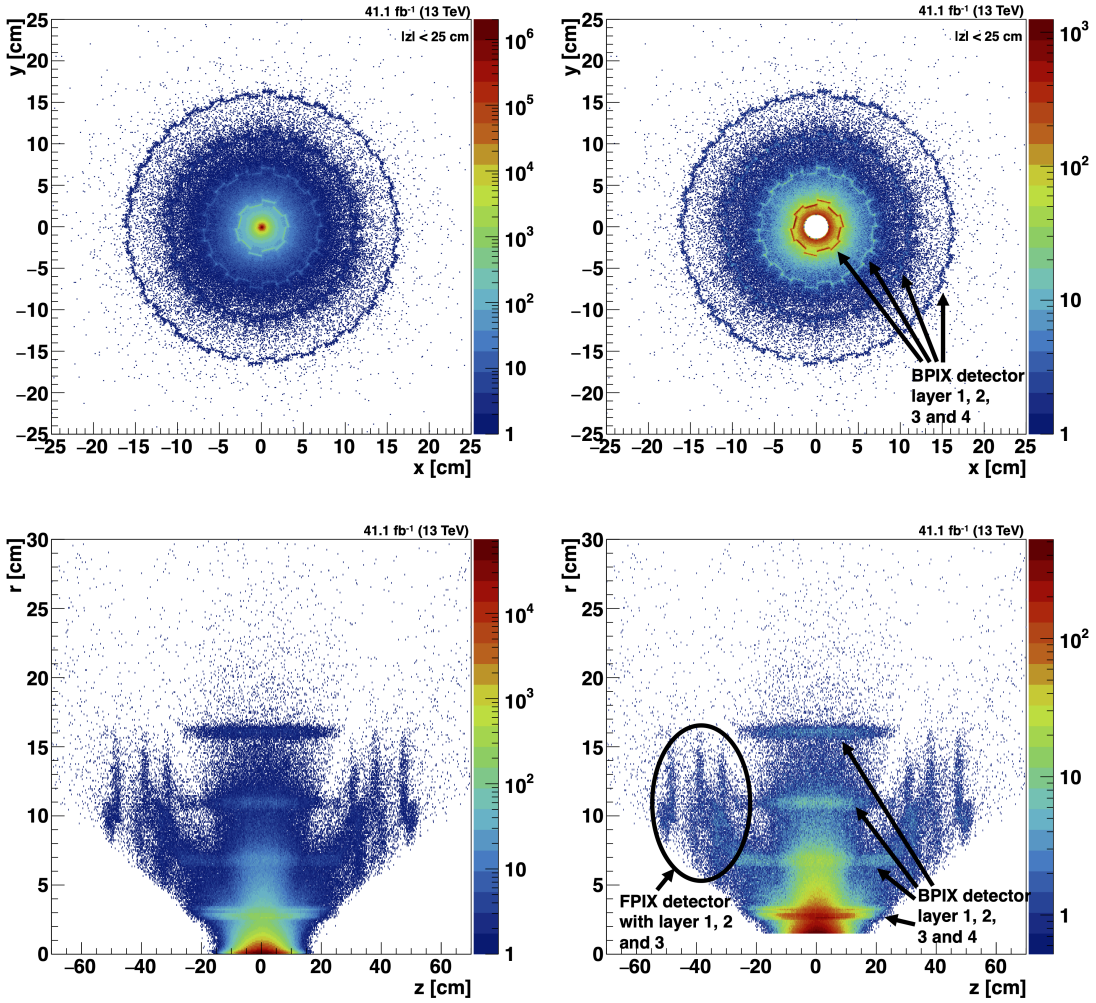

Figure 8.7: The SVs found with the IVF algorithm with relaxed requirements for SVs selection are shown with data recorded in 2017 at $\sqrt{s} = 13\,\text{TeV}$. The upper left and right plots present this distribution in the (x,y) plane with a cut applied at $|z| < 25\,\text{cm}$ to focus on the barrel part only. The lower left and right plots show the distribution in the (z,r) plane. For the upper and lower right plots, all SVs within the beam pipe are removed, so the structure of the NIs with the detector material is better visible. Arrows indicate the barrel (BPIX) and forward (FPIX) pixel detector positions.

reconstructed in that region. In order to get a better profile view of the SVs happening farther away from the interaction point, all SVs within the beam pipe, located at radius $r = 2.1\,\text{cm}$ around the interaction point, are removed. The remaining SVs are shown in upper and lower right plots in Figure 8.7. The four layers of the barrel pixel (BPIX) detector at around $r = 2.8, 6.7, 10.8$ and $16.0\,\text{cm}$ [80] are visible, as well as the three layers

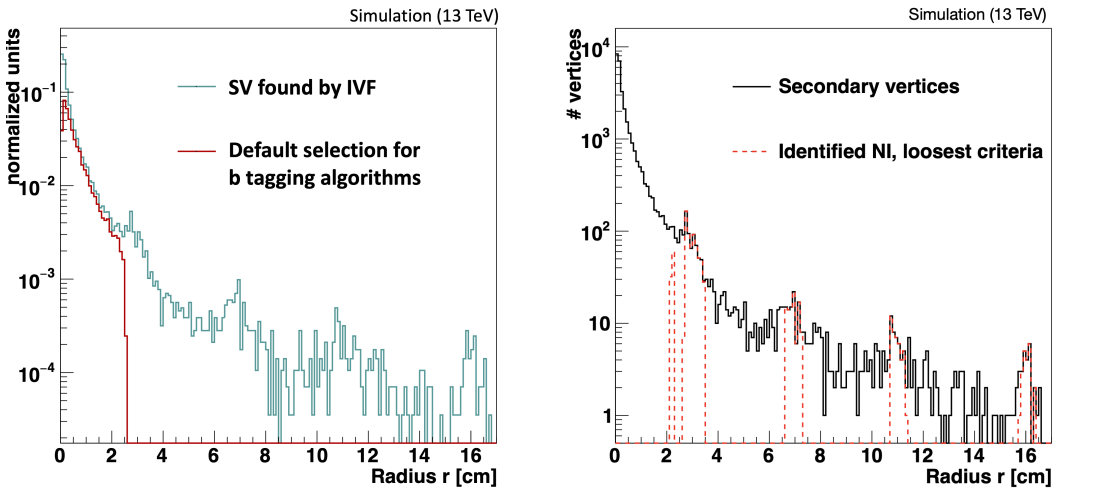

Figure 8.8: The SVs found by the IVF algorithm with the default requirements applied (red) and with relaxed requirements and all SVs found (turquoise) in the left plot. The right plot shows all SVs found by the IVF algorithm (black) and those identified as NIs with the position of the beam pipe and the barrel pixel layers only.

of the forward pixel detector (FPIX) at around $z = 29, 40$ and $42\,\text{cm}$ [80], where NIs took place. This shows that many SVs outside the beam pipe can be identified as NIs and should be rejected as input to b tagging algorithms.

In order to study different rejection requirements with $t\bar{t}$ simulation events are used since the amount of b quark decays makes this SM process ideally suited. As mentioned above, the SVs found with the IVF algorithm are selected by several requirements to serve as input for b tagging algorithms. The impact of such requirements is visible in the left plot of Figure 8.8, where the SVs are plotted versus the decay radius. The red curve shows the distribution when the default requirements are applied, and the turquoise curve represents all SVs found with the IVF algorithm. The study aims to regain efficiency by recovering SVs from b hadrons above the radius $r > 2.5\,\text{cm}$, where roughly $4\,\%$ of the SVs by b hadrons decay. Therefore, the entire collection of SVs found with the IVF algorithm is used, and potential NIs are removed by requirements explained in the following. The first scenario is to remove all SVs at the pixel layer and the beam pipe position, shown in the right plot of Figure 8.8. The following different categories are defined by information of either generator level or from Geant4 simulation, to get an idea of the true origin of the remaining SVs, as: NIs, the decay of b, c or K^0_s hadrons, photon conversion and fake SVs. Fake SVs are used if the SVs are caused by PU, or nothing else was recorded

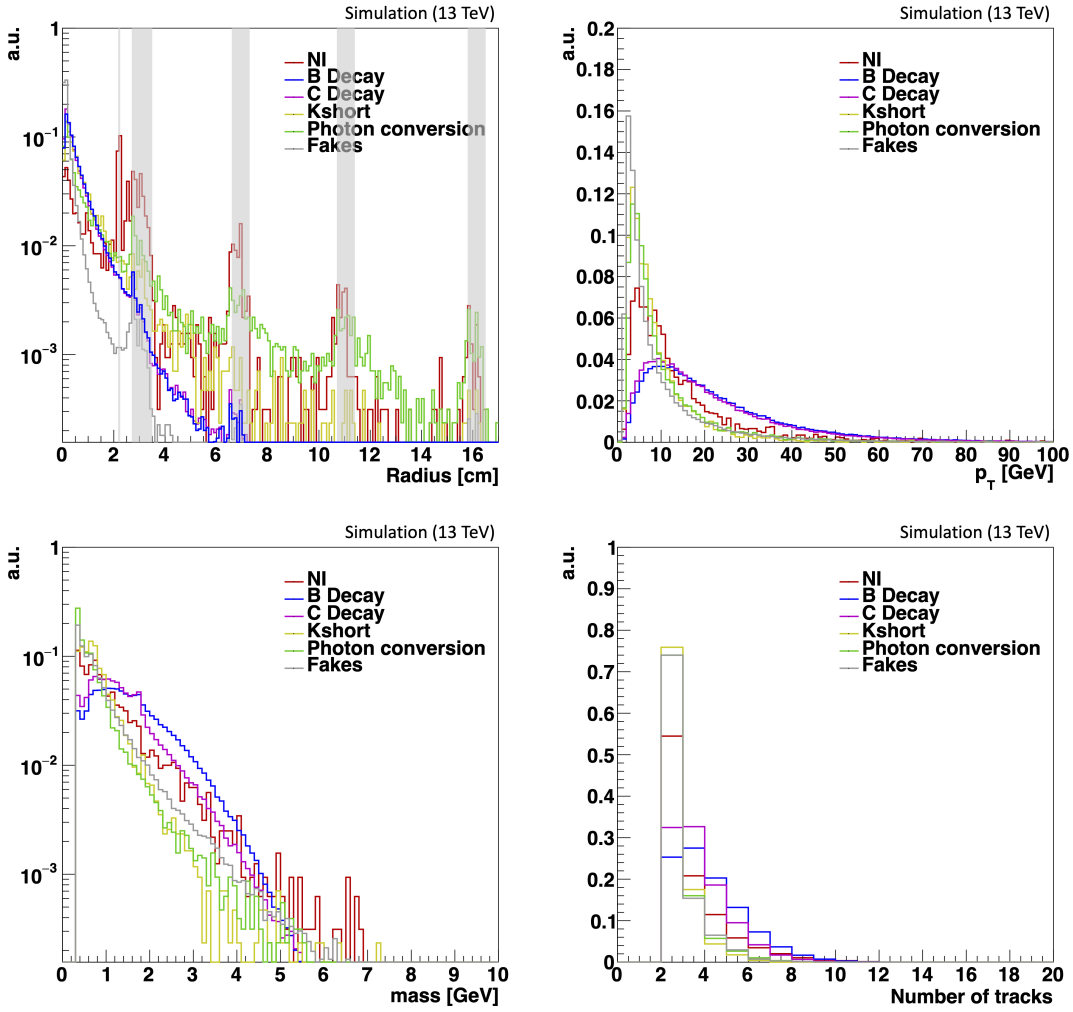

Figure 8.9: The SVs found by the IVF algorithm are sorted into several categories. NI (red), decays of b (blue) and c (purple) hadrons, decays of K^0_s (yellow), photon conversion (green) and fake (grey) SVs. SVs are plotted depending on the decay radius position (upper left), p_T (upper right), the invariant mass of the vertex (lower left) and the number of tracks associated with the vertex (lower right).

around these specific SVs. Each category is normalised to unity. Within the entire SVs collection, there are roughly 1 % NIs. The distribution of the decay radius with the different categories can be found in the upper left plot of Figure 8.9. Highlighted in grey are the position of the beam pipe and the four layers of the barrel pixel detector. As visible, NIs are peaking around these grey shaded areas. NIs in between the positions can be explained by supporting material and electronics, which is placed around the pixel

modules. Furthermore, it indicates that decays of b and c hadrons mainly happen below the beam pipe position (around 95 %), and only a small fraction is exceeding further (around 5 %). Differences between the categories are also visible in the distribution of the p_{T} of the vertex (upper right plot of Figure 8.9), the vertex mass (lower left plot of Figure 8.9) and the number of charged particles produced per vertex (lower right plot of Figure 8.9), where no further selections of the SVs are applied. In addition to the radius, other tunable parameters can be used to refine the selection of the NIs. These are the vertex mass and the number of tracks, the distance between an already identified NI candidate and the closest SV, as well as the number of flight lengths, defined as:

$$Nc_{\tau} = \frac{\text{flightDistance2D} \times \text{mass}}{p_{\mathrm{T}} \times 0.05\text{cm}}, \tag{8.4}$$

normalised to a typical decay length of b hadrons. The effect of these requirements on the performance of the CSVv2 and DeepCSV algorithms was studied in ROC curves and compared to the performance with the default SV collection. Only jets within the tracking system acceptance $|\eta| < 2.4$ were used for this study. The ROC curves present the efficiency of b vs $udsg$[4] jets and are shown in Figure 8.10. One of the default requirements for SVs selection for the 2017 data taking period was set to the maximum decay radius of 2.5 cm. With the old geometry of the pixel detector, the beam pipe position was outside this radius, but with the new geometry, the beam pipe is positioned closer to the interaction point. Hence, NIs happening with that material are still taken into account for b tagging algorithms. The impact of this requirement is shown in Figure 8.10, left plot for CSVv2 algorithm and right plot for DeepCSV algorithm. In both cases, the default SV selection (blue line) performs better than the red line, where all SVs within the position of the beam pipe are set as NIs and removed. This indicates that both CSVv2 and DeepCSV can distinguish NIs within the beam pipe position and SVs coming from b hadron decays. Taking the whole SV collection without any further selection, several different combinations of the before mentioned tunable parameters were tested. The best performance was found when SVs within the beam pipe and pixel layer positions were only removed, when their number of track ≤ 2, they have an invariant mass ≤ 1.5 GeV and their number of flight lengths ≥ 3.5. The following results are all performed with these requirements, which are summarised in Table 8.1. The results are shown in Figure 8.11, the right plot for CSVv2 and the left plot for DeepCSV tagging. These indicate that the performance for both taggers is equally good as for the default SV selection. The main reason for this

[4]The $udsg$ or non b-jet efficiency is now also called mistag rate, but means the same.

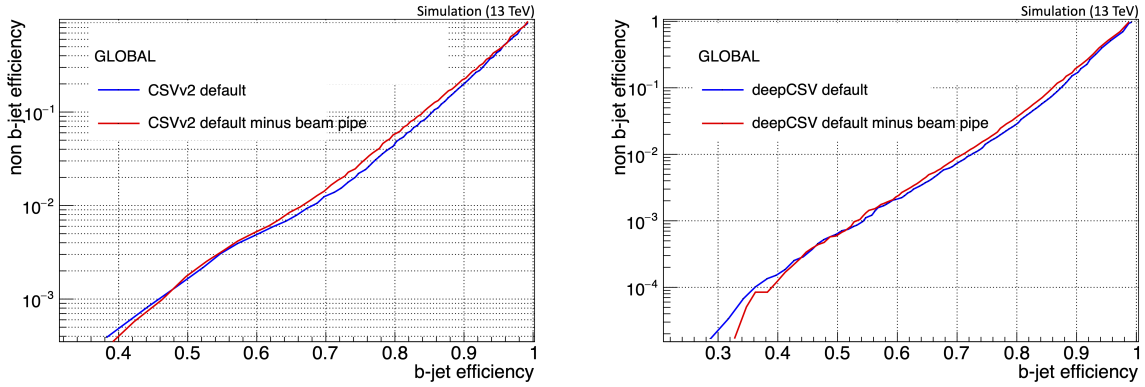

Figure 8.10: ROC curves to compare the performance of default SV selection (blue line) with modified SV collection (red line). Results are shown for the CSVv2 algorithm in the left plot, while the results of the DeepCSV algorithm can be found in the right plot. The plots show the impact of SVs removed, which lay within the beam pipe position.

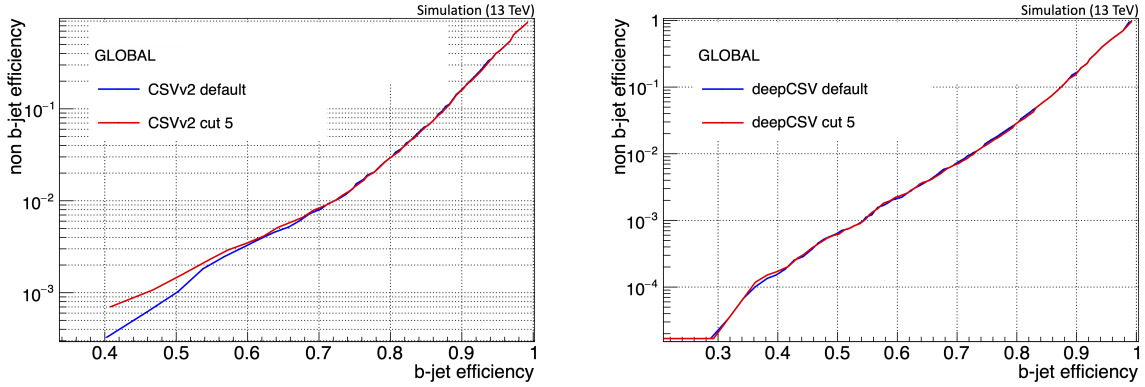

Figure 8.11: ROC curves to compare the performance of default SV selection (blue line) with modified SV collection (red line). Results are shown for the CSVv2 algorithm in the left plot, while the results of the DeepCSV algorithm can be found in the right plot. The plots show the result of the best found SV collection, where SVs within the beam pipe and pixel layer positions were only removed, when their number of track ≤ 2, they have an invariant mass $\leq 1.5\,\text{GeV}$ and their number of flight lengths ≥ 3.5.

result can be that around 95 % of the b hadron decays happen before the position of the beam pipe is reached. The performance was also studied in different regions of transverse momentum and pseudorapidity of the jet. The splitting in two regions of $0 \leq |\eta| < 1.4$ and $1.4 \leq |\eta| < 2.4$ are shown in the left and right-handed plots in Figure 8.12, respectively. The upper row shows the performance for the CSVv2 algorithm, while the lower

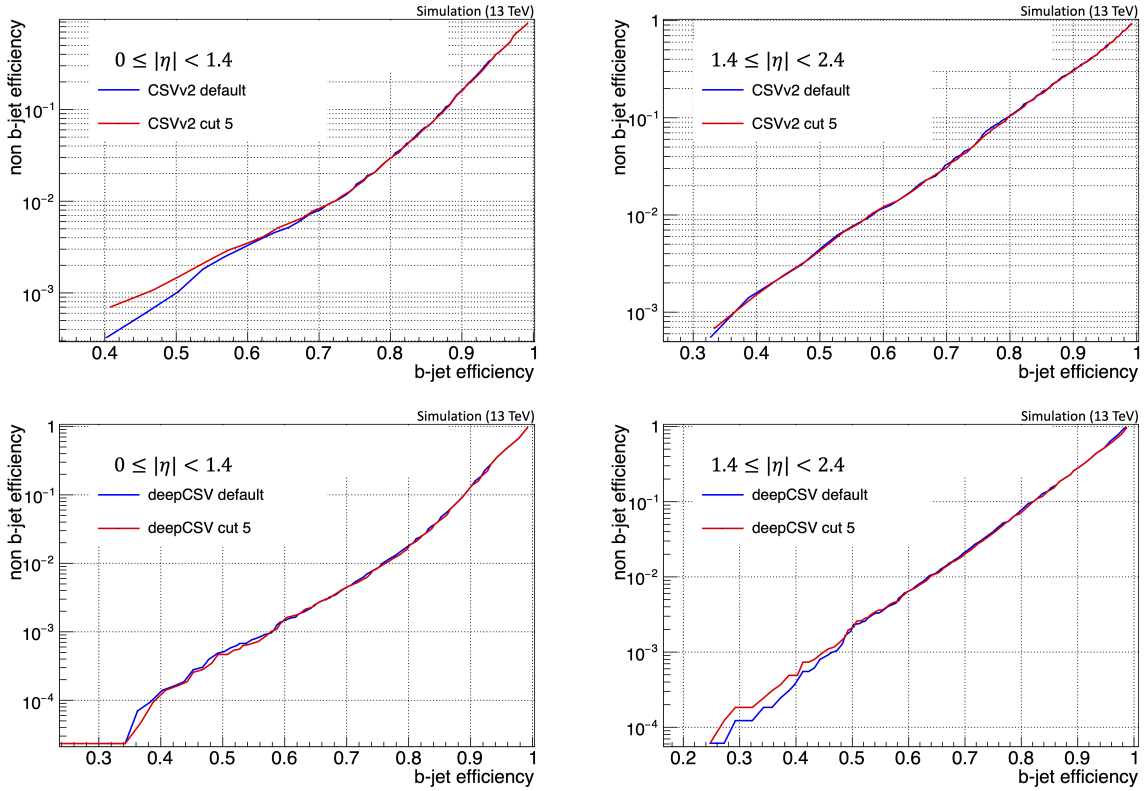

Figure 8.12: ROC curves to compare the performance of default SV selection (blue line) with modified SV collection (red line) within different jet $|\eta|$ regions. Results are shown for the CSVv2 algorithm in the upper row, while the results of the DeepCSV algorithm can be found in the lower row. All plots show the result of the best found SV collection as in Figure 8.10. The left upper and lower plot show the region of $0 \leq |\eta| < 1.4$. The region $1.4 \leq |\eta| < 2.4$ is shown in the right upper and lower plot.

row represents the DeepCSV algorithm results. In general, the plots with the higher $|\eta|$ region show a worse performance for both SV collections. In that region, the track reconstruction efficiency is worse (see Section 8.1.1) than the barrel part, which also impacts vertex and jet reconstruction, and hence b tagging is affected. Visible on all plots is that the same behaviour as in the upper and lower right plots in Figure 8.10. A different result can be found by splitting the jets up into two region of $30 < p_{\mathrm{T}} < 150\,\mathrm{GeV}$ and $150 < p_{\mathrm{T}} < 3000\,\mathrm{GeV}$, which is shown in the left and right-handed plots in Figure 8.13, respectively. Again the upper and lower row are split up into CSVv2 and DeepCSV tagger results. While the lower p_{T} region shows a similar behaviour as in the previous result, the higher jet p_{T} region shows an improvement in the upper and lower right plots in Fig-

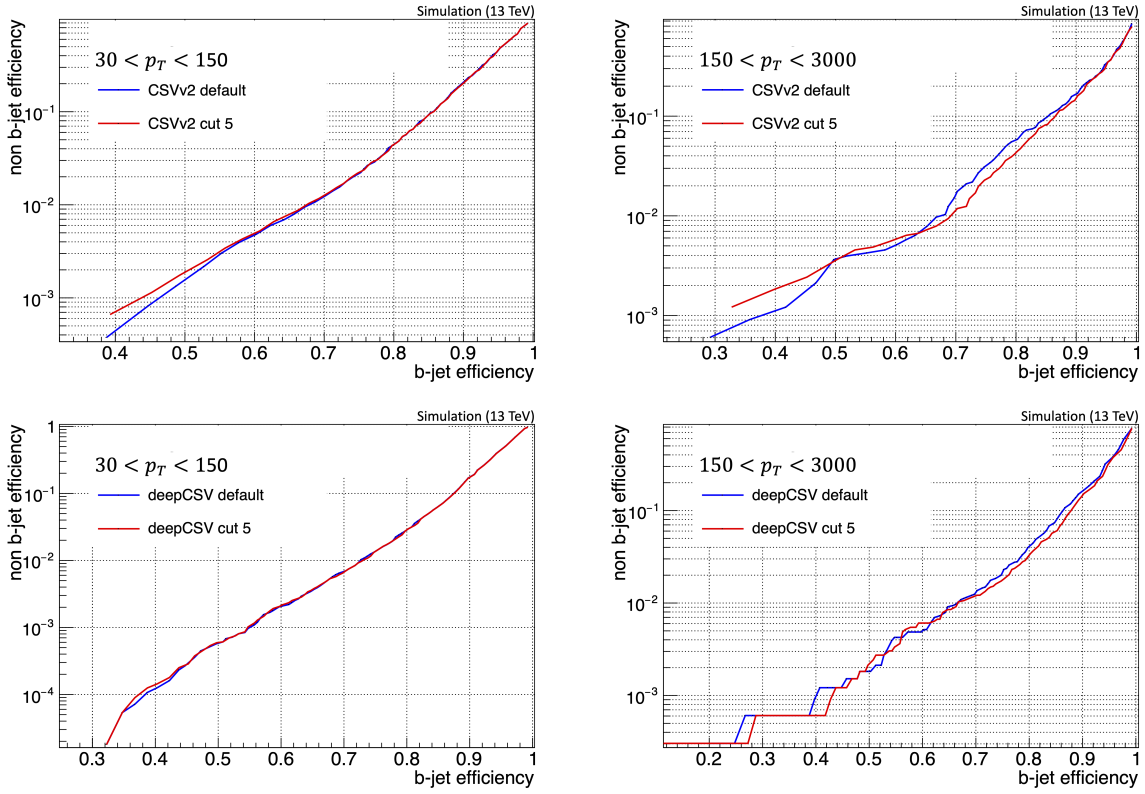

Figure 8.13: ROC curves to compare the performance of default SV selection (blue line) with modified SV collection (red line) within different jet p_{T} regions. Results are shown for the CSVv2 algorithm in the upper row, while the results of the DeepCSV algorithm can be found in the lower row. All plots show the result of the best found SV collection as in Figure 8.10. The left upper and lower plot show the region of $30 \leq p_{\mathrm{T}} < 150\,\mathrm{GeV}$. The region $150 \leq p_{\mathrm{T}} < 3000\,\mathrm{GeV}$ is shown in the right upper and lower plot.

ure 8.13. Especially for b jet efficiencies between 0.7 and 0.9, the selection of SVs with the requirements applied an improvement of around 1 % can be achieved for both the tagging algorithms studied. The wiggling structure in these two plots indicate that the statistics might be a bit low, particularly for lower b jet efficiencies. This result can be of interest for analyses searching for slightly more displaced b hadron decays with expected high p_{T} jets, as it could be for some processes with new, so far not found particles.

The combined results show on average, that a similar performance between two SV collections studied for both CSVv2 and DeepCSV algorithms. A similar performance for the default SV collection and the selected requirements was shown, without retraining the two taggers. This indicates that either the improvement of selection potentially more SVs

Table 8.1: Requirements and thresholds for SV, which are removed when requirements fulfilled and position is within the beam pipe and pixel layer positions.

Requirement	Threshold
Number of tracks	≤ 2
Invariant mass	$\leq 1.5\,\text{GeV}$
Number of flight lengths	≥ 3.5

from b hadrons (up to 4 %) was not enough or that without a re-training no improvement can be achieved. Nevertheless, the study shows there might be some improvement possible for analyses searching for new physics with high p_T jets and vertex displacement using CSVv2 or DeepCSV as tagging algorithm.
The performance of the DeepJet algorithm was not studied since it uses no hard requirements to select SVs applied, as described in Section 8.4.1.

8.5 Electrons and Photons

Electrons produce photons by bremsstrahlung in the presence of the Coulomb field of an atomic core. Photons, on the other hand, produce electron-positron pairs in the presence of a Coulomb field. Due to the detector material of the tracking system, these processes happen frequently. Therefore, the reconstruction of both particles has to take place in parallel.

As discussed in Section 8.2, the misidentification rate for electrons is increased by the combined procedure of the two seeding strategies. In order to lower the misidentification rate, several additional properties of the candidates are checked and have to fulfil certain thresholds. For example, the amount of radiated energy of the track, distances between the track extrapolation and the ECAL seeding clusters or the ratio between energies deposited in HCAL and ECAL associated with the track are evaluated, amongst others [79]. In addition, specific electron identification requirements (IDs) are provided by the CMS Collaboration and can be applied to selections of analyses to increase purity. The IDs use of different variables related to tracking properties, as well as shower shapes, differences between track and ECAL clusters and some more. A detailed description of these variables can be found in [98]. Since there are no or only very few events expected to have electrons in the signal analysed in this thesis, events are vetoed if electrons with $p_{\mathrm{T}} > 10\,\mathrm{GeV}$ are present, fulfilling the veto ID working point [99].

Photons are instead defined if no track can be linked to the cluster in the ECAL and a specific ratio between energy deposits in ECAL and HCAL is fulfilled [79]. As for the electrons, there are as well IDs defined for photons by the CMS Collaboration. In this analysis, events with photons of $p_{\mathrm{T}} > 15\,\mathrm{GeV}$ fulfilling a loose ID working point [100] are vetoed.

8.6 Muons

Depending on which information muons are reconstructed with, they are called differently, and different purity is achieved. Tracker muons are reconstructed by a track found in the tracking system with at least one additional hit in the muon chambers. If hits in the muon system alone are added together, this muon will be called standalone muon. Finally, global muons define muons, which are a combination of standalone muons and tracks in the tracking system. When global muons and tracker muons overlap, they are merged. Global muons have the advantage of information from two tracks, resulting in

better momentum resolution than tracker muons alone. Muon candidates can be further purified by using specific IDs [101]. The so-called loose working point with the highest efficiency is achieved if the muon is either a global or a tracker muon. Events with muons of $p_{\mathrm{T}} > 10\,\mathrm{GeV}$ fulfilling the loose working point are vetoed for the signal region. Nevertheless, a validation region is defined, and exactly one muon fulfilling the tight working point with $p_{\mathrm{T}} > 35\,\mathrm{GeV}$ is required. This working point has the lowest efficiency but the highest purity of the collection. The tight working point requires, on top of the criteria of the loose working point, criteria on the number of hits in the tracking system and the muon chambers, the goodness-of-fit parameter and transverse and longitudinal distances from the PV.

8.7 Taus

Taus are leptons of the third generation and with a mass of approximately 1777 MeV the heaviest copy of the electron. They are not stable and decay via different decay modes. They can decay into one lighter lepton, electron or muon, and two neutrinos, conserving the lepton number. Furthermore, decays into one neutrino and hadrons, as for example pions or kaons, are possible. Unfortunately, these decays mimic different other processes and taus can easily be misidentified. Nevertheless, it is possible to lower the misidentification rate with isolation criteria [102], since tau decays happen often well isolated from other particles in an event. The sum of the p_{T} all the particles within a cone size of $\Delta\mathrm{R}< 0.5$ around the tau candidate is used to increase the efficiency of the identification. Furthermore, an identification of tau candidates is performed using the numbers of charged hadrons and neutral pions. In addition rejections against muons or electron misidentification can be applied, but are not used for the analysis presented in this thesis.
Events containing tau candidates are removed in this analysis, if they are identified with $p_{\mathrm{T}} > 18\,\mathrm{GeV}$, $|\eta| < 2.3$, contain one neutral pion and one charged hadron, and if the transverse momentum within $\Delta\mathrm{R}< 0.5$ is below 2.0 GeV.

8.8 Missing Transverse Momentum

The initial state of the pp collision has negligible transverse momentum. Therefore, the sum of the transverse momentum of all final state particles of this collision is expected to

be close to zero again due to momentum conservation. Nevertheless, some particles do not or only rarely interact with the detector material, and escape it undetected, for example, the SM neutrinos or potentially new, so far undiscovered particles. Furthermore, very soft particles may be unrecorded. In addition, the precision of momentum measurements of reconstructed PF candidates affects as well the defined quantity called missing transverse momenta:

$$p_{\mathrm{T}}^{\mathrm{miss}} = |\vec{p}_{\mathrm{T}\ \mathrm{miss}}| = \left| -\sum_{i} \overrightarrow{p_{\mathrm{T},i}} \right|, \tag{8.5}$$

defined as the negative vectorial sum of the transverse momenta of all the PF candidates in the event. Since PU, as well as jet corrections for simulations, have an impact on the missing transverse momentum, both are taken into account for the calculation. This is done via the so-called *type-I* correction, where jet energy scale and jet energy correction is applied to the jets, which are propagated through the $p_{\mathrm{T}}^{\mathrm{miss}}$ calculation.
A $p_{\mathrm{T}}^{\mathrm{miss}} > 35\,\mathrm{GeV}$ requirement is applied to the validation region, where a W boson is reconstructed via the decay products of a tight ID muon and a neutrino.

Part III

Search for Long-Lived Particles Produced in Higgs Decays with b Quark-like Signature

This part presents a search for LLPs produced in SM Higgs boson decays, as predicted by different BSM theories (see Chapter 4). The search is sensitive to a LLP decaying into two b quarks with short lifetimes, corresponding to a physical decay lengths of up to 1 mm in the rest frame of the LLP[5]. An exemplary Feynman diagram of the Higgs boson and the LLP decay can be found in the left part of Figure 8.14. Translated to reconstructed objects, the search is targeting b jets, with slightly larger displacements than for SM b jets. Therefore, analysis techniques such as triggers using b tagging algorithms can be used, while identifying signal jets with standard reconstructed objects is not sufficient. The search is split into two analyses, a boosted and a resolved analysis, targeting LLPs with different masses; both are presented in the following.
Previous analyses probed similar theory models so far, for example, for LLP decays in the muon chamber [103], searches for displaced jets [104, 105] or for prompt decays [14]. Nevertheless, the phase spaces investigated in the two analyses described in this thesis are still unexplored with CMS data. While published analyses mainly focused on the associated production of the Higgs boson, the presented analyses focus on VBF and ggF Higgs boson production modes. An advantage of this is a higher cross section of the signal process. On the other hand, the events have not such a clear signature as for the other production modes, which results in signal events being similar to SM background events. Depending on the LLP mass, the signal signature consists of two (boosted analysis) or up to four (resolved analysis) b jets plus additional light jets from the VBF production per event. The dominant background consists of the QCD multijet production, and a ML technique is used to distinguish the background from the signal.
The following Chapter 9 describes fundamental components used for both analyses. Afterwards, the analyses for LLPs with boosted and resolved signatures of the b quark like jets are presented in Chapter 10 and Chapter 11, respectively. Finally, the results of both analyses are summarised in Chapter 12.

[5]Lifetimes of up to 10 mm are investigated, while the strategy aims for up to 1 mm.

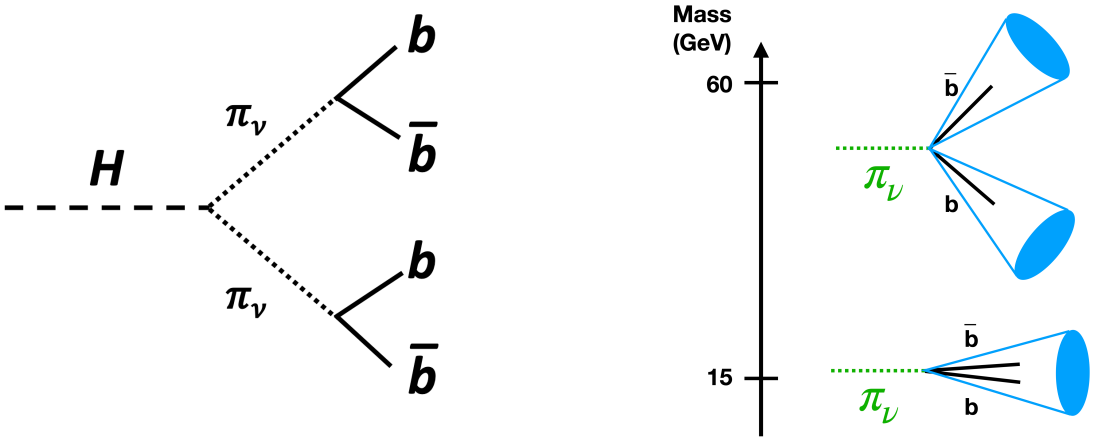

Figure 8.14: Feynman diagram for the decay of Higgs boson into a pair of LLPs and their subsequent decay into b quark-antiquark pairs (left). Impact of the mass of the LLP on the angular separation of its decay products (right).

9 Fundamental Analysis Components

Several fundamental concepts are shared in the two analyses (with boosted and resolved topology) described in this thesis. These concepts are described in the following, whereas more details and the analysis dependent strategies will be described in the corresponding analysis chapters.

9.1 Analysis Strategy

The signal events investigated in this thesis are expected to contain slightly displaced b jets. However, the reconstructed signal jets, i.e. jets matched to the decay products of the LLPs, have a relatively soft p_{T} (see Section 4.1), making it even more challenging to distinguish them from SM backgrounds. The displacement of the signature is depending on the LLP lifetime. In addition, the mass of the LLP has an impact on the signature of the signal. The distances in ΔR are not only different between the LLPs for different masses, but also for their decay products, as shown in Section 4.1.1. Low mass LLPs (15 GeV) result in collimated decay products and a boosted topology, while for higher masses (40 GeV and 55 GeV) the decay products are further apart in ΔR and have a resolved topology, as displayed in the right schematic of Figure 8.14.
Events are selected by triggers requiring a high jet multiplicity and b-tagged jets. Events containing photons or leptons are rejected. The signal properties are significantly affected by these selections, and the study results are presented in Section 9.3.1.
An event selection requiring jets of the VBF kinematics did not result in improvements to the signal efficiency and was therefore not applied.
The jets of interest, i.e. those originating from the LLP decay products, are chosen among all jets in a selected event based on their invariant mass. For example, the two jets per event of the boosted topology should give an invariant mass close to the mass of the SM Higgs boson. A ΔR requirement between the selected jets further suppresses SM background processes and completes the definition of the signal region (SR). A region to validate the background estimation is defined by inverting the Higgs mass window and

will be called in the following $\overline{\text{SR}}$. The $\overline{\text{SR}}$ has the same ΔR requirement applied as the SR, to make them similar.
After the selection the signal over background yield is further enhanced using a DNN (see Section 9.5). The DNN jet tagger is trained with mixtures of LLP masses and lifetimes and the two main backgrounds QCD multijet and $t\bar{t}$ production. Per jet quantities are used as input features. In addition, the mass and lifetime of the LLPs are used to parametrise the DNN. Therefore for each jet a discriminating value for each mass-lifetime combination can be obtained. A more detailed description can be found in Section 9.5.
An ABCD method is used to estimate the QCD multijet background in the SR from data. The regions are defined by the DNN discriminating values of the selected[1] signal jets. The $\overline{\text{SR}}$ and a $t\bar{t}$ control region (CR) are used to validate the ABCD method. Furthermore, the data-to-simulation agreement of the DNN discriminant is studied in the blinded SR, the $\overline{\text{SR}}$ and the $t\bar{t}$ CR.
The statistical analysis for both topologies is a counting experiment where the number of data events is compared to the sum of the signal and non-QCD background events expected from SM simulation and the number of QCD multijet background events expected from the data-driven background estimation.

9.2 Dataset, Simulated Events and Triggers

The data analysed in this thesis were produced in pp collisions by the LHC at $\sqrt{s} = 13\,\text{TeV}$ in 2016 and recorded by the CMS detector. The integrated luminosity is $\mathcal{L} = 36.3\,\text{fb}^{-1}$ [15]. For the analysis, a logical *or* of two triggers is applied. Both triggers require at least four jets of which three jets to be b tagged. A more detailed description of the triggers can be found in Section 9.2.1.
The signal samples contain events simulated according to the twin Higgs model [106] as described in Section 4.1. In this theory, a SM Higgs boson decays via a portal into two neutral LLP. Each LLP decays into a pair of fermions, with an expected predominant decay into b quark pairs. The branching ratio for the decay of the Higgs boson to two LLPs to four b quarks is set to 100 %. For the production of the Higgs boson in the signal events, the VBF channel with a cross section of $\sigma = 3.782\,\text{pb}$ [10] and the ggF channel with a cross section of $\sigma = 48.58\,\text{pb}$ [10] are considered. The numbers of simulated events for the different production modes and for each simulated LLP mass and lifetime are listed in

[1] The jets which are meant to differ for the boosted and resolved analysis, and a detailed description can be found in the corresponding chapters.

Table 9.1: Twin Higgs model signal samples for VBF Higgs production with a cross section of $\sigma = 3.782\,\text{pb}$. All samples in the list are generated with POWHEG, and the showering is simulated with PYTHIA8. Listed are the masses and lifetimes of the LLPs within the samples, as well as the number of simulated events.

Mass [GeV]	Lifetime [mm]	Events [10^3]
15	0	50
	0.05	246
	0.1	246
	1	240
	5	180
	10	1,019
40	0	181
	0.05	259
	0.1	247
	1	1,022
	5	249
	10	251
55	0	237
	0.05	230
	0.1	262
	1	244
	5	249
	10	233

Tables 9.1 and 9.2, respectively. For the phase space investigated in this analysis, masses and lifetimes of the LLP between 15-55 GeV and 0-10 mm are considered. The samples are generated with POWHEG [59], the parton showering is simulated with PYTHIA8 [60], and the underlying event is tuned according to CUETP8M1 [107, 108].

Several SM background processes are taken into account in this analysis. For visibility reasons, processes are combined, and groups are used in the following chapters: *QCD*, $t\bar{t}$, *SM Higgs* and *Others*. A complete list is given in Table 9.3. If not stated otherwise, the parton showering process for the background simulation is performed using PYTHIA8. QCD multijet samples, split up in H_T bins, are generated with MADGRAPH with the MLM matching scheme [61] applied. Events for the $t\bar{t}$ background were generated with POWHEG and contain all $t\bar{t}$ decay channels. Within the *SM Higgs* group, different SM Higgs production modes are taken into account. For the generation of the VBF di-Higgs production, MADGRAPH is used, while Higgs boson events produced via VBF, ggF, and

Table 9.2: Twin Higgs model signal samples for ggF Higgs production with a cross section of $\sigma = 48.58\,\text{pb}$. All samples in the list are generated with POWHEG, and the showering is simulated with PYTHIA8. Listed are the masses and lifetimes of the LLPs within the samples, as well as the number of simulated events.

Mass [GeV]	lifetime [mm]	Events [10^3]
15	1	48
	10	1,905
40	1	1,847
	10	1,927
55	1	1,857
	10	1,934

$W/Z/t\bar{t}$ associated Higgs production modes are generated using POWHEG. In all these samples, a decay of the Higgs boson into two b quarks is required[2], while different decay channels for the W and Z bosons are taken into account. The $b\bar{b}$ associated Higgs boson production sample generation follows the instructions in Reference [109] and is produced with MADGRAPH5_aMC@NLO [62]. The group *Others* contains various other SM processes which will be discussed in the following. Diboson samples (WW, WZ and ZZ) are generated with PYTHIA8. Samples with W boson in association with additional jet radiation, where the W boson decays to qq and $l\nu$ are generated with MADGRAPH. The same generation is used for the DY process, where a Z boson or a γ decays to qq. Finally, three different single *top* quark production modes are taken into account. The samples with t- and tW-channel production are generated with POWHEG, while for the s-channel MADGRAPH5_aMC@NLO is used for the generation. The cross sections used for the normalisation of the background processes can be found in Tables 9.4 and 9.5.

All signal and background samples are generated using the NNPDF3.0 [54] PDFs sets. The interaction of all simulated particles with the detector material is simulated with the GEANT4 toolkit [63].

All simulated events are corrected to match the PU profile in data. The total inelastic pp cross section of approximately 69 mb [110] is taken into account to calculate the mean number of expected pp interactions in recorded data with similar detector conditions (called lumi-block). These values are then compared to simulated events, and a weight is derived and applied. The JEC, as described in Section 8.3.2 is applied to data and

[2]The large branching fraction from the Higgs boson to b quarks makes this process the most important one.

Table 9.3: Simulated SM background processes taken into account for this analysis. Listed are the group of the samples, the SM process, the number of events and the generator used for simulation.

Group	Process	Events [10^6]	Generator
QCD	QCD, $H_T \in [100, 200)$	76.9	MadGraph + Pythia
	QCD, $H_T \in [200, 300)$	18.7	MadGraph + Pythia
	QCD, $H_T \in [300, 500)$	12.9	MadGraph + Pythia
	QCD, $H_T \in [500, 700)$	16.5	MadGraph + Pythia
	QCD, $H_T \in [700, 1000)$	15.6	MadGraph + Pythia
	QCD, $H_T \in [1000, 1500)$	3.7	MadGraph + Pythia
	QCD, $H_T \in [1500, 2000)$	3.9	MadGraph + Pythia
	QCD, $H_T \in [2000, \infty)$	1.4	MadGraph + Pythia
$t\bar{t}$	$t\bar{t}$	67.4	Powheg + Pythia
SM Higgs	VBFH: H$\to b\bar{b}$	1.0	Powheg + Pythia
	VBFHH: HH$\to 4b$	0.3	MadGraph + Pythia
	ggFH: H$\to b\bar{b}$	4.9	Powheg + Pythia
	$b\bar{b}$H: H$\to b\bar{b}$	0.7	aMC@NLO
	$t\bar{t}$H: H$\to b\bar{b}$	3.6	Powheg + Pythia
	ZH: H$\to b\bar{b}$, Z$\to qq$	0.5	Powheg + Pythia
	ZH: H$\to b\bar{b}$, Z$\to \nu\nu$	2.9	Powheg + Pythia
	ZH: H$\to b\bar{b}$, Z$\to ll$	2.0	Powheg + Pythia
	W$^-$H: H$\to b\bar{b}$, W$^- \to qq$	0.5	Powheg + Pythia
	W$^+$H: H$\to b\bar{b}$, W$^+ \to qq$	0.5	Powheg + Pythia
	W$^-$H: H$\to b\bar{b}$, W$^- \to l\nu$	1.0	Powheg + Pythia
	W$^+$H: H$\to b\bar{b}$, W$^+ \to l\nu$	1.0	Powheg + Pythia
Others	WW	1.0	Pythia
	WZ	1.0	Pythia
	ZZ	1.0	Pythia
	W + jets: W$\to qq$	15.8	MadGraph + Pythia
	W + jets: W$\to l\nu$	24.1	MadGraph + Pythia
	DY: Z/$\gamma \to qq$	10.0	MadGraph + Pythia
	Single t, t-channel	56.8	Powheg + Pythia
	Single $\bar{t}$, t-channel	38.8	Powheg + Pythia
	Single t, s-channel	1.0	aMC@NLO + Pythia
	Single t, tW-channel	7.0	Powheg + Pythia
	Single $\bar{t}$, tW-channel	6.9	Powheg + Pythia

Table 9.4: Listed are the cross sections of the QCD multijet productions.

Group	Process	Cross section [pb]
QCD	QCD, $H_T \in [100, 200)$	$2.8 \cdot 10^7$
	QCD, $H_T \in [200, 300)$	$1.7 \cdot 10^6$
	QCD, $H_T \in [300, 500)$	$3.5 \cdot 10^5$
	QCD, $H_T \in [500, 700)$	$3.2 \cdot 10^4$
	QCD, $H_T \in [700, 1000)$	$6.8 \cdot 10^3$
	QCD, $H_T \in [1000, 1500)$	$1.2 \cdot 10^3$
	QCD, $H_T \in [1500, 2000)$	120.0
	QCD, $H_T \in [2000, \infty)$	25.3

simulation, while simulated events are afterwards corrected for JER. The b tagging corrections are applied to simulated events (see Section 8.4.1). In 2016 and 2017, the ECAL timing was not correctly propagated to different detector parts. Therefore, jets with high pseudorapidity ($2.0 < |\eta| < 3.0$) have a certain probability of being wrongly associated with the previous bunch crossing, called *prefiring*. This is not described in simulated events. Therefore, a weight representing the probability of an event to prefire is derived and applied to simulated events. This probability-based weight reproduces the behaviour in data. This issue was fixed for the 2018 data taking period.

Simulated samples are normalised to allow comparisons to recorded data. The normalisation weight is calculated as:

$$w = \frac{\sigma \mathcal{L}}{N}, \tag{9.1}$$

with the cross section σ of the dedicated process, the integrated luminosity $\mathcal{L} = 36.3\,\text{fb}^{-1}$ of the recorded dataset and N the number of events of the sample. The cross sections of the QCD multijet productions can be found in Table 9.4, and in Table 9.5 for the remaining SM backgrounds.

9.2.1 Trigger

The two triggers, which are combined by a logical *or* requiring at least four jets of which at least three have to be b-tagged jets. The HLT path of each trigger consists of several filter steps, requiring different objects to be within the event. The HLT path for both triggers are:

Table 9.5: Cross section and uncertainty for simulated SM background processes. The value given for the uncertainty combines the uncertainties of scale and PDFs and α_S.

Group	Process	Cross section [pb]	Uncertainty [%]	Reference
$t\bar{t}$	$t\bar{t}$	831.76	$^{+6.6}_{-7.8}$	[111–115]
SM Higgs	VBFH: H$\to b\bar{b}$	3.78	$^{+2.5}_{-2.4}$	[10]
	VBFHH: HH$\to$4b	$1.6 \cdot 10^{-3}$	10	[10]
	ggFH: H$\to b\bar{b}$	48.6	$^{+7.8}_{-9.9}$	[10]
	$b\bar{b}$H: H$\to b\bar{b}$	0.49	$^{+20.2}_{-23.9}$	[10]
	$t\bar{t}$H: H$\to b\bar{b}$	0.51	$^{+9.4}_{-12.8}$	[10]
	ZH: H$\to b\bar{b}$, Z$\to qq$	0.68	$^{+5.4}_{-4.7}$	[10]
	ZH: H$\to b\bar{b}$, Z$\to \nu\nu$	0.18	$^{+5.4}_{-4.7}$	[10]
	ZH: H$\to b\bar{b}$, Z$\to ll$	$2.98 \cdot 10^{-2}$	$^{+5.4}_{-4.7}$	[10]
	W$^-$H: H$\to b\bar{b}$, W$^- \to qq$	0.47	$^{+2.4}_{-2.6}$	[10]
	W$^+$H: H$\to b\bar{b}$, W$^+ \to qq$	0.75	$^{+2.4}_{-2.6}$	[10]
	W$^-$H: H$\to b\bar{b}$, W$^- \to l\nu$	$5.98 \cdot 10^{-2}$	$^{+2.4}_{-2.7}$	[10]
	W$^+$H: H$\to b\bar{b}$, W$^+ \to l\nu$	$9.43 \cdot 10^{-2}$	$^{+2.3}_{-2.5}$	[10]
Others	WW	118.7	$^{+2.5}_{-2.2}$	[116]
	WZ	46.7	10	[117]
	ZZ	16.0	$^{+3.7}_{-2.6}$	[117]
	W + jets: W$^- \to qq$	$3.1 \cdot 10^3$	20	
	W + jets: W$^- \to l\nu$	$5.0 \cdot 10^4$	20	
	DY: Z/$\gamma \to qq$	$1.2 \cdot 10^3$	10	[118]
	Single t, t-channel	136.0	$^{+5.6}_{-4.9}$	[119, 120]
	Single $\bar{t}$, t-channel	81.0	$^{+7.1}_{-6.0}$	[119, 120]
	Single t, s-channel	3.36	$^{+5.4}_{-5.1}$	[119, 120]
	Single t, tW-channel	35.9	$^{+7.3}_{-7.3}$	[121, 122]
	Single $\bar{t}$, tW-channel	35.9	$^{+7.3}_{-7.3}$	[121, 122]

Trigger name: **HLT_QuadJet45_TripleBTagCSV**

1. **hltL1sQuadJetCIorTripleJetVBFIorHTT**: Specific L1 trigger found required objects.
2. **hltQuadCentralJet45**: At least four jets with $p_{\mathrm{T}} \geq 45\,\mathrm{GeV}$ within $|\eta| \leq 2.6$ were found.
3. **hltBTagCaloCSVp087Triple**: At least three out of eight leading jets fulfil a b tag requirement at HLT level. The online CSV discriminant of 0.56 needs to be fulfilled.
4. **hltQuadPFCentralJetLooseID45**: The jet reconstruction efficiency has to exceeds 99 % for all four jets from filter 2.

Trigger name: **HLT_DoubleJet90_Double30_TripleBTagCSV**

1. **hltL1sTripleJetVBFIorHTTIorDoubleJetCIorSingleJet**: Specific L1 trigger found requried objects.
2. **hltQuadCentralJet30**: At least four jets with $p_{\mathrm{T}} \geq 30\,\mathrm{GeV}$ within $|\eta| \leq 2.6$ were found.
3. **hltDoubleCentralJet90**: At least two jets with $p_{\mathrm{T}} \geq 90\,\mathrm{GeV}$ within $|\eta| \leq 2.6$ were found.
4. **hltBTagCaloCSVp087Triple**: At least three out of eight leading jets fulfil a b tag requirement at HLT level. The online CSV discriminant of 0.56 needs to be fulfilled.
5. **hltQuadPFCentralJetLooseID30**: The jet reconstruction efficiency has to exceeds 99 % for all four jets from filter 2.
6. **hltDoublePFCentralJetLooseID90**: The jet reconstruction efficiency has to exceeds 99 % for all four jets from filter 3.

Both HLT paths require the same online b tagging requirement, which is similar to offline b tagging. Online b tagging uses objects found at trigger level and these objects can differ from the ones reconstructed offline, as described in Section 7.2.6.
The efficiency of the trigger requirement, calculated as the number of events passing the trigger divided by the total number of events, is shown in Figure 9.1 for VBF (upper

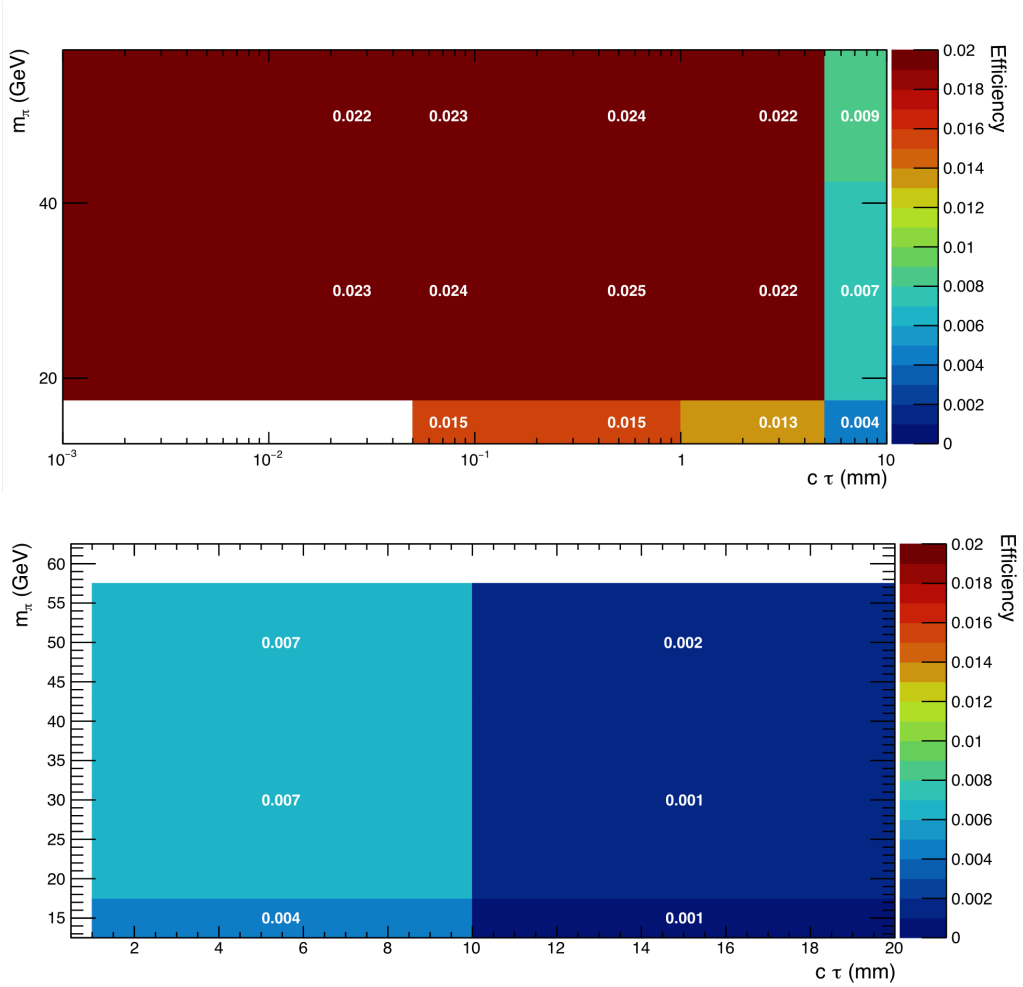

Figure 9.1: Trigger efficiencies for the two triggers combined by a logical *or* for VBF (upper) and ggF (lower plot) signal, depending on masses and lifetimes of the LLPs. Masses of 15, 40 and 55 GeV with lifetimes between 0 mm and 5 mm for VBF samples and 1 mm and 10 mm for ggF samples are shown.

plot) and ggF (lower plot) signal, depending on the masses (15, 40 and 55 GeV) and the lifetimes (0-5 mm and 1-10 mm, respectively) of the LLPs. The lower trigger efficiency of the ggF compared to the VBF Higgs production is due to the lower jet multiplicity in the event. Since the cross section for ggF is about an order of magnitude larger than for VBF production, ggF events are still a significant contribution even with a smaller trigger efficiency. The trigger efficiency decreases for both production modes above 1 mm lifetimes. This happens because longer lifetimes correspond to larger displacements which lead to worse jet reconstruction and b tagging efficiency. The efficiency is also worse for lighter LLPs due to the boosted topology, where instead of four, only two signal jets

originating from the LLPs are expected.
The trigger efficiency in simulation is corrected to match the efficiency in data, as described in Reference [123]. The same online object can be used across the different steps of the HLT path, to fulfil the requirements. Therefore, the trigger efficiency needs to be calculated step by step, taking all steps in the HLT paths into account. For this efficiency calculation, data and simulated $t\bar{t}$ events are used. The efficiency of each filter step takes only events into account which passed the previous steps, the jets are ordered in p_{T}. This procedure has to be adjusted for the filter with the b tagging requirement, since only two b jets are expected for the simulated $t\bar{t}$ events. The jets are ordered now via their b tagging discriminant. Out of that value, the probability is derived that three jets are able to pass the online b tagging requirement. This probability is used to derive the efficiency of the filter. The different filter efficiencies are fitted by different functions, matching each efficiency the best. The different filter efficiencies are combined into a trigger efficiency for each HLT trigger separately. Finally, the efficiency that the event fulfils one or both HLT triggers is derived and functions are fitted to the efficiency curves. Out of that fitted efficiencies a combined correction factor is calculated comparing the efficiencies in data and simulated events.

9.3 Event Preselection

As mentioned before, two triggers requiring jets and b-tagged jets are combined by a logical *or* to select events of interest. Online trigger objects are matched with $\Delta\mathrm{R} \leq 0.5$ to the offline reconstructed objects used in the analysis to ensure trigger objects are reconstructed and used in the analysis. Therefore, events only fulfil this requirement if all online trigger objects are matched, while one offline object can be matched to one or multiple online objects.
Events used for the analysis have to contain at least four AK4 CHS jets, as required from the triggers. The jets have to fulfil optimised selections such that the jet reconstruction efficiency exceeds 90 % with a noise jet rejection of more than 90 % (also referred to as tight ID). Furthermore, the jets are required to fulfil $p_{\mathrm{T}} \geq 30\,\mathrm{GeV}$ and $|\eta| \leq 2.4$. In addition, the sum of all jet p_{T}, called H_{T}, needs to be above 250 GeV. Events are removed if they contain loose ID photons (defined in Section 8.5) with $p_{\mathrm{T}} > 15\,\mathrm{GeV}$, loose ID μ (defined in Section 8.6) with $p_{\mathrm{T}} > 10\,\mathrm{GeV}$, veto ID e with $p_{\mathrm{T}} > 10\,\mathrm{GeV}$ (see Section 8.5) or τ with $p_{\mathrm{T}} > 18\,\mathrm{GeV}$ (see Section 8.7). In Figure 9.2, distributions of H_{T} (upper left), $p_{\mathrm{T}}^{\mathrm{miss}}$ (upper right) and the number of CHS jets with tight ID (lower) after these preselection

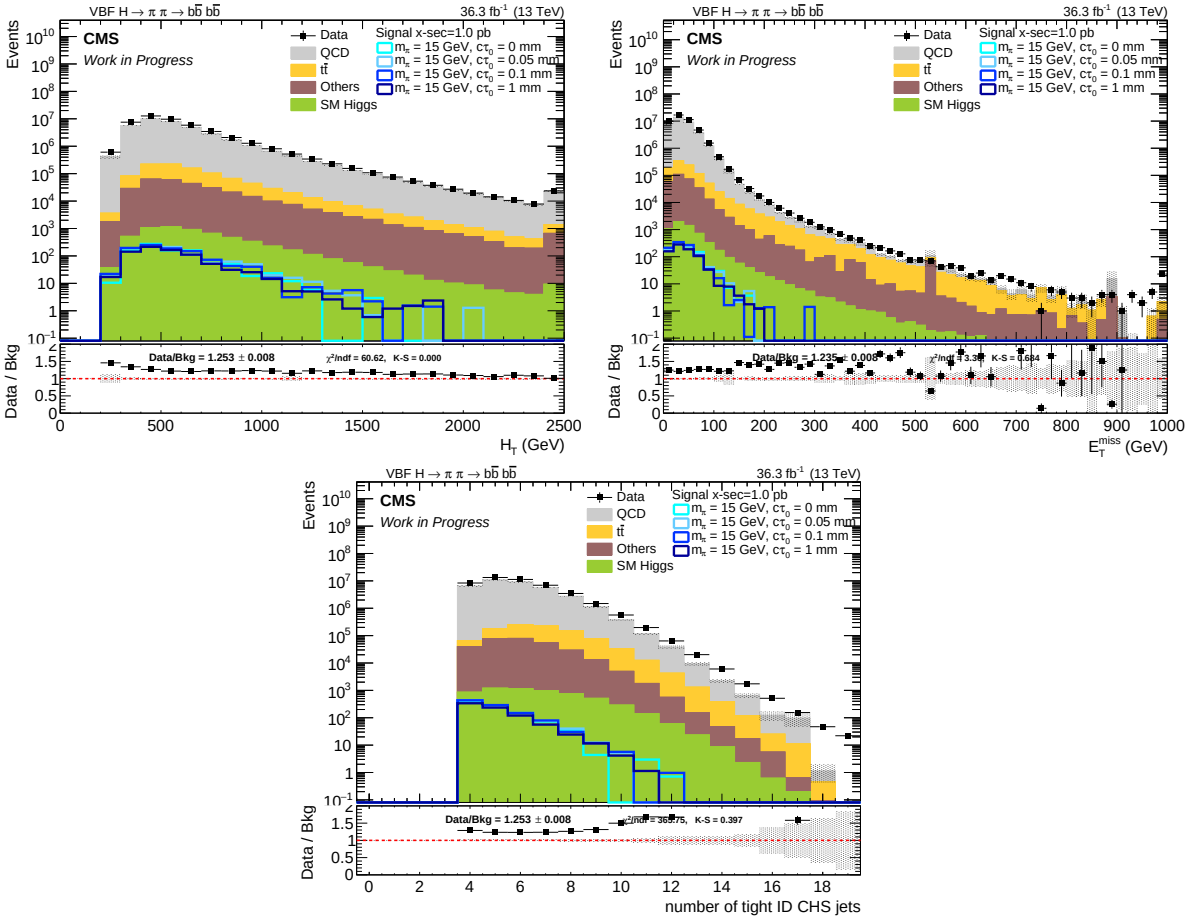

Figure 9.2: Distribution of H_{T} (upper left), $p_{\mathrm{T}}^{\mathrm{miss}}$ (upper right) and number of AK4 CHS jets with tight ID (lower) after preselection. Black filled squares represent data. The SM background events are stacked and represented by the coloured areas and lines indicate the signal prediction. All simulated evens are normalised with the weight from Equation 9.1. The lower panel shows the ratio of data and the predicted background yield per bin. Only statistical uncertainties are shown.

steps can be found. Furthermore, the p_{T} (left plots) and η (right plots) distributions of the four leading jets, sorted via p_{T}, are shown in Figure 9.3, where each row represents one jet. In both sets of plots, only statistical uncertainties are shown. Data and simulation are, beside a constant offset, in good agreement.

The impacts of each requirement on signal and SM background samples are presented in Sections 10.1 and 11.1, with the complete analysis selection for each topology separately.

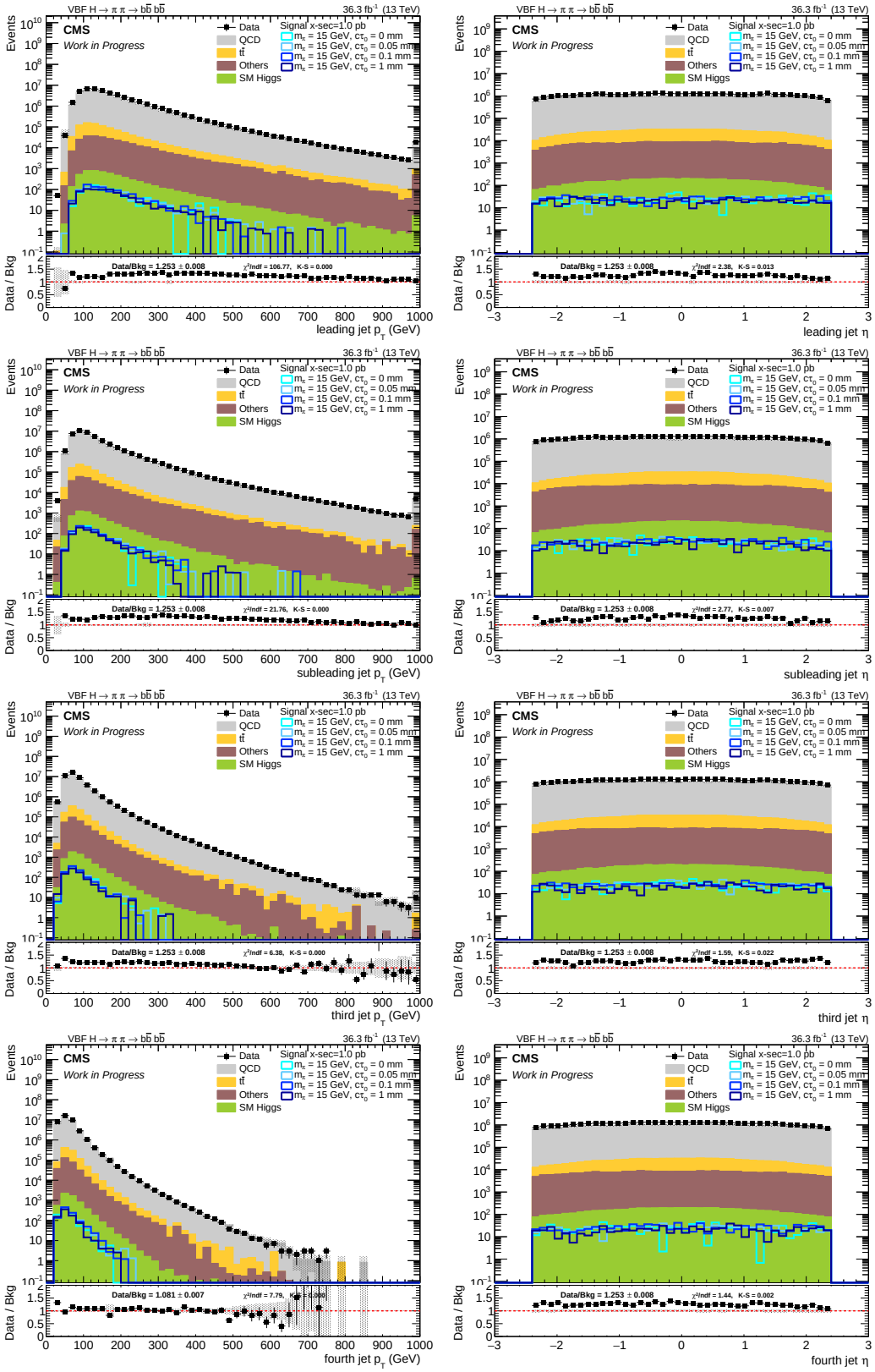

Figure 9.3: Distributions of the p_{T} (left) and η (right) of the jets with the largest (top row) through fourth largest (lowest row) p_{T}. Only statistical uncertainties are shown.

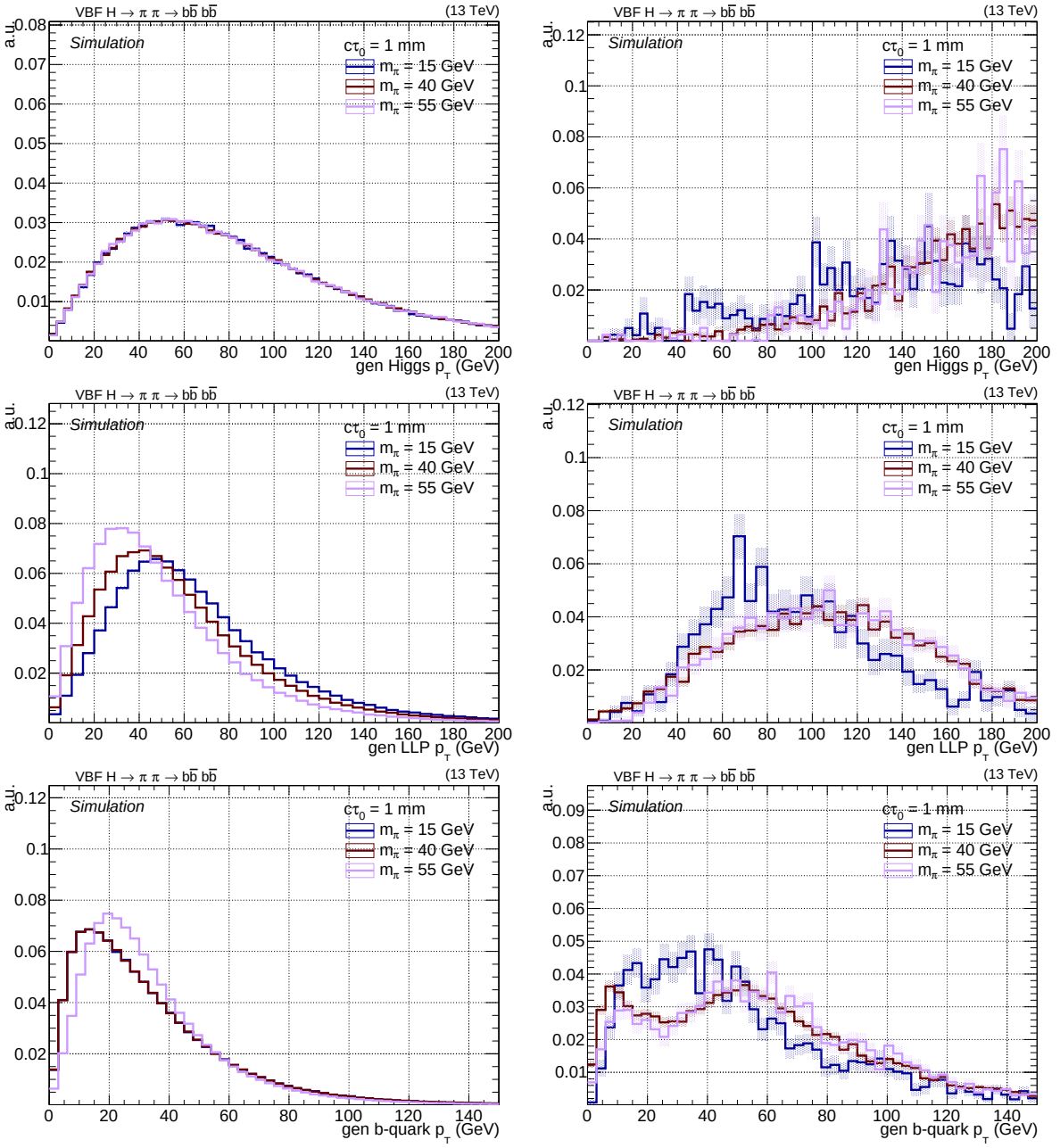

Figure 9.4: The p_{T} distribution of signal with VBF Higgs production mode without any selection (left) and after preselection (right) of the Higgs boson (upper row), the two LLPs (middle row) and the four b quarks originated from the LLPs (last row).

9.3.1 Signal Properties after Preselection

The signal properties without any selections are presented in Section 4.1.1. However, these properties are significantly changed by the preselection. Therefore, a study was performed

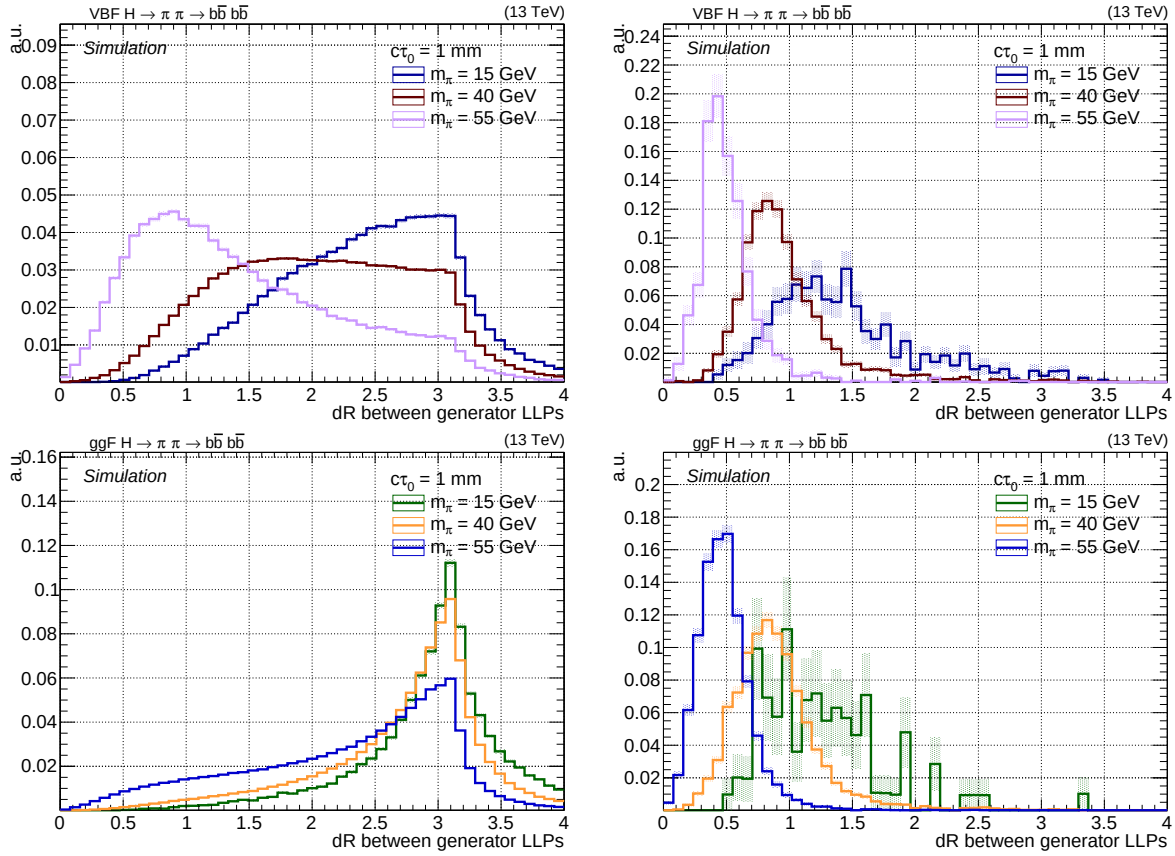

Figure 9.5: The ΔR distributions between the two LLPs of signal with VBF (upper) and ggF (lower) Higgs production mode without any selection (left) and after preselection (right).

to understand the properties after the preselections, and the results are presented in the following.

In the following, distributions without any selections (left) are compared with those after the preselections (right). The p_{T} distributions for the signal produced with the VBF Higgs boson production mode is shown in Figure 9.4. The distributions of the Higgs boson, the LLPs and the b quarks are presented. Especially the distributions of the Higgs boson and the LLPs are shifted towards higher p_{T} values. These events with higher p_{T} values are preferably selected by the requirements of the two triggers, presented in Section 9.2. The probability that at least four jets, fulfilling the p_{T} requirements of the triggers, are reconstructed, is more likely when the Higgs boson has enough p_{T}. Even though the p_{T} distribution without any selection are different for the VBF and ggF Higgs boson production mode, they are similar after the preselection requirements, and therefore, they are not presented here.

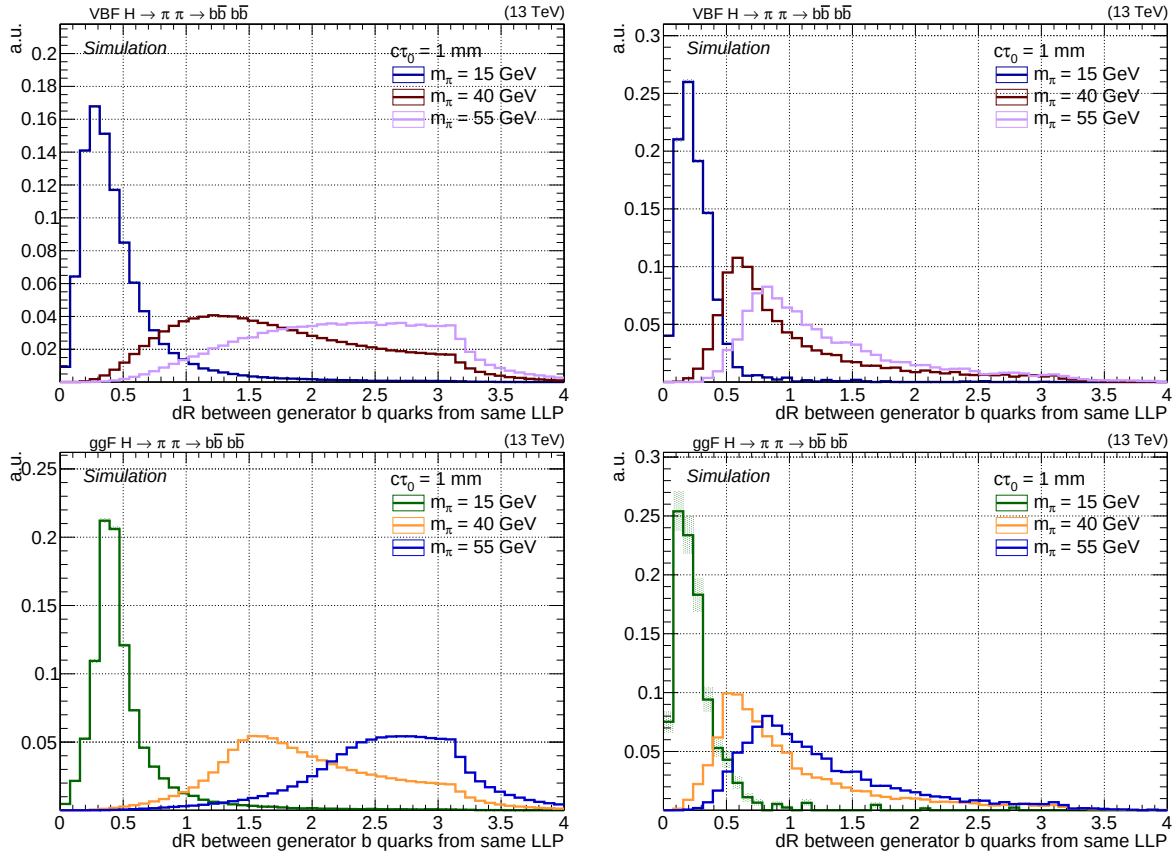

Figure 9.6: The ΔR distributions between the two b quarks, originated from the same LLP of signal with VBF (upper) and ggF (lower) Higgs production mode without any selection (left) and after preselection (right).

The change in the p_{T} distributions also affects the ΔR distributions of the decay processes. The ΔR distributions between the two LLPs with the VBF (upper) and ggF (lower) Higgs boson production modes are shown in Figure 9.5. After the preselection requirements, the LLPs are closer together across all different masses, and the distributions of both production modes become very similar. An impact is also visible in the decay products of the LLPs. The ΔR distributions of the b quarks originating from the same LLP are presented in Figure 9.6. The boost induced by the higher p_{T} of the LLPs is, in particular, observable for the higher masses of the LLPs, but also affects the lower masses. Again the distributions become very similar for the two Higgs boson production modes. Furthermore, the distributions of the closest and farthest b quarks originating from different LLPs are shown in Figures 9.7 and 9.8, respectively. For both distributions, events are selected by the preselection requirements with smaller distances between the b quarks.
The change in the kinematics is important for the selections of the two different analyses

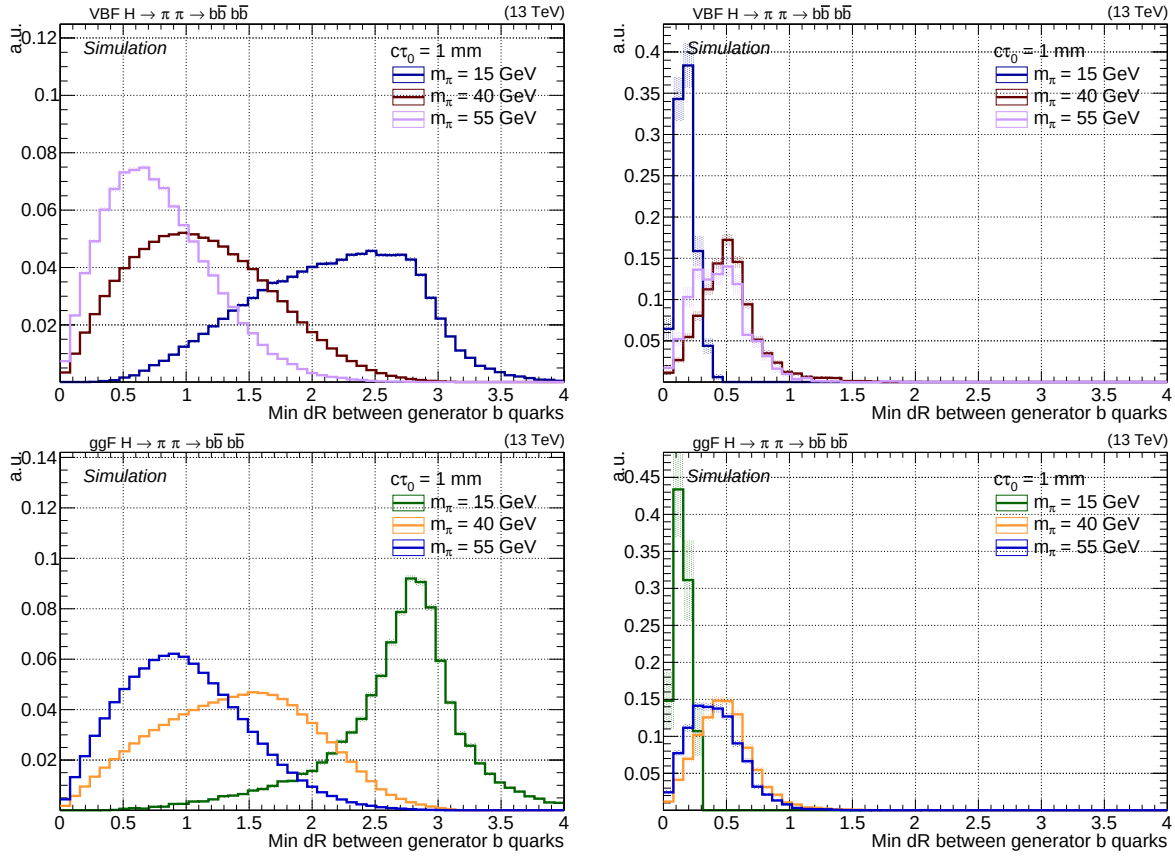

Figure 9.7: The ΔR distributions between the two closest b quarks, originated from different LLPs of signal with VBF (upper) and ggF (lower) Higgs production mode without any selection (left) and after preselection (right).

in the following and affect, for example, the reconstructed jet multiplicity of signal events.

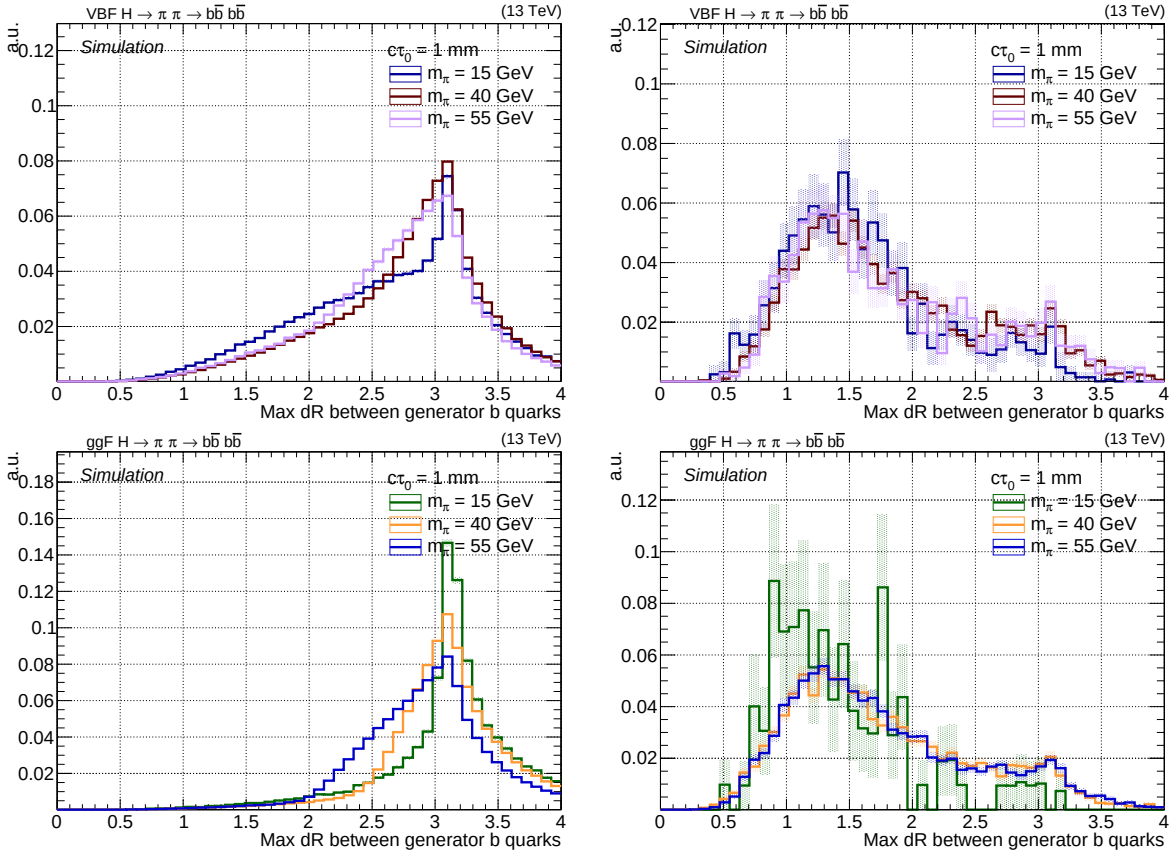

Figure 9.8: The ΔR distributions between the two farthest b quarks, originated from different LLPs of signal with VBF (upper) and ggF (lower) Higgs production mode without any selection (left) and after preselection (right).

9.4 $t\bar{t}$ Control Region

A $t\bar{t}$ CR is defined and mainly used to test the background estimation method. The same preselection with triggers, H_T, jets and veto of photons, e and τ leptons is applied as described in Section 9.3, but instead of zero muons, exactly one tight ID muon with $p_T > 35\,\text{GeV}$ is required in each event. In addition, $p_T^{\text{miss}} > 35\,\text{GeV}$ and a minimum $\Delta\phi > 0.2$ between the muon and p_T^{miss} needs to be fulfilled. Furthermore, the transverse mass of the combined object of muon and p_T^{miss} needs to be above 100 GeV. The latter requirement serves to remove potential signal events where a Higgs boson is produced in association with a W boson. Corrections to the simulated events due to μ ID and isolation criterion depending on p_T and η are applied in addition to those described in Section 9.2.

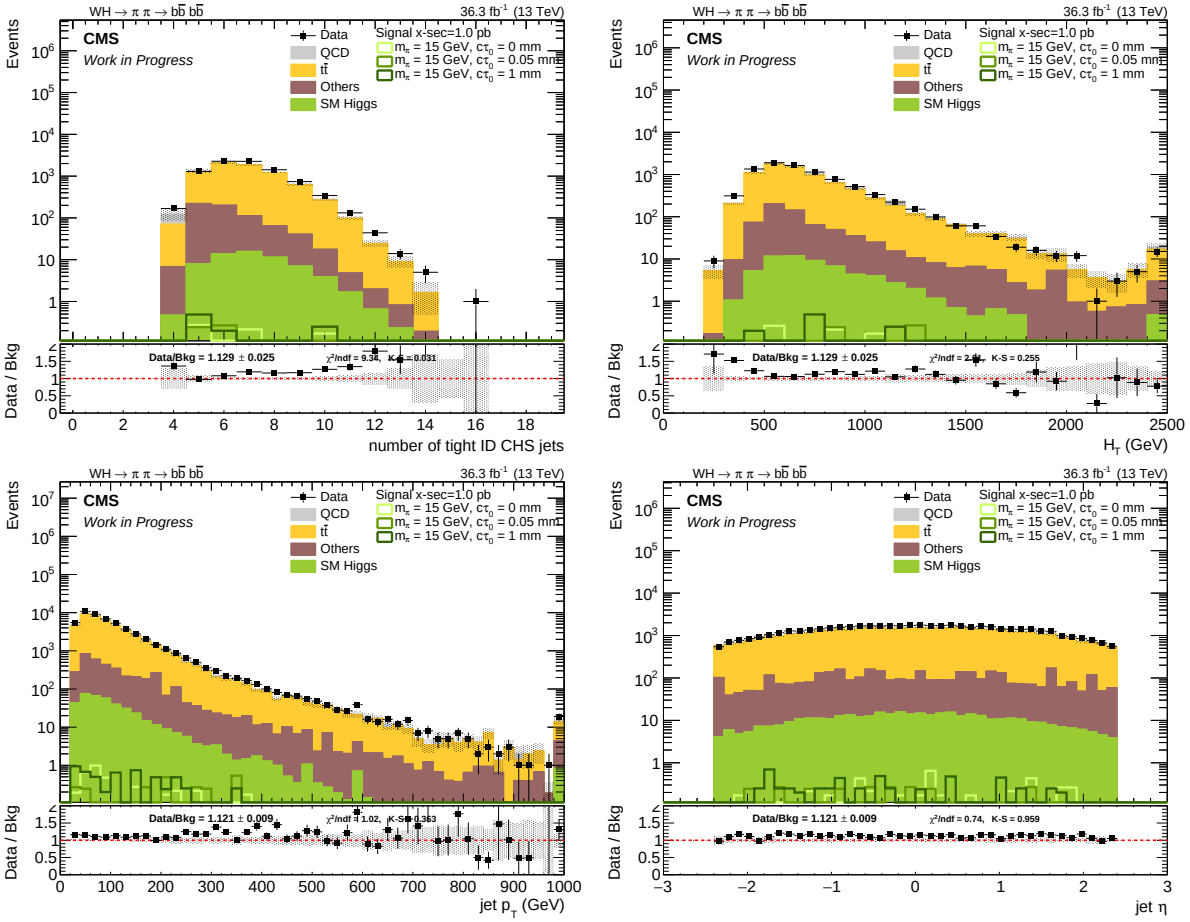

Figure 9.9: Distribution in $t\bar{t}$ CR after the baseline section of the number of CHS jets (upper left), H_T (upper right), p_T and η of all jets (lower left and right). Only statistical uncertainties are shown.

Distributions of the jet multiplicity (upper left), H_{T} (upper right) as well as p_{T} and η of all jets (lower left and right) for events in this $t\bar{t}$ CR are shown in Figure 9.9. As can be seen, the CR is dominated by $t\bar{t}$ events, and a good agreement between simulation and data is observed.

9.5 Parametrised Jet Tagger

The signal of the analyses presented in this thesis is quite similar to QCD multijet background events, as already visible after the preselection (see Figure 9.2). A DNN-based jet tagging method has been developed, to identify jets originated by decay products of LLPs, and discriminate those of SM background jets. A basic description of ML applications for high-energy physics can be found in Chapter 6.
The analyses in this thesis cover the boosted and resolved signal event topology. The properties of the jets are different due to the two topologies, but also differ with the lifetime of the LLP. Typically, a single DNN would only show good performance on sub-parts of the investigated signal, and therefore the training of several DNN would have been needed. Instead, the parametrised DNN [124], used in this thesis, takes the masses and lifetimes of the LLPs as input features and provides discriminating values for each of these combinations. The advantage is, that only one DNN is trained and the amount of jets needed for training is reduced. Furthermore, discriminating values for mass-lifetime combinations of the LLPs not used for training can be provided. The values for the background of the LLP mass-lifetime combinations are randomly sampled from

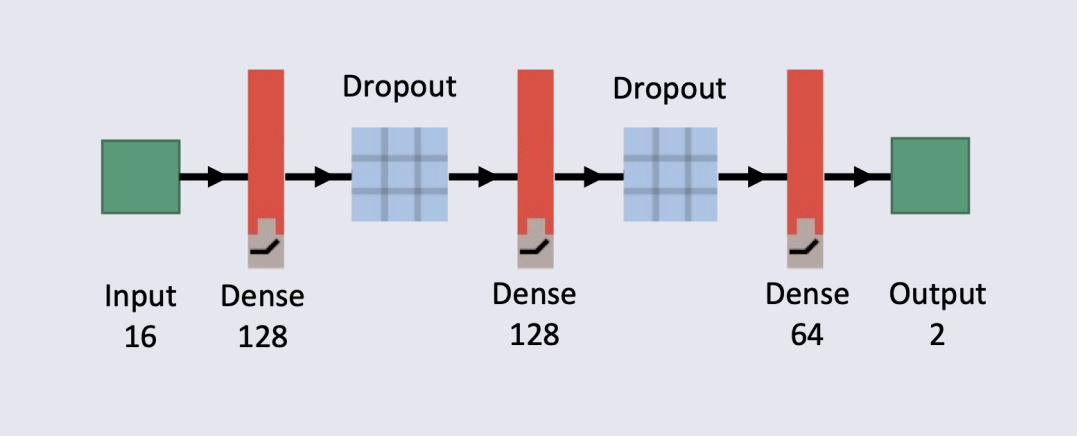

Figure 9.10: Architecture used for the parametrised DNN with 16 input features, three dense layers and two dropout stages.

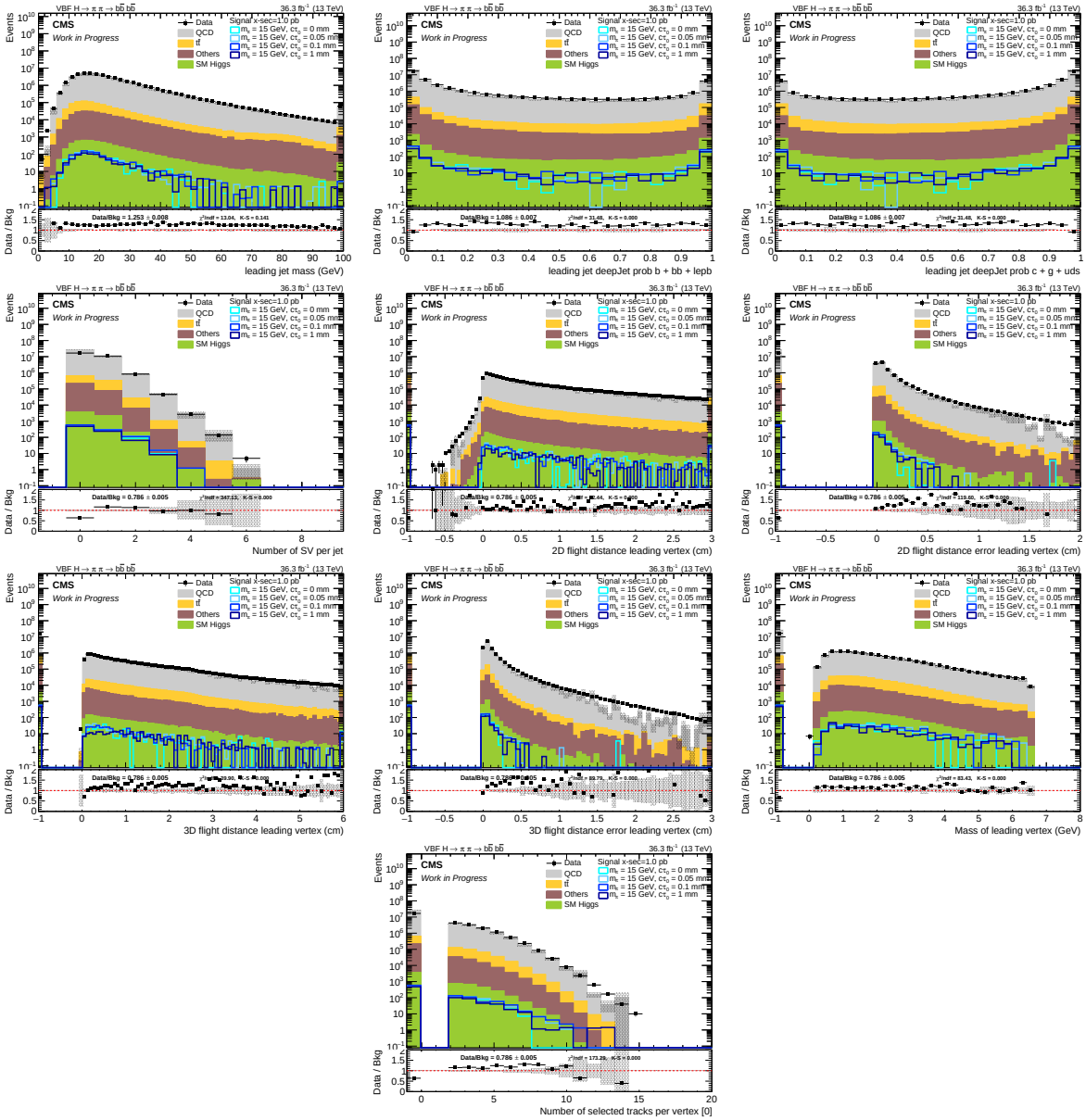

Figure 9.11: Distribution of several of the DNN input features of the leading jet after preselection are shown. In the first row are the jet mass (right), and the added DeepJet probabilities of $b + bb + lep\,b$ (middle) and $c + g + uds$ (right). The following rows present the number of SV per jet (second row left), the leading vertex's flight distance in 2D (second row middle) and its error (second row right), and in 3D (third row left and middle), mass of the leading vertex (third row right) and the number of selected tracks of the leading vertex (fourth row). For the last six plots an underflow bin shows the default values if no SV was found for this jet. Only statistical uncertainties are shown.

the combinations of signal for training. For the evaluation each specific LLP mass and lifetime only this signal is used, while the remaining signal and background values are set as well to this combination.
The DNN architecture, used in this thesis, is shown in Figure 9.10. There are three hidden layers used with 128, 128 and 64 units, respectively. Furthermore, the dropout technique [70] is used. The dropout rate in the DNN used is set to 30 %. The ADAM optimiser [71] is used in training with a learning rate of 0.0008. For the loss function the sparse categorical cross-entropy is used in the minimisation process. The two output nodes provide values that represent the probability that a jet is more signal or background like. Early stopping with a patience level of 16 is included. The rectified linear unit activation function are applied on the three dense layers, while softmax is applied to the output nodes. In total, 16 input features per jet are used and fed into the DNN. They can be grouped into four main categories and are:

- **Jet kinematics (4):** p_{T}, η, mass and energy.
- **DeepJet probabilities (2):** $b + bb + lep\,b$, $c + g + uds$.
- **Input features of the *b* tagging algorithm (8):** number of SVs, number of tracks assigned to all vertices in the jet, flight distances in 2D and 3D of the leading SV[3] as well as their uncertainties, mass of the SV and number of tracks of the leading SV.
- **Parametrisation (2):** mass and lifetime of the LLPs.

Distributions of the input features for the leading jet are shown in Figure 9.11. Shown are from the top left to the bottom right: the jet mass, the added DeepJet probabilities of $b + bb + lep\,b$, and $c + g + uds$, the number of SV per jet, the leading vertex's flight distance in 2D and 3D and their errors, the mass and the number of selected tracks. For the last six plots, the bin with the value -1 represents the events having the default values[4] set when no SV was found for this jet. Overall a good agreement between data and simulation can be observed. One requirement of the b tagging algorithms is that the mass of a vertex is requried to be below 6.5 GeV, which is visible in the right plot of the third row. In all of these plots, a similar shape between signal and SM background can be observed.

[3]The so called *leading* SV is the one with the highest p_{T} within the jet.
[4]The default values are -1 for the number of selected tracks and -100 for all flight distance features and the mass of the vertex.

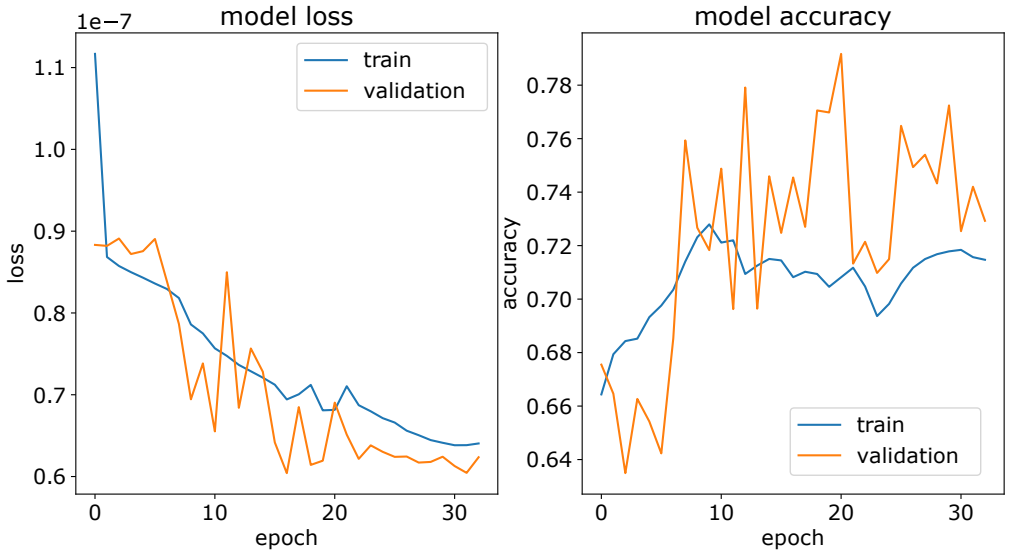

Figure 9.12: Loss and accuracy at each epoch during the training of the DNN.

The DNN is trained with a mixture of all studied LLP masses: $m_{\pi_\nu} = [15, 40, 55]$ GeV and a combination of the lifetimes $c \times \tau = [0.05, 0.1, 1]$ mm. For the SM background jets used for the training, the values for the m_{π_ν} and $c \times \tau$ are randomly sampled from the possible combinations, considering that the different combinations occur with different rates. About 140k signal jets matched by $\Delta R < 0.4$ to generator b quarks originated by LLP decays, and 12 million jets from multijet and $t\bar{t}$ backgrounds are used for the training of the DNN. The jets used for the training of the DNN are set aside and independent from those used for the analyses later on. Loss and accuracy behaviour during training is shown in Figure 9.12. Samples used for training are split in the following way: 50 % of the events are used for analysis, 50 % for ML procedure. Out of the latter one, 80 % and 20 % are used for training and validation, respectively. The fluctuation in the validation curve of loss and accuracy comes from low signal statistics in the validation sample.
The parametrisation of the DNN has the advantage that the LLP mass-lifetime combination can be set for each jet, and hence a discrimination value for each of these combinations can be assigned. The DNN was evaluated with $\approx$ 25k jets of signal jets matched by $\Delta R < 0.4$ to generator b quarks which are direct decay products from a LLP and $\approx$ 3 million jets of backgrounds. The performance of the DNN was studied for the different mass-lifetime combinations. The DNN was evaluated with signal jets matched to generator b quarks, of a specific mass-lifetime combination, while the parametrisation values of the background jets were set to this specific model. The ROC (defined in Section 6.2) for

all masses and lifetimes can be found in the upper plot of Figure 9.13. On average, the boosted signal with a mass of 15 GeV performs better than the resolved masses. Across the masses 40 GeV and 55 GeV the performance is very similar. While the resolved signal behaves more like SM background and is harder to distinguish, the probability that the boosted signal has differences in some of the input features is higher. For all masses the 1 mm lifetime has the best performance, while the lifetimes not used for training perform worse. The performance of the parametrised DNN can be compared to the black line, which corresponds to the DeepJet performance to b tag the jet, of combined signal jets with all masses and lifetimes between 0 mm and 1 mm. Almost all different parametrised DNN discriminants outperform the DeepJet tagger up to high signal efficiencies. The performance of the DeepJet tagger for jets of each mass and lifetime separately evaluated can be found in the lower plot of Figure 9.13. Again, jets of the boosted topology with masses of the LLPs of 15 GeV show the best results. In addition, the 1 mm lifetimes for each mass has the best performance across the different lifetimes. The DeepJet probabilities to tag jets originating from b quarks, and input features of the DeepJet tagger are used for the parametrised DNN, hence it is expected that similar performance is observed. Comparing the ROC AUC (defined in Section 6.2) values of one mass-lifetime combination between the parametrised DNN and DeepJet, the values are quite close together. However, for the remaining analyses steps include a jet selection, based on the topology of the signal jets. Afterwards, a clear difference in the discrimination between signal and background jets with DeepJet and the parametrised DNN tagger were seen.
The LLP lifetimes of 5 and 10 mm result in quite displaced jets, which differ from jets originated by SM b quarks. As already shown the trigger efficiency drops and there are not enough events left for the training. Therefore, the DNN is not trained with these signal jets, which results in a performance decrease with larger lifetimes (see Appendix A). In the following, the DNN discriminant for 1 mm is used as an approximation for these two lifetimes.

9.6 Background Estimation

When SM processes are difficult to simulate and the simulation does not describe data well, a data-driven background estimation is performed. The main background for the boosted and the resolved analysis is the QCD multijet production. A data-driven background estimation is used for this QCD multijet background, while all non-QCD processes are used from simulation. The basic idea is described in the following, while more specific

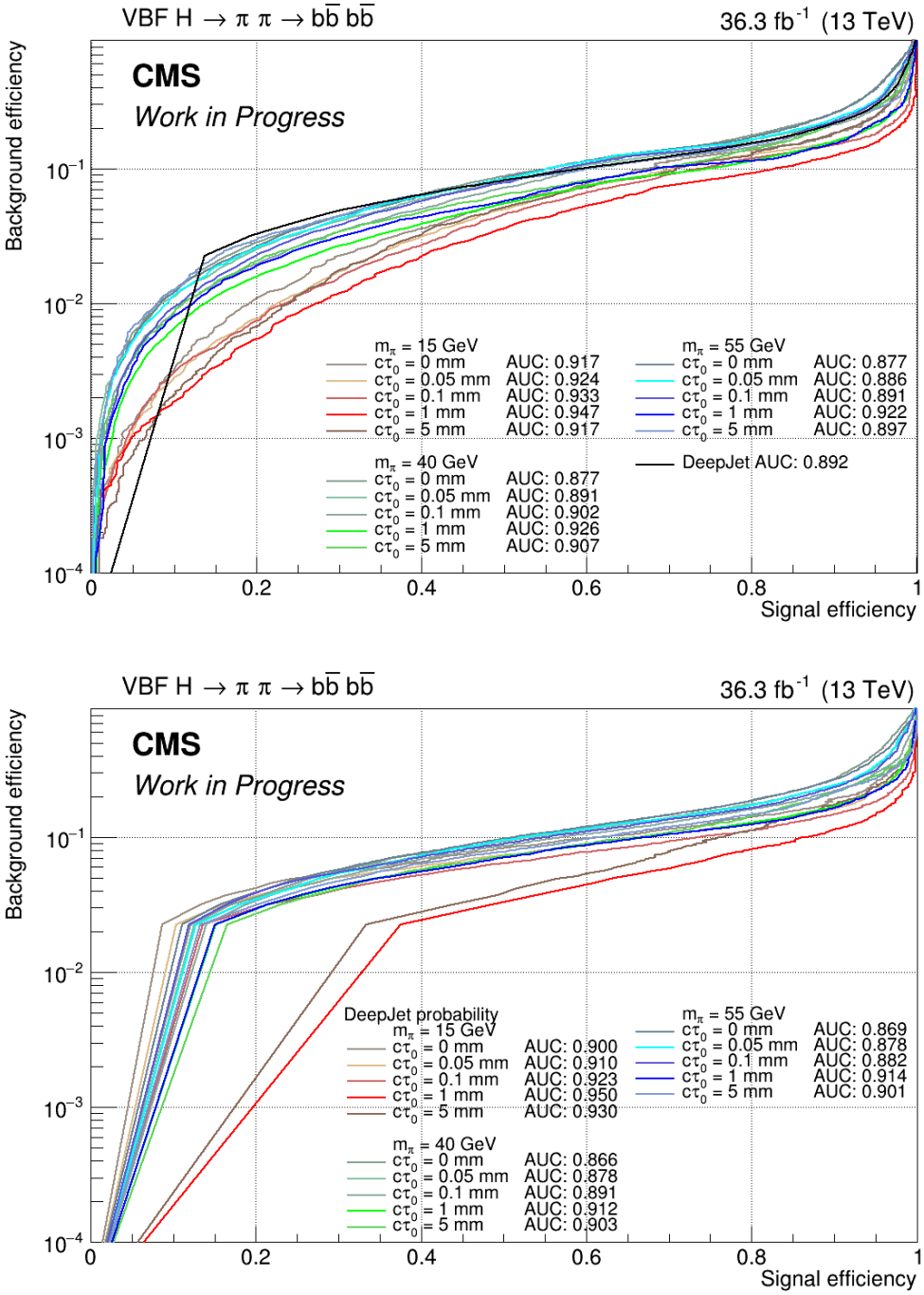

Figure 9.13: The ROC shows background efficiencies determined for different signal efficiencies. For the upper plot different DNN discriminants are evaluated with signal jets of the different LLP masses and lifetimes and the black curve shows the behaviour for all signal masses with lifetimes between 0 mm and 1 mm evaluated with the DeepJet tagger. The lower plot presents the performance of the DeepJet tagger on different LLP mass-lifetime signal jets.

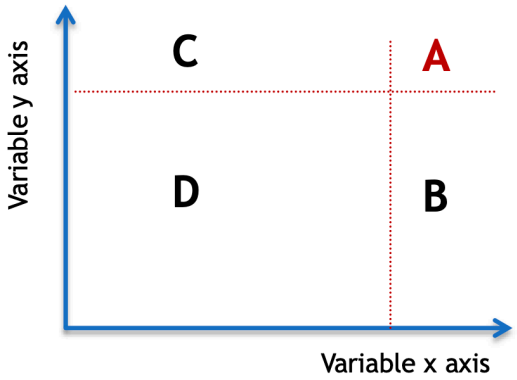

Figure 9.14: A schematic of the ABCD method is shown. The two variables are plotted against each other. The red dotted lines indicate thresholds, which divide the area into four regions, A, B, C and D.

details for the analysis are given in Sections 10.2 and 11.2.

The background estimation method uses two independent variables to define the so-called ABCD regions [125]. In general, the two variables are event contents and can be chosen depending on the relevant analysis specification. A schematic of the ABCD method can be found in Figure 9.14. Two variables are plotted against each other, and thresholds, indicated as red dotted lines, divide the distributions into the four regions: A, B, C and D. Region A is defined as the signal region of interest, while background events dominate ideally region D. The data-driven background estimation method estimates the background event yield in region A N_A by the event yields of the other three regions:

$$N_{\mathrm{A}} = \frac{N_{\mathrm{B}} \cdot N_{\mathrm{C}}}{N_{\mathrm{D}}}, \tag{9.2}$$

where N_{X} is the event yield of the region X. This equation is only valid if the two variables are independent and not correlated. The statistical uncertainty of this method is derived by the statistical uncertainties of the yields in region B, C and D and error propagation.

In order to define the final thresholds separating the regions, several things need to be considered and are listed in the following. The two variables should be uncorrelated. If a correlation is observed, it might help to shrink the ABCD plane by excluding events in certain areas, for example, by lower bounds. Clear disagreements in some parts or trends across the distribution indicate that the method might fail. Data and simulated events are compared in the non-signal regions B, C and D. The ratio of signal over background yield ($\frac{S}{\sqrt{B}}$) for the signal region A should be approximately one order of magnitude larger

than for each other region. Furthermore, a closure test is performed in which the event yield predicted by Equation 9.2 is compared to the number of simulated events actually observed in region A. This closure is studied using the $\overline{\text{SR}}$, which is expected to represent the SR. In addition, the ABCD method is validated with sideband regions defined by removing the right (or upper) part of the ABCD plane and therefore removing the signal region A. The closure tests of these sideband regions can be performed again for $\overline{\text{SR}}$, but now as well for the SR. For both validations, first, the systematic uncertainty of the background estimation is derived by the statistical uncertainties of the data minus non-QCD event yields and error propagating these uncertainties with Equation 9.2. If deviations from the closure are observed in these sideband regions, which are not covered by the statistical uncertainties, they can be considered as an additional uncertainty.
For the analyses discussed in this thesis, the DNN discriminant of two jets are used. The parametrised DNN approach, provides a discriminating value for each investigated mass and lifetime combination. Depending on the mass-lifetime combination, a different signal and background behaviour is expected. Therefore, the thresholds for the ABCD regions are optimised separately for each mass-lifetime hypothesis. Lower bounds, removing events with low discriminating DNN values, help to stabilise the ABCD method. The yields of the remaining backgrounds are subtracted in regions B, C and D from the data yield. This procedure is possible since the non-QCD backgrounds describe data well, as shown in the $t\bar{t}$ CR (see Section 10.2.3), and are small compared to the QCD background. After calculating N_A with Equation 9.2, this predicted yield is used instead of the QCD background in region A, while all non-QCD multijet backgrounds yields are taken from simulation.

9.7 Systematic Uncertainties

Simulated processes never describe recorded data perfectly. Therefore, correction factors of different sources are applied. Each of these corrections comes with an uncertainty, which needs to be taken into account. In addition, uncertainties from theoretical predictions, as for example the cross section of the SM backgrounds, are used. Since the analyses described in the following are counting experiments, all systematic uncertainties affect only the yield. The effect of the different uncertainty sources is studied for each analysis separately. The event yields in the final region A are varied within the systematic uncertainties, and the effect on the final event yield is measured. All of them are taken into account for the statistical evaluation in Chapter 12.

The following different systematic uncertainties are taken into account for both analyses:

- **Luminosity:** The data recorded by the CMS detector in 2016 at 13 TeV correspond to an integrated luminosity of $\mathcal{L} = 36.3\,\text{fb}^{-1}$ with an uncertainty of 1.2 % [15]. Simulated events are additionally weighted in such a way that the predicted total number of events corresponds to that expected for this integrated luminosity.

- **PDFs:** The PDFs [54,126] are an essential estimation to simulate pp collision events. For the NNPDF3.0 PDF set, used for the analyses investigated in this thesis, the uncertainty calculation is derived by using 100 different PDFs replicas. The root-mean-square of the 100 variations compared to the final result is used to estimate the uncertainty, as described in Reference [127].

- **PU:** Simulated events need to match the PU distributions in data and are reweighted accordingly. The number of PU interactions of recorded data is evaluated by using the inelastic pp cross section at a centre-of-mass energy of $\sqrt{s} = 13\,\text{TeV}$, which is approximately 69 mb [110]. The minimum bias cross section is varied up and down by its uncertainty of 4.6 % to evaluate the PU uncertainty.

- **Production cross section:** Uncertainties on the production cross sections are considered for the SM processes as listed in Table 9.5. The uncertainties of different processes grouped in the analyses are weighted accordingly to the yield fraction within the group.

- **JEC and JER:** JEC and JER are taken into account as described in Section 8.3.2. The variation within the JEC and JER uncertainties [93] can affect the event yield of the final result. Therefore, the effect was studied and evaluated within the complete analysis with independently varied values.

- **Trigger:** The trigger and the method to estimate the associated uncertainties published in [123] is applied, and uncertainties are taken into account. Details for the correction factor derivation can be found in Section 9.2. The correction factor is derived from fitted curves of the different filter steps in the HLT paths. Therefore, the uncertainty of the fitted curves of each filter are used, and the combined uncertainty is calculated, taking all filter steps as fully correlated, resulting in the largest possible uncertainty.

- b **tagging:** The correction procedure is described in Section 8.4.1. Uncertainties due to the correction procedure are derived by applying additional correction factors

that were calculated with variations of the underlying uncertainty sources. The additional correction factors correspond for example to contamination from light flavour ($udsg$) jets in the region of b jets or statistical fluctuations.

- **Background estimation method:** The uncertainty of the background estimation method consists of two parts. For the first part, the closure in the sideband regions of SR is studied. Deviations to unity of the closure, which are not covered by the statistical uncertainties, are used as an additional uncertainty, as described in Section 10.2.2. The second part is derived by error propagation of the statistical uncertainties of the event yields with Equation 9.2. The uncertainties of the data and the subtracted non-QCD processes are taken into account. Both parts are taken as fully correlated and are quadratically added.

- **Renormalisation and factorization scales:** The scale uncertainties of renormalisation (μ_R) and factorization (μ_F) are derived following Reference [128]. From both scales, μ_R and μ_F, the nominal value plus the up and down variation by factor 2 are considered. This results in six different variations. The envelope of these different variations is used as uncertainties for the analyses.

- **Prefiring:** As discussed in Section 9.2 a correction factor for a timing problem was derived and applied. The associated uncertainty is encoded in additional correction factors and propagated to the final results of this analysis.

For the signal samples information needed to calculate the uncertainties on the PDF sets, as well as the renormalisation and factorization scales had not been stored during event generation. Therefore, values were taken from Reference [10], since they depend on the SM Higgs boson production mechanisms.
All uncertainties were derived for each analysis and can be found in Sections 10.3 and 11.3.

10 Search for Long-Lived Particles with Boosted Signatures

This analysis describes an approach sensitive to light LLPs, and a LLP mass of 15 GeV is investigated. In this topology, the decay products of each LLP are expected to be close together in ΔR, leading to the so-called boosted topology. They are reconstructed within one AK4 jet, resulting in two signal jets per event. These two jets of interest can be selected by requiring an invariant mass close to the SM Higgs boson. SM background processes are further suppressed by a ΔR requirement between the selected jets. An ABCD method is used to estimate the QCD multijet background in the SR from data[1]. The regions of the ABCD method are defined by the DNN discriminants of the two selected jets. Finally, a validation region and a $t\bar{t}$ CR are used to validate the ABCD method and the data-to-simulation agreement for the DNN discriminant is investigated. Each of these steps is described in detail in the following.

10.1 Full Event Selection

In the boosted topology, the decay products of each LLP tend to be merged into one jet, leading to a dijet final state. In many cases, the signal jets are not the two jets with the highest p_{T}. Especially in the VBF production, one of the leading jets often originates from one of the two quarks produced in association with the Higgs boson (compare e.g. Figure 2.1). Therefore, the following procedure was used to select the two potential signal jets, based on the observation that the invariant mass of the dijet final state should be close to the SM Higgs boson mass. A χ^2 value is defined as:

$$\chi^2_{ij} = \frac{(m_{\mathrm{reco},ij} - m_{\mathrm{Higgs}})^2}{125\,\mathrm{GeV}^2}, \tag{10.1}$$

[1]The difference between the QCD multijet background from simulation and the data-driven background estimation of the QCD background is indicated by the key words *simulated* and *predicted*, respectively.

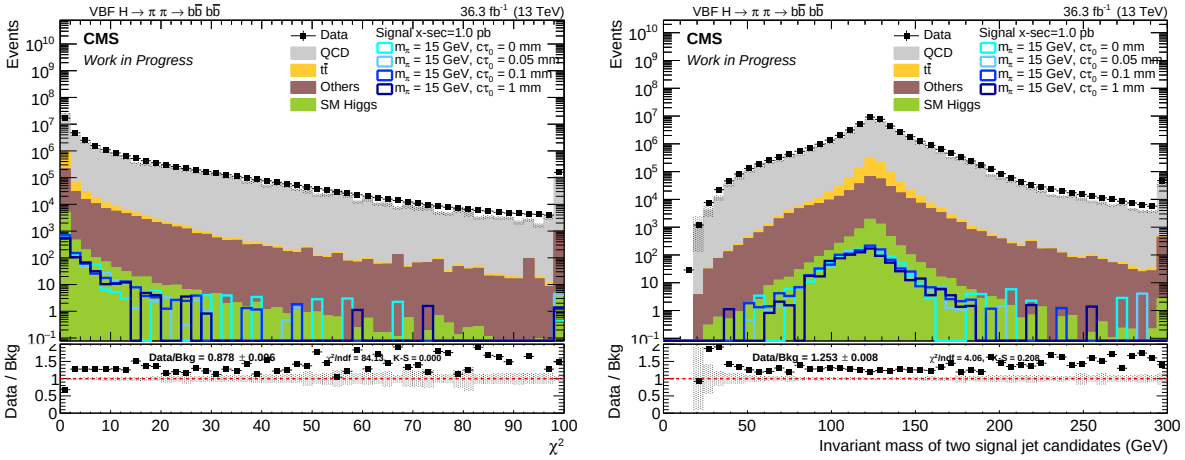

Figure 10.1: Distribution of the smallest χ^2 per event (left) and the corresponding invariant mass of the corresponding dijet combination (right) used for the boosted topology after the preselection.

with $m_{\text{reco},ij}$ being the invariant mass of two jets i and j and $m_{\text{Higgs}} = 125\,\text{GeV}$ the mass of the SM Higgs boson. For each event, the χ^2_{ij} value is calculated for all possible dijet combinations. In each signal event, jets associated with the LLP decay are expected to provide the smallest χ^2 value, and hence only this combination is used in the following. The distribution of the smallest χ^2 in each event is shown on the left, and the distribution of the invariant masses of the associated dijet pairs is shown on the right of Figure 10.1. The mass dependence of the χ^2 leads to the mass peak around the Higgs boson mass in the distribution. Neutrinos that are produced within the b hadronisation, for example, during the decays of charged pions, slightly reduce the achievable mass, visible as a tail towards lower masses in the signal. Nevertheless, selecting the two potential signal jets of interest is achievable with this requirement. Only events with $\chi^2 \leq 10$ are used for the SR in the following analysis steps, this selection corresponds to a mass window of $90\,\text{GeV} \leq m_{\text{reco},ij} \leq 160\,\text{GeV}$. The distribution of the transverse momenta p_{T} of these two selected jets (upper left and right plot) and the ΔR (lower plot) between them are shown in Figure 10.2. In all three distributions, a constant difference between data and simulated events can be observed, which is most likely due to the simulated QCD multijet events which typically do not describe data perfectly.

The χ^2 method selects the two signal jets but does not provide significant discrimination from the background. However, further discrimination can be achieved by exploiting the ΔR between the two selected jets. Therefore, a selection with $\Delta\text{R} \leq 1.55$ is applied.

A validation region close to the SR is used to validate the background estimation method.

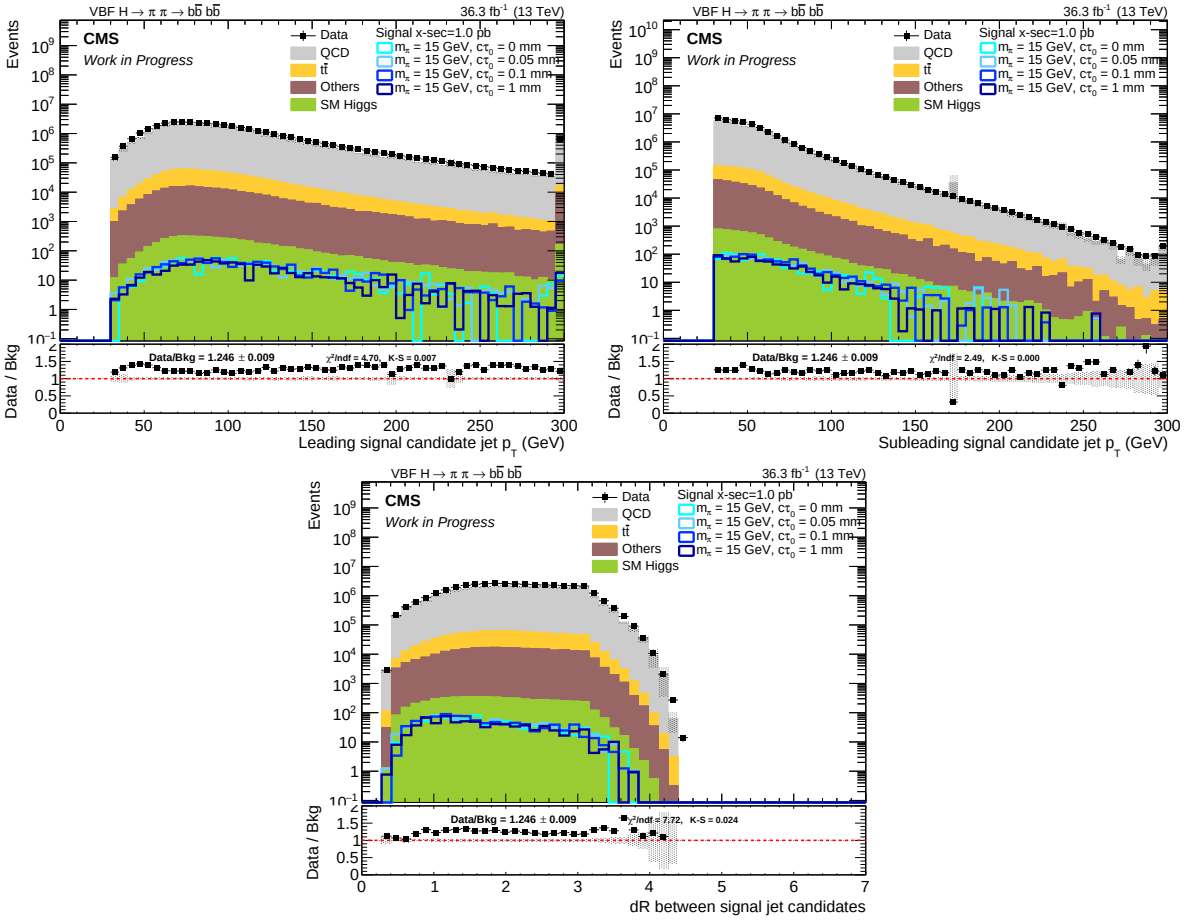

Figure 10.2: The distribution of the p_{T} of the two selected jets (upper row) and the ΔR between the two signal candidate jets (lower plot) after the $\chi^2 < 10$ requirement.

This region is defined by selecting only events where the lowest χ^2 value fulfils $\chi^2 > 10$, and $\Delta\mathrm{R} \leq 1.55$, and is called $\overline{\mathrm{SR}}$ in the following. The distributions of the transverse momenta p_{T} of the two selected jets (upper left and right) and the ΔR between them (lower) after the $\chi^2 > 10$ requirement are shown in Figure 10.3. In addition, the DNN signal probabilities of the two selected jets, ordered via the ϕ variable, after the full $\overline{\mathrm{SR}}$ selections are presented in Figure 10.4. As before, the data agree reasonably well with the simulation.

Two additional regions, defined by the inversion of the ΔR requirement were studied, but this inversion changes the kinematic properties of the selected jets significantly, which also affects the distribution in the ABCD plane. These additional validation regions are studied in Appendix B.

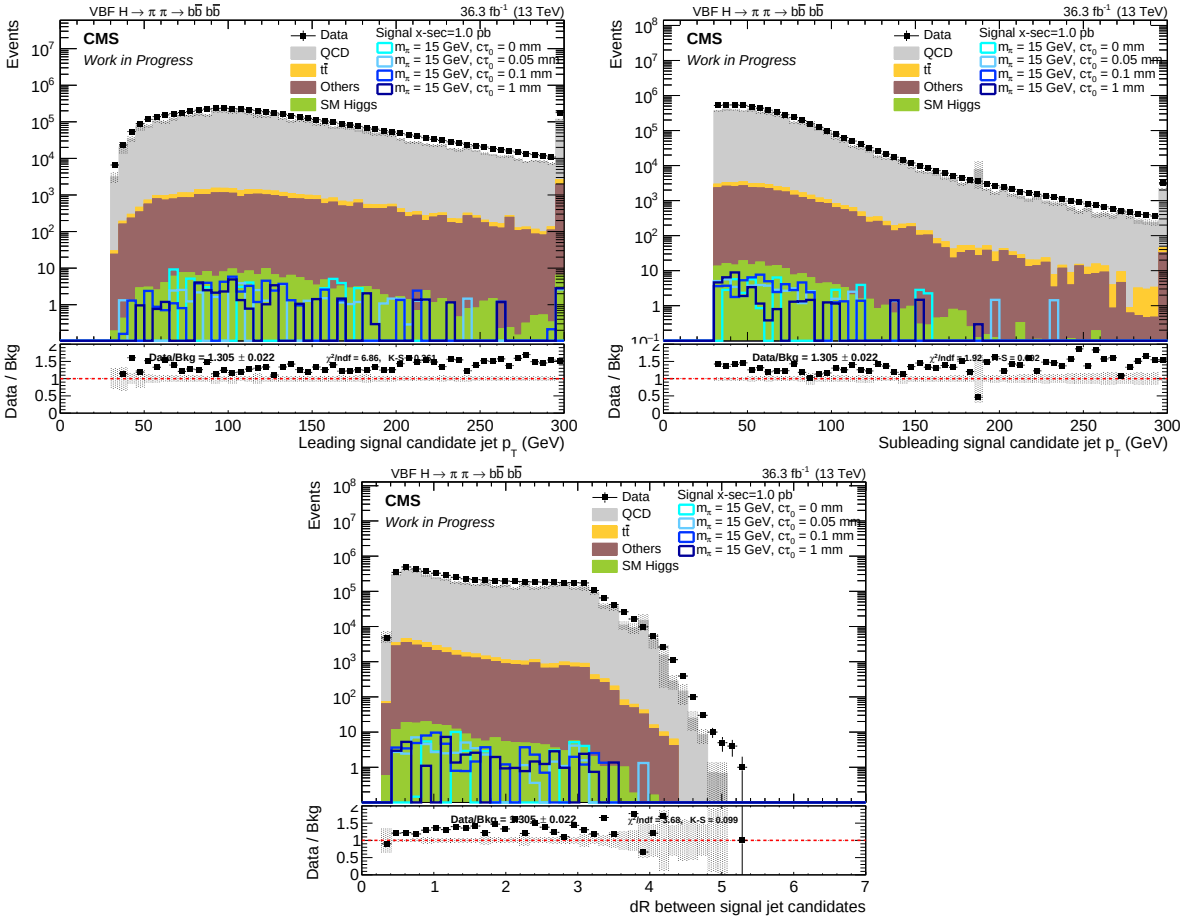

Figure 10.3: The distribution of the p_{T} of the two selected jets (upper row) and the ΔR between the two signal candidate jets (lower plot) for events fulfilling the $\chi^2 > 10$ requirement.

The efficiency of each requirement defining the SR, taking the previous requirements into account, are shown in Figure 10.5 and Table 10.1 for the VBF induced signal process (upper), as well as for the simulated QCD multijet and $t\bar{t}$ background (lower). The specific requirements[2] are:

- Triggers: Events fulfil the logic *or* of the two triggers.
- Trigger Filters: All online trigger objects must be matched by $\Delta\mathrm{R} < 0.4$ to reconstructed jets in the event.
- $\mathrm{N}_{\mathrm{jets,tight\,ID}}$: At least four jets with tight ID[3] requirements must be found in the

[2]Only the χ^2 and the ΔR requirements are different for the resolved topology, while the remaining ones are the same.

[3]The jet reconstruction efficiency exceeds 90 % with a noise jet rejection of more than 90 %.

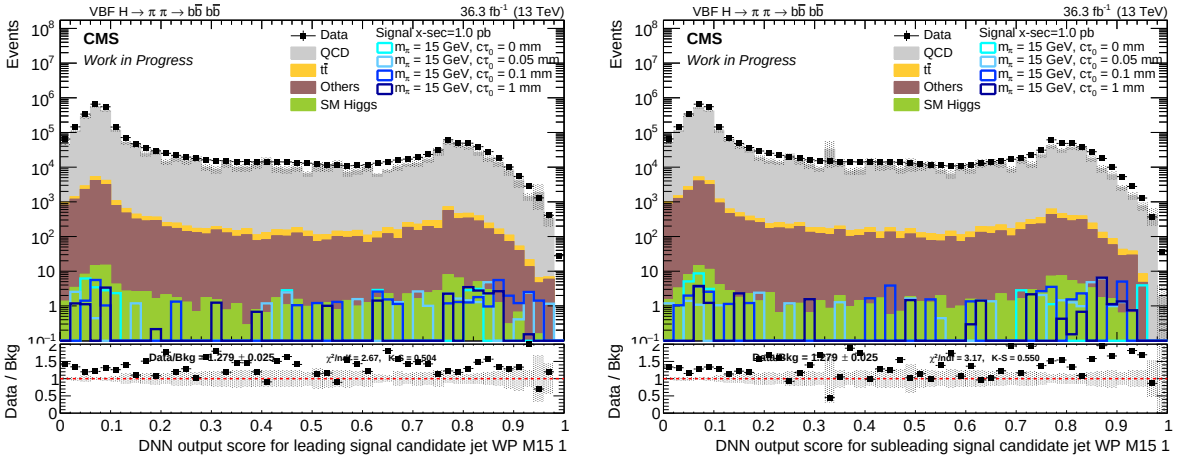

Figure 10.4: The distribution of the DNN discriminant of the two selected, ϕ ordered jets for events in the $\overline{\text{SR}}$ validation region defined by the $\chi^2 > 10$ and $\Delta\text{R} \leq 1.55$ requirements.

event.

- Preselection: The remaining preselection requirements on H_T, as well as lepton and photon vetos.
- χ^2 method: Two jets are selected with $\chi^2 \leq 10$, following Equation 10.1.
- ΔR: The distance in ΔR between the two selected jets does not exceed 1.55.

As already shown in Section 9.2, the trigger efficiency is relatively low for signal, especially for the longer lifetimes. The requirements for matching to the trigger filter objects and the jet multiplicity are applied to ensure that the trigger works efficiently. The ΔR requirement has a similar efficiency reduction for signal and SM background. However, this requirement decreases the number of signal events with low DNN signal probabilities of either one or both jets, while for the SM background the requirement decreases the number of events, which are evenly distributed with the DNN discriminant.
The final selections lead to the following simulated background proportions in the SR: QCD 96.5 %, $t\bar{t}$ 2.4 %, Others 1.0 % and SM Higgs < 0.1 %.
The DNN discriminants of the selected two jets are used to define the four regions of the ABCD method with which the background is estimated as discussed in the following. Up until this point in the analysis, the jets are ordered via the transversal momenta p_T, with the leading jet having the highest p_T. The p_T of the jets are used as input features of the DNN and therefore the DNN discriminant is correlated with p_T. If the

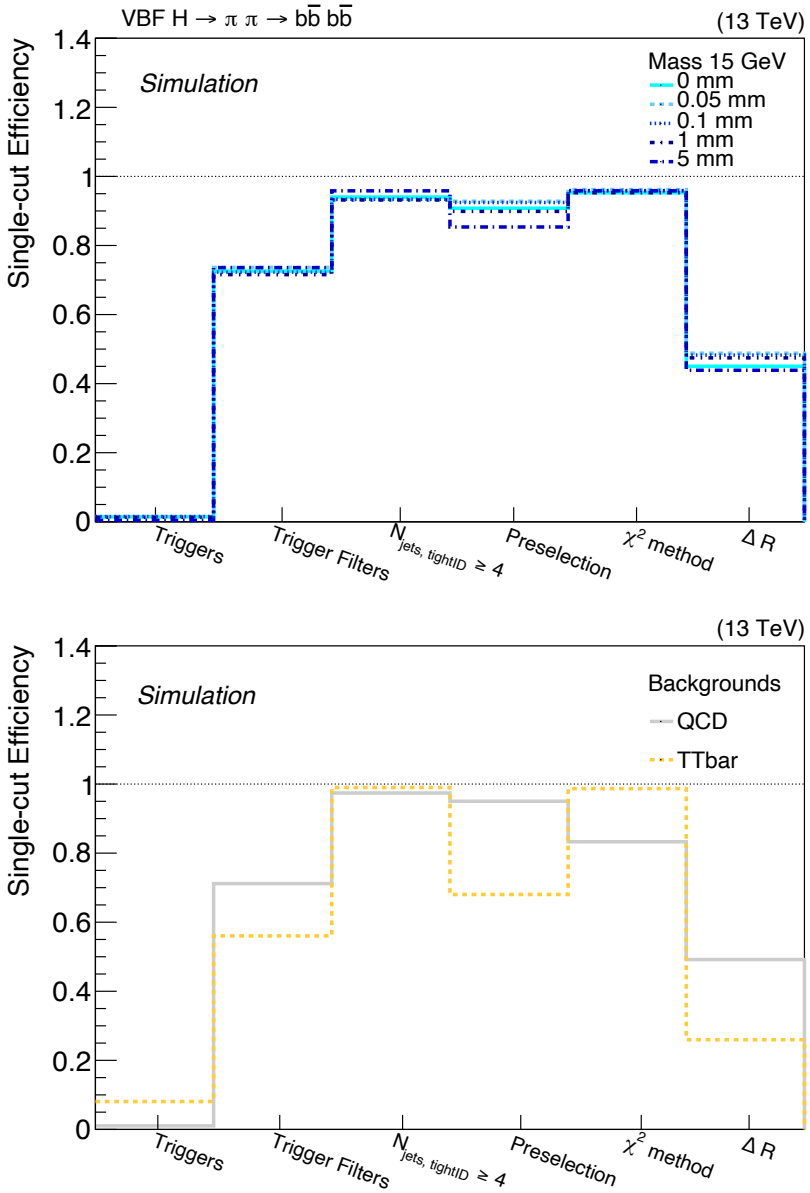

Figure 10.5: The efficiencies of all selection requirements applied, with respect to the events passing the previous step, on signal (upper) and background (lower) for the boosted topology. The requirements are applied in the following order: The two triggers, matching between objects of the trigger filters to reconstructed objects, jet multiplicity, the remaining preselections, jet selection with the χ^2 method and the ΔR requirement.

Table 10.1: The efficiencies of all selection requirements for the signal and background events for the boosted topology. Each efficiency is calculated with respect to the events passing the previous step. The order of application of the requirements is from left to right.

Mass [GeV]	Mode	Lifetime [mm]	Trigger	Trigger Filters	$N_{\text{jets,tight ID}}$	Preselection	χ^2 method	ΔR
15	VBF	0 mm	0.014	0.726	0.940	0.908	0.953	0.450
		0.05 mm	0.015	0.736	0.932	0.928	0.962	0.488
		0.1 mm	0.015	0.723	0.934	0.925	0.959	0.483
		1 mm	0.013	0.716	0.932	0.899	0.953	0.475
		5 mm	0.004	0.736	0.958	0.854	0.958	0.439
		10 mm	0.002	0.749	0.959	0.875	0.959	0.430
	ggF	1 mm	0.005	0.630	0.958	0.912	0.960	0.517
		10 mm	0.001	0.661	0.965	0.881	0.967	0.423
Background sample								
QCD			0.010	0.712	0.974	0.950	0.833	0.492
$t\bar{t}$			0.081	0.560	0.990	0.680	0.987	0.259

p_{T} sorted jets are used for the definition of the x- and y-axis of the ABCD method, the distribution is affected. Therefore, the ϕ coordinates of the jets were used for the sorting, since jets should be randomly distributed around the azimuthal angle ϕ and should not carry relevant information.

The parametrised DNN was found to outperform standard b tagging algorithms in discriminating LLP signal from SM background. Comparisons were performed using the DeepJet b tagging algorithm and are presented in Appendix C.

10.2 Background Estimation

The main SM background of QCD multijet production is estimated using the data-driven method, described in Section 9.6, with ABCD planes defined by the DNN discriminants of the two selected jets. All non-QCD background processes are taken from simulation.

For each investigated lifetime of the boosted topology, a specific DNN discriminant is available, due to the parametrisation based on the mass and the lifetime of the LLP. Depending on the lifetime, a different signal and background behaviour is expected. Therefore, the thresholds for the definition of the ABCD regions are optimised for each lifetime. Symmetric distributions are expected due to the pseudo randomisation, and thresholds on the diagonal are selected. In the following, all values are always provided for all lifetimes,

while plots are shown for a LLP mass of 15 GeV and 1 mm lifetime. The plots for the remaining lifetimes can be found in Appendix D.

The distributions used for the ABCD method for LLPs of 15 GeV and 1 mm lifetime can be found in Figure 10.6. Shown are: signal with VBF (first row) and ggF (second row) Higgs production mode, data (third row) and simulated QCD multijet production (fourth row) in the SR (left) and $\overline{\text{SR}}$ (right). The area close to the maximum values of the discriminants is defined as signal region A. While signal can be mainly found in the region A of the SR, the events of the simulated QCD multijet background and data are mainly distributed in the other areas (B, C and D). In the distribution of data in the SR (third row left), region A is not shown. The accumulation of events with DNN discriminant of 0.76 is due to jets, where no SV was assigned. Those jets have default values for several input features of the DNN, and the DNN returns discriminants between zero and 0.76. Red empty squares show the mean y-value in each bin, visualising the correlation between the two values. The ϕ ordering of the jets induces a symmetric behaviour, therefore the correlation visualised for one axis is similar to that of the second axis. A correlation is visible for data, which is very similar in the SR and $\overline{\text{SR}}$, ignoring the blinded area. A similar correlation can also be observed in the simulated QCD multijet production. This correlation might be due to events in which a gluon splits into two quarks and whose jets are then selected as the two candidate jets. In measurements of $t\bar{t}H$, $H \to b\bar{b}$ production a main background is due to the production of $t\bar{t} + b\bar{b}$, where the $b\bar{b}$ pair originates from the splitting of a gluon. In a study [129, 130] it was found that some requirements, which should enrich $H \to b\bar{b}$ events, also enriches $t\bar{t} + b\bar{b}$ events. In the case of the analysis in this thesis, when a gluon splitting produces for example two b quarks the two jets reconstructed from their hadronisation are selected with high probability by the χ^2 method. In addition, these jets would show potentially high DNN discriminants, leading to a correlation in the ABCD plane.

Studies showed that removing events with one or both jets having low DNN discriminants decreases the correlation. Therefore, the DNN discriminants are bounded from below to remove these events from the ABCD plane. For the boosted topology, a lower bound of 0.3 was found to sufficiently decrease the correlation and in the following the ABCD planes are always shown without these events. In addition, the lower bounds do significantly reduce the number of background events and the efficiency of this additional selection, with respect to the previous ΔR selection, is 0.06 for $t\bar{t}$, 0.08 for simulated QCD multijet production and $\approx$0.75 for signal with VBF and ggF production mode.

The SR distributions without the events below the lower bound of 0.3 for LLPs of 15 GeV

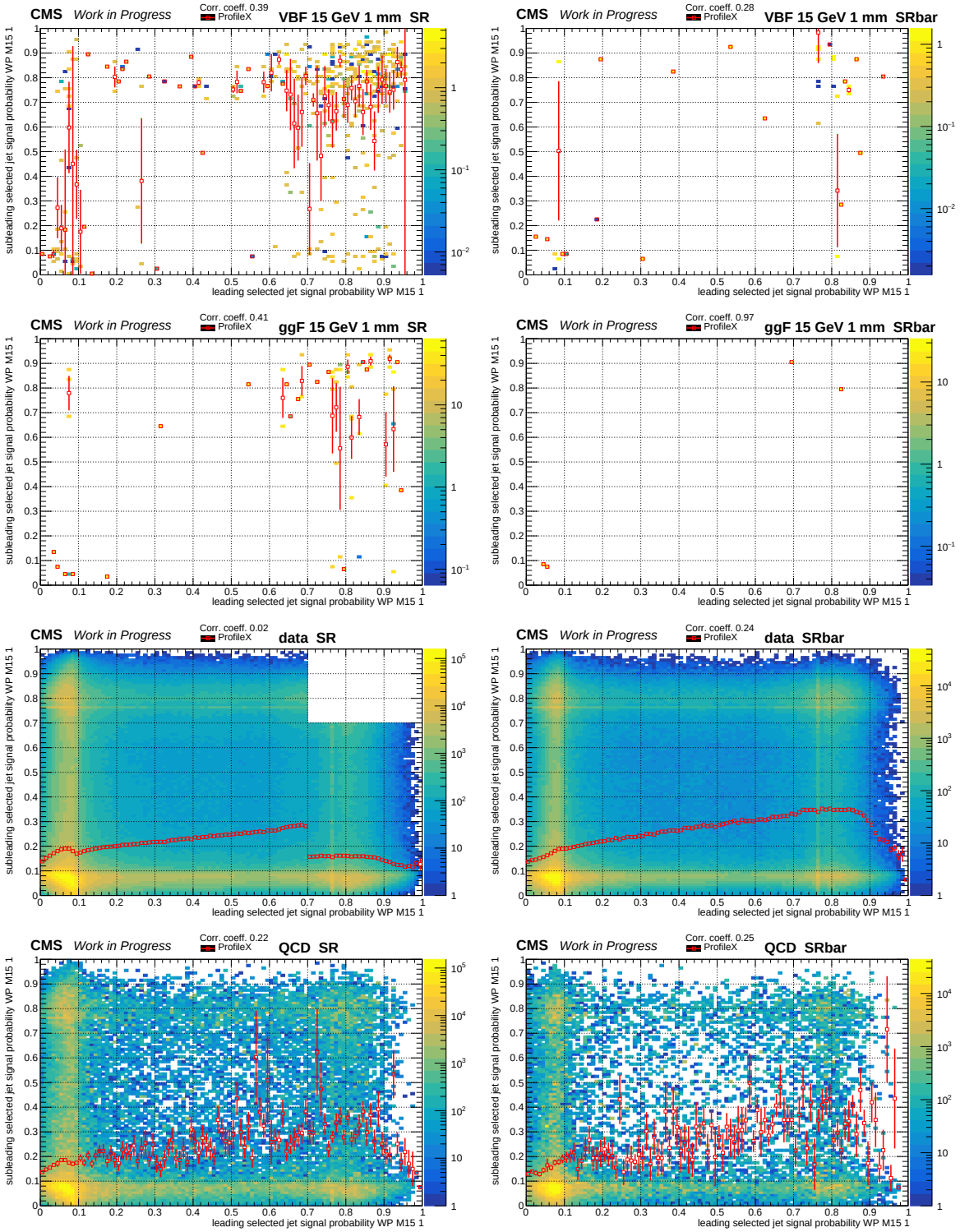

Figure 10.6: Distributions of the ABCD planes in the SR (left) and $\overline{\text{SR}}$ (right) for the analysis of the LLP with 15 GeV mass and 1 mm lifetime for: VBF and ggF induced signal (first and second row), data (third row) and simulated QCD multijet production (fourth row). Red empty squares with error bars indicate the mean y-value of each bin. The upper right region of the plots, depending on the chosen thresholds, is the signal region (region A), and is not shown for data in the SR (third row left).

and 1 mm lifetime can be found in Figure 10.7. Shown are signal events of the VBF and ggF Higgs production modes (upper left and right), simulated QCD multijet production (second row left), $t\bar{t}$ (second row right), SM Higgs (third row left), Others (third row right) and data (last row). In the distribution of data the region A is again not shown. Compared to the plots of Figure 10.6 the correlation is greatly reduced in the plots of simulated QCD multijet production and data.

The relative contributions of the different simulated background sources to the total background are: QCD multijet production 96.5 %, $t\bar{t}$ 1.79 %, SM Higgs 0.26 %, Others 1.48 %. A correlation is still visible for the $t\bar{t}$ distribution even with the lower bounds, and therefore, the ABCD method is not used for this background and it is instead taken from simulation. The remaining two backgrounds (SM Higgs and Others) have small event yields, and are also taken from simulation. This means that these three background yields are subtracted from the data yields in the regions B, C and D, before the Equation 9.2 is used to estimate the QCD background.

The analogous distributions are shown for the $\overline{\text{SR}}$ in Figure 10.8, where it can be seen that the number of signal events is very small. The amount of data and the overall size of the backgrounds are also smaller than in the SR. Nevertheless, the $\overline{\text{SR}}$ distributions of the simulated QCD multijet production and data are very similar to those of the SR and, for example, the correlations observed in data are very close to each other. Even though the distributions are very similar, the selection based on the χ^2 method has the effect of a kinematic selection of the jets which also impacts the DNN discriminants (see Appendix B). In addition to these comparisons, additional studies are also performed in sidebands of the SR and $\overline{\text{SR}}$, and described in Section 10.2.1.

The thresholds defining the ABCD regions were finalised by comparing results for many different possible thresholds, shown in Figures 10.9 and 10.10. Each bin represents the specific combination of DNN discriminants used to define the ABCD regions. White bins indicate such regions where either the SM background yield or the signal yield was zero. The signal significance $S/\sqrt{B}$ in region A of the VBF Higgs production mode[4] (Figure 10.9 upper) is smoothly distributed, with the exception of the upper right area, in which the thresholds are set to tight values and the significance is increased. However, the values with thresholds above 0.9 have to be used carefully, since the number of simulated events of SM background is very small and carry large statistical uncertainties, which results in large values of the signal significance. The significance enhancement Σ_{signal} (Figure 10.9

[4]The cross section of the Higgs production mode is used as the signal cross section.

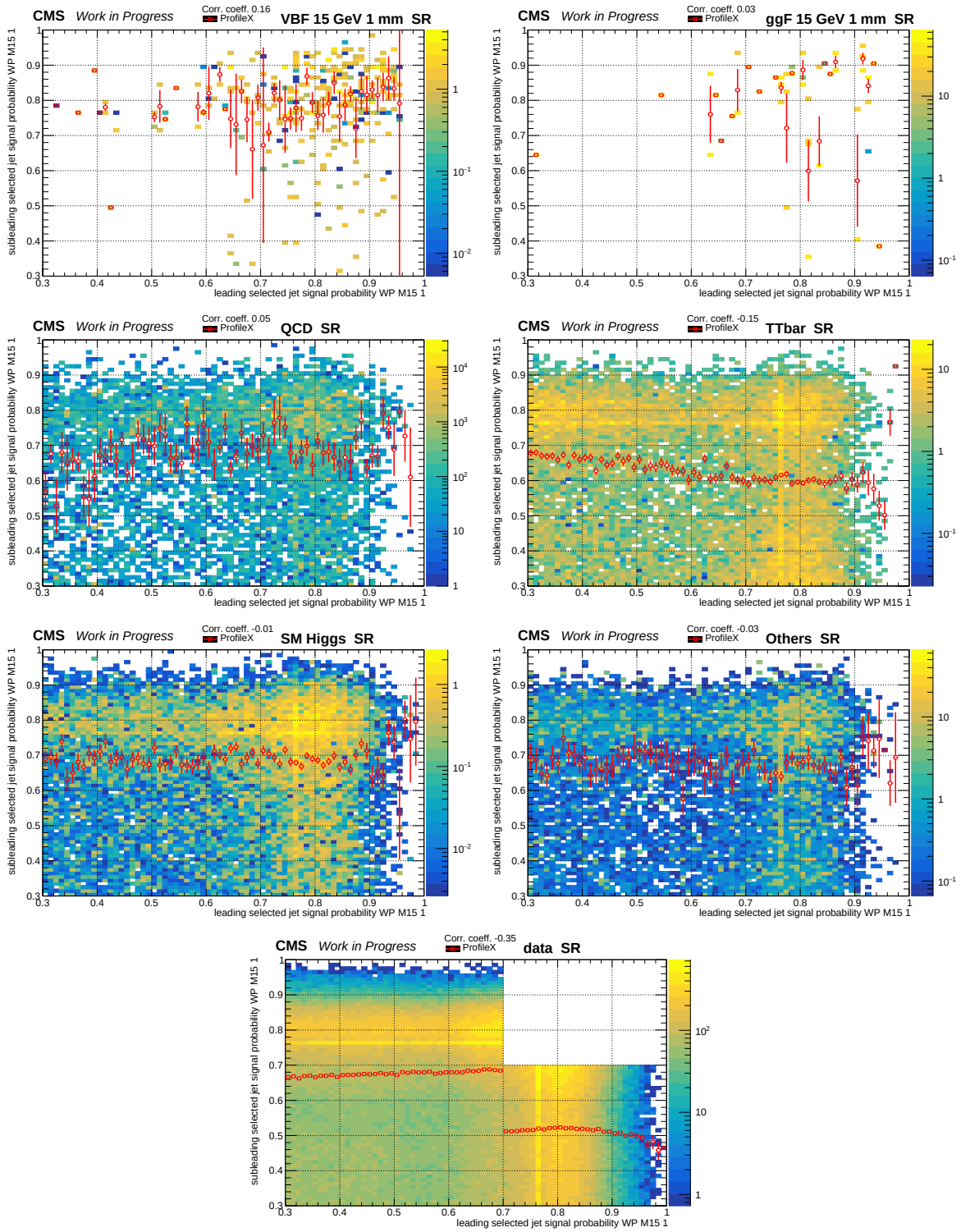

Figure 10.7: Distributions of the ABCD planes for the two selected jets in the SR for the analysis of the LLP with 15 GeV mass and 1 mm lifetime with a lower bound of 0.3 for: VBF and ggF produced signal (first row left and right), simulated QCD multijet production (second row left), $t\bar{t}$ (second row right), SM Higgs (third row left) and Others (third row right). The upper right region of the plots is not shown for data (last row).

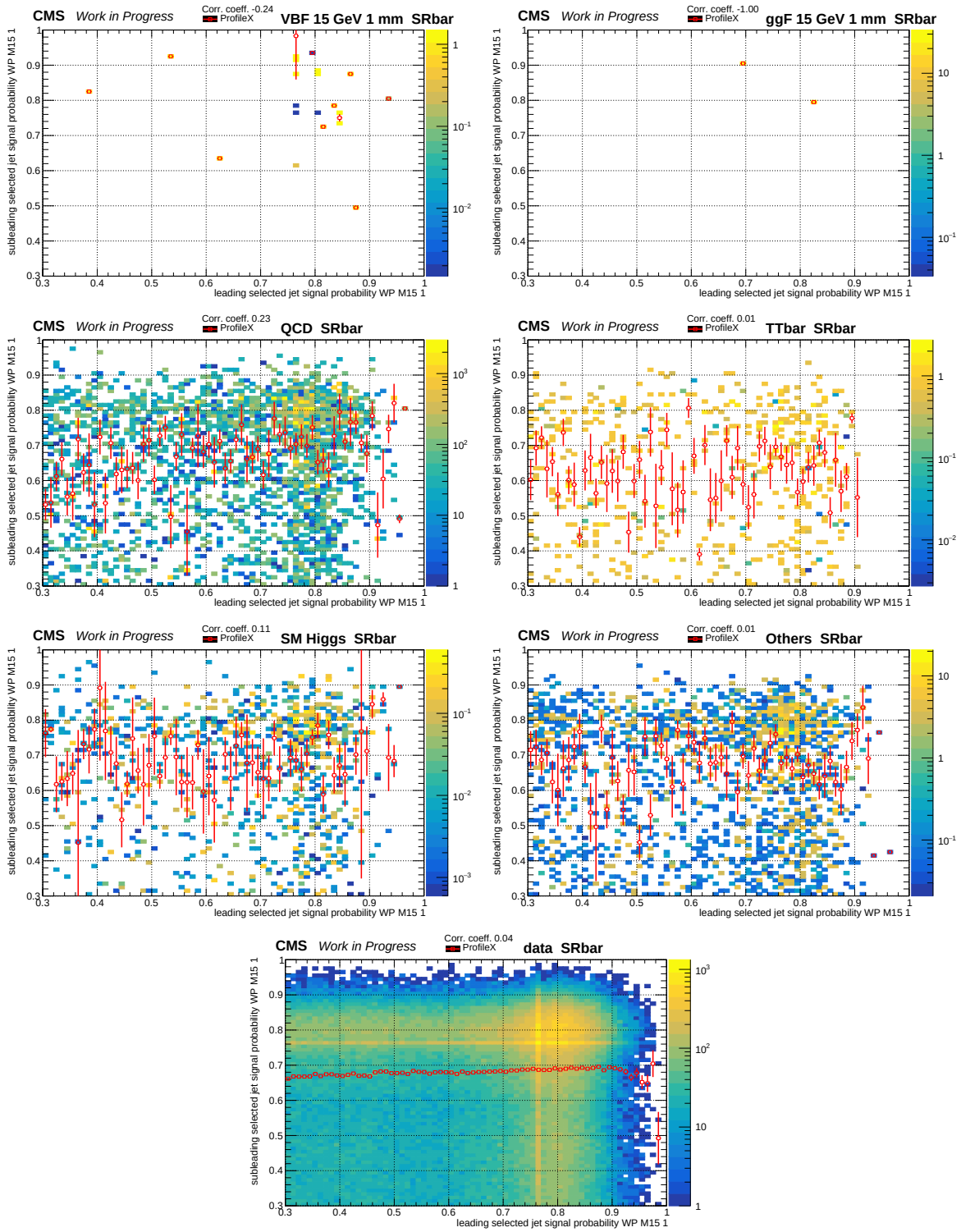

Figure 10.8: Distributions of the DNN discriminants for the two selected jets in the $\overline{\text{SR}}$ for the analysis of the LLP with 15 GeV mass and 1 mm lifetime for: VBF and ggF produced signal (first row left and right), simulated QCD multijet production (second row left), $t\bar{t}$ (second row right), SM Higgs (third row left), Others (third row right) and data (last row).

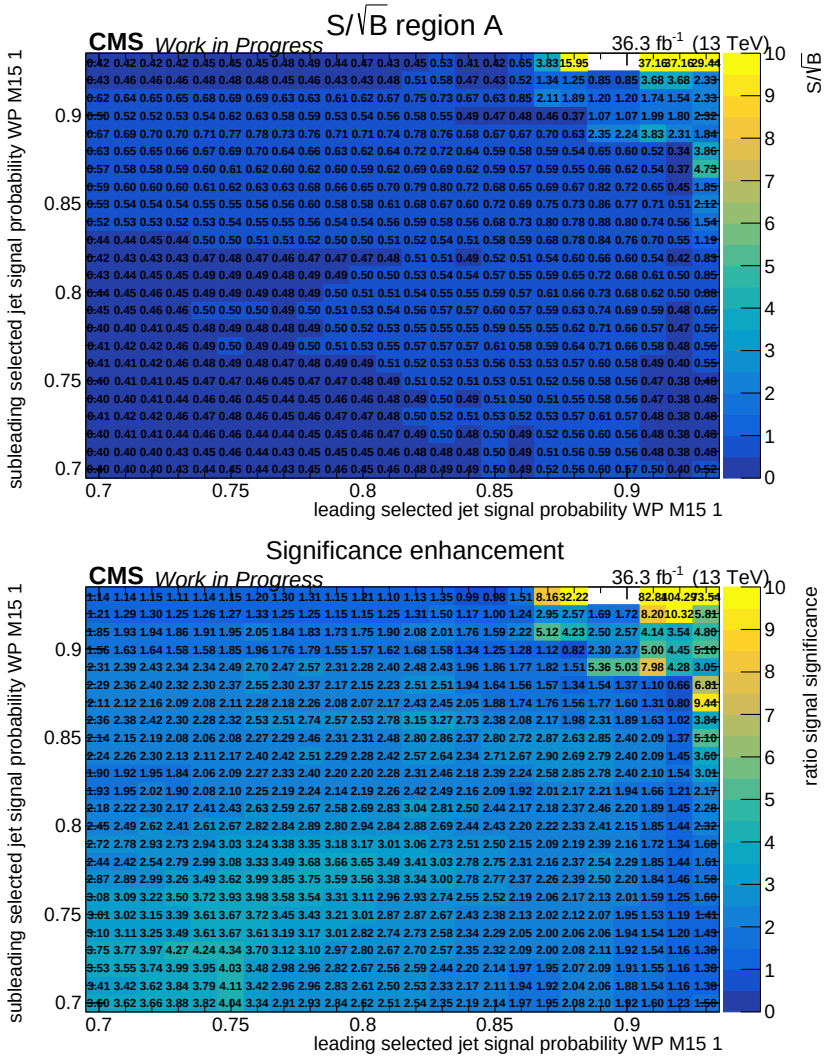

Figure 10.9: Effect of various thresholds for the ABCD method on the analysis of LLPs with a mass of 15 GeV and a lifetime of 1 mm on: Signal significance (upper) and the significance enhancement Σ_{signal} (lower).

lower), is defined as:

$$\Sigma_{\text{signal}} = \frac{\text{sign}_{\text{A}}}{\max(\text{sign}_{\text{B}}, \text{sign}_{\text{C}}, \text{sign}_{\text{D}})}, \tag{10.2}$$

$$\text{with } \text{sign}_{\text{X}} = \frac{\text{yield}_{\text{signal,X}}}{\sqrt{\text{yield}_{\text{background,X}}}}.$$

This value gives an overview on the enrichment of signal in region A, compared to the regions B, C and D. Similar to the signal significance, it is smoothly distributed over several threshold combinations and only the region towards tighter thresholds shows out-

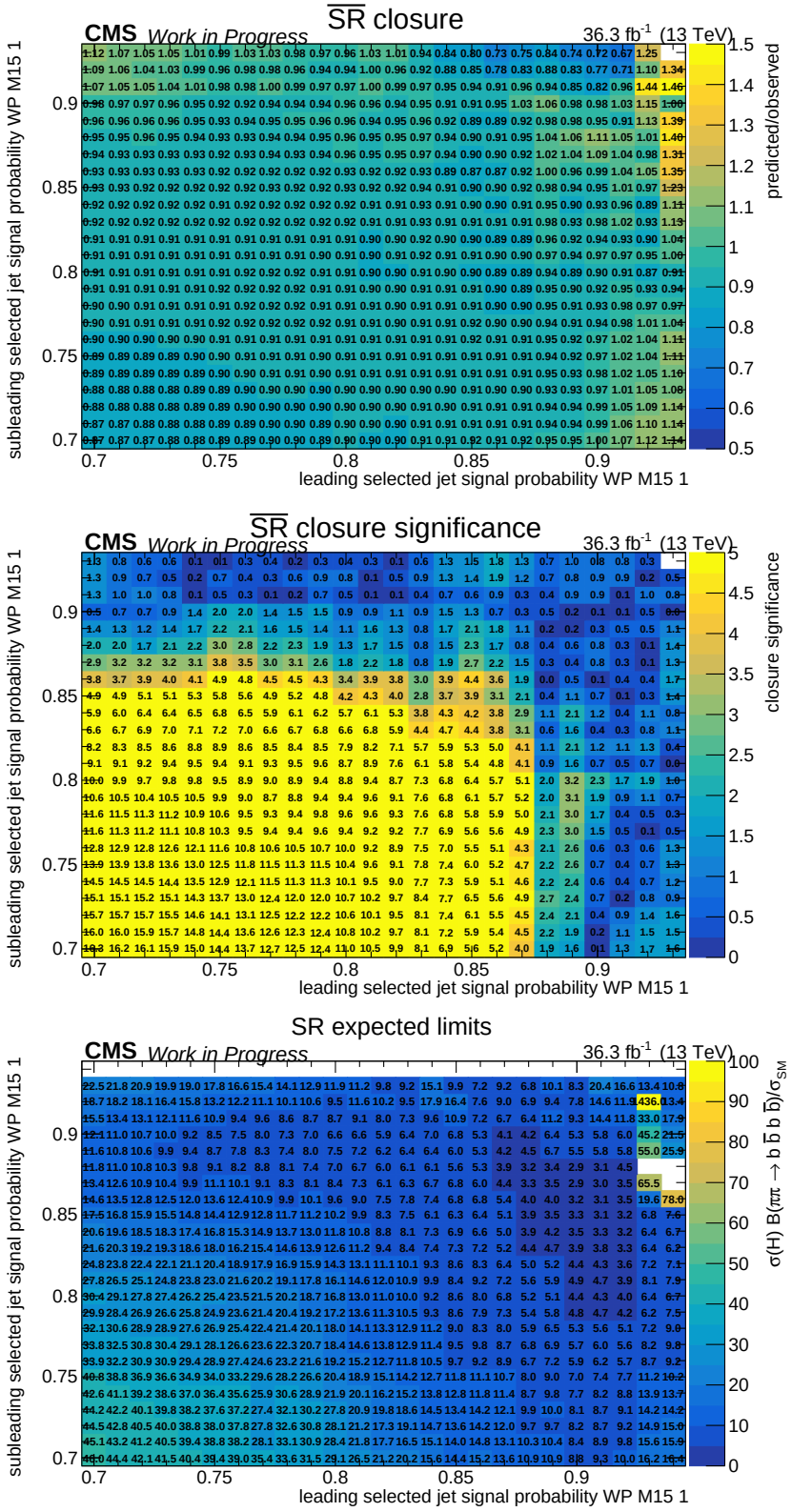

Figure 10.10: Effect of various thresholds for the ABCD method on the analysis of LLPs with a mass of 15 GeV and a lifetime of 1 mm on: Closure using data (upper) and its significance (middle) in $\overline{\text{SR}}$, and the expected upper limits in the SR (lower).

liers, due to the same reason as for the signal significance. In addition to the measures on simulation in the SR, the prediction of the ABCD method is studied in the $\overline{\text{SR}}$ using the closure and its significance. As described in Section 9.6, the non-QCD backgrounds are first subtracted from data in regions B, C and D to predict the QCD background yield in region A. The closure (Figure 10.10 upper) of the ABCD method is then derived as:

$$\text{closure} = \frac{\text{yield}_{\text{nonQCD,A}} + \text{yield}_{\text{predictedQCD,A}}}{\text{yield}_{\text{data,A}}}. \tag{10.3}$$

The closure improves, the tighter the thresholds are, up to a certain point, where too few events in regions B or C lower the prediction probability of the ABCD method. The closure significance in the $\overline{\text{SR}}$ (Figure 10.10 middle), is calculated as:

$$\text{significance}_{\text{closure}} = \frac{|\text{yield}_{\text{predictedQCD,A}} + \text{yield}_{\text{nonQCD,A}} - \text{yield}_{\text{data,A}}|}{\text{unc}_{\text{total}}}. \tag{10.4}$$

The total uncertainty $\text{unc}_{\text{total}}$ is the quadratic sum of statistical uncertainties of the observed, the predicted and the non-QCD yields in region A. The closure significance shows a better performance in the upper right part. The blinded expected upper limits at 95 % CL on the value of cross section times branching ratio, with respect to the SM Higgs boson cross section in the SR are shown in the last row of Figure 10.10. The expected limits are found to be larger at looser threshold values, and reach a minimum at tighter thresholds, before increasing again due to a decrease of the signal yield for very tight thresholds. For the expected limits shown here, all systematic uncertainties discussed in Section 9.7 are taken into account for signal and the non-QCD background processes, while only the statistical uncertainty of the background estimation is used for the predicted QCD yield. Additional uncertainties on the predicted QCD yield will be discussed in Section 10.2.2 and are applied to the final results. With these additional uncertainties the expected limits will be worse than the values presented in Figure 10.10. The five discussed measures are essential indicators for a good ABCD method and compared with each other for each lifetime and Higgs production mode separately. The final thresholds were selected based on these comparisons and can be found for all lifetimes in Table 10.2. For the signal of the LLP lifetimes of 5 mm and 10 mm the DNN parametrised for the 1 mm lifetime is used (as discussed in Section 9.5). The significance enhancement is expected to be different for the different lifetimes, but all other measures are the same as for the signal with 1 mm lifetime. The chosen thresholds for the 1 mm and the 5 mm cases are identical, while for the 10 mm case a slightly different threshold was chosen. Furthermore, the LLP

Table 10.2: The chosen thresholds for each lifetime of the boosted topology together with the resulting values of the discussed measures for the VBF and ggF Higgs production modes of the signal.

	Lifetime in mm	Threshold	$S/\sqrt{B}$ region A	Σ_{signal}	Closure $\overline{\text{SR}}$	$\overline{\text{SR}}$ closure significance	Blinded expected limits
VBF	0	0.92x0.92	1.462	4.129	1.069 ± 0.204	0.360	11.4
	0.05	0.90x0.90	0.296	0.538	1.030 ± 0.073	0.417	9.7
	0.1	0.91x0.91	1.296	3.384	0.937 ± 0.107	0.558	4.5
	1	0.89x0.89	2.345	5.366	0.978 ± 0.114	0.190	3.4
	5		0.216	1.714			62.8
	10	0.88x0.88	0.020	0.483	1.036 ± 0.084	0.440	140.0
ggF	1	0.89x0.89	11.297	5.400	0.978 ± 0.114	0.190	1.1
	10	0.88x0.88	0.067	0.474	1.036 ± 0.084	0.440	78.5

lifetimes with the VBF and the ggF Higgs production modes were studied independently of each other, but they perform similarly in the same areas, hence the same thresholds were chosen for the same lifetime, which has the additional benefit, that results can also be calculated for the combination of both production modes.

The proportions of the remaining backgrounds in region A, as an example for the DNN discriminants for the signal with a mass of 15 GeV and 1 mm lifetime are: predicted QCD 98.7 %, $t\bar{t}$ 1.16 %, SM Higgs 0.10 %, Others 0.04 %.

Table 10.2 includes the blinded expected limits at the chosen thresholds for each lifetime, with the uncertainty on the predicted QCD yield being only of statistical nature, which can be used to investigate some key points. The results show that the analysis is more sensitive to the ggF production mode than to the VBF produced mode, which can be attributed to the larger production cross section. In addition, the best sensitivity is, as expected, reached with the LLP lifetime of 1 mm, due to the displacement. The shorter the lifetimes are, the more similar are the final states of the signal to that of SM backgrounds with b quarks, which leads to a decreasing separation power of the DNN discriminants. However, the LLP lifetimes of 5 mm and 10 mm behave differently to this expectation due to the lower trigger efficiency.

In addition, distributions of the DNN discriminants in the regions B, C and D for the simulated background and signal are compared to those in data in Figure 10.11. The distributions of region B are shown in the upper row, for region C in the middle row and for region D in the last row. Data and simulation generally agree in shape and overall

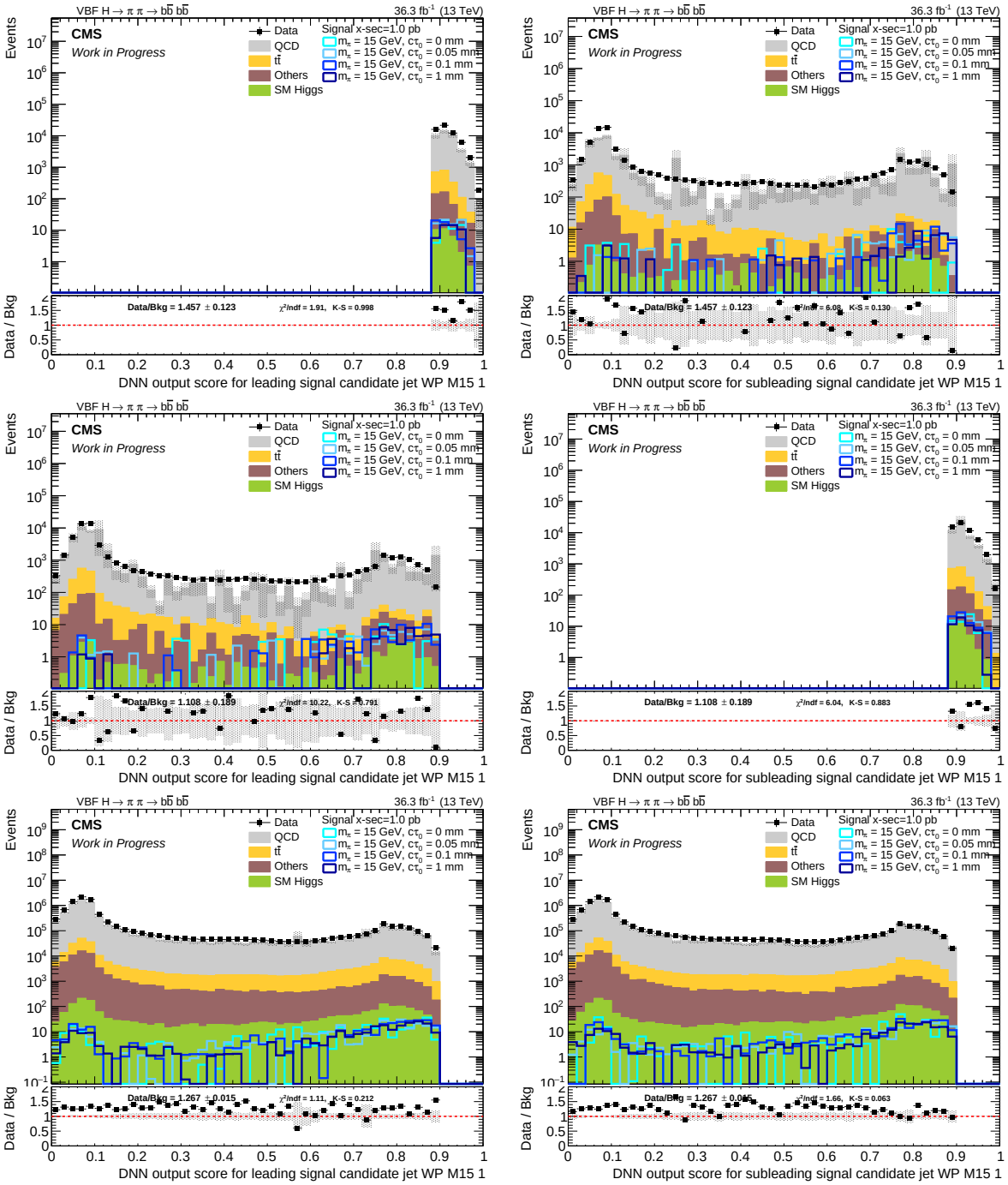

Figure 10.11: Distributions of the DNN discriminant of the two selected jets in region B (upper row), region C (middle row) and region D (last row) in the SR. Shown are the simulated QCD multijet production and the uncertainty bands contain the statistical uncertainties of the simulated SM background.

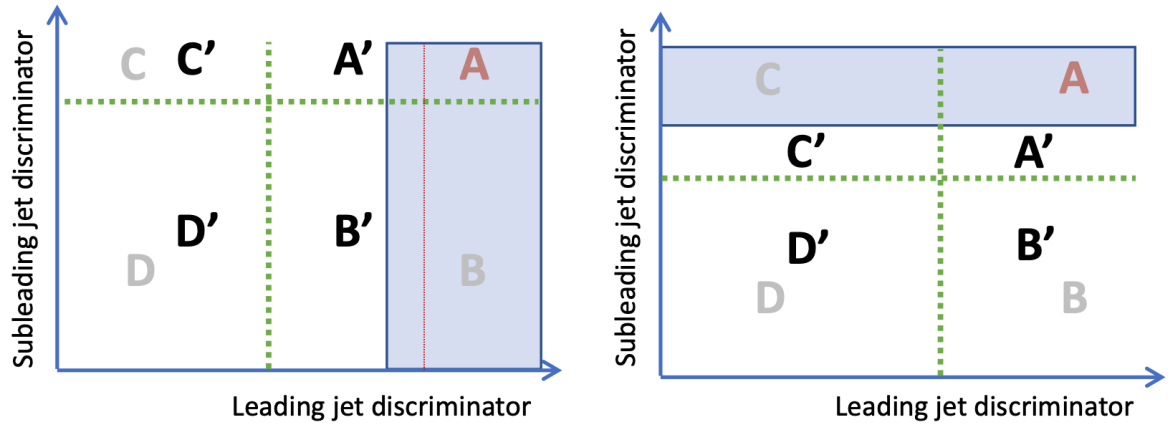

Figure 10.12: Schematics of sideband 1 (left) and sideband 2 (right) of the ABCD method. Events in the light blue areas are removed. Green dotted lines indicate the thresholds, which define the regions A', B', C' and D'.

yield, when the statistical uncertainties are taken into account. Small disagreements can be explained by simulated QCD multijet production events, where the simulation does not describe the data well. The large fluctuations in the background shape and the large statistical uncertainties are caused by simulated QCD multijet events with large event weights.

10.2.1 Sideband Studies

The $\overline{\text{SR}}$ is used to validate the background estimation. The difference between SR and $\overline{\text{SR}}$ is based on the χ^2 method and induces differences on the kinematic properties of the jets in both regions (see Appendix B), which might result in a slightly different distribution in the ABCD plane and affect the closures. In order to study such possible differences and to derive an uncertainty for the background estimation, the ABCD method was also investigated in sidebands of the SR and $\overline{\text{SR}}$.

Two different sideband regions, sideband 1 and sideband 2, are defined, as visualised in the left and right schematic of Figure 10.12, respectively. As before, the lower bounds of 0.3 are applied. The two sidebands are defined by removing either the right or upper part of the ABCD plane, indicated by the light blue area in the schematics, which leaves the actual region A blinded. The new regions A', B', C' and D' are defined by applying the thresholds indicated by the green dotted lines in the schematics.

As before, scans over several thresholds for sidebands 1 and 2 were performed and pre-

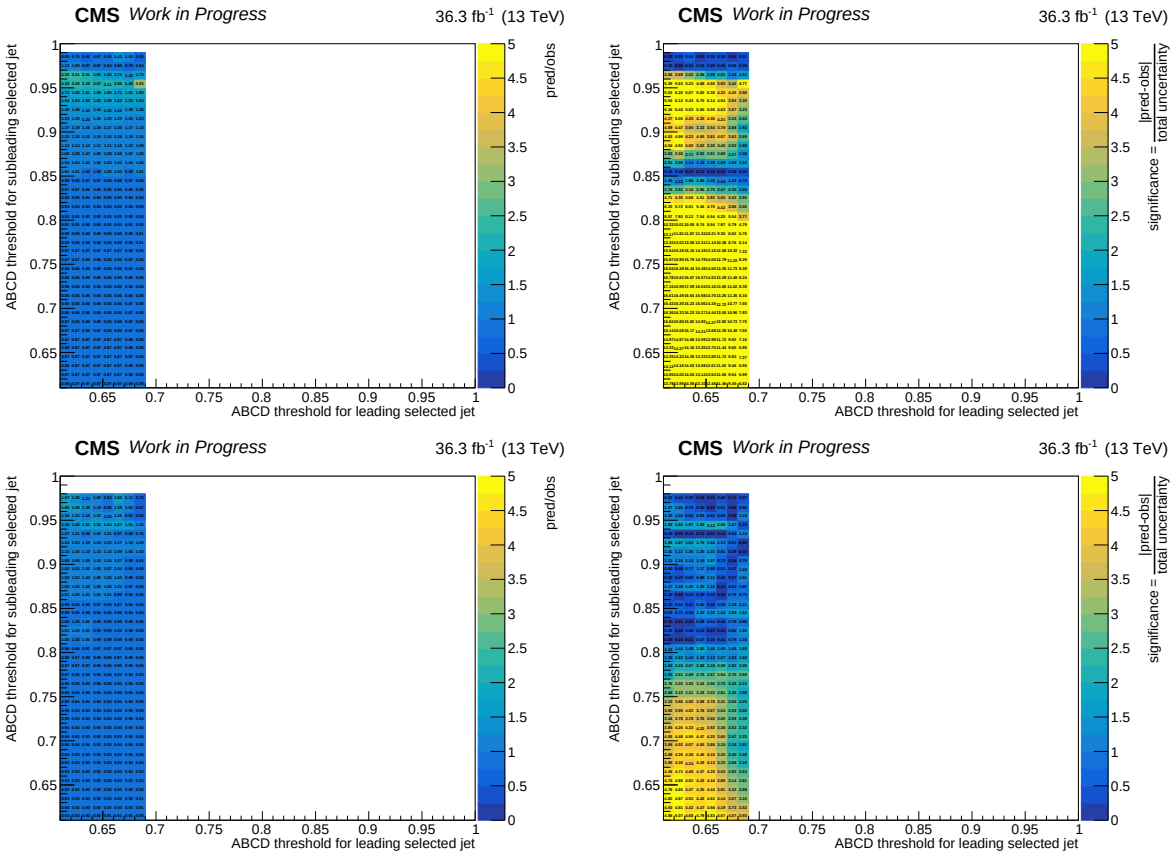

Figure 10.13: The closure (left) and its significance (right) in sideband 1 for SR (upper row) and $\overline{\text{SR}}$ (lower row).

sented in Figures 10.13 and 10.14, respectively. The closure (left) and its significance (right) are shown for SR (upper row) and $\overline{\text{SR}}$ (lower row). For the significance the total uncertainty is used, which is the quadratic sum of the statistical uncertainties of the observed yield, the predicted QCD yield and the non-QCD yield. The closure shows an underprediction for loose, an overprediction for very tight thresholds, and a good closure between these two areas. This behaviour is similar in the SR and the $\overline{\text{SR}}$. On average, the closure, as well as its significance are a bit better in the $\overline{\text{SR}}$. The latter one is related to the smaller event yields, and hence relative statistical uncertainties are larger.

For specifically chosen thresholds the yields in both sidebands are shown in Table 10.3 for the DNN discriminants used for the analysis of 1 mm lifetime. The closures and the statistical uncertainties for all lifetimes in the sideband 1 and 2 are presented in Table 10.4. The thresholds for this study are chosen such that the region A' is as close as possible to the actual region A while still containing sufficient numbers of events. For the

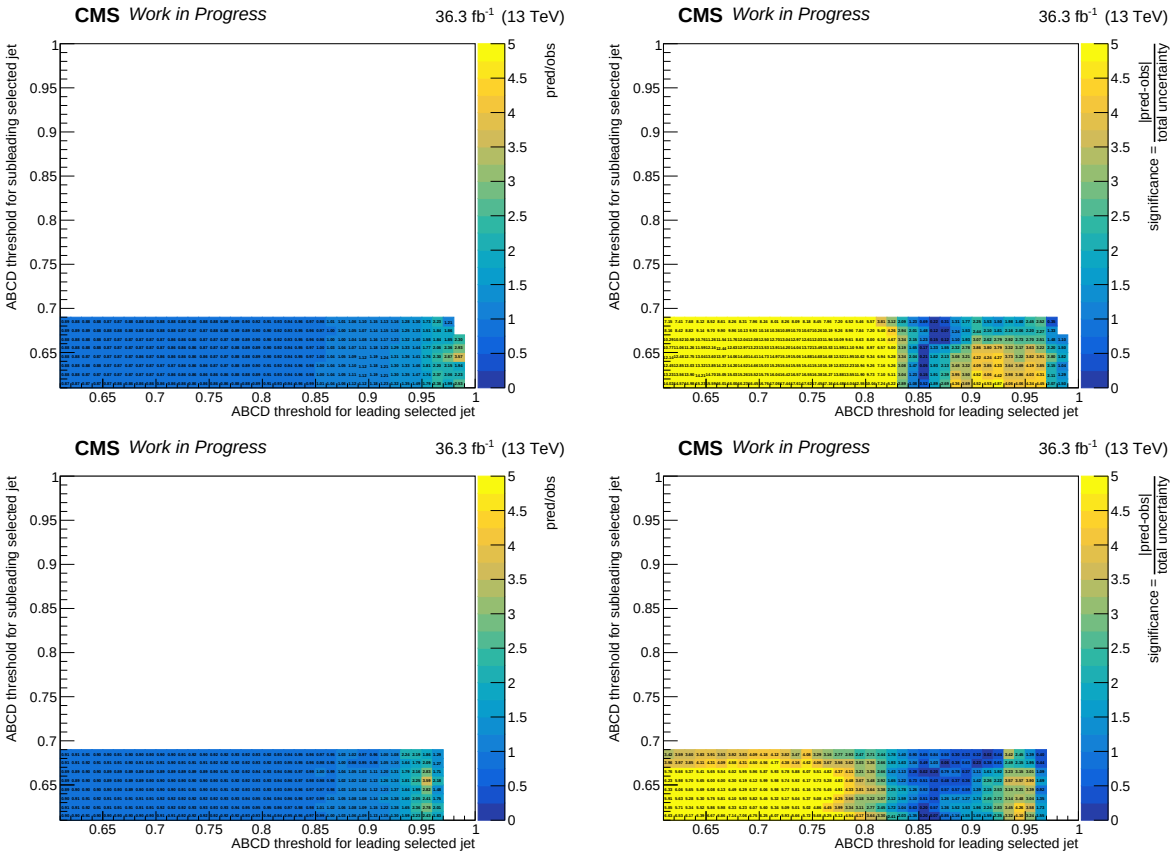

Figure 10.14: The closure (left) and its significance (right) in sideband 2 for SR (upper row) and $\overline{\text{SR}}$ (lower row).

present case of the 1 mm lifetime, the actual region A is defined by thresholds of 0.89x0.89, and therefore the sidebands are defined by thresholds of 0.65x0.89 or 0.89x0.65. In all presented cases, an overprediction can be observed, and the closures in the SR and $\overline{\text{SR}}$ agree within one or two standard deviations in each sideband. The results also show, that the statistical uncertainty is not able to cover the non-closure in all cases. Therefore, an additional uncertainty is derived from these sideband studies, as further discussed in Section 10.2.2. Comparing the plots of the $\overline{\text{SR}}$ in the sidebands to the closure and its significance in the full ABCD plane in Figure 10.10 (upper and middle), it is visible that the values are quite similar. In addition, the closure and its significance are better for the actual thresholds, than for the sideband values.

Table 10.3: Observed and predicted yields, the closure and its significance of SR and $\overline{\text{SR}}$ in sideband 1 with the thresholds 0.65x0.89 and in sideband 2 with the thresholds 0.89x0.65 for the signal with 1 mm lifetime.

		Observed yield	Predicted plus non-QCD yield	Closure	Closure significance
Sideband 1	SR	840.0 ± 29.0	968.3 ± 17.2	1.153 ± 0.045	3.805
	$\overline{\text{SR}}$	264.0 ± 16.2	282.2 ± 8.921	1.069 ± 0.074	0.984
Sideband 2	SR	910.0 ± 30.2	1006.5 ± 17.1	1.106 ± 0.041	2.784
	$\overline{\text{SR}}$	275.0 ± 16.6	281.8 ± 9.1	1.025 ± 0.070	0.360

Table 10.4: The closure and the statistical uncertainty in sideband 1 and 2 of the SR and $\overline{\text{SR}}$ for all lifetimes.

Lifetime	SR		$\overline{\text{SR}}$	
[mm]	Sideband 1	Sideband 2	Sideband 1	Sideband 2
0	1.372 ± 0.082	1.354 ± 0.077	1.124 ± 0.121	1.093 ± 0.122
0.05	1.164 ± 0.043	1.231 ± 0.045	1.086 ± 0.074	1.015 ± 0.069
0.1	1.241 ± 0.058	1.281 ± 0.059	1.012 ± 0.084	1.018 ± 0.087
1 & 5	1.153 ± 0.045	1.106 ± 0.041	1.069 ± 0.074	1.025 ± 0.070
10	1.096 ± 0.035	1.072 ± 0.033	1.063 ± 0.060	1.020 ± 0.057

10.2.2 Uncertainty Determination

Motivated by the results presented in the previous section, an additional uncertainty for the predicted QCD yield is derived. The total uncertainty on this predicted yield is composed of two parts, as explained in the following.

The first part of the uncertainty for the QCD background estimation procedure is estimated from the sidebands. The closures of the SR and the $\overline{\text{SR}}$ sideband 1 and 2 are compared for each lifetime, and the value further away from unity is used to define the uncertainty. As can be seen in Table 10.4, the closures in the sidebands of the SR are always worse than the closures in the $\overline{\text{SR}}$. For example, the values for LLPs with 1 mm lifetime, shown in Table 10.4, have a closure of 1.153 in sideband 1 and a closure of 1.106 in sideband 2, while the closures in the sidebands of the $\overline{\text{SR}}$ are significantly better, hence the first value is chosen and 15.3 % are used as the additional uncertainty. This procedure is slightly overestimating the uncertainty, such that a closure within less than one standard deviation is achieved[5]. The uncertainty is derived for each lifetime separately.

The second part of the uncertainty is derived from the statistical uncertainties of the data minus non-QCD yields in regions B, C and D, by propagating these statistical uncertainties through Equation 9.2 to the predicted QCD yield using standard error propagation.

Both parts are quadratically added and used as a systematic uncertainty for the final

[5]Studies were performed where the exact uncertainty to achieve one standard deviation was calculated, but the values and the final blinded fit results did not differ much, hence the more conservative procedure was chosen.

Table 10.5: The derived uncertainties from sideband and predicted QCD yield by the background estimation method with the first and second part of the uncertainty is listed for the two Higgs production modes and different LLP lifetimes.

Higgs production mode	Lifetime [mm]	Thresholds	Derived uncertainties from sidebands [%]	Predicted QCD yield in SR
VBF	0	0.92x0.92	37.2	167.8 ± 62.4 ± 2.3
	0.05	0.90x0.90	23.1	1061.6 ± 245.2 ± 9.5
	0.1	0.91x0.91	28.1	407.4 ± 114.5 ± 4.5
	1 5	0.89x0.89	15.3	297.4 ± 45.5 ± 3.8
	10	0.88x0.88	9.6	645.0 ± 61.9 ± 6.9
ggF	1	0.89x0.89	15.3	297.4 ± 45.5 ± 3.8
	10	0.88x0.88	9.6	645.0 ± 61.9 ± 6.9

statistical evaluation. For each lifetime of the LLPs, the systematic uncertainty was derived separately. The derived uncertainties of the first part and the predicted QCD yields with both parts of the uncertainties separately are presented in Table 10.5. The LLP lifetimes 1 mm and 5 mm for both Higgs production mechanisms share the same threshold of the same parametrised DNN discriminant, hence the values are identical.

10.2.3 Validation in $t\bar{t}$ Control Region

A validation for the simulated $t\bar{t}$ and minor backgrounds was performed in the $t\bar{t}$ CR, defined in Section 9.4. The same correction factors as for the SR are applied to describe data well by simulated events. Since the $t\bar{t}$ CR requires the presence of one muon, an additional correction due to the ID and isolation of the muon is applied. Furthermore, requirements for the missing transverse momenta $p_{\mathrm{T}}^{\mathrm{miss}}$ and the invariant mass of the combination of muon and $p_{\mathrm{T}}^{\mathrm{miss}}$ are set. The latter one is not allowed to be lower than 100 GeV to not unblind another potential signal region with the WH associated production mode. Distributions after the baseline selection can be found in Figure 10.15. The χ^2 value (left) and the corresponding invariant mass of the two selected jets (right) are shown. Furthermore, plots after the $\chi^2 < 10$ requirement are shown in Figure 10.16. The ΔR between the two selected jets (upper) and their DNN discriminants (lower left and right) are shown. For the latter two, in addition the requirement on ΔR is applied, to reproduce the selections of the SR. All plots show good agreement between data and simulated

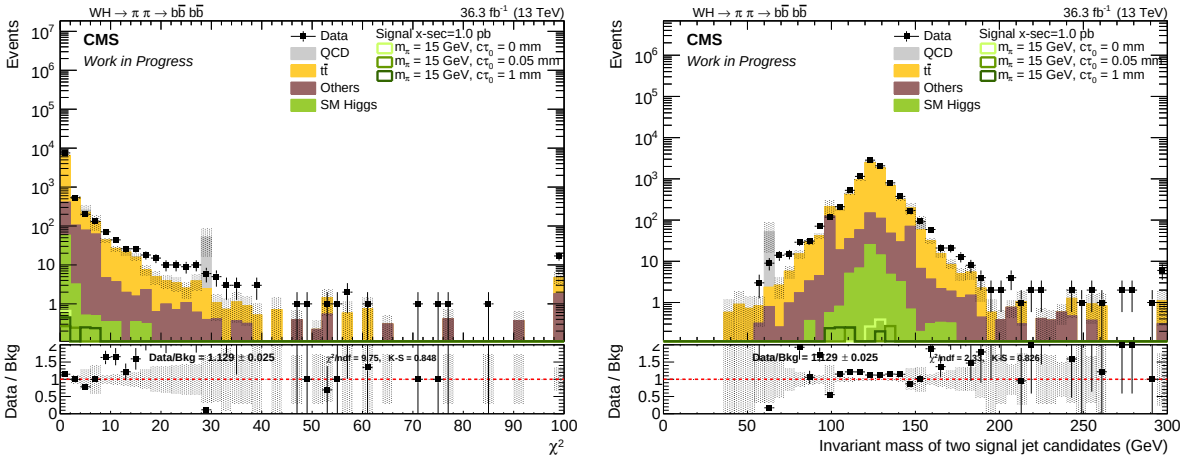

Figure 10.15: Distributions of the χ^2 (left) and invariant mass of the two selected jets (right) in the $t\bar{t}$ CR after the baseline section. The statistical uncertainties of the simulated SM background event yields are visualised.

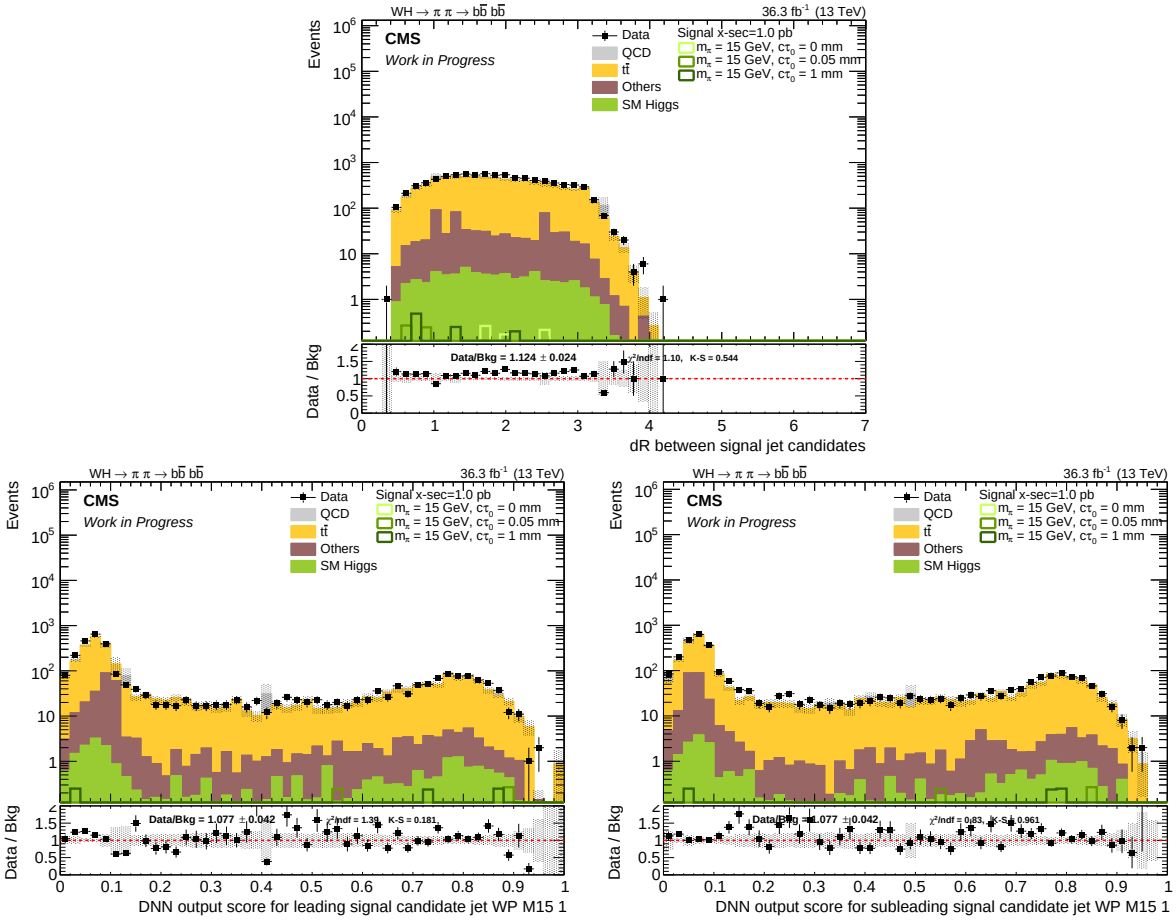

Figure 10.16: Distributions of the ΔR between the selected two jets (upper) in $t\bar{t}$ CR after χ^2 requirement. The DNN discriminants for mass 15 GeV, lifetime 1 mm of the selected two jets (lower left and right) in $t\bar{t}$ CR after ΔR requirement. The statistical uncertainties of the simulated SM background event yields are visualised.

events, and no trend is visible.

10.3 Systematic Uncertainties

Correction factors of different sources are applied to simulated processes to achieve a better agreement to recorded data. Each correction factor of the different sources (discussed in Section 9.7), comes with a corresponding systematic uncertainty. The different sources of uncertainties, including the derived uncertainty on the QCD background estimation from Section 10.2.2, are used as nuisance parameters in the final statistical evaluation (see Section 12.1). A log-normal prior distribution is used to model the impact on the

Table 10.6: Changes of the signal yields due to the different uncertainty sources for the different lifetimes of the boosted topology. The threshold values from Table 10.2 for each lifetime are also applied here.

Production mode	Lifetime [mm]	JEC [%]	JER [%]	PU [%]	Trigger [%]	μ_R/μ_F [%]	PDFs [%]	b tagging [%]
VBF	0.1	±20.6	±12.6	−2.81 +2.33	+61.9 −28.5	+0.4 −0.3	±2.1	+5.57 −5.45
	1	−33.4 +0.53	±12.0	+10.1 −11.0	+97.4 −32.1	+0.4 −0.3	±2.1	+4.87 −4.82
ggF	1	±1.09	±0.01	+1.61 −1.00	+67.2 −30.0	±7.6	±1.8	+5.01 −5.14

yield of each uncertainty in the fit. The fit is performed for each lifetime separately.
The sizes of the different uncertainty sources for different signals are presented in Table 10.6. For the b tagging uncertainty, the largest one across the different uncertainty sources[6] is presented. The difference of uncertainties across the different production modes or lifetimes might come from the different signatures, introduced, for example, by the displacement or the jet multiplicity. Especially the trigger uncertainty is large, compared to the other uncertainties. These large values come from the accumulation of the uncertainties of the different filter steps, which are considered to be fully correlated, resulting in the largest and most conservative possible value. Similar values for the trigger uncertainties are also observed for the SM background processes, which are listed in Table 10.7 as an example for the thresholds of 1 mm LLP lifetime. The JEC is, compared to the other uncertainties, for some signal lifetimes and background processes quite asymmetric. This is expected, since the procedure of the uncertainty derivation includes a slight variation of the p_{T}. This procedure in combination with the relative low selection threshold of 30 GeV for the jets, and the soft signal jets, removes jets by the down variation, but not by the up variation, hence an asymmetric uncertainty is observed.

[6]For example the light flavour contamination of the heavy flavour region, where the correction factors are derived. All these uncertainties are included as separate nuisance parameters for the final results.

Table 10.7: Changes of the non-QCD SM background yields due to the different uncertainty sources for 1 mm of the boosted topology. The threshold values from Table 10.2 are applied.

Background process	JEC [%]	JER [%]	PU [%]	Trigger [%]	μ_R/μ_F [%]	PDFs [%]	b tagging [%]
$t\bar{t}$	-21.0 $+7.53$	$+6.01$ -0.01	-3.57 $+5.64$	$+80.4$ -27.4	$+27.7$ -20.0	$+2.56$ -2.63	$+6.23$ $+6.05$
SM Higgs	$+4.35$ -41.7	$+5.38$ -33.9	$+6.30$ -7.10	$+98.0$ -32.6	$+8.74$ -9.26	$+7.02$ -11.7	$+6.57$ -6.39
Others	± 98.0	± 0.01	-5.37 $+4.14$	$+55.8$ -27.6	$+15.9$ -12.4	–	$+5.22$ -5.13

11 Search for Long-Lived Particles with Resolved Signatures

The following sections describe the search for LLPs with a resolved topology, for which masses of 40 GeV and 55 GeV are investigated. The overall procedure is similar to the boosted analysis, described in Chapter 10, but differs in relevant details. The LLPs with the investigated masses are expected to be closer in ΔR to each other, than they were for the boosted signature. In addition, the ΔR between the two b quarks originating from one LLP, is expected to be larger, than in the boosted signature (see Sections 4.1.1 and 9.3.1). Hence, the hadronisation of the two decay products originating from one LLP is expected to be reconstructed within one or two AK4 jets, resulting in up to four signal jets for the resolved topology. However, the fourth jet is often too soft to fulfil the $p_{\mathrm{T}} > 30\,\mathrm{GeV}$ requirement (see Section 4.1.1). Therefore, only three reconstructed signal jets of interest are required to reconstruct the Higgs boson and an invariant mass out of these three jets is used in a χ^2 method to find the three signal candidate jets of interest. As for the boosted analysis, only the jet combination with the lowest χ^2 value is used and only events below a χ^2 threshold are selected for the SR. A ΔR requirement amongst two of the three jets suppresses background. Again an ABCD method is used to estimate the QCD multijet background in the SR from data[1], validations of the ABCD method are performed in the $t\bar{t}$ CR and a validation region. Each step is described in detail in the following.

11.1 Full Event Selection

First of all, a strategy needs to be found to select the three signal jets of interest for events fulfilling the preselection (described in Section 9.3). In contrast to the boosted topology, more than two jets are expected, and the SM Higgs boson mass is not the

[1]The difference between the simulate QCD multijet background from simulation and the data-driven background estimation of the QCD background is indicated by the key words *simulated* and *predicted*, respectively.

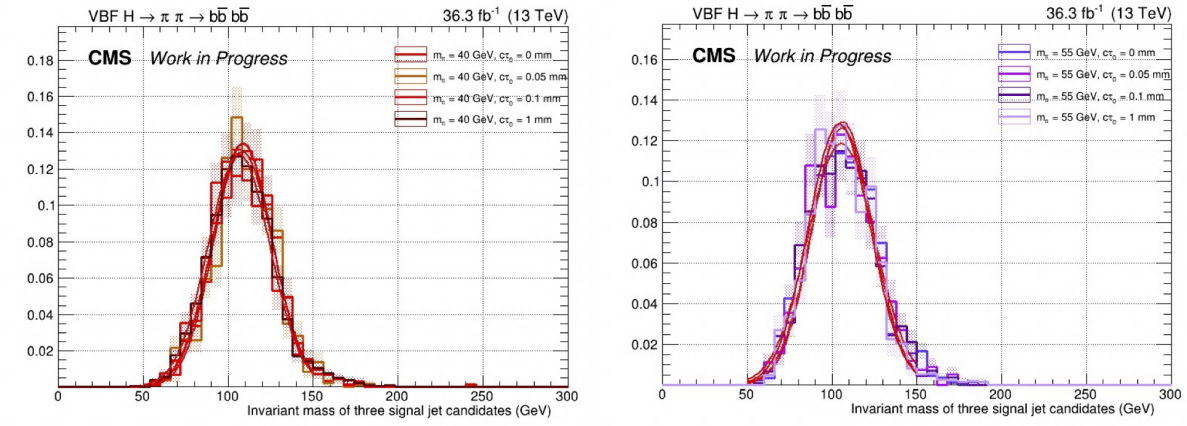

Figure 11.1: The invariant mass of three jets, where each is matched to generator b quarks originated by LLPs in events where exactly three jets are matched and for LLP masses of 40 GeV (left) and 55 GeV (right). A Gaussian function is fitted to each histogram.

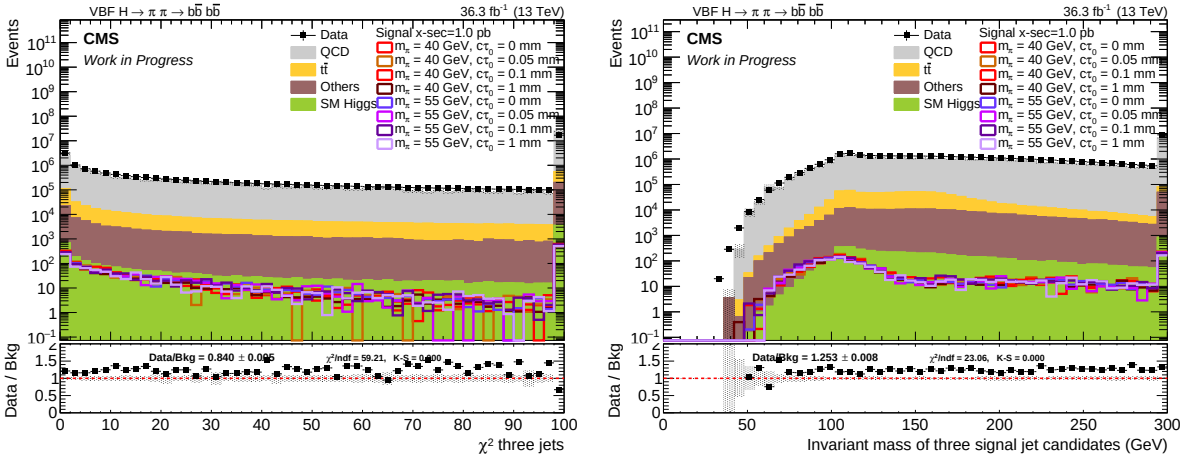

Figure 11.2: The distribution of the lowest χ^2 (left) and the corresponding invariant mass of three jets (right) after preselection for the resolved topology.

proper criteria to select these jets, since for most events, the fourth jet does not fulfil the $p_{\mathrm{T}} > 30\,\mathrm{GeV}$ requirement, and the Higgs boson can not be fully reconstructed using the remaining three jets only. Therefore, instead of reconstructing the Higgs boson from four jets, only three jets are used to calculate an invariant mass used for the χ^2 selection. Events in which exactly three jets could be matched, using a $\Delta\mathrm{R} < 0.4$ criteria, to different b quarks resulting from the decays of the LLPs are selected to derive a value m_{fit} for the invariant mass of the three-jet combination. The invariant three-jet masses for matched jets in samples with LLPs masses of 40 GeV (left) and 55 GeV (right) are shown

in Figure 11.1. Across the masses and lifetimes of the LLP, no significant difference is visible, as expected. Therefore, the invariant masses of all these events were combined in one histogram, and a Gaussian function was fitted to determine the mean value as the invariant mass $m_{\text{fit}} \approx 107\,\text{GeV}$ and the width as $\sigma_{\text{fit}} \approx 18\,\text{GeV}$. These two variables are used to define the selection criteria χ^2 as:

$$\chi^2_{ijk} = \frac{(m_{\text{reco},ijk} - m_{\text{fit}})^2}{\sigma_{\text{fit}}}, \tag{11.1}$$

with $m_{\text{reco},ijk}$ being the invariant mass of the three jets i, j and k. For each event, a χ^2_{ijk} value is calculated for each possible three-jet combination and the combination with the lowest χ^2_{ijk} value is chosen for the following steps. The lowest χ^2_{ijk} value and the corresponding invariant mass of the three jets are shown in Figure 11.2 left and right, respectively. The selection of the lowest χ^2 value leads to an invariant mass around the m_{fit} value for signal, and the SM background events show a long tail towards higher masses. Both distribution show an acceptable agreement between data and simulation. Possible selection thresholds of the χ^2 observable were studied using the punzi significance [131], and a selection of events with $\chi^2 \leq 30$, corresponding to an invariant mass window of $84\,\text{GeV} \leq m_{\text{reco},ijk} \leq 130\,\text{GeV}$, was chosen for the selection of events in the SR. The distribution of the transverse momenta p_{T} of the three selected jets can be found in Figure 11.3 (upper left, right and lower left plot). Furthermore, the largest ΔR value amongst the three selected jets is shown in the lower right plot of Figure 11.3. Events are only selected into the SR if the largest ΔR between the three chosen jets fulfils $\Delta\text{R}_{\text{max}} \leq 1.45$. This selection increases the probability of selecting the correct jets from the decay products of the LLPs, to select reconstructed signal jets from decay products of different LLPs, and further reduces the background contribution. The value was chosen based on the punzi significance. The selection might also reduce the probability of events in which gluons split into b quark pairs, reducing possible correlations between the DNN discriminant values.

The ABCD method used to predict the QCD background is validated in an additional region called $\overline{\text{SR}}$, defined by selecting events with the lowest χ^2 value of the three jet combination fulfilling $\chi^2 > 30$, and $\Delta\text{R}_{\text{max}} \leq 1.45$. The distribution of the transverse momenta p_{T} of the three selected jets and the $\Delta\text{R}_{\text{max}}$ after the $\chi^2 > 30$ selection can be found in Figure 11.4. The difference between data and simulated events is slightly worse in the $\overline{\text{SR}}$ compared to the SR, a small offset but no trend is visible.

The distributions of the DNN discriminant in the $\overline{\text{SR}}$ for a LLP mass of 40 GeV and 1 mm

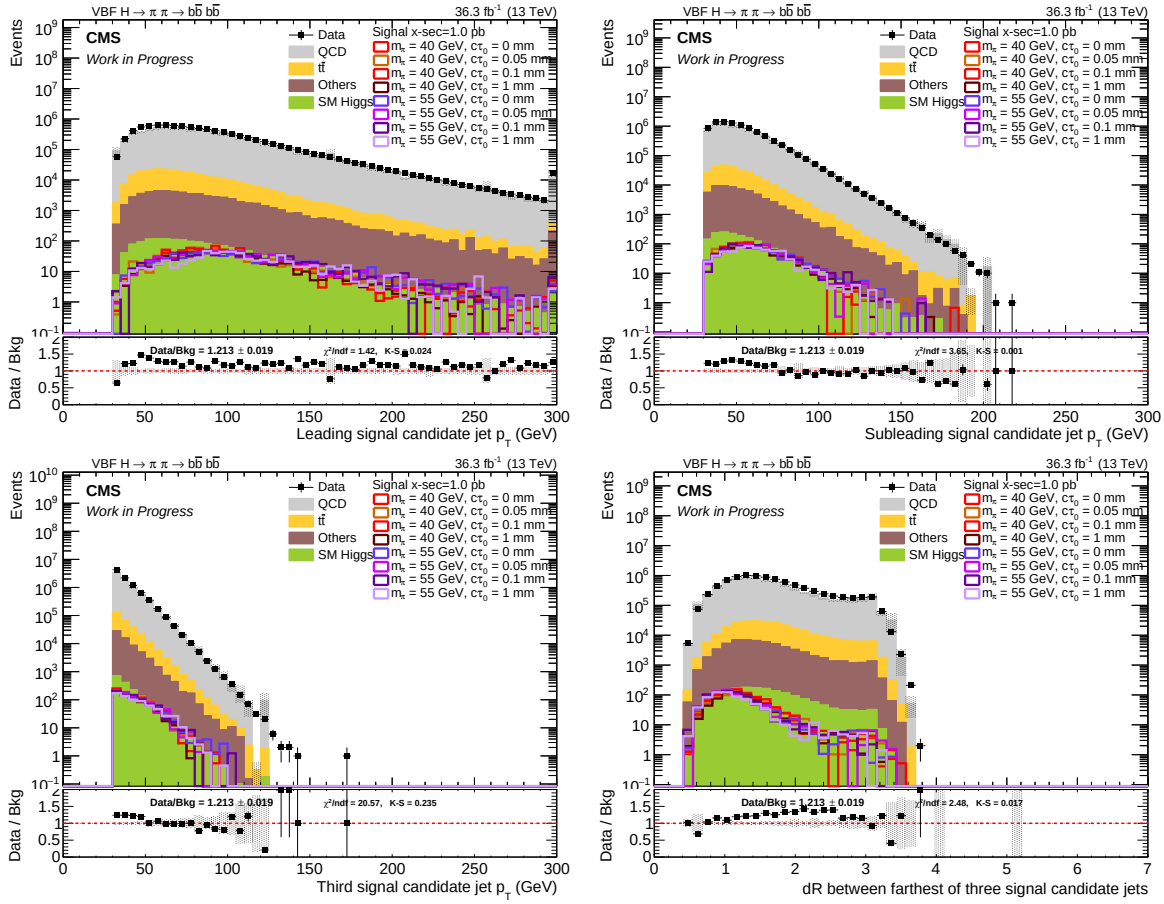

Figure 11.3: The distribution of the p_{T} of the three selected jets (upper left and right and lower left) and the largest ΔR amongst the three selected jets (lower right) after the $\chi^2 \leq 30$ requirement.

lifetime for the three selected, ϕ ordered jets are shown in Figure 11.5. For lower values the data-to-simulation agreement is similar to the previous plots, while for very high DNN discriminants the difference is larger.

The efficiency of each requirement, taking the previous requirements into account, can be found in Figure 11.6 for signal with LLP mass of 40 GeV (upper row), 55 GeV (middle row) and simulated QCD multijet and $t\bar{t}$ background (last row), as well as in Table 11.1. The single requirements[2] are:

- Triggers: Events fulfil the logic *or* of the two triggers.
- Trigger Filters: All online trigger objects must be matched by $\Delta\mathrm{R} < 0.4$ to recon-

[2]Only the χ^2 and the ΔR requirements are different for the boosted topology, while the remaining ones are the same.

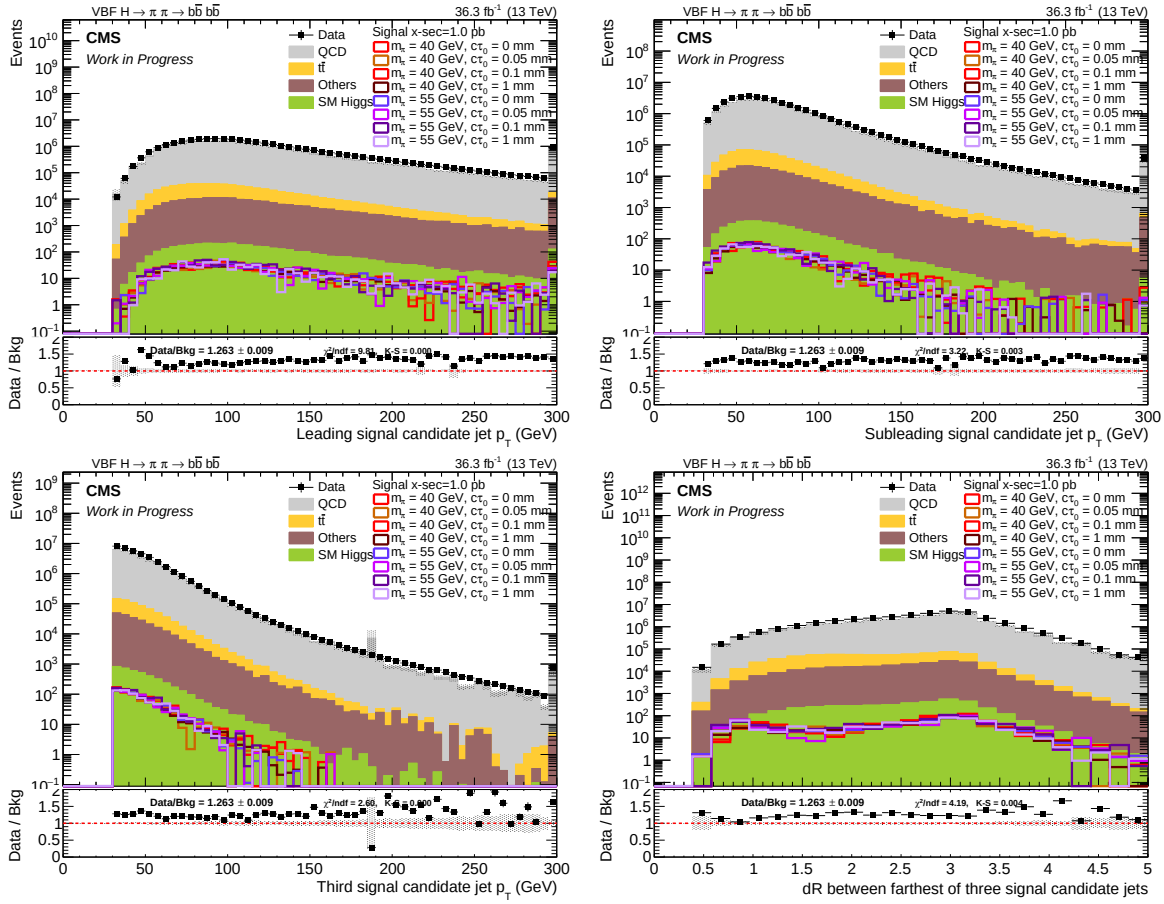

Figure 11.4: The distribution of the p_T of the three selected jets (upper left and right and lower left) and the ΔR_{max} amongst the three selected jets (lower right) after the $\chi^2 > 30$ requirement.

structed jets in the event.

- $N_{jets,tight\,ID}$: At least four jets with tight ID[3] requirements must be found in the event.
- Preselection: The remaining preselection requirements on H_T, as well as lepton and photon vetos.
- χ^2 method: Three jets are selected with $\chi^2 \leq 30$, following Equation 11.1.
- ΔR: The largest distance in ΔR between two amongst the three selected jets does not exceed 1.45.

[3]The jet reconstruction efficiency exceeds 90 % with a noise jet rejection of more than 90 %.

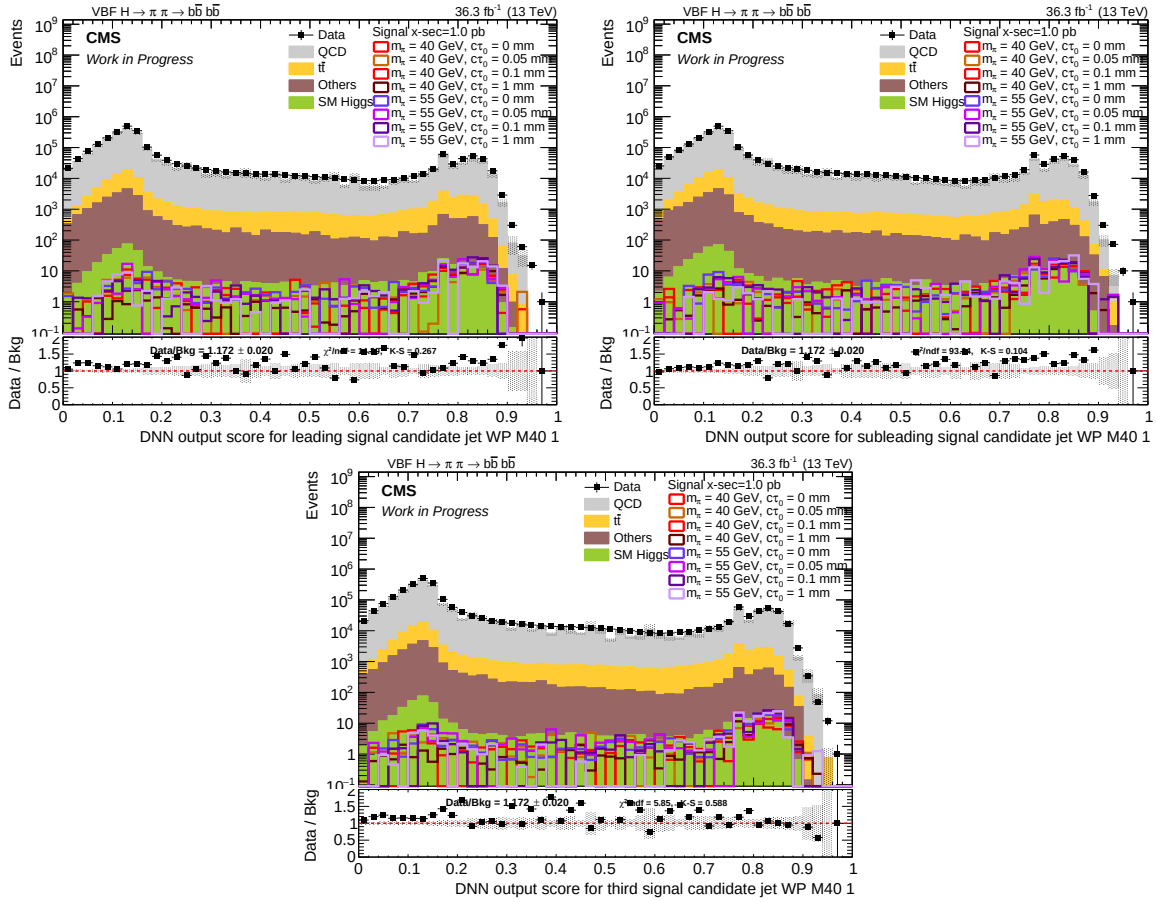

Figure 11.5: The distribution of the DNN discriminant in $\overline{\text{SR}}$ for 40 GeV and 1 mm of the three selected, ϕ ordered jets for events with $\chi^2 > 30$ and $\Delta\text{R} \leq 1.45$.

The trigger efficiency is relatively low for signal, as presented in Section 9.2. The requirements of χ^2 and ΔR show better discrimination between signal and background in the resolved topology compared to the boosted selection.

The final selections lead to the following simulated background proportions in the SR: QCD 96.8 %, $t\bar{t}$ 2.35 %, Others 0.83 %, and SM Higgs < 0.05 %.

As for the boosted analysis, QCD multijet production is the dominant background, and is similarly estimated using an ABCD method. Two out of the three selected jets define the ABCD region with the DNN discriminant. The DNN is parametrised with the LLP masses and lifetimes, making the use of the same network for both topologies possible. As already discussed in Section 10.1, the p_T of the jets is correlated with the DNN discriminant, which would affect the ABCD method. Instead of the typical p_T sorting of the jets, they are reordered using the ϕ coordinates. This introduces a reproducible way of sorting which

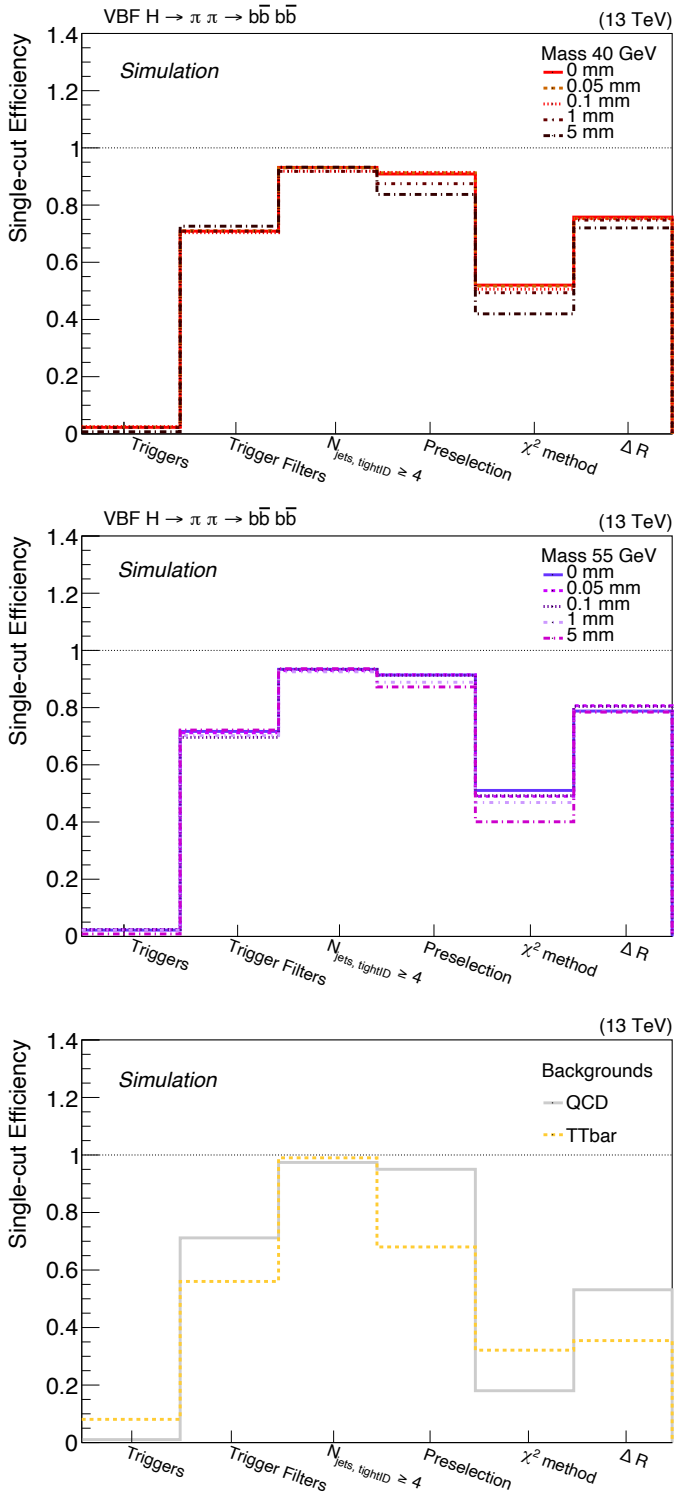

Figure 11.6: The efficiencies of all selection requirements applied, with respect to the events passing the previous step, on signal with LLP mass of 40 GeV (upper row) and 55 GeV (middle row) and background (last row) for the resolved topology. The requirements are applied in the following order: The two triggers, matching between objects of the trigger filters to reconstructed objects, jet multiplicity, the remaining preselections, jet selection with the χ^2 method and the ΔR requirement.

Table 11.1: The efficiencies of all selection requirements for the signal with LLP masses of 40 GeV and 55 GeV, as well as simulated background events for the resolved topology. Each efficiency is calculated with respect to the events passing the previous step. The order of application of the requirements is from left to right.

Mass [GeV]	Mode	Lifetime [mm]	Trigger	Trigger Filters	$N_{\text{jets,tight ID}}$	Preselection	χ^2 method	ΔR
40	VBF	0	0.023	0.709	0.932	0.909	0.520	0.758
		0.05	0.024	0.710	0.930	0.913	0.517	0.753
		0.1	0.025	0.704	0.919	0.914	0.506	0.752
		1	0.022	0.709	0.918	0.875	0.493	0.747
		5	0.007	0.726	0.932	0.837	0.420	0.720
		10	0.004	0.744	0.939	0.842	0.400	0.636
	ggF	1	0.007	0.583	0.960	0.891	0.458	0.669
		10	0.001	0.611	0.969	0.870	0.371	0.672
55	VBF	0	0.022	0.717	0.934	0.914	0.510	0.788
		0.05	0.023	0.712	0.929	0.915	0.490	0.807
		0.1	0.024	0.696	0.933	0.913	0.492	0.804
		1	0.022	0.702	0.925	0.889	0.468	0.786
		5	0.009	0.721	0.936	0.872	0.401	0.784
		10	0.004	0.733	0.944	0.874	0.370	0.750
	ggF	1	0.007	0.584	0.959	0.901	0.450	0.720
		10	0.002	0.634	0.961	0.874	0.377	0.685
Background sample								
QCD			0.010	0.712	0.974	0.950	0.180	0.531
$t\bar{t}$			0.081	0.560	0.990	0.680	0.321	0.354

should not be correlated to the DNN discriminant.

11.2 Background Estimation

The main SM background is, as for the boosted analysis, the QCD multijet production. An ABCD method is used to estimate the QCD background from data, while all non-QCD backgrounds are taken from simulation (see Sections 9.6 and 10.2).

However, instead of only two jets as in the boosted analysis, three jets are now selected by the χ^2 method. The separation between the SR and the $\overline{\text{SR}}$ is based on the χ^2 value, while the same selection on the ΔR_{max} between the three jets is required in both regions. The event selection of the $\overline{\text{SR}}$ aims to define a region that describes the actual SR well. The inversion of the ΔR requirement defines two additional regions, but the selection

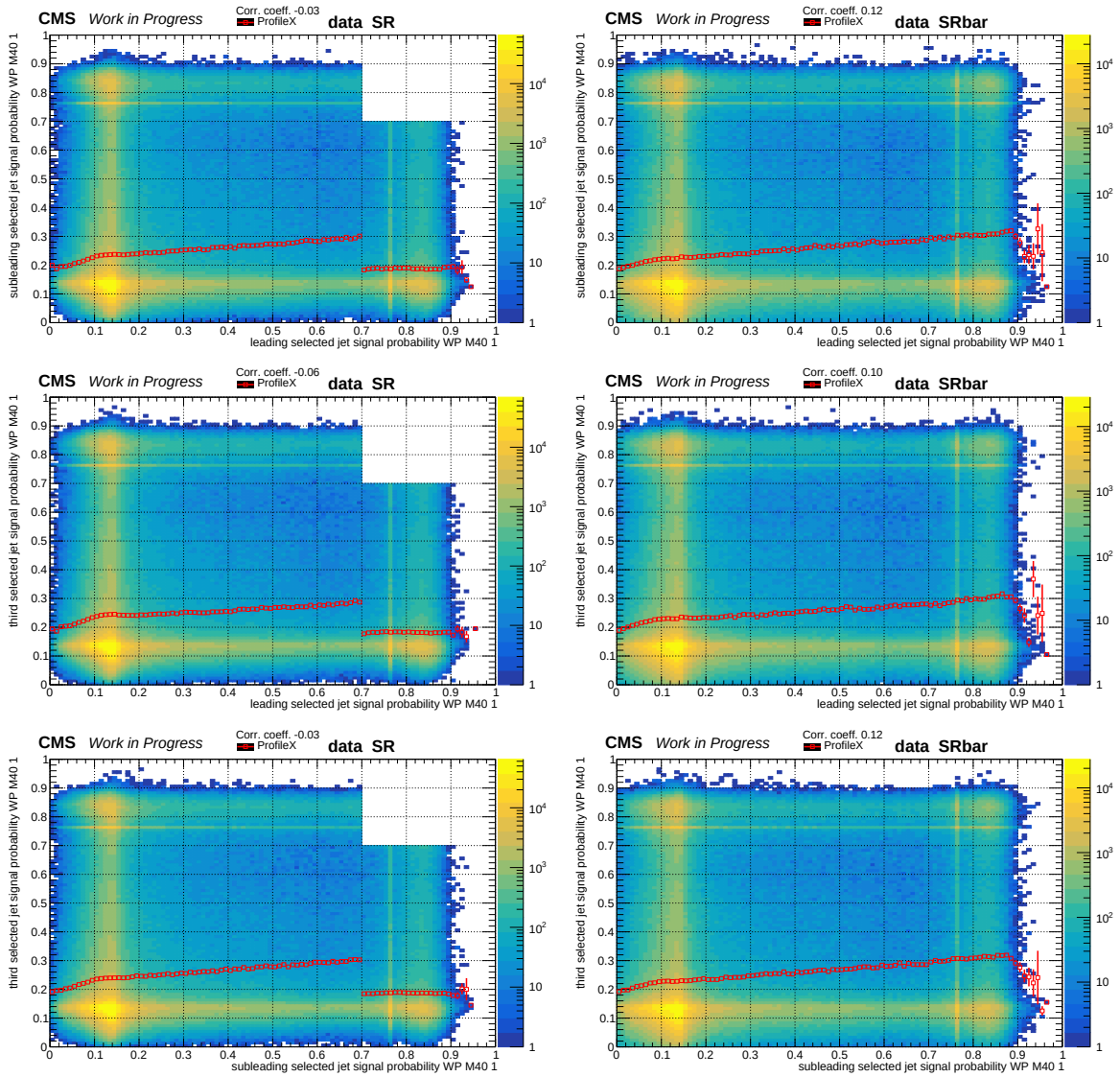

Figure 11.7: Distributions of the DNN discriminant in the SR (left) and $\overline{\text{SR}}$ (right) for the LLPs mass of 40 GeV and 1 mm lifetime in data. Different combinations of the three ϕ sorted jets are used: leading-subleading jets (upper row), leading-third jet (middle row), and subleading-third jet (last row). The upper right region is not shown for the distributions in the SR.

induces differences on the kinematic properties of the jets, as studied in Appendix B. While there are three jets used for the reconstruction of the Higgs boson, only two are required to define the ABCD regions. There are three possible jet combinations and their corresponding ABCD regions are shown in Figure 11.7 for the SR (left column) and the $\overline{\text{SR}}$ (right column) for the case of the analysis of LLPs with a mass of 40 GeV and

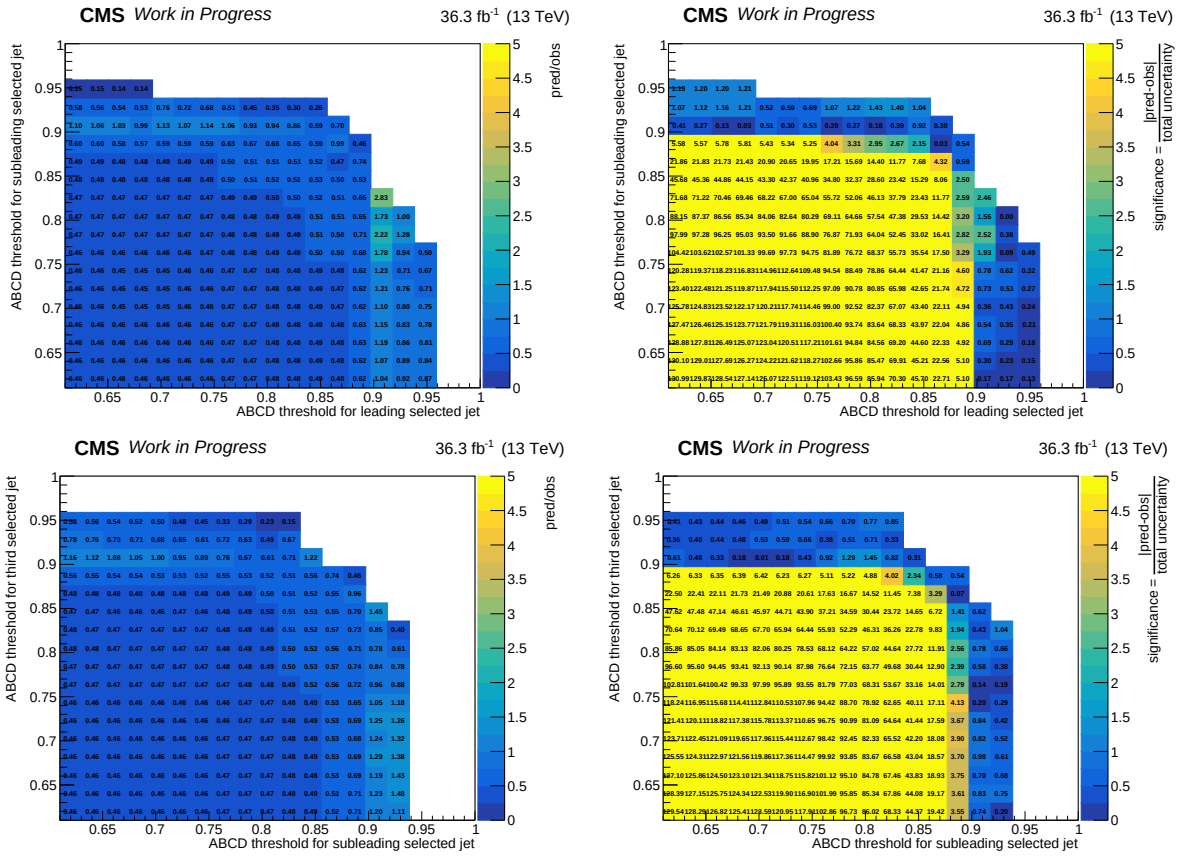

Figure 11.8: The closure (left) of the ABCD method and its significance (right) in the $\overline{\text{SR}}$ using data of LLPs of 40 GeV and 1 mm lifetime. The different combinations of the three ϕ sorted jets are: leading and subleading jet (upper row) and subleading and third jet (last row).

1 mm lifetime. As in the boosted analyses, the jet ordering is randomised by ordering the jets according to their ϕ value. For the SR the region A is not shown. The first row represents the distributions of the leading-subleading jets the second row for leading-third and the last row for subleading-third jet. The mean value of the y-axis for each bin of the x-axis is indicated by the red empty squares. Due to the ϕ sorting the distributions are approximately symmetric for both axes and therefore, only the mean values of one axis is shown. If the shape and the slope of this profile are similar in the SR and the $\overline{\text{SR}}$ this indicates that the $\overline{\text{SR}}$ is describing the SR well. For the leading-subleading jets (first row) and the subleading-third (last row) combinations the profiles in SR and $\overline{\text{SR}}$ are very similar, while the profile of the middle row is slightly flatter in the $\overline{\text{SR}}$, which can also be seen by the correlation coefficient in the $\overline{\text{SR}}$. Slight differences between the plots can be related to the kinematic selection of the ΔR. The definition of ΔR also includes the

azimuthal angle ϕ (see Equation 7.4), therefore a connection between these two variables is expected. Jets with a large ΔR between each other have also a certain probability to have a large $\Delta\phi$ value. Therefore, the two jets would be ordered as the leading and third jet. Hence, this jet combination (middle row) is not used for defining the ABCD regions. For the remaining two combinations, the closure and its significance of data in $\overline{\text{SR}}$ are shown in Figure 11.8. In both cases the data closure in $\overline{\text{SR}}$ is quite bad, which stems most likely from a correlation of the DNN discriminant of the two jets. For the leading-subleading jet (upper row), the closure is a bit more fluctuating and not as stable as for the subleading-third jet (last row). Therefore, the subleading-third jet combination is taken for the remaining part of the analysis. In addition, studies were performed to remove events where either one or both jets have a low DNN discriminant, which helps to reduce the correlation and, in addition, significantly decreases the background yields. For the resolved topology, a lower bound of 0.5 was considered sufficient and all the following ABCD distributions are presented with this selection applied. The efficiency of the lower bound selection with respect to the previous ΔR requirement, is 0.03 for $t\bar{t}$, 0.04 for the simulated QCD multijet production and > 0.70 for signal with VBF and ggF production mode.

In the following, all values are provided for LLPs with masses of 40 and 55 GeV and all lifetimes, while plots are shown for the LLP of 40 GeV and 1 mm as example. The remaining plots for the other mass-lifetime combinations can be found in Appendix E.

The ABCD distributions in the SR for the analysis of the LLPs with mass of 40 GeV and lifetime of 1 mm are shown in Figure 11.9. As for the boosted analysis, the upper right area is the potential signal region A. Shown are the signal with VBF and ggF Higgs production mode (upper left and right), the different SM processes of simulated QCD multijet (second row left), $t\bar{t}$ (second row right), SM Higgs (third row left) and Others (third row right). For the distribution of data (last row) region A is not shown. Again, the prominent accumulation of events around values of 0.76 is due to jets without assigned SV, leading to default values in several input features and therefore the DNN discriminant has values between zero and 0.76 with a hard cut-off at the upper value. The lower bound leaves only very little correlation in the distribution of data, compared to the left plot in the last row in Figure 11.7. While signal is accumulated in the upper right area, also the events of the different background processes are distributed there, and the difference is not as large as for the boosted topology. The discrimination between the resolved signal and SM background was expected to perform not as well as for the boosted topology. For the resolved topology, the hadronisation products of mainly one

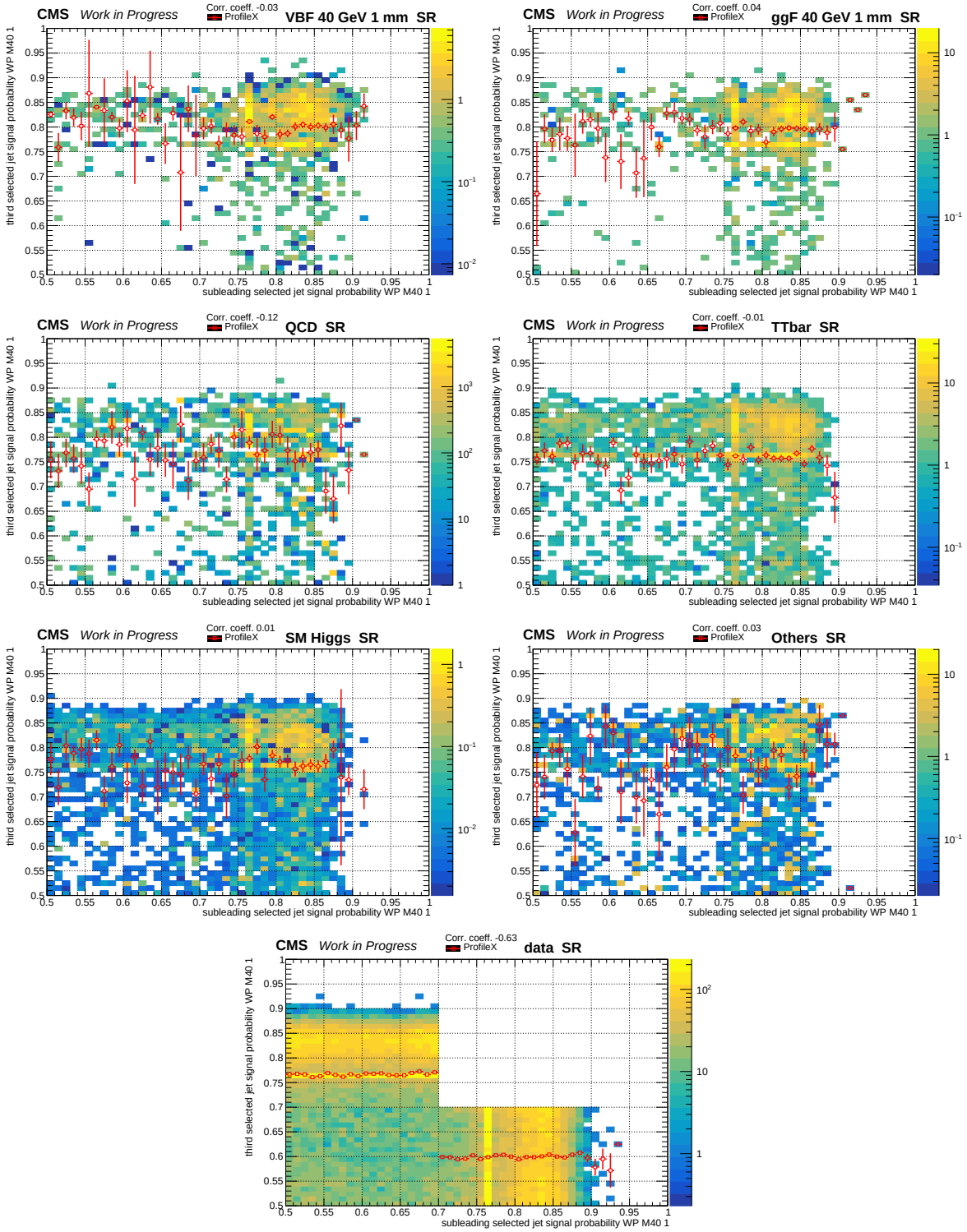

Figure 11.9: Distributions of the DNN discriminant in the SR of LLPs of 40 GeV and 1 mm lifetime of the subleading and third selected jets for: VBF (upper left) and ggF (upper right) Higgs production mode signal, simulated QCD multijet production (second row left), $t\bar{t}$ (second row right), SM Higgs (third row left). For the distribution of data (last row), region A is not shown.

b quark are reconstructed in one jet, and beside the possible displacement, the jets are more similar to SM objects. The proportions of the different simulated backgrounds are: QCD 96.9 %, $t\bar{t}$ 1.98 %, Others 1.00 %, and SM Higgs 0.05 %. For the three non-QCD backgrounds, the correlation between the DNN discriminants is rather small, but as for the boosted analysis, the background estimation method models the QCD background only, while the remaining backgrounds are taken from simulations.

In addition, the analogous distributions, are shown for the $\overline{\text{SR}}$ in Figure 11.10. In the $\overline{\text{SR}}$ less signal is present, and the SM background distributions have fewer events, but the distributions are similar to the ones in the SR. Furthermore, the distribution of data has only very little correlation, and is very similar to the distribution in the SR, up to the blinded area. Especially, the profiles of both distribution agree well.

The impacts of different thresholds to define the ABCD regions are studied using the VBF Higgs production mode. The signal with the ggF Higgs production mode was studied in addition, but the results are on average better with respect to the VBF mode, and hence the latter one has more constraints. The different distributions are shown in Figures 11.11 and 11.12, where each bin represents the specific combination of the two thresholds on DNN discriminants defining the ABCD regions. White bins indicate regions where either the SM background yield or the signal yield is zero. The signal significance $S/\sqrt{B}$ in region A (Figure 11.11 first row) shows higher values for looser threshold combinations. The large values at the edge indicate values where the background yield is close to zero. The significance enhancement Σ_{signal} (Figure 11.11 last row), defined in Equation 10.2, is higher for looser thresholds, since the signal yield in region A is enriched. The closure in the $\overline{\text{SR}}$ (Figure 11.12 first row) is defined in Equation 10.3. Loose thresholds tend to result in an underprediction, while for tighter thresholds overpredictions can be observed. In between these two areas thresholds can be found where the method closes well. The closure significance of data in the $\overline{\text{SR}}$ (Figure 11.12 second row) is calculated as in Equation 10.4. The distribution shows a closure within 1.5 standard deviations with thresholds above 0.83, while for looser thresholds the closure is much worse. The blinded expected upper limits at 95 % CL on the value of cross section times branching ratio, with respect to the SM Higgs boson cross section is presented in the last row of Figure 11.12. For these expected limits all systematic uncertainties of the non-QCD backgrounds and signals are taken into account, while only the statistical uncertainties of the background estimation is used for the predicted QCD yield. Additional systematic uncertainties for the background estimation were derived and are described in Section 11.2.2, which will affect the final results. On average, the results of the limits are worse, the looser the threshold values

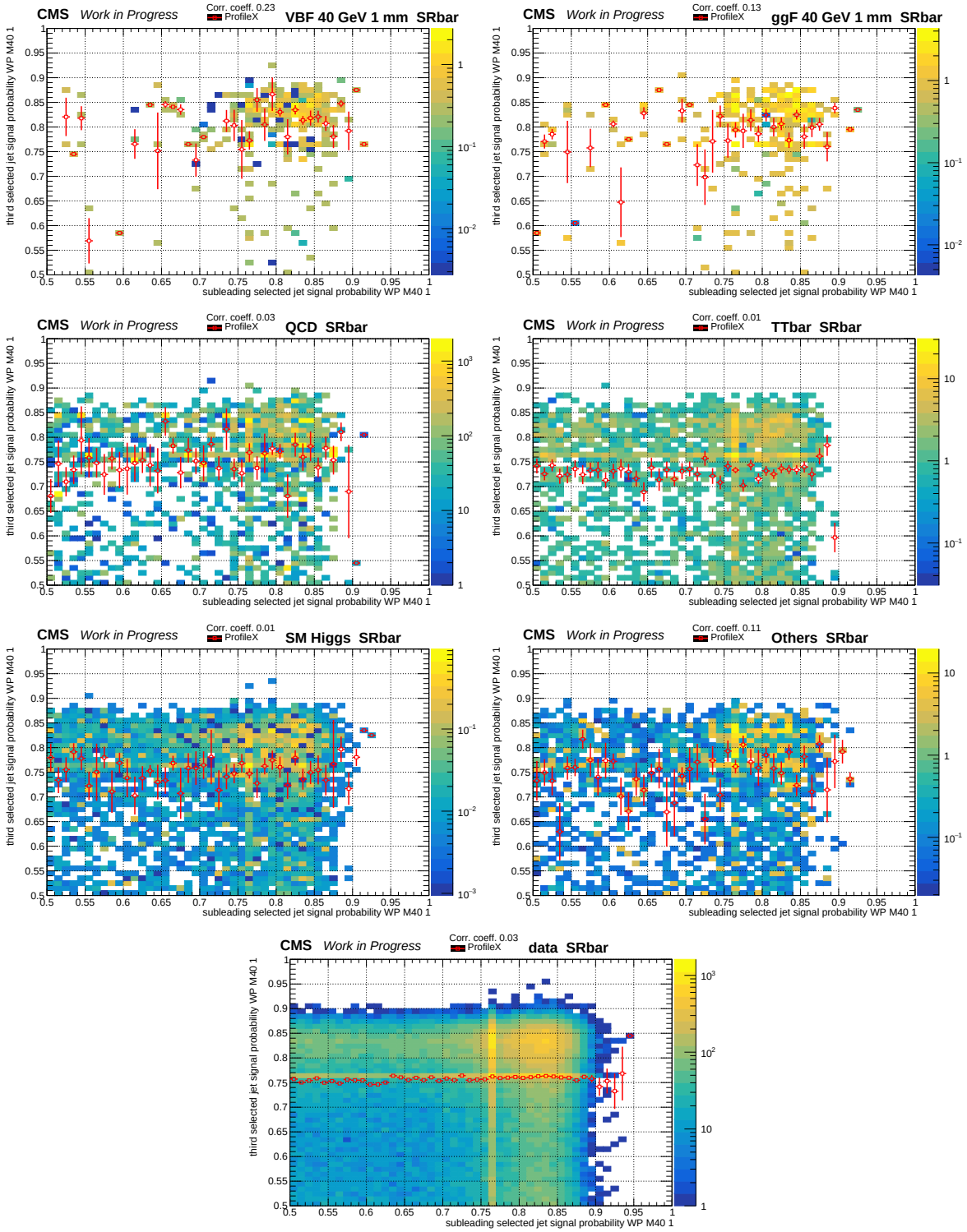

Figure 11.10: Distributions of the DNN discriminant in the $\overline{\text{SR}}$ of LLPs of 40 GeV and 1 mm lifetime of the subleading and third selected jets for: VBF (upper left) and ggF (upper right) Higgs production mode signal, simulated QCD multijet production (second row left), $t\bar{t}$ (second row right), SM Higgs (third row left), Others (third row right) and data (last row).

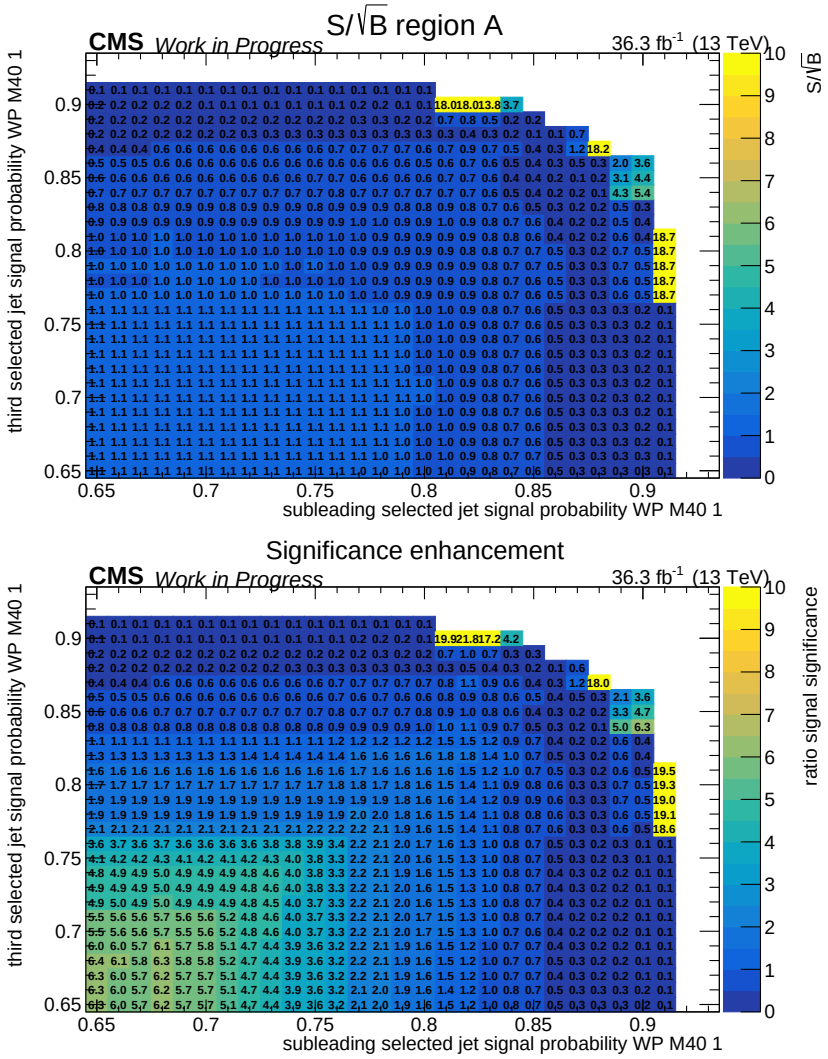

Figure 11.11: Effect of various thresholds for the ABCD method on the analysis of LLPs with a mass of 40 GeV and a lifetime of 1 mm on: Signal significance (upper), the significance enhancement Σ_{signal} (lower).

are.

The presented measures are essential indicators for a valid ABCD method, hence they were compared and the final threshold values were selected as presented in Tables 11.2 and 11.3 for LLP masses of 40 GeV and 55 GeV, respectively. Again the DNN discriminant of 1 mm is used for 5 mm and 10 mm lifetimes. The same thresholds have been found sufficient for all three lifetimes and, as well for the ggF production mode, which has the advantage that combined limits for both production modes can be calculated. The signal enhancement in region A and Σ_{signal} are smaller compared to the values found for the boosted topology.

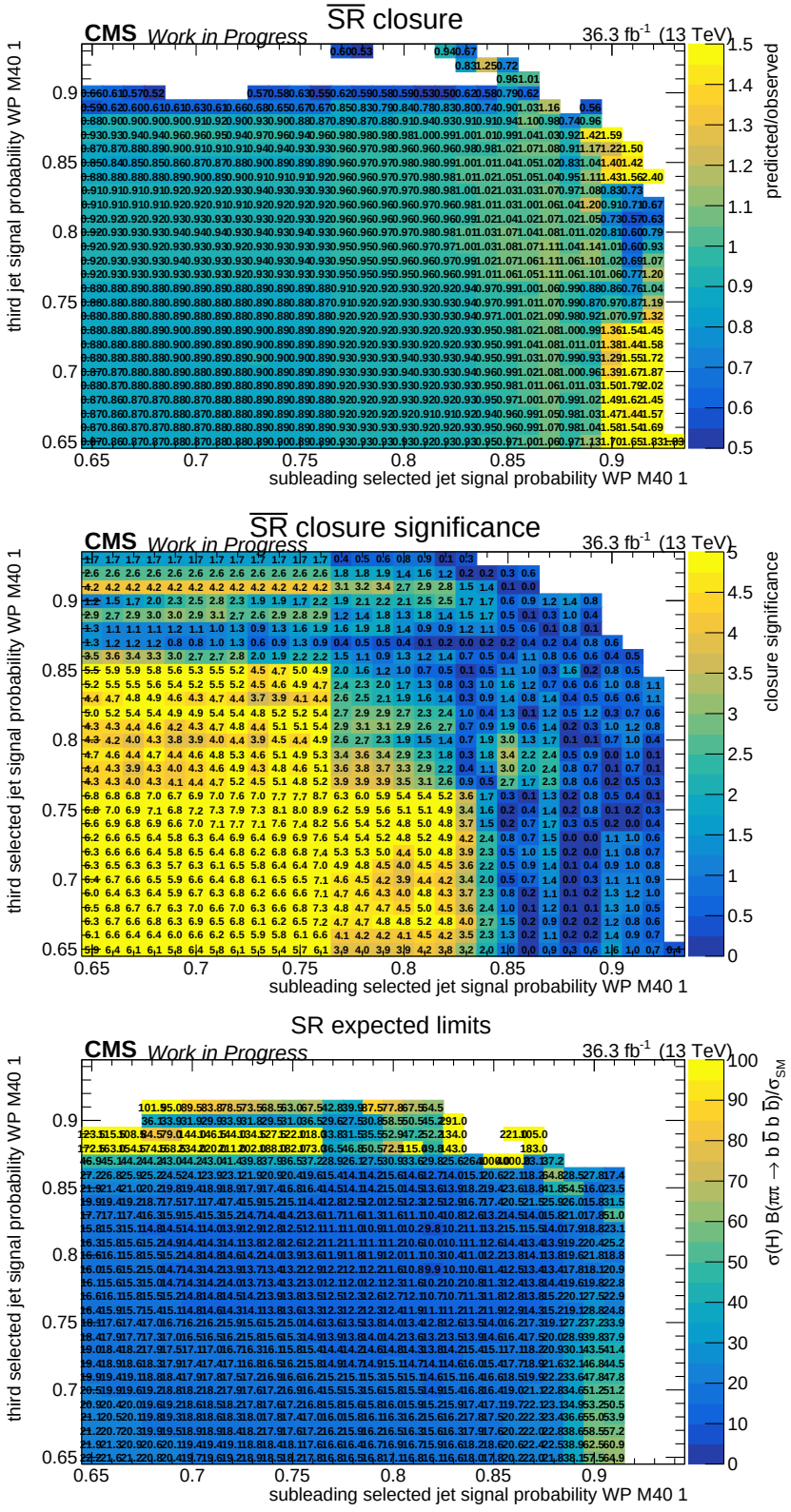

Figure 11.12: Effect of various thresholds for the ABCD method on the analysis of LLPs with a mass of 40 GeV and a lifetime of 1 mm on: The closure using data in the $\overline{\text{SR}}$ (upper) and its significance (second row), and blinded expected upper limits in the SR (last row).

Table 11.2: The chosen thresholds for each lifetime of the LLP mass of 40 GeV with the resulting values of the discussed indicators for the VBF and ggF Higgs production modes in signal.

	Lifetime in mm	Threshold	$S/\sqrt{B}$ region A	Σ_{signal}	Closure $\overline{\text{SR}}$	$\overline{\text{SR}}$ closure significance	Blinded expected limits
VBF	0	0.84x0.84	0.232	0.360	0.988 ± 0.017	0.724	29.3
	0.05	0.85x0.85	0.403	0.509	0.996 ± 0.024	0.153	16.0
	0.1	0.84x0.84	0.702	0.950	0.998 ± 0.017	0.089	9.5
	1	0.83x0.83	0.723	1.203	0.995 ± 0.018	0.273	10.2
	5		0.150	1.079			57.5
	10		0.072	1.014			126.0
ggF	1	0.83x0.83	2.024	1.259	0.995 ± 0.018	0.273	3.8
	10		0.065	0.317			204.5

Table 11.3: The chosen thresholds for each lifetime of the LLP mass of 55 GeV with the resulting values of the discussed indicators for the VBF and ggF Higgs production modes in signal.

	Lifetime in mm	Threshold	$S/\sqrt{B}$ region A	Σ_{signal}	Closure $\overline{\text{SR}}$	$\overline{\text{SR}}$ closure significance	Blinded expected limits
VBF	0	0.86x0.86	0.351	0.622	0.997 ± 0.014	0.186	25.9
	0.05	0.86x0.86	0.369	0.623	1.001 ± 0.015	0.057	22.8
	0.1	0.86x0.86	0.535	0.832	1.006 ± 0.015	0.407	15.6
	1	0.86x0.86	0.562	0.830	1.010 ± 0.018	0.563	13.0
	5		0.134	0.523			56.3
	10		0.029	0.337			681.0
ggF	1	0.86x0.86	1.439	0.723	1.010 ± 0.018	0.563	5.1
	10		0.039	0.120			548.0

This is a direct result of the similar shapes of signal and SM background at the high values of the DNN discriminant, due to the similarity between the final states of signal and SM backgrounds containing b quarks. The best discrimination is reached for both LLP masses for lifetimes of 0.1 mm and 1 mm, which results in the best blinded expected limits. This indicates again that the displacement increases the sensitivity of the analysis, since for shorter lifetimes the limits are getting worse. However, for lifetimes of 5 mm and 10 mm worse limits are again caused by lower trigger efficiencies for both masses.
The proportions of the remaining backgrounds in region A, as an example for the DNN discriminants for the signal with a mass of 40 GeV and 1 mm lifetime are: predicted QCD 98.5 %, $t\bar{t}$ 0.96 %, SM Higgs 0.03 %, Others 0.48 %.
The distribution of the DNN discriminant, for the parametrisation of LLPs with a mass of 40 GeV and a lifetime of 1 mm, of the subleading (left) and the third (right) of the ϕ ordered selected jets in regions B (first row), C (middle row) and D (last row) are shown in Figure 11.13. Data and the simulation-based SM background agree generally well within the statistical uncertainties. Some events from the simulated QCD multijet productions have high weights, leading to fluctuations and high statistical uncertainties. No trends or constant offsets are visible for the different regions, while small disagreements are most likely due to the simulated QCD multijet productions, which do not describe the data well.

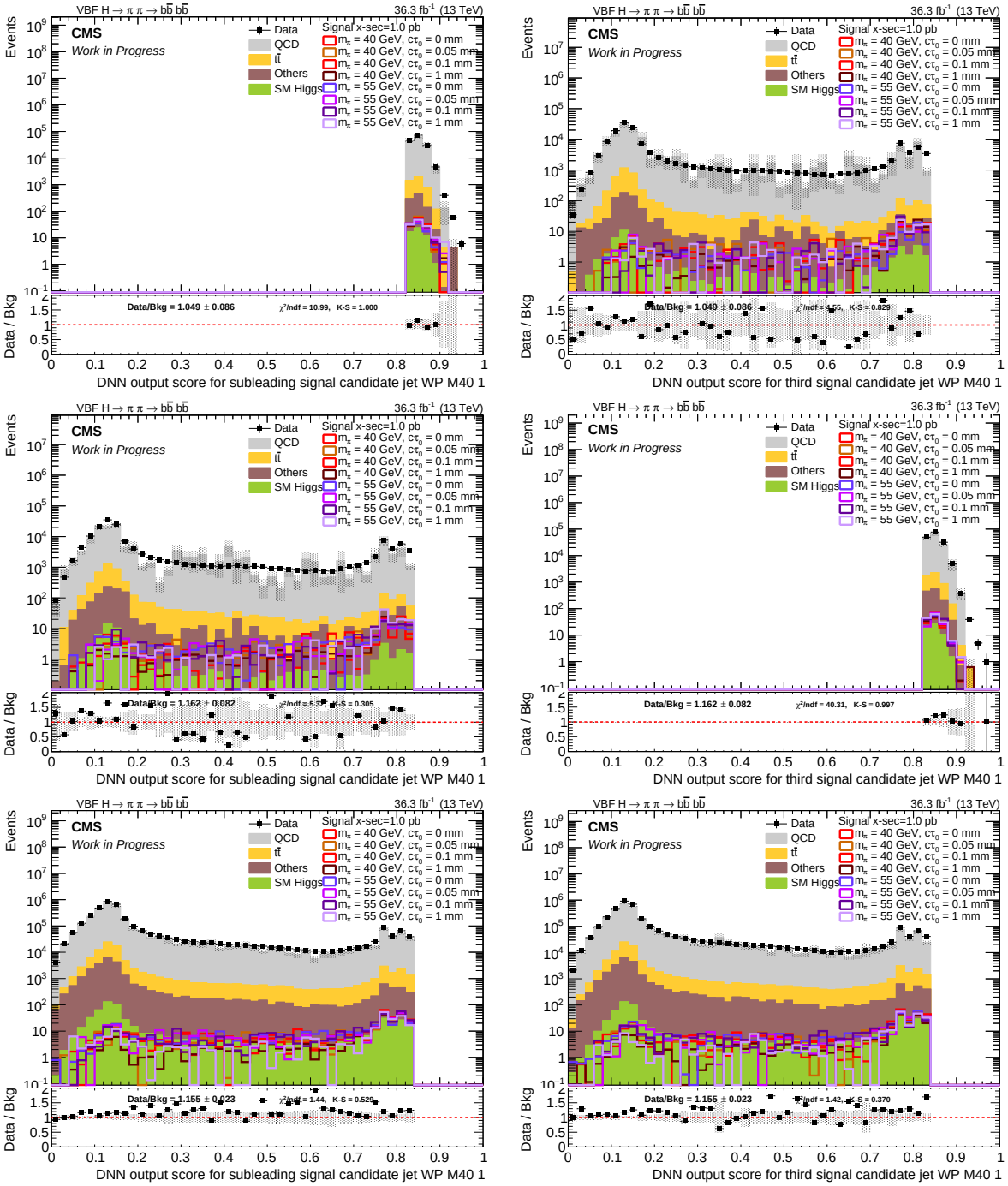

Figure 11.13: Distribution of the DNN discriminant for the resolved topology evaluated for the parametrised DNN with 40 GeV and 1 mm for the subleading (left) and third (right) jet out of the three selected jets in region B (upper row), region C (middle row) and region D (last row).

11.2.1 Sideband Studies

The background estimation method is validated in the $\overline{\text{SR}}$, but it was observed that the χ^2 selection, used to separate SR and $\overline{\text{SR}}$, leads to differences in the kinematic properties of the jets (see Appendix B). Such differences might lead to different DNN discriminant distributions, different distributions in the ABCD planes and therefore to different closures. In addition, there is a relation between the ΔR selection and the ϕ ordering of the jets, which might also affect the distributions. Therefore, the sideband studies complement the studies for possible differences between the SR and the $\overline{\text{SR}}$ and are used to derive an uncertainty for the QCD background estimation.

The sidebands 1 and 2 are defined by removing the right or the upper part of the ABCD plane, leaving the actual region A blinded. The two sidebands are visualised in Figure 10.12. The blue shaded areas are the removed parts and the green dotted lines indicate the thresholds, defining the new regions in these reduced planes are called A',

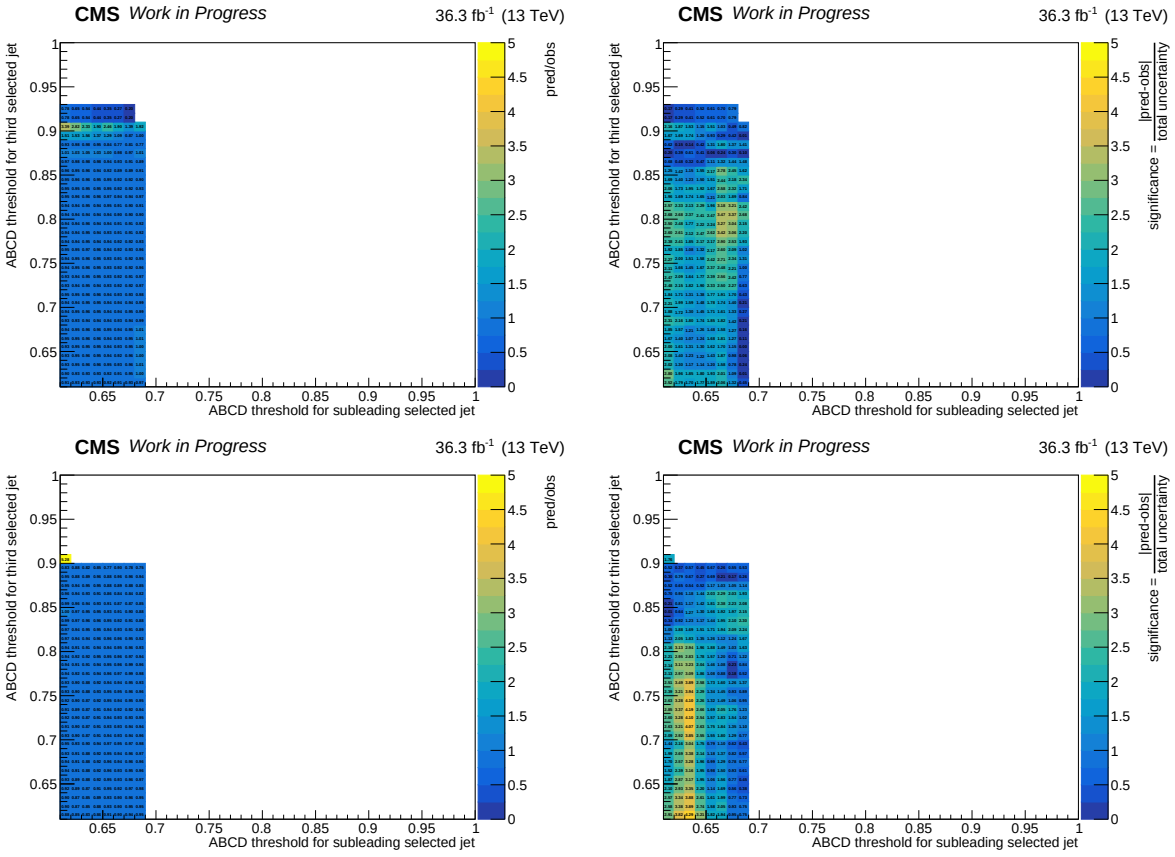

Figure 11.14: The closure (left) and its significance (right) in sideband 1 for SR (upper row) and $\overline{\text{SR}}$ (lower row) for the DNN discriminant of 40 GeV and 1 mm.

B', C' and D'.

Scans over several thresholds in the sidebands 1 and 2 were performed and are presented in Figures 11.14 and 11.15, respectively. The distributions of SR (upper row) and $\overline{\text{SR}}$ (lower row) of the closure (left) and its significance (right) are presented. The closure significance uses the total uncertainty, which is the quadratic sum of the statistical uncertainties of the observed yield, the QCD yield predicted by the ABCD-method and the non-QCD yield. The figures show that the background is underpredicted almost everywhere, for both the SR and the $\overline{\text{SR}}$ and both sidebands. However, at very tight thresholds, for which only few events are present in the regions B' or C' the background is overpredicted. The shapes of the distributions of the closure significance differs between SR and $\overline{\text{SR}}$ and especially in sideband 2 the values are much smaller for the latter region, which might come from the smaller event yields and larger relative statistical uncertainties.

For specifically chosen thresholds, the closures, their significances and associated yields in

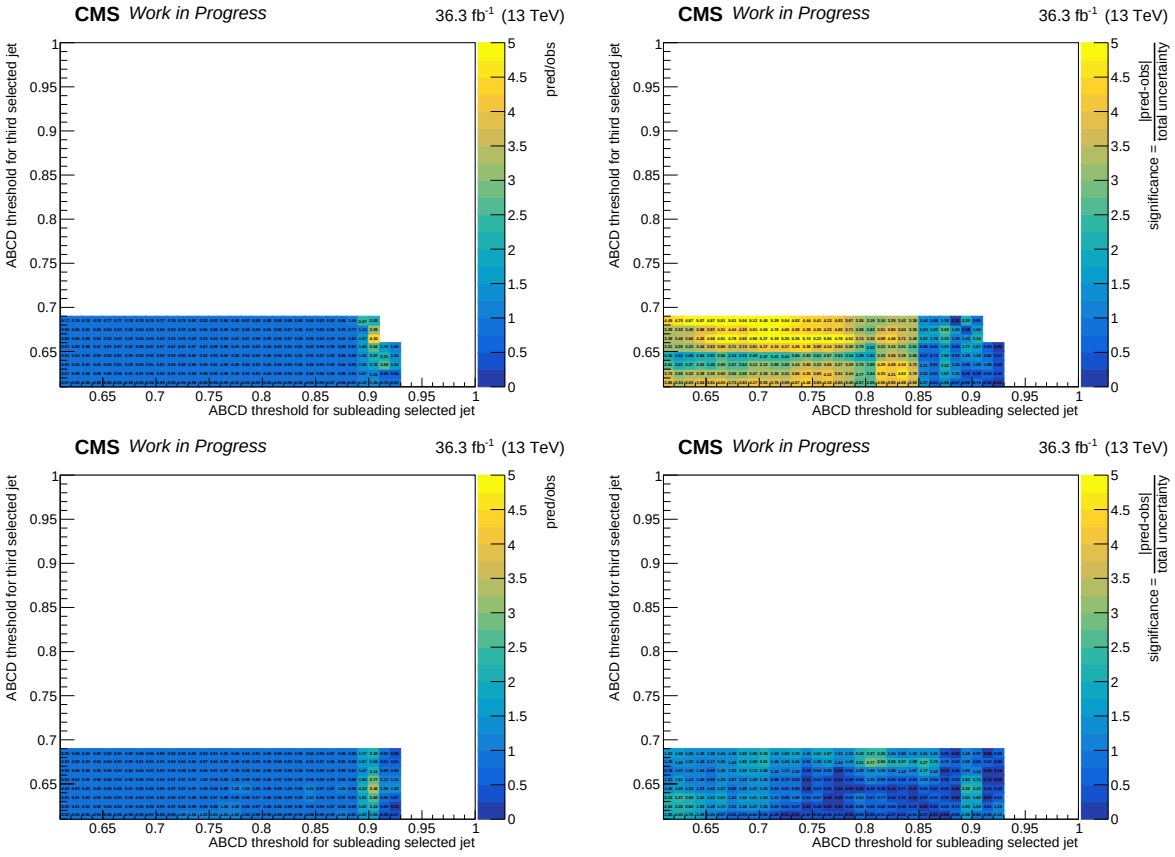

Figure 11.15: The closure (left) and its significance (right) in sideband 2 for SR (upper row) and $\overline{\text{SR}}$ (lower row) for the DNN discriminant of 40 GeV and 1 mm.

Table 11.4: Observed and predicted yields, the closure and its significance of SR and $\overline{\text{SR}}$ in sideband 1 with the thresholds 0.65x0.83 and in sideband 2 with the thresholds 0.83x0.65 for the signal with a mass of 40 GeV and 1 mm lifetime.

		Observed yield	Predicted plus non-QCD yield	Closure	Closure significance
Sideband 1	SR	2245.0 ± 47.4	2136.0 ± 45.2	0.951 ± 0.028	1.666
	$\overline{\text{SR}}$	1308.0 ± 36.2	1237.6 ± 32.7	0.946 ± 0.036	1.445
Sideband 2	SR	2128.0 ± 46.1	1939.6 ± 42.5	0.941 ± 0.028	3.005
	$\overline{\text{SR}}$	1283.0 ± 35.8	1252.8 ± 33.4	0.976 ± 0.038	0.616

Table 11.5: The closure and the statistical uncertainty in sideband 1 and 2 of the SR and $\overline{\text{SR}}$ for a LLP mass of 40 GeV and all lifetimes.

Lifetime	SR		$\overline{\text{SR}}$	
[mm]	Sideband 1	Sideband 2	Sideband 1	Sideband 2
0	0.897 ± 0.028	0.928 ± 0.028	0.980 ± 0.037	1.038 ± 0.038
0.05	0.919 ± 0.034	0.882 ± 0.032	1.006 ± 0.045	0.996 ± 0.024
0.1	0.933 ± 0.030	0.903 ± 0.028	0.919 ± 0.035	1.027 ± 0.039
1 & 5 & 10	0.951 ± 0.028	0.941 ± 0.028	0.946 ± 0.036	0.976 ± 0.038

the two sideband regions for a LLP mass of 40 GeV and a lifetimes of 1 mm can be found in Table 11.4. Region A' is defined by the thresholds in such a way, that it is as close as possible to the actual region A, while still containing a sufficient number of events. For the presented case of 40 GeV and 1 mm, the chosen thresholds for the sidebands is 0.65x0.83 or 0.83x0.65. The closures in the SR and the $\overline{\text{SR}}$ agree within one or two standard deviations in each sideband. The statistical uncertainty is clearly not large enough to cover a potentially difference to unity of the closure, hence an additional uncertainty was derived from the sidebands, which is explained in Section 11.2.2.

The closures for all lifetimes in both sidebands for the SR and the $\overline{\text{SR}}$ can be found in Tables 11.5 and 11.6 for LLP masses of 40 GeV and 55 GeV, respectively. On average an underestimation in almost all sidebands was observed.

Table 11.6: The closure and the statistical uncertainty in sideband 1 and 2 of SR and $\overline{\text{SR}}$ for a LLP mass of 55 GeV and all lifetimes.

Lifetime	SR		$\overline{\text{SR}}$	
[mm]	Sideband 1	Sideband 2	Sideband 1	Sideband 2
0	0.943 ± 0.024	0.930 ± 0.023	0.936 ± 0.030	0.933 ± 0.029
0.05	0.959 ± 0.025	0.936 ± 0.024	0.925 ± 0.031	0.946 ±0.030
0.1	0.955 ± 0.025	0.959 ± 0.025	0.912 ± 0.030	0.948 ± 0.031
1 & 5 & 10	0.911 ± 0.029	0.936 ± 0.028	0.998 ± 0.039	1.013 ± 0.040

11.2.2 Uncertainty Determination

The uncertainty derivation for the QCD background estimation method follows the approach discussed in Section 10.2.2 for the boosted analysis. The uncertainty again consists of two parts. The first part is estimated from closure of the sideband regions, where the value further away from unity is taken as the uncertainty. The sidebands in the SR and the $\overline{\text{SR}}$ are investigated, and the latter one closes on average better. The values can be found for the LLP masses of 40 GeV and 55 GeV in Tables 11.7 and 11.8, respectively. The second part of the uncertainty is derived from the statistical uncertainties of the data minus non-QCD yields in regions B, C and D, using standard error propagation.
Both parts are quadratically added and used as the systematic uncertainty for the final statistical fit. This systematic uncertainty was derived for each mass and lifetime individually. The predicted QCD yields with both parts of the uncertainties separately can also be found in Tables 11.7 and 11.8. The lifetimes between 1 mm and 10 mm share the same thresholds of the parametrised DNN discriminant and are therefore identical.
The uncertainties on the QCD background estimations are on average smaller than for the boosted topology, but the predicted event yields are much larger for the resolved topology.

11.2.3 Validation in $t\bar{t}$ Control Region

The $t\bar{t}$ CR requiring exactly one muon is used for the validation of the simulated $t\bar{t}$ and minor backgrounds. The full requirements of the baseline selection for the $t\bar{t}$ CR are

Table 11.7: The derived uncertainties from sidebands and predicted QCD yields with the first and second part of the total uncertainty quoted separately for a LLP mass of 40 GeV and the two Higgs production modes and different LLP lifetimes.

Higgs production mode	Lifetime [mm]	Thresholds	Derived uncertainties from sidebands [%]	Predicted QCD yield in SR
VBF	0	0.84x0.84	10.3	13045 ± 1347 ± 98
	0.05	0.85x0.85	11.8	5227 ± 618 ± 47
	0.1	0.84x0.84	9.7	12248 ± 1192 ± 95
	1 5 10	0.83x0.83	5.9	14176 ± 845 ± 125
ggF	1 10	0.83x0.83	5.9	14176 ± 845 ± 125

Table 11.8: The derived uncertainties from sidebands and predicted QCD yields with the first and second part of the total uncertainty quoted separately for a LLP mass of 55 GeV and the two Higgs production modes and different LLP lifetimes.

Higgs production mode	Lifetime [mm]	Thresholds	Derived uncertainties from sidebands [%]	Predicted QCD yield in SR
VBF	0	0.86x0.86	7.0	19119 ± 1344 ± 127
	0.05	0.86x0.86	6.4	18746 ± 1206 ± 126
	0.1	0.86x0.86	4.5	18483 ± 841 ± 126
	1 5 10	0.86x0.86	8.9	13277 ± 1187 ± 109
ggF	1 10	0.86x0.86	8.9	13277 ± 1187 ± 109

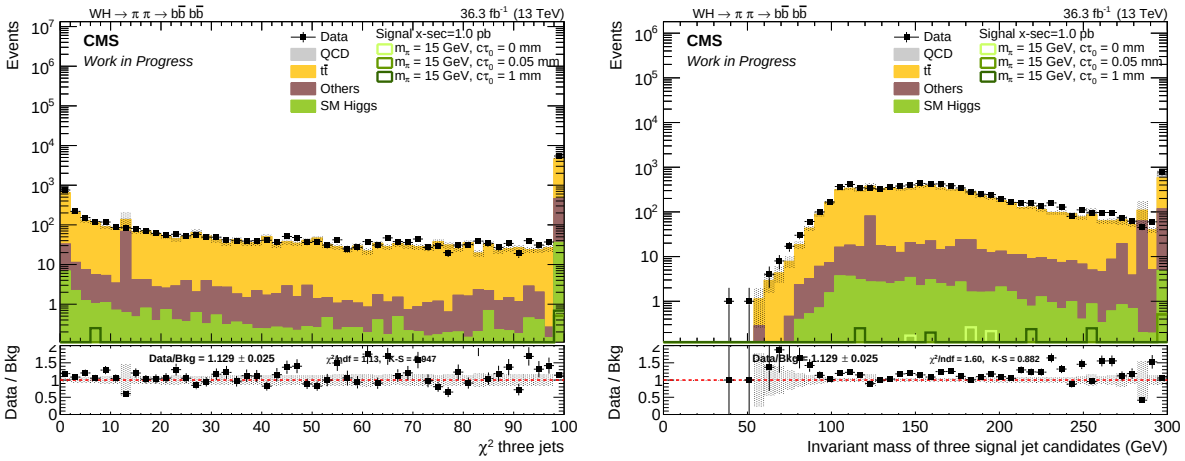

Figure 11.16: Distribution of the χ^2 (left) and invariant mass of the three selected jets (right) in the $t\bar{t}$ CR after the baseline section. The statistical uncertainties of the simulated SM background event yields are visualised.

described in Section 9.4. Similar agreement studies as for the boosted analysis (described in Section 10.2.3) have been performed.

The distribution after the CR baseline selection can be found in Figure 11.16. The χ^2 value to potentially find the three signal candidate jets of the resolved analysis and the corresponding invariant mass of the three selected jets are shown in the left and right plot, respectively. The χ^2 requirement is additionally applied for the plots shown in Figure 11.17. There, the largest ΔR between two amongst the three selected jets can be found on the upper left. Furthermore, the DNN discriminant for the parametrisation

with 40 GeV and 1 mm, of the three selected jets, are shown. In all plots the agreement between data and simulated event is good, and no offset or trend is visible.

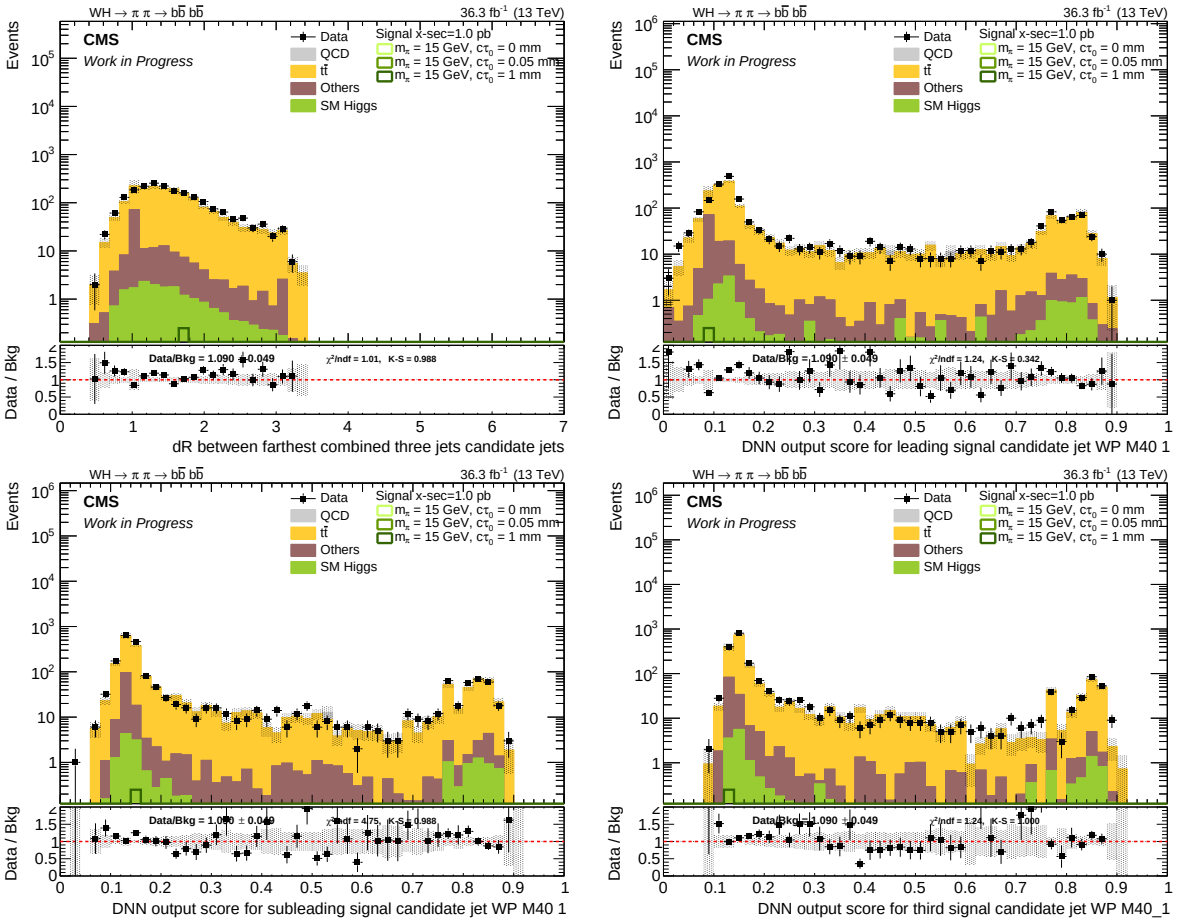

Figure 11.17: Distribution of the ΔR between the selected two jets (upper left) and DNN discriminant for mass 40 GeV, lifetime 1 mm of the three selected jets (upper right and lower left and right) are shown. The statistical uncertainties of the simulated SM background event yields are visualised.

11.3 Systematic Uncertainties

The correction factors, to achieve a better agreement between recorded data and simulation, come with systematic uncertainties. All relevant systematic uncertainties are summarised in Section 9.7. They, including the additional derived uncertainty of the predicted QCD yield, are used as nuisance parameters in the final limit calculation (see Section 12.1), which can slightly change the yield in the final signal region A. A log-normal prior distribution is used to model the impact on the yield of each uncertainty in the fit. The fit is performed for each lifetime separately. A summary of the uncertainties on different signals are presented in Table 11.9. Furthermore, the uncertainties on all non-QCD SM background processes for the thresholds of the LLP mass of 40 GeV and 1 mm lifetime is given in Table 11.10. Only the largest across the different uncertainties for b tagging is shown. The trigger uncertainty clearly dominates again the uncertainties on signal and SM background. The large uncertainties on the trigger correction factors are the result of the handling of the different uncertainties across the trigger filters, which are taken as fully correlated. Another important uncertainty is the JEC, which can be understood from the relative low jet p_{T} selection criteria of 30 GeV and the soft signal candidate jets leading to a large impact of the slight p_{T} variation to define the uncertainties. Overall, the uncertainties are compatible with the ones derived for the boosted topology, taking into account that a different jet multiplicity leads to slightly different values.

Table 11.9: Changes of the signal yields due to the different uncertainty sources for the signal for a LLP mass of 40 GeV. The threshold values from Tables 11.2 for each mass and lifetime is also applied here.

Production mode	Lifetime [mm]	JEC [%]	JER [%]	PU [%]	Trigger [%]	μ_R/μ_F [%]	PDFs [%]	b tagging [%]
VBF	0.1	±19.2	$^{+1.27}_{-10.7}$	$^{+0.52}_{-1.21}$	$^{+82.0}_{-29.2}$	±0.4	±2.1	$^{+9.98}_{-9.40}$
	1	±20.7	±5.82	$^{-2.12}_{+2.30}$	$^{+98.0}_{-30.5}$	±0.4	±2.1	$^{+10.2}_{-9.59}$
ggF	1	$^{-20.7}_{+9.30}$	$^{+1.13}_{-2.90}$	$^{-1.25}_{+1.07}$	$^{+68.0}_{-26.6}$	±7.6	±1.8	$^{+10.3}_{-9.68}$

Table 11.10: Changes of the non-QCD SM background yields due to the different uncertainty sources for a LLP mass of 40 GeV and 1 mm lifetime. The threshold values from Table 11.2 are applied.

Background process	JEC [%]	JER [%]	PU [%]	Trigger [%]	μ_R/μ_F [%]	PDFs [%]	b tagging [%]
$t\bar{t}$	-20.4 $+7.24$	$+0.23$ -2.75	$+2.12$ -2.28	$+62.4$ -25.5	$+20.6$ -16.2	± 2.60	$+7.48$ -7.31
SM Higgs	-18.9 $+12.6$	$+11.1$ -5.89	-2.04 $+1.65$	$+52.6$ -23.2	$+42.6$ -20.5	± 2.14	$+6.32$ -7.23
Others	-48.2 $+1.28$	$+8.82$ -79.2	$+0.87$ -1.72	$+98$ -31.8	$+10.5$ -8.97	–	$+7.60$ -7.42

12 Results

The final results of the search for LLPs and the statistical procedures to obtain them are discussed in this chapter. The studied signal models include Higgs bosons with production modes of the VBF and the ggF, which subsequently decay into a pair of LLPs. Two separate analyses were performed targeting different LLP masses. The analysis for the boosted topology targeting LLPs with masses of 15 GeV and the analysis for the resolved topologies targeting masses of 40 GeV and 55 GeV. For each topology optimised requirements select potential signal jets, and for each LLP mass-lifetime combination, the parametrised DNN discriminant defines the ABCD regions. The event yield in the signal region A of the ABCD method is used in a counting experiment to set upper limits on the presence of the LLPs.

First, a brief discussion of the statistical procedures used for the final evaluation is given. Afterwards, expected upper limits at 95 % CL on the value of the cross section times branching ratio with respect to the SM Higgs boson cross section are set for each LLP mass-lifetime combination with an Asimov pseudodata. Finally, observed upper limits with recorded data are presented. Finally, the results for the two SM Higgs production modes are presented separately and combined.

12.1 Statistical Procedures

The final statistical calculations were performed using the Combine Tool [132] software package.

The signal strength modifier μ is defined in this thesis as:

$$\mu = \frac{\sigma(H) \cdot \mathrm{BR}(H \to \pi\pi \to b\bar{b}b\bar{b})}{\sigma_{\mathrm{SM}}}, \tag{12.1}$$

where the observed cross section of the Higgs boson $\sigma(H)$, the branching ratio $\mathrm{BR}(H \to$

$\pi\pi \to b\bar{b}b\bar{b}$) of the Higgs boson to two LLPs into the four b quark final state[1], and the predicted SM Higgs boson cross section σ_{SM} are taken into account. The signal strength modifier is used to describe either the background-only hypothesis ($\mu = 0$) or the signal-plus-background hypothesis, with $\mu = 1$ being the nominal signal hypothesis. The yield is defined with the expected yields in signal s and background b:

$$\lambda = \mu \cdot s(\theta) + b(\theta), \tag{12.2}$$

where both depend on the nuisance parameters θ. These nuisance parameters are the systematic uncertainties of different sources. The ones used for this thesis are listed in Section 9.7. They either affect several processes so that they are correlated (such as uncertainties due to JEC or trigger) or only affect specific processes and are uncorrelated (such as the uncertainty due to the size of the simulated sample).

The statistical evaluation for this thesis investigates the event yield in one final bin. Therefore, the likelihood function for n observed events and k nuisance parameters has the form:

$$\mathcal{L}(n|\mu, \theta) = P(n|\lambda) \cdot \prod_k p(\tilde{\theta}_k|\theta_k), \tag{12.3}$$

where the probability $p(\tilde{\theta}_k|\theta_k)$ of an observed value $\tilde{\theta}_k$ given a particular default value θ_k is used. Furthermore, is the Poisson probability distribution of the following form used:

$$P(n|\lambda) = \frac{(\lambda)^n}{n!} \exp(-\lambda). \tag{12.4}$$

In this thesis, the log-normal probability density function is used for the nuisance parameters in the fit:

$$p(\tilde{\theta}|\theta) = \frac{1}{\sqrt{2\pi}\theta \ln(\kappa)} \exp\left(-\frac{\ln(\theta/\tilde{\theta})^2}{2(\ln(\kappa))^2}\right), \tag{12.5}$$

where the relative uncertainty κ can be directly interpreted as the width of this distribution.

The model is fit to the data to obtain an estimate for the value of the signal strength modifier μ that describes the data best. During this fit, the likelihood function is maximised with respect to the signal strength modifier and the nuisance parameters θ_k. Due to the probability density functions of the nuisance parameters, increasing pulls of these parameters away from their central values lead to decreasing likelihood values, effectively

[1] This branching ratio is set to 100 % in this thesis.

penalising large pulls during the fit. The signal strength modifier does not have such a penalising probability density function and is left free-floating. In practice, rather than maximising the function, its negative logarithm is minimised. This minimisation is performed using the MINUIT algorithm [133] implemented in the COMBINE software.

The background-only and the signal-plus-background hypotheses are tested against the observed data using the *test statistic*, defined as:

$$q_\mu = -2 \ln \frac{\mathcal{L}(n|\mu, \hat{\theta}_\mu)}{\mathcal{L}(n|\hat{\mu}, \hat{\theta})}, \text{with } 0 \leq \hat{\mu} \leq \mu. \tag{12.6}$$

Here $\hat{\mu}$ and $\hat{\theta}$ minimises the negative log-likelihood globally, while $\hat{\theta}_\mu$ minimises the negative log-likelihood for a fixed value of μ. Large disagreements between the hypotheses and the observed data result in large values of q_μ.

The *p-value* is calculated taking the probability for a given hypothesis μ which is assumed to be correct into account:

$$p = \int_{q_\mu^{\text{obs}}}^{\infty} f(q_\mu|\mu, \hat{\theta}_\mu^{\text{obs}}) \mathrm{d}q_\mu, \tag{12.7}$$

where $f(q_\mu|\mu, \hat{\theta}_\mu^{\text{obs}})$ is the probability density function for the test statistic q_μ.

The upper limits are calculated using an asymptotic approximation of a modified frequentist approach called the *Asymptotic CLs method* [134, 135]. Here the CL_s is defined as:

$$CL_s(\mu) = \frac{p_\mu}{1 - p_b}, \tag{12.8}$$

with p_μ and p_b being the p-values for the signal-plus-background and background-only hypotheses, respectively. The level of disagreement between data and the used hypothesis is quantified with p_μ and $1 - p_b$. The upper limit at 95 % CL_s excludes a given hypothesis μ, for which $CL_s = 0.95$.

For all calculations, n can either be observed data or pseudodata. The so-called *observed limits* are calculated using observed data, while pseudodata are used to calculate so-called *expected limits* without unblinding the observed data. Therefore, an expectation of the upper limits can be calculated. At the same time, changes in the analysis are still possible, and improvements in the sensitivity can be made without being biased by the actual data yield. A typical set of pseudodata is the Asimov dataset [136]. For several iterations, the sum of all the background plus the signal yields are smeared within their nuisance parameters, and the median set of such produced pseudodata is used as the Asimov

dataset. The blinded expected upper limits in Section 12.2 were calculated, using that description of the Asimov dataset. However, for the expected upper limits in Section 12.3, the background-only hypothesis was used, where only the sum of the background yield is smeared within their nuisance parameters.

12.2 Expected Results Before Unblinding

Before the observed upper limits are calculated using data in the regions A of the ABCD planes for all LLP mass-lifetime combinations, the approach of the analyses was studied and validated with Asimov pseudodata. The blinded expected upper limits were calculated to estimate the sensitivity of the analyses. The pulls and their impacts were used to study the behaviour of the nuisance parameters for fits to Asimov pseudodata. The different studies are further explained in the following.

12.2.1 Boosted Topology

For the boosted analysis with a LLP mass of 15 GeV, the following lifetimes are taken into account: 0, 0.05, 0.1, 1, 5 and 10 mm.
The impact of each systematic uncertainty, handled as a nuisance parameter with a log-normal prior distribution, is studied with Asimov pseudodata for the $\mu = r = 1$ hypothesis and shown in Figure 12.1. First, a fit is performed with all nuisance parameters and the signal strength modifier. The postfit yields and uncertainties σ of all nuisance parameters of this fit are used for the next step. For each nuisance parameter, the affected background yields are changed to their $+\sigma$ or $-\sigma$ postfit value separately, and a new fit is performed. For each of these new fits, the impact is expressed by the shift $\Delta\hat{r} = \hat{r} - r_{\text{shift}}$, by how much the signal strength modifier is shifted r_{shift} to compensate for the yield change concerning the best-fit value of the signal strength modifier in the first fit $\hat{r}$. The data-driven QCD background estimation method has the largest impact, followed by the trigger uncertainty, the JEC, the uncertainty on the size of the signal yield and JER. All other impacts are distinctively smaller. The impact of the uncertainty on the JEC is quite asymmetric, which can be understood by comparing the derived uncertainties on signal and SM background processes in Tables 10.6 and 10.7, respectively. These asymmetric values are a result of the loose selection criteria on jets of $p_{\text{T}} > 30$ GeV and the soft signal candidate jets, as already mentioned earlier. The pull, shown in the middle column, represents the difference between the postfit and prefit values, where the postfit uncertainty

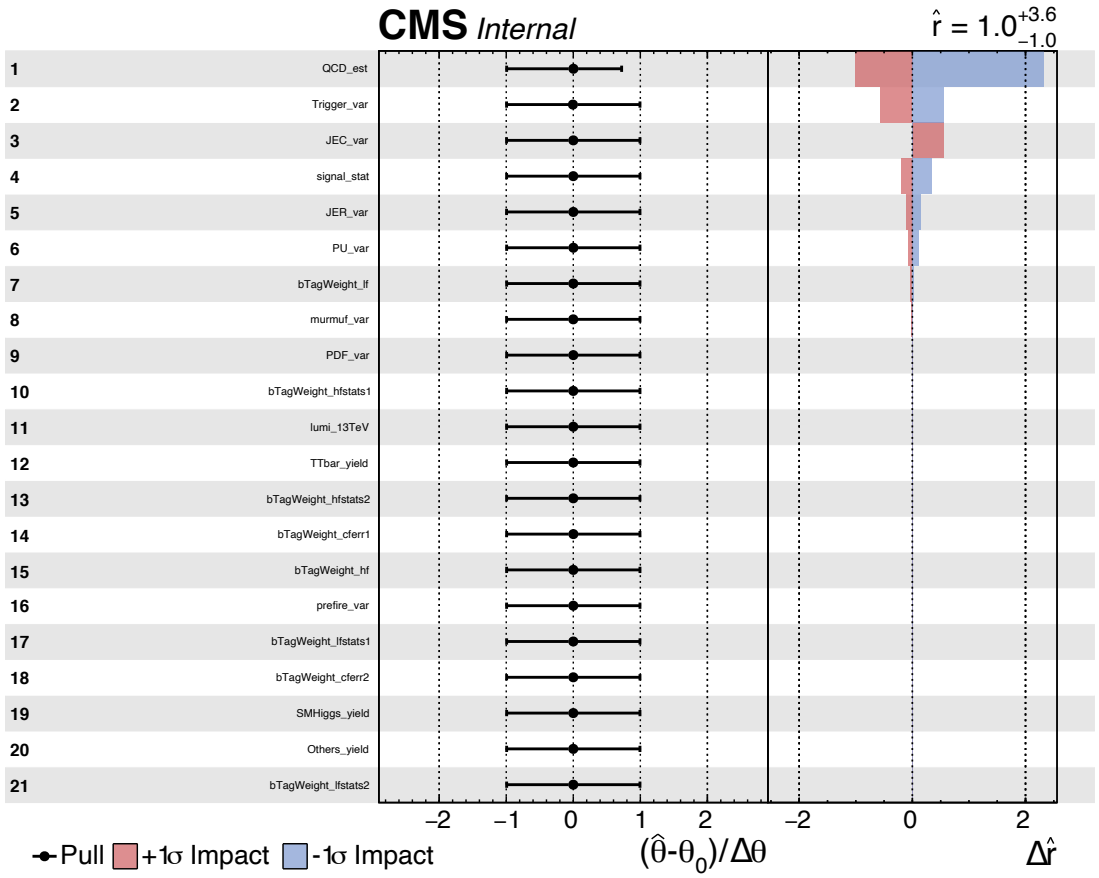

Figure 12.1: The impact of different nuisance parameters calculated with $\mu = 1$ Asimov pseudodata for the boosted topology and 1 mm lifetime. Each row represents one nuisance parameter, where the name is shown on the left, the pull in the middle, and the impact in the right column.

divided by the prefit uncertainty represents the error bars. Values below ± 1 mean those parameters are constrained in the fit [132]. These constraints can be asymmetric for the presented pull in Figure 12.1, while for the following study of the pulls, they are treated as symmetric.

Pulls were calculated for the background-only hypothesis and compared to the signal-plus-background hypothesis with Asimov pseudodata, and the results can be found in Figure 12.2. In the signal-plus-background fit, the difference between the background yields and the Asimov pseudodata, which are the sum of all background plus signal yields, can be compensated by fitting a finite value for the signal strength modifier μ, and the nuisance parameters are not expected to be pulled. However, the background-only fit does not contain the signal strength modifier μ, and several nuisance parameters need to be

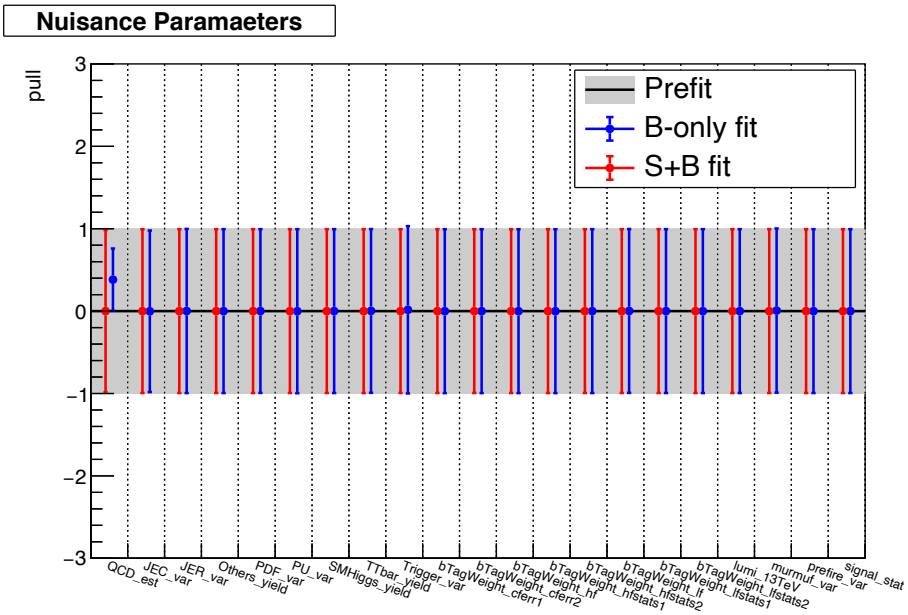

Figure 12.2: The pulls of different nuisance parameters for the background-only signal-plus-background fits to the Asimov pseudodata with $\mu = 1$ hypothesis for the boosted topology and 1 mm lifetime.

Table 12.1: The mean values of the blinded expected limits for the different lifetimes of the boosted topology with VBF and ggF Higgs production modes and of the lifetimes with both production modes combined.

Mass [GeV]	Lifetime [mm]	Thresholds	Blinded Expected Limit		
			VBF	ggF	combined
15	0	0.92x0.92	48.3	-	-
	0.05	0.90x0.90	65.0	-	-
	0.1	0.91x0.91	22.1	-	-
	1	0.89x0.89	8.7	2.8	2.8
	5	0.89x0.89	164.0	-	-
	10	0.88x0.88	314.0	174.0	106.8

pulled to account for the difference between the background yields and the pseudodata. The largest pull is related to the uncertainty of the estimation of the QCD background *QCD_est*, which can be understood by considering that the predicted QCD background is the dominant one and the uncertainty is very large. The remaining uncertainties, for example, of the trigger, are pulled as well, but by a much smaller amount, only barely visible in the plot.

Blinded expected upper limits at 95 % CL on the signal strength modifier are calculated.

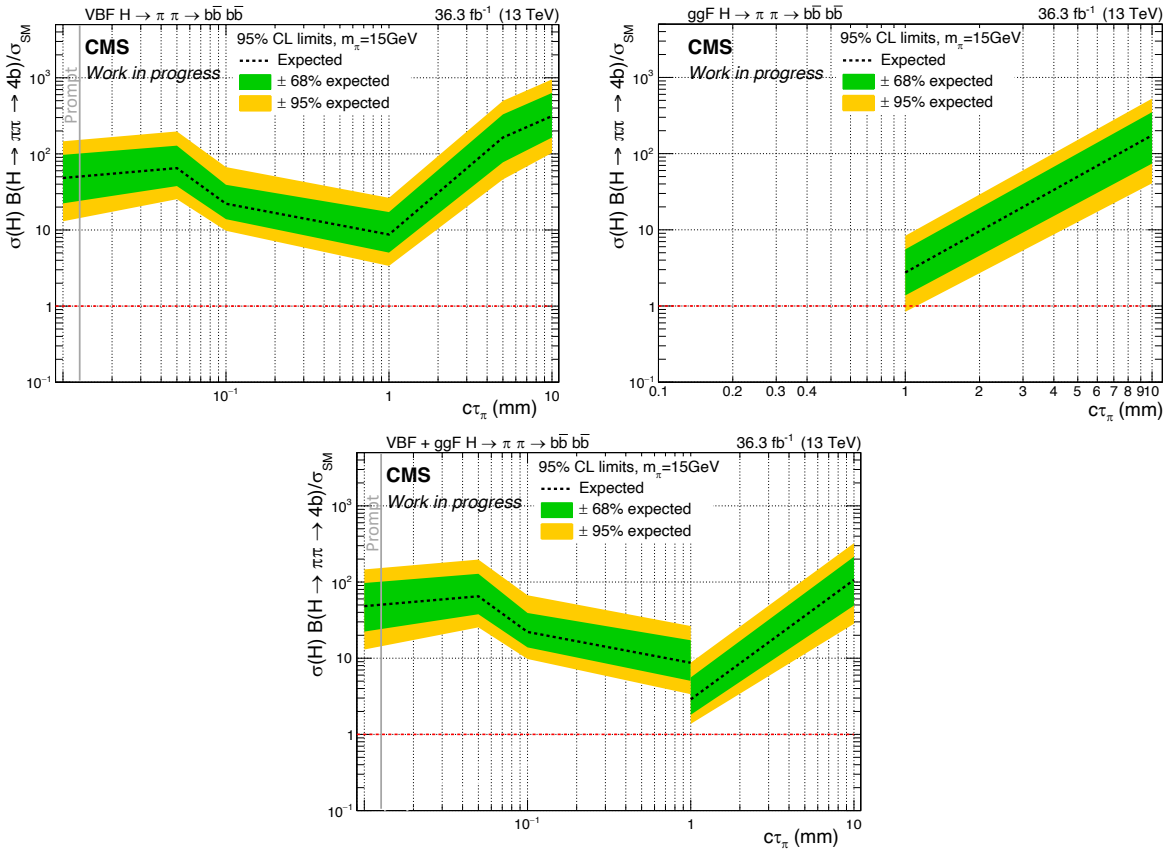

Figure 12.3: Expected upper limits on the signal strength modifier for LLPs with a mass of 15 GeV with VBF (upper left), ggF (upper right) and the combined (lower) Higgs boson production modes in the four b final state. For lifetimes, where no signal prediction for the ggF production mode exists, the result for the VBF signal only is used instead of the ggF+VBF result.

Table 12.2: Expected event yields in region A of the LLP mass of 15 GeV with the VBF and ggF Higgs production mode signal.

Production mode	Lifetime [mm]	Signal	Predicted QCD	$t\bar{t}$	SM Higgs	Others
VBF	0	9.6	167.8	1.8	0.3	-
	0.05	13.2	1061.6	12.6	1.0	2.9
	0.1	15.1	407.4	4.0	0.5	0.1
	1 5	19.5 1.8	297.4	3.5	0.3	0.1
	10	1.1	645.0	4.9	1.0	3.6
ggF	1	94.1	297.4	3.5	0.3	0.1
	10	3.6	645.0	4.9	1.0	3.6

The branching ratio of the Higgs boson decaying to two LLPs to four b quarks was chosen and fixed to be 100 %. The resulting limits are presented in Figure 12.3 for the VBF (upper left) and ggF (upper right) production modes, depending on the lifetime of the LLP. The corresponding mean values of these expected limits can be found in Table 12.1. The expected event yields can be found in Table 12.2 for the signal with VBF and ggF Higgs production modes. The best sensitivity is reached for the LLP lifetime of 1 mm for both Higgs boson production modes. The expected limits increase for lifetimes above 1 mm, since the trigger efficiency decreases, and standard reconstruction techniques used for this analysis perform worse for such displaced signal objects. For shorter LLP lifetimes and corresponding smaller flight distances, the b quarks are harder to distinguish from those produced in SM processes, decreasing the expected sensitivity. Since the cross section for ggF Higgs boson production is higher than that for VBF production, the expected signal yields are higher, and the sensitivity is overall better. The lower plot of Figure 12.3 shows the results for combining both production modes. Both predicted signal yields were used to calculate upper limits on a single signal strength modifier. For lifetimes for which no ggF sample exists, no combined limit could be calculated, and the expected limits are those of the VBF analysis. The combination increases the total signal yield and, depending on the relative yield change, results in improved sensitivity.

12.2.2 Resolved Topology

For the resolved analysis, the two LLP masses, 40 GeV and 55 GeV, were investigated with the following lifetimes: 0, 0.05, 0.1, 1, 5 and 10 mm.
The impact of each nuisance parameter on the signal strength modifier is studied with Asimov pseudodata and shown in Figure 12.4 for the LLP masses of 40 GeV (upper) and 55 GeV (lower) with a lifetime of 1 mm. The results for both LLP masses are relatively similar. For both masses, the uncertainty on the data-driven QCD background estimation has the most significant impact, followed by the trigger uncertainty. In contrast, the impacts of the remaining uncertainties are distinctively more minor. The pulls are shown in the middle column, and again only the uncertainty related to the QCD background estimation was constrained in the fit.
Comparisons between the pulls obtained in background-only and signal-plus-background fits are shown in Figure 12.5 for the LLP lifetime of 1 mm with masses of 40 GeV (upper) and 55 GeV (lower). Since the signal yields are much smaller than the background yields, as shown in Table 12.3, the pulls of the background are much smaller than in the boosted

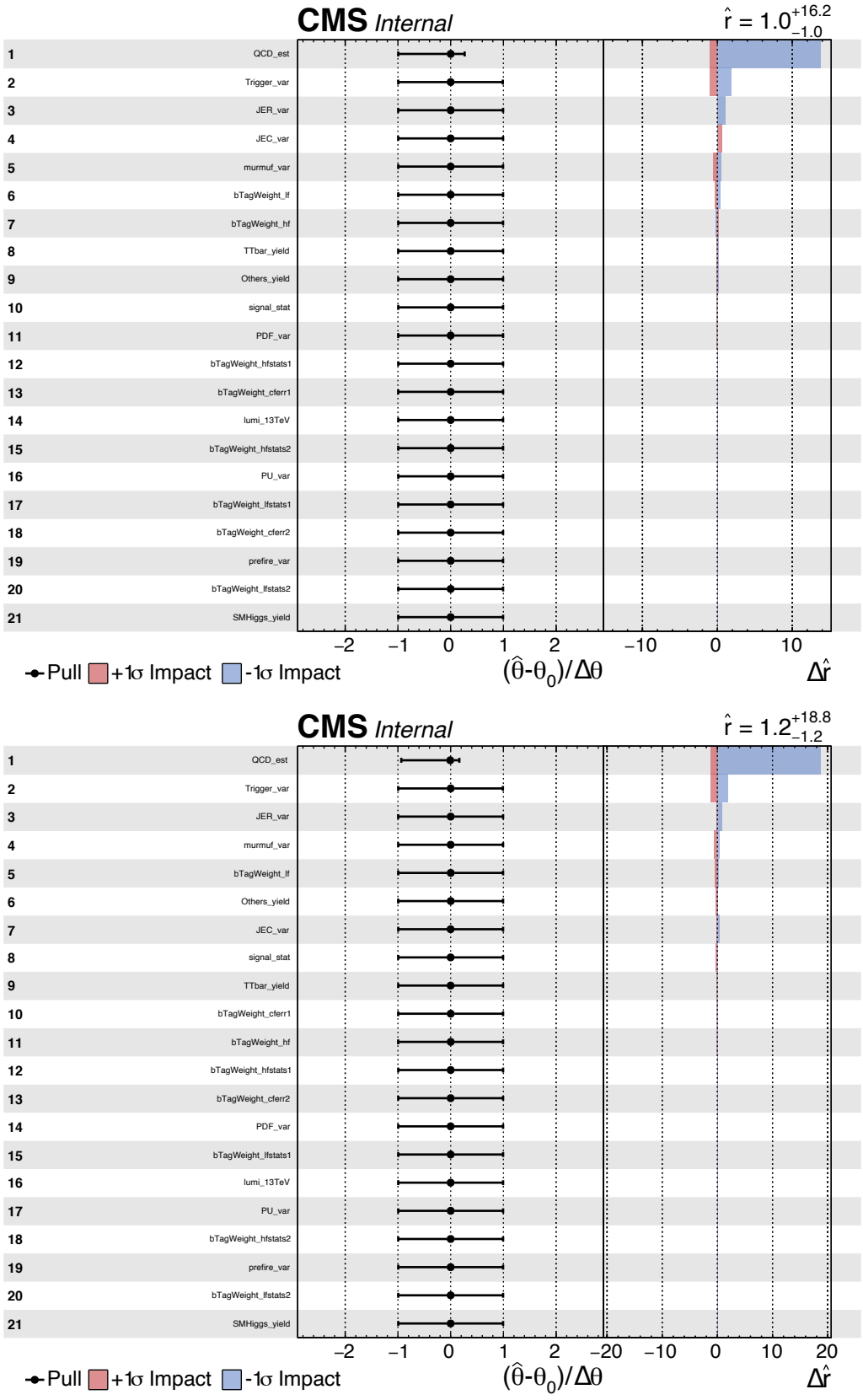

Figure 12.4: The impact of different nuisance parameters for the resolved topology for a LLP mass of 40 GeV (upper) and 55 GeV (lower) with a 1 mm lifetime.

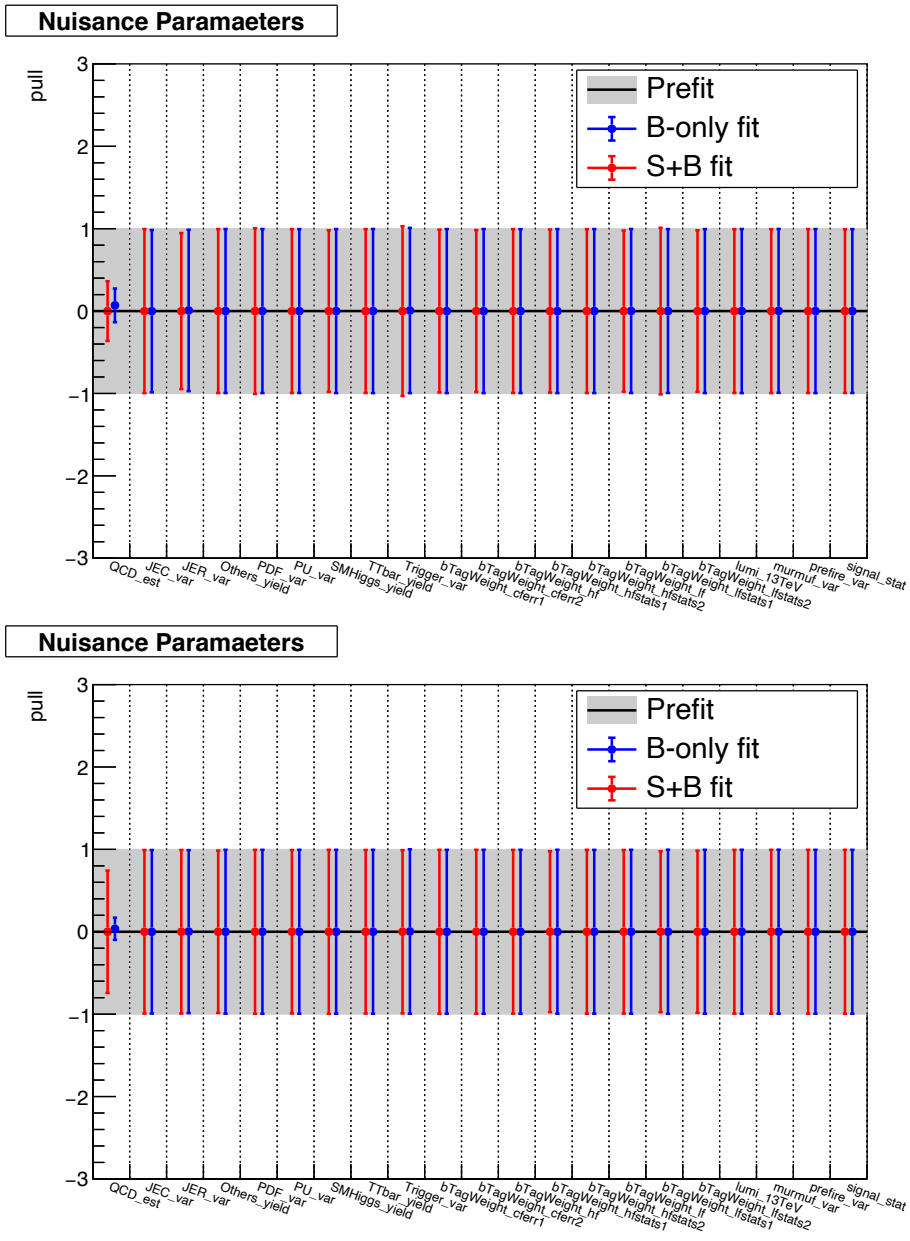

Figure 12.5: The pulls of different nuisance parameters calculated with $\mu = 1$ Asimov pseudodata for the LLP mass of 40 GeV (upper) and 55 GeV (lower) with a 1 mm lifetime.

topology. Again, the background yield consist to $> 98\,\%$ of the predicted QCD multijet production, hence all other uncertainties are pulled by a much smaller amount.
As for the light LLP mass analysis, blinded expected upper limits on the signal strength modifier were calculated. Figures 12.6 and 12.7 show the results for LLP masses of 40 GeV and 55 GeV, respectively. The mean values of the blinded expected limits can be found in Table 12.4 for the different production modes separately and combined. For both masses, expected limits were calculated for the VBF (upper left) and ggF (upper right) Higgs production mechanisms. For the different LLP masses and lifetimes, the expected event yields of region A are listed in Table 12.3 for the VBF and ggF Higgs boson production modes. Both production mechanisms are combined and presented separately for both masses in the lower rows of Figures 12.6 and 12.7. For those lifetimes for which no ggF induced signal sample was available, the result of the VBF mode is shown instead of the combination. Since the analyses of the different masses were not performed on orthogonal phase spaces, the analyses of different masses can not be combined. The results for the ggF Higgs boson production mode are more sensitive than the results for the VBF production mode, and their combination leads to further improvement of the sensitivity.
For all LLP masses and lifetimes, the blinded expected limits calculated for the resolved topology analyses are worse than those found for the analysis of the boosted topology. The expected limits also differ between the analyses of the two LLP masses of 40 GeV and 55 GeV. For 1 mm and longer lifetimes, better limits are found for the 40 GeV analysis, while the 55 GeV analysis performs better for shorter lifetimes.
Since the sideband studies performed for the resolved topology in Section 11.2.1 have shown that the QCD background is underpredicted for all lifetimes, additional studies are performed to better understand the effects of this systematic underprediction. For all LLP masses and lifetimes behave the closures similarly. The QCD background is overpredicted for tight thresholds, while it is underpredicted for loose thresholds, as visible in the upper and middle row plots of Figures 10.10 and 11.12. The thresholds for the boosted topology, e.g. listed in Table 12.1, are on average tighter than for the resolved topology, see e.g. Table 12.4. Therefore, the underprediction in the $\overline{\text{SR}}$ might be a direct result of the looser thresholds chosen for the resolved topology.
The expected effect of an underprediction on the results was studied by first creating singal+background pseudodata with varying positive signal contributions corresponding to up to three standard deviations of the uncertainty on the QCD prediction. Therefore, an assumption of an underprediction of the QCD yield of up to three standard deviations was made. Next, expected and observed limits were calculated for each set of pseudo-

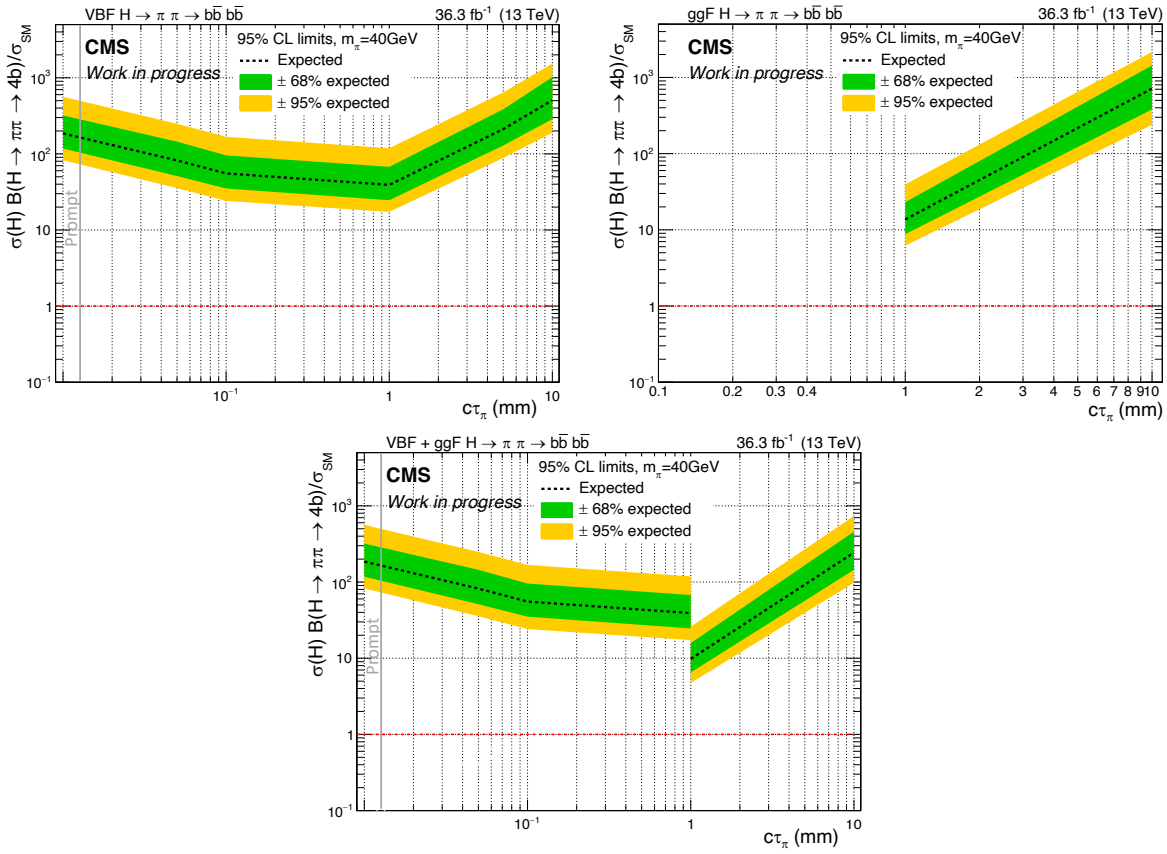

Figure 12.6: Expected upper limits on the signal strength modifier for LLPs with a mass of 40 GeV with VBF (upper left), ggF (upper right) and the combined (lower) Higgs boson production modes in the four b final state. For lifetimes, where no signal prediction for the ggF production mode exists, the result for the VBF signal only is used, instead of the ggF+VBF result.

data, treating the pseudodata as if they were observed data. Since the created pseudodata were larger than the predicted background, the expected limits increased with increasing pseudodata, and the observed limits were higher than the expected limits and increased faster. The maximal signal contribution for which the observed limit was still within two standard deviations of the expected limit was found to be between mu=22 and mu=170, depending on the LLP mass-lifetime combination and the Higgs boson production mode and the assumption that the QCD prediction was underpredicted by at most three standard deviations. Such a large overprediction is rather unlikely with the performed studies for both topologies. Nevertheless, the unblinding process, described in the following, was started with the boosted topology.

However, the resolved topology with the three selected jets and the possible correla-

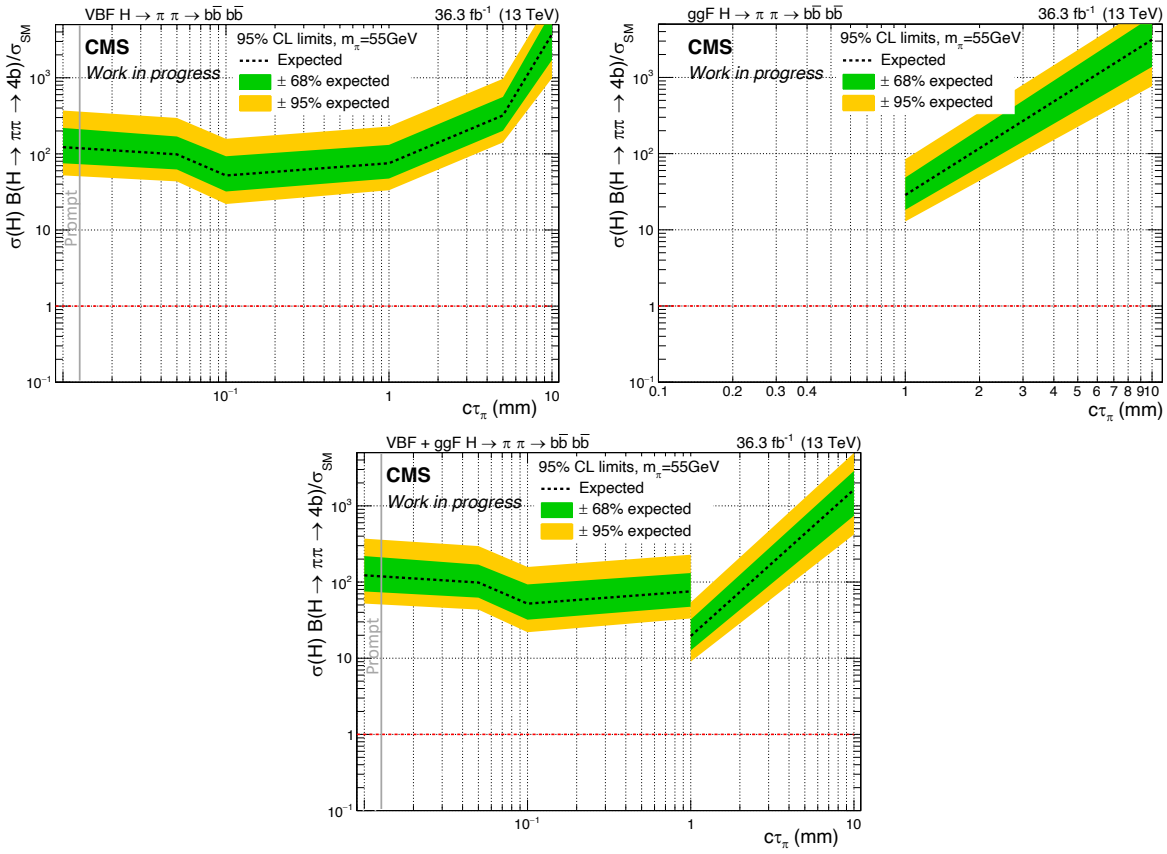

Figure 12.7: Expected upper limits on the signal strength modifier for LLPs with a mass of 55 GeV with VBF (upper left), ggF (upper right) and the combined (lower) Higgs boson production modes in the four b final state.

tion between the ϕ ordering and the ΔR requirement further complicate the predictions. Therefore, the unblinding was performed with these issues in mind, and additional control studies were performed at various steps.

Table 12.3: Expected event yields in region A of the resolved analysis with the VBF and ggF Higgs production mode signal.

Mass [GeV]	Production mode	Lifetime [mm]	Signal	Predicted QCD	$t\bar{t}$	SM Higgs	Others
40	VBF	0	19.6	12825.4	142.3	3.3	74.4
		0.05	21.9	5138.1	52.9	1.0	34.9
		0.1	58.5	12046.4	132.9	3.2	66.4
		1 5 10	60.1 12.5 6.0	13968.4	135.6	3.5	68.3
	ggF	1 10	168.1 5.4	13968.4	135.6	3.5	68.3
55	VBF	0	32.4	18793.2	219.1	4.5	101.8
		0.05	34.0	18434.6	207.2	4.4	99.3
		0.1	48.8	18180.0	199.1	4.3	99.2
		1 5 10	43.2 10.3 2.2	13095.7	115.0	2.8	63.1
	ggF	1 10	110.5 3.0	13095.7	115.0	2.8	63.1

Table 12.4: The mean values of the blinded expected limits for the different lifetimes of the LLP masses of 40 GeV and 55 GeV with VBF and ggF Higgs production modes and the lifetimes with both production modes combined.

Mass [GeV]	Lifetime [mm]	Thresholds	Blinded Expected Limit		
			VBF	ggF	combined
40	0	0.84x0.84	185.5	-	-
	0.05	0.85x0.85	82.0	-	-
	0.1	0.84x0.84	55.4	-	-
	1	0.83x0.83	39.1	13.7	9.8
	5	0.83x0.83	211.5	-	-
	10	0.83x0.83	507.0	714.0	243.5
55	0	0.86x0.86	122.5	-	-
	0.05	0.86x0.86	98.5	-	-
	0.1	0.86x0.86	52.0	-	-
	1	0.86x0.86	75.4	28.6	19.6
	5	0.86x0.86	320.0	-	-
	10	0.86x0.86	3726.0	3130.0	1633.0

12.3 Unblinding Process and Unblinded Results

Up to this point, the data in regions A of the SR were blinded, and all previous studies were performed either with Asimov pseudodata from simulated samples or data outside of region A. The unblinding is performed using a stepwise process to ensure that possible remaining biases due to the analysis design or other unexpected issues are caught early. First, the data-to-simulation agreement of the DNN discriminant distributions is studied, and the distributions of data in the ABCD planes are compared between the SR and the $\overline{\text{SR}}$. Afterwards, the observed event yields in regions A and the closures are studied. These results are also compared to the closures in the $\overline{\text{SR}}$ and the sideband studies of Sections 10.2.1 and 11.2.1. Next, the pulls studied with Asimov pseudodata are compared to pulls obtained from fits to data under the background-only and the signal-plus-background hypotheses. In addition, the prefit and postfit values of the signal and background yields are investigated. Next, the blinded expected limits of the previous section are compared to the expected limits, which are calculated with pseudodata close to the observed data yield. Finally, observed limits are calculated and compared to the expected limits from the previous step.
Each step was studied separately for each LLP mass-lifetime combination, and details are presented in the following.

12.3.1 Boosted Topology

The entire ranges of the 1D distribution of the DNN discriminant, as well as in the entire ABCD planes were so far not shown in data of the SR. The DNN discriminant distributions of the leading (left) and subleading (right) jets are shown in Figure 12.8 for events in the SR of the analysis for a 1 mm lifetime. The simulation-based background describes the overall shape of the data relatively well over the whole range of the distributions. Nevertheless, a slight general offset is visible, and several data points do not agree with the prediction within the given uncertainties. However, the error bands in the figures contain only the statistical uncertainty of the background simulation, and systematic uncertainties might cover the disagreements. The regions above a value of 0.7 were previously blinded. The data-to-simulation agreement in these high-value regions is similar to that in the low-value regions. Since the simulated QCD multijet process is the dominant contribution, it is reasonable to assume that the miss-modelling of the data is mainly caused by this process, which does not sufficiently describe the data. The lack of simulated events in the

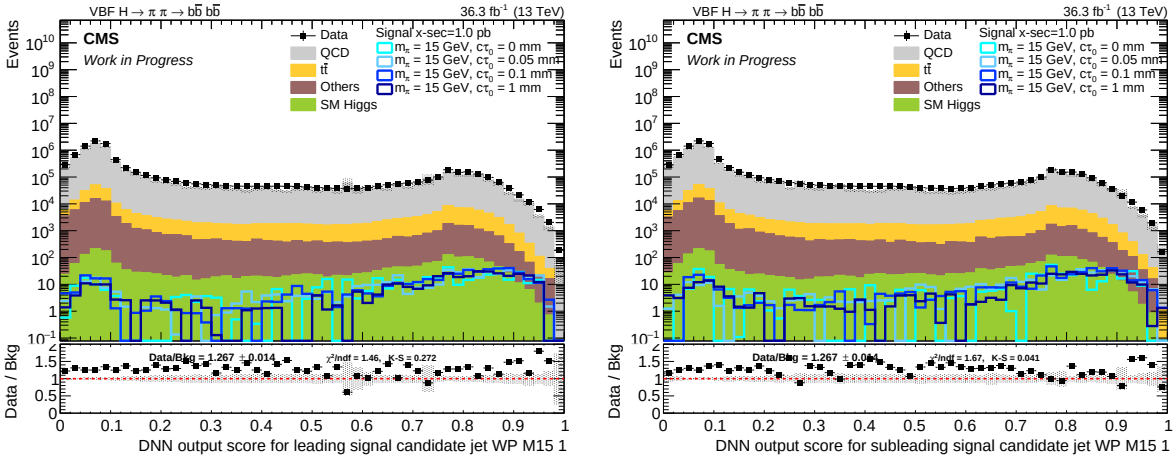

Figure 12.8: Distributions of the DNN discriminant for the leading (left) and subleading (right) selected jet in the SR for the analysis of the LLP with 15 GeV mass. The QCD multijet process is taken from simulation. The error band constraints statistical uncertainties only.

high DNN discriminant value regions also worsens the effect, leading to large statistical fluctuations of events with large weights. These expected shortcomings were the reason for applying the ABCD method to predict the QCD background in regions A. The full ABCD planes of the SR (left) can be compared to the distributions of the $\overline{\text{SR}}$ (right), presented in Figure 12.9. Each row contains the planes for one lifetime, starting with 0 mm in the first row and ending with 1 mm in the last row. The distribution for the 1 mm lifetime is also used for the signals with lifetimes of 5 mm and 10 mm. Since the ABCD method was validated in the $\overline{\text{SR}}$, the distributions should ideally be similar in the SR and the $\overline{\text{SR}}$. For each lifetime, the two distributions and the profiles seem to be very similar, while the slopes of the profiles are slightly different. The accumulation of events in the upper right part of the ABCD planes are at similar positions. Furthermore, the regions containing hardly any events in the right and upper parts of the plots are also very similar in the SR and the $\overline{\text{SR}}$. However, differences are visible when comparing the distributions across different lifetimes. The profiles of the 1 mm lifetime are much flatter than the profiles of the other lifetimes. In addition, it is visible that the events in the upper right parts are more evenly distributed. Their distribution in this region has a rounder shape for the signal with 1 mm than for the other lifetimes where this seems to have harder borders. Nevertheless, all distributions look as expected, and no huge differences were investigated. Therefore, it was continued with the next step.

During the unblinding step, the observed and the predicted yields are compared. The

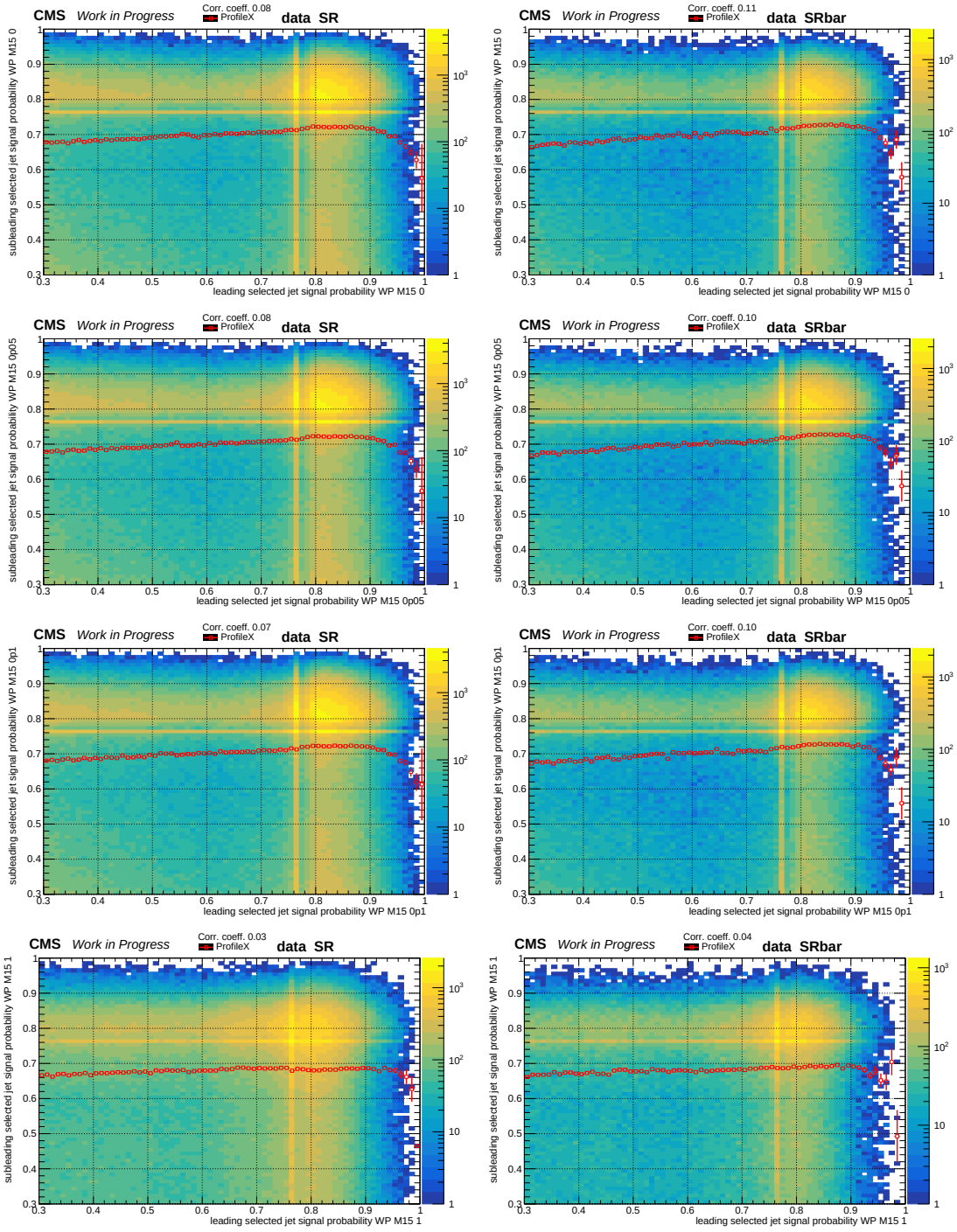

Figure 12.9: Distributions of data in the ABCD planes defined by the DNN discriminants of the two selected jets in the SR (left) and $\overline{\text{SR}}$ (right) for the LLP with 15 GeV mass and lifetimes of 0 mm (first row), 0.05 mm (second row), 0.1 mm (third row) and 1 mm (fourth row).

Table 12.5: Observed and predicted event yields in region A, the closure of the background prediction, and its significance for all lifetimes investigated in the analysis of the boosted topology.

Mass [GeV]	Lifetime [mm]	Data yield	Predicted background $\pm\sigma_{\text{QCD\_est}} \pm \sigma_{\text{stat}}$	Closure	Closure significance
15	0	99	169.8 ± 63.2 ± 2.6	1.716 ± 0.661	1.107
	0.05	748	1078.1 ± 249.1 ± 10.2	1.441 ± 0.337	1.317
	0.1	269	412.0 ± 115.9 ± 4.8	1.532 ± 0.441	1.222
	1 & 5	281	301.2 ± 46.3 ± 4.2	1.072 ± 0.177	0.411
	10	628	654.5 ± 63.2 ± 7.7	1.042 ± 0.109	0.390

values for all lifetimes, as well as the closures of the background estimation method and their significances can be found in Table 12.5. The predicted background yield is the sum of the non-QCD backgrounds and the predicted QCD multijet process using the ABCD method. The total uncertainty of the background prediction has two contributions which are shown separately, one from the prediction of the QCD process and one from the statistical uncertainties of the predicted QCD and the non-QCD backgrounds. Both uncertainties are taken into account to calculate the closure significance. The QCD multijet background is overpredicted for all lifetimes, and the deviation of the closure from unity increases with decreasing LLP lifetime. However, the closure is compatible with unity within 1.5 standard deviations for all lifetimes. Comparing the closures to the ones from the $\overline{\text{SR}}$ in Table 10.2, it is visible that the closure of the background estimation is much better for the $\overline{\text{SR}}$. Although the distributions in the ABCD planes of the SR and $\overline{\text{SR}}$ looked similar, a difference was observed in this step. One possible explanation is that the χ^2 selection criterion separates not only the events into the SR and the $\overline{\text{SR}}$ but it might also induce kinematic differences of the jets (see Chapter 10 and Appendix B). As discussed in Section10.2.2, the closures in the actual region A and the sidebands of the $\overline{\text{SR}}$ were relatively similar. Therefore, the uncertainty on the background estimation was derived based on the closures in the sidebands regions of the SR. However, a comparison between the closures in the unblinded region A of the SR (Table 12.5) and those in the sidebands (Table 10.4) shows that the closures differ significantly for smaller lifetimes. Therefore, additional studies were performed to understand better why the SR behaves differently from the $\overline{\text{SR}}$ in this regard.

Normalised distributions of the DNN discriminants of the leading and subleading jets for data in the SR and $\overline{\text{SR}}$ of the analyses of different lifetimes are shown in Figure 12.10.

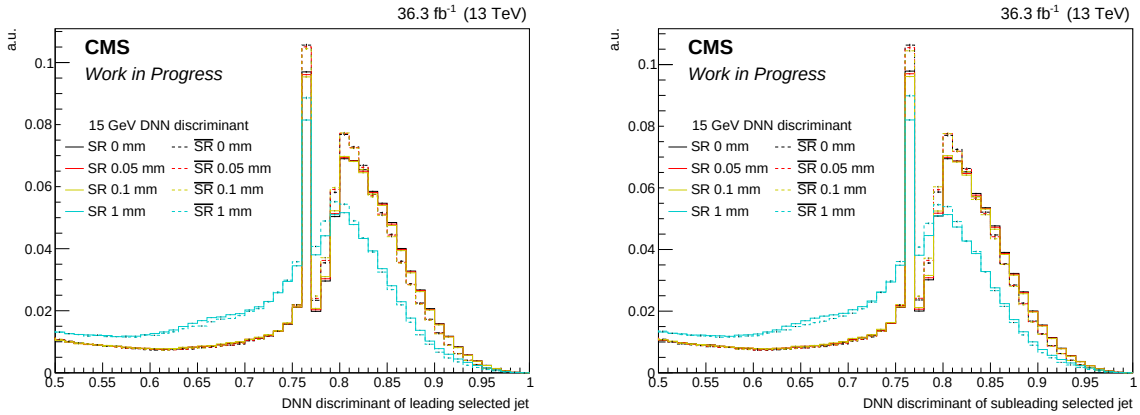

Figure 12.10: Distributions of the DNN discriminant of the leading (left) and subleading (right) jet for data in the SR (solid lines) and $\overline{\text{SR}}$ (dashed lines) used for the analyses of different lifetimes. The distributions are normalised to unity over the whole range of discriminant values, while only the region above 0.5 is shown.

The distributions of the DNN discriminant targeting the LLP lifetimes of 0 mm, 0.05 mm and 0.1 mm are very similar to each other, while the distribution for 1 mm is significantly different. The peak of the 1 mm distribution is shifted further to the left, the slope to its left is not as steep, and the distributions around the peak are broader and seem to be more symmetric than the peaks in the distributions for the shorter lifetimes. Minor differences are also visible between the SR and $\overline{\text{SR}}$ distributions for the same lifetimes. For example, for the 1 mm case, the SR and $\overline{\text{SR}}$ distributions are similar, while the right-hand side tail is much steeper for shorter lifetimes in the $\overline{\text{SR}}$ distributions. This difference between the SR and the $\overline{\text{SR}}$ can be explained by the difference in the jet kinematics, which affects the DNN distribution, as explained in Appendix B. Since the ABCD planes, shown in Figure 12.9, are defined by the discriminant values of the two selected jets, these differences could lead to the observed dissimilarities in the closures of the SR and $\overline{\text{SR}}$ and the different lifetimes. For events in regions A, both jets have a DNN discriminant of at least 0.88 (see Table 12.1). Therefore, the jets are on the right-handed tail of the peak in the 1D distributions. Similarly, for events in regions B and C, only one jet has to fulfil the DNN discriminant above 0.88, while the other jet has a lower discriminant value. Hence only one jet of the right-handed tail is selected. The differences in the peak shapes for the different lifetimes are also visible in Figure 12.9, where it can be seen that the slope of the events on the right-hand and upper side of the peak is smaller for the 1 mm case than for the shorter lifetimes. In addition, longer tails reaching into regions

B and C are visible for the shorter lifetimes, while for the 1 mm case, the shape of the peak seems to be rounder without the appearance of these tails. These tails seem to be also generally less pronounced in the $\overline{\text{SR}}$, even for smaller lifetimes. Based on the ABCD relation of Equation 9.2, an overprediction of region A can occur when there are too many events in regions B and C or too few events in region D. As investigations have shown, the numbers of events in regions B and C are very similar and much smaller than those in region D. Therefore, large overpredictions in A would require a large change to the number of events in region D or a relatively much smaller change in regions B and C. The tails reaching into regions B and C in the SR for the lifetimes below 1 mm could increase the number of events in regions B and C which might explain the overpredictions observed for these lifetimes. The tails are less pronounced, and the closures are better for the 1 mm lifetime in the SR and for all lifetimes in the $\overline{\text{SR}}$. Therefore, the differences in the closures of the different lifetimes and regions could be explained by the differences of the jet kinematics, which influence the shapes of the DNN discriminants in the relevant high value regions and the correlations between these jets. It was found that increasing the threshold values decreases the number of events in regions A, B and C, which improves the closures. However, sufficiently tight thresholds also lead to tiny numbers of events in those regions and, therefore, to huge statistical uncertainties. Another option would be to select looser thresholds so that more events end up in region A, resulting in a better closure in the SR. However, since the closure in the $\overline{\text{SR}}$ is different from the closure in the SR, this could not have been studied without knowing the distribution in the actual region A of the SR. These investigations were helpful in understanding the differences between the SR and the $\overline{\text{SR}}$, and this knowledge will be used for the unblinding of the resolved topology.

In the next step of the unblinding procedure, the behaviour of the nuisance parameters was studied based on the fit with unblinded data. First, the correlations between the different nuisance parameters and the signal strength modifier were investigated. Figure 12.11 shows the postfit correlations between the parameters found in a signal-plus-background fit to data used in the analysis of the LLPs with a 1 mm lifetime. The signal strength modifier, denoted as r in this figure, was for this and the following studies set to be equal or above zero and was found, as expected, very strongly anticorrelated to the uncertainty on the QCD background estimation. All other correlation coefficients are much smaller.

Next, the pull distributions were calculated for the background-only and the signal-plus-background fits to unblinded data, and the results are presented in Figure 12.12. In

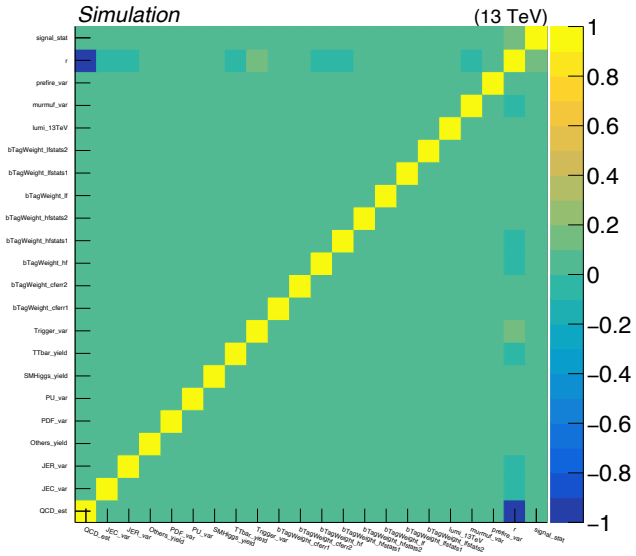

Figure 12.11: The correlations between the nuisance parameters and the signal strength modifier, denoted here as r in the signal-plus-background fit for the analysis of the 1 mm LLP lifetime.

contrast to the pulls found in the fit to Asimov pseudodata, presented in Figure 12.2, the QCD background estimation uncertainty *QCD_est* is now used to pull the yield downwards, as expected by the overprediction of the QCD multijet background. The remaining nuisances are only pulled by a small amount. The pull distribution for the signal-plus-background fit to data is similar to the background-only result. This is because the signal strength modifier is limited to non-negative values. The remaining difference between observed data and the overpredicted background yield is closed by pulling the nuisance parameter controlling the dominant QCD background downward. This behaviour is also visible in Table 12.6, where it can be seen that in the signal-plus-background fit, the signal strength is fitted to zero, and mainly the yield of the QCD multijet background is reduced. The pull distributions and the corresponding prefit and postfit yields for the fits with the remaining LLP lifetimes and the ggF Higgs production mode of the signal can be found in Appendix F. All these pulls show similar distributions, as the presented one here, where mainly the predicted QCD background was pulled downwards by the background estimation uncertainty.

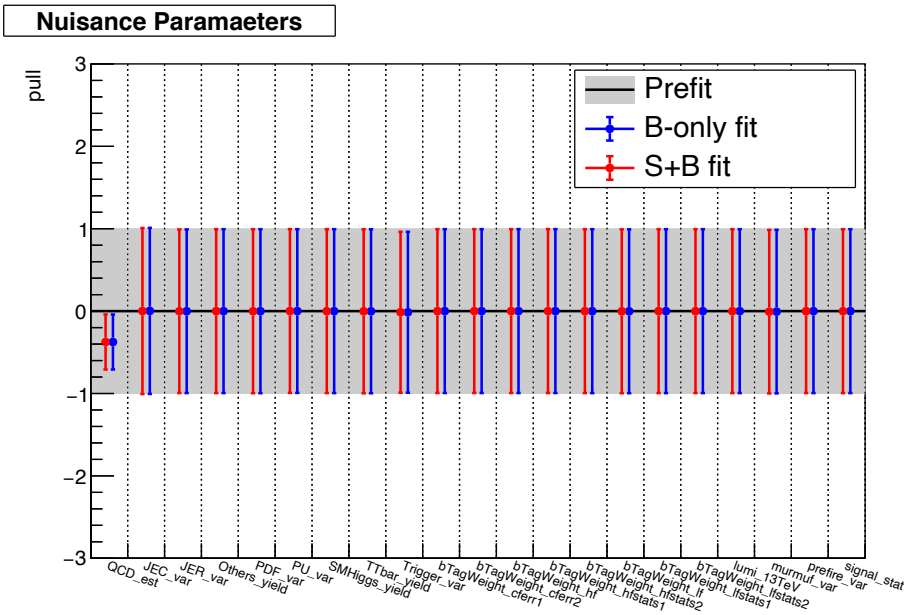

Figure 12.12: The pull distribution of the nuisance parameters in the background-only (blue) and signal-plus-background (red) fits to data in the analysis with a 1 mm LLP lifetime.

Table 12.6: Prefit and postfit yields for background-only and signal-plus-background hypotheses for the analysis of LLPs with 15 GeV mass and 1 mm lifetime.

	Prefit yield	Postfit yield	
Sample		b-only	s+b
Signal	19.5 ± 21.7	0.0 ± 0.0	0.0 ± 0.1
QCD pred.	297.4 ± 45.3	279.4 ± 15.6	279.4 ± 15.5
$t\bar{t}$	3.5 ± 3.3	3.4 ± 3.0	3.5 ± 3.0
SM Higgs	0.3 ± 0.2	0.3 ± 0.2	0.3 ± 0.2
Others	0.1 ± 0.2	0.1 ± 0.2	0.1 ± 0.2
Data	281	281	281
total signal	19.5 ± 21.7	0.0 ± 0.0	0.0 ± 0.1
total background	301.2 ± 45.3	283.2 ± 15.4	283.2 ± 15.8
total	320.8 ± 50.8	283.2 ± 15.4	283.2 ± 15.8

Only the closures of the shorter lifetimes differ from the expectation but were still within 1.5 standard deviations, while the remaining presented results are very close to the expected behaviour. Therefore, the unblinded expected and observed upper limits at the 95 % CL on the signal strength modifier were calculated for all lifetimes, and the results are presented in Figure 12.13. As for the blinded expected limits, the signal with the VBF (upper left) and the ggF (upper right) Higgs production modes are shown separately. The

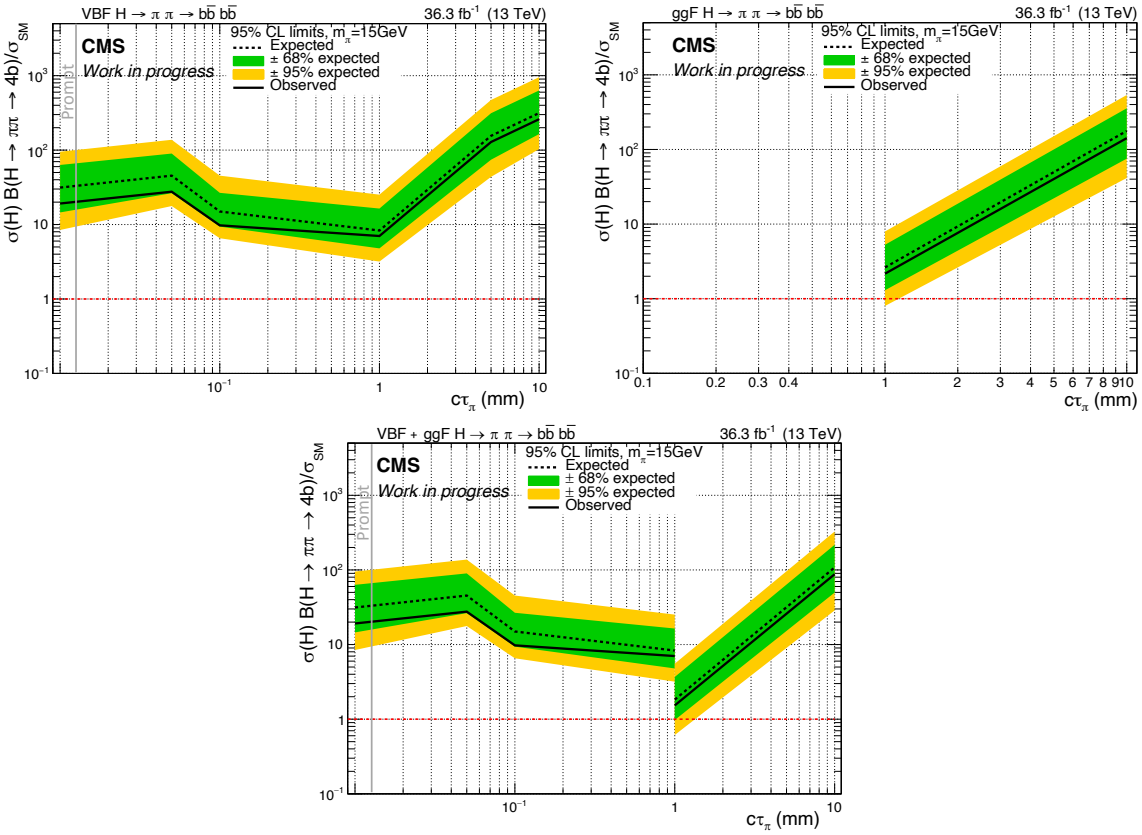

Figure 12.13: The expected and observed limits on the signal strength modifier for the production of the LLPs with a mass of 15 GeV as a function of the LLP lifetime for the VBF (upper left), ggF (upper right) and the combined (lower) Higgs production modes.

combined (lower) limits were calculated for the lifetimes that exist for both production modes, while for the remaining lifetimes, the VBF signal only result was used instead of the VBF+ggF result. Table 12.7 summarises the mean values of the blinded and the unblinded expected, as well as the observed limits for all lifetimes and the different Higgs production modes. The unblinded expected limits are lower than the blinded expected limit, which is due to the overprediction of the QCD multijet background. Furthermore, the observed limit is below the unblinded expected limit for all lifetimes. The observed limits can be found below the unblinded expected limits for all lifetimes due to the smaller observed yield compared to the predicted background. The observed limit is within the 1σ band of the expected limit for all lifetimes. The signal with the ggF Higgs production mode is more sensitive due to the higher production cross section, and hence the limits are better than for the VBF production mode. The combination of both production modes

Table 12.7: The mean values of the blinded and unblinded expected and observed limits for the different lifetimes of the boosted topology with VBF and ggF Higgs production modes and the lifetimes with both production modes combined.

Production mode	Lifetime [mm]	Thresholds	Blinded	Unblinded	
			Expected	Expected	Observed
VBF	0	0.92x0.92	48.3	31.4	19.2
	0.05	0.90x0.90	65.0	45.4	27.6
	0.1	0.91x0.91	22.1	15.0	9.8
	1	0.89x0.89	8.7	8.3	7.0
	5	0.89x0.89	164.0	155.5	128.4
	10	0.88x0.88	314.0	314.5	259.9
ggF	1	0.89x0.89	2.8	2.6	2.2
	10	0.88x0.88	174.0	177.0	141.9
combined	1	0.89x0.89	2.8	1.8	1.5
	10	0.88x0.88	106.8	108.0	87.6

further reduces the observed and expected limits.

12.3.2 Resolved Topology

The studies of the closures in the $\overline{\text{SR}}$ and the sideband regions of the resolved topology discussed in Section 11.2 indicated that the QCD background is almost everywhere underpredicted. Furthermore, were the closures in the sideband regions of the SR and $\overline{\text{SR}}$ very similar. Based on these results, the assumption was made that the closures in the regions A of the SR and the $\overline{\text{SR}}$ would behave similarly. Similar assumptions were found for the boosted topology. However, during the unblinding of the boosted topology, it was observed that the closures in the SR and $\overline{\text{SR}}$ were only similar for lifetimes of 1 mm and above. In contrast, for shorter lifetimes, the closures in the SR were much worse than in the $\overline{\text{SR}}$. Studies indicated that this might be caused by differences in the jet kinematics of the SR and the $\overline{\text{SR}}$ (see Appendix B). Therefore, before the unblinding process of the resolved topology, the input features of the DNN were investigated, and it was observed that the differences between the jet kinematics of the SR and the $\overline{\text{SR}}$ selections are not as large as for the boosted topology (see Appendix B). Especially the η distributions are very similar, and the peaks in the p_{T} and mass distributions are at very similar positions. At the same time, there are larger differences in the tails of the distribution where the statistical uncertainty also increases.

Next, normalised 1D distributions of the DNN discriminants evaluated on data were compared for the SR and the $\overline{\text{SR}}$ of different LLP mass-lifetime combinations and are presented in Figure 12.14. The subleading (left) and the third-leading (right) of the selected jets are shown for the LLP masses of 40 GeV (upper) and 55 GeV (lower). Two significant differences to the boosted topology can be observed. Firstly, the peaks of the distributions for the different lifetimes are at the same position. Secondly, the shapes of the distribution of the SR and the $\overline{\text{SR}}$ are very similar per lifetime, especially at the tail to the right side. The left side of the peak of the LLP mass of 55 GeV shows a small plateau instead of the constantly falling distribution of the 40 GeV distribution. However, the SR and the $\overline{\text{SR}}$ are still in good agreement, and therefore a similar behaviour of both regions is expected.

The ABCD planes in the $\overline{\text{SR}}$ (left) and the unblinded SR (right) in data are presented in Figures 12.15 and 12.16 for the LLP masses of 40 GeV and 55 GeV, respectively. The plots for the lifetimes of 0 mm to 1 mm are shown in the first to last row. Since the same DNN discriminant is used for the 1 mm, 5 mm and 10 mm lifetimes, only the plot for the 1 mm lifetime is shown. The distributions and the profiles are very similar, including

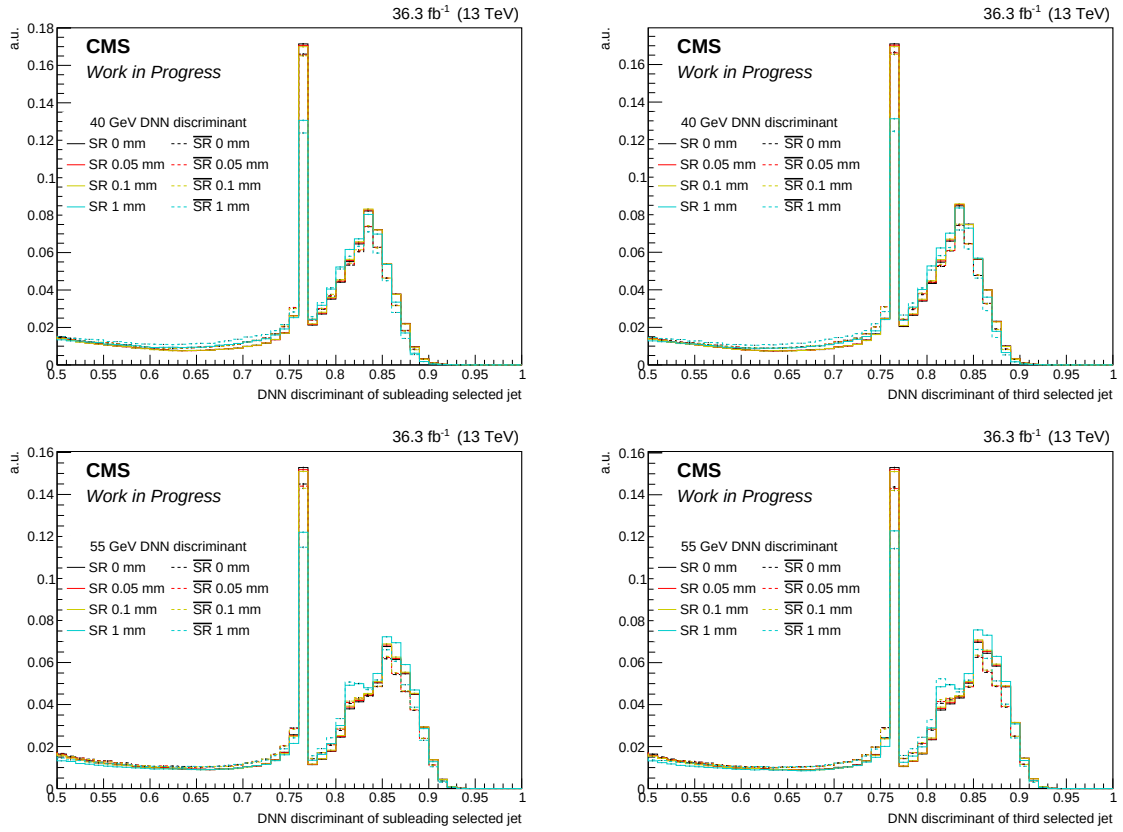

Figure 12.14: Distributions of the DNN discriminant in data of the subleading (left) and the third-leading (right) selected jet for LLP masses of 40 GeV (upper) and 55 GeV (lower). The DNN discriminants are shown for different lifetimes. The distributions in the SR and the $\overline{\text{SR}}$ are indicated by solid and dashed lines, respectively. The distributions are normalised to unity over the whole range of the discriminant, while only the region above 0.5 is shown.

the shapes and positions of the accumulation of events around values of 0.83. Compared to the boosted topology, the accumulations found in the resolved topology seem to be rounder and without obvious borders or tails towards particular directions. Based on this observation, as well as the results of the normalised 1D distribution and of the input features, which show minor difference between the $\overline{\text{SR}}$ and the SR, it is expected that both regions behave more similarly and that the blinded and unblinded expected limits might agree better, as it was the case for the 1 mm lifetime in the boosted topology analysis.

The 1D distributions of the full DNN discriminant range for LLP masses of 40 GeV (upper) and 55 GeV (lower) and 1 mm lifetime are presented in Figure 12.17. The QCD multijet processes are taken from simulations. The data-to-simulation agreement over the whole

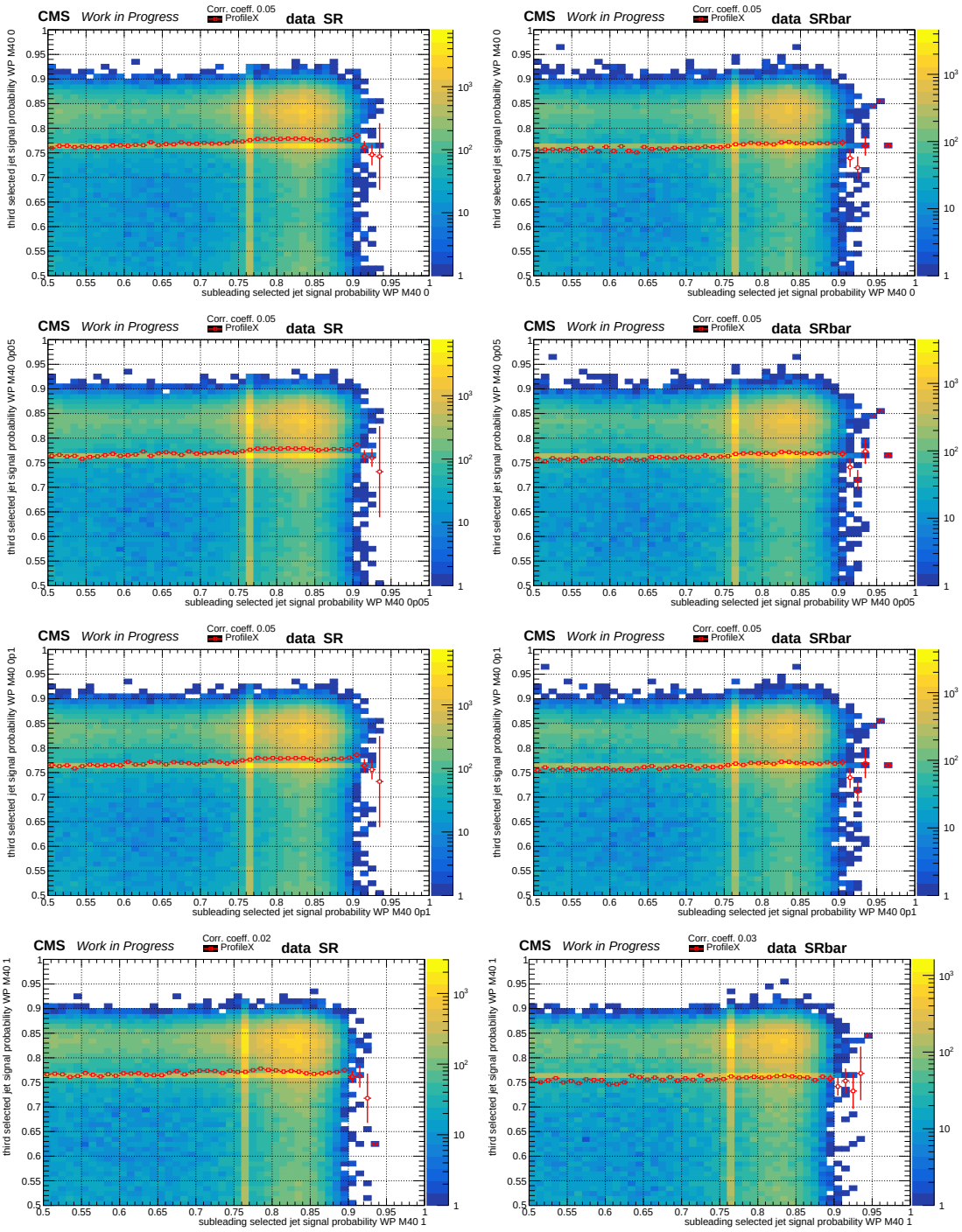

Figure 12.15: Distributions of data in the ABCD planes defined by the DNN discriminants for the subleading and third-leading selected jet in the SR (left) and $\overline{\text{SR}}$ (right) for the analysis of the LLP with 40 GeV mass and lifetimes of 0 mm (first row), 0.05 mm (second row), 0.1 mm (third row) and 1 mm (fourth row).

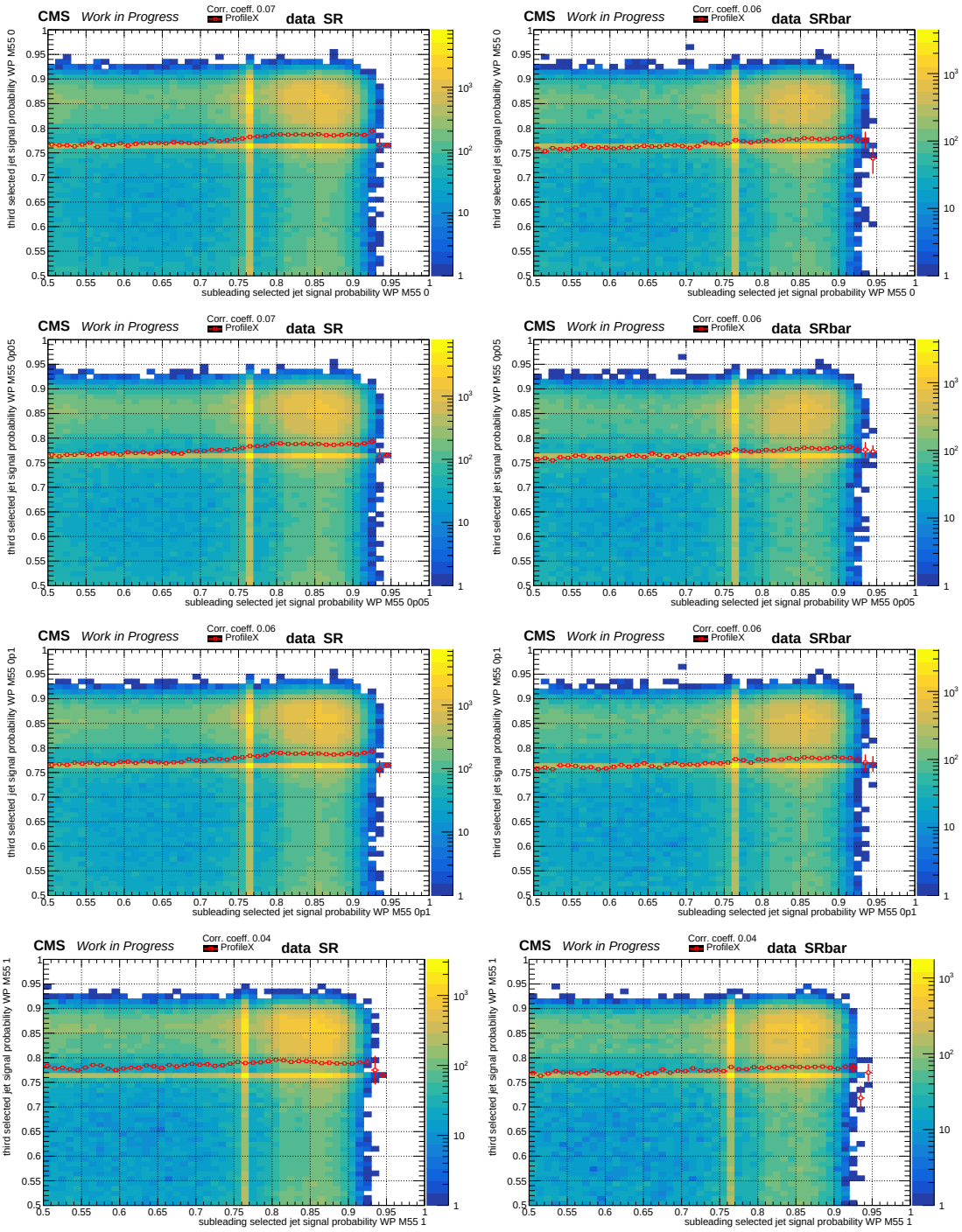

Figure 12.16: Distributions of data in the ABCD planes defined by the DNN discriminants for the subleading and third-leading selected jet in the SR (left) and $\overline{\text{SR}}$ (right) for the analysis of the LLP with 55 GeV mass and lifetimes of 0 mm (first row), 0.05 mm (second row), 0.1 mm (third row) and 1 mm (fourth row).

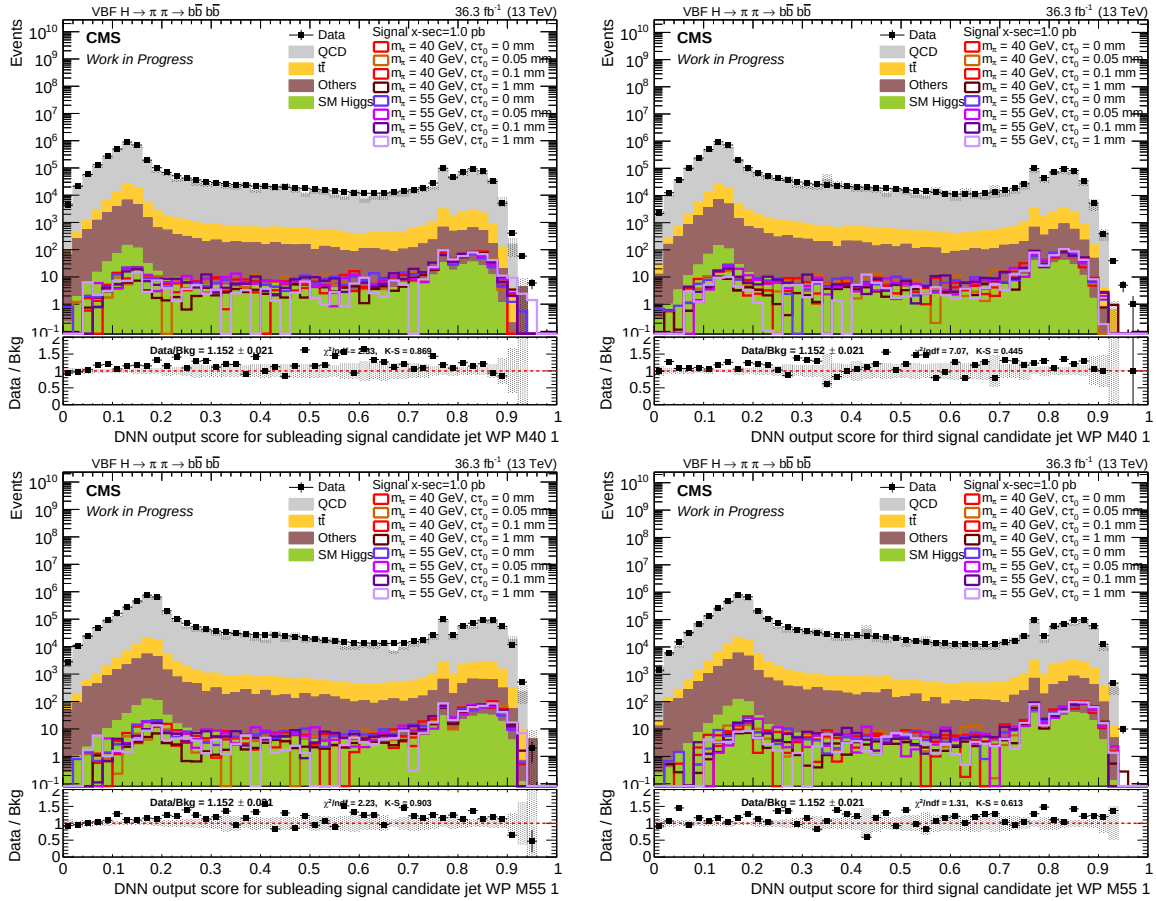

Figure 12.17: Distributions of the DNN discriminants for the subleading (left) and third (right) of the selected jets in the SR for the analysis of the LLP with 40 GeV (upper) and 55 GeV (lower) mass. The simulated QCD multijet process is shown, and the error band consists of the statistical uncertainties only.

range is acceptable and similar to the previous agreements. A perfect agreement was not expected, which is the reason for the background estimation method.

The observed and predicted QCD plus non-QCD background yields with their closures and its significances for the different LLP mass-lifetime combinations can be found in Table 12.8. The closures in the regions A are for all mass-lifetimes combinations significantly greater than one, indicating overpredictions, in contrast to the underpredictions expected from the sideband studies. In addition, all closures are of similar size, in contrast to the closures of the boosted topology, where differences between the lifetimes were observed. The significances of the closure's deviations from unity are between 1 and 2.7 standard deviations, and without the additional uncertainty term, explained in Section 11.2.2, these

Table 12.8: Observed and predicted event yields in region A, the closure of the background prediction, and its significance for all LLP masses and lifetimes investigated in the analysis of the resolved topology.

Mass [GeV]	Lifetime [mm]	Data yield	Predicted background $\pm\sigma_{\text{QCD\_est}} \pm \sigma_{\text{stat}}$	Closure	Closure significance
40	0	11568	13045 ± 1347 ± 98	1.128 ± 0.117	1.093
	0.05	4440	5227 ± 618 ± 47	1.177 ± 0.140	1.265
	0.1	10743	12248 ± 1192 ± 95	1.140 ± 0.111	1.259
	1 & 5 & 10	12211	14176 ± 845 ± 125	1.161 ± 0.070	2.304
55	0	16895	19118 ± 1344 ± 127	1.132 ± 0.080	1.646
	0.05	16550	18746 ± 1206 ± 126	1.133 ± 0.073	1.810
	0.1	16229	18483 ± 841 ± 126	1.139 ± 0.053	2.649
	1 & 5 & 10	11121	13277 ± 1187 ± 109	1.194 ± 0.107	1.809

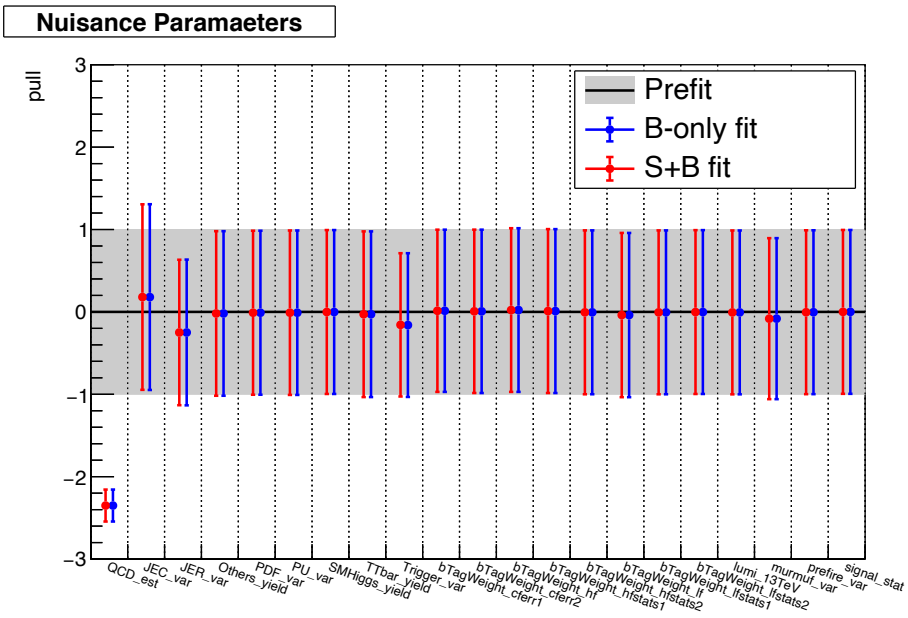

Figure 12.18: The pull distribution of the nuisance parameters of the LLP with a mass of 40 GeV and a lifetime of 1 mm for the fit with background-only (blue) and signal-plus-background (red) hypothesis.

significances would be much higher. In the boosted topology, the significances are smaller due to either better closures or larger additional uncertainties.

The correlation matrices for the fits in the resolved topology are similar to those in the boosted topology, presented in Figure 12.11 for 1 mm lifetime, and hence not shown. As for the boosted topology, the most significant correlations occur between the signal

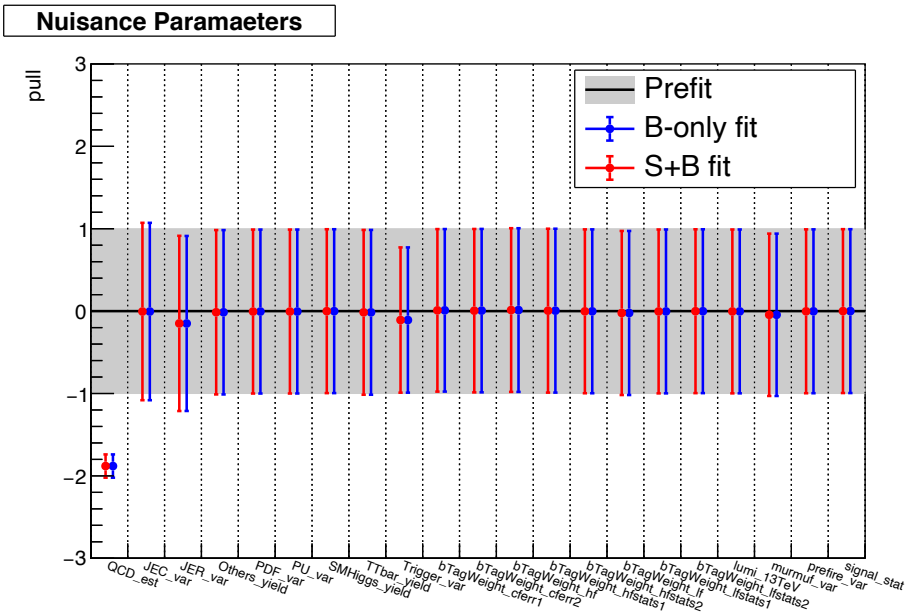

Figure 12.19: The pull distribution of the nuisance parameters of the LLP with a mass of 55 GeV and a lifetime of 1 mm for the fit with background-only (blue) and signal-plus-background (red) hypothesis.

Table 12.9: Prefit and postfit yields for background-only and signal-plus-background hypotheses for the LLP analysis with 40 GeV mass and 1 mm lifetime.

	Prefit yield	Postfit yield	
Sample		b-only	s+b
Signal	60.1 ± 71.4	0.0 ± 0.0	0.0 ± 0.3
QCD pred.	13968.4 ± 825.7	12086.7 ± 146.8	12086.7 ± 145.8
$t\bar{t}$	135.6 ± 90.7	120.5 ± 64.8	120.6 ± 61.0
SM Higgs	3.5 ± 2.9	3.1 ± 2.1	3.1 ± 2.0
Others	68.3 ± 63.4	39.2 ± 36.5	39.3 ± 35.2
Data	12211	12211	12211
total signal	60.1 ± 71.4	0.0 ± 0.0	0.0 ± 0.3
total background	14175.9 ± 833.7	12249.7 ± 127.1	12249.7 ± 134.1
total	14235.9 ± 841.2	12249.7 ± 127.1	12249.7 ± 134.1

strength modifier and the QCD background estimation uncertainty.

The pull distributions of the nuisance parameters for the background-only and the signal-plus-background fits to data for the 1 mm lifetime and LLP masses of 40 GeV and 55 GeV in Figures 12.18 and 12.19, and the corresponding prefit and postfit yields are presented in Tables 12.9 and 12.10, respectively. The fits to data behave differently from those

Table 12.10: Prefit and postfit yields for background-only and signal-plus-background hypotheses for the LLP analysis with 55 GeV mass and 1 mm lifetime.

	Prefit yield	Postfit yield	
Sample		b-only	s+b
Signal	43.2 ± 51.6	0.0 ± 0.0	0.0 ± 0.2
QCD pred.	13095.7 ± 1159.7	10981.0 ± 147.7	10981.0 ± 146.8
$t\bar{t}$	115.0 ± 95.2	108.1 ± 73.6	108.1 ± 67.9
SM Higgs	2.8 ± 2.6	2.6 ± 2.3	2.6 ± 2.2
Others	63.1 ± 73.7	49.6 ± 50.4	49.7 ± 50.6
Data	11121	11121	11121
total signal	43.2 ± 51.6	0.0 ± 0.0	0.0 ± 0.2
total background	13276.6 ± 1164.7	11141.4 ± 128.0	11141.4 ± 135.4
total	13319.8 ± 1168.2	11141.4 ± 128.0	11141.4 ± 135.4

to Asimov pseudodata, performed before the unblinding and shown in Figure 12.5. In the signal-plus-background and background-only fits to data, is the uncertainty with the largest pulls and strongest constraints the QCD background estimation, which is strongly pulled downwards to compensate for the larger overpredictions of the background yields. Compared to the boosted topology, the nuisance parameters for the uncertainties on JEC, JER, trigger, as well as the renormalization and factorization scales are pulled more strongly, leading to a larger reduction of the non-QCD backgrounds, which additionally compensates for the larger overpredictions. Since the signal-plus-background fits again result in signal strength modifiers of zero, being bound to non-negative values, the pull distributions of the background-only and the signal-plus-background hypotheses are very similar.

The observed and expected limits at 95 % CL on the signal strength modifier are shown as a function of the lifetime for LLPs with masses of 40 GeV and 55 GeV in Figures 12.20 and 12.21, respectively. Presented are the limits on the signal produced in the VBF (upper left) and ggF (upper right) Higgs production modes and the combination of both production modes (lower), where the VBF-only result is shown if no ggF sample was available for the relevant lifetime. Comparisons between the mean values of the blinded and unblinded expected limits, as well as the observed limits, are presented in Tables 12.11 and 12.12 for the different lifetimes of both masses. Due to the overprediction, are the unblinded expected limits again lower than the blinded expected limits. In addition, the observed limits are below the unblinded expected limits. The overall sensitivity for the signal with a mass of 40 GeV is slightly better than for longer lifetimes, while the sensitivity for the

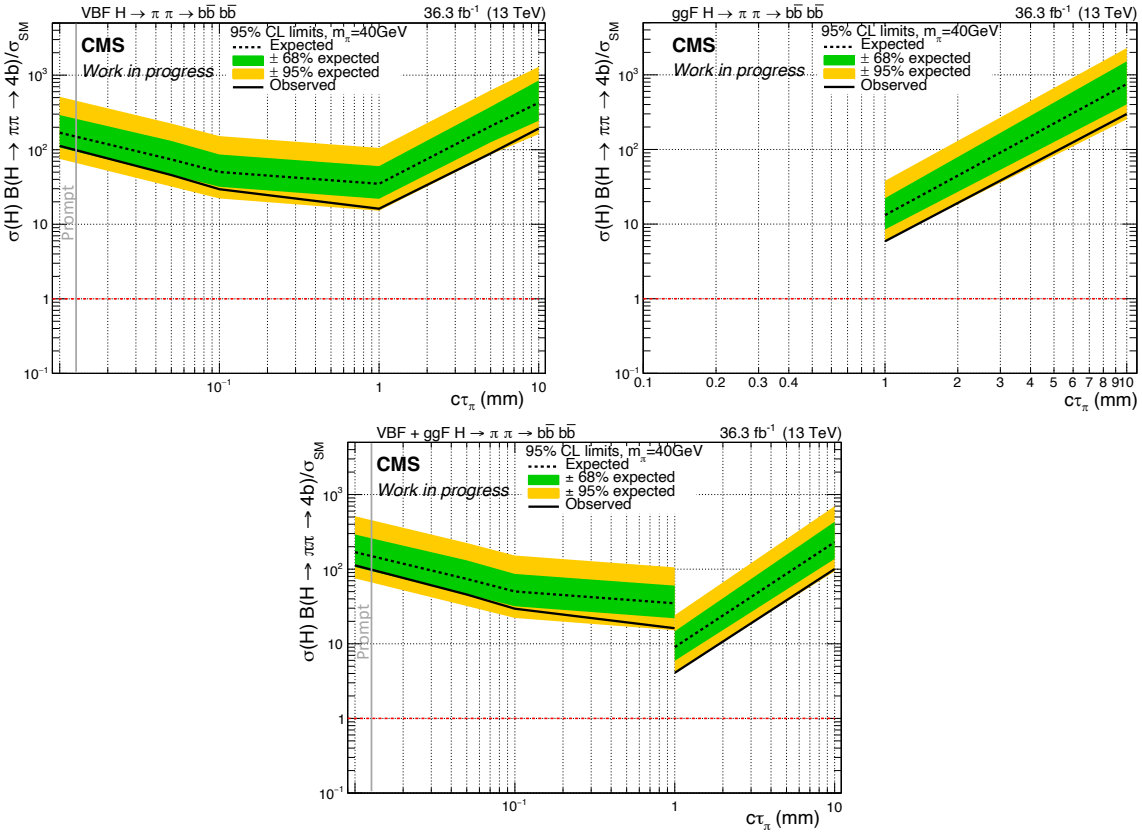

Figure 12.20: The expected and observed limits on the signal strength modifier of the different lifetimes of the LLP mass of 40 GeV with the signal of VBF (upper left), ggF (upper right) and the combined (lower) Higgs production modes.

mass of 55 GeV is better for shorter lifetimes. The ggF Higgs production mode signal is more sensitive due to the higher production cross section. The combination of both production modes also increases the sensitivity slightly compared to the result of the ggF production mode alone. The observed limit is within the 2σ band of the expected limit for all LLP mass-lifetime combinations.

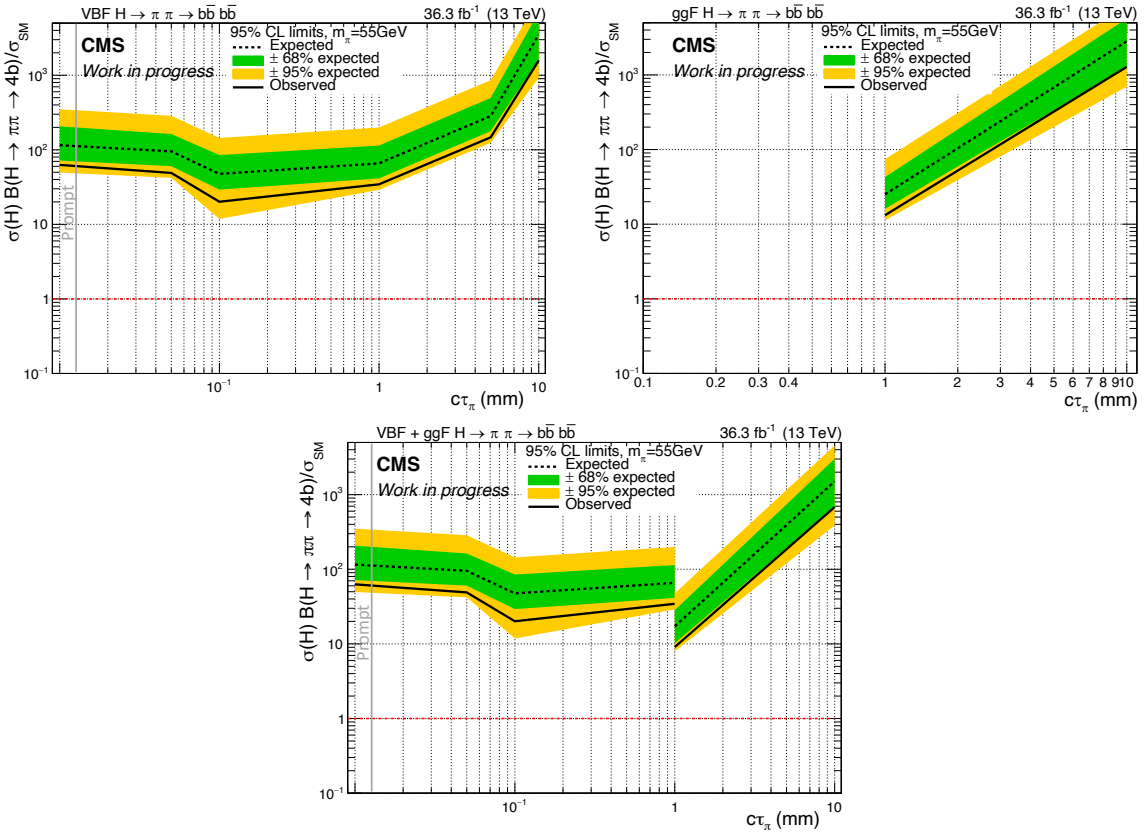

Figure 12.21: The expected and observed limits on the signal strength modifier of the different lifetimes of the LLP mass of 55 GeV with the signal of VBF (upper left), ggF (upper right) and the combined (lower) Higgs production modes.

Table 12.11: The mean values of the blinded and unblinded expected and observed limits for the different lifetimes of the LLP mass of 40 GeV with VBF and ggF Higgs production modes and of the lifetimes with both production modes combined.

Production mode	Lifetime [mm]	Thresholds	Blinded	Unblinded	
			Expected	Expected	Observed
VBF	0	0.84x0.84	185.5	169.0	112.4
	0.05	0.85x0.85	82.0	74.0	45.7
	0.1	0.84x0.84	55.4	50.3	29.5
	1	0.83x0.83	39.1	34.9	16.2
	5	0.83x0.83	211.5	206.5	89.2
	10	0.83x0.83	507.0	427.0	192.7
ggF	1	0.83x0.83	13.7	13.2	5.9
	10	0.83x0.83	714.0	754.0	299.0
combined	1	0.83x0.83	9.8	9.0	4.1
	10	0.83x0.83	243.5	230.0	100.5

Table 12.12: The mean values of the blinded and unblinded expected and observed limits for the different lifetimes of the LLP mass of 55 GeV with VBF and ggF Higgs production modes and of the lifetimes with both production modes combined.

Production mode	Lifetime [mm]	Thresholds	Blinded	Unblinded	
			Expected	Expected	Observed
VBF	0	0.86x0.86	122.5	115.5	62.8
	0.05	0.86x0.86	98.5	95.3	48.9
	0.1	0.86x0.86	52.0	47.5	20.1
	1	0.86x0.86	75.4	65.8	34.5
	5	0.86x0.86	320.0	283.5	146.9
	10	0.86x0.86	3726.0	3493.0	1577.1
ggF	1	0.86x0.86	28.6	25.1	13.2
	10	0.86x0.86	3130.0	2828.0	1282.2
combined	1	0.86x0.86	19.6	17.2	9.1
	10	0.86x0.86	1633.0	1500.0	681.0

Part IV

Future Perspectives and Summary

13 Future Perspectives of the Search for Long-Lived Particles with b Quark-like Signature

The presented search for LLPs with lifetimes on the order of few millimetres and decays to b quarks produced in Higgs boson decays with boosted and resolved final state is the first search in this phase space analysing data with an integrated luminosity of $\mathcal{L} = 36.3\,\text{fb}^{-1}$ recorded by the CMS experiment in 2016. The search targeted LLPs with various masses and lifetimes originating from Higgs bosons produced via the ggF and VBF channels. Upper limits at 95 % CL are set on the signal strength modifier for the different LLP mass-lifetime combinations for the two Higgs production mechanisms separately and combined. Due to the selection based on triggers requiring standard jets and b-tagged jets, the main background of the search is the QCD multijet processes. In addition, very short lifetimes of LLPs are probed in this search, making the b quarks originating from the LLP decays very hard to distinguish from that originating from SM processes. Altogether, this search is rather challenging and, in the following, ideas are discussed to improve the sensitivity of the search.

The results of the presented search in this thesis were obtained using data with an integrated luminosity of $\mathcal{L} = 36.3\,\text{fb}^{-1}$ recorded in 2016. One improvement in the sensitivity of the search can be expected by analysing more data. For example, the data recorded between 2016-2018 have an integrated luminosity of $\mathcal{L} = 139\,\text{fb}^{-1}$, roughly four times more than in 2016 only. In addition, changing methods or using different technologies in the search might improve the sensitivity. Such ideas are presented in the following and are partially based on the results of the presented work of this thesis.

The trigger needs to be reevaluated for the data recorded in 2017-2018. Preliminary studies of the trigger paths for the data recorded in 2016-2018 showed that, unfortunately, the two trigger paths used for the presented analysis with 2016 data are not available since the pp collision rate was increased, resulting in the adjustment of the trigger requirements.

In addition to the triggers used in this analysis, which are listed again below:

- **2016:** HLT_QuadJet45_TripleBTagCSV *or* HLT_DoubleJet90_Double30_TripleBTagCSV

The following triggers would be appropriate for the additional years:

- **2017:** HLT_PFHT300PT30_QuadPFJet_75_60_45_40_TriplePFBTagCSV_3p0
- **2018:** HLT_PFHT330PT30_QuadPFJet_75_60_45_40_TriplePFBTagDeepCSV_4p5

All those trigger paths have in common that they require at least four jets of which at least three have to be b-tagged jets, but with increased p_{T} requirements for the two trigger paths of 2017 and 2018. In addition, a requirement on the H_{T}, defined as the scalar sum of the p_{T} of the jets, needs to be fulfilled. These two additional requirements could potentially lower the trigger efficiency for signal events, which has rather soft jets, for the data taking period of 2017-2018. The trigger efficiency for the VBF Higgs production mode and the different LLP mass-lifetime combinations are presented in Figure 13.1. The efficiency of the two triggers combined by a logical *or* in 2016 is presented in Figure 9.1. Comparing the results of the different data-taking periods show that adding the additional datasets would only double the signal efficiency, while the integrated luminosity is roughly four times larger.
Another option to increase the sensitivity would be to use trigger paths which are prescaled to lower the event rate. As described in Section 7.2.6, the HLT filters are selected so that the event rate is on the order of 100 Hz. Only a subset of the events passing those trigger paths is stored to consider trigger paths that would select events with higher rates during data taking. Therefore, looser requirements can be chosen to potentially select events of interest which are not selected by non-prescaled triggers. The looser requirements might increase the efficiency for signal events, but depending on the value of the prescale, potential signal events might also be randomly removed and not recorded. These triggers are preferably not used for the first setup of an analysis, but could be considered in the future.

Some improvements are motivated by studies or shortcomings of the analysis presented in this thesis. One of these shortcomings is the overprediction of the QCD multijet background by the ABCD method, which was observed for all LLP masses and lifetimes. Furthermore, the most significant uncertainty is related to the estimation of the dominant QCD multijet background. Any improvement in the background estimation and the uncertainty would directly result in increased sensitivity. This could be made possible by

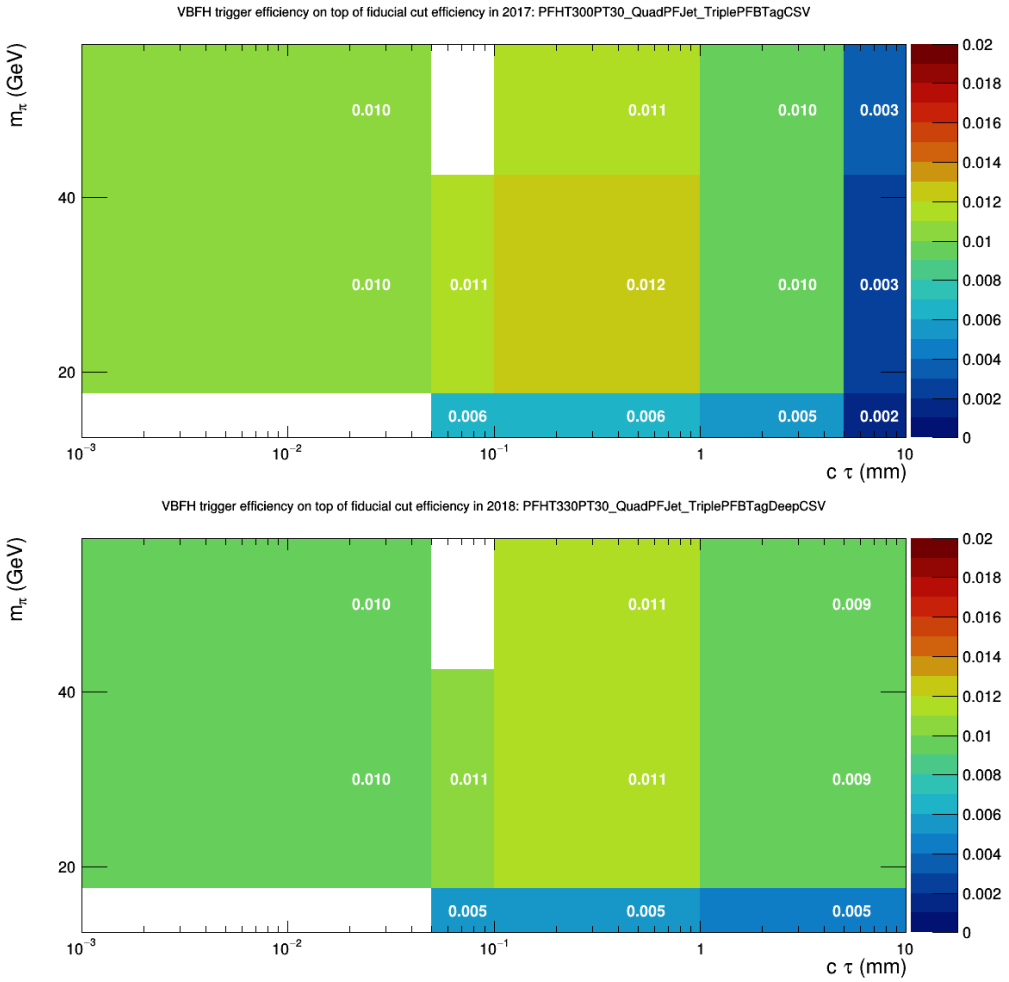

Figure 13.1: Trigger efficiency plots for data taking period 2017 (upper) and 2018 (lower) evaluated on simulated VBF signal events, as a function of masses and lifetimes of the LLPs. For 2017 lifetimes between 0 mm and 5 mm and for 2018 only up to 1 mm are shown for LLP masses of 15, 40 and 55 GeV.

using validation or control regions to calculate the upper limits, making it more complicated than the currently used simple counting experiment in one bin. By including these different regions that do not have signal contamination, the predictions of different uncertainties could be improved. Apart from that, a more complex fit, like using the shape of a variable would also benefit from additionally fitted regions. The shape fit would require a change in the analysis strategy. For example, a multi-classifier DNN could select the jets of interest based on event and jet information. This would replace the χ^2 method, and the invariant mass of the selected jets could be used to calculate upper limits. Unfortunately, the shape fit makes the estimation of the QCD multijet background more complicated,

but it is not impossible.
The second-largest uncertainty of the presented search comes from the trigger correction factor uncertainty. This uncertainty was derived conservatively, treating all HLT filter efficiencies as fully correlated, resulting in the largest possible uncertainty, as described in Section 9.2.1. A smaller uncertainty could be derived by studying the actual correlations between the different HLT filter steps, which would result in an improvement of the sensitivity.
Improving the sensitivity could also be achieved by also considering the production of the Higgs boson in association with vector bosons, with subsequent decays of the W and the Z boson to quarks. The combined WH and ZH production modes have roughly the same cross section as the VBF Higgs production mode. Furthermore, enough jets are expected from the decay of vector bosons, which might result in a sufficient trigger efficiency. However, Z boson decays to b quark pairs could complicate the selection of the signal signatures. Another Higgs boson production mode that could be considered for further analysis is that of the associated production with heavy quarks, such as ttH, which has roughly one order of magnitude lower production cross section than the VBF production mode. The associated production mode would then most likely need a different analysis strategy, where identifications of the decay processes of the *top* quarks are included. If the decays of the *top* quarks are considered full hadronically, the main background still might be the QCD multijet processes. Instead, an event selection where one or both *top* quarks are considered with a leptonic decay potentially leads to a clearer signature, and the QCD multijet processes would not be the main background any longer.
More LLP masses and lifetimes could be easily added to the search since the parametrised DNN can also predict combinations which it was not trained on. In the presented search, the centrally produced LLP signal samples were used, as described in Chapter 9.2. Additional samples with more masses and lifetime combinations could be produced. Instead, an interpolation from an existing sample to a different combination is possible, and not as many different mass-lifetime combinations would need to be produced.
Furthermore, the existing strategy could be extended to use potential signal events which end up in region A of a different mass-lifetime combination. For example, events which end up in the boosted topology with a LLP mass of 15 GeV and 1 mm lifetime but refer to the signal with a mass of 55 GeV and 1 mm could be used as an additional bin for the limit calculation of the latter signal model. Events might end up in both bins, and therefore, careful investment and removal of such events would be essential so that they are not used twice for the limit calculation. The number of additional signal events ending up in the

selection of the other topology is expected to be small. However, the sensitivity of the combined Higgs boson production modes is better than the ggF mode alone. Therefore, any increase in the signal event yield improves the sensitivity.

The used DNN is currently parametrised with the LLP lifetime in the rest frame of the particle. However, it would also be possible to parametrise the DNN using the nominal lifetime in the rest frame of the detector by using generator level information of the signal events. This procedure would require careful consideration of what values for the SM background processes would be used.

With the current analysis strategy, it was observed that the DNN discriminant was correlated to the jet kinematics, which can be understood as the jet kinematics are used as input features. Therefore, the separation into the SR and the $\overline{\text{SR}}$ based on the value of the χ^2 method induces differences in the ABCD planes. These correlations could be decreased by either removing the relevant input features from the DNN or normalising the jet kinematics. Such a decorrelation might result in a better closure of the SR or that the $\overline{\text{SR}}$ describes the SR better, or both. In any case, using two variables for the ABCD plane, which are not at all or only very little correlated to each other, improves the ABCD method.

A possible addition to the ΔR requirement would be to veto events where jets with a certain invariant mass are present in the other hemisphere of the detector since especially simulated QCD multijet processes tend to have jets produced back-to-back to conserve the momentum. Such an event veto would further reduce the QCD multijet background.

The two topologies might benefit from different analysis strategies. Instead of optimising each preselection of the analyses so that both topologies can be investigated, a complete split into two independent analyses could help improve the sensitivity. For example, jets with a radius parameter $R = 0.8$ might have been large enough to cover the hadronisation objects of the two b quarks originated by the same LLP of the resolved[1] topology.

Sensitivity could also be gained by applying new and more sophisticated algorithms or analysis techniques.

One of such new developments was achieved by the CMS collaboration. The jets used for the search are cleaned from the effects of PU using the CHS algorithm. From the data taking period of 2022 onwards, the algorithm called PUPPI should be used by default (see Section 8.1.2). Early studies on the performance of the two algorithms showed that

[1]The studies on generator level after the preselection in Section 9.3.1 show that the AK4 jets are most likely large enough to reconstruct the hadronisation processes of two b quarks in the boosted topology.

there is not much difference for the lifetimes used in the presented search, while a clear drop in the efficiency was observed for longer lifetimes.
Given the speed of development in the research field of machine learning, the strategy of using the parametrised DNN could be rethought. In addition to the changes mentioned above in the analysis strategy, a different tagger for jets might show a better performance. For example, the currently used b tagging architecture of DeepJet (explained in Section 8.4.1) retrained with LLP signal signatures could be used. Careful adjustments of the selections on the input features, such as the mass of the vertex, the maximum displacement of a vertex or the maximum impact parameter of tracks to be used, would be needed to increase the performance. A completely different method, like a graph convolutional neural network [137], could also be considered.
All in all, there are many different ways to improve the sensitivity of the search for LLPs with decays to b quarks and short lifetimes. Moreover, the ongoing development of new analysis techniques, new trigger paths and future colliders are important aspects for the improvements in the sensitivity of many analyses.

14 Summary

The SM of particle physics is a well motivated and extensively tested theory, and almost all measurements agree with its predictions. However, the theory leaves some questions unanswered, such as the hierarchy problem. Therefore, many theories extending the SM of particle physics have been developed to answer one or several of the open questions. Some of them predict a twin sector to the SM, with new, long-lived particles that are uncharged under the SM. The Higgs boson is a suitable candidate to allow decays to the twin sector and back to SM particles. The decay to two b quarks is predicted to be the dominant decay mode for LLPs. The existence of such a twin sector would solve the little hierarchy problem, which would extend the validity of the SM of particle physics.
Searches for signatures of such LLPs are therefore of great interest and performed by experiments at the LHC. Previous searches for LLPs focused mainly on LLPs originating from Higgs boson decays with Higgs bosons produced via the associated production with leptonically decaying vector bosons. This Higgs boson production channel has a relatively low production cross section, but the presence of the leptons from the vector boson decays leads to a clean final state signature. So far, none of these searches resulted in any evidence for LLPs. However, there are still phase spaces that have not yet been analysed.
This thesis presents the first search for LLPs decaying to b quark-antiquark pairs using data recorded with the CMS experiment. The analysis was performed with data from pp collisions at the LHC at a centre-of-mass energy of 13 TeV with an integrated luminosity of $36.3\,\mathrm{fb}^{-1}$, recorded in 2016. The search considered a benchmark model, predicting a Higgs boson decay into two LLPs, where each LLP decays back to two b quarks, with the Higgs boson being produced via the ggF and the VBF modes. LLP masses between 15-55 GeV and lifetimes up to 10 mm have been investigated. The displacement of the decays of the b quarks originating from a LLP depends on the lifetime of the LLP and is expected to be slightly larger than for b quarks produced via SM processes. The different masses of the LLPs impact the topology, therefore the search is split into an analysis targeting LLP decays with a boosted topology and an analysis targeting decays with a resolved topology. The b quarks originating from a light mass LLP are closer together and

reconstructed within one jet, while the radial distance between the two b quarks is larger for heavier masses. The main background for both topologies is QCD multijet production, which is estimated by a data-driven method. A NN was developed to identify the signal and is parametrised as a function of the masses and lifetimes of the LLPs. Input features of the network are based on the b tagging algorithm DeepJet.

One complication that arises by the identification of b jets is that neutral particles interacting with the detector material lead to displaced vertices that mimic those created by the signal process. The impact of these vertices on b tagging algorithms has been studied on previously used b tagging algorithms, which consider vertices selected based on specific requirements. It was found that variations of these requirements neither impact the signal jets used in this thesis, which are rather soft in p_{T} and have small displacements nor the more sophisticated b tagging algorithm DeepJet.

Limits with 95 % CL were calculated on the signal strength modifier for all LLP mass-lifetime combinations. The sensitivity of the search with the boosted topology was found to be better than for the resolved topology, while for both, the LLP lifetimes of 1 mm result in the best upper limit. No evidence for the production of LLPs decaying into b quark-antiquark pairs was found.

Additionally, future perspectives of the presented search for LLPs with the four b quark final state and short lifetimes were discussed to improve the sensitivity. Since theories predicting new and long-lived particles are suitable extensions to the SM of particle physics, the search for them will be ongoing not only at the LHC but also at future colliders such as the HL-LHC. The higher luminosities or centre-of-mass energies provided by such future colliders, combined with improved analyses methods, will increase the sensitivity to LLP and the possibility of finding such predicted new particles that might exist.

Bibliography

Bibliography

[1] J. J. Thomson, "XL. Cathode Rays", *The Lond. Edinb. Dublin Philos. Mag. J. Sci.* **44** (1897), no. 269, 293–316, doi:10.1080/14786449708621070.

[2] CMS Collaboration, "Observation of a new boson at a mass of 125 GeV with the CMS experiment at the LHC", *Phys. Lett. B* **716** (2012), no. 1, 30–61, doi:https://doi.org/10.1016/j.physletb.2012.08.021.

[3] ATLAS Collaboration, "Observation of a new particle in the search for the Standard Model Higgs boson with the ATLAS detector at the LHC", *Phys. Lett. B* **716** (2012), no. 1, 1–29, doi:https://doi.org/10.1016/j.physletb.2012.08.020.

[4] L. Evans and P. Bryant, "LHC Machine", *J. Instrum.* **3** (Aug, 2008) S08001–S08001, doi:10.1088/1748-0221/3/08/s08001.

[5] ATLAS Collaboration, "The ATLAS Experiment at the CERN Large Hadron Collider", *J. Instrum.* **3** (Aug, 2008) S08003–S08003, doi:10.1088/1748-0221/3/08/s08003.

[6] CMS Collaboration, "The CMS experiment at the CERN LHC", *J. Instrum.* **3** (Aug, 2008) S08004–S08004, doi:10.1088/1748-0221/3/08/s08004.

[7] B. T. Cleveland, T. Daily, J. Raymond Davis et al., "Measurement of the Solar Electron Neutrino Flux with the Homestake Chlorine Detector", *Astrophys. J.* **496** (mar, 1998) 505–526, doi:10.1086/305343.

[8] Y. Fukuda, T. Hayakawa, E. Ichihara et al., "Evidence for Oscillation of Atmospheric Neutrinos", *Phys. Rev. Lett.* **81** (Aug, 1998) 1562–1567, doi:10.1103/physrevlett.81.1562.

[9] F. P. An, J. Z. Bai, A. B. Balantekin et al., "Observation of Electron-Antineutrino Disappearance at Daya Bay", *Phys. Rev. Lett.* **108** (Apr, 2012) doi:10.1103/physrevlett.108.171803.

[10] L. H. C. S. W. Group, "Handbook of LHC Higgs Cross Sections: 4. Deciphering the Nature of the Higgs Sector", doi:10.23731/CYRM-2017-002. https://cds.cern.ch/record/2227475.

[11] Z. Chacko, H.-S. Goh, and R. Harnik, "Natural Electroweak Breaking from a Mirror Symmetry", *Phys. Rev. Lett.* **96** (Jun, 2006) doi:10.1103/physrevlett.96.231802.

[12] Z. Chacko, Y. Nomura, M. Papucci et al., "Natural little hierarchy from a partially goldstone twin Higgs", *J. High Energy Phys.* **2006** (Jan, 2006) 126–126, doi:10.1088/1126-6708/2006/01/126.

[13] R. Barbieri, T. Gregoire, and L. J. Hall, "Mirror world at the large hadron collider", arXiv:hep-ph/0509242.

[14] ATLAS Collaboration, "Search for Higgs boson decays into two new low-mass spin-0 particles in the 4b channel with the ATLAS detector using pp collisions at $\sqrt{s}$=13 TeV", *Phys. Rev. D* **102** (Dec, 2020) doi:10.1103/physrevd.102.112006.

[15] CMS Collaboration, "Precision luminosity measurement in proton-proton collisions at $\sqrt{s} = 13$ TeV in 2015 and 2016 at CMS", *Eur. Phys. J. C* **81** (Apr, 2021) 800. 42 p, doi:10.1140/epjc/s10052-021-09538-2, arXiv:2104.01927.

[16] M. Thomson, "Modern Particle Physics". Cambridge University Press, New York, 2013.

[17] D. Griffiths, "Introduction to elementary particles". WILEY-VCH, Weinheim, 2004.

[18] A. Zannoni, "On the Quantization of the Monoatomic Ideal Gas", doi:10.48550/ARXIV.COND-MAT/9912229. Translation of the original work of Enrico Fermi.

[19] P. Dirac, "On the theory of quantum mechanics", *Royal Society* **112** (1926) doi:10.1098/rspa.1926.0133.

[20] S. Bose, "Planck's law and the light quantum hypothesis", *Journal of Astrophysics and Astronomy volume* **15** (1994) doi:10.1007/BF03010400.

[21] Particle Data Group, "Review of Particle Physics", *PTEP* **2020** (2020), no. 8, 083C01, doi:10.1093/ptep/ptaa104.

[22] KATRIN Collaboration, "Improved Upper Limit on the Neutrino Mass from a Direct Kinematic Method by KATRIN", *Phys. Rev. Lett.* **123** (Nov, 2019) doi:10.1103/physrevlett.123.221802.

[23] R. S. Bhalerao, "Relativistic heavy-ion collisions", *First Asia-Europe-Pacific School of High-Energy Physics* (2012) arXiv:1404.3294.

[24] E. Fermi, "Versuch einer Theorie der β-Strahlen I.", *Z. Phys.* **88** (1934) 161–177, doi:10.1007/BF01351864.

[25] S. L. Glashow, "Partial-symmetries of weak interactions", *Nucl. Phys.* **22** (1961), no. 4, 579–588, doi:https://doi.org/10.1016/0029-5582(61)90469-2.

[26] S. Weinberg, "A Model of Leptons", *Phys. Rev. Lett.* **19** (Nov, 1967) 1264–1266, doi:10.1103/PhysRevLett.19.1264.

[27] F. Englert and R. Brout, "Broken Symmetry and the Mass of Gauge Vector Mesons", *Phys. Rev. Lett.* **13** (Aug, 1964) 321–323, doi:10.1103/PhysRevLett.13.321.

[28] P. W. Higgs, "Broken Symmetries and the Masses of Gauge Bosons", *Phys. Rev. Lett.* **13** (Oct, 1964) 508–509, doi:10.1103/PhysRevLett.13.508.

[29] A. Aivazis, "A javascript application for creating feynman diagrams". Webpage: https://feynman.aivazis.com/.

[30] ATLAS Collaboration, "Observation of Higgs boson production in association with a top quark pair at the LHC with the ATLAS detector", *Phys. Lett. B* **784** (Sep, 2018) 173–191, doi:10.1016/j.physletb.2018.07.035.

[31] CMS Collaboration, "Observation of $t\bar{t}H$ Production", *Phys. Rev. Lett.* **120** (Jun, 2018) doi:10.1103/physrevlett.120.231801.

[32] CMS Collaboration, "Observation of Higgs Boson Decay to Bottom Quarks", *Phys. Rev. Lett.* **121** (Sep, 2018) doi:10.1103/physrevlett.121.121801.

[33] CMS Collaboration, "Observation of the Higgs boson decay to a pair of τ leptons with the CMS detector", *Phys. Lett. B* **779** (Apr, 2018) 283–316, doi:10.1016/j.physletb.2018.02.004.

[34] CMS Collaboration, "A search for the standard model Higgs boson decaying to charm quarks", *J. High Energy Phys.* **2020** (Mar, 2020) doi:10.1007/jhep03(2020)131.

[35] ATLAS Collaboration, "Evidence for Higgs boson decay to a pair of muons", *J. High Energy Phys.* **2021** (Jan, 2021) doi:10.1007/jhep01(2021)148.

[36] CMS Collaboration, "Measurements of properties of the Higgs boson decaying into the four-lepton final state in pp collisions at $\sqrt{s} = 13\,\text{TeV}$", *J. High Energy Phys.* **2017** (Nov, 2017) doi:10.1007/jhep11(2017)047.

[37] CMS Collaboration, "Measurements of Higgs boson properties in the diphoton decay channel in proton-proton collisions at $\sqrt{s} = 13\,\text{TeV}$", *J. High Energy Phys.* **2018** (Nov, 2018) doi:10.1007/jhep11(2018)185.

[38] CMS Collaboration, "Constraints on the spin-parity and anomalous HVV couplings of the Higgs boson in proton collisions at 7 and 8 TeV", *Phys. Rev. D* **92** (Jul, 2015) doi:10.1103/physrevd.92.012004.

[39] ATLAS Collaboration, "Evidence for the spin-0 nature of the Higgs boson using ATLAS data", *Phys. Lett. B* **726** (Oct, 2013) 120–144, doi:10.1016/j.physletb.2013.08.026.

[40] G. Hooft, "Naturalness, Chiral Symmetry, and Spontaneous Chiral Symmetry Breaking", doi:10.1007/978-1-4684-7571-5_9.

[41] G. F. Giudice, "Naturally Speaking: The Naturalness Criterion and Physics at the LHC", *Perspectives on LHC Physics* (Jun, 2008) 155–178, doi:10.1142/9789812779762_0010.

[42] KATRIN Collaboration, "Direct neutrino-mass measurement with sub-electronvolt sensitivity", *Nat. Phys.* **18** (02, 2022) 160–166, doi:10.1038/s41567-021-01463-1.

[43] Muon $g-2$ Collaboration, "Measurement of the anomalous precession frequency of the muon in the Fermilab Muon $g-2$ Experiment", *Phys. Rev. D* **103** (Apr, 2021) 072002, doi:10.1103/PhysRevD.103.072002.

[44] Muon $g-2$ Collaboration, "Measurement of the Positive Muon Anomalous Magnetic Moment to 0.46 ppm", *Phys. Rev. Lett.* **126** (Apr, 2021) 141801, doi:10.1103/PhysRevLett.126.141801.

[45] H. P. Nilles, "Supersymmetry, Supergravity and Particle Physics", *Phys. Rept.* **110** (1984) 1–162, doi:10.1016/0370-1573(84)90008-5.

[46] S. P. MARTIN, "A Supersymmetry Primer", *Adv. Ser. Dir. High Energy Phys.* (Jul, 1998) 1–98, doi:10.1142/9789812839657_0001.

[47] D. Curtin and C. B. Verhaaren, "Discovering uncolored naturalness in exotic Higgs decays", *J. High Energy Phys.* **2015** (Dec, 2015) 1–36, doi:10.1007/jhep12(2015)072.

[48] N. Craig, A. Katz, M. Strassler et al., "Naturalness in the Dark at the LHC", arXiv:1501.05310.

[49] J. E. Juknevich, "Pure-glue hidden valleys through the Higgs portal", *J. High Energy Phys.* **08** (2010) 121, doi:10.1007/JHEP08(2010)121, arXiv:0911.5616.

[50] H. Beauchesne, E. Bertuzzo, G. G. di Cortona et al., "Collider phenomenology of Hidden Valley mediators of spin 0 or 1/2 with semivisible jets", *J. High Energy Phys.* **2018** (Aug, 2018) doi:10.1007/jhep08(2018)030.

[51] C. Csáki, E. Kuflik, S. Lombardo et al., "Searching for displaced Higgs boson decays", *Phys. Rev. D* **92** (Oct, 2015) doi:10.1103/physrevd.92.073008.

[52] M. Cepeda, S. Gori, V. M. Outschoorn et al., "Exotic Higgs Decays", arXiv:2111.12751.

[53] H1 and ZEUS Collaborations, "Combination of Measurements of Inclusive Deep Inelastic $e^{\pm}p$ Scattering Cross Sections and QCD Analysis of HERA Data", 2015. doi:10.48550/ARXIV.1506.06042.

[54] NNPDF Collaboration, "Parton distributions for the LHC run II", *J. High Energy Phys.* **2015** (Apr, 2015) doi:10.1007/jhep04(2015)040.

[55] Particle Data Group, "Review of Particle Physics", *Phys. Rev. D* **98** (Aug, 2018) 030001, doi:10.1103/PhysRevD.98.030001.

[56] J. C. Collins, D. E. Soper, and G. Sterman, "Factorization of Hard Processes in QCD", doi:10.48550/ARXIV.HEP-PH/0409313.

[57] J. C. Collins and D. E. Soper, "The Theorems of Perturbative QCD", *Ann. Rev. Nucl. Part. Sci.* **37** (1987) 383–409, doi:10.1146/annurev.ns.37.120187.002123.

[58] CMS Collaboration, "Summaries of CMS cross section measurements". *https://twiki.cern.ch/twiki/bin/view/CMSPublic/PhysicsResultsCombined*, Accessed: 2021-09-02.

[59] S. Alioli, P. Nason, C. Oleari et al., "A general framework for implementing NLO calculations in shower Monte Carlo programs: the POWHEG BOX", *J. High Energy Phys.* **2010** (Jun, 2010) doi:10.1007/jhep06(2010)043.

[60] T. Sjöstrand, S. Ask, J. R. Christiansen et al., "An introduction to PYTHIA 8.2", *Comput. Phys. Commun.* **191** (Jun, 2015) 159–177, doi:10.1016/j.cpc.2015.01.024.

[61] J. Alwall, S. Höche, F. Krauss et al., "Comparative study of various algorithms for the merging of parton showers and matrix elements in hadronic collisions", *Eur. Phys. J. C* **53** (Dec, 2007) 473–500, doi:10.1140/epjc/s10052-007-0490-5.

[62] J. Alwall, R. Frederix, S. Frixione et al., "The automated computation of tree-level and next-to-leading order differential cross sections, and their matching to parton shower simulations", *J. High Energy Phys.* **2014** (Jul, 2014) doi:10.1007/jhep07(2014)079.

[63] GEANT4 Collaboration, "Geant4—a simulation toolkit", *Nucl. Instrum. Methods. Phys. Res. A* **506** (2003), no. 3, 250–303, doi:https://doi.org/10.1016/S0168-9002(03)01368-8.

[64] CMS Collaboration, "Machine learning-based identification of highly Lorentz-boosted hadronically decaying particles at the CMS experiment",. http://cds.cern.ch/record/2683870.

[65] CMS Collaboration, "Identification of heavy-flavour jets with the CMS detector in pp collisions at 13 TeV", *J. Instrum.* **13** (May, 2018) P05011–P05011, doi:10.1088/1748-0221/13/05/p05011.

[66] CMS Collaboration, "Performance of the DeepJet b tagging algorithm using 41.9/fb of data from proton-proton collisions at 13 TeV with Phase 1 CMS detector", *CMS-DP-2018-058* (Nov, 2018). http://cds.cern.ch/record/2646773.

[67] I. Goodfellow, Y. Bengio, and A. Courville, "Deep Learning". MIT Press, 2016. http://www.deeplearningbook.org.

[68] P. Mehta, M. Bukov, C.-H. Wang et al., "A high-bias, low-variance introduction to Machine Learning for physicists", *Phys. Rep.* **810** (May, 2019) 1–124, doi:10.1016/j.physrep.2019.03.001.

[69] T. Heimel, G. Kasieczka, T. Plehn et al., "QCD or what?", *SciPost Phys.* **6** (Mar, 2019) doi:10.21468/scipostphys.6.3.030.

[70] N. Srivastava, G. Hinton, A. Krizhevsky et al., "Dropout: A Simple Way to Prevent Neural Networks from Overfitting", *J. Mach. Learn.* **15** (2014), no. 56, 1929–1958. http://jmlr.org/papers/v15/srivastava14a.html.

[71] D. P. Kingma and J. Ba, "Adam: A Method for Stochastic Optimization", arXiv:1412.6980.

[72] Christopher Olah, "Understanding LSTM Networks", 2015. https://colah.github.io/posts/2015-08-Understanding-LSTMs/ Accessed: 2022-01-17.

[73] S. Hochreiter and J. Schmidhuber, "Long Short-Term Memory", *Neural Comput. Appl.* **9** (11, 1997) 1735–1780, doi:10.1162/neco.1997.9.8.1735.

[74] F. Chollet et al., "Keras". https://github.com/fchollet/keras, 2015.

[75] M. Abadi, A. Agarwal, P. Barham et al., "TensorFlow: Large-Scale Machine Learning on Heterogeneous Distributed Systems", arXiv:1603.04467.

[76] G. A. et al., "High Luminosity Large Hadron Collider HL-LHC", *Technical Design Report. CERN Yellow Report* **Monographs 4** (2017) doi:10.5170/CERN-2015-005.1.

[77] LHCb Collaboration, "The LHCb Detector at the LHC", *J. Instrum.* **3** (Aug, 2008) S08005–S08005, doi:10.1088/1748-0221/3/08/s08005.

[78] ALICE Collaboration, "The ALICE experiment at the CERN LHC", *J. Instrum.* **3** (Aug, 2008) S08002–S08002, doi:10.1088/1748-0221/3/08/s08002.

[79] CMS Collaboration, "Particle-flow reconstruction and global event description with the CMS detector", *J. Instrum.* **12** (Oct, 2017) P10003–P10003, doi:10.1088/1748-0221/12/10/p10003.

[80] CMS Collaboration, "CMS Technical Design Report for the Pixel Detector Upgrade", *CERN-LHCC-2012-016, CMS-TDR-11* (Sep, 2012) doi:10.2172/1151650.

[81] CMS Collaboration, "Description and performance of track and primary-vertex reconstruction with the CMS tracker", *J. Instrum.* **9** (Oct, 2014) P10009–P10009, doi:10.1088/1748-0221/9/10/p10009.

[82] CMS Collaboration, "Pileup mitigation at CMS in 13 TeV data", *J. Instrum.* **15** (Sep, 2020) P09018–P09018, doi:10.1088/1748-0221/15/09/P09018.

[83] M. Swartz, "CMS pixel simulations", *Nucl. Instrum. Methods. Phys. Res. A* **511** (2003), no. 1, 88–91, doi:10.1016/S0168-9002(03)01757-1. Proceedings of the 11th International Workshop on Vertex Detectors.

[84] T. Speer, W. Adam, R. Fruhwirth et al., "Track Reconstruction in the CMS tracker", *CMS-NOTE-2006-041, CERN, Geneva* (Dec, 2006) doi:10.1016/j.nima.2005.11.207.

[85] R. Frühwirth, W. Waltenberger, P. Vanlaer, "Adaptive Vertex Fitting", *Technical Design Report CMS-NOTE-2007-008* (2007). https://cds.cern.ch/record/1027031/files/NOTE2007_008.pdf.

[86] A. Sirunyan, A. Tumasyan, W. Adam et al., "Particle-flow reconstruction and global event description with the CMS detector", *J. Instrum.* **12** (Oct, 2017) P10003–P10003, doi:10.1088/1748-0221/12/10/p10003.

[87] CMS Collaboration, "Measurement of $B\overline{B}$ angular correlations based on secondary vertex reconstruction at $\sqrt{s} = 7\,\text{TeV}$", *J. High Energy Phys.* **2011** (Mar, 2011) doi:10.1007/jhep03(2011)136.

[88] S. Moortgat, "When charm and beauty adjoin the top. First cross section of top quark pair production with additional charm jets with the CMS experiment.", *CERN-THESIS-2019-051* (2019). https://cds.cern.ch/record/2676133/files/CERN-THESIS-2019-051.pdf.

[89] CMS Collaboration, "Event displays from the b–tagging and vertexing (BTV) group of CMS, using 2016 data". https://twiki.cern.ch/twiki/bin/viewauth/CMS/BTVEventDisplaysInternal Accessed: 2021-05-26.

[90] Y. Dokshitzer, G. Leder, S. Moretti et al., "Better jet clustering algorithms", *J. High Energy Phys.* **1997** (Aug, 1997) 001–001, doi:10.1088/1126-6708/1997/08/001.

[91] S. Ellis and D. Soper, "Successive combination jet algorithm for hadron collisions", *Phys. Rev. D* **48** (Oct, 1993) 3160–3166, doi:10.1103/physrevd.48.3160.

[92] M. Cacciari, G. P. Salam, and G. Soyez, "The anti-k_T jet clustering algorithm", *J. High Energy Phys.* **2008** (Apr, 2008) 063–063, doi:10.1088/1126-6708/2008/04/063.

[93] CMS Collaboration, "Jet energy scale and resolution in the CMS experiment in pp collisions at 8 TeV", *J. Instrum.* **12** (Feb, 2017) P02014–P02014, doi:10.1088/1748-0221/12/02/p02014.

[94] CMS Collaboration, "Search for the associated production of the Higgs boson with a top-quark pair", *J. High Energy Phys.* **2014** (Sep, 2014) doi:10.1007/jhep09(2014)087.

[95] CMS Collaboration, "Phase 1 Pixel Material Budget", *CMS-DP-2019-006* (Mar, 2019). http://cds.cern.ch/record/2668396.

[96] CMS Collaboration, "Description and performance of track and primary-vertex reconstruction with the CMS tracker", *J. Instrum.* **9** (Oct, 2014) P10009–P10009, doi:10.1088/1748-0221/9/10/p10009.

[97] D. Nowatschin, "Search for vector-like quarks using jet substructure techniques with the CMS experiment", doi:10.3204/PUBDB-2017-07360.

[98] CMS Collaboration, "Performance of electron reconstruction and selection with the CMS detector in proton-proton collisions at $\sqrt{s} = 8\,\text{TeV}$", *J. Instrum.* **10** (jun, 2015) P06005–P06005, doi:10.1088/1748-0221/10/06/p06005.

[99] CMS Collaboration, "Electron Cut Based ID for 94X samples", 2018. https://indico.cern.ch/event/732971/contributions/3022843/attachments/1658685/2656462/eleIdTuning.pdf Accessed: 2021-06-04.

[100] CMS Collaboration, "Cut Based Photon ID", 2016. https://indico.cern.ch/event/491548/contributions/2384977/attachments/1377936/2117789/CutBasedPhotonID_25-11-2016.pdf Accessed: 2021-06-04.

[101] CMS Collaboration, "Performance of the CMS muon detector and muon reconstruction with proton-proton collisions at $\sqrt{s} = 13\,\text{TeV}$", *J. Instrum.* **13** (Jun, 2018) P06015–P06015, doi:10.1088/1748-0221/13/06/p06015.

[102] CMS Collaboration, "Reconstruction and identification of τ lepton decays to hadrons and τ neutrino at CMS", *J. Instrum.* **11** (Jan, 2016) P01019–P01019, doi:10.1088/1748-0221/11/01/p01019.

[103] CMS Collaboration, "Search for long-lived particles decaying in the CMS endcap muon detectors in proton-proton collisions at $\sqrt{s} = 13$ TeV", arXiv:2107.04838.

[104] CMS Collaboration, "Search for long-lived particles using displaced jets in proton-proton collisions at $\sqrt{s} = 13\,\text{TeV}$", *Phys. Rev. D* **104** (Jul, 2021) doi:10.1103/physrevd.104.012015.

[105] ATLAS Collaboration, "Search for long-lived neutral particles produced in pp collisions at $\sqrt{s} = 13\,\text{TeV}$ decaying into displaced hadronic jets in the ATLAS inner detector and muon spectrometer", *Phys. Rev. D* **101** (Mar, 2020) doi:10.1103/physrevd.101.052013.

[106] Z. Chacko, H.-S. Goh, and R. Harnik, "Natural Electroweak Breaking from a Mirror Symmetry", *Phys. Rev. Lett.* **96** (Jun, 2006) doi:10.1103/physrevlett.96.231802.

[107] P. Skands, S. Carrazza, and J. Rojo, "Tuning PYTHIA 8.1: the Monash 2013 tune", *Eur. Phys. J. C* **74** (Aug, 2014) doi:10.1140/epjc/s10052-014-3024-y.

[108] CMS Collaboration, "Event generator tunes obtained from underlying event and multiparton scattering measurements", *Eur. Phys. J. C* **76** (Mar, 2016) doi:10.1140/epjc/s10052-016-3988-x.

[109] M. Wiesemann, R. Frederix, S. Frixione et al., "Higgs production in association with bottom quarks", *J. High Energy Phys.* **2015** (Feb, 2015) doi:10.1007/jhep02(2015)132.

[110] A. M. Sirunyan, A. Tumasyan, W. Adam et al., "Measurement of the inelastic proton-proton cross section at $\sqrt{s} = 13\,\text{TeV}$", *J. High Energy Phys.* **2018** (Jul, 2018) doi:10.1007/jhep07(2018)161.

[111] M. Czakon and A. Mitov, "Top++: A Program for the Calculation of the Top-Pair Cross-Section at Hadron Colliders", *Comput. Phys. Commun.* **185** (2014) 2930, doi:10.1016/j.cpc.2014.06.021, arXiv:1112.5675.

[112] M. Botje, J. Butterworth, A. Cooper-Sarkar et al., "The PDF4LHC Working Group Interim Recommendations", 2011. doi:10.48550/ARXIV.1101.0538.

[113] A. D. Martin, W. J. Stirling, R. S. Thorne et al., "Uncertainties on α_S in global PDF analyses and implications for predicted hadronic cross sections", *Eur. Phys. J. C* **64** (Oct, 2009) 653–680, doi:10.1140/epjc/s10052-009-1164-2.

[114] J. Gao, M. Guzzi, J. Huston et al., "CT10 next-to-next-to-leading order global analysis of QCD", *Phys. Rev. D* **89** (Feb, 2014) doi:10.1103/physrevd.89.033009.

[115] NNPDF Collaboration, "Parton distributions with LHC data", *Nucl. Phys. B* **867** (Feb, 2013) 244–289, doi:10.1016/j.nuclphysb.2012.10.003.

[116] T. Gehrmann, M. Grazzini, S. Kallweit et al., "W^+W^- Production at Hadron Colliders in Next to Next to Leading Order QCD", *Phys. Rev. Lett.* **113** (Nov, 2014) doi:10.1103/physrevlett.113.212001.

[117] J. M. Campbell, R. K. Ellis, and C. Williams, "Vector boson pair production at the LHC", *J. High Energy Phys.* **2011** (Jul, 2011) doi:10.1007/jhep07(2011)018.

[118] CMS Collaboration, "Measurement of Inclusive W and Z Boson Production Cross Sections in pp Collisions at $\sqrt{s} = 8\,\text{TeV}$", *Phys. Rev. Lett.* **112** (May, 2014) doi:10.1103/physrevlett.112.191802.

[119] M. Aliev, H. Lacker, U. Langenfeld et al., "HATHOR – HAdronic Top and Heavy quarks crOss section calculatoR", *Comput. Phys. Commun.* **182** (Apr, 2011) 1034–1046, doi:10.1016/j.cpc.2010.12.040.

[120] P. Kant, O. Kind, T. Kintscher et al., "HatHor for single top-quark production: Updated predictions and uncertainty estimates for single top-quark production in hadronic collisions", *Comput. Phys. Commun.* **191** (Jun, 2015) 74–89, doi:10.1016/j.cpc.2015.02.001.

[121] N. Kidonakis, "Top Quark Production", 2013. doi:10.48550/ARXIV.1311.0283.

[122] N. Kidonakis, "Two-loop soft anomalous dimensions for single top quark associated production with a W^- or H^-", *Phys. Rev. D* **82** (Sep, 2010) doi:10.1103/physrevd.82.054018.

[123] CMS Collaboration, "Search for resonant pair production of Higgs bosons decaying to bottom quark-antiquark pairs in proton-proton collisions at 13 TeV", *J. High Energy Phys.* **2018** (Aug, 2018) doi:10.1007/jhep08(2018)152.

[124] P. Baldi, K. Cranmer, T. Faucett et al., "Parameterized neural networks for high-energy physics", *Eur. Phys. J. C* **76** (apr, 2016) doi:10.1140/epjc/s10052-016-4099-4.

[125] S. Choi and H. Oh, "Improved Extrapolation Methods of Data-driven Background Estimation in HEP", 2021. doi:10.48550/ARXIV.1906.10831.

[126] J. Butterworth, S. Carrazza, A. Cooper-Sarkar et al., "PDF4LHC recommendations for LHC Run II", *J. Phys. G Nucl. Part. Phys.* **43** (Jan, 2016) 023001, doi:10.1088/0954-3899/43/2/023001.

[127] A. Buckley, J. Ferrando, S. Lloyd et al., "LHAPDF6: parton density access in the LHC precision era", *Eur. Phys. J. C* **75** (12, 2014) doi:10.1140/epjc/s10052-015-3318-8.

[128] M. Cacciari, S. Frixione, M. Mangano et al., "The $t\bar{t}$ cross-section at 1.8 and 1.96 TeV: a study of the systematics due to parton densities and scale dependence", *J. High Energy Phys.* **2004** (Apr, 2004) 068–068, doi:10.1088/1126-6708/2004/04/068.

[129] CMS Collaboration, "Measurement of $\mathrm{t\bar{t}H}$ production in the $\mathrm{H} \to \mathrm{b\bar{b}}$ decay channel in $41.5\,\mathrm{fb}^{-1}$ of proton-proton collision data at $\sqrt{s} = 13\,\mathrm{TeV}$", , CERN, Geneva, (2019). https://cds.cern.ch/record/2675023.

[130] CMS Collaboration, "Search for $\mathrm{t\bar{t}H}$ production in the $\mathrm{H} \to \mathrm{b\bar{b}}$ decay channel with leptonic $\mathrm{t\bar{t}}$ decays in proton-proton collisions at $\sqrt{s} = 13\,\mathrm{TeV}$", *J. High Energy Phys.* **2019** (mar, 2019) doi:10.1007/jhep03(2019)026.

[131] G. Punzi, "Sensitivity of searches for new signals and its optimization", 2003. doi:10.48550/ARXIV.PHYSICS/0308063.

[132] The ATLAS Collaboration, The CMS Collaboration, The LHC Higgs Combination Group, "Procedure for the LHC Higgs boson search combination in Summer 2011", , CERN, Geneva, (Aug, 2011). Technical Report CMS-NOTE-2011-005. ATL-PHYS-PUB-2011-11, https://cds.cern.ch/record/1379837.

[133] F. a. James, "MINUIT: Function Minimization and Error Analysis Reference Manual",. CERN Program Library Long Writeups, https://cds.cern.ch/record/2296388.

[134] A. L. Read, "Presentation of search results: the CL_s technique", *J. Phys. G Nucl. Part. Phys.* **28** (sep, 2002) 2693–2704, doi:10.1088/0954-3899/28/10/313.

[135] G. Cowan, K. Cranmer, E. Gross et al., "Asymptotic formulae for likelihood-based tests of new physics", *Eur. Phys. J. C* **71** (Feb, 2011) doi:10.1140/epjc/s10052-011-1554-0.

[136] G. Cowan, K. Cranmer, E. Gross et al., "Asymptotic formulae for likelihood-based tests of new physics", *Eur. Phys. J. C* **71** (feb, 2011) doi:10.1140/epjc/s10052-011-1554-0.

[137] H. Qu and L. Gouskos, "Jet tagging via particle clouds", *Phys. Rev. D* **101** (mar, 2020) doi:10.1103/physrevd.101.056019.

Appendices

Appendix A DNN Performance for Lifetimes above 1 mm

The DNN is parametrised as functions of the masses and lifetimes of the LLPs, as described in Section 9.5. It was trained with the LLP masses of 15 GeV, 40 GeV and 55 GeV and lifetimes between 0.05 mm and 1 mm. The performance of the b tagging algorithm Deep is expected to be worse for larger lifetimes, due to the different signature of tracks and the displacement of the vertices, which also affects the performance of the parametrised DNN. The DNN performance of signal and simulated QCD multi-jet and $t\bar{t}$ background jets at the evaluation step of the ML procedure are shown in Figure A.1. While for the lifetimes 0.05 mm (upper left) and 1 mm (upper right) a difference between signal and background is visible, this is not the case for 5 mm (lower left) and 10 mm (lower right). Limits for the lifetimes 5 mm and 10 mm are set using the DNN discriminant of the 1 mm signal.

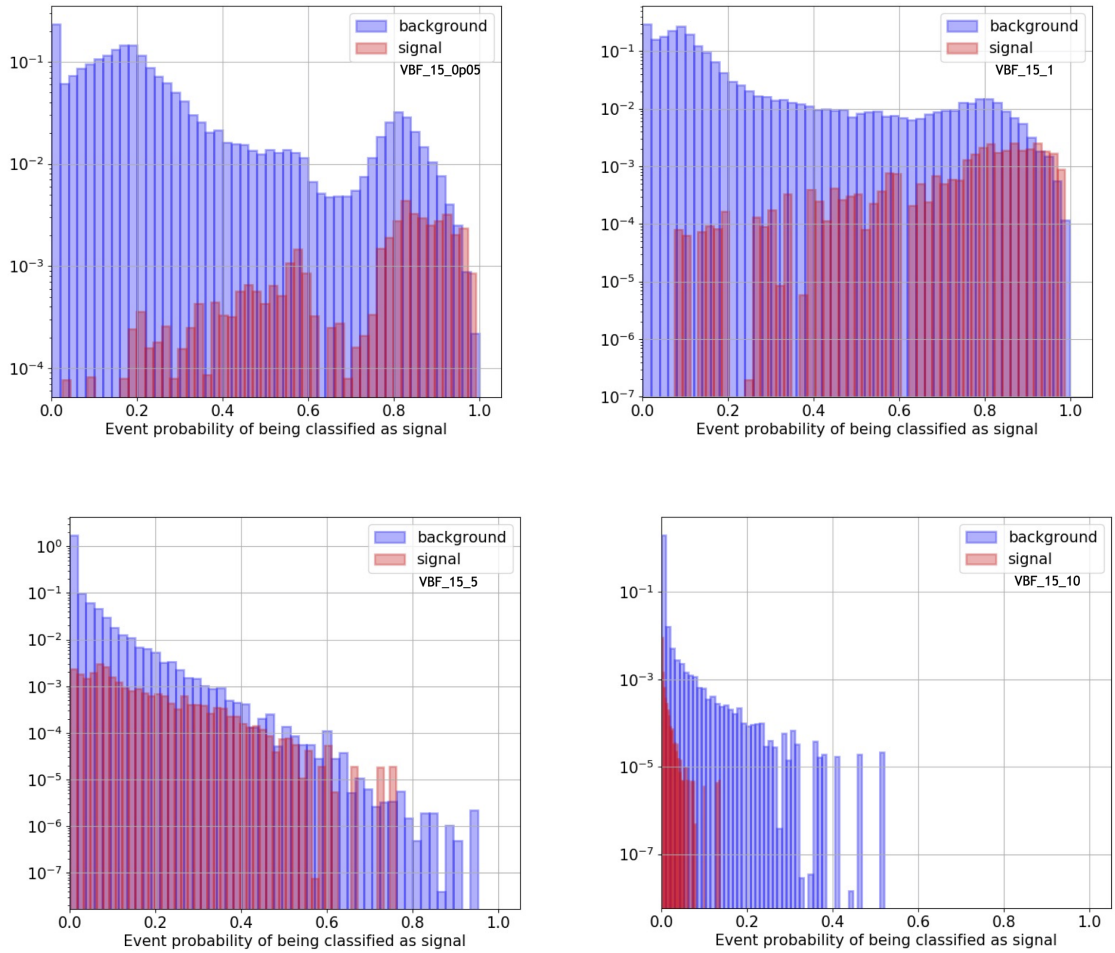

Figure A.1: The discriminant for jets of background (blue), consisting of QCD multi-jet and $t\bar{t}$ an signal (red). Different presented LLP lifetimes of the boosted topology are: 0.05 mm (upper left), 1 mm (upper right), 5 mm (lower left) and 10 mm (lower right) of the .

Appendix B Additional Studies of the Background Estimation Method

B.1 Validation Regions

For the presented search in this thesis, at least one additional region is needed to validate the background estimation method. This validation region should describe the SR well. The selections of the SR leave the possibility to define three additional regions by inverting the χ^2 and the ΔR requirements. A schematic of these different selection combinations is shown in Figure B.1, with the values of the boosted topology. The three studied regions are defined by the different selections with respect to the actual SR and are called $\overline{\text{SR}}$ (inverting χ^2), VR (inverting ΔR) and $\overline{\text{VR}}$ (inverting both χ^2 and ΔR). The difference between the boosted and the resolved topology are not only different thresholds for the two requirements but also a different jet multiplicity of the χ^2 method. Therefore, differences between both topologies are also expected, and since both selections affect the kinematic properties of the selected jets, careful studies of the different regions of the two topologies are necessary.

Lets focus for a moment on the simpler case of the boosted topology, where two jets are selected by the χ^2 method. The method selects the two jets of an event with the invariant mass being closest to the SM Higgs boson mass. For the SR are only these events used where this smallest χ^2 value is below 10, which corresponds to a mass window of 90 GeV $\leq m_{\text{reco},ij} \leq$ 160GeV. By inverting this selection criterion and selecting events instead with the smallest $\chi^2 > 10$, the invariant mass of the two jets is outside this mass window, and a difference in the kinematic properties of the jets is expected to some degree. On top are the ΔR requirements to be taken into account. A schematic of the jets distributed in space is shown on the right side of Figure B.2. Since the invariant mass depends on the

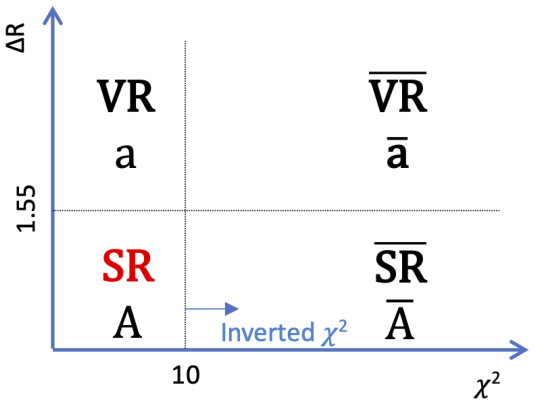

Figure B.1: Schematics of the selections for the SR and three possible validation regions with the values of the boosted topology.

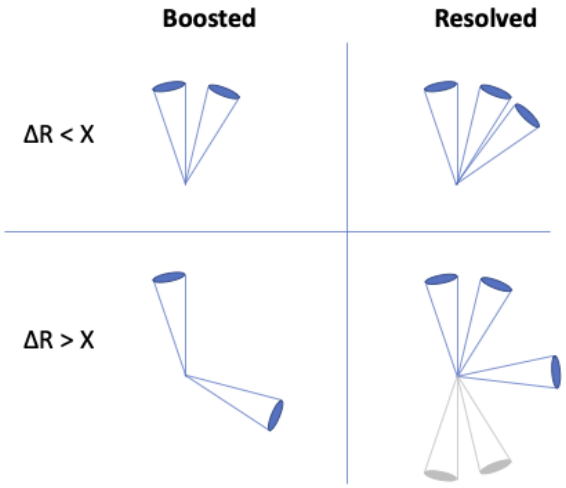

Figure B.2: Schematics of the jet distributed in space with different ΔR selections for the χ^2 method requirements of the boosted and the resolved topology.

transverse momentum, the pseudorapidity and the azimuthal angle, a correlation to the ΔR requirement, which depends on the latter two, is expected. And a difference of the kinematic properties of the jets for the ΔR of the inverted selection is already visualised in the schematic. In addition, have the simulated QCD multijet processes the tendency that jets are produced back-to-back to conserve the momentum. The normalised distributions of data of the leading jet[1] used as input features for the DNN are shown in Figure B.3. Applied are the different selections of the boosted topology to define the SR and the three

[1]Due to the jet ordering via the ϕ variable, the distributions of the subleading jet are very similar and hence not shown.

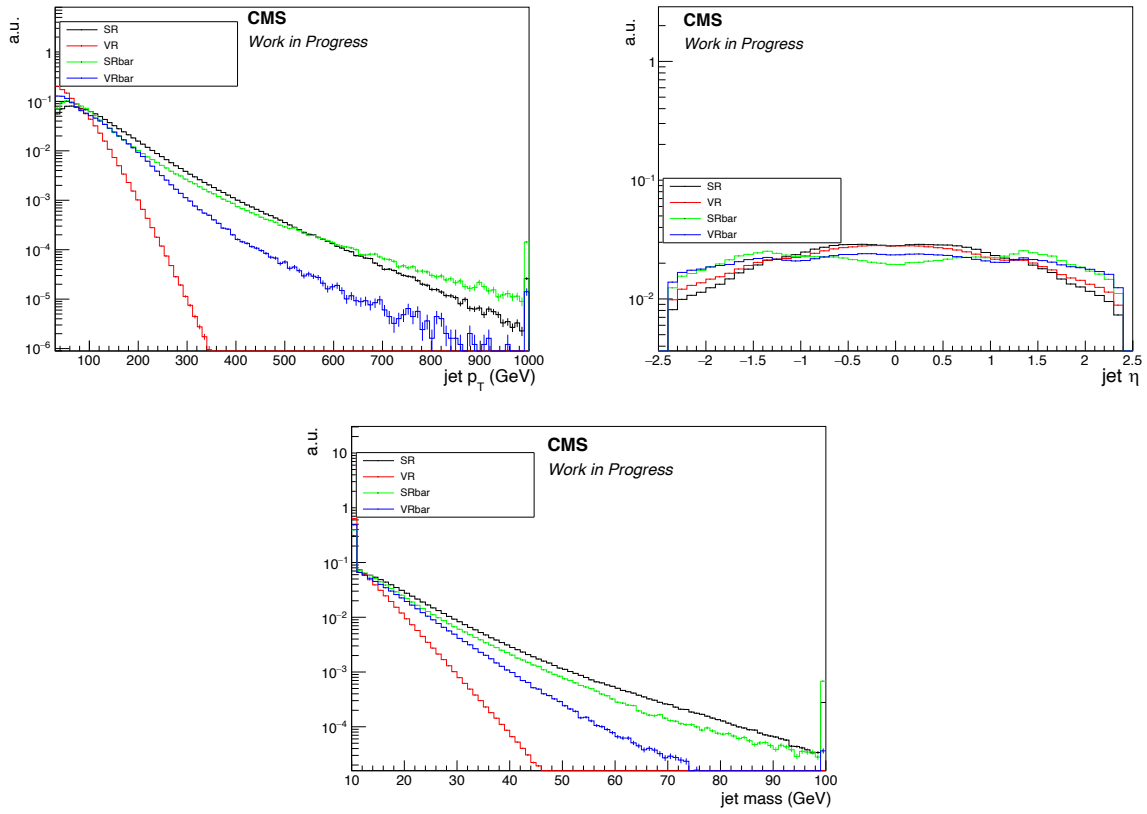

Figure B.3: Jet distributions with selections for the boosted topology of: p_T (upper left), η (upper right) and mass (lower).

additional regions. While the p_T (upper left) and the mass distributions are similar in the SR (black line) and $\overline{\text{SR}}$ (green line), are the remaining distributions of the other two regions rather different, as expected. In addition, are the distributions in η rather similar for the same selections with the χ^2 method, so the SR do agree with the VR (red line) and the $\overline{\text{SR}}$ with the $\overline{\text{VR}}$ as well. Due to this study, the VR and the $\overline{\text{VR}}$ are not used as validation regions since the jet kinematic are too different. Furthermore, a difference of the DNN discriminant between the SR and the $\overline{\text{SR}}$ is to some degree expected since the presented input features related to the kinematic properties of the jets are not identical.

With the understanding of the boosted topology, the slightly more complicated resolved topology is now easier. As seen in the right part of the schematic in Figure B.2, three jets have now to fulfil the χ^2 requirement. Again the selection for the SR corresponds to a mass window, which is inverted for the regions $\overline{\text{SR}}$ and $\overline{\text{VR}}$. As for the boosted topology, a difference of the kinematic properties of the jets is expected to fulfil the different invariant mass criterium. The ΔR requirement changes the distributions of the jets in space and

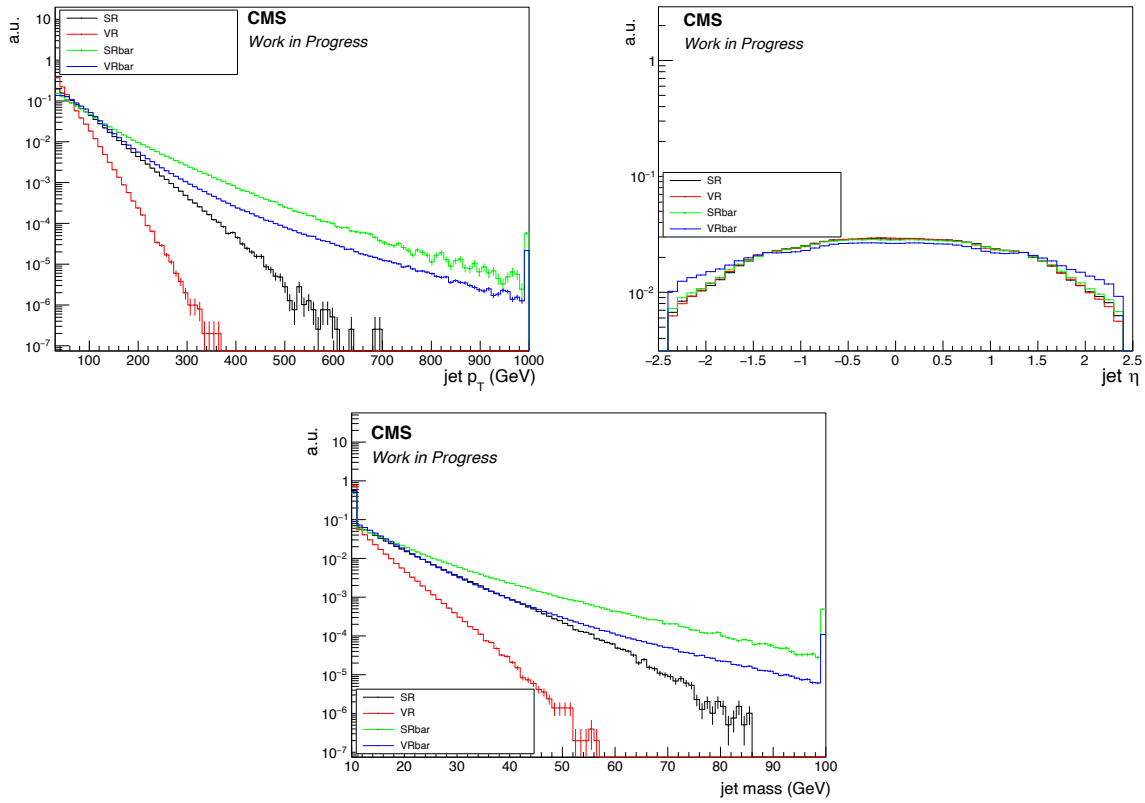

Figure B.4: Jet distributions with selections for the resolved topology of: p_{T} (upper left), η (upper right) and mass (lower).

hence affects the invariant mass additionally. Furthermore, are more jets expected for the simulated QCD multijet process, as indicated by the grey jets of the inverted ΔR criteria[2]. These additional jets change the kinematic of the entire event and have as well an impact on the three selected jets. This can be seen in the normalised distribution of the subleading jet[3] in data with the different selections of the resolved topology in Figure B.4. For the p_{T} (upper left) and the mass (lower) distribution are the peaks of the SR, the $\overline{\mathrm{SR}}$ and $\overline{\mathrm{VR}}$ are similar and differ only in the tails, while the distribution of the VR is different. The η distribution is instead similar for all four regions. Again the VR and the $\overline{\mathrm{VR}}$ are not used as validation regions due to the aforementioned reasons. Depending on which events of the distribution in SR and $\overline{\mathrm{SR}}$ end up in region A, a larger difference between both regions might be present than the boosted topology.

[2]These additional jets can be present in all other selections as well, for visibility reasons they are only shown for the one selection.

[3]Due to the jet ordering via the ϕ variable, the distribution of the leading and third jets are very similar and hence not shown.

Appendix C Performance of DeepJet

The DeepJet b tagger was used to compare the performance of a standard b tagging algorithm to the DNN used for this thesis. The whole analysis process, including the final event selection of the boosted analysis (described in Section 10.1), was applied and instead of the DNN discriminant, the DeepJet probability of b jets (b+bb+$lepb$) of the two selected jets were used to build the ABCD planes. The corresponding plots are shown in Figure C.1. The red dashed lines indicate the thresholds for ABCD method, which are chosen to be 0.995 for each jet. For signal (upper left) the events accumulate at region A, while the SM background events are ending up in all four corners. The signal over background ratio ($S/\sqrt{B}$) is shown in Table C.1. The difference between region A and the others is not as clear as for the DNN used and explained in Section 10.2.2. The limit of the VBF Higgs production signal sample of mass 15 GeV and 1 mm lifetime was in addition found to be approximately two orders of magnitudes worse than with the parametrised DNN.

Table C.1: The signal over background ratios ($\frac{S}{\sqrt{B}}$) of the different regions using the DeepJet probability to build the ABCD planes, for a LLP signal with a mass of 15 GeV and a lifetime of 1 mm.

Region	($\frac{S}{\sqrt{B}}$)
A	0.43
B	0.13
C	0.15
D	0.07

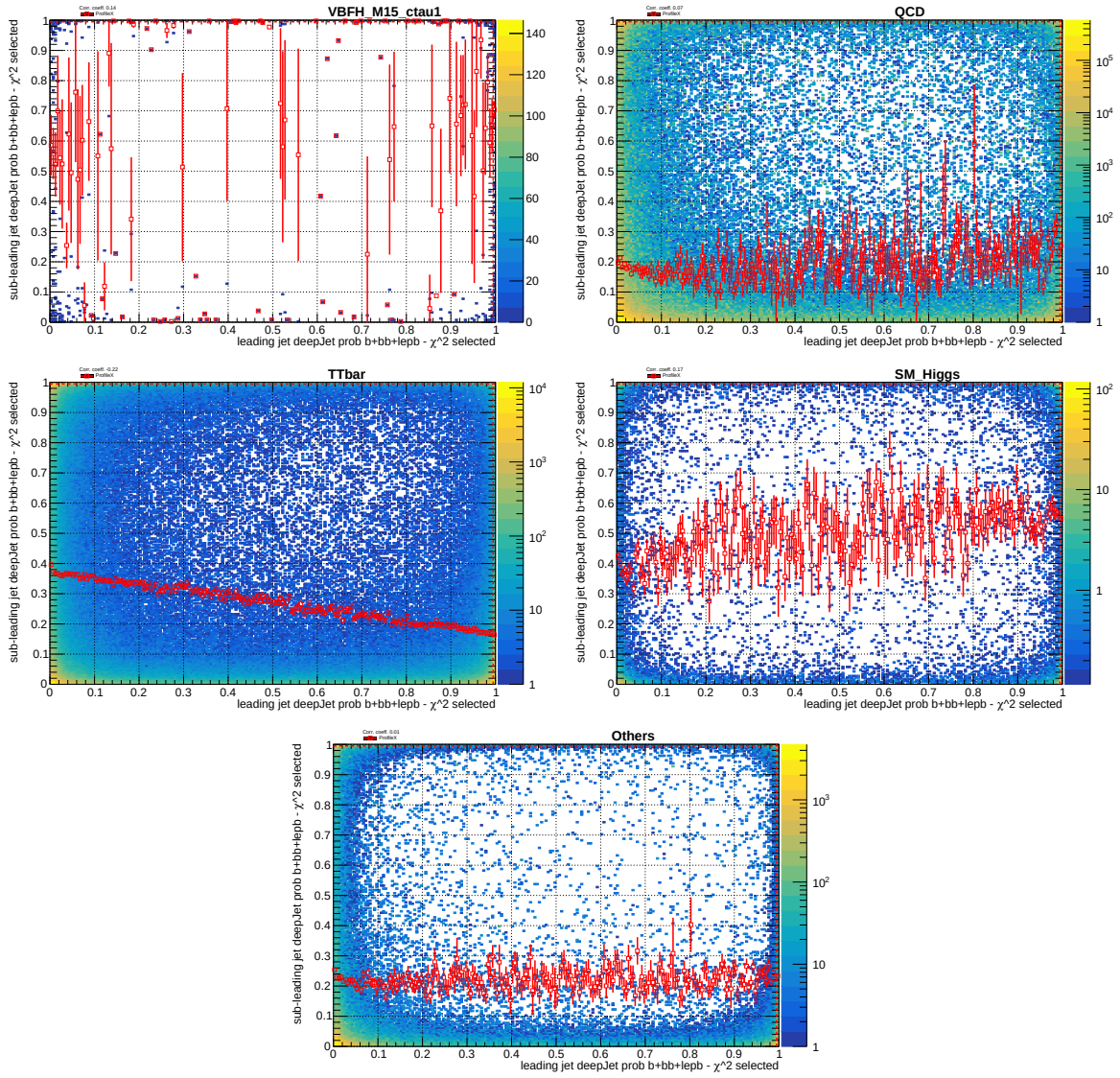

Figure C.1: The ABCD planes defined by the DeepJet probability of the two selected jets. Red dashed lines indicate the borders between the different regions A, B, C and D, where the upper right region is the signal region (A). Red empty squares with error bars indicate the mean y-value of each bin. Distributions for signal (upper left), QCD multi-jet (upper right), $t\bar{t}$ (middle left), SM Higgs (middle right) and Others (lower) are shown.

Appendix D Boosted Signature

Studies for all lifetimes of the boosted topology were performed, but only distributions of the 1 mm lifetime were shown in Chapter 10.2. In the following, the distributions of all lifetimes can be found. Presented are: ABCD planes in the SR and the $\overline{\text{SR}}$, 2D scans for different thresholds of several variables, as well as closures and their significances in the sideband regions of the SR and the $\overline{\text{SR}}$.

D.1 Signal with LLP mass 15 GeV, lifetime 0 mm

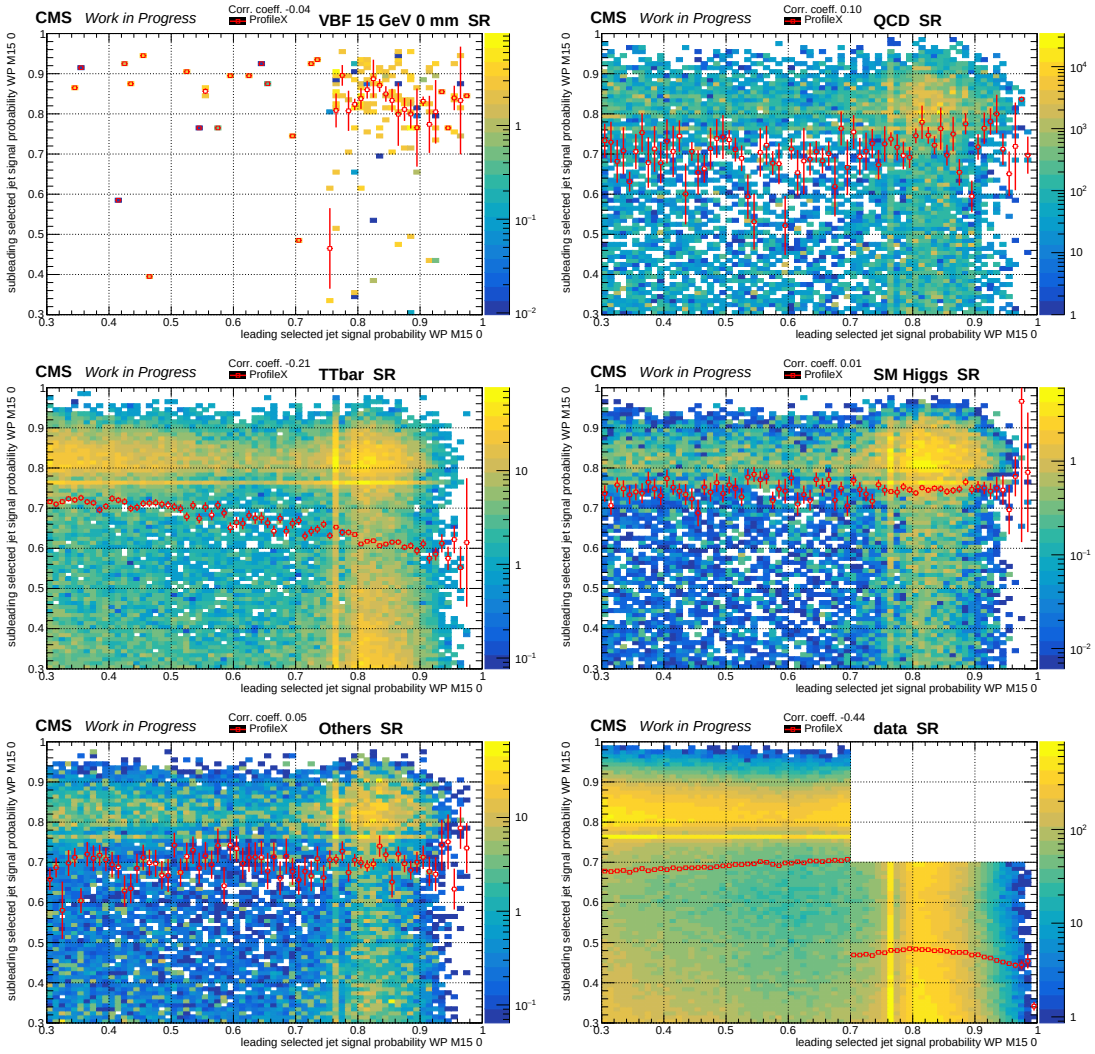

Figure D.1: The plots represent the DNN discriminant for the probability of LLPs of 15 GeV and 0 mm lifetime of the two selected jets in SR and define the regions for the background estimation method. Distributions for signal (upper left), QCD multijet (upper right), $t\bar{t}$ (middle left), SM Higgs (middle right) and Others (lower left) are shown. For the distribution of data (lower right), an extended area of region A is not shown.

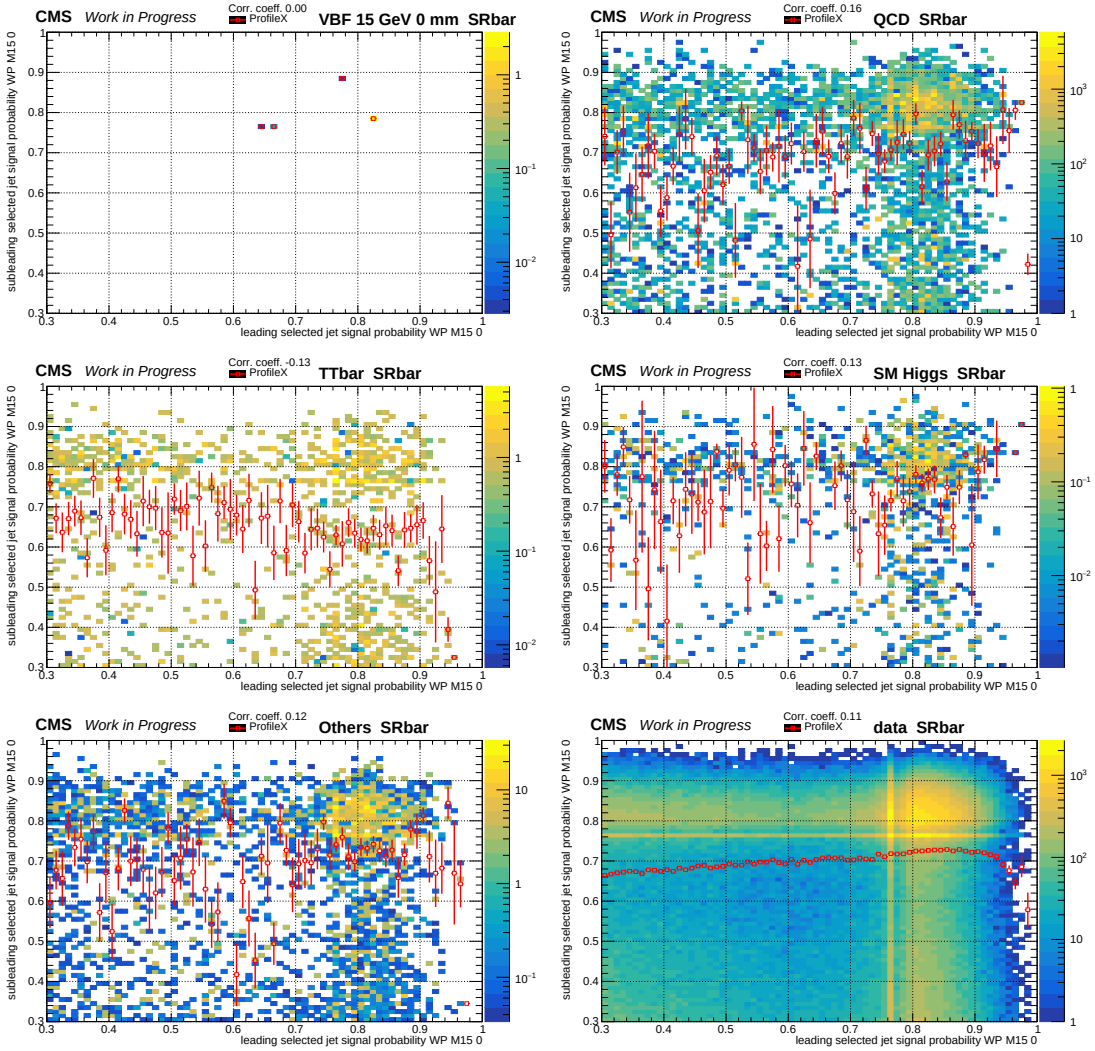

Figure D.2: Distributions of the DNN discriminant of the LLP with 15 GeV mass and 0 mm lifetime of the two selected jets in $\overline{\text{SR}}$ to verify the background estimation method applied in SR. Distributions for signal (upper left), QCD multijet (upper right), $t\bar{t}$ (middle left), SM Higgs (middle right), Others (lower left) and data (lower right) are shown.

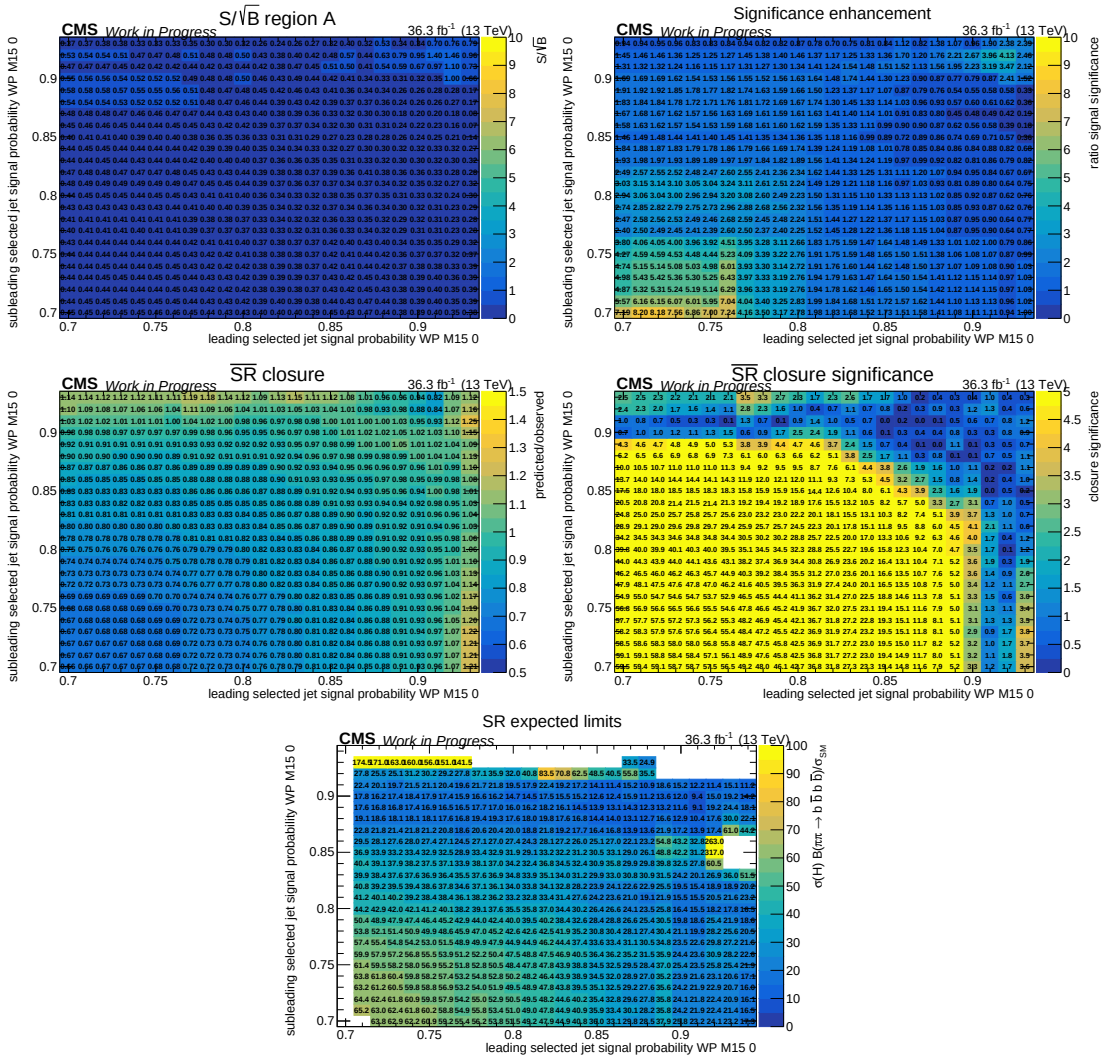

Figure D.3: Effect of various thresholds for the ABCD method on the analysis of LLPs with a mass of 15 GeV and a lifetime of 0 mm on: Signal significance (first row left), the significance enhancement Σ_{signal} (first row right), the closure using data in the $\overline{\text{SR}}$ (second row left) and its significance (second row right), and the expected upper limits on the signal strength modifier in the SR (lower).

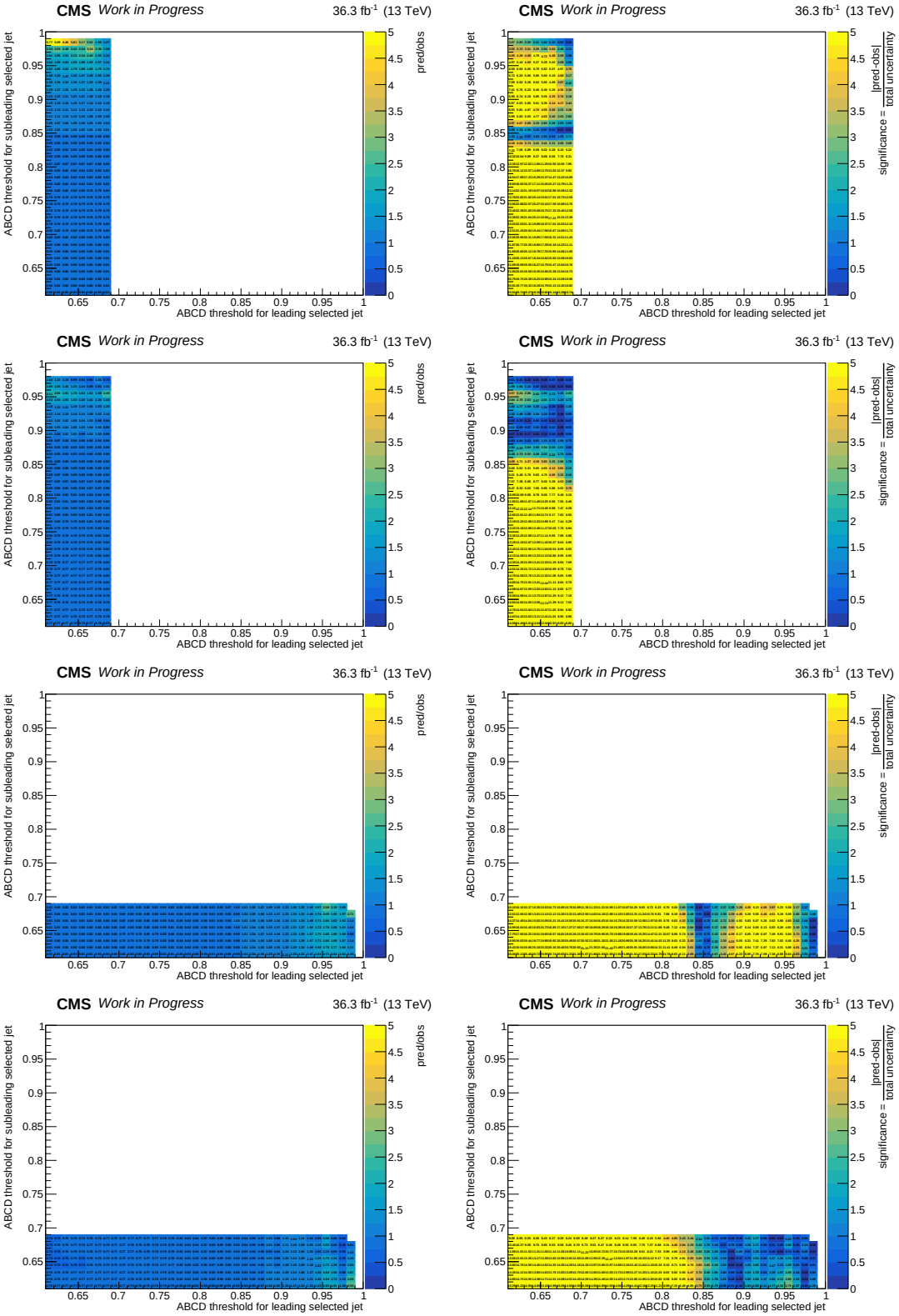

Figure D.4: The closure (left) and its significance (right) for the LLP mass of 15 GeV and 0 mm of the SR (first and third row) and $\overline{\text{SR}}$ (second and fourth row) of sideband 1 (upper two rows) and 2 (lower two rows).

D.2 Signal with LLP mass 15 GeV, lifetime 0.05 mm

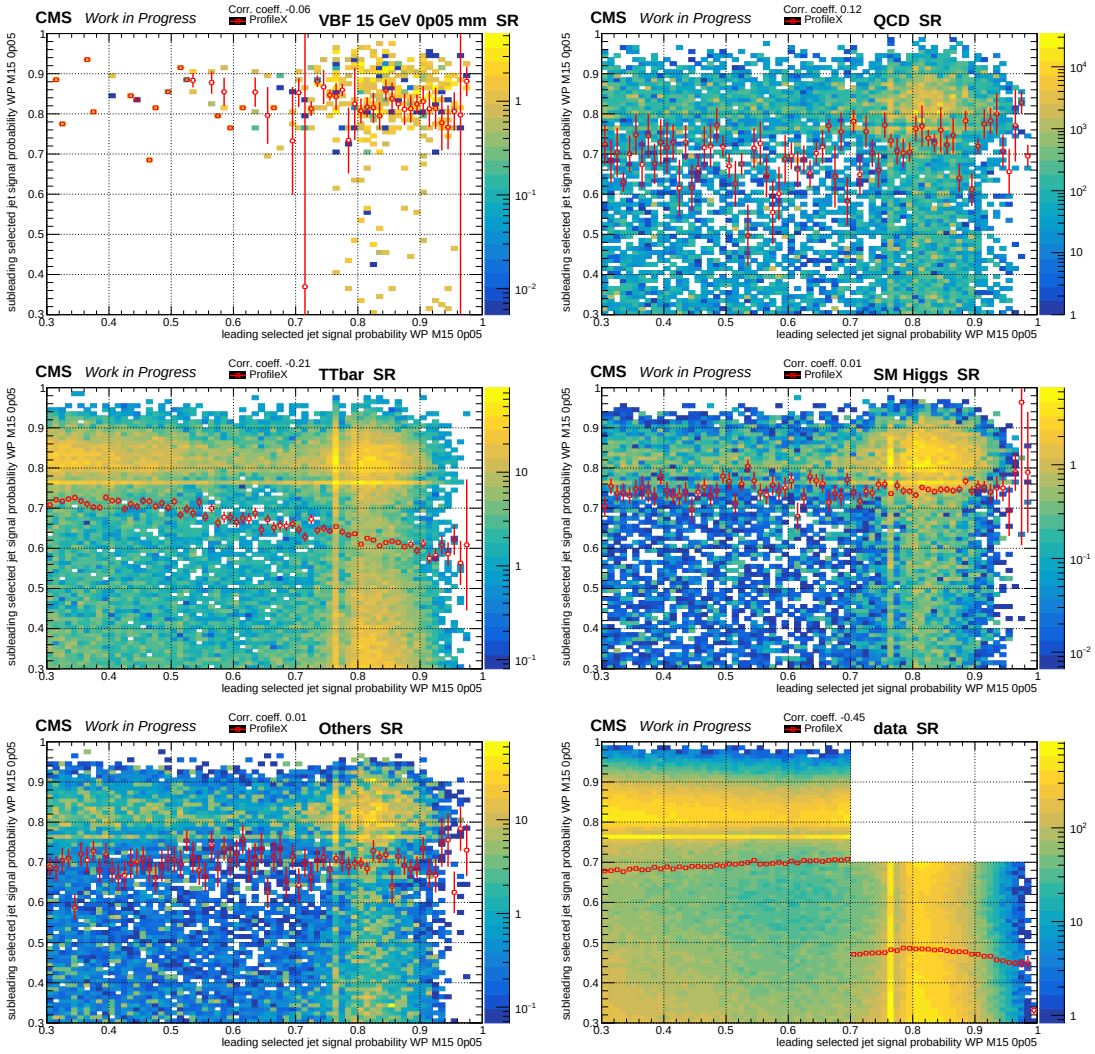

Figure D.5: Distributions of the DNN discriminant of the LLP with 15 GeV mass and 0.05 mm lifetime of the two selected jets in SR and define the regions for the background estimation method. Distributions for signal (upper left), QCD multijet (upper right), $t\bar{t}$ (middle left), SM Higgs (middle right) and Others (lower left) are shown. For the distribution of data (lower right), an extended area of region A is not shown.

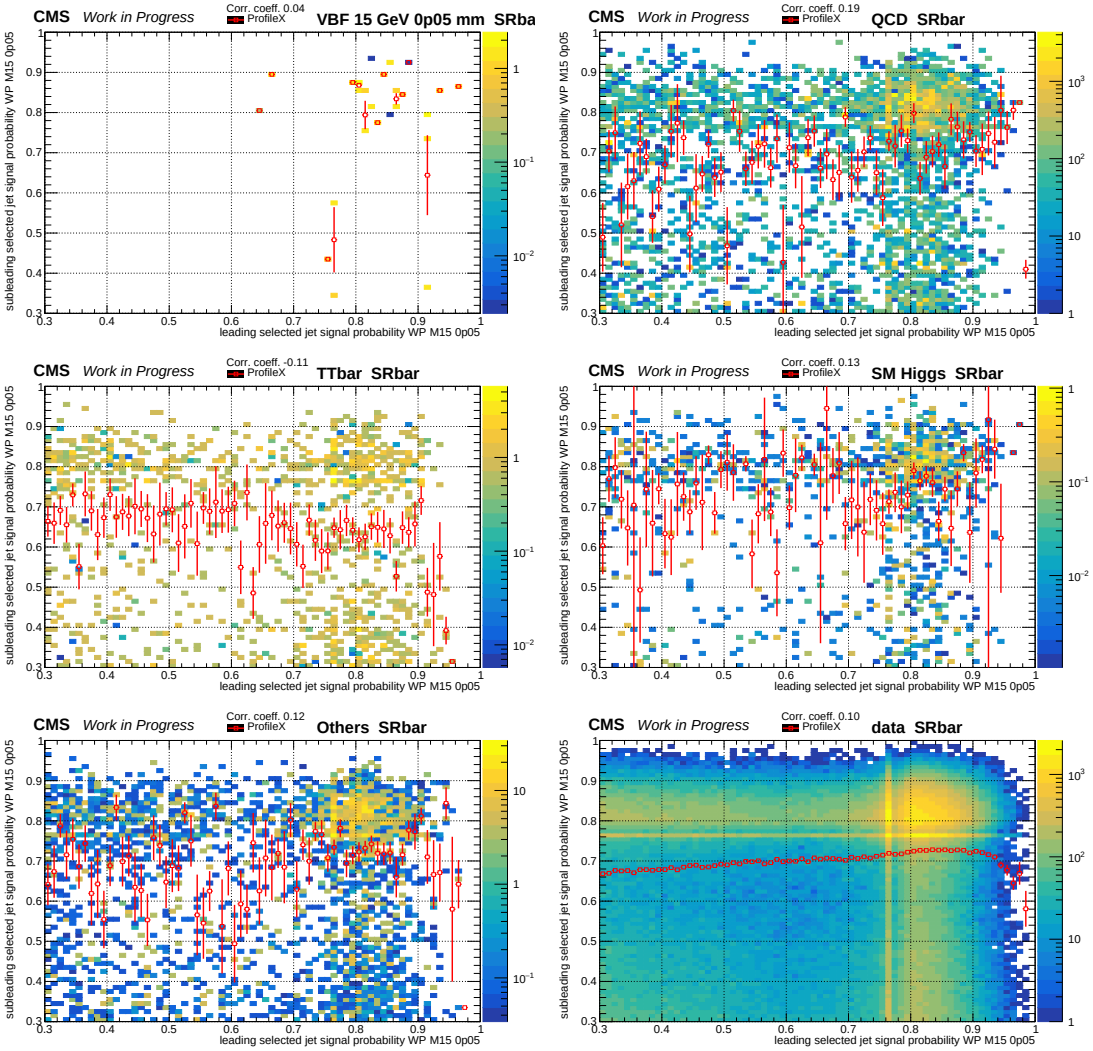

Figure D.6: Distributions of the DNN discriminant of the LLP with 15 GeV mass and 0.05 mm lifetime of the two selected jets in $\overline{\text{SR}}$ to verify the background estimation method applied in SR. Distributions for signal (upper left), QCD multijet (upper right), $t\bar{t}$ (middle left), SM Higgs (middle right), Others (lower left) and data (lower right) are shown.

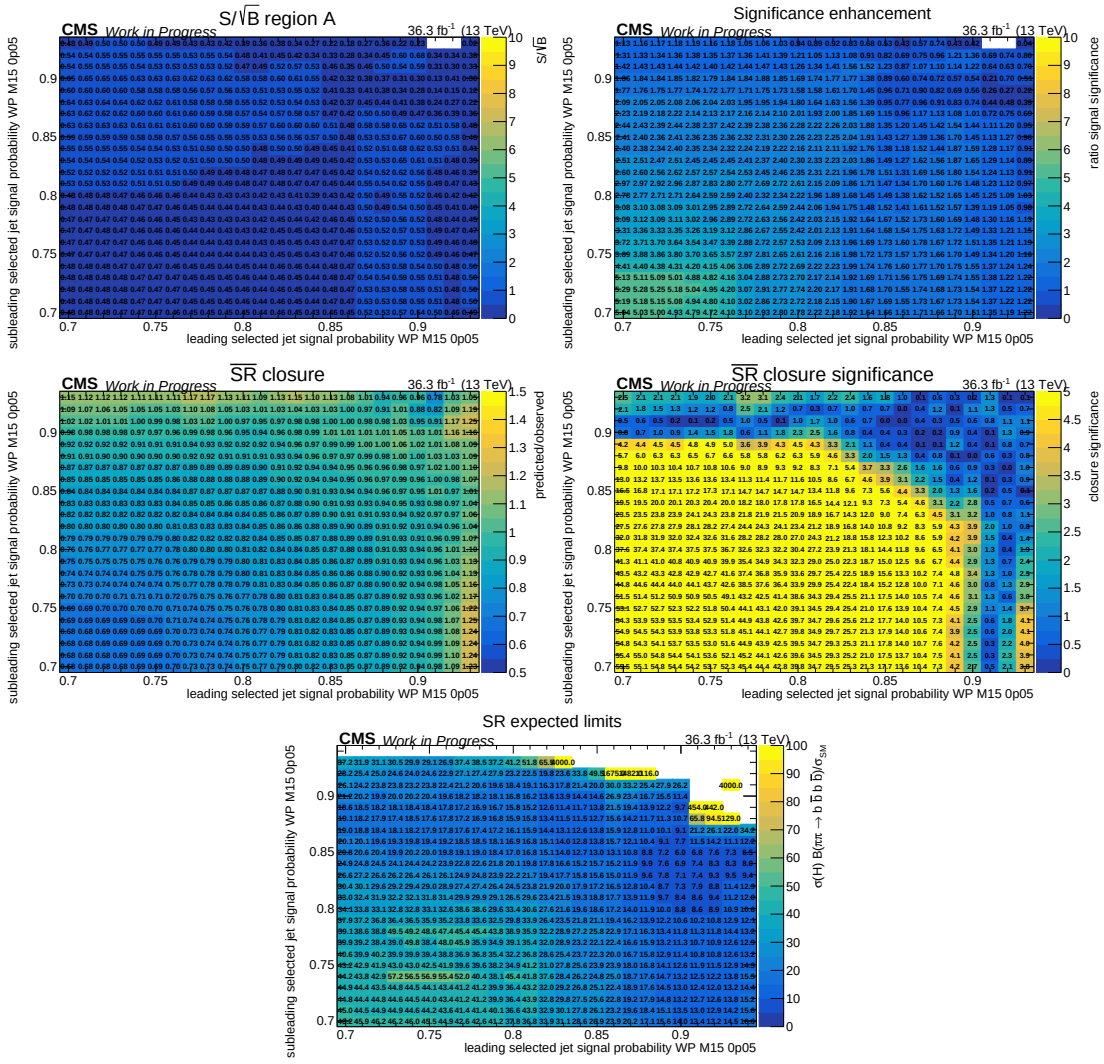

Figure D.7: Effect of various thresholds for the ABCD method on the analysis of LLPs with a mass of 15 GeV and a lifetime of 0.05 mm on: Signal significance (first row left), the significance enhancement Σ_{signal} (first row right), the closure using data in the $\overline{\text{SR}}$ (second row left) and its significance (second row right), and the expected upper limits on the signal strength modifier in the SR (lower). White bins indicate such regions where either the SM background yield or the signal yield was zero.

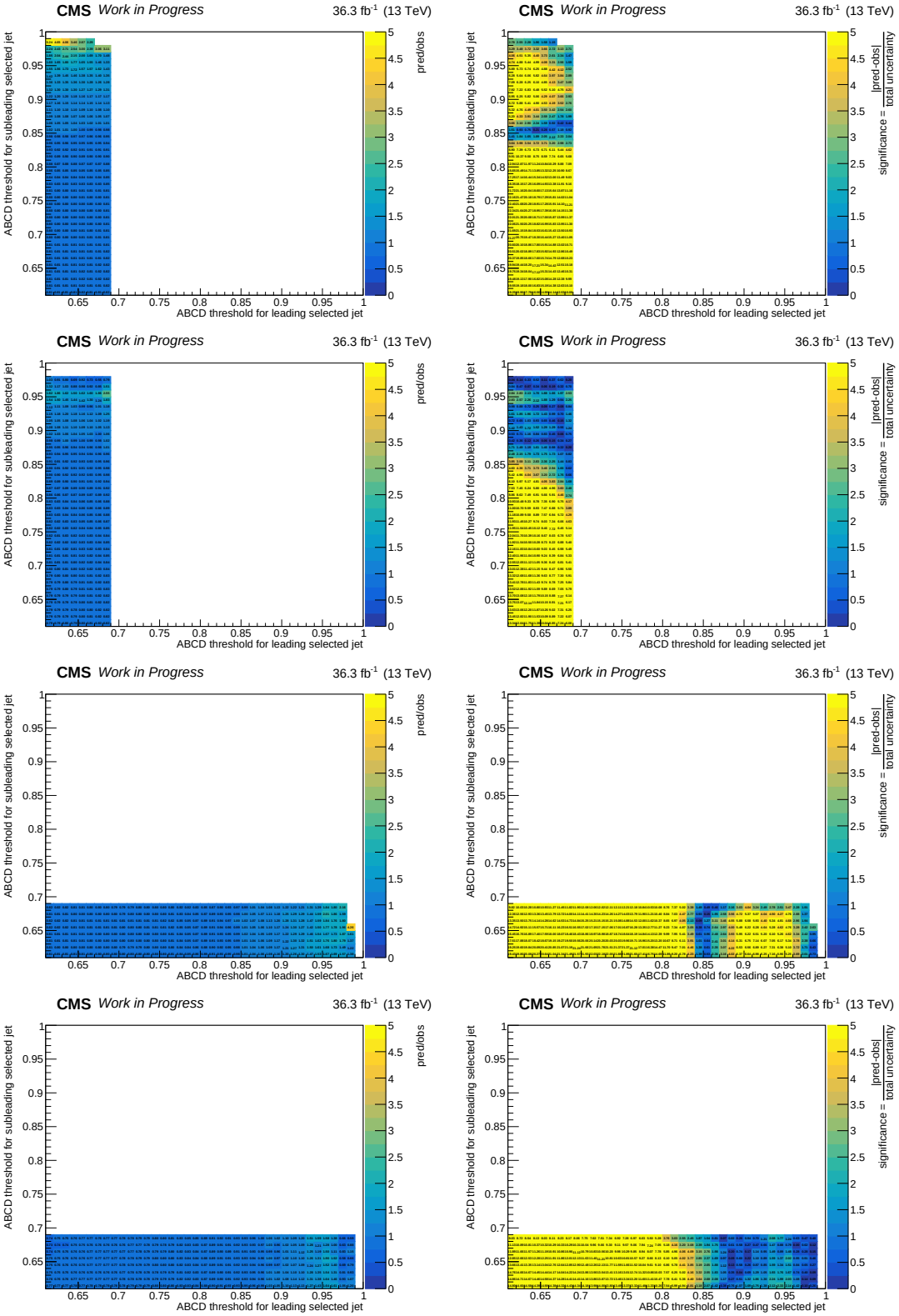

Figure D.8: The closure (left) and its significance (right) for the LLP mass of 15 GeV and 0.05 mm of the SR (first and third row) and $\overline{\text{SR}}$ (second and fourth row) of sideband 1 (upper two rows) and 2 (lower two rows).

D.3 Signal with LLP mass 15 GeV, lifetime 0.1 mm

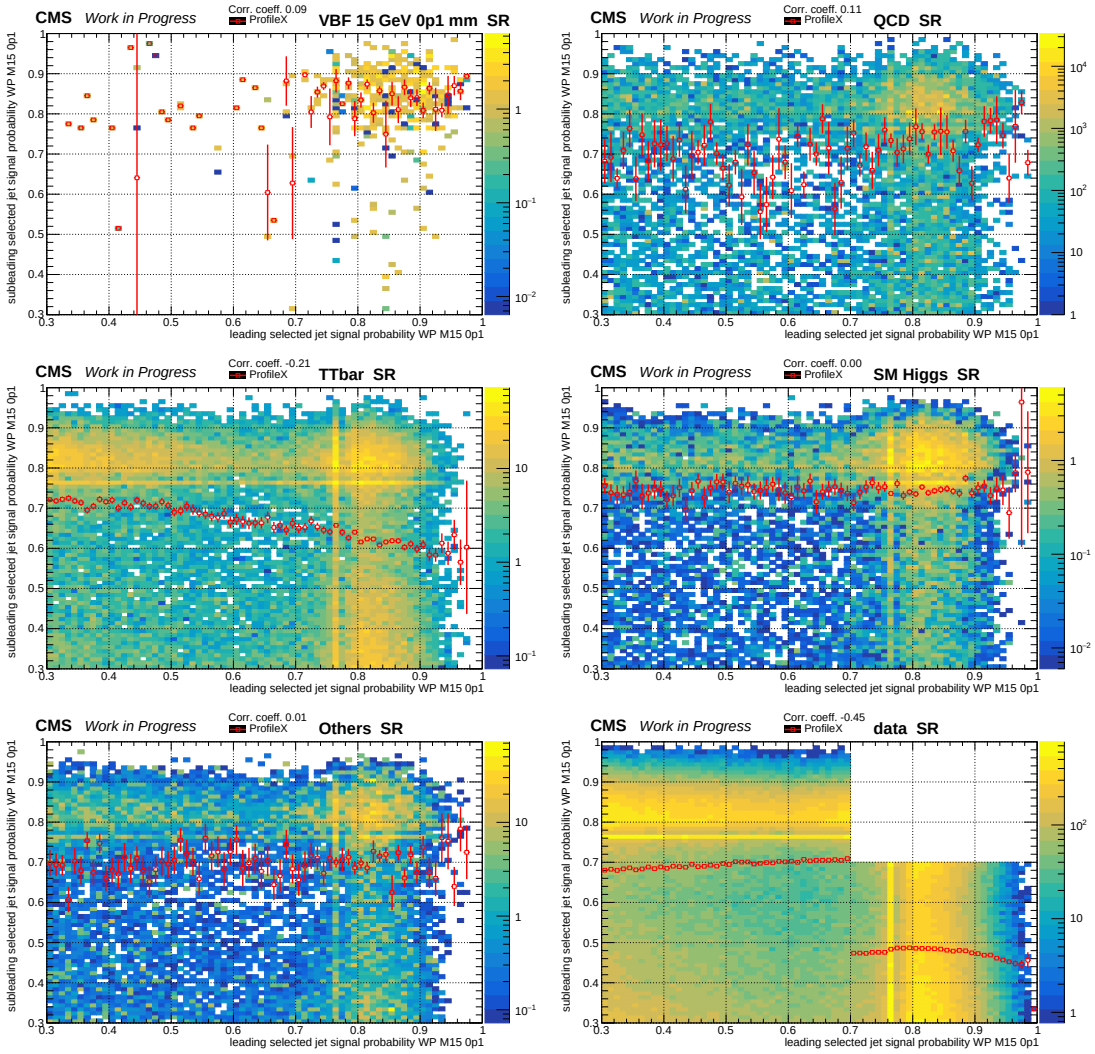

Figure D.9: Distributions of the DNN discriminant of the LLP with 15 GeV mass and 0.1 mm lifetime of the two selected jets in SR and define the regions for the background estimation method. Distributions for signal (upper left), QCD multijet (upper right), $t\bar{t}$ (middle left), SM Higgs (middle right) and Others (lower left) are shown. For the distribution of data (lower right), an extended area of region A is not shown.

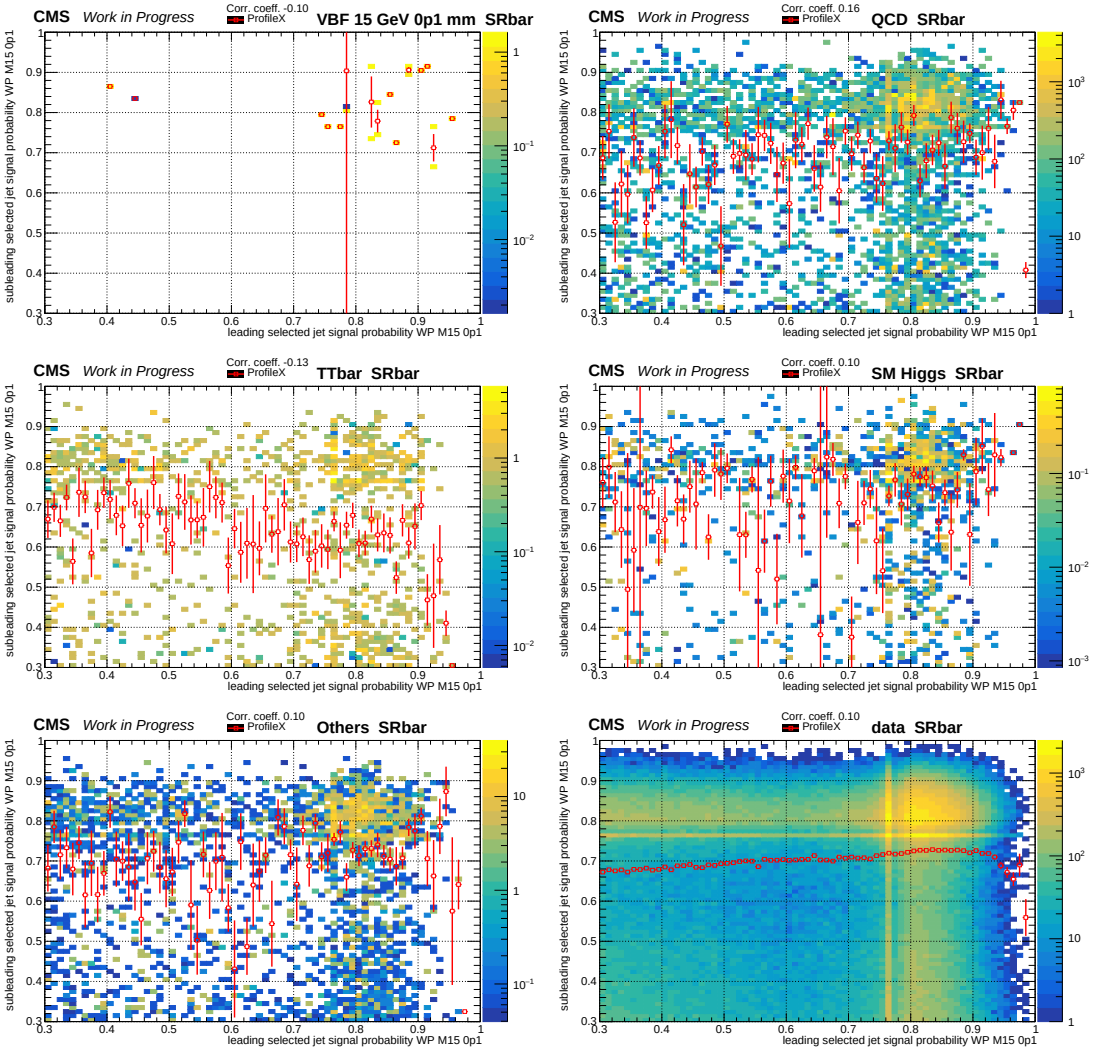

Figure D.10: Distributions of the DNN discriminant of the LLP with 15 GeV mass and 0.1 mm lifetime of the two selected jets in $\overline{\text{SR}}$ to verify the background estimation method applied in SR. Distributions for signal (upper left), QCD multijet (upper right), $t\bar{t}$ (middle left), SM Higgs (middle right), Others (lower left) and data (lower right) are shown.

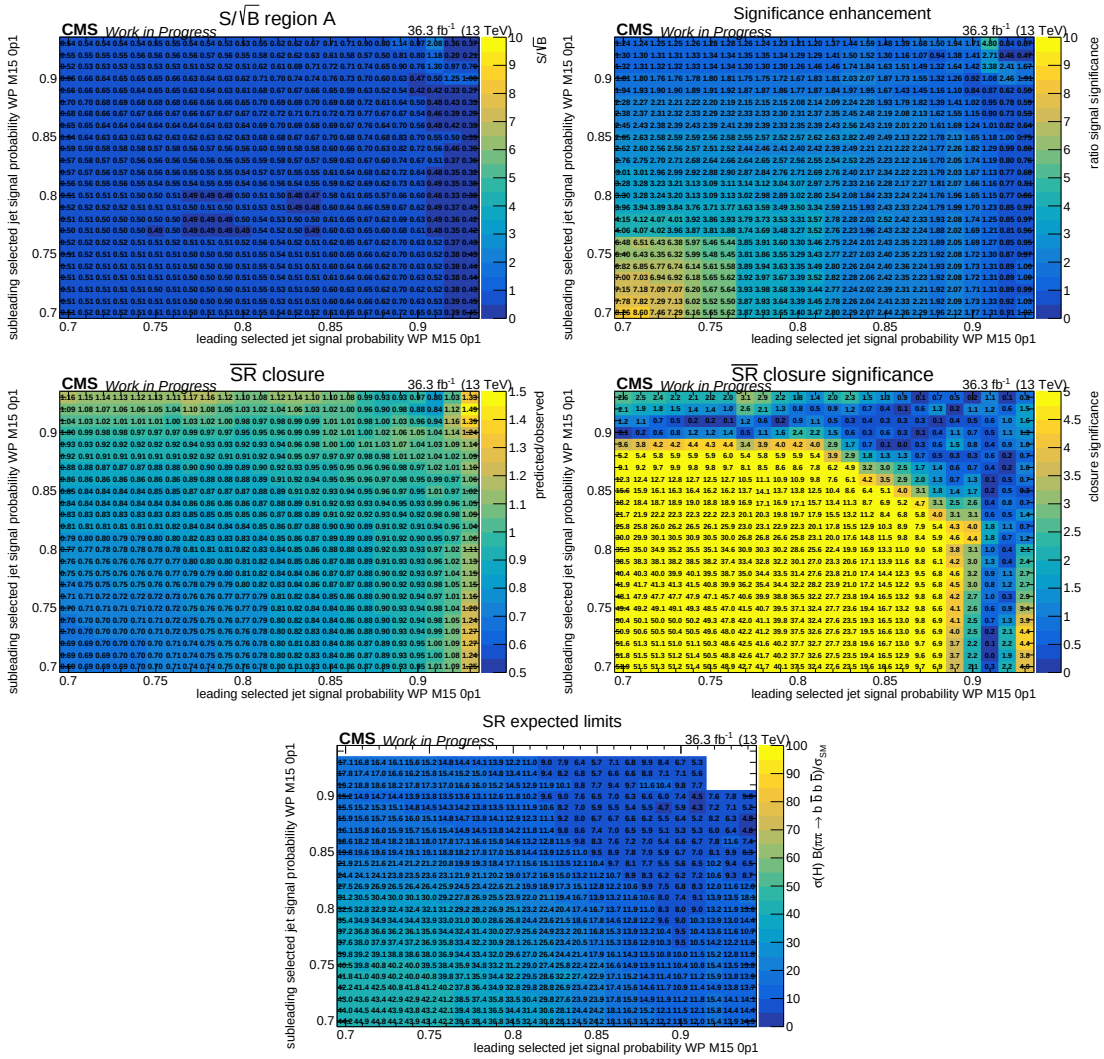

Figure D.11: Effect of various thresholds for the ABCD method on the analysis of LLPs with a mass of 15 GeV and a lifetime of 0.1 mm on: Signal significance (first row left), the significance enhancement Σ_{signal} (first row right), the closure using data in the $\overline{\text{SR}}$ (second row left) and its significance (second row right), and the expected upper limits on the signal strength modifier in the SR (lower). White bins indicate such regions where either the SM background yield or the signal yield was zero.

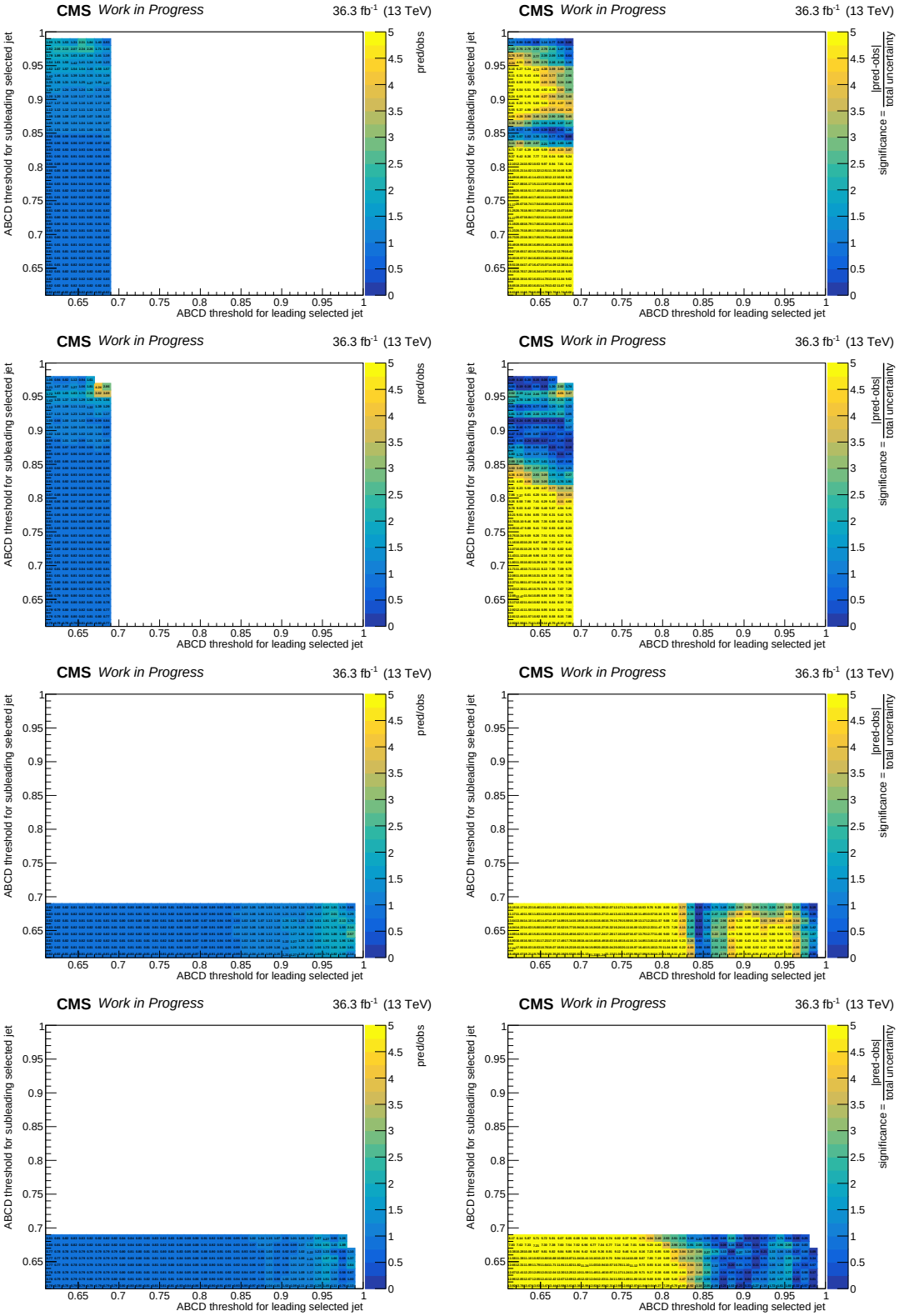

Figure D.12: The closure (left) and its significance (right) for the LLP mass of 15 GeV and 0.1 mm of the SR (first and third row) and $\overline{\text{SR}}$ (second and fourth row) of sideband 1 (upper two rows) and 2 (lower two rows).

D.4 Signal with LLP mass 15 GeV, lifetime 1 mm

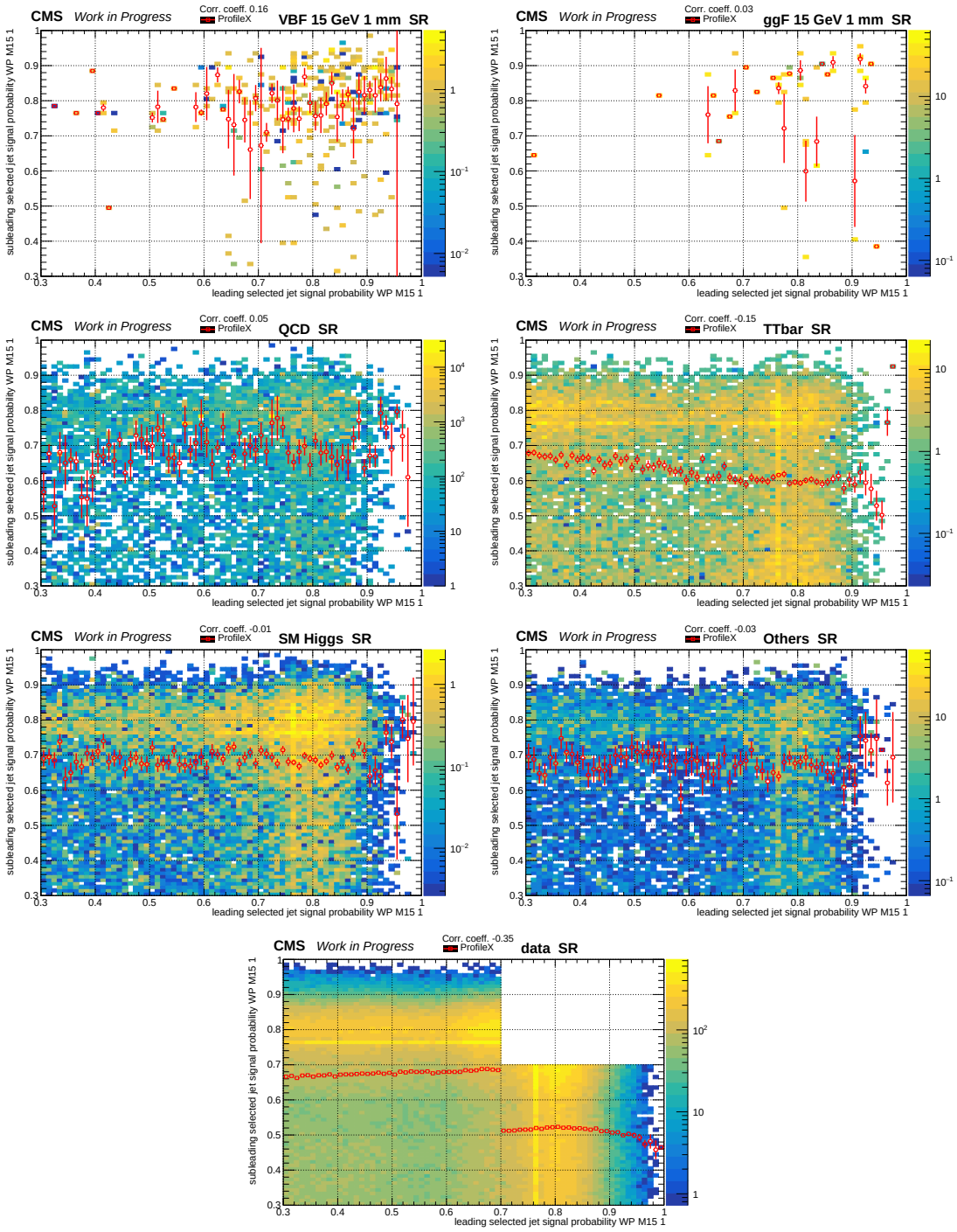

Figure D.13: Distributions in the SR of the DNN discriminant for the two selected jets for the analysis of the LLP with 15 GeV mass and 1 mm lifetime with a lower bound of 0.3 for: VBF and ggF produced signal (upper left and right, respectively), QCD multijet (second row left), $t\bar{t}$ (second row right), SM Higgs (third row left) and Others (third row right). The upper right region of the plots, depending on the chosen thresholds, is the signal region (region A), and is not shown for data (lower).

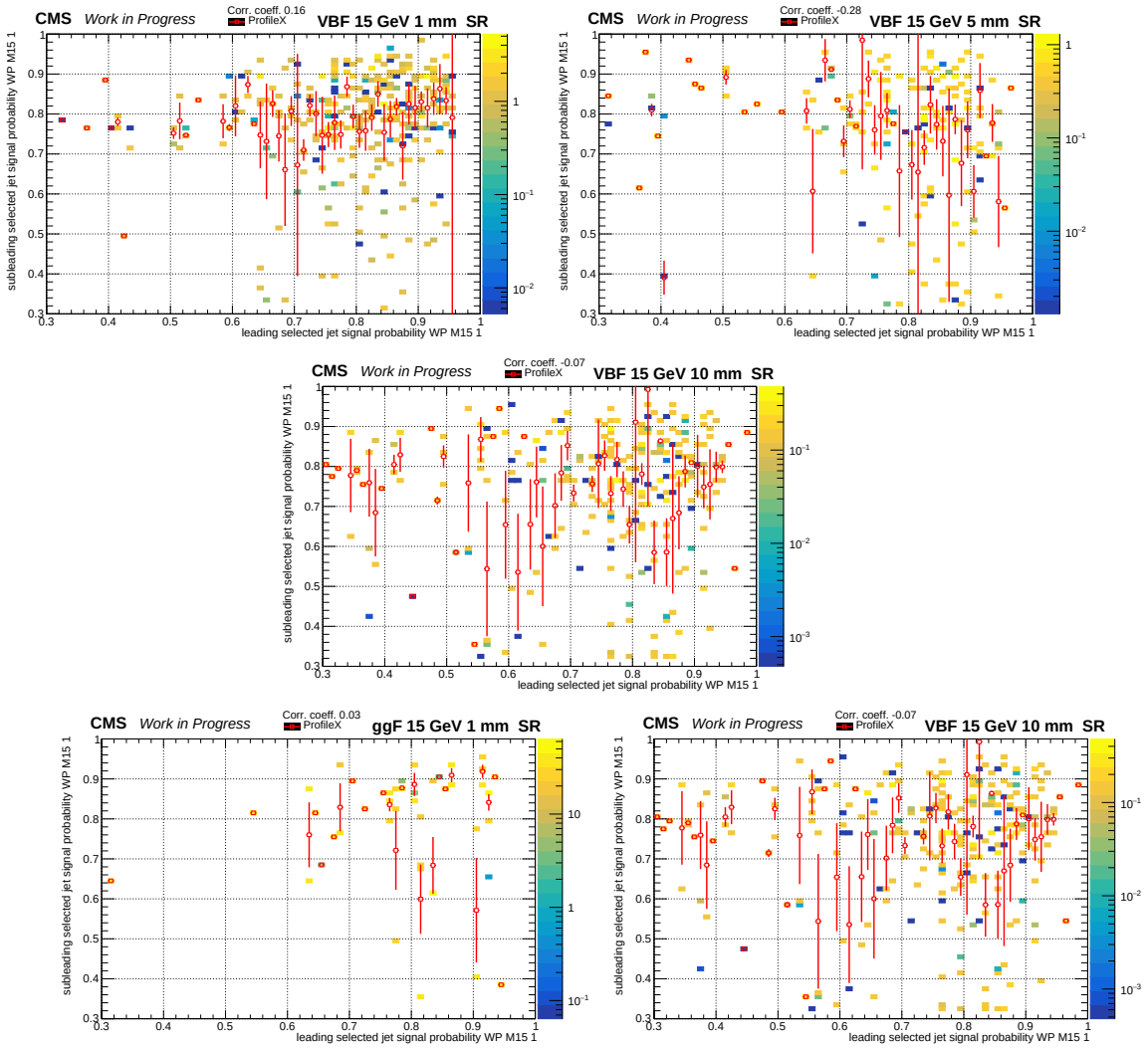

Figure D.14: Distributions of the DNN discriminant for different signal models evaluated of the LLP with 15 GeV mass and 1 mm lifetime of the two selected jets in SR and define the regions for the background estimation method. Distributions for VBF Higgs produced signal with LLPs of 1 mm lifetime (upper left), 5 mm (upper right) and 10 mm (second row). ggF Higgs production mode with 1 mm (third row left) and 10 mm (third row right).

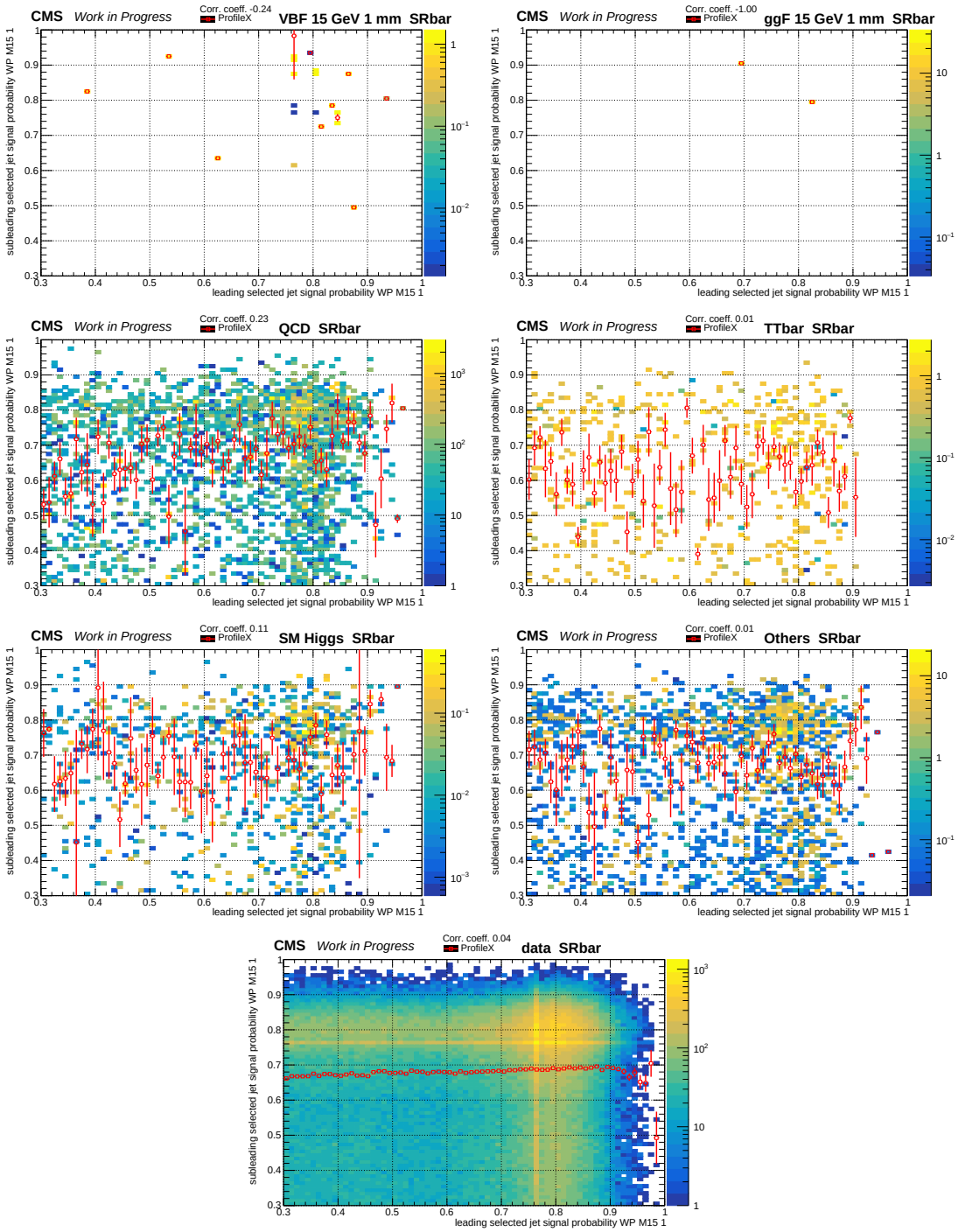

Figure D.15: Distributions in the $\overline{\text{SR}}$ of the DNN discriminant for the two selected jets for the analysis of the LLP with 15 GeV mass and 1 mm lifetime for: VBF and ggF produced signal (upper left and right, respectively), QCD multijet (second row left), $t\bar{t}$ (second row right), SM Higgs (third row left), Others (third row right) and data (lower).

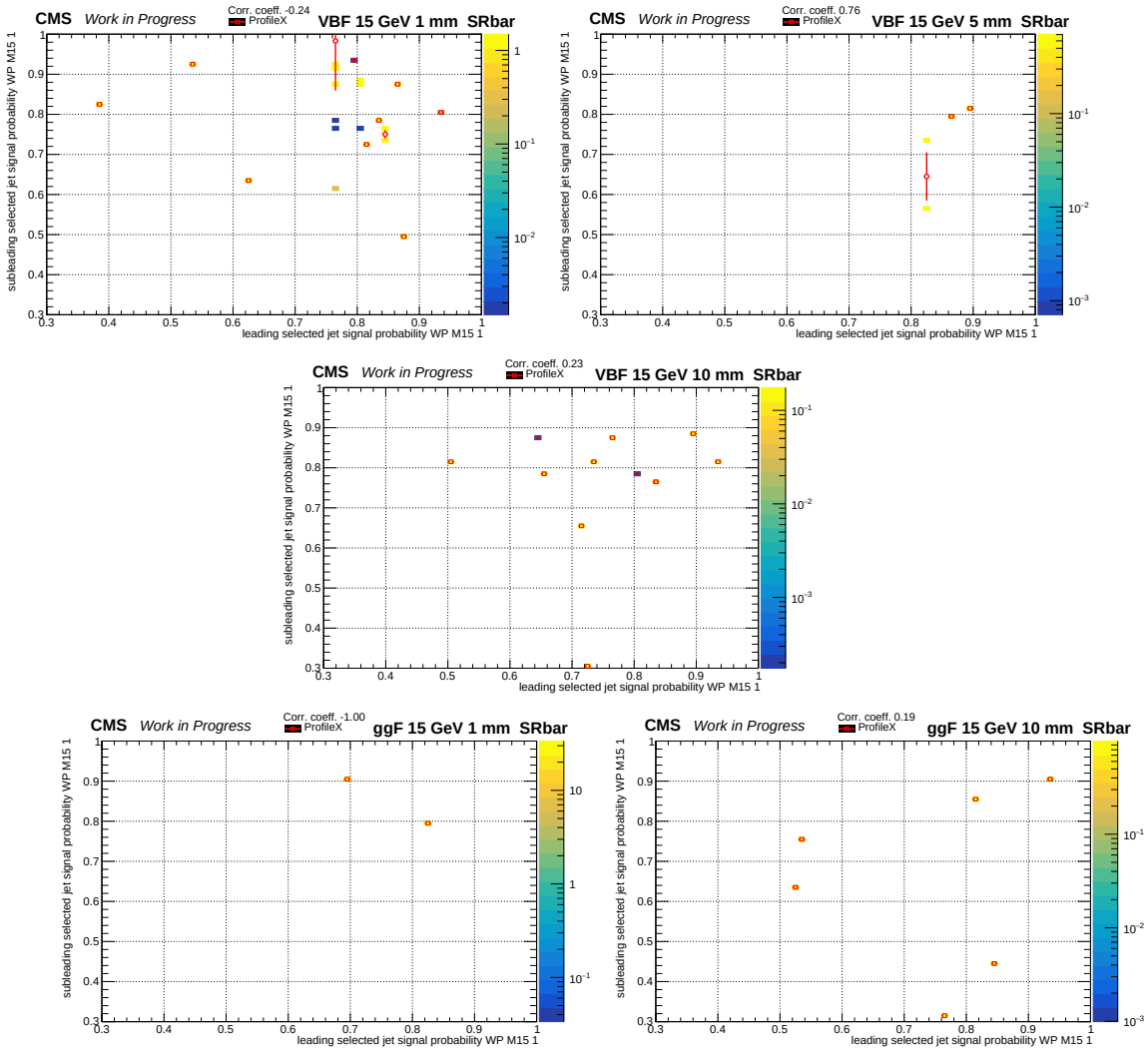

Figure D.16: Distributions of the DNN discriminant for different signal models evaluated of the LLP with 15 GeV mass and 1 mm lifetime of the two selected jets in $\overline{\text{SR}}$ and define the regions for the background estimation method. Distributions for VBF Higgs produced signal with LLPs of 1 mm lifetime (upper left), 5 mm (upper right) and 10 mm (second row). ggF Higgs production mode with 1 mm (third row left) and 10 mm (third row right).

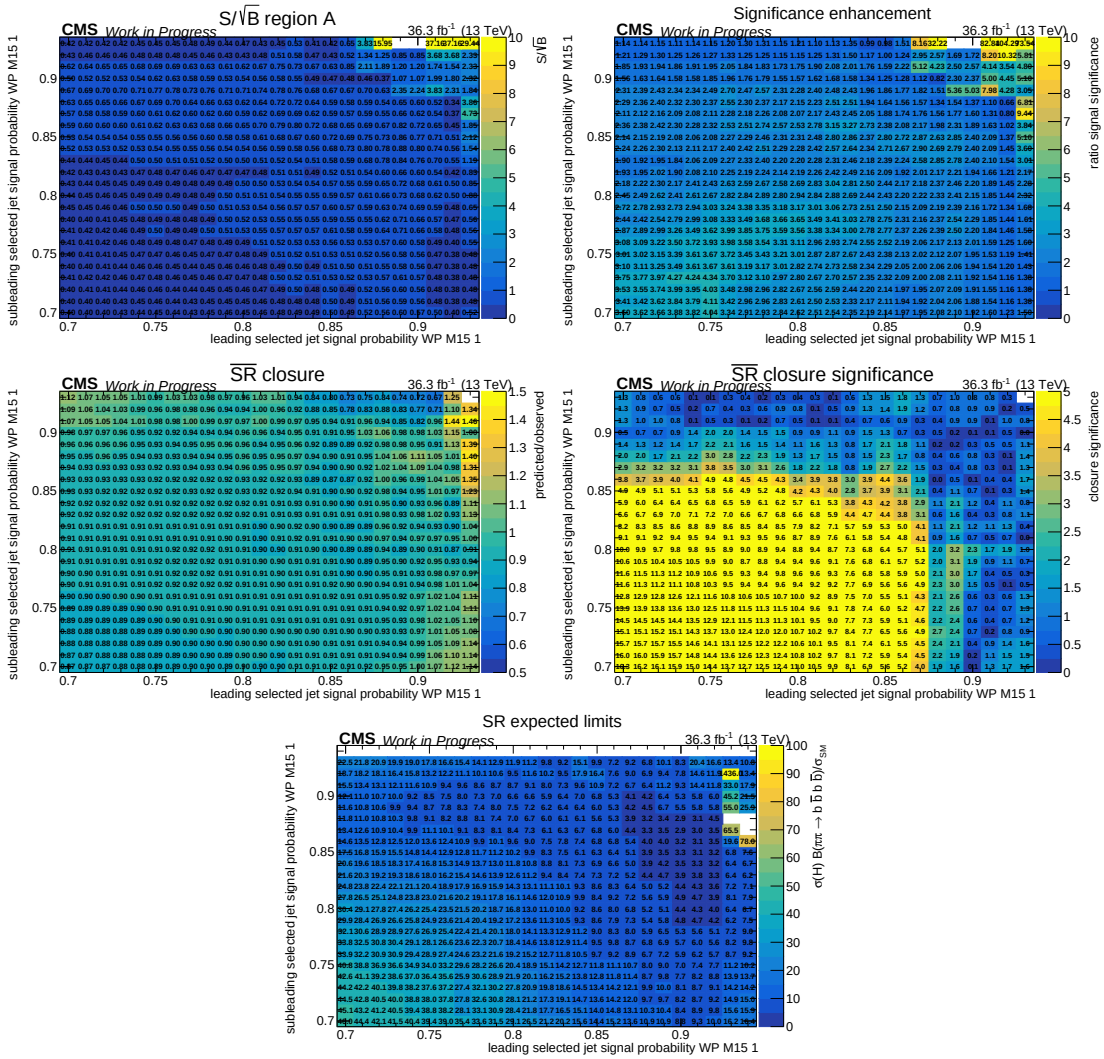

Figure D.17: Effect of various thresholds for the ABCD method on the analysis of LLPs with a mass of 15 GeV and a lifetime of 1 mm produced with VBF Higgs production mode on: Signal significance (first row left), the significance enhancement Σ_{signal} (first row right), the closure using data in the $\overline{\text{SR}}$ (second row left) and its significance (second row right), and the expected upper limits on the signal strength modifier in the SR (lower). White bins indicate such regions where either the SM background yield or the signal yield was zero.

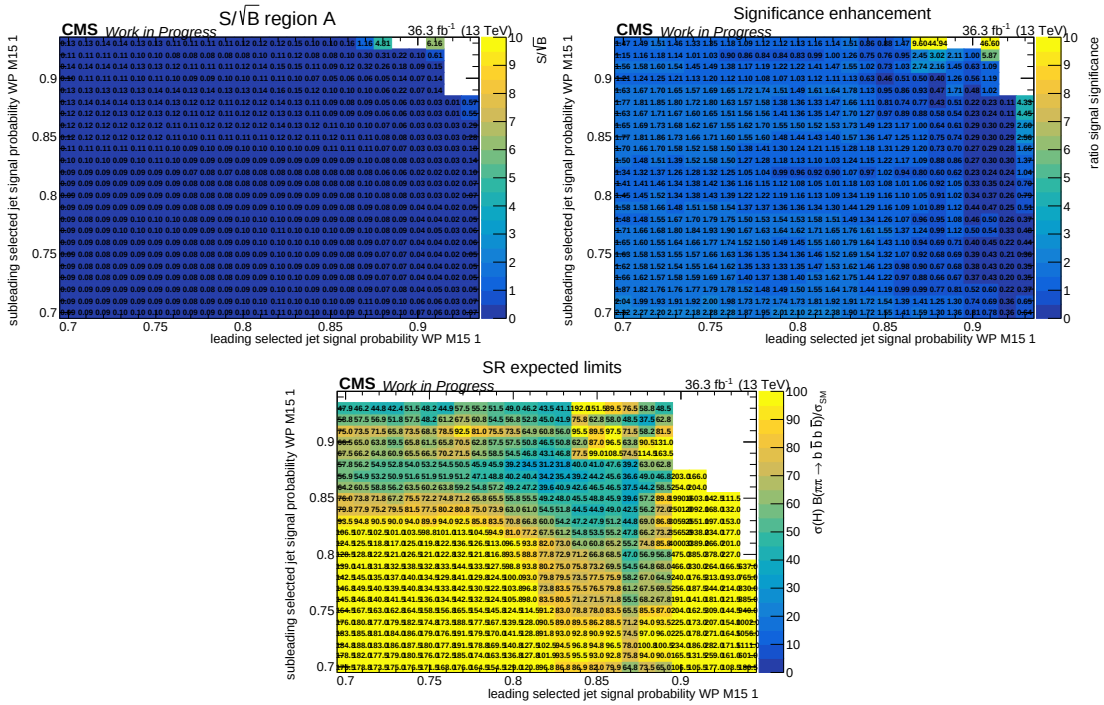

Figure D.18: Effect of various thresholds for the ABCD method on the analysis of LLPs with a mass of 15 GeV and a lifetime of 5 mm on: Signal significance (first row left), the significance enhancement Σ_{signal} (first row right), and the expected upper limits on the signal strength modifier in the SR (lower).

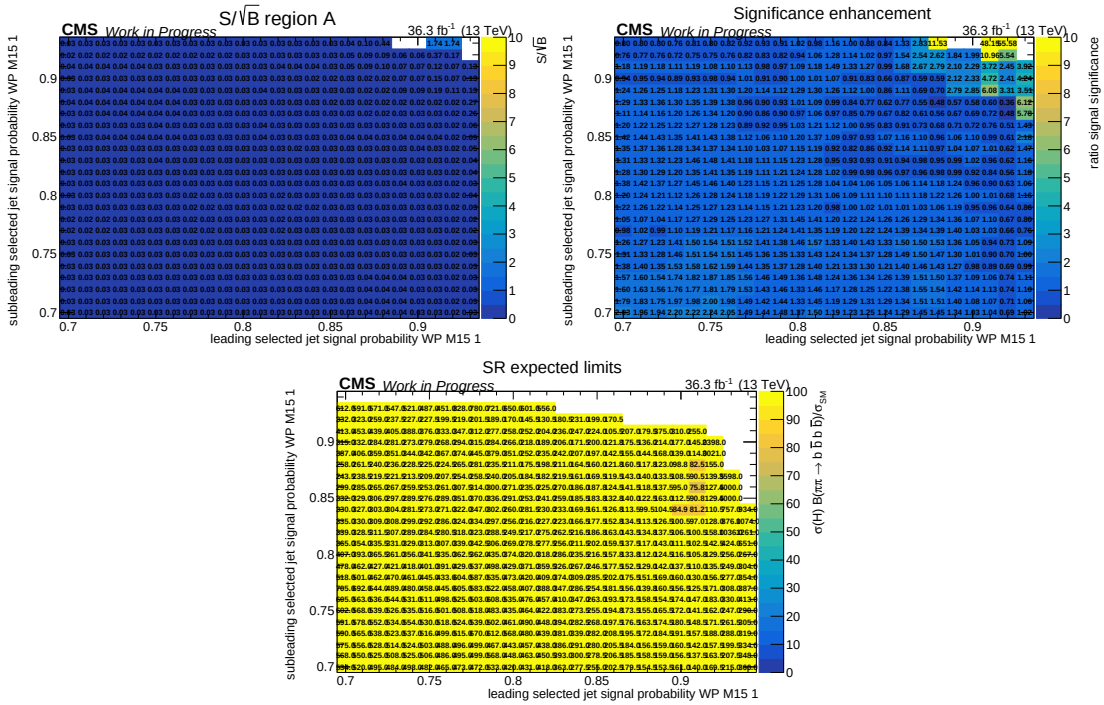

Figure D.19: Effect of various thresholds for the ABCD method on the analysis of LLPs with a mass of 15 GeV and a lifetime of 10 mm produced with VBF Higgs production mode on: Signal significance (first row left), the significance enhancement Σ_{signal} (first row right), and the expected upper limits on the signal strength modifier in the SR (lower).

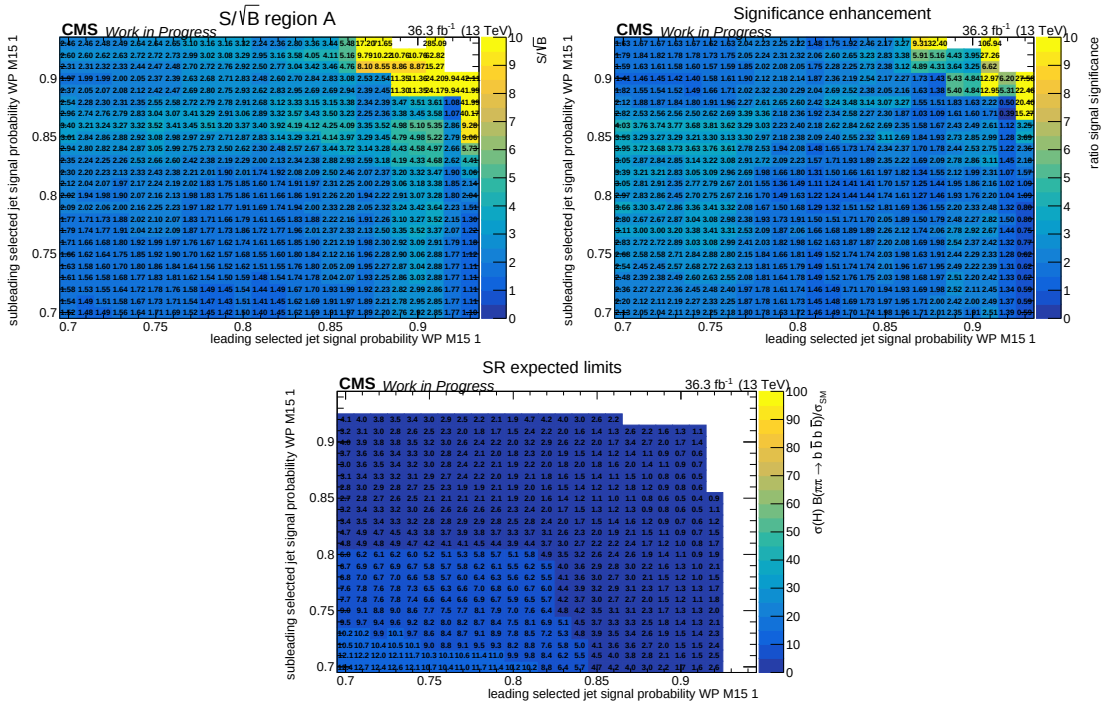

Figure D.20: Effect of various thresholds for the ABCD method on the analysis of LLPs with a mass of 15 GeV and a lifetime of 1 mm produced with ggF Higgs production mode on: Signal significance (first row left), the significance enhancement Σ_{signal} (first row right), and the expected upper limits on the signal strength modifier in the SR (lower).

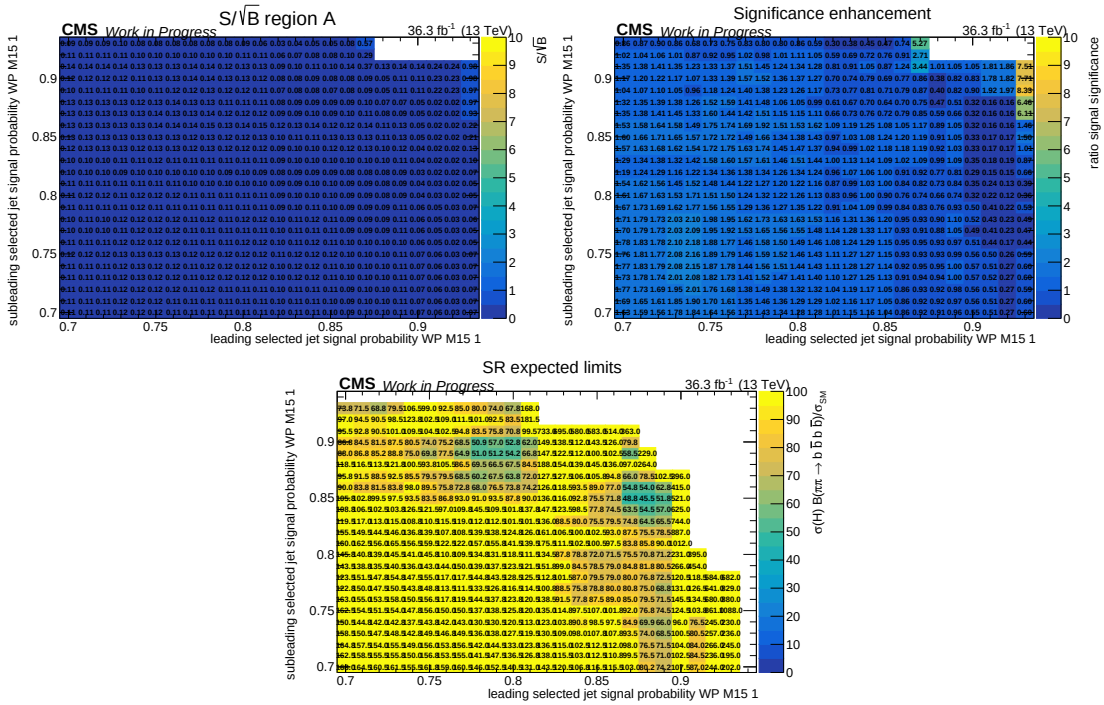

Figure D.21: Effect of various thresholds for the ABCD method on the analysis of LLPs with a mass of 15 GeV and a lifetime of 10 mm produced with ggF Higgs production mode on: Signal significance (first row left), the significance enhancement Σ_{signal} (first row right), and the expected upper limits on the signal strength modifier in the SR (lower).

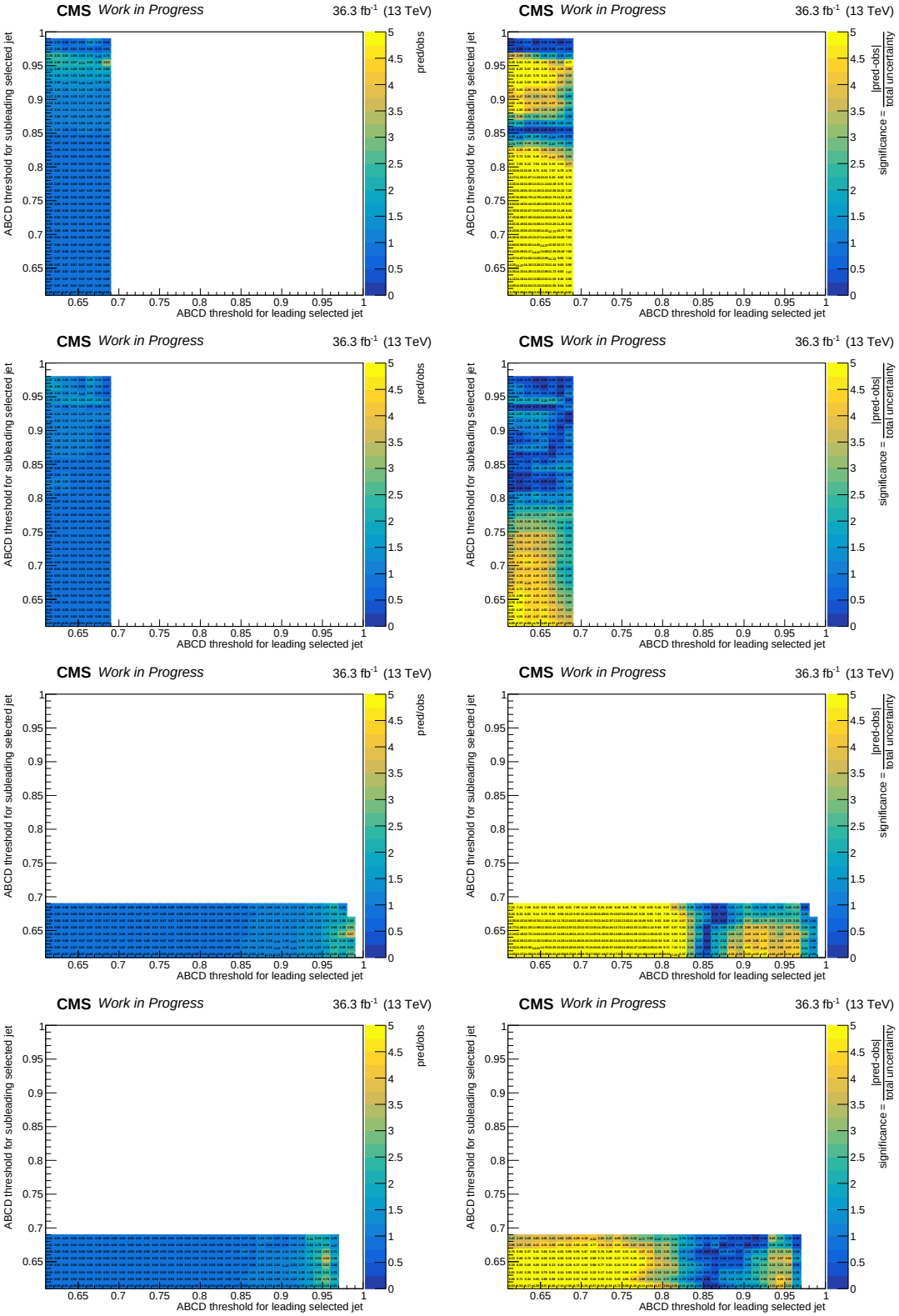

Figure D.22: The closure (left) and its significance (right) for SR (first and third row) and $\overline{\text{SR}}$ (second and fourth row) of sideband 1 (upper two rows) and 2 (lower two rows).

Appendix E Resolved Signature

Studies for the LLP masses of 40 GeV and 55 GeV and all lifetimes of the resolved topology were performed, but only distributions of the 40 GeV 1 mm combination were shown in Chapter 11.2. In the following, the distributions of all mass-lifetime combinations can be found. Presented are: ABCD planes in the SR and the $\overline{\text{SR}}$, 2D scans for different thresholds of several variables, as well as closures and their significances in the sideband regions of the SR and the $\overline{\text{SR}}$.

E.1 Signal with LLP mass 40 GeV, lifetime 0 mm

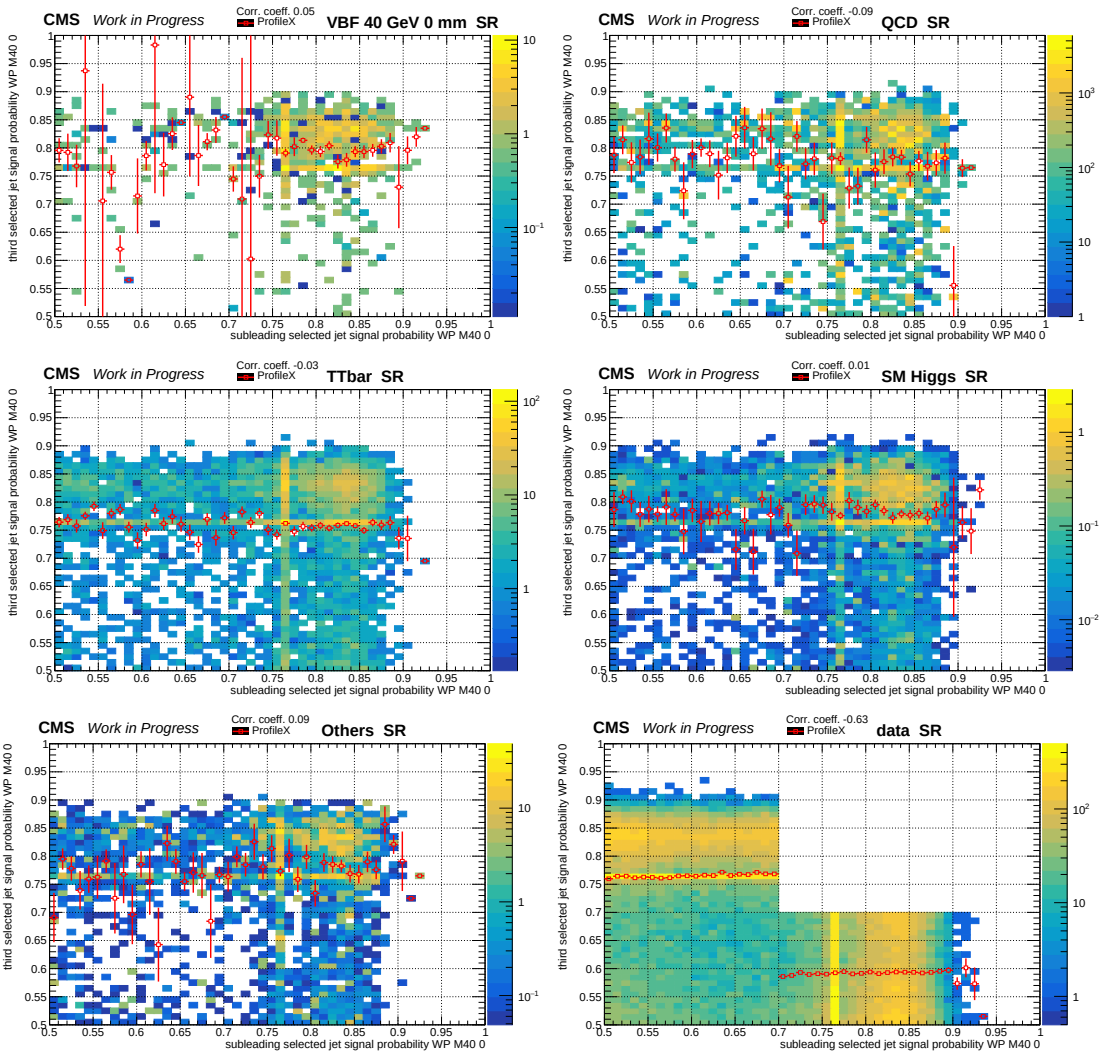

Figure E.1: Distributions of the DNN discriminant for the probability of LLPs of 40 GeV and 0 mm lifetime of the subleading and third of the selected jets in SR and define the regions for the background estimation method. The upper right region is the signal region (A). Red empty squares with error bars indicate the mean y-value of each bin. Distributions for signal (upper left), QCD multijet (upper right), $t\bar{t}$ (middle left), SM Higgs (middle right) and Others (lower left) are shown. For the distribution of data (lower right), an extended area of region A is not shown.

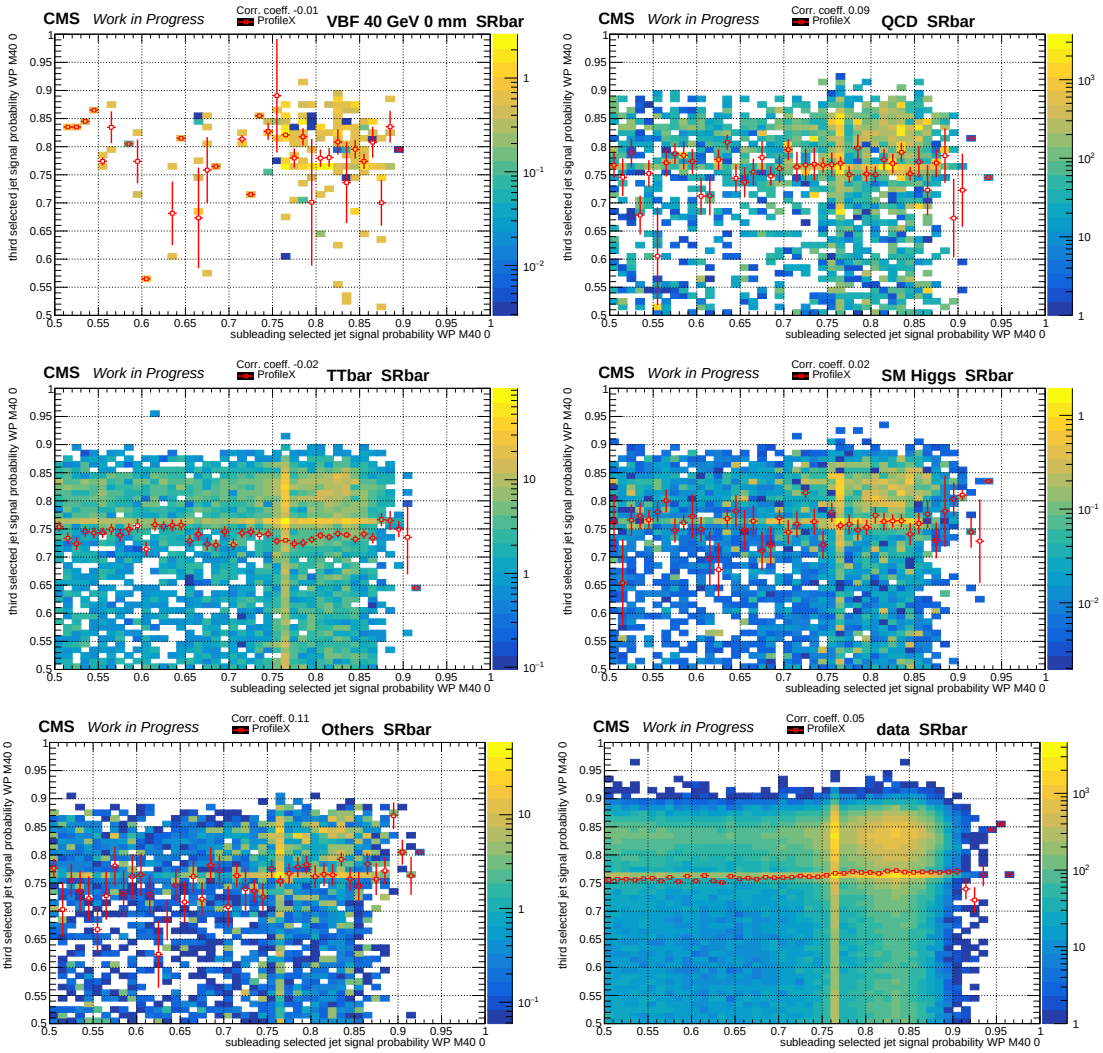

Figure E.2: Distributions in the $\overline{\text{SR}}$ of the DNN discriminant for the probability of LLPs of 40 GeV and 0 mm lifetime of the subleading and third selected jets for: VBF (upper left) and ggF (upper right) Higgs production mode signal, QCD multijet (second row left), $t\bar{t}$ (second row right), SM Higgs (third row left), Others (third row right) and data (lower).

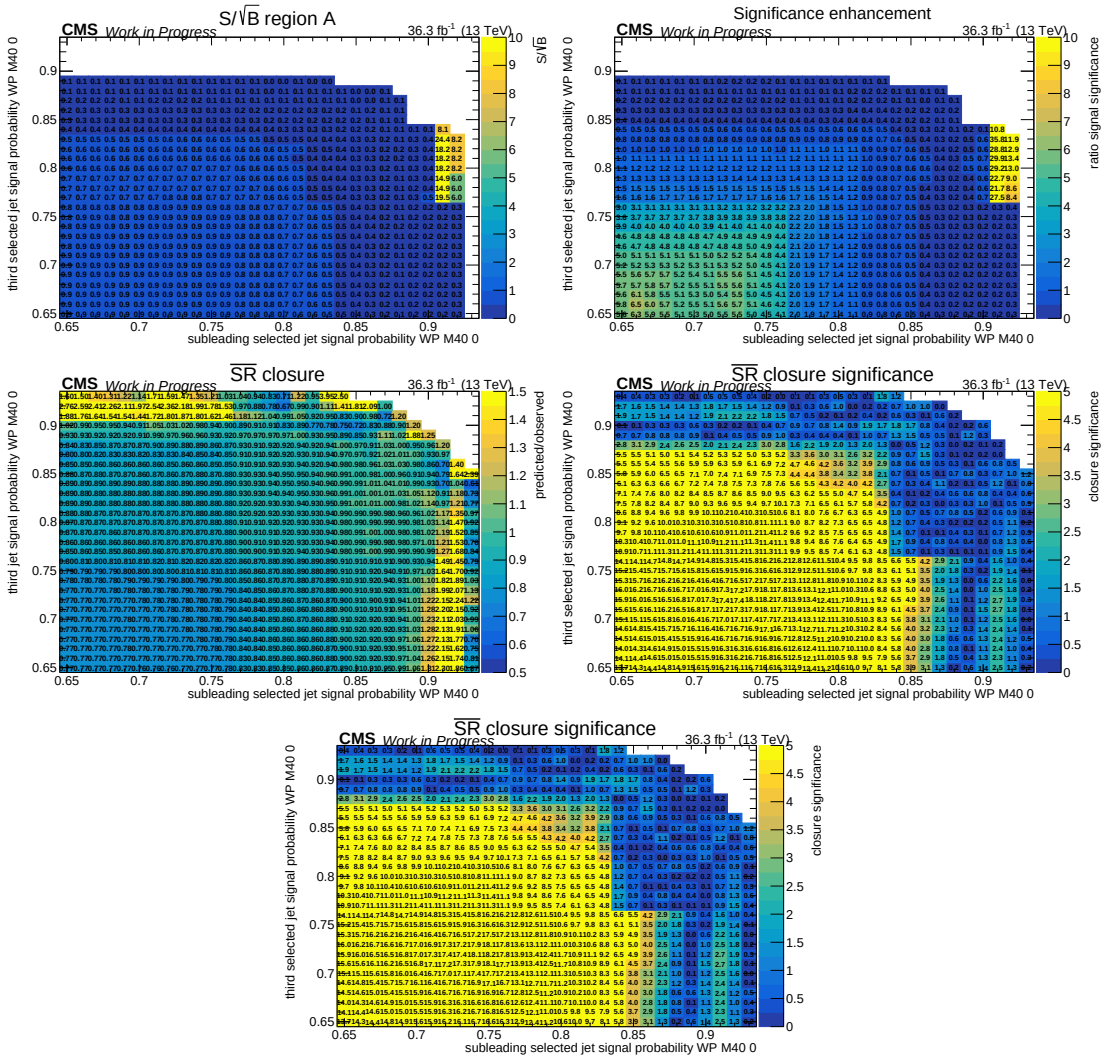

Figure E.3: Effect of various thresholds for the ABCD method on the analysis of LLPs with a mass of 40 GeV and a lifetime of 0 mm on: Signal significance (first row left), the significance enhancement Σ_{signal} (first row right), the closure using data in the $\overline{\text{SR}}$ (second row left) and its significance (second row right), and blinded expected upper limits on the signal strength modifier in the SR (lower). White bins indicate such regions where either the SM background yield or the signal yield was zero.

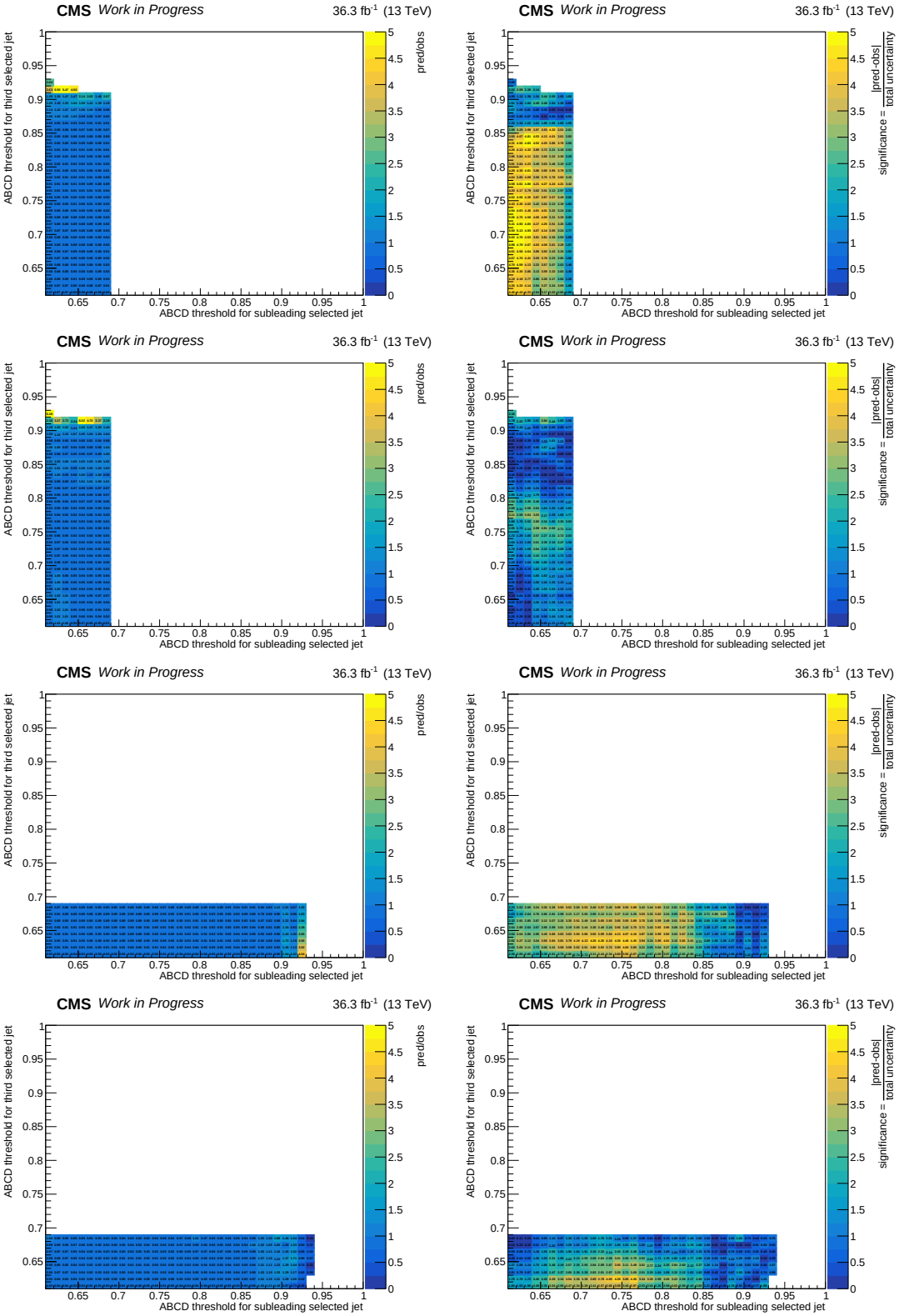

Figure E.4: The closure (left) and its significance (right) for the LLP mass of 40 GeV and 0 mm of the SR (first and third row) and $\overline{\text{SR}}$ (second and fourth row) of sideband 1 (upper two rows) and 2 (lower two rows).

E.2 Signal with LLP mass 40 GeV, lifetime 0.05 mm

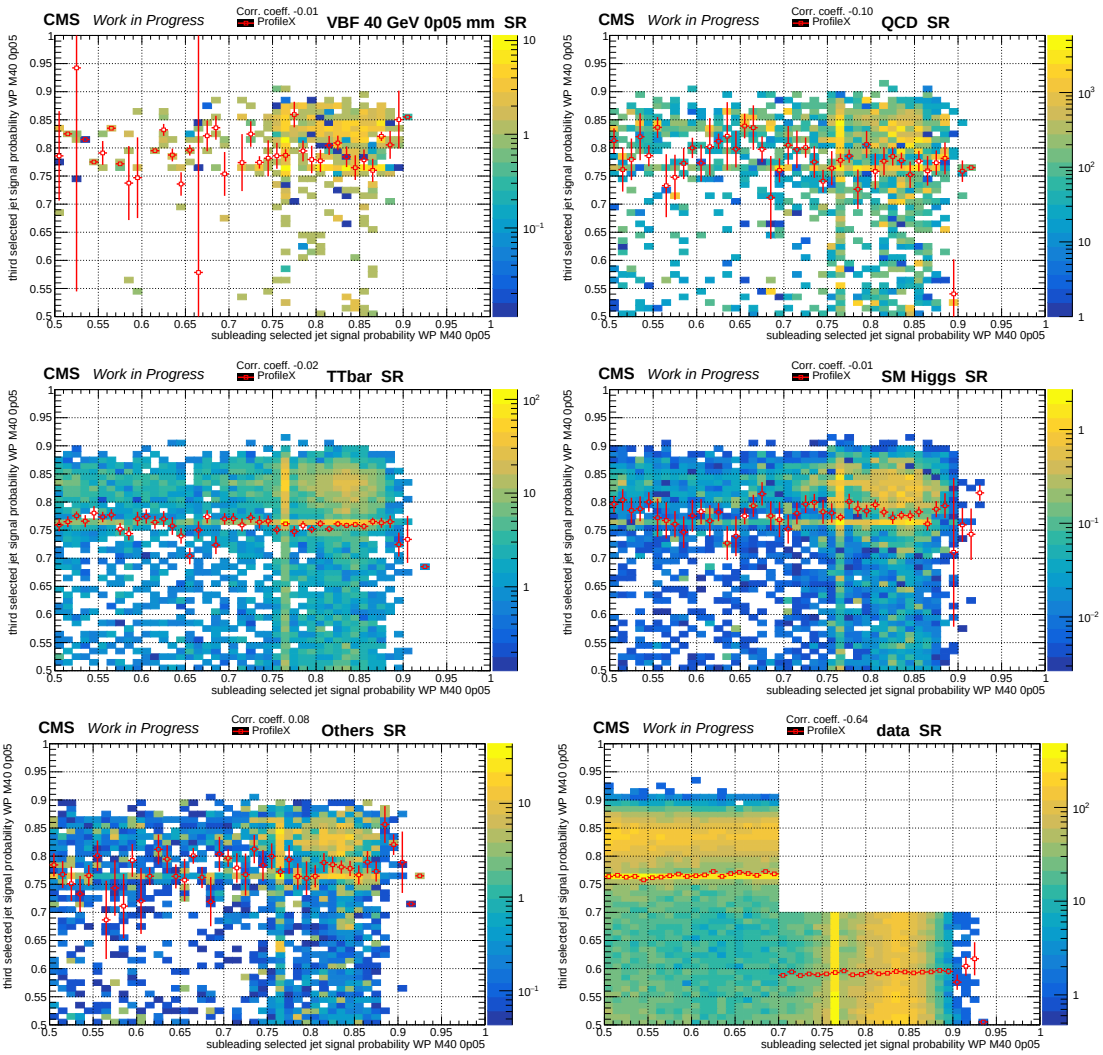

Figure E.5: Distributions of the DNN discriminant for the probability of LLPs of 40 GeV and 0.05 mm lifetime of the subleading and third of the selected jets in SR and define the regions for the background estimation method. The upper right region is the signal region (A). Red empty squares with error bars indicate the mean y-value of each bin. Distributions for signal (upper left), QCD multijet (upper right), $t\bar{t}$ (middle left), SM Higgs (middle right) and Others (lower left) are shown. For the distribution of data (lower right), an extended area of region A is not shown.

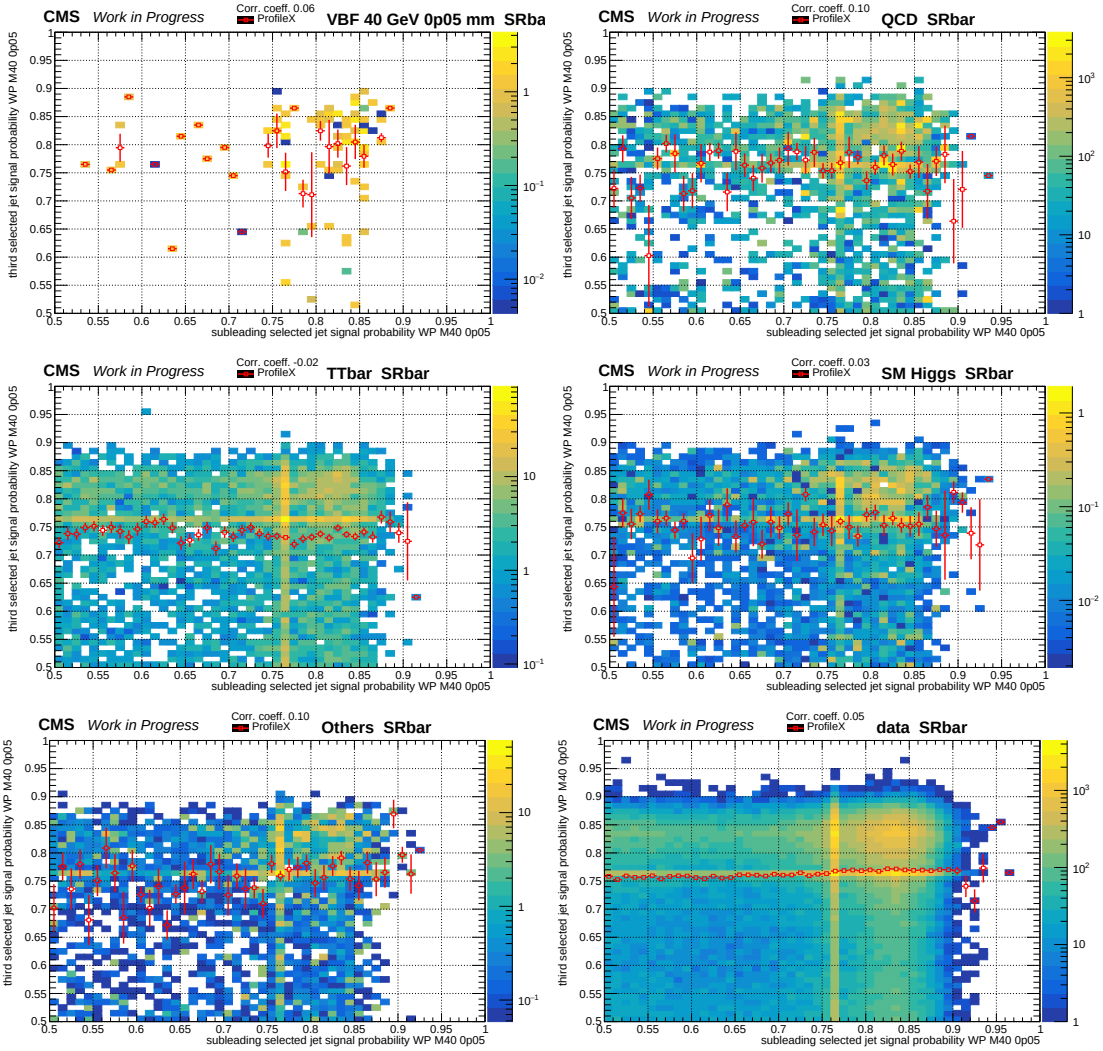

Figure E.6: Distributions of the DNN discriminant for the probability of LLPs of 40 GeV and 0.05 mm lifetime of the subleading and third of the selected jets in $\overline{\text{SR}}$ and define the regions for the background estimation method. Distributions for signal (upper left), QCD multijet (upper right), $t\bar{t}$ (middle left), SM Higgs (middle right), Others (lower left) and data (lower right) are shown.

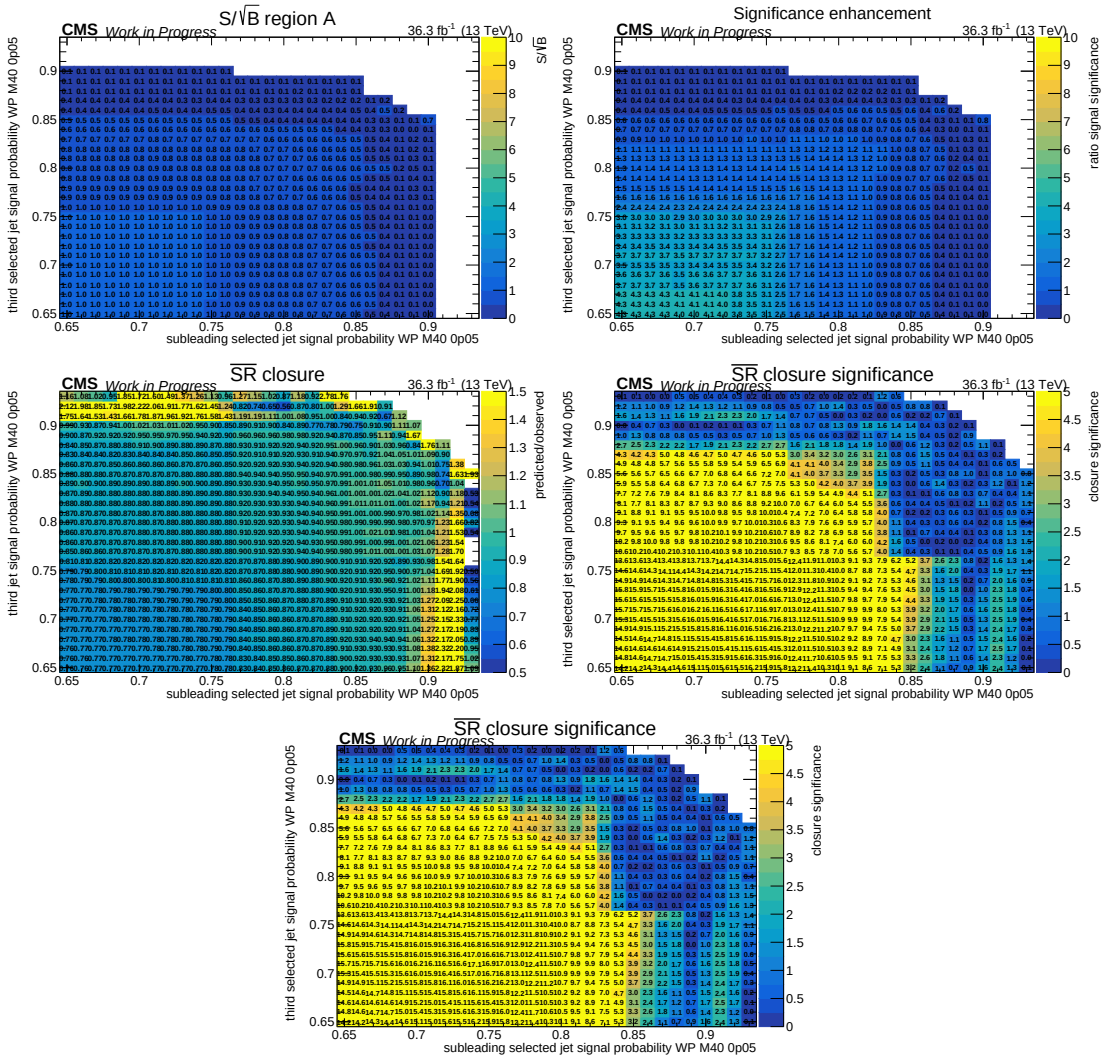

Figure E.7: Effect of various thresholds for the ABCD method on the analysis of LLPs with a mass of 40 GeV and a lifetime of 0.05 mm on: Signal significance (first row left), the significance enhancement Σ_{signal} (first row right), the closure using data in the $\overline{\text{SR}}$ (second row left) and its significance (second row right), and blinded expected upper limits on the signal strength modifier in the SR (lower). White bins indicate such regions where either the SM background yield or the signal yield was zero.

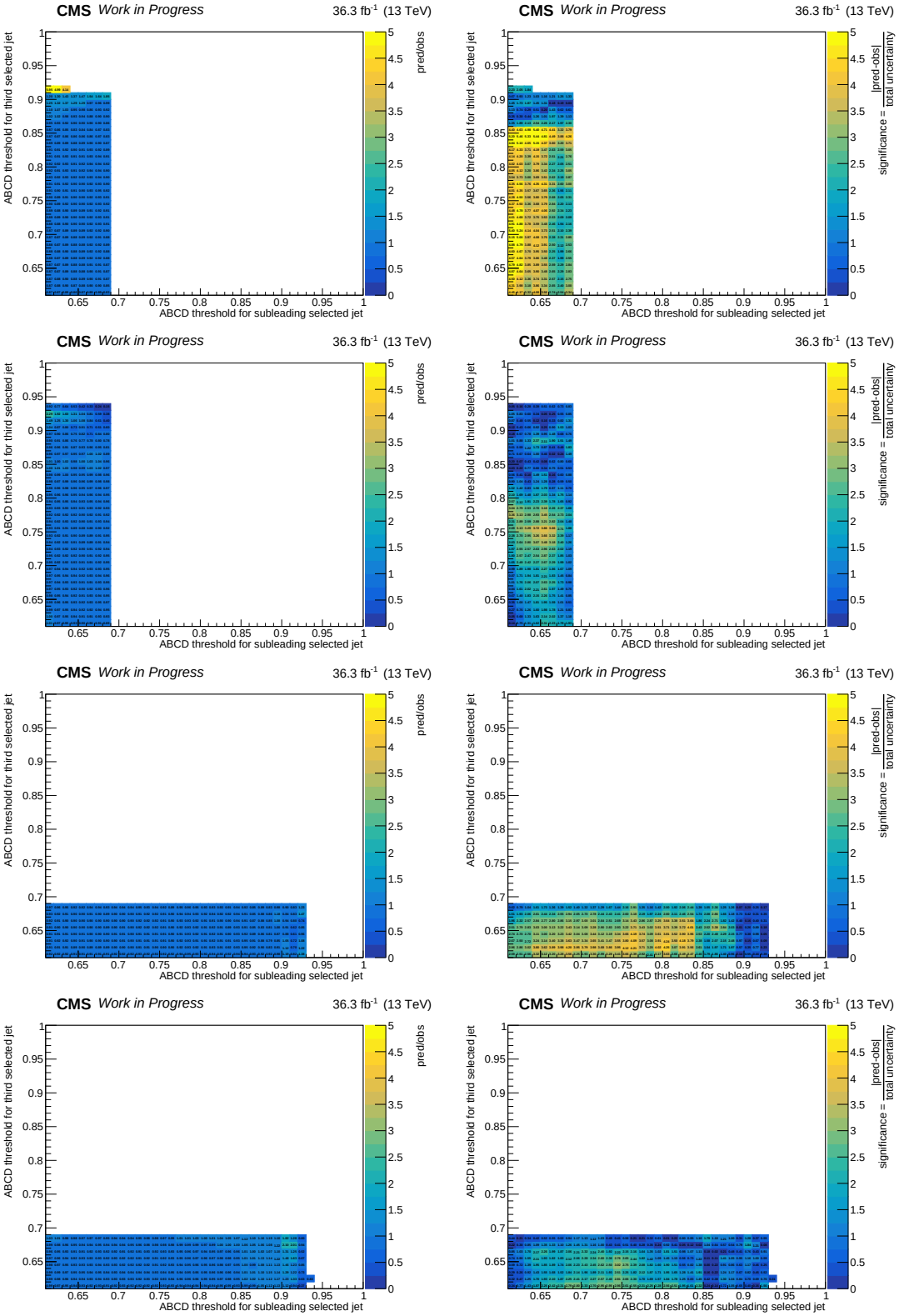

Figure E.8: The closure (left) and its significance (right) for the LLP mass of 40 GeV and 0.05 mm of the SR (first and third row) and $\overline{\text{SR}}$ (second and fourth row) of sideband 1 (upper two rows) and 2 (lower two rows).

E.3 Signal with LLP mass 40 GeV, lifetime 0.1 mm

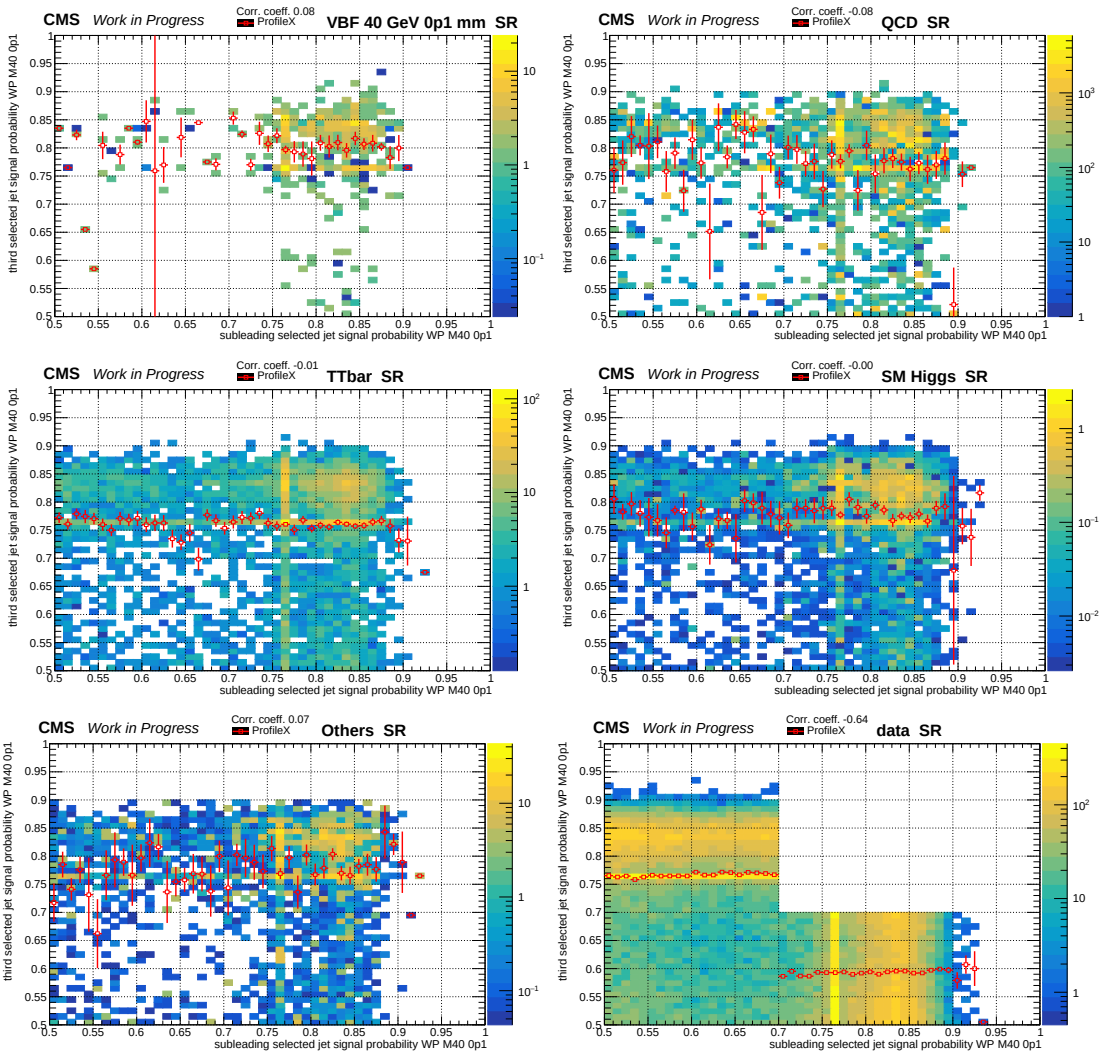

Figure E.9: Distributions of the DNN discriminant for the probability of LLPs of 40 GeV and 0.1 mm lifetime of the subleading and third of the selected jets in SR and define the regions for the background estimation method. The upper right region is the signal region (A). Red empty squares with error bars indicate the mean y-value of each bin. Distributions for signal (upper left), QCD multijet (upper right), $t\bar{t}$ (middle left), SM Higgs (middle right) and Others (lower left) are shown. For the distribution of data (lower right), an extended area of region A is not shown.

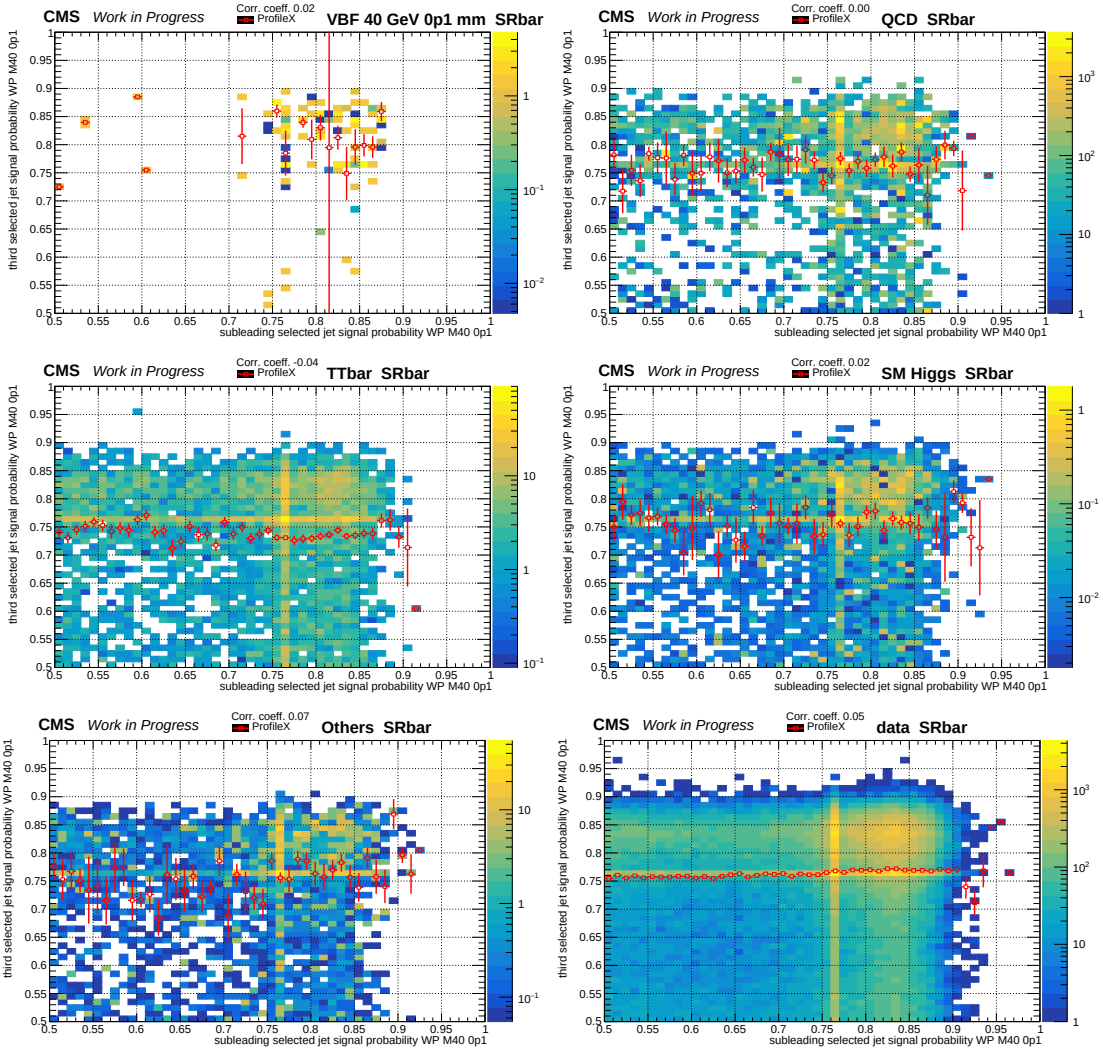

Figure E.10: Distributions of the DNN discriminant for the probability of LLPs of 40 GeV and 0.1 mm lifetime of the subleading and third of the selected jets in $\overline{\text{SR}}$ and define the regions for the background estimation method. Distributions for signal (upper left), QCD multijet (upper right), $t\bar{t}$ (middle left), SM Higgs (middle right), Others (lower left) and data (lower right) are shown.

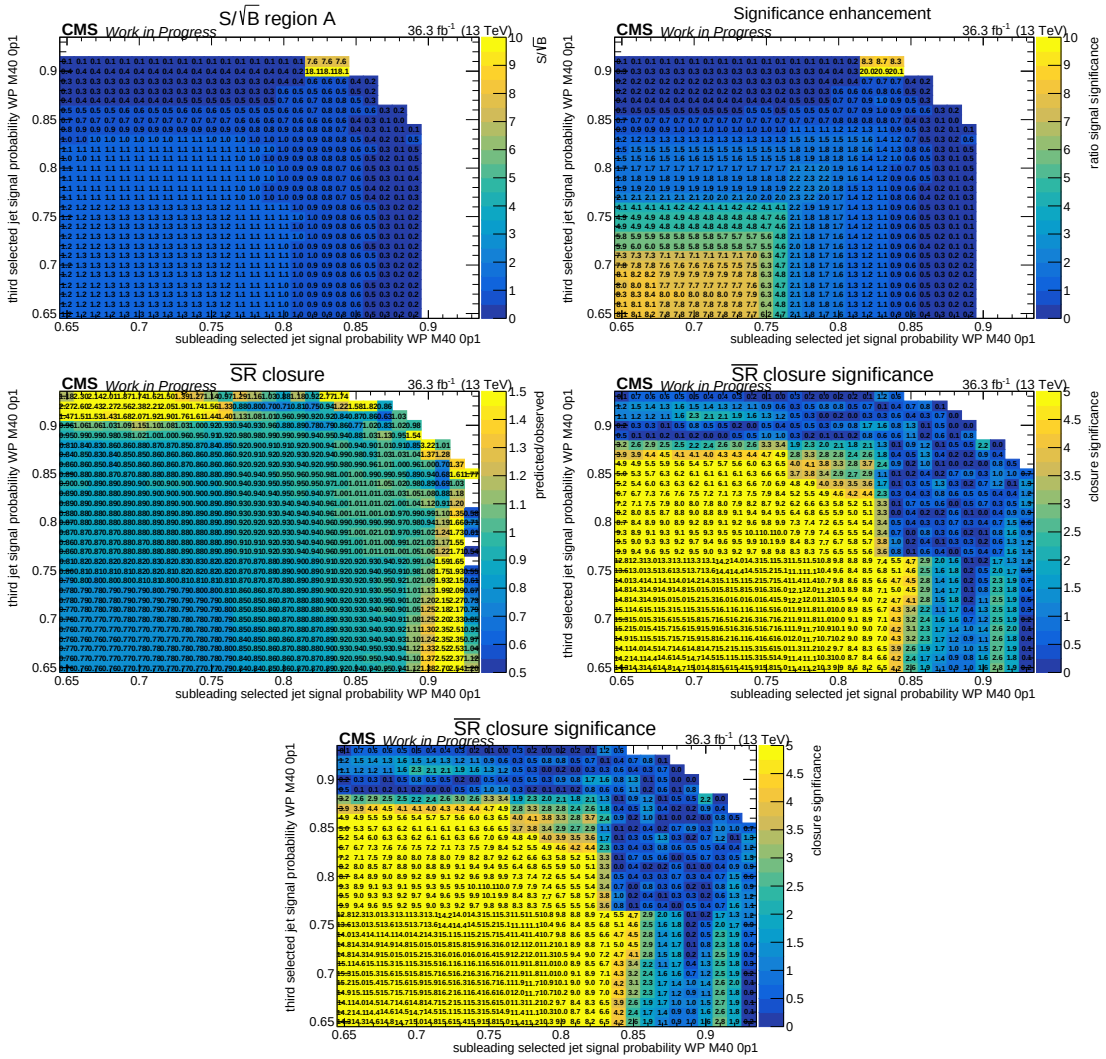

Figure E.11: Effect of various thresholds for the ABCD method on the analysis of LLPs with a mass of 40 GeV and a lifetime of 0.1 mm on: Signal significance (first row left), the significance enhancement Σ_{signal} (first row right), the closure using data in the $\overline{\text{SR}}$ (second row left) and its significance (second row right), and blinded expected upper limits on the signal strength modifier in the SR (lower). White bins indicate such regions where either the SM background yield or the signal yield was zero.

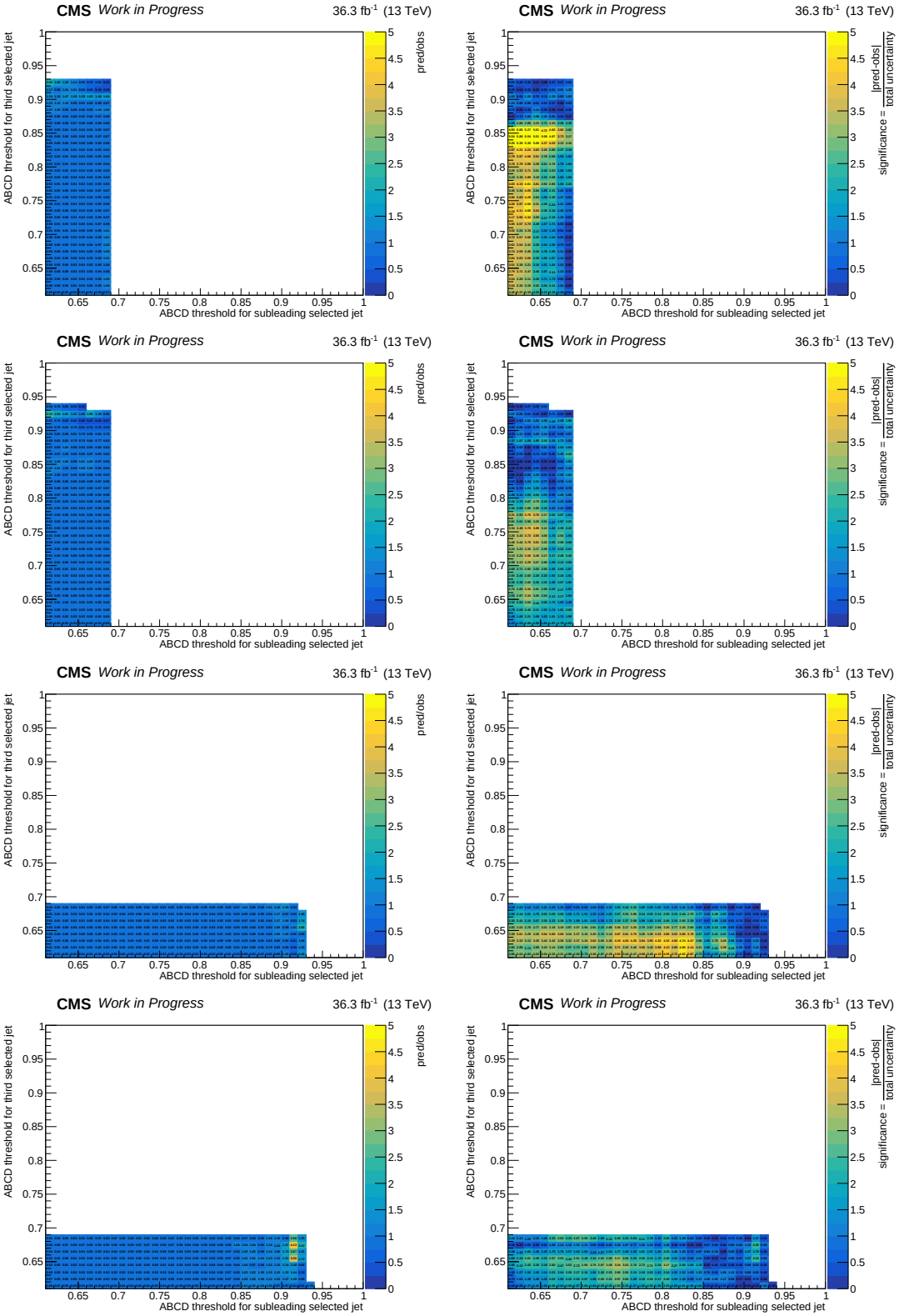

Figure E.12: The closure (left) and its significance (right) for the LLP mass of 40 GeV and 0.1 mm of the SR (first and third row) and $\overline{\text{SR}}$ (second and fourth row) of sideband 1 (upper two rows) and 2 (lower two rows).

E.4 Signal with LLP mass 40 GeV, lifetime 1 mm

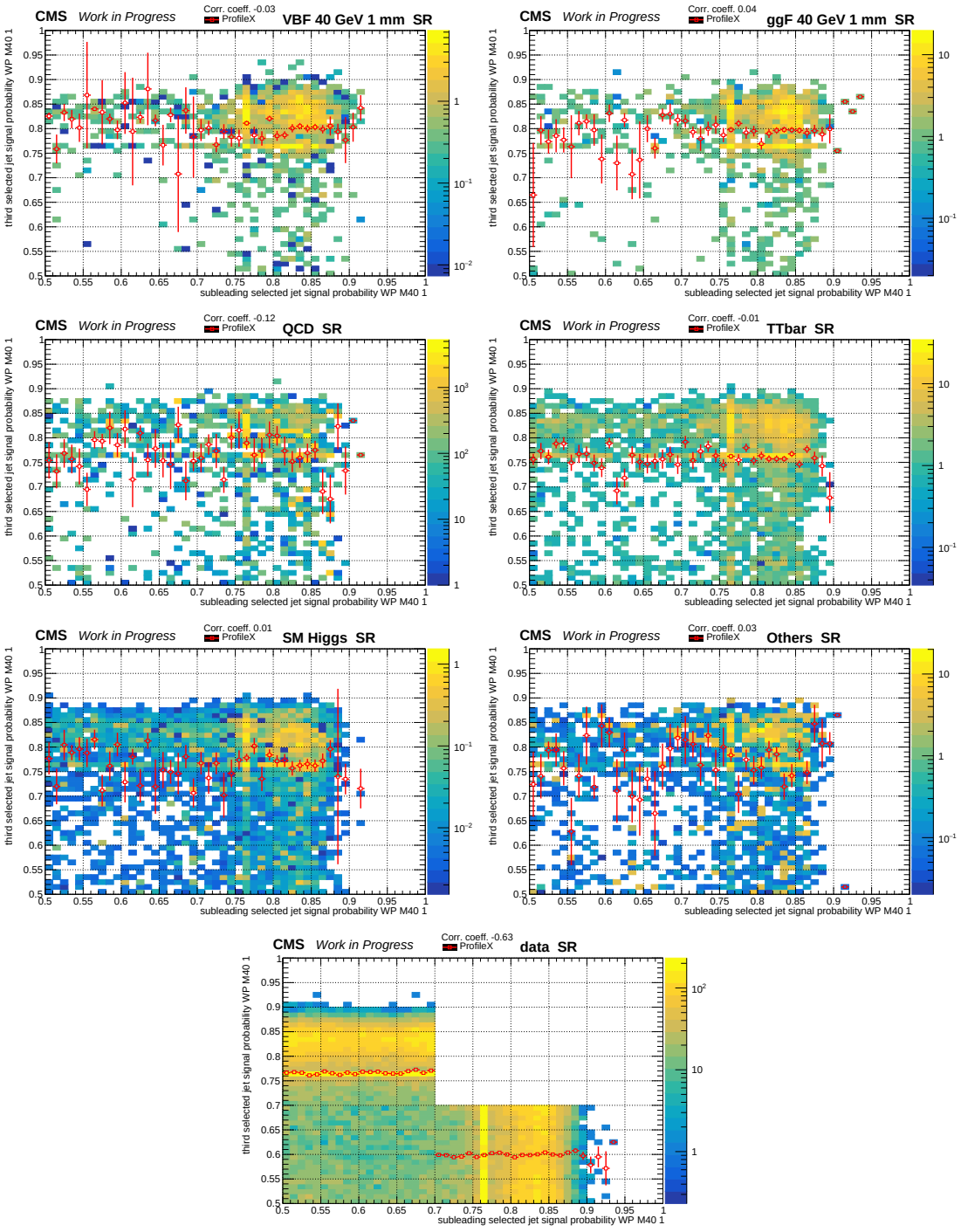

Figure E.13: Distributions in the SR of the DNN discriminant for the probability of LLPs of 40 GeV and 1 mm lifetime of the subleading and third selected jets for: VBF (upper left) and ggF (upper right) Higgs production mode signal, QCD multijet (second row left), $t\bar{t}$ (second row right), SM Higgs (third row left). For the distribution of data (lower), region A is not shown.

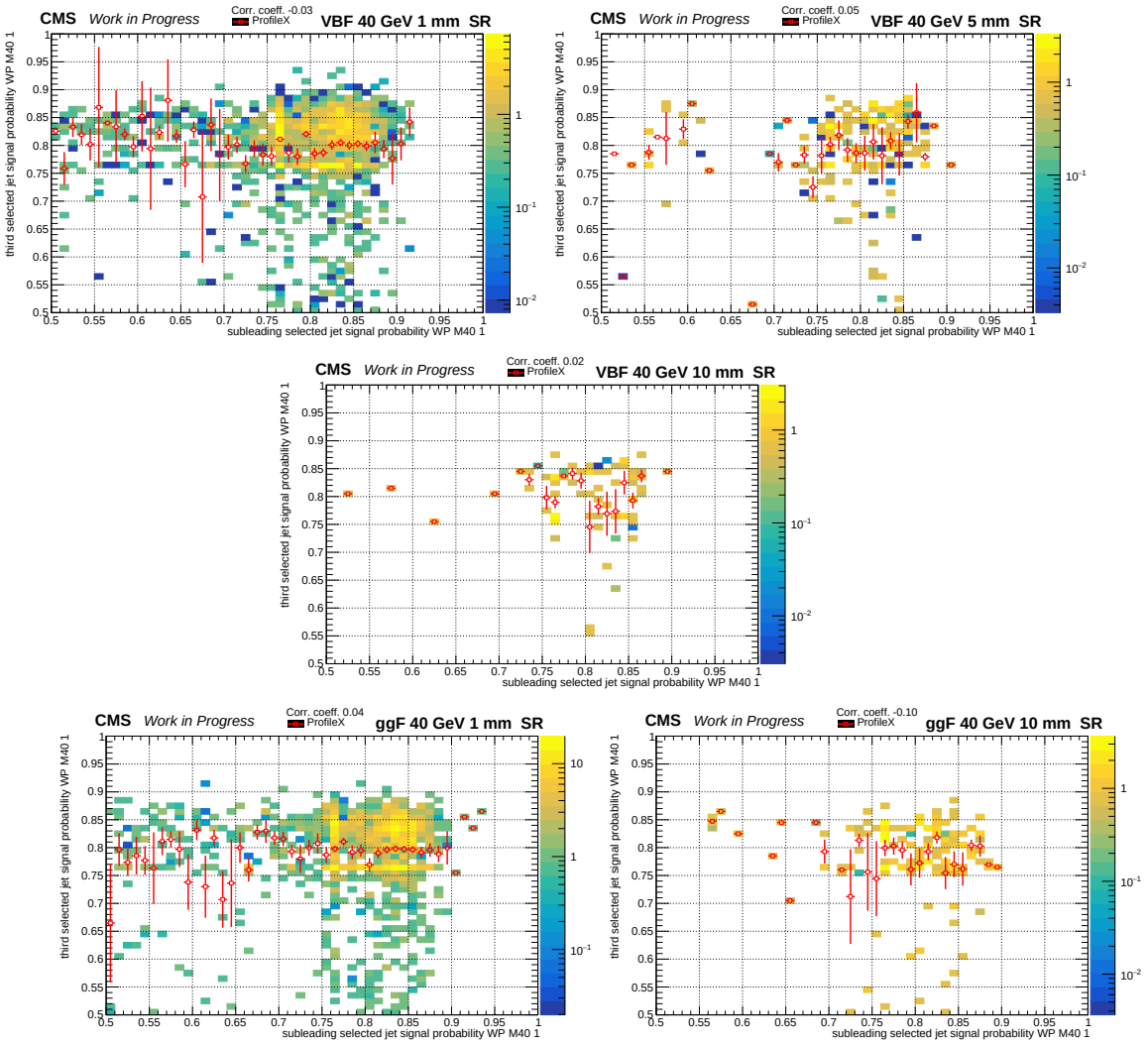

Figure E.14: Distributions of the DNN discriminant for different signal models for the analysis of LLPs of 40 GeV and 1 mm lifetime of the two selected jets in SR and define the regions for the background estimation method. Distributions for VBF Higgs produced signal with LLPs of 1 mm lifetime (upper left), 5 mm (upper right) and 10 mm (second row). ggF Higgs production mode with 1 mm (third row left) and 10 mm (third row right).

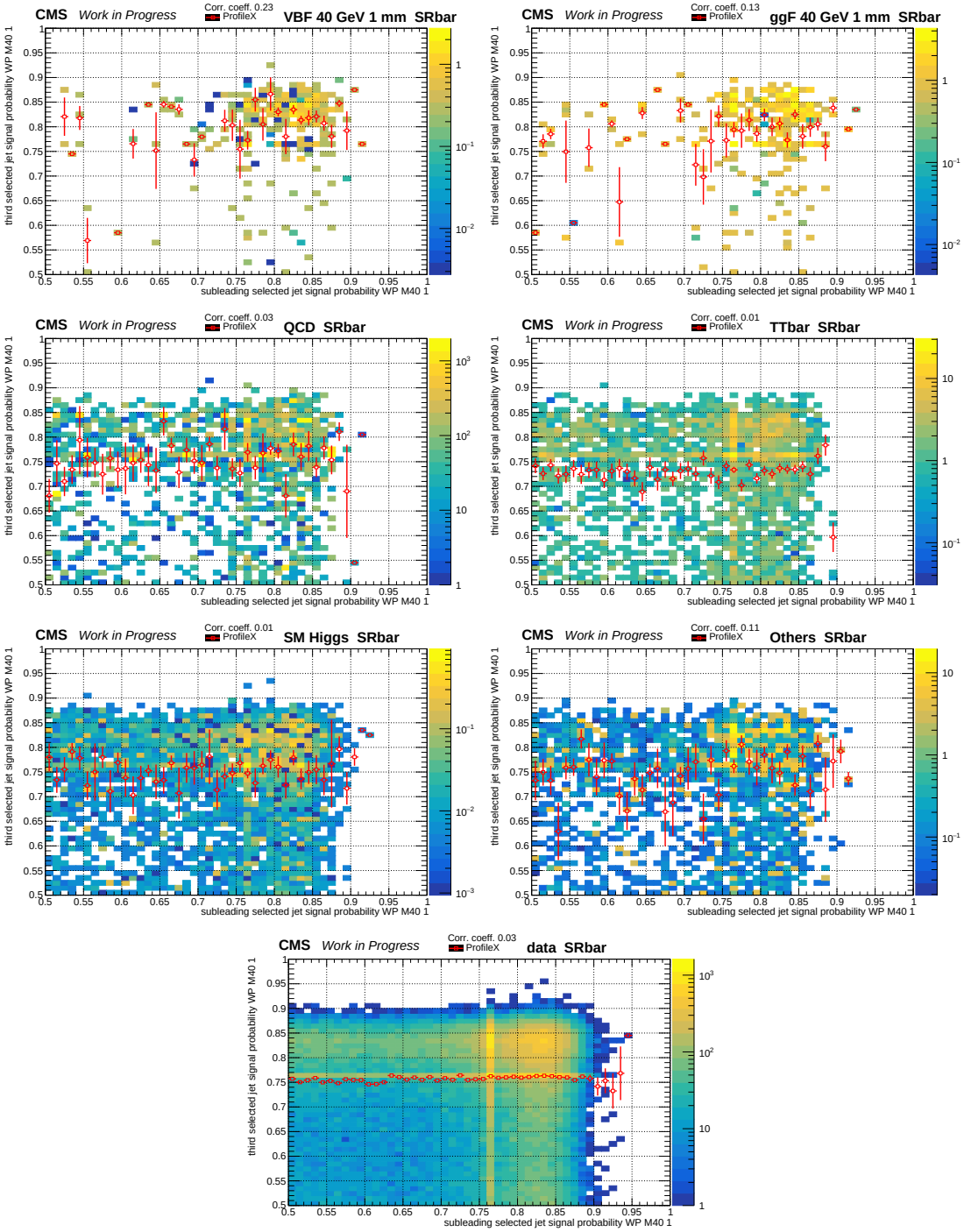

Figure E.15: Distributions in the $\overline{\text{SR}}$ of the DNN discriminant for the probability of LLPs of 40 GeV and 1 mm lifetime of the subleading and third selected jets for: VBF (upper left) and ggF (upper right) Higgs production mode signal, QCD multijet (second row left), $t\bar{t}$ (second row right), SM Higgs (third row left), Others (third row right) and data (lower).

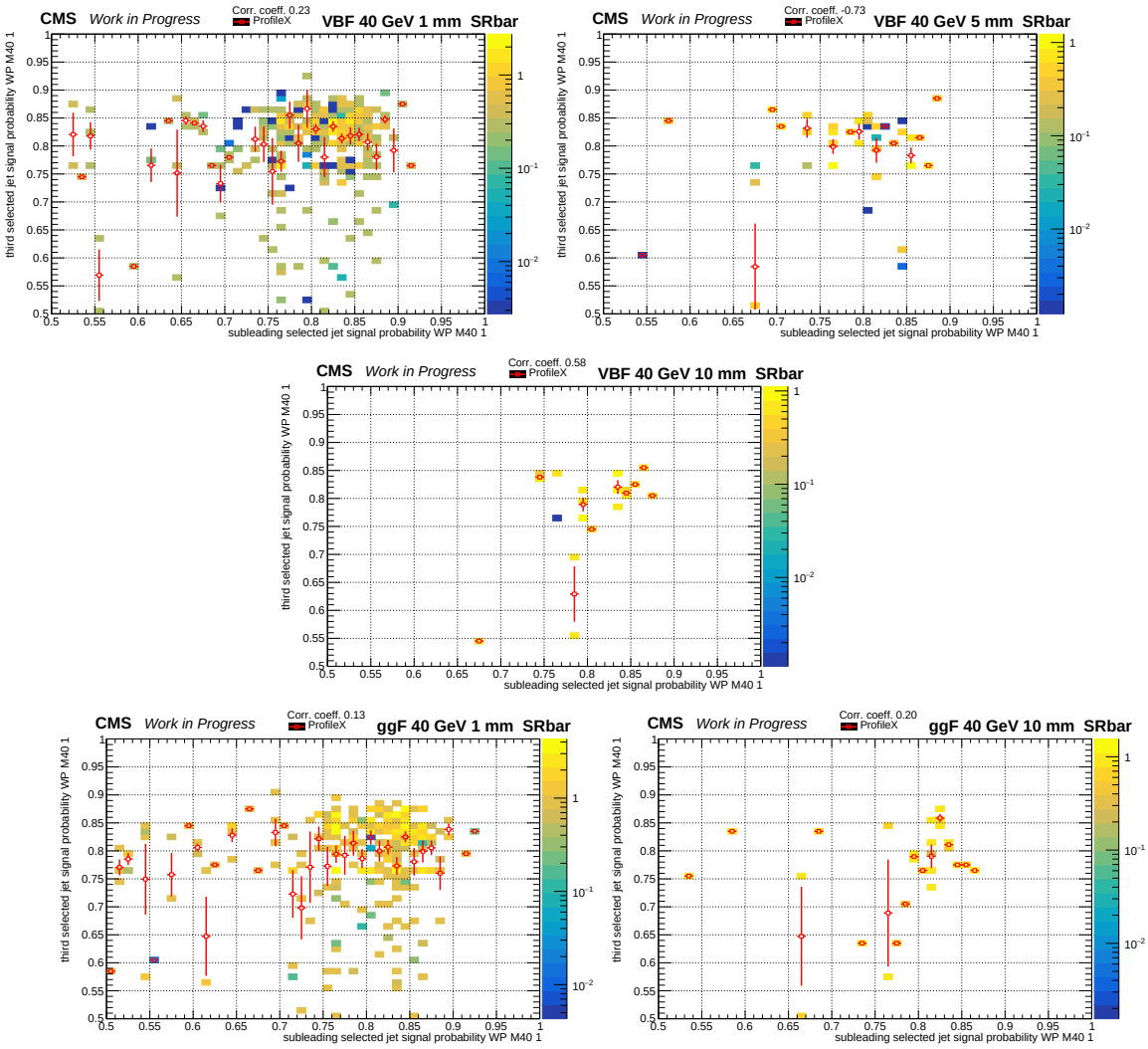

Figure E.16: Distributions of the DNN discriminant for different signal models for the analysis of LLPs of 40 GeV and 1 mm lifetime of the two selected jets in $\overline{\text{SR}}$ and define the regions for the background estimation method. Distributions for VBF Higgs produced signal with LLPs of 1 mm lifetime (upper left), 5 mm (upper right) and 10 mm (second row). ggF Higgs production mode with 1 mm (third row left) and 10 mm (third row right).

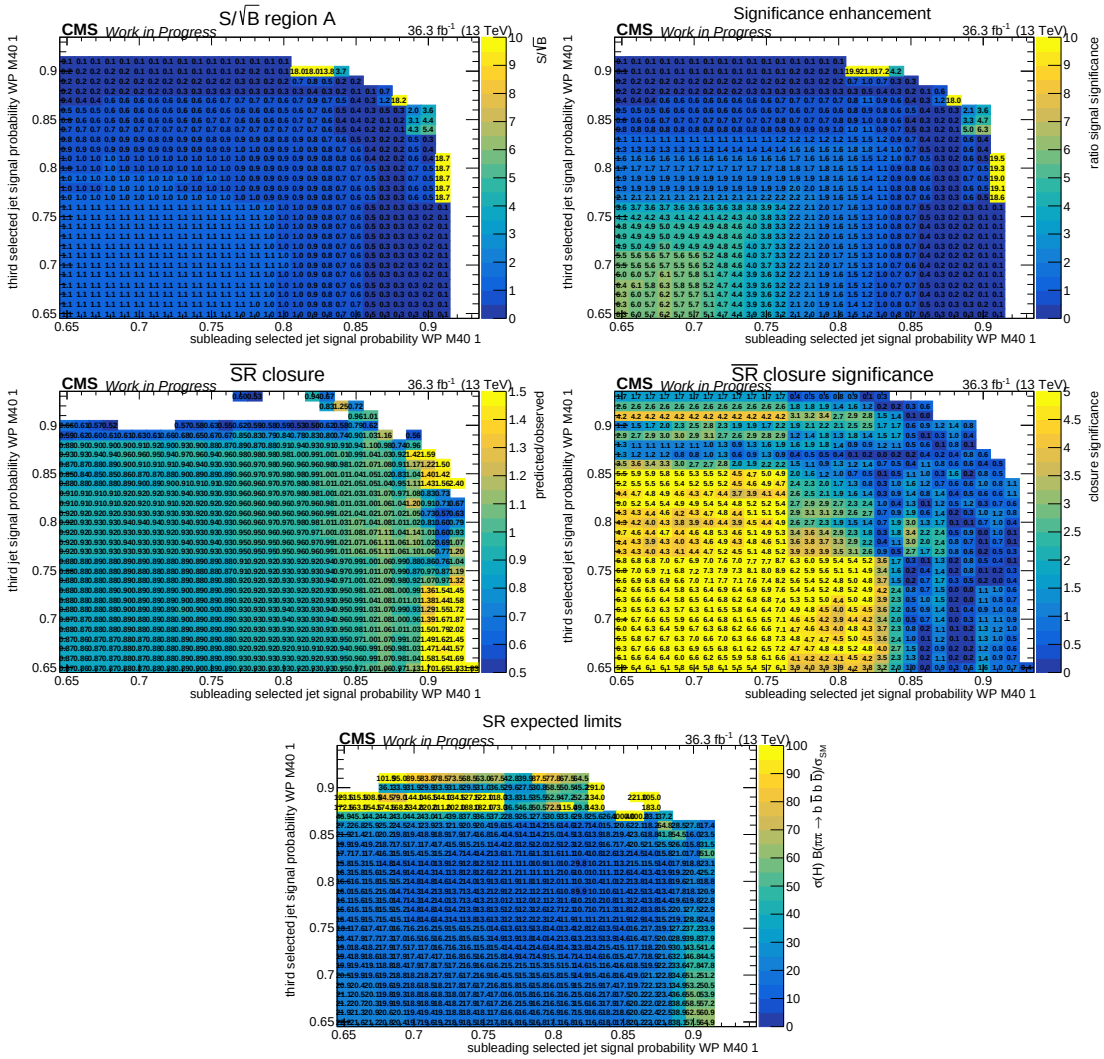

Figure E.17: Effect of various thresholds for the ABCD method on the analysis of LLPs with a mass of 40 GeV and a lifetime of 1 mm and the VBF Higgs production mode on: Signal significance (first row left), the significance enhancement Σ_{signal} (first row right), the closure using data in the $\overline{\text{SR}}$ (second row left) and its significance (second row right), and blinded expected upper limits on the signal strength modifier in the SR (lower). White bins indicate such regions where either the SM background yield or the signal yield was zero.

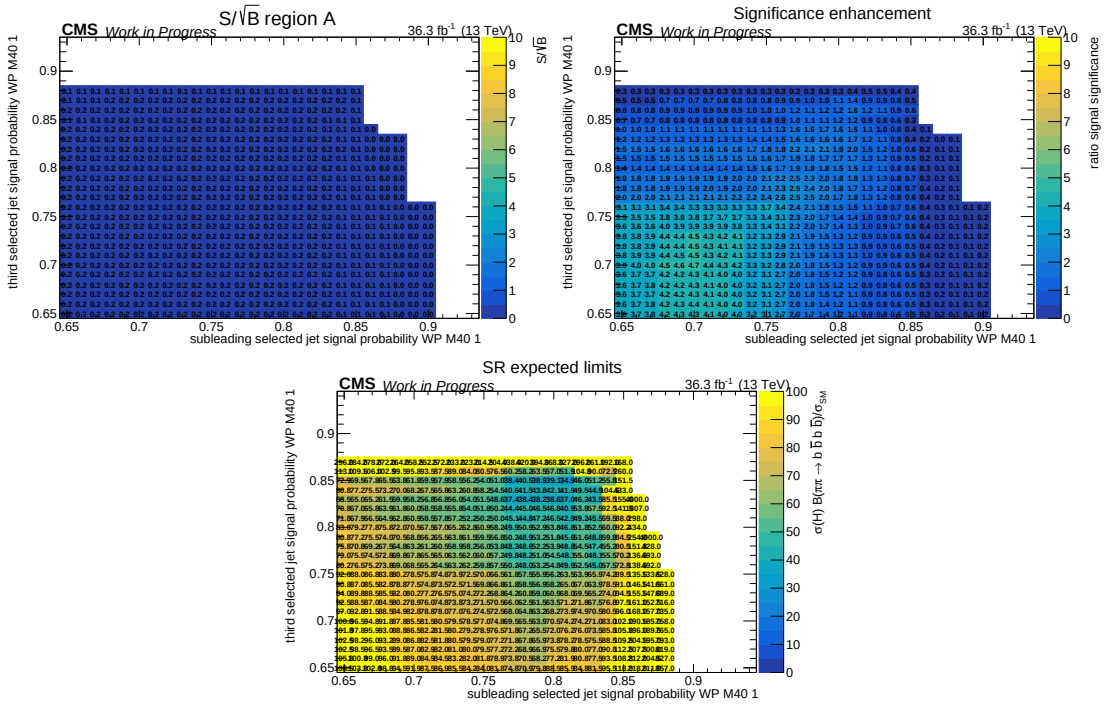

Figure E.18: Effect of various thresholds for the ABCD method on the analysis of LLPs with a mass of 40 GeV and a lifetime of 5 mm and the VBF Higgs production mode on: Signal significance (first row left), the significance enhancement Σ_{signal} (first row right), and blinded expected upper limits on the signal strength modifier in the SR (lower). Closure and its significance in $\overline{\text{SR}}$ can be found in Figure E.17.

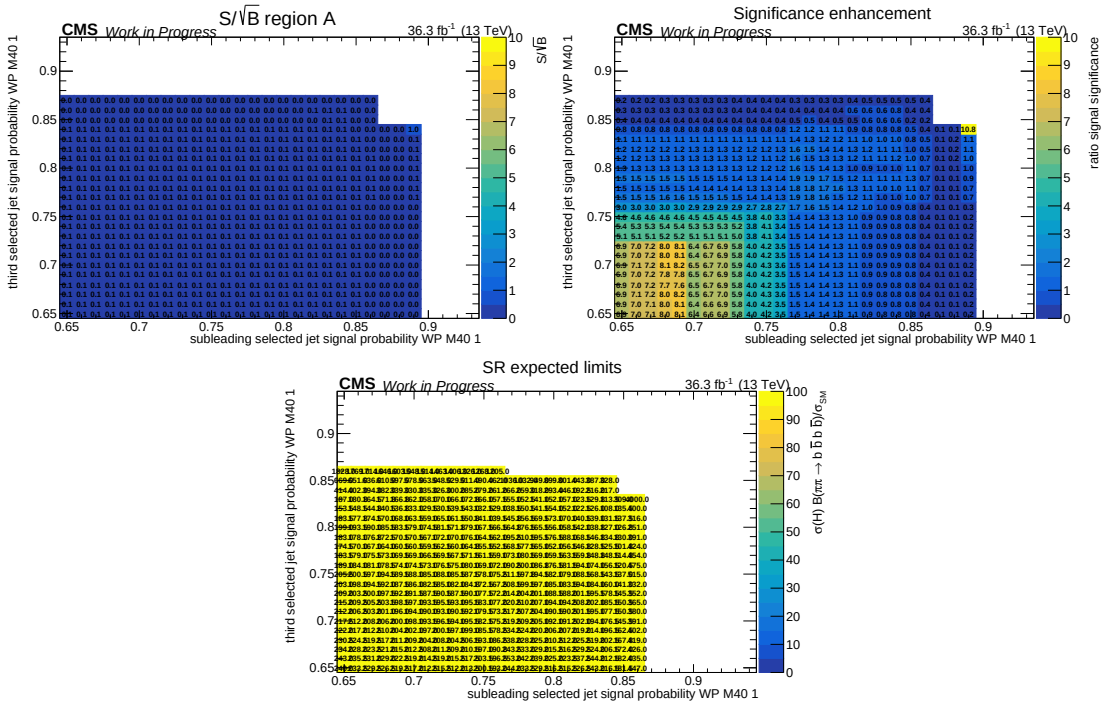

Figure E.19: Effect of various thresholds for the ABCD method on the analysis of LLPs with a mass of 40 GeV and a lifetime of 10 mm and the VBF Higgs production mode on: Signal significance (first row left), the significance enhancement Σ_{signal} (first row right), and blinded expected upper limits on the signal strength modifier in the SR (lower). Closure and its significance in $\overline{\text{SR}}$ can be found in Figure E.17.

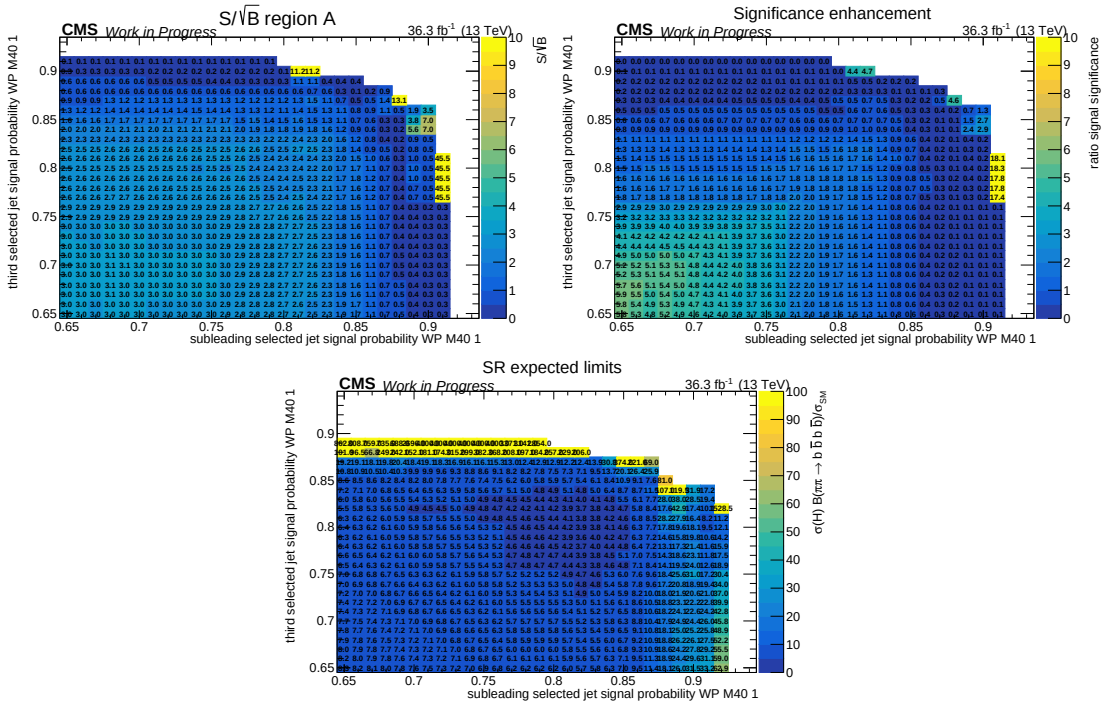

Figure E.20: Effect of various thresholds for the ABCD method on the analysis of LLPs with a mass of 40 GeV and a lifetime of 1 mm and the ggF Higgs production mode on: Signal significance (first row left), the significance enhancement Σ_{signal} (first row right), and blinded expected upper limits on the signal strength modifier in the SR (lower). Closure and its significance in $\overline{\text{SR}}$ can be found in Figure E.17.

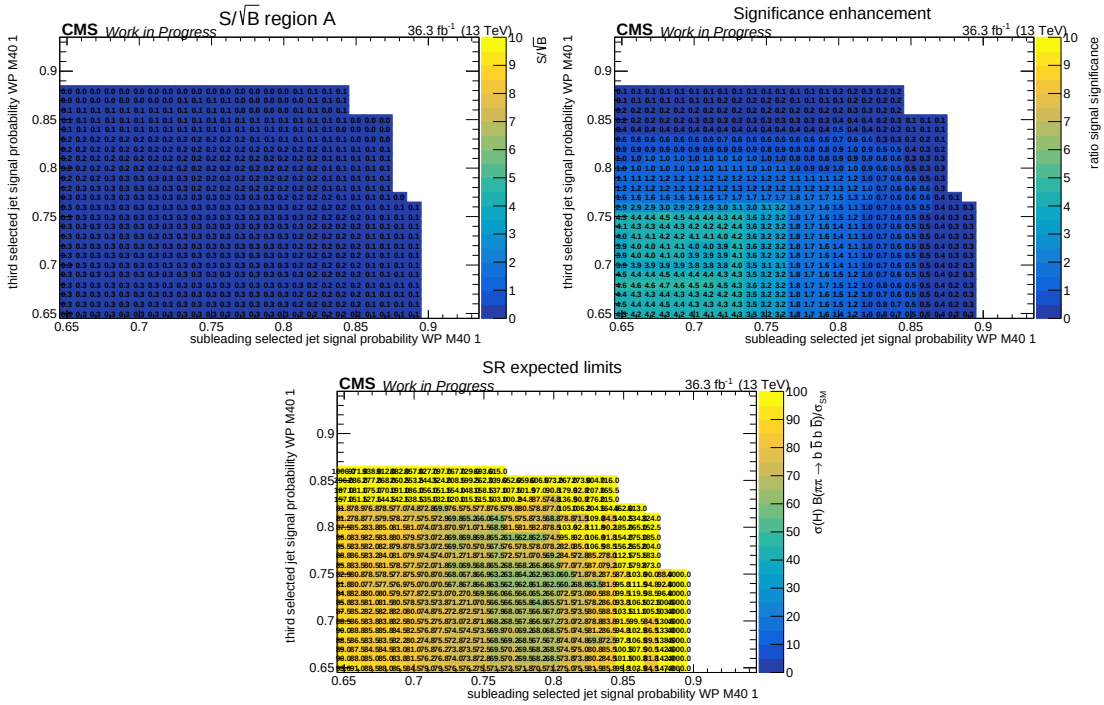

Figure E.21: Effect of various thresholds for the ABCD method on the analysis of LLPs with a mass of 40 GeV and a lifetime of 10 mm and the ggF Higgs production mode on: Signal significance (first row left), the significance enhancement Σ_{signal} (first row right), and blinded expected upper limits on the signal strength modifier in the SR (lower). Closure and its significance in $\overline{\text{SR}}$ can be found in Figure E.17.

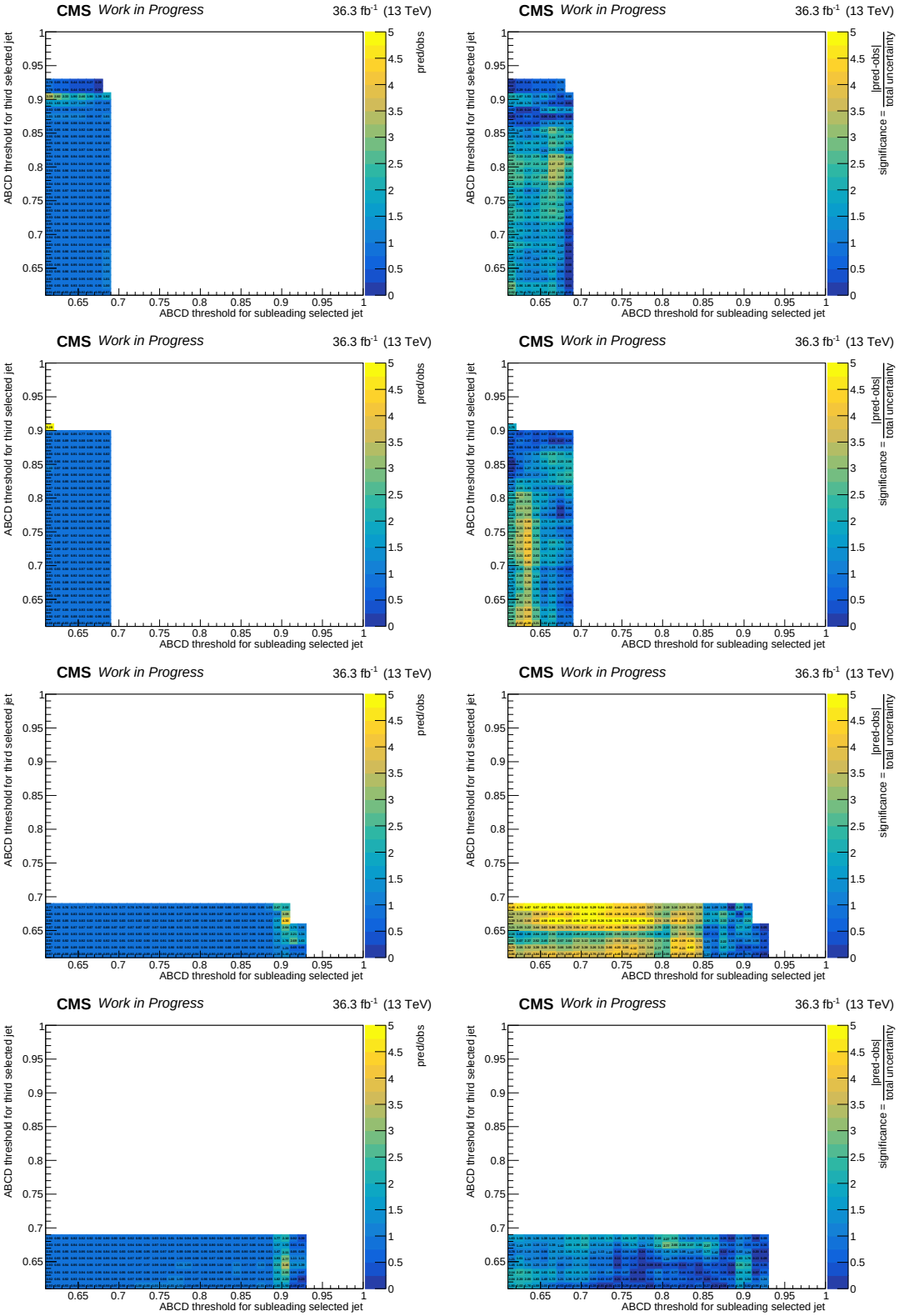

Figure E.22: The closure (left) and its significance (right) for the LLP mass of 40 GeV and 1 mm of the SR (first and third row) and $\overline{\text{SR}}$ (second and fourth row) of sideband 1 (upper two rows) and 2 (lower two rows).

E.5 Signal with LLP mass 55 GeV, lifetime 0 mm

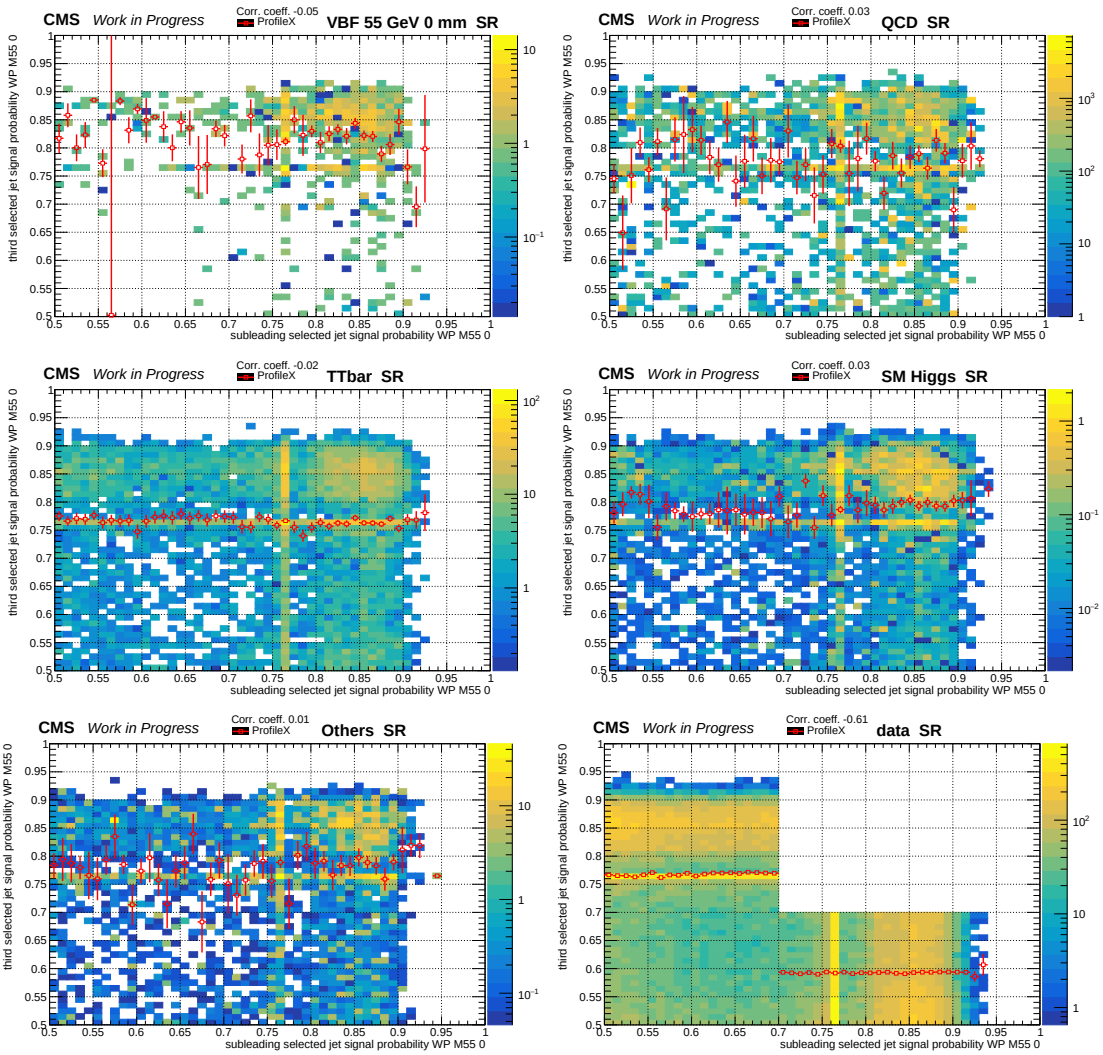

Figure E.23: Distributions of the DNN discriminant for the probability of LLPs of 55 GeV and 0 mm lifetime of the subleading and third of the selected jets in SR and define the regions for the background estimation method. The upper right region is the signal region (A). Red empty squares with error bars indicate the mean y-value of each bin. Distributions for signal (upper left), QCD multijet (upper right), $t\bar{t}$ (middle left), SM Higgs (middle right) and Others (lower left) are shown. For the distribution of data (lower right), an extended area of region A is not shown.

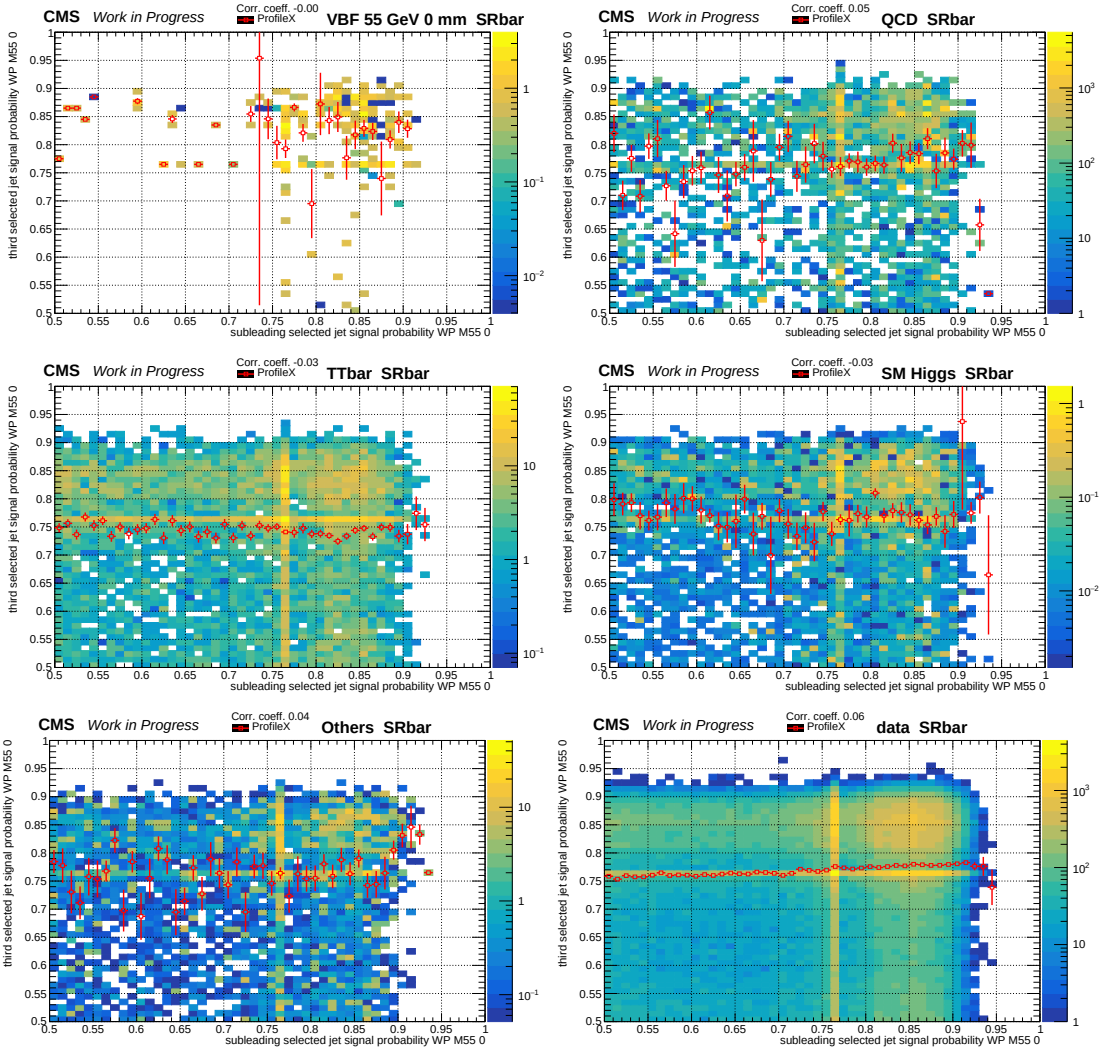

Figure E.24: Distributions of the DNN discriminant for the probability of LLPs of 55 GeV and 0 mm lifetime of the subleading and third of the selected jets in $\overline{\text{SR}}$ and define the regions for the background estimation method. Distributions for signal (upper left), QCD multijet (upper right), $t\bar{t}$ (middle left), SM Higgs (middle right), Others (lower left) and data (lower right) are shown.

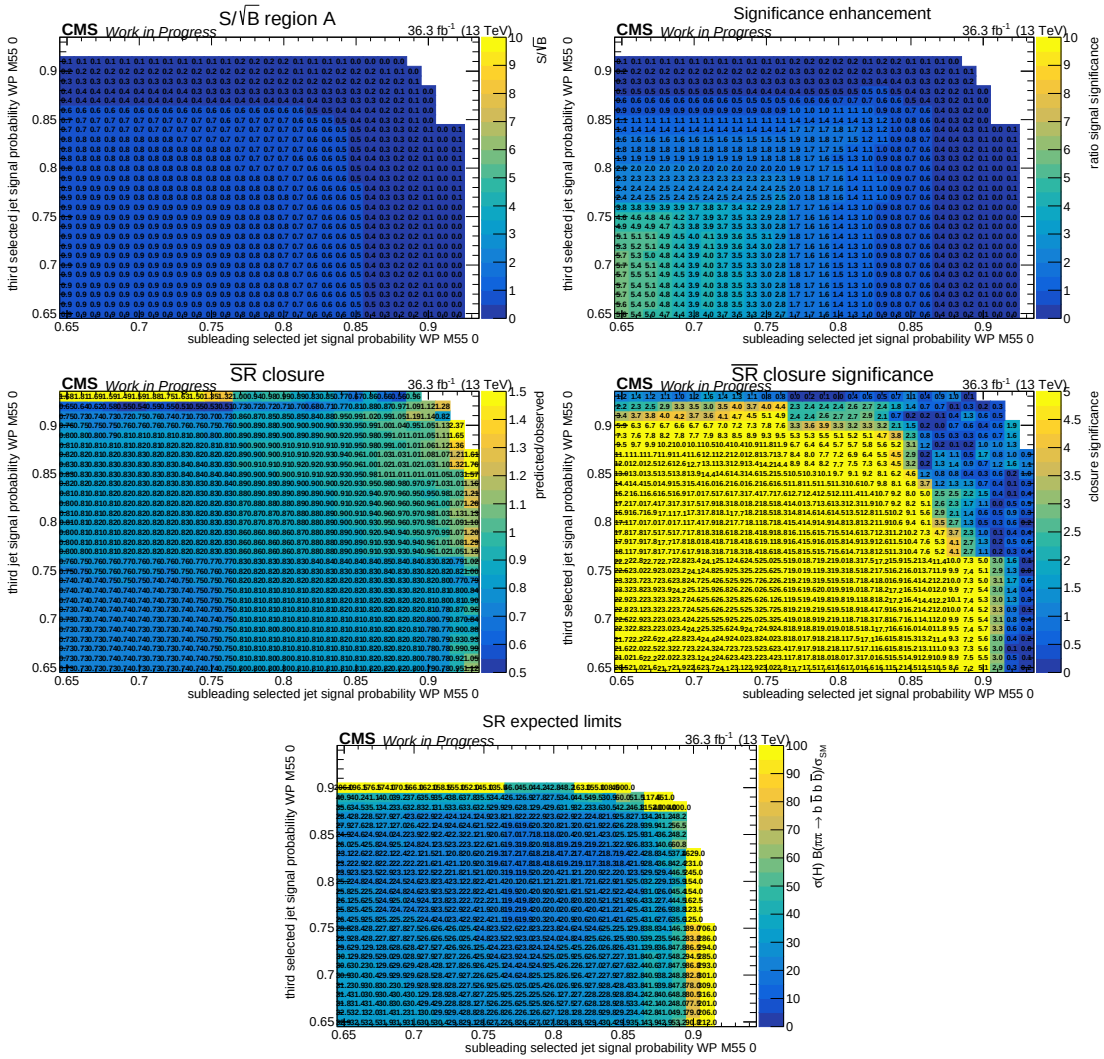

Figure E.25: Effect of various thresholds for the ABCD method on the analysis of LLPs with a mass of 55 GeV and a lifetime of 0 mm on: Signal significance (first row left), the significance enhancement Σ_{signal} (first row right), the closure using data in the $\overline{\text{SR}}$ (second row left) and its significance (second row right), and blinded expected upper limits on the signal strength modifier in the SR (lower). White bins indicate such regions where either the SM background yield or the signal yield was zero.

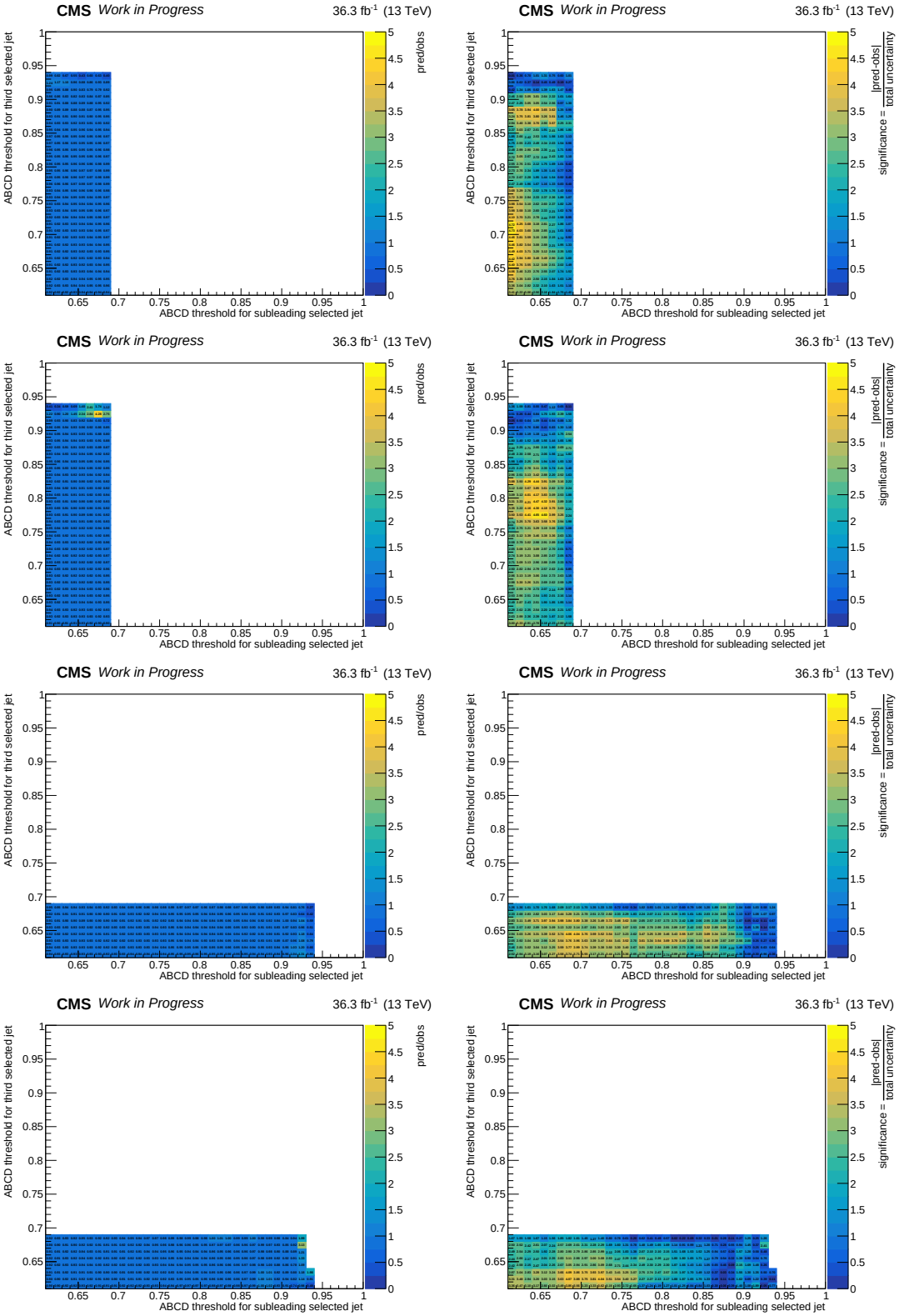

Figure E.26: The closure (left) and its significance (right) for the LLP mass of 55 GeV and 0 mm of the SR (first and third row) and $\overline{\text{SR}}$ (second and fourth row) of sideband 1 (upper two rows) and 2 (lower two rows).

E.6 Signal with LLP mass 55 GeV, lifetime 0.05 mm

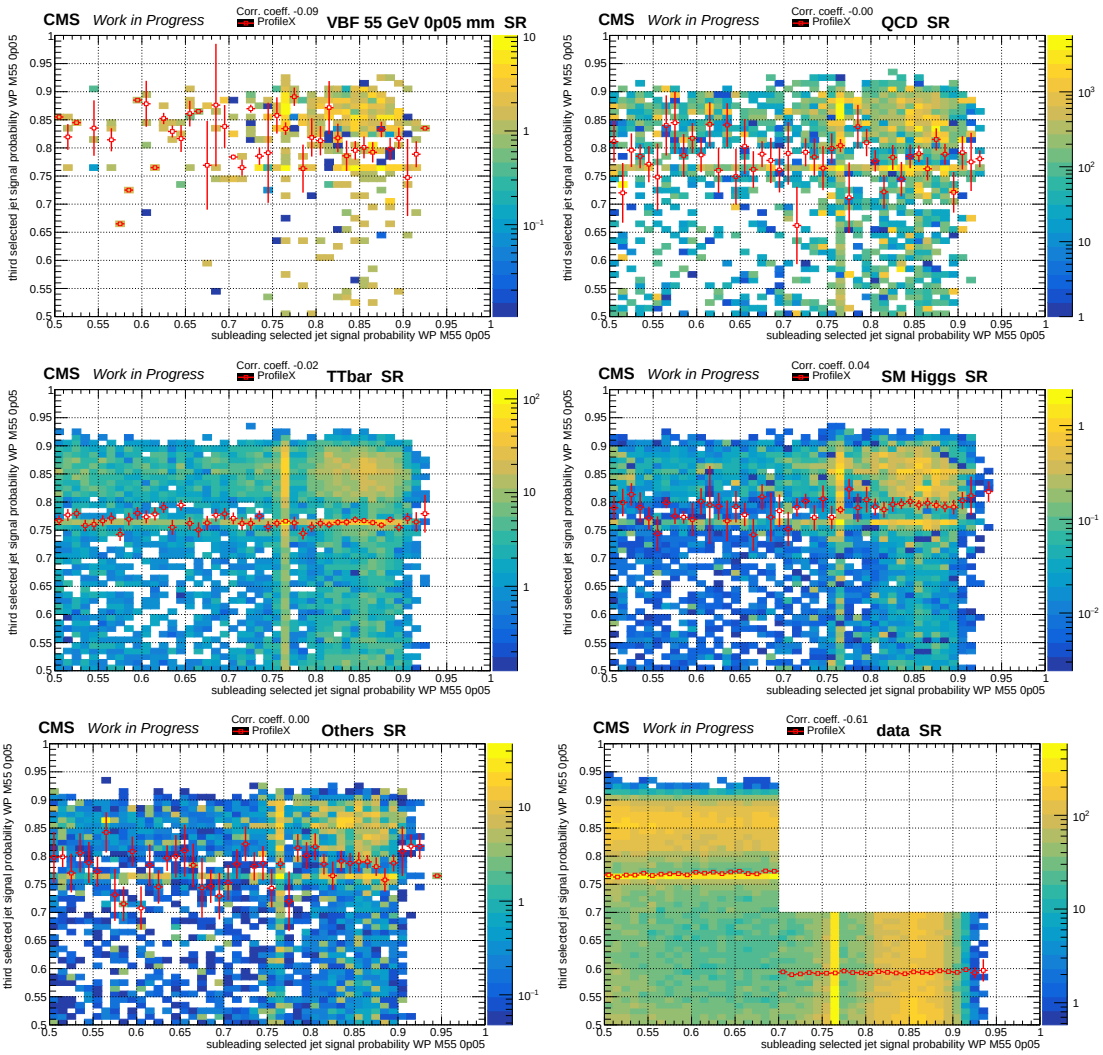

Figure E.27: Distributions of the DNN discriminant for the probability of LLPs of 55 GeV and 0.05 mm lifetime of the subleading and third of the selected jets in SR and define the regions for the background estimation method. The upper right region is the signal region (A). Red empty squares with error bars indicate the mean y-value of each bin. Distributions for signal (upper left), QCD multijet (upper right), $t\bar{t}$ (middle left), SM Higgs (middle right) and Others (lower left) are shown. For the distribution of data (lower right), an extended area of region A is not shown.

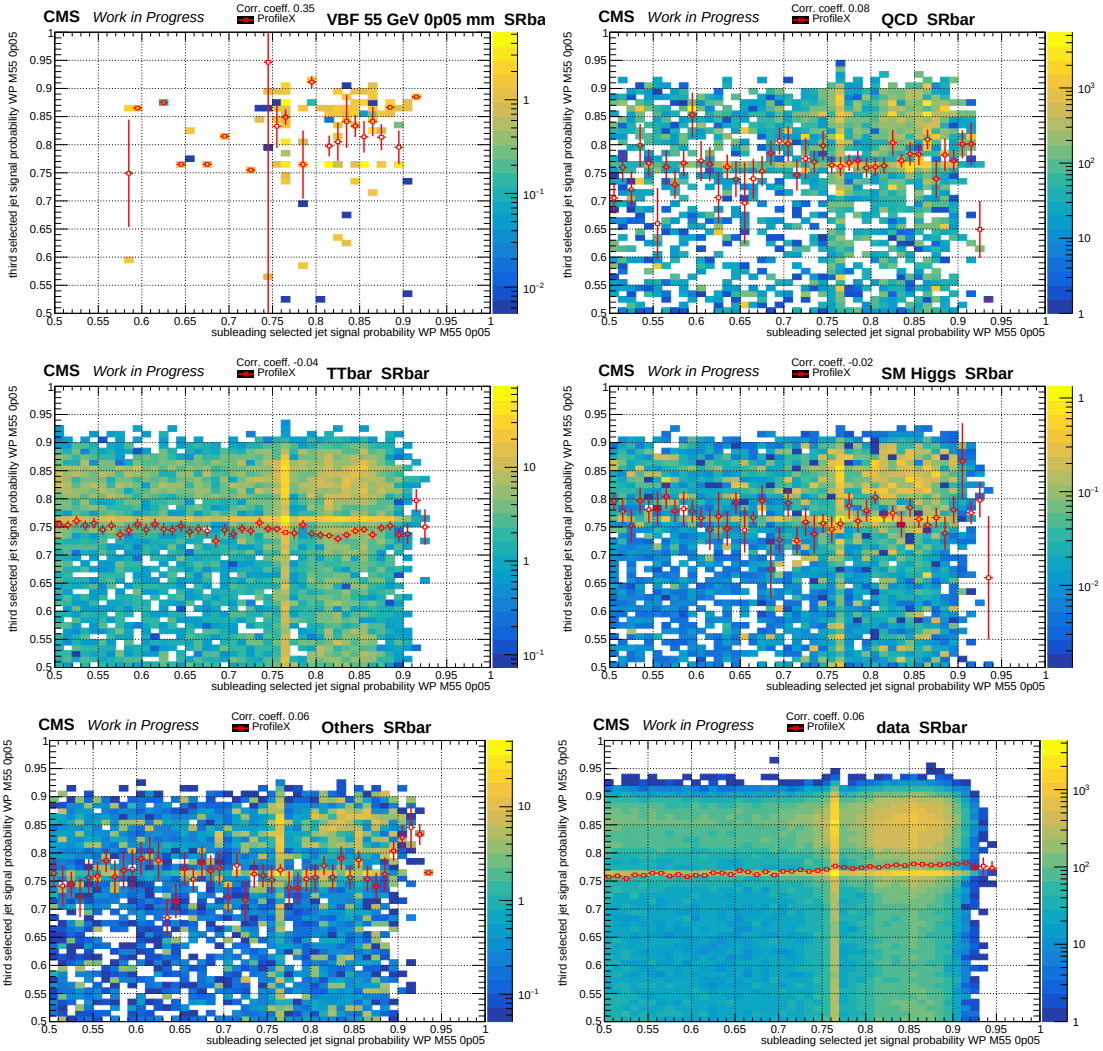

Figure E.28: Distributions of the DNN discriminant for the probability of LLPs of 55 GeV and 0.05 mm lifetime of the subleading and third of the selected jets in $\overline{\text{SR}}$ and define the regions for the background estimation method. Distributions for signal (upper left), QCD multijet (upper right), $t\bar{t}$ (middle left), SM Higgs (middle right), Others (lower left) and data (lower right) are shown.

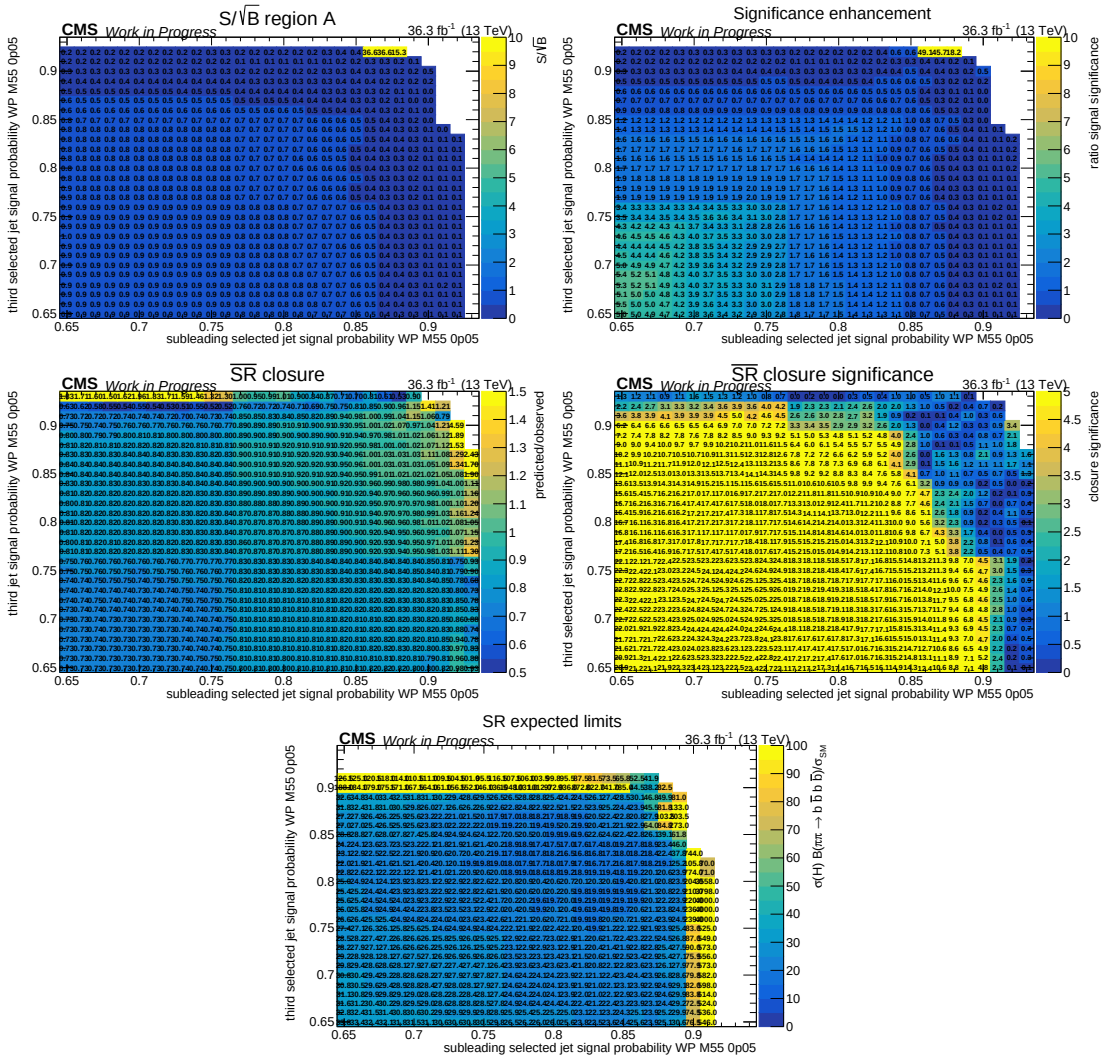

Figure E.29: Effect of various thresholds for the ABCD method on the analysis of LLPs with a mass of 55 GeV and a lifetime of 0.05 mm on: Signal significance (first row left), the significance enhancement Σ_{signal} (first row right), the closure using data in the $\overline{\text{SR}}$ (second row left) and its significance (second row right), and blinded expected upper limits on the signal strength modifier in the SR (lower). White bins indicate such regions where either the SM background yield or the signal yield was zero.

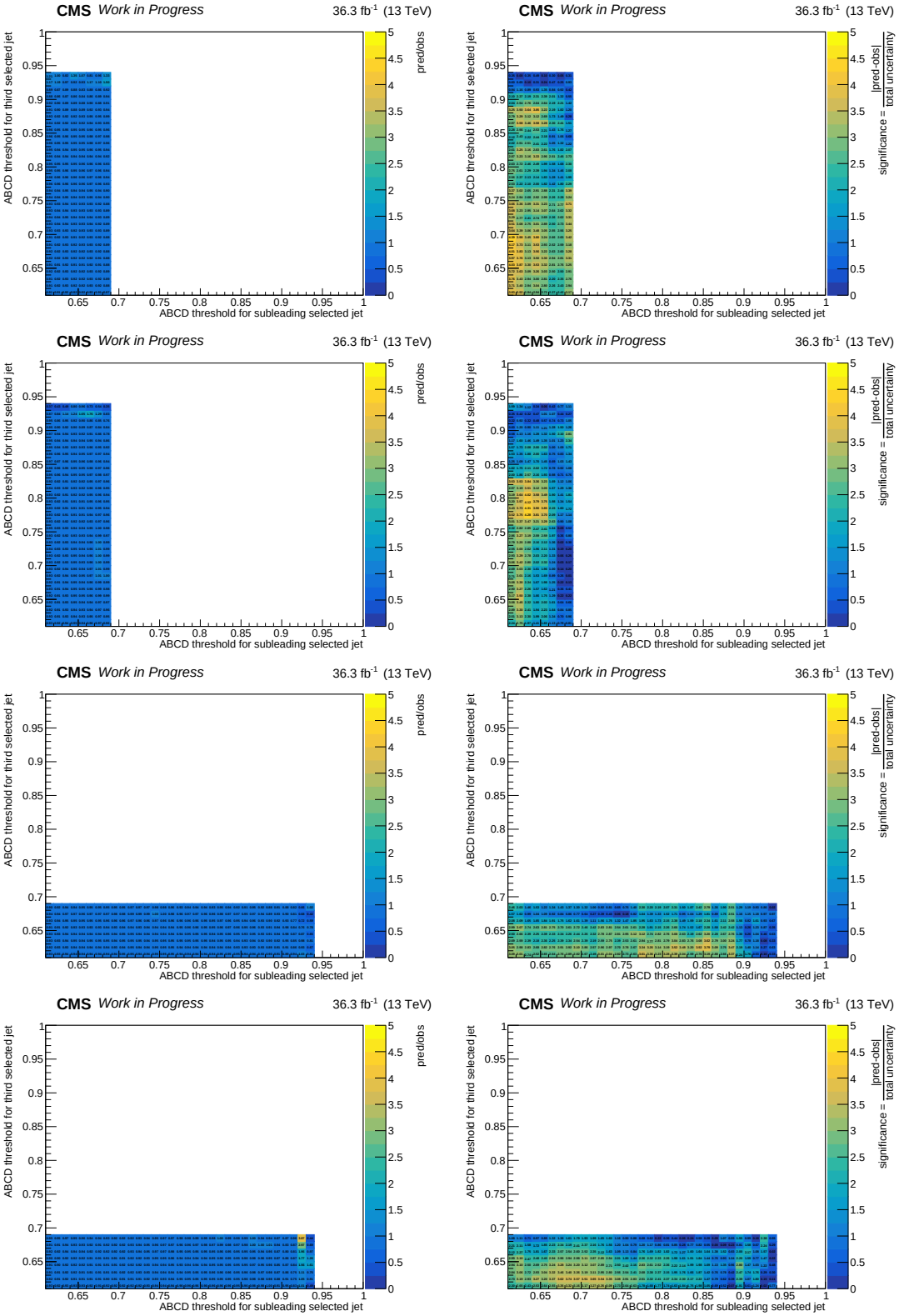

Figure E.30: The closure (left) and its significance (right) for the LLP mass of 55 GeV and 0.05 mm of the SR (first and third row) and $\overline{\text{SR}}$ (second and fourth row) of sideband 1 (upper two rows) and 2 (lower two rows).

E.7 Signal with LLP mass 55 GeV, lifetime 0.1 mm

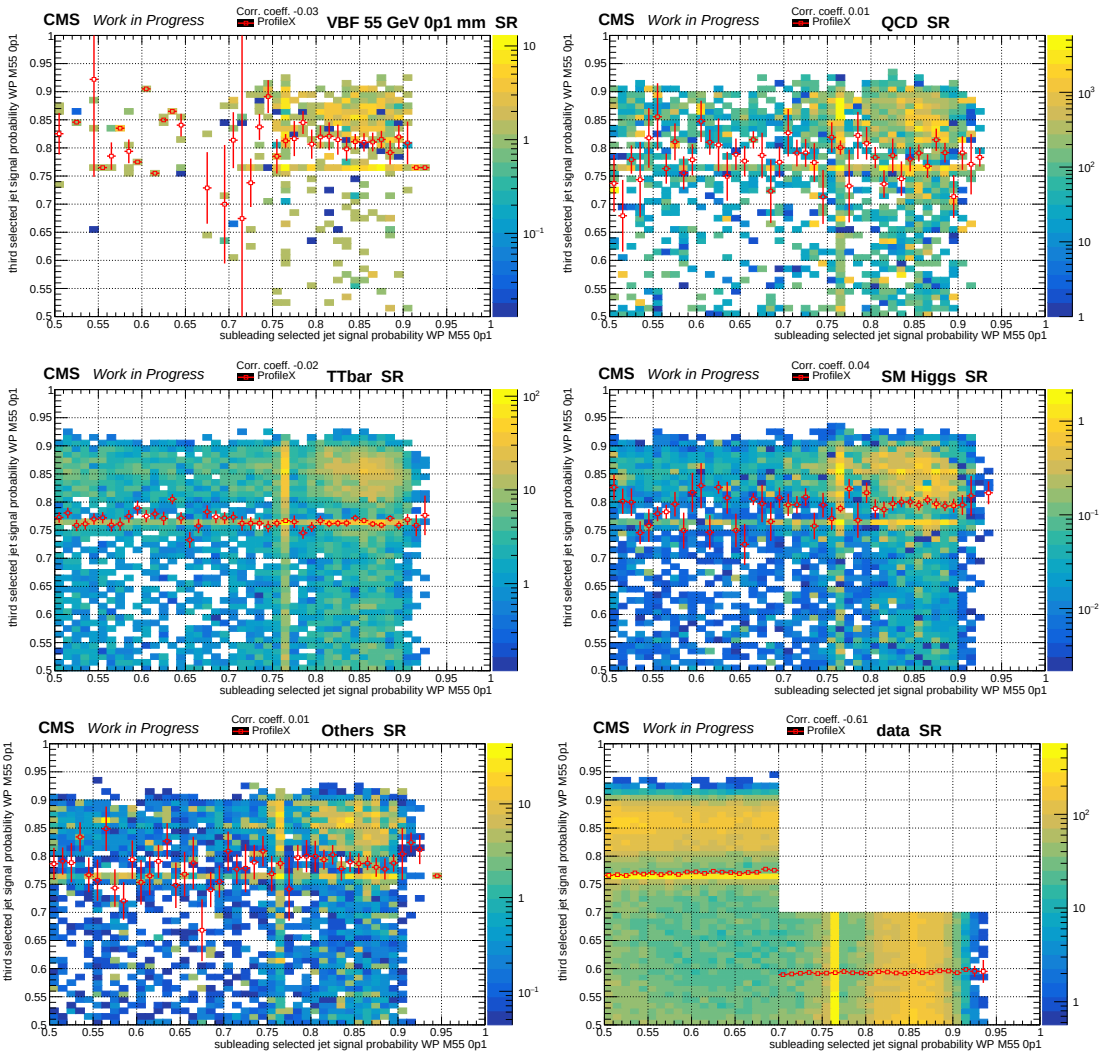

Figure E.31: Distributions of the DNN discriminant for the probability of LLPs of 55 GeV and 0.1 mm lifetime of the subleading and third of the selected jets in SR and define the regions for the background estimation method. The upper right region is the signal region (A). Red empty squares with error bars indicate the mean y-value of each bin. Distributions for signal (upper left), QCD multijet (upper right), $t\bar{t}$ (middle left), SM Higgs (middle right) and Others (lower left) are shown. For the distribution of data (lower right), an extended area of region A is not shown.

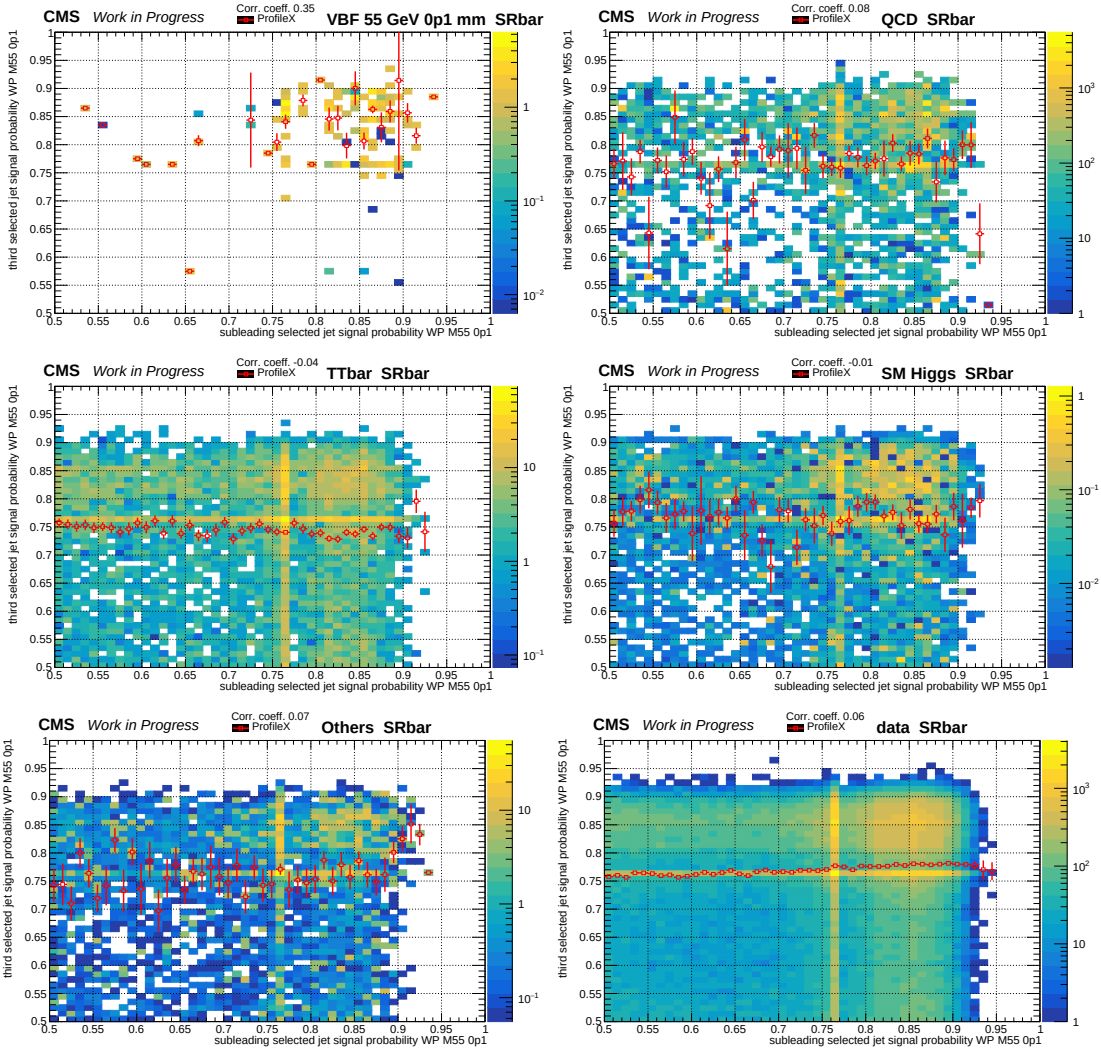

Figure E.32: Distributions of the DNN discriminant for the probability of LLPs of 55 GeV and 0.1 mm lifetime of the subleading and third of the selected jets in $\overline{\text{SR}}$ and define the regions for the background estimation method. Distributions for signal (upper left), QCD multijet (upper right), $t\bar{t}$ (middle left), SM Higgs (middle right), Others (lower left) and data (lower right) are shown.

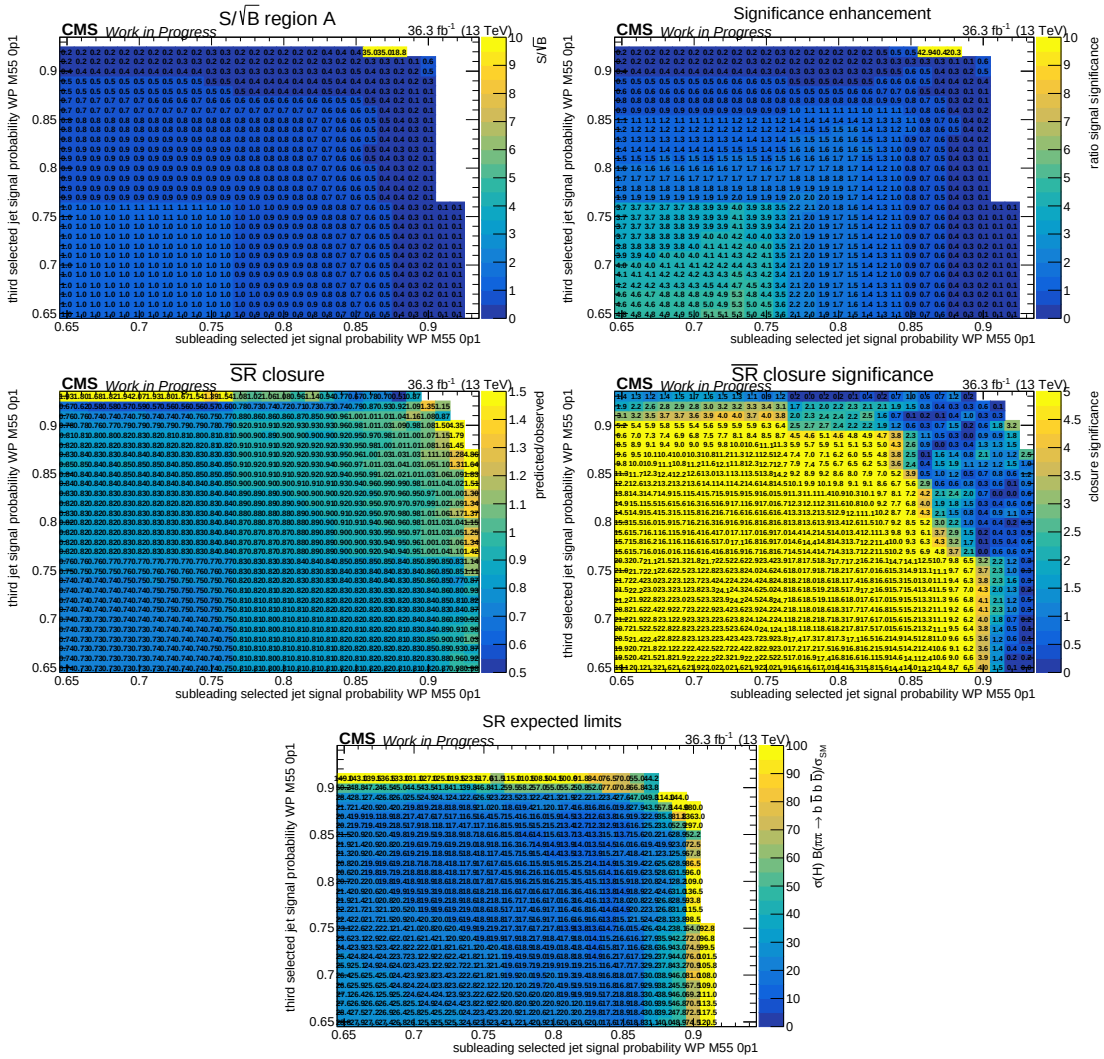

Figure E.33: Effect of various thresholds for the ABCD method on the analysis of LLPs with a mass of 55 GeV and a lifetime of 0.1 mm on: Signal significance (first row left), the significance enhancement Σ_{signal} (first row right), the closure using data in the $\overline{\text{SR}}$ (second row left) and its significance (second row right), and blinded expected upper limits on the signal strength modifier in the SR (lower). White bins indicate such regions where either the SM background yield or the signal yield was zero.

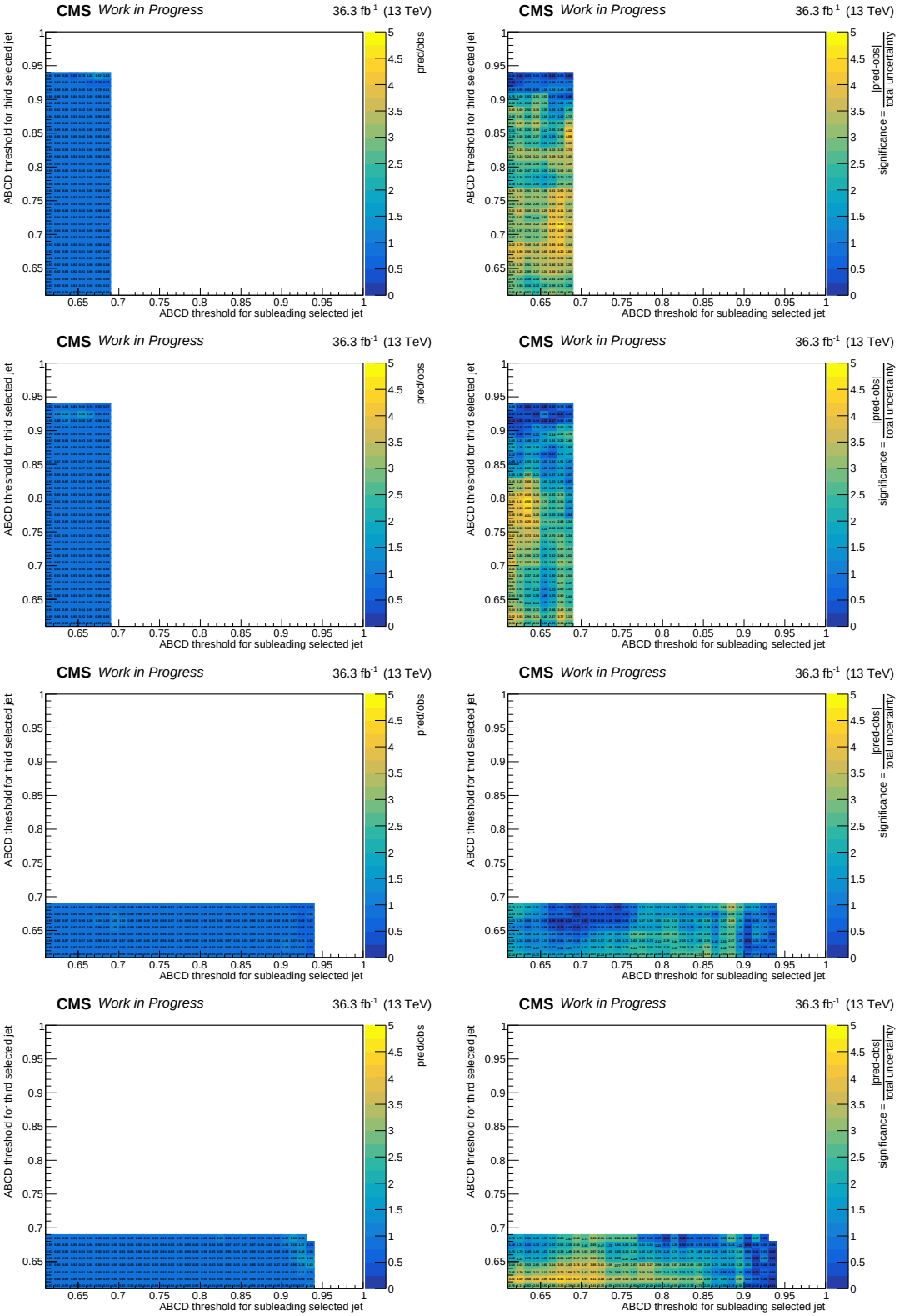

Figure E.34: The closure (left) and its significance (right) for the LLP mass of 55 GeV and 0.1 mm of the SR (first and third row) and $\overline{\text{SR}}$ (second and fourth row) of sideband 1 (upper two rows) and 2 (lower two rows).

E.8 Signal with LLP mass 55 GeV, lifetime 1 mm

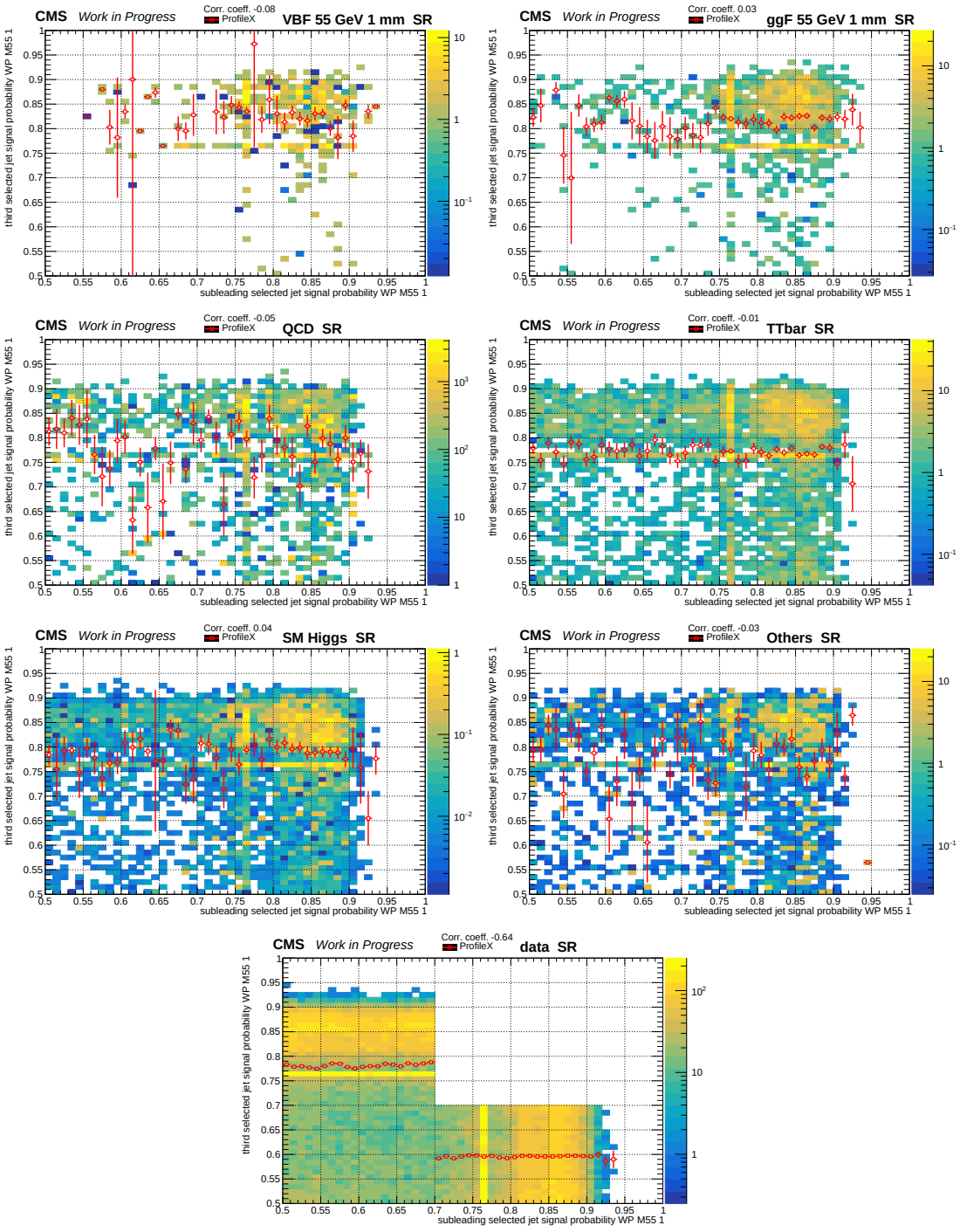

Figure E.35: Distributions in the SR of the DNN discriminant for the probability of LLPs of 55 GeV and 1 mm lifetime of the subleading and third selected jets for: VBF (upper left) and ggF (upper right) Higgs production mode signal, QCD multijet (second row left), $t\bar{t}$ (second row right), SM Higgs (third row left). For the distribution of data (lower), region A is not shown.

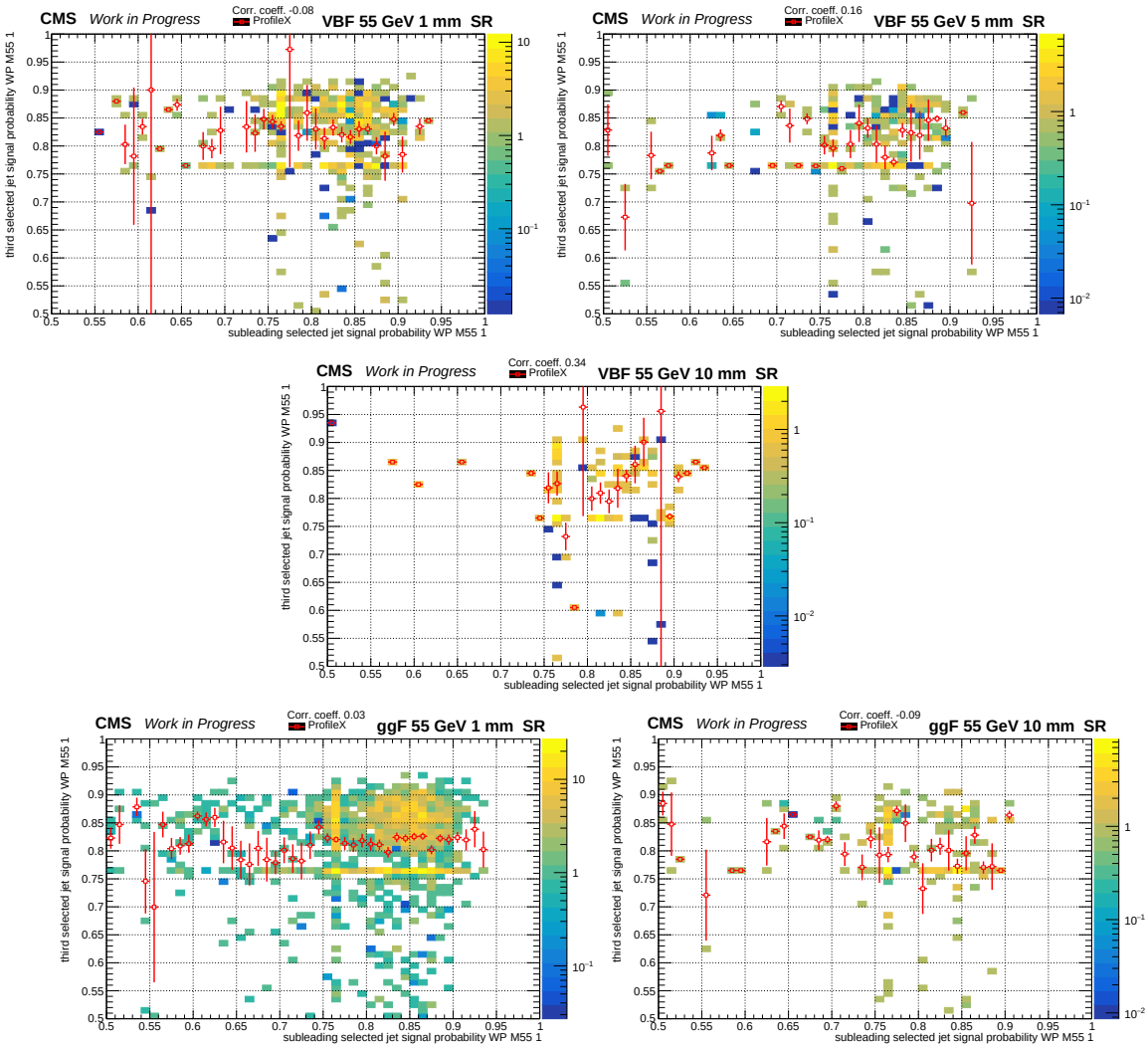

Figure E.36: Distributions of the DNN discriminant for different signal models for the analysis of LLPs of 55 GeV and 1 mm lifetime of the two selected jets in SR and define the regions for the background estimation method. Distributions for VBF Higgs produced signal with LLPs of 1 mm lifetime (upper left), 5 mm (upper right) and 10 mm (second row). ggF Higgs production mode with 1 mm (third row left) and 10 mm (third row right).

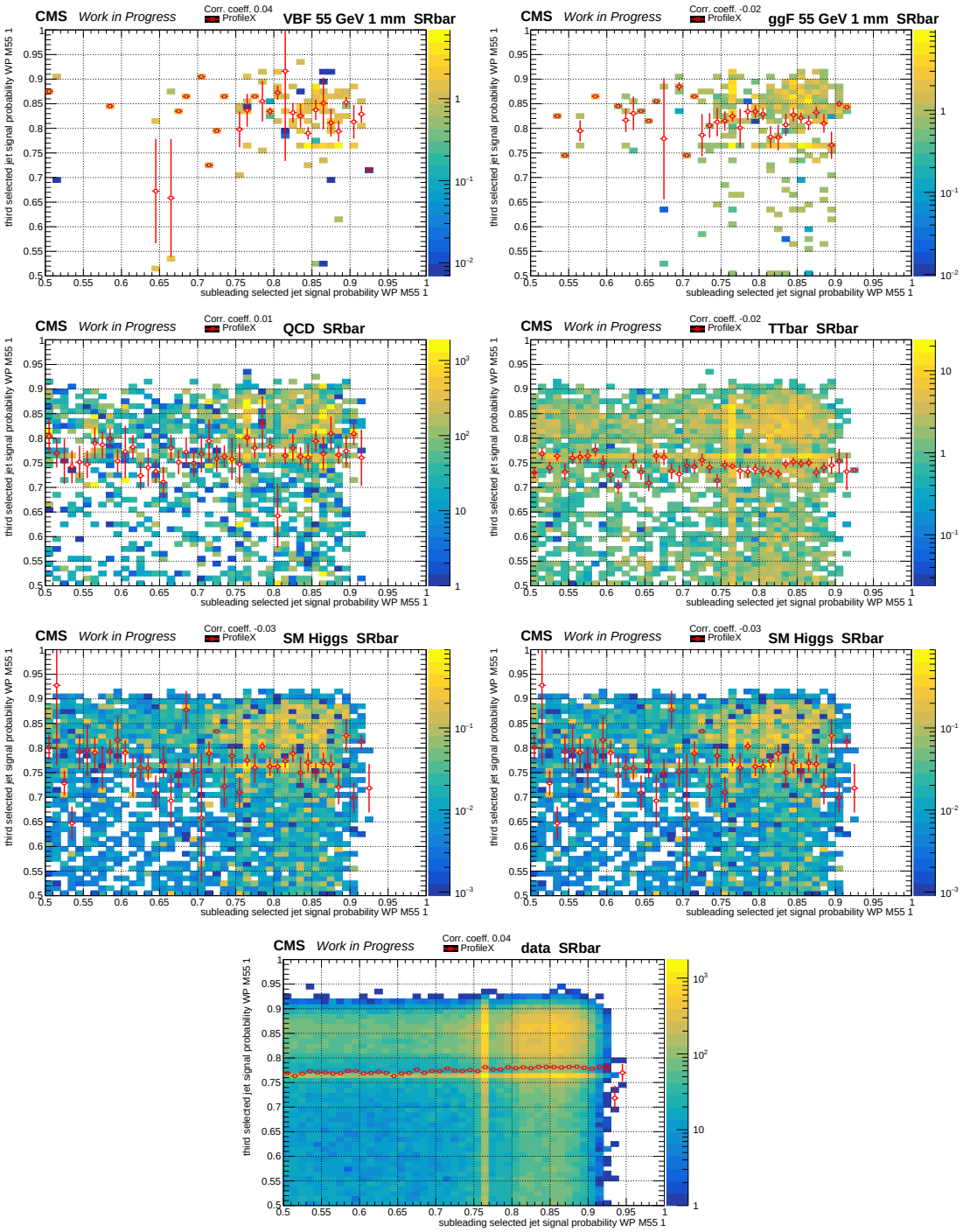

Figure E.37: Distributions in the $\overline{\text{SR}}$ of the DNN discriminant for the probability of LLPs of 55 GeV and 1 mm lifetime of the subleading and third selected jets for: VBF (upper left) and ggF (upper right) Higgs production mode signal, QCD multijet (second row left), $t\bar{t}$ (second row right), SM Higgs (third row left), Others (third row right) and data (lower).

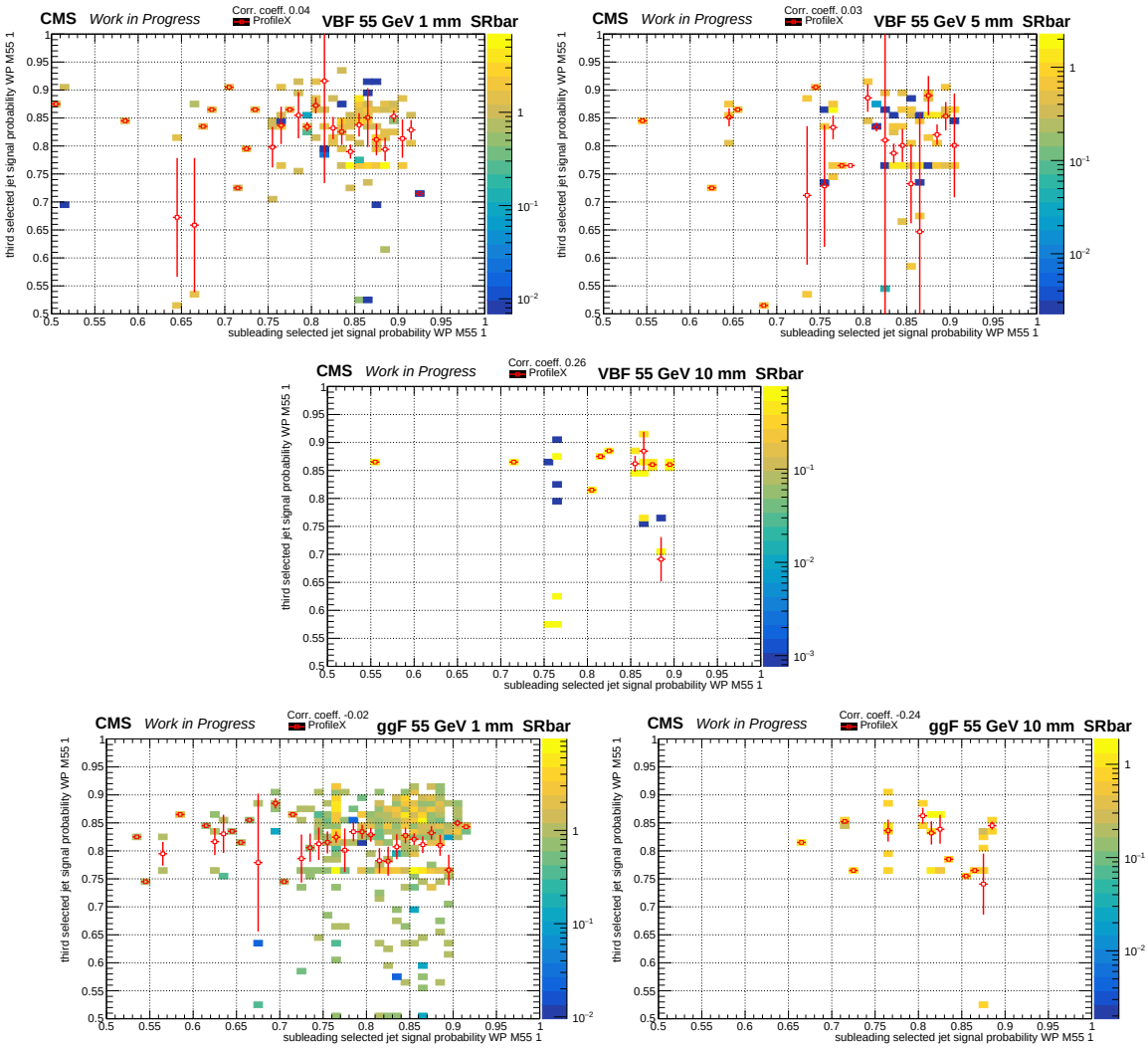

Figure E.38: Distributions of the DNN discriminant for different signal models for the analysis of LLPs of 55 GeV and 1 mm lifetime of the two selected jets in $\overline{\text{SR}}$ and define the regions for the background estimation method. Distributions for VBF Higgs produced signal with LLPs of 1 mm lifetime (upper left), 5 mm (upper right) and 10 mm (second row). ggF Higgs production mode with 1 mm (third row left) and 10 mm (third row right).

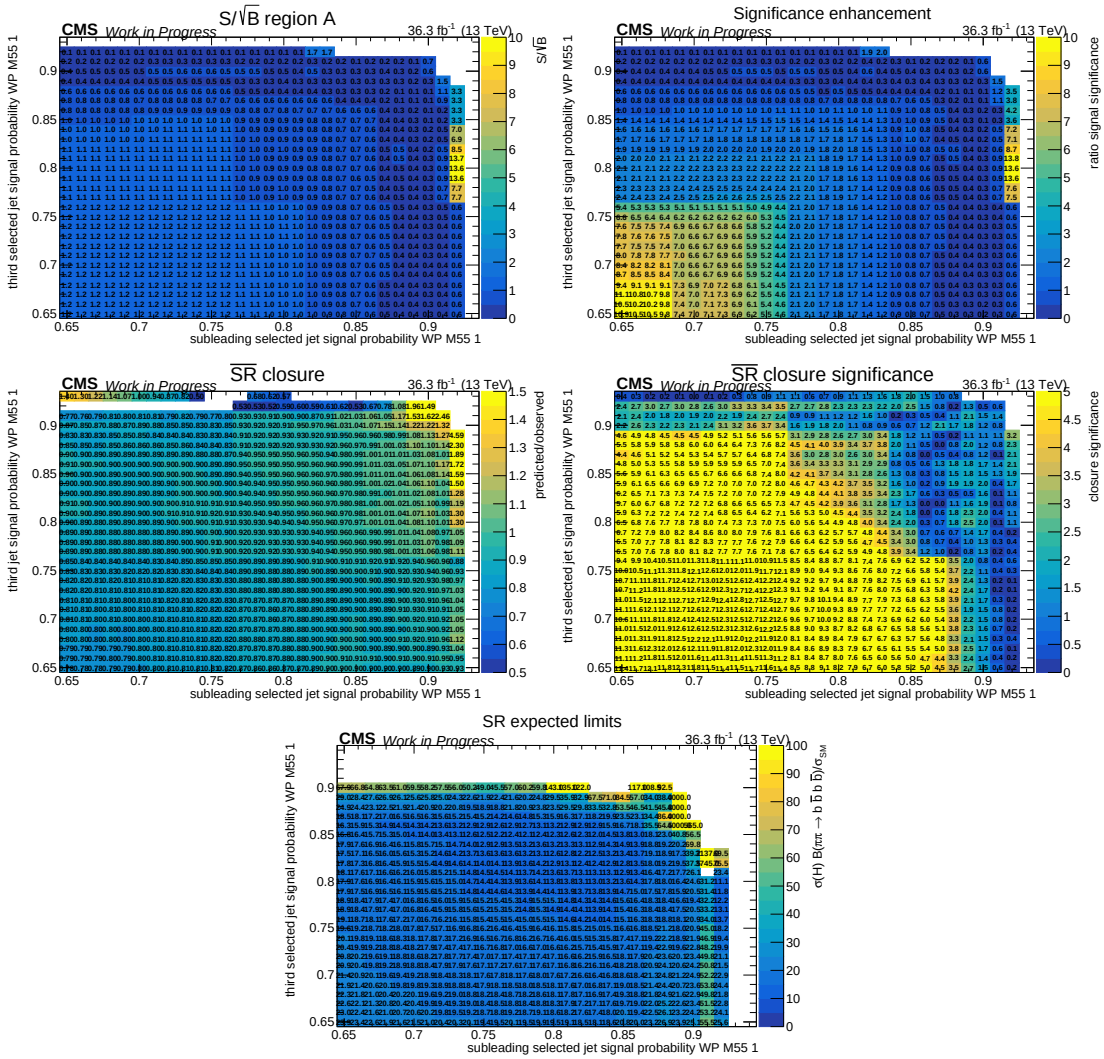

Figure E.39: Effect of various thresholds for the ABCD method on the analysis of LLPs with a mass of 55 GeV and a lifetime of 1 mm on: Signal significance (first row left), the significance enhancement Σ_{signal} (first row right), the closure using data in the $\overline{\text{SR}}$ (second row left) and its significance (second row right), and blinded expected upper limits on the signal strength modifier in the SR (lower). White bins indicate such regions where either the SM background yield or the signal yield was zero.

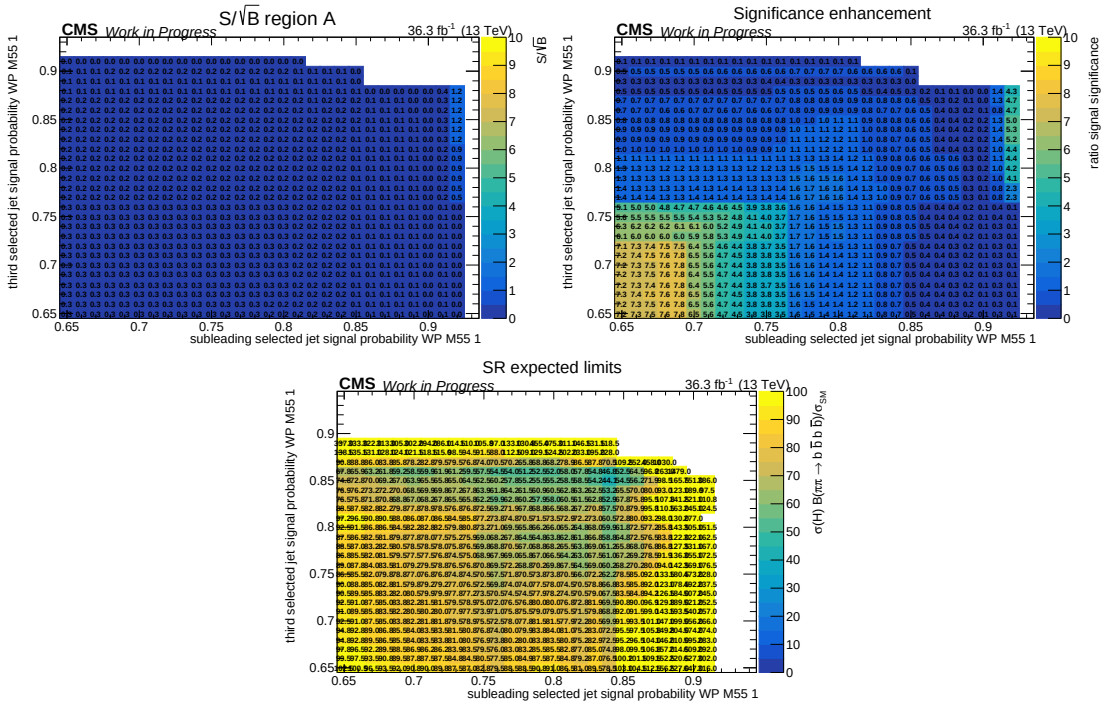

Figure E.40: Effect of various thresholds for the ABCD method on the analysis of LLPs with a mass of 55 GeV and a lifetime of 5 mm and the VBF Higgs production mode on: Signal significance (first row left), the significance enhancement Σ_{signal} (first row right), the closure using data in the $\overline{\text{SR}}$ (second row left) and its significance (second row right), and blinded expected upper limits on the signal strength modifier in the SR (lower). White bins indicate such regions where either the SM background yield or the signal yield was zero.

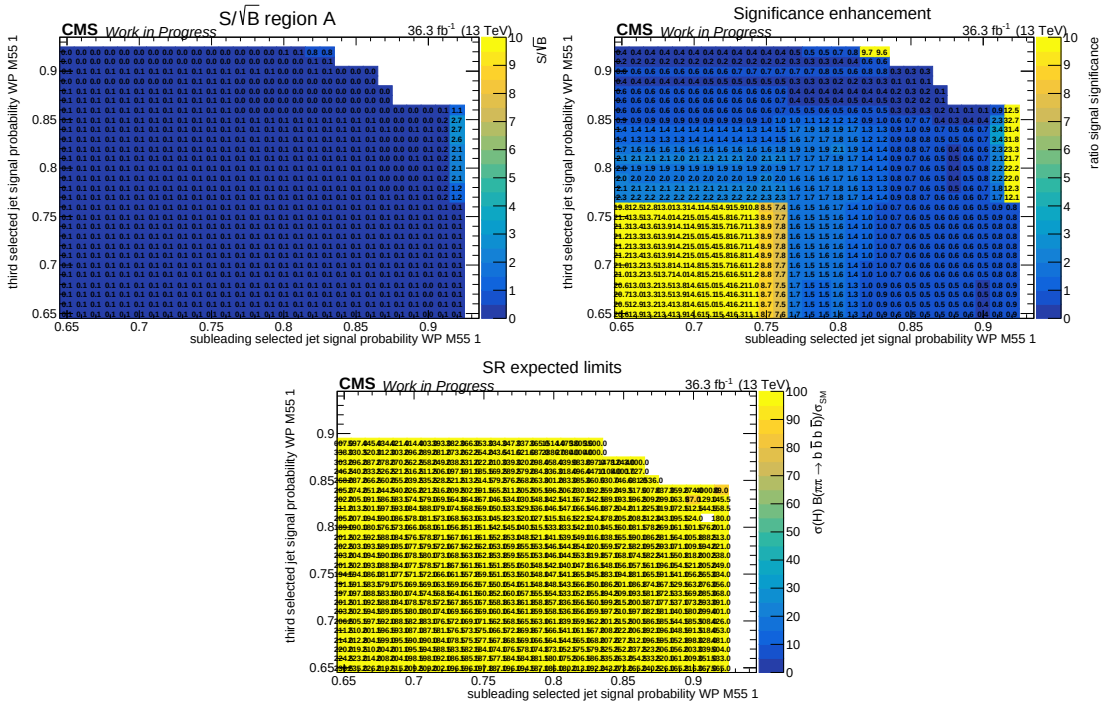

Figure E.41: Effect of various thresholds for the ABCD method on the analysis of LLPs with a mass of 55 GeV and a lifetime of 10 mm and the VBF Higgs production mode on: Signal significance (first row left), the significance enhancement Σ_{signal} (first row right), the closure using data in the $\overline{\text{SR}}$ (second row left) and its significance (second row right), and blinded expected upper limits on the signal strength modifier in the SR (lower). White bins indicate such regions where either the SM background yield or the signal yield was zero.

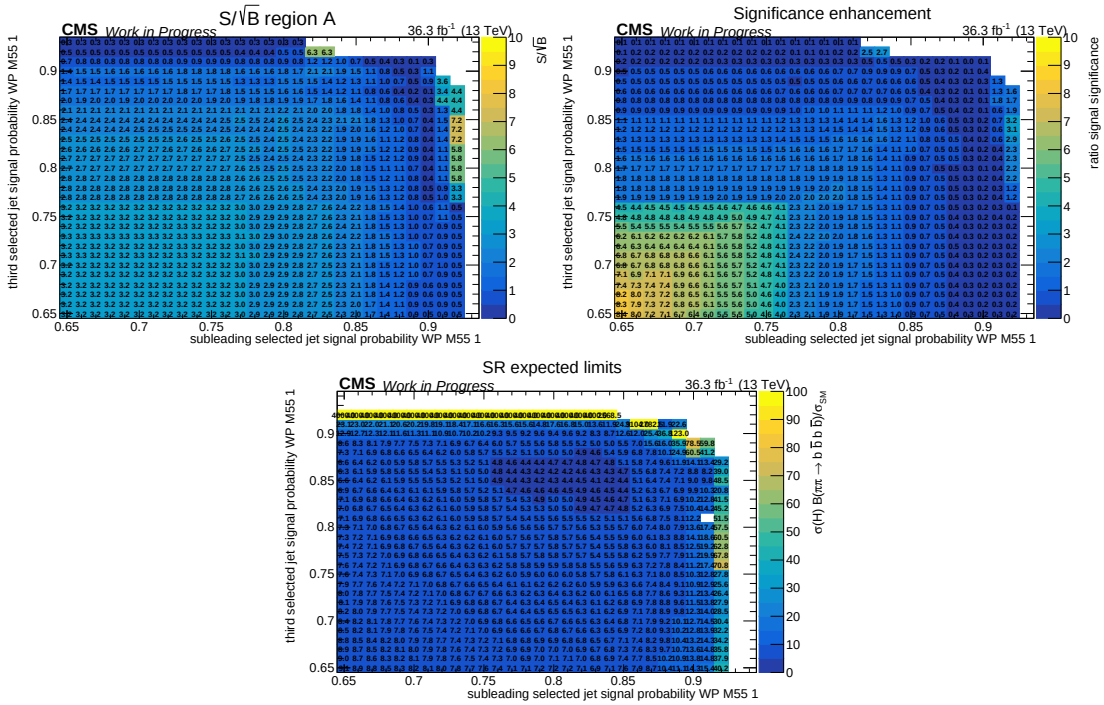

Figure E.42: Effect of various thresholds for the ABCD method on the analysis of LLPs with a mass of 55 GeV and a lifetime of 1 mm and the ggF Higgs production mode on: Signal significance (first row left), the significance enhancement Σ_{signal} (first row right), the closure using data in the $\overline{\text{SR}}$ (second row left) and its significance (second row right), and blinded expected upper limits on the signal strength modifier in the SR (lower). White bins indicate such regions where either the SM background yield or the signal yield was zero.

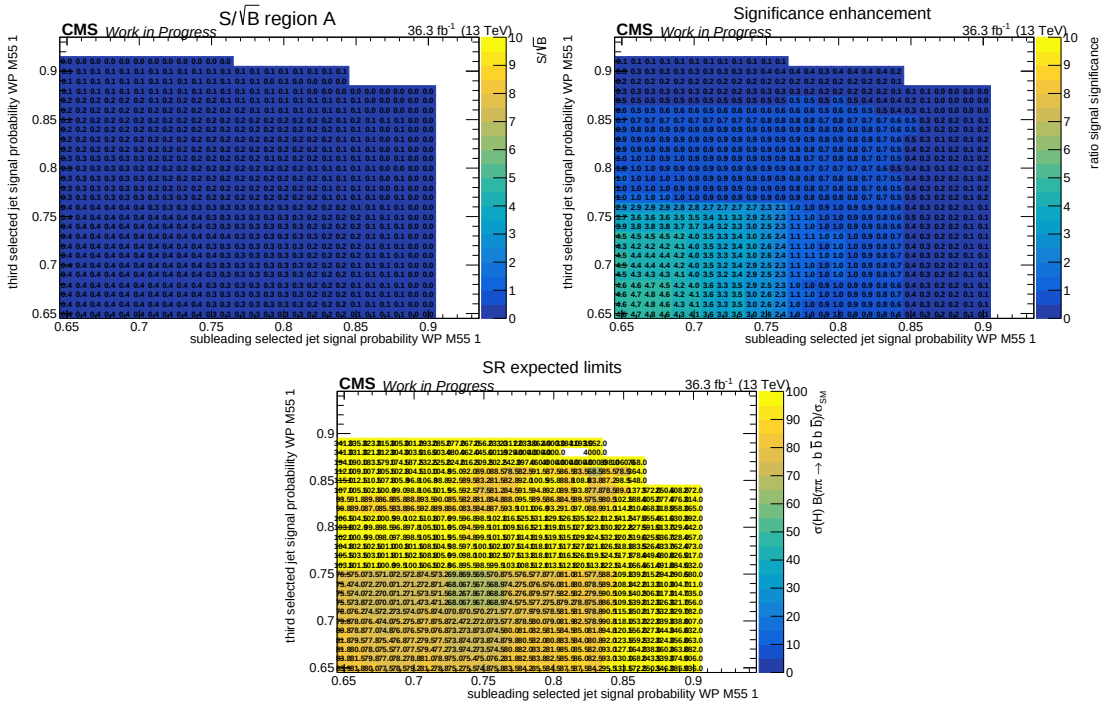

Figure E.43: Effect of various thresholds for the ABCD method on the analysis of LLPs with a mass of 55 GeV and a lifetime of 10 mm and the ggF Higgs production mode on: Signal significance (first row left), the significance enhancement Σ_{signal} (first row right), the closure using data in the $\overline{\text{SR}}$ (second row left) and its significance (second row right), and blinded expected upper limits on the signal strength modifier in the SR (lower). White bins indicate such regions where either the SM background yield or the signal yield was zero.

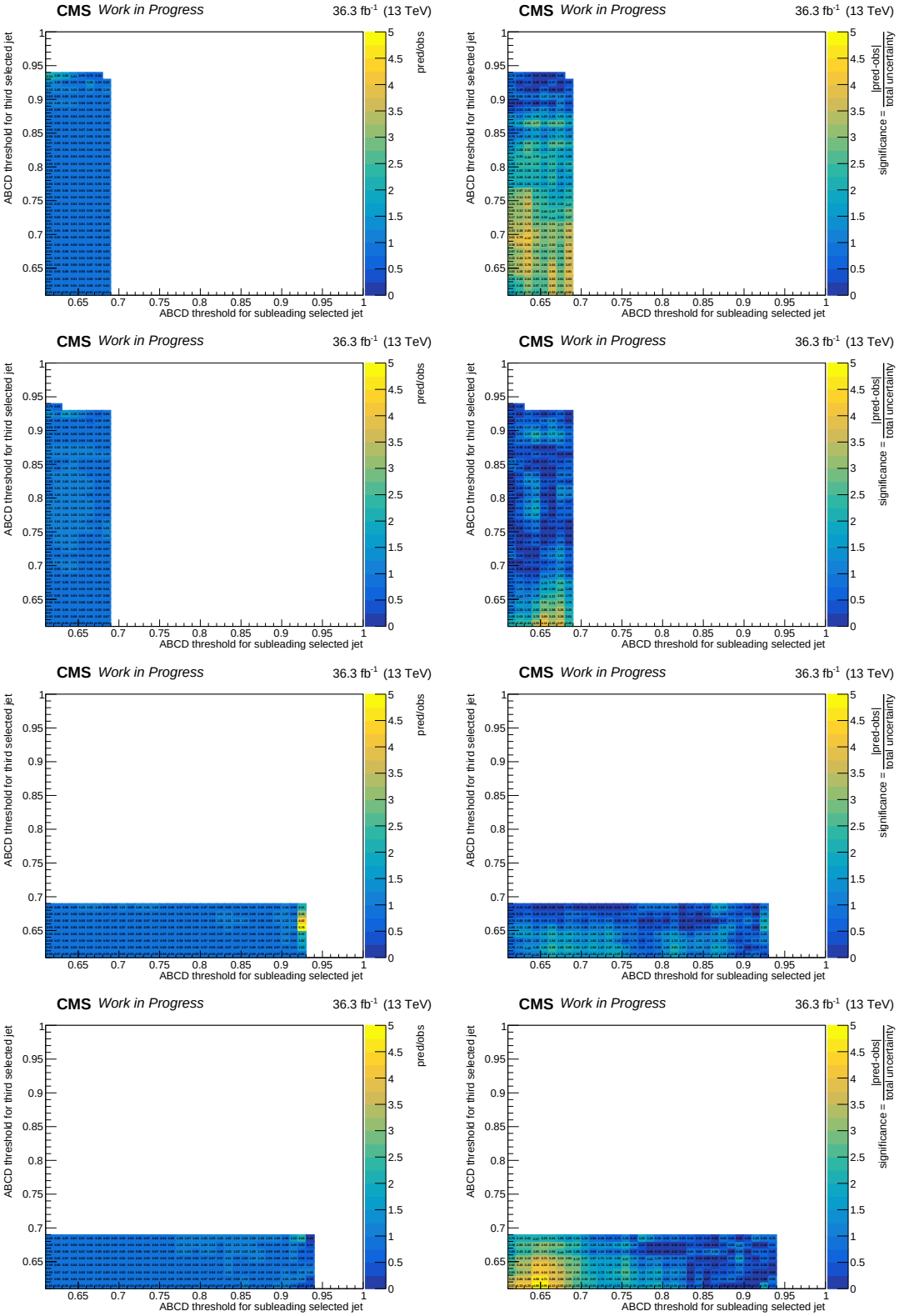

Figure E.44: The closure (left) and its significance (right) for the LLP mass of 55 GeV and 1 mm of the SR (first and third row) and $\overline{\text{SR}}$ (second and fourth row) of sideband 1 (upper two rows) and 2 (lower two rows).

Appendix F Unblinding Procedure

During the unblinding procedure, pull distributions, as well as the prefit and postfit yields of all mass-lifetime combinations and the background-only and signal-plus-background hypotheses were investigated. In the following the remaining distributions and tables of the boosted and the resolved topology can be found in Sections F.1 and F.2, respectively.

F.1 Boosted Topology

F.1.1 Lifetime 0 mm

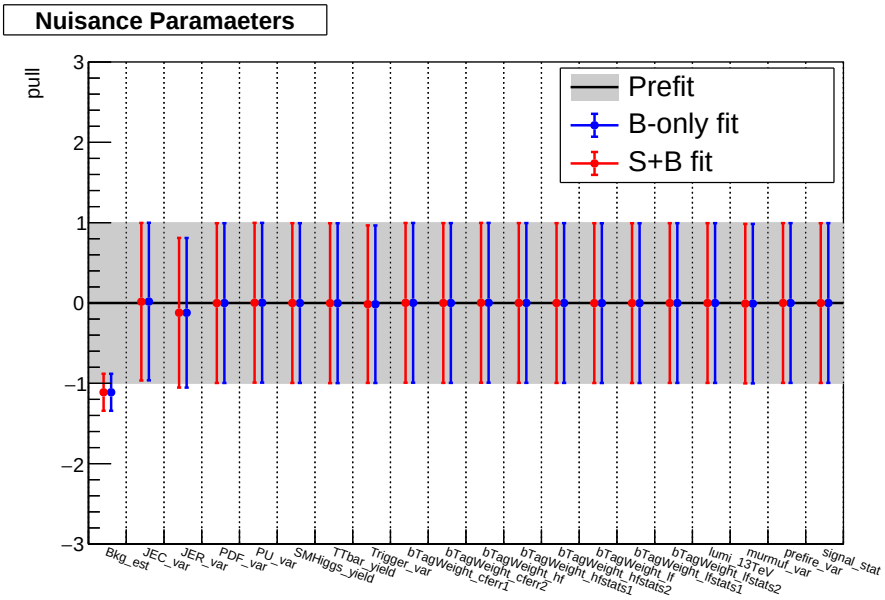

Figure F.1: The pulls of different nuisance parameters for the background-only and signal-plus-background fits to the Asimov pseudodata with $\mu = 1$ hypothesis for the LLP lifetime of 0 mm.

Table F.1: Prefit and postfit yields for background-only and signal-plus-background hypotheses of analysis for 15 GeV 0 mm.

	Prefit yield	Postfit yield	
Sample		b only	s+b
Signal	9.583 ± 11.709	0.000 ± 0.000	0.000 ± 0.002
QCD pred	167.821 ± 61.716	100.035 ± 10.776	100.041 ± 10.994
$t\bar{t}$	1.776 ± 5.366	1.207 ± 5.561	1.211 ± 4.663
SM Higgs	0.245 ± 0.476	0.169 ± 0.358	0.169 ± 0.390
Data	99.000	99.000	99.000
total signal	9.583 ± 11.709	0.000 ± 0.000	0.000 ± 0.002
total background	169.842 ± 62.067	101.411 ± 11.037	101.422 ± 10.932
total	179.425 ± 63.724	101.411 ± 11.037	101.422 ± 10.932

F.1.2 Lifetime 0.05 mm

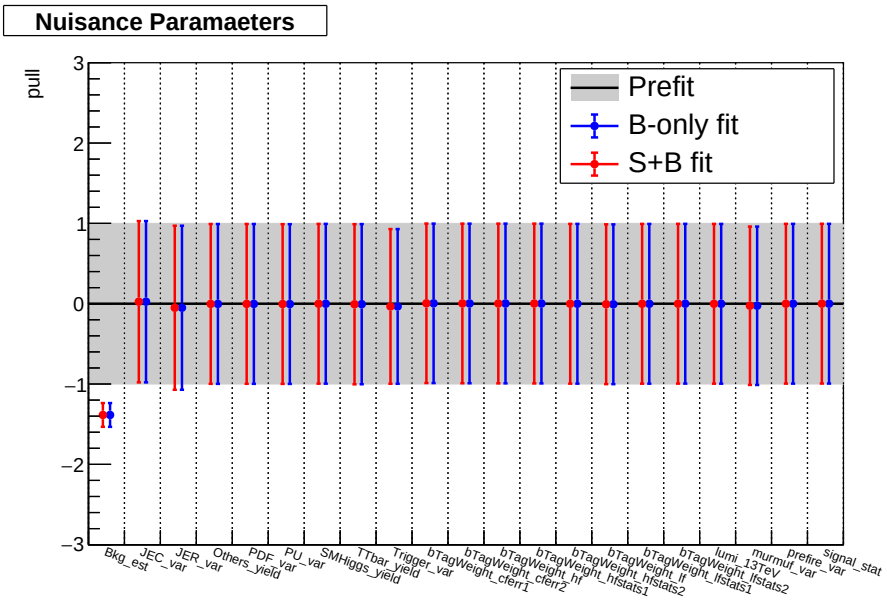

Figure F.2: The pulls of different nuisance parameters for the background-only and signal-plus-background fits to the Asimov pseudodata with $\mu = 1$ hypothesis for the LLP lifetime of 0.05 mm.

Table F.2: Prefit and postfit yields for background-only and signal-plus-background hypotheses of analysis for 15 GeV 0.05 mm.

	Prefit yield	Postfit yield	
Sample		b only	s+b
Signal	13.205 ± 13.830	0.000 ± 0.000	0.000 ± 0.073
QCD pred	1061.624 ± 244.284	737.591 ± 29.182	737.603 ± 29.050
$t\bar{t}$	12.597 ± 8.870	12.125 ± 8.014	12.124 ± 7.302
SM Higgs	0.986 ± 1.769	0.945 ± 1.650	0.945 ± 1.542
Others	2.932 ± 6.451	2.720 ± 5.678	2.720 ± 5.563
Data	748.000	748.000	748.000
total signal	13.205 ± 13.830	0.000 ± 0.000	0.000 ± 0.073
total background	1078.139 ± 244.736	753.381 ± 27.555	753.391 ± 29.246
total	1091.344 ± 244.634	753.381 ± 27.555	753.391 ± 29.253

F.1.3 Lifetime 0.1 mm

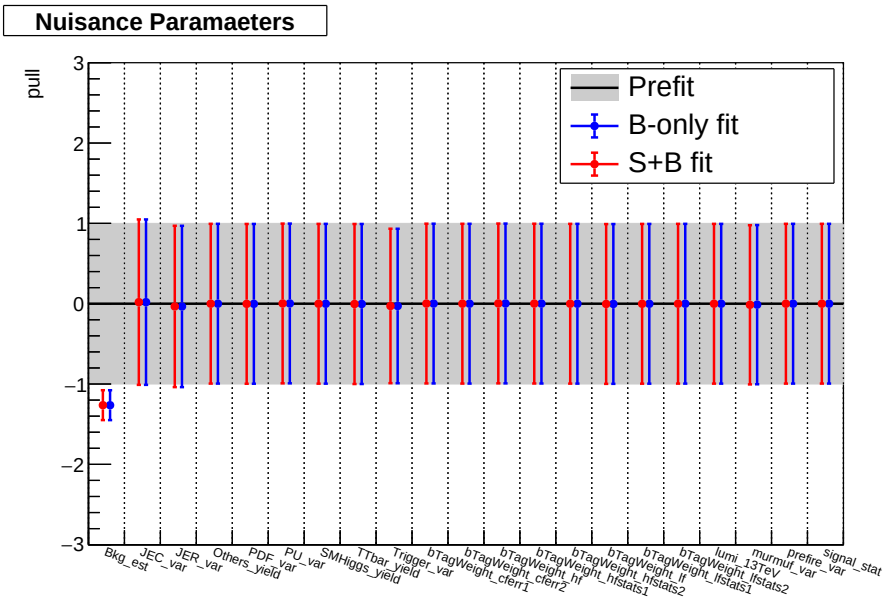

Figure F.3: The pulls of different nuisance parameters for the background-only and signal-plus-background fits to the Asimov pseudodata with $\mu = 1$ hypothesis for the LLP lifetime of 0.1 mm.

Table F.3: Prefit and postfit yields for background-only and signal-plus-background hypotheses of analysis for 15 GeV 0.1 mm.

	Prefit yield	Postfit yield	
Sample		b only	s+b
Signal	15.080 ± 13.004	0.000 ± 0.000	0.000 ± 0.024
QCD pred	407.387 ± 114.335	268.440 ± 16.786	268.461 ± 16.739
$t\bar{t}$	4.037 ± 5.483	3.864 ± 4.677	3.864 ± 4.135
SM Higgs	0.515 ± 0.966	0.503 ± 0.824	0.503 ± 0.857
Others	0.067 ± 0.230	0.068 ± 0.270	0.068 ± 0.243
Data	269.000	269.000	269.000
total signal	15.080 ± 13.004	0.000 ± 0.000	0.000 ± 0.024
total background	412.006 ± 114.526	272.876 ± 16.391	272.896 ± 17.092
total	427.085 ± 115.191	272.876 ± 16.391	272.896 ± 17.094

F.1.4 Lifetime 1 mm

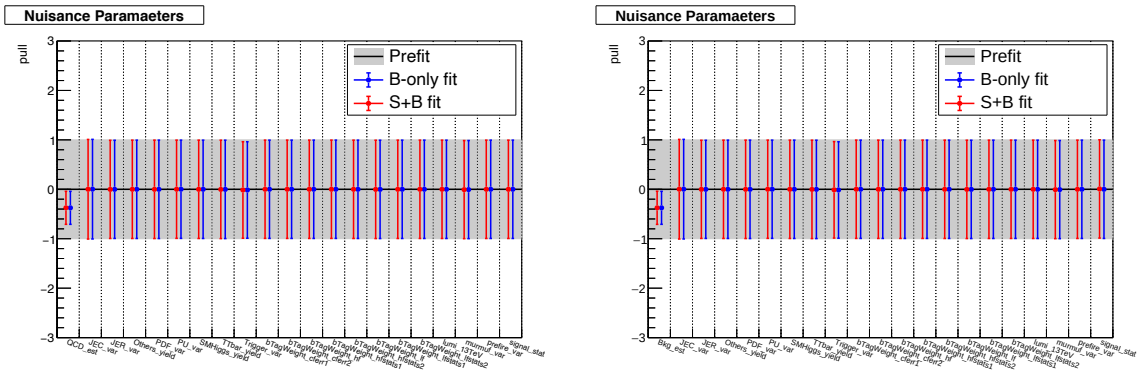

Figure F.4: The pulls of different nuisance parameters for the background-only and signal-plus-background fits to the Asimov pseudodata with $\mu = 1$ hypothesis for the LLP lifetime of 1 mm with the VBF (left) and the ggF Higgs production mode.

Table F.4: Prefit and postfit yields for background-only and signal-plus-background hypotheses of analysis for 15 GeV 1 mm.

	Prefit yield	Postfit yield	
Sample		b only	s+b
Signal	19.540 ± 21.726	0.000 ± 0.000	0.000 ± 0.039
QCD pred	297.357 ± 45.283	279.395 ± 15.554	279.391 ± 15.464
$t\bar{t}$	3.479 ± 3.274	3.449 ± 2.977	3.450 ± 2.996
SM Higgs	0.286 ± 0.246	0.284 ± 0.200	0.284 ± 0.229
Others	0.113 ± 0.191	0.113 ± 0.177	0.113 ± 0.182
Data	281.000	281.000	281.000
total signal	19.540 ± 21.726	0.000 ± 0.000	0.000 ± 0.039
total background	301.236 ± 45.309	283.241 ± 15.378	283.238 ± 15.796
total	320.775 ± 50.832	283.241 ± 15.378	283.238 ± 15.800

Table F.5: Prefit and postfit yields for background-only and signal-plus-background hypotheses of analysis for 15 GeV 1 mm with ggF Higgs production mode.

	Prefit yield	Postfit yield	
Sample		b only	s+b
Signal	94.124 ± 118.723	0.000 ± 0.000	0.007 ± 1.379
QCD pred	297.357 ± 45.283	279.395 ± 15.554	279.398 ± 15.517
$t\bar{t}$	3.479 ± 3.274	3.449 ± 2.977	3.454 ± 3.001
SM Higgs	0.286 ± 0.246	0.284 ± 0.200	0.285 ± 0.230
Others	0.113 ± 0.191	0.113 ± 0.177	0.113 ± 0.182
Data	281.000	281.000	281.000
total signal	94.124 ± 118.723	0.000 ± 0.000	0.007 ± 1.379
total background	301.236 ± 45.309	283.241 ± 15.378	283.251 ± 15.848
total	395.360 ± 127.847	283.241 ± 15.378	283.258 ± 15.974

F.1.5 Lifetime 5 mm

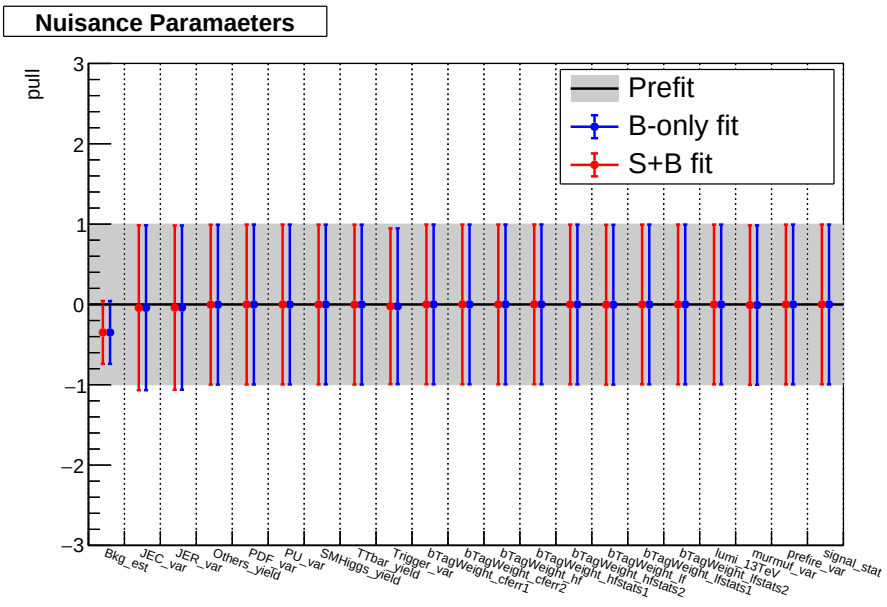

Figure F.5: The pulls of different nuisance parameters for the background-only and signal-plus-background fits to the Asimov pseudodata with $\mu = 1$ hypothesis for the LLP lifetime of 5 mm.

Table F.6: Prefit and postfit yields for background-only and signal-plus-background hypotheses of analysis for 15 GeV 5 mm.

	Prefit yield	Postfit yield	
Sample		b only	s+b
Signal	1.801 ± 3.106	0.000 ± 0.000	0.000 ± 0.033
QCD pred	297.357 ± 45.283	279.395 ± 15.554	279.397 ± 15.464
$t\bar{t}$	3.479 ± 3.274	3.449 ± 2.977	3.450 ± 2.996
SM Higgs	0.286 ± 0.246	0.284 ± 0.200	0.284 ± 0.229
Others	0.113 ± 0.191	0.113 ± 0.177	0.113 ± 0.182
Data	281.000	281.000	281.000
total signal	1.801 ± 3.106	0.000 ± 0.000	0.000 ± 0.033
total background	301.236 ± 45.309	283.241 ± 15.378	283.244 ± 15.796
total	303.037 ± 45.461	283.241 ± 15.378	283.244 ± 15.799

F.1.6 Lifetime 10 mm

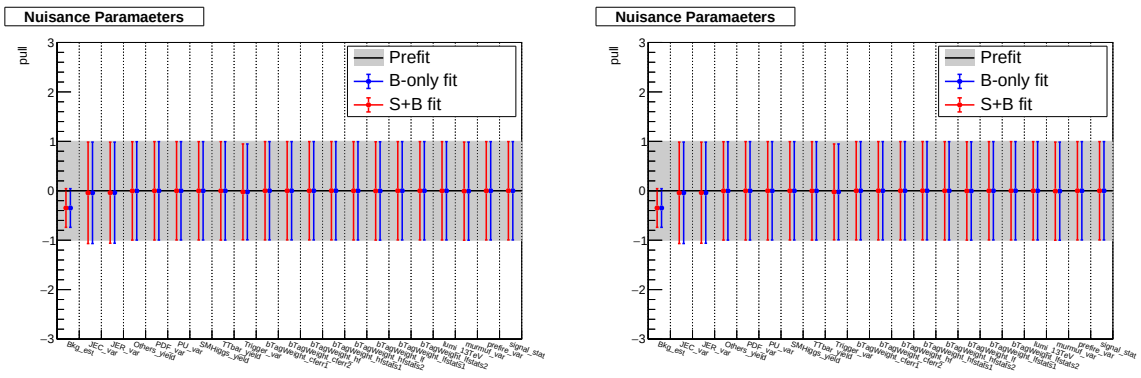

Figure F.6: The pulls of different nuisance parameters for the background-only and signal-plus-background fits to the Asimov pseudodata with $\mu = 1$ hypothesis for the LLP lifetime of 10 mm with the VBF (left) and the ggF Higgs production mode.

Table F.7: Prefit and postfit yields for background-only and signal-plus-background hypotheses of analysis for 15 GeV 10 mm.

	Prefit yield	Postfit yield	
Sample		b only	s+b
Signal	1.052 ± 1.736	0.000 ± 0.000	0.000 ± 0.022
QCD pred	644.966 ± 61.723	622.587 ± 24.761	622.603 ± 24.602
$t\bar{t}$	4.889 ± 5.786	4.685 ± 4.872	4.684 ± 4.862
SM Higgs	1.009 ± 0.859	0.979 ± 0.680	0.979 ± 0.733
Others	3.642 ± 12.052	3.173 ± 9.564	3.170 ± 8.824
Data	628.000	628.000	628.000
total signal	1.052 ± 1.736	0.000 ± 0.000	0.000 ± 0.022
total background	654.506 ± 64.156	631.424 ± 24.794	631.436 ± 25.610
total	655.558 ± 64.434	631.424 ± 24.794	631.436 ± 25.613

Table F.8: Prefit and postfit yields for background-only and signal-plus-background hypotheses of analysis for 15 GeV 10 mm with ggF Higgs production mode.

	Prefit yield	Postfit yield	
Sample		b only	s+b
Signal	3.575 ± 6.824	0.000 ± 0.000	0.000 ± 0.208
QCD pred	644.966 ± 61.723	622.587 ± 24.761	622.601 ± 24.601
$t\bar{t}$	4.889 ± 5.786	4.685 ± 4.872	4.683 ± 4.862
SM Higgs	1.009 ± 0.859	0.979 ± 0.680	0.979 ± 0.732
Others	3.642 ± 12.052	3.173 ± 9.564	3.170 ± 8.825
Data	628.000	628.000	628.000
total signal	3.575 ± 6.824	0.000 ± 0.000	0.000 ± 0.208
total background	654.506 ± 64.156	631.424 ± 24.794	631.433 ± 25.611
total	658.081 ± 65.633	631.424 ± 24.794	631.433 ± 25.633

F.2 Resolved Topology

F.2.1 40 GeV

Lifetime 0 mm

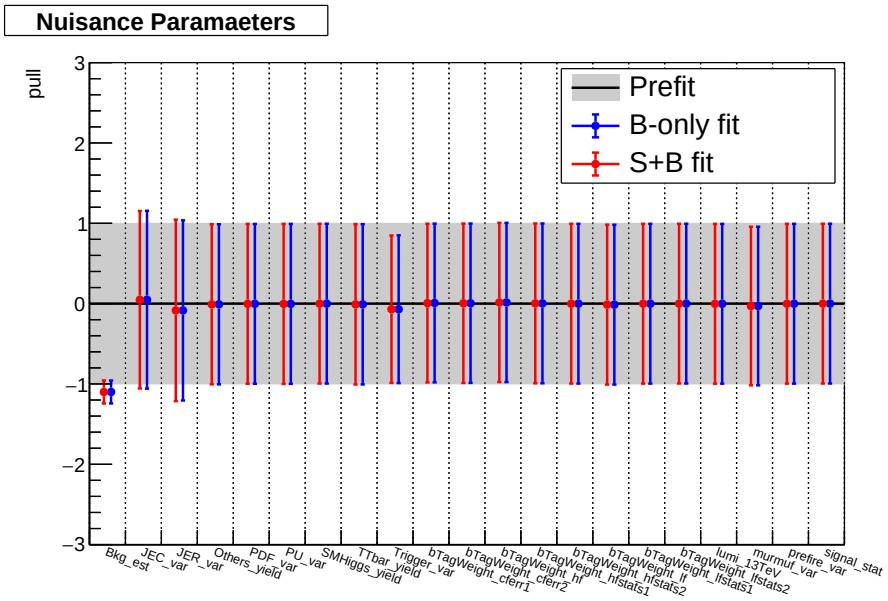

Figure F.7: The pulls of different nuisance parameters for the background-only and signal-plus-background fits to the Asimov pseudodata with $\mu = 1$ hypothesis for the LLP with a mass of 40 GeV and a lifetime of 0 mm.

Table F.9: Prefit and postfit yields for background-only and signal-plus-background hypotheses of analysis for 40 GeV 0 mm.

	Prefit yield	Postfit yield	
Sample		b only	s+b
Signal	19.640 ± 22.547	0.000 ± 0.000	0.000 ± 0.352
QCD pred	12825.414 ± 1312.683	11375.859 ± 180.018	11375.853 ± 179.479
$t\bar{t}$	142.287 ± 104.686	135.547 ± 88.863	135.576 ± 81.923
SM Higgs	3.339 ± 3.030	3.180 ± 2.650	3.180 ± 2.446
Data	11568.000	11568.000	11568.000
total signal	19.640 ± 22.547	0.000 ± 0.000	0.000 ± 0.352
total background	13045.391 ± 1318.271	11578.263 ± 145.790	11578.298 ± 149.270
total	13065.031 ± 1319.211	11578.263 ± 145.790	11578.298 ± 149.301

Lifetime 0.05 mm

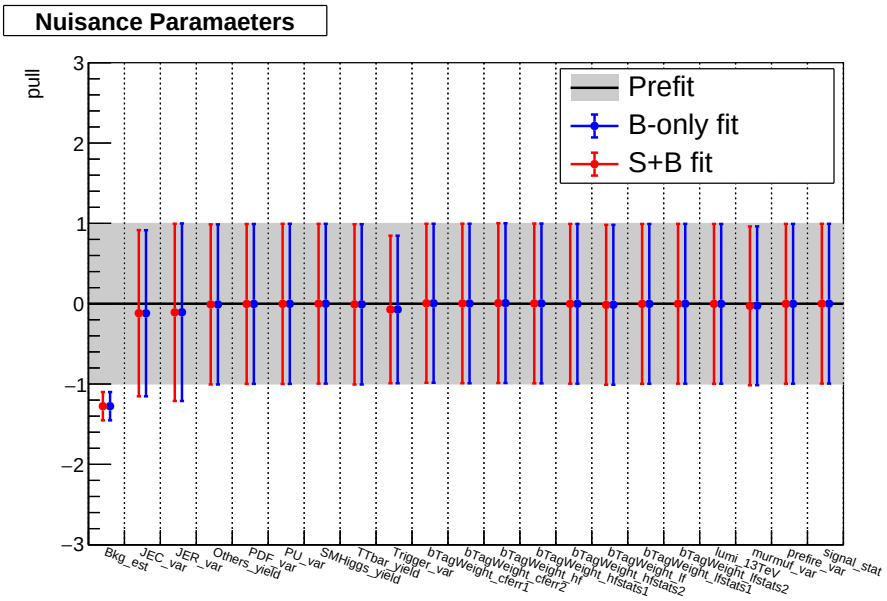

Figure F.8: The pulls of different nuisance parameters for the background-only and signal-plus-background fits to the Asimov pseudodata with $\mu = 1$ hypothesis for the LLP with a mass of 40 GeV and a lifetime of 0.05 mm.

Table F.10: Prefit and postfit yields for background-only and signal-plus-background hypotheses of analysis for 40 GeV 0.05 mm.

	Prefit yield	Postfit yield	
Sample		b only	s+b
Signal	21.869 ± 22.171	0.000 ± 0.000	0.000 ± 0.038
QCD pred	5138.051 ± 602.439	4375.480 ± 98.816	4375.549 ± 98.248
$t\bar{t}$	52.884 ± 55.985	48.246 ± 41.499	48.244 ± 38.095
SM Higgs	1.033 ± 1.011	0.951 ± 0.814	0.951 ± 0.756
Others	34.868 ± 52.753	25.608 ± 36.654	25.568 ± 33.360
Data	4440.000	4440.000	4440.000
total signal	21.869 ± 22.171	0.000 ± 0.000	0.000 ± 0.038
total background	5226.836 ± 608.046	4450.286 ± 82.139	4450.312 ± 84.661
total	5248.705 ± 610.125	4450.286 ± 82.139	4450.312 ± 84.666

Lifetime 0.1 mm

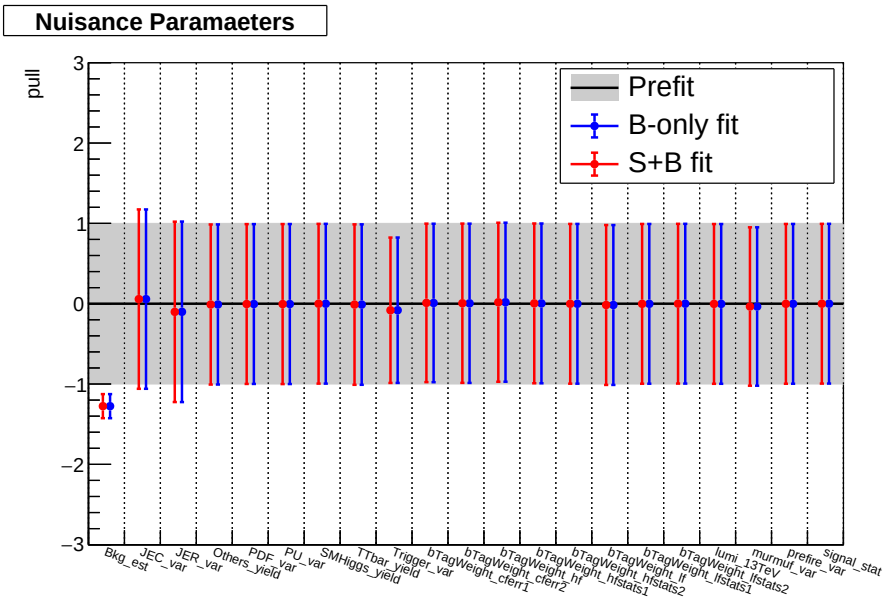

Figure F.9: The pulls of different nuisance parameters for the background-only and signal-plus-background fits to the Asimov pseudodata with $\mu = 1$ hypothesis for the LLP with a mass of 40 GeV and a lifetime of 0.1 mm.

Table F.11: Prefit and postfit yields for background-only and signal-plus-background hypotheses of analysis for 40 GeV 0.1 mm.

	Prefit yield	Postfit yield	
Sample		b only	s+b
Signal	58.455 ± 55.026	0.000 ± 0.000	0.001 ± 1.033
QCD pred	12046.353 ± 1161.198	10571.856 ± 164.934	10571.997 ± 163.822
$t\bar{t}$	132.903 ± 99.475	125.859 ± 81.455	125.828 ± 76.001
SM Higgs	3.159 ± 2.557	3.000 ± 2.100	3.000 ± 2.044
Others	66.429 ± 63.808	54.952 ± 49.358	54.896 ± 45.507
Data	10743.000	10743.000	10743.000
total signal	58.455 ± 55.026	0.000 ± 0.000	0.001 ± 1.033
total background	12248.844 ± 1166.463	10755.668 ± 137.357	10755.720 ± 141.192
total	12307.299 ± 1169.638	10755.668 ± 137.357	10755.721 ± 141.268

Lifetime 1 mm

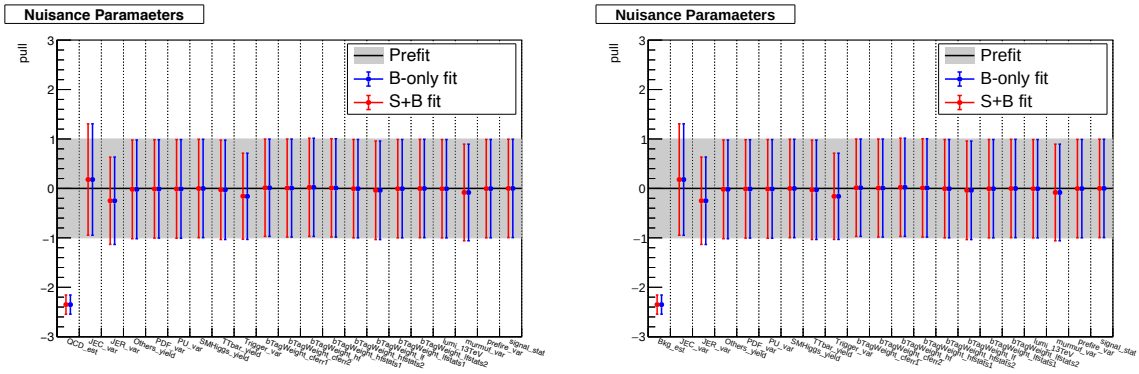

Figure F.10: The pulls of different nuisance parameters for the background-only and signal-plus-background fits to the Asimov pseudodata with $\mu = 1$ hypothesis for the LLP with a mass of 40 GeV and a lifetime of 1 mm with the VBF (left) and the ggF Higgs production mode.

Table F.12: Prefit and postfit yields for background-only and signal-plus-background hypotheses of analysis for 40 GeV 1 mm.

	Prefit yield	Postfit yield	
Sample		b only	s+b
Signal	60.072 ± 71.436	0.000 ± 0.000	0.000 ± 0.315
QCD pred	13968.438 ± 825.711	12086.749 ± 146.831	12086.650 ± 145.784
$t\bar{t}$	135.609 ± 90.657	120.526 ± 64.788	120.616 ± 60.952
SM Higgs	3.545 ± 2.933	3.141 ± 2.129	3.144 ± 2.045
Others	68.264 ± 63.448	39.283 ± 36.498	39.305 ± 35.228
Data	12211.000	12211.000	12211.000
total signal	60.072 ± 71.436	0.000 ± 0.000	0.000 ± 0.315
total background	14175.854 ± 833.747	12249.700 ± 127.093	12249.716 ± 134.088
total	14235.927 ± 841.188	12249.700 ± 127.093	12249.716 ± 134.124

Table F.13: Prefit and postfit yields for background-only and signal-plus-background hypotheses of analysis for 40 GeV 1 mm with ggF Higgs production mode.

	Prefit yield	Postfit yield	
Sample		b only	s+b
Signal	168.092 ± 116.003	0.000 ± 0.000	0.000 ± 0.002
QCD pred	13968.438 ± 825.711	12086.749 ± 146.831	12086.749 ± 145.845
$t\bar{t}$	135.609 ± 90.657	120.526 ± 64.788	120.526 ± 61.044
SM Higgs	3.545 ± 2.933	3.141 ± 2.129	3.141 ± 2.047
Others	68.264 ± 63.448	39.283 ± 36.498	39.284 ± 35.239
Data	12211.000	12211.000	12211.000
total signal	168.092 ± 116.003	0.000 ± 0.000	0.000 ± 0.002
total background	14175.854 ± 833.747	12249.700 ± 127.093	12249.699 ± 134.172
total	14343.946 ± 855.002	12249.700 ± 127.093	12249.699 ± 134.172

Lifetime 5 mm

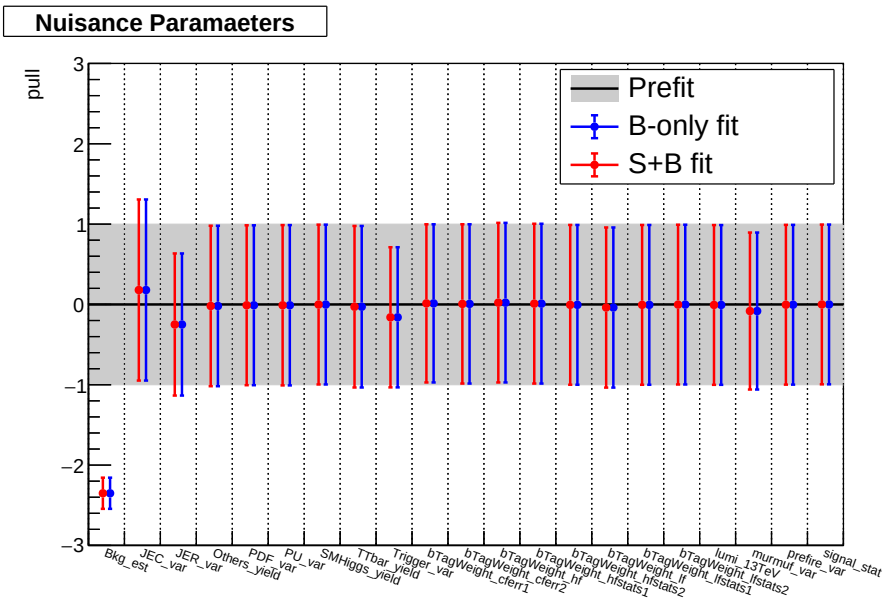

Figure F.11: The pulls of different nuisance parameters for the background-only and signal-plus-background fits to the Asimov pseudodata with $\mu = 1$ hypothesis for the LLP with a mass of 40 GeV and a lifetime of 5 mm.

Table F.14: Prefit and postfit yields for background-only and signal-plus-background hypotheses of analysis for 40 GeV 5 mm.

	Prefit yield	Postfit yield	
Sample		b only	s+b
Signal	12.481 ± 17.004	0.000 ± 0.000	0.000 ± 0.007
QCD pred	13968.438 ± 825.711	12086.749 ± 146.831	12086.753 ± 145.868
$t\bar{t}$	135.609 ± 90.657	120.526 ± 64.788	120.526 ± 61.055
SM Higgs	3.545 ± 2.933	3.141 ± 2.129	3.141 ± 2.047
Others	68.264 ± 63.448	39.283 ± 36.498	39.286 ± 35.222
Data	12211.000	12211.000	12211.000
total signal	12.481 ± 17.004	0.000 ± 0.000	0.000 ± 0.007
total background	14175.854 ± 833.747	12249.700 ± 127.093	12249.707 ± 134.221
total	14188.335 ± 835.649	12249.700 ± 127.093	12249.707 ± 134.222

Lifetime 10 mm

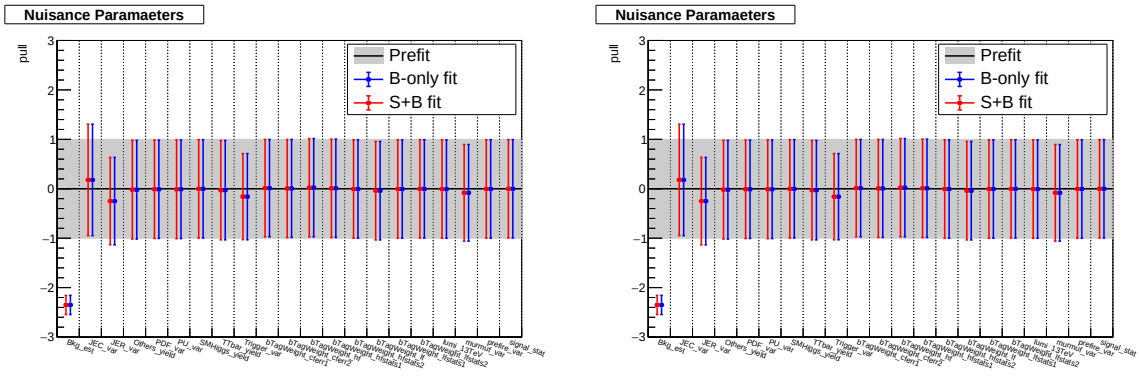

Figure F.12: The pulls of different nuisance parameters for the background-only and signal-plus-background fits to the Asimov pseudodata with $\mu = 1$ hypothesis for the LLP with a mass of 40 GeV and a lifetime of 10 mm with the VBF (left) and the ggF Higgs production mode.

Table F.15: Prefit and postfit yields for background-only and signal-plus-background hypotheses of analysis for 40 GeV 10 mm.

	Prefit yield	Postfit yield	
Sample		b only	s+b
Signal	5.983 ± 6.177	0.000 ± 0.000	0.000 ± 0.114
QCD pred	13968.438 ± 825.711	12086.749 ± 146.831	12086.564 ± 145.869
$t\bar{t}$	135.609 ± 90.657	120.526 ± 64.788	120.614 ± 60.989
SM Higgs	3.545 ± 2.933	3.141 ± 2.129	3.143 ± 2.046
Others	68.264 ± 63.448	39.283 ± 36.498	39.368 ± 35.251
Data	12211.000	12211.000	12211.000
total signal	5.983 ± 6.177	0.000 ± 0.000	0.000 ± 0.114
total background	14175.854 ± 833.747	12249.700 ± 127.093	12249.689 ± 134.174
total	14181.837 ± 833.893	12249.700 ± 127.093	12249.689 ± 134.189

Table F.16: Prefit and postfit yields for background-only and signal-plus-background hypotheses of analysis for 40 GeV 10 mm with ggF Higgs production mode.

	Prefit yield	Postfit yield	
Sample		b only	s+b
Signal	5.419 ± 8.524	0.000 ± 0.000	0.000 ± 0.003
QCD pred	13968.438 ± 825.711	12086.749 ± 146.831	12086.752 ± 145.866
$t\bar{t}$	135.609 ± 90.657	120.526 ± 64.788	120.526 ± 61.056
SM Higgs	3.545 ± 2.933	3.141 ± 2.129	3.141 ± 2.047
Others	68.264 ± 63.448	39.283 ± 36.498	39.285 ± 35.223
Data	12211.000	12211.000	12211.000
total signal	5.419 ± 8.524	0.000 ± 0.000	0.000 ± 0.003
total background	14175.854 ± 833.747	12249.700 ± 127.093	12249.704 ± 134.221
total	14181.274 ± 834.707	12249.700 ± 127.093	12249.704 ± 134.221

F.2.2 55 GeV

Lifetime 0 mm

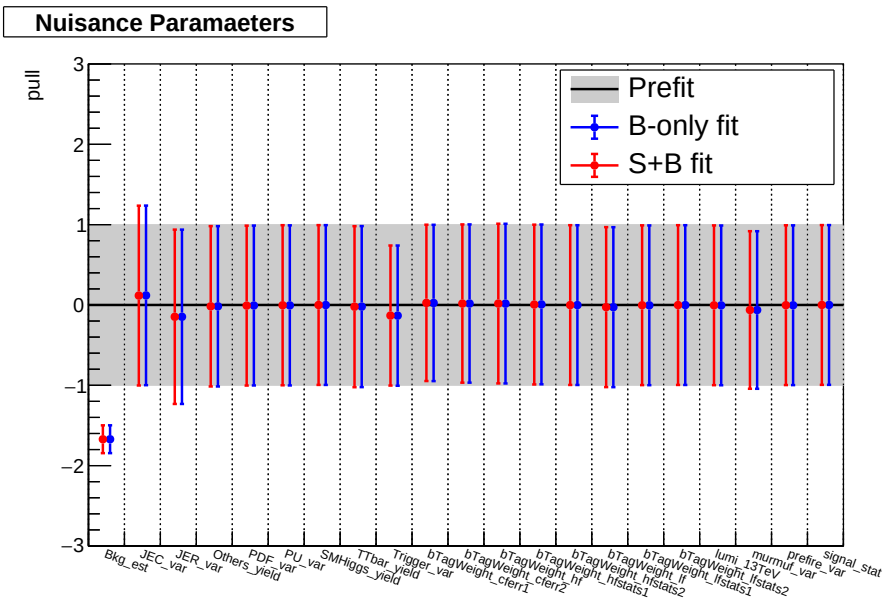

Figure F.13: The pulls of different nuisance parameters for the background-only and signal-plus-background fits to the Asimov pseudodata with $\mu = 1$ hypothesis for the LLP with a mass of 55 GeV and a lifetime of 0 mm.

Table F.17: Prefit and postfit yields for background-only and signal-plus-background hypotheses of analysis for 55 GeV 0 mm.

	Prefit yield	Postfit yield	
Sample		b only	s+b
Signal	32.398 ± 33.985	0.000 ± 0.000	0.001 ± 1.208
QCD pred	18793.227 ± 1308.319	16637.672 ± 213.634	16637.305 ± 212.277
$t\bar{t}$	219.113 ± 171.428	198.295 ± 125.659	198.482 ± 115.308
SM Higgs	4.457 ± 3.446	4.033 ± 2.692	4.037 ± 2.502
Others	101.763 ± 107.303	78.308 ± 73.419	78.440 ± 65.439
Data	16895.000	16895.000	16895.000
total signal	32.398 ± 33.985	0.000 ± 0.000	0.001 ± 1.208
total background	19118.561 ± 1327.321	16918.309 ± 175.568	16918.264 ± 177.056
total	19150.959 ± 1331.970	16918.309 ± 175.568	16918.266 ± 177.256

Lifetime 0.05 mm

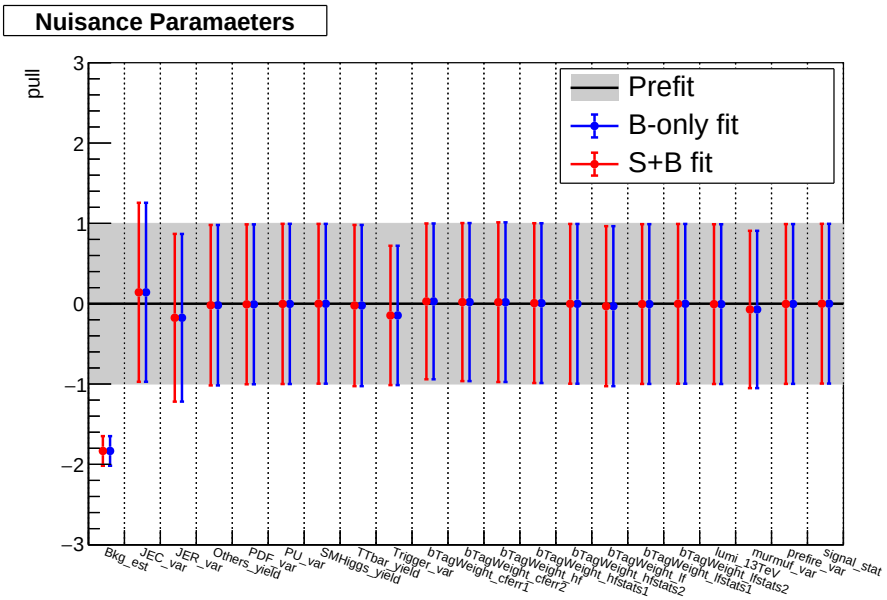

Figure F.14: The pulls of different nuisance parameters for the background-only and signal-plus-background fits to the Asimov pseudodata with $\mu = 1$ hypothesis for the LLP with a mass of 55 GeV and a lifetime of 0.05 mm.

Table F.18: Prefit and postfit yields for background-only and signal-plus-background hypotheses of analysis for 55 GeV 0.05 mm.

	Prefit yield	Postfit yield	
Sample		b only	s+b
Signal	33.981 ± 37.098	0.000 ± 0.000	0.000 ± 0.013
QCD pred	18434.643 ± 1175.568	16316.909 ± 203.591	16316.919 ± 202.423
$t\bar{t}$	207.234 ± 166.250	184.691 ± 118.021	184.687 ± 108.246
SM Higgs	4.411 ± 3.330	3.929 ± 2.492	3.929 ± 2.339
Others	99.343 ± 105.120	72.450 ± 68.358	72.452 ± 61.205
Data	16550.000	16550.000	16550.000
total signal	33.981 ± 37.098	0.000 ± 0.000	0.000 ± 0.013
total background	18745.631 ± 1196.336	16577.980 ± 169.727	16577.986 ± 172.619
total	18779.611 ± 1201.973	16577.980 ± 169.727	16577.986 ± 172.621

Lifetime 0.1 mm

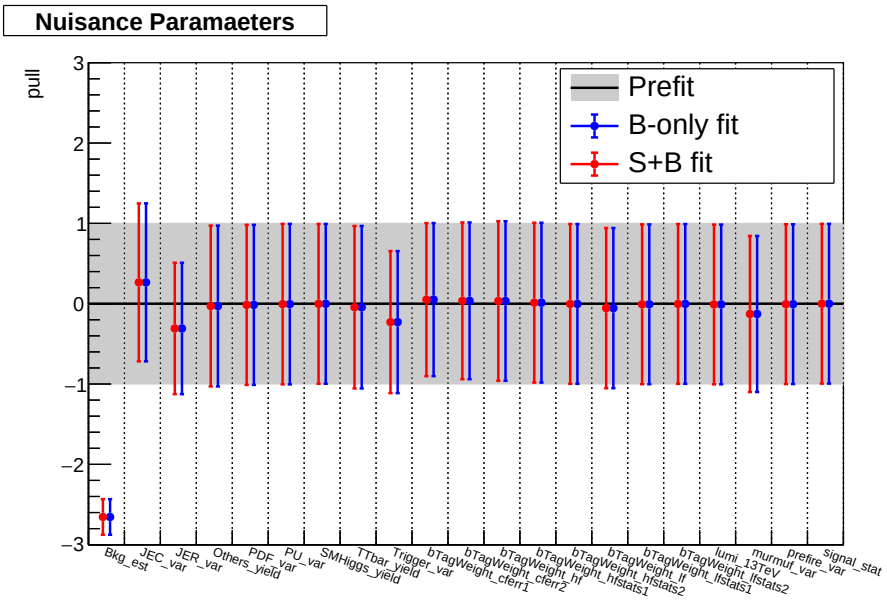

Figure F.15: The pulls of different nuisance parameters for the background-only and signal-plus-background fits to the Asimov pseudodata with $\mu = 1$ hypothesis for the LLP with a mass of 55 GeV and a lifetime of 0.1 mm.

Table F.19: Prefit and postfit yields for background-only and signal-plus-background hypotheses of analysis for 55 GeV 0.1 mm.

	Prefit yield	Postfit yield	
Sample		b only	s+b
Signal	48.816 ± 49.326	0.000 ± 0.000	0.000 ± 0.003
QCD pred	18180.047 ± 818.959	16065.566 ± 168.560	16065.565 ± 167.432
$t\bar{t}$	199.100 ± 162.115	164.364 ± 103.084	164.364 ± 95.189
SM Higgs	4.346 ± 3.343	3.561 ± 2.183	3.561 ± 2.082
Others	99.222 ± 104.515	53.316 ± 55.049	53.314 ± 51.047
Data	16229.000	16229.000	16229.000
total signal	48.816 ± 49.326	0.000 ± 0.000	0.000 ± 0.003
total background	18482.715 ± 849.982	16286.808 ± 154.275	16286.805 ± 160.852
total	18531.531 ± 858.512	16286.808 ± 154.275	16286.805 ± 160.852

Lifetime 1 mm

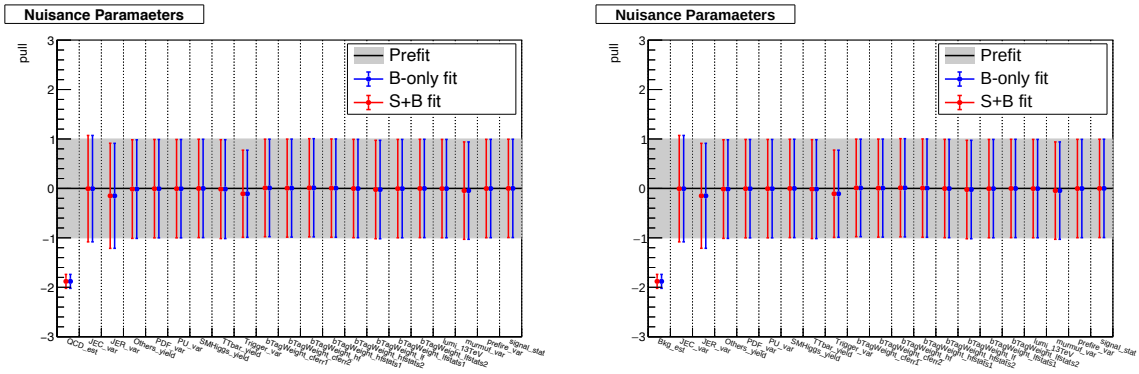

Figure F.16: The pulls of different nuisance parameters for the background-only and signal-plus-background fits to the Asimov pseudodata with $\mu = 1$ hypothesis for the LLP with a mass of 55 GeV and a lifetime of 1 mm with the VBF (left) and the ggF Higgs production mode.

Table F.20: Prefit and postfit yields for background-only and signal-plus-background hypotheses of analysis for 55 GeV 1 mm.

	Prefit yield	Postfit yield	
Sample		b only	s+b
Signal	43.184 ± 51.615	0.000 ± 0.000	0.000 ± 0.235
QCD pred	13095.727 ± 1159.697	10981.017 ± 147.710	10980.969 ± 146.805
$t\bar{t}$	114.981 ± 95.185	108.103 ± 73.599	108.109 ± 67.857
SM Higgs	2.780 ± 2.642	2.627 ± 2.319	2.627 ± 2.210
Others	63.145 ± 73.746	49.626 ± 50.368	49.668 ± 50.611
Data	11121.000	11121.000	11121.000
total signal	43.184 ± 51.615	0.000 ± 0.000	0.000 ± 0.235
total background	13276.632 ± 1164.745	11141.372 ± 128.017	11141.373 ± 135.427
total	13319.815 ± 1168.231	11141.372 ± 128.017	11141.373 ± 135.464

Table F.21: Prefit and postfit yields for background-only and signal-plus-background hypotheses of analysis for 55 GeV 1 mm with ggF Higgs production mode.

	Prefit yield	Postfit yield	
Sample		b only	s+b
Signal	110.512 ± 83.885	0.000 ± 0.000	0.000 ± 0.009
QCD pred	13095.727 ± 1159.697	10981.017 ± 147.720	10981.037 ± 146.798
$t\bar{t}$	114.981 ± 95.185	108.103 ± 73.611	108.109 ± 67.992
SM Higgs	2.780 ± 2.642	2.627 ± 2.320	2.627 ± 2.212
Others	63.145 ± 73.746	49.626 ± 50.376	49.625 ± 50.618
Data	11121.000	11121.000	11121.000
total signal	110.512 ± 83.885	0.000 ± 0.000	0.000 ± 0.009
total background	13276.632 ± 1164.745	11141.372 ± 128.024	11141.397 ± 135.314
total	13387.144 ± 1173.640	11141.372 ± 128.024	11141.397 ± 135.316

Lifetime 5 mm

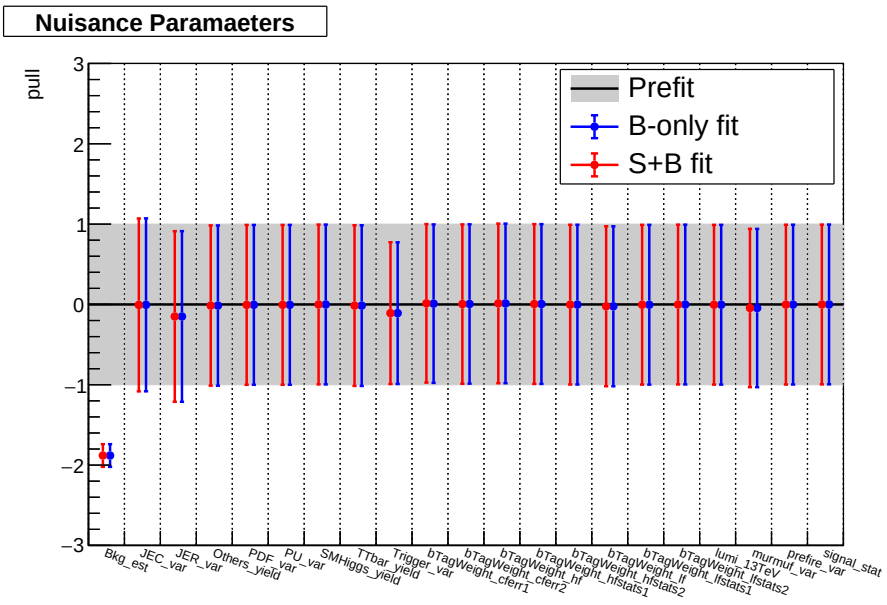

Figure F.17: The pulls of different nuisance parameters for the background-only and signal-plus-background fits to the Asimov pseudodata with $\mu = 1$ hypothesis for the LLP with a mass of 55 GeV and a lifetime of 5 mm.

Table F.22: Prefit and postfit yields for background-only and signal-plus-background hypotheses of analysis for 55 GeV 5 mm.

	Prefit yield	Postfit yield	
Sample		b only	s+b
Signal	10.295 ± 11.928	0.000 ± 0.000	0.000 ± 0.712
QCD pred	13095.727 ± 1159.697	10981.017 ± 147.710	10980.974 ± 146.760
$t\bar{t}$	114.981 ± 95.185	108.103 ± 73.599	108.109 ± 67.911
SM Higgs	2.780 ± 2.642	2.627 ± 2.319	2.628 ± 2.211
Others	63.145 ± 73.746	49.626 ± 50.368	49.608 ± 50.610
Data	11121.000	11121.000	11121.000
total signal	10.295 ± 11.928	0.000 ± 0.000	0.000 ± 0.712
total background	13276.632 ± 1164.745	11141.372 ± 128.017	11141.317 ± 135.412
total	13286.927 ± 1165.522	11141.372 ± 128.017	11141.317 ± 135.516

Lifetime 10 mm

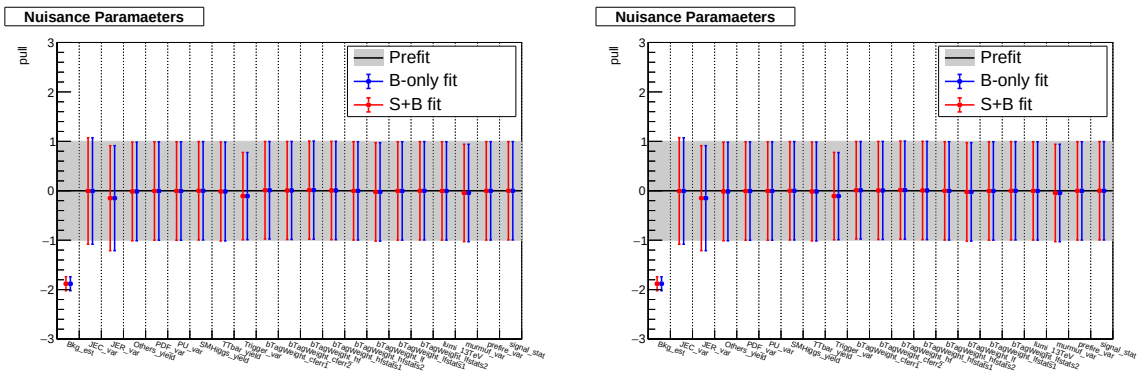

Figure F.18: The pulls of different nuisance parameters for the background-only and signal-plus-background fits to the Asimov pseudodata with $\mu = 1$ hypothesis for the LLP with a mass of 55 GeV and a lifetime of 10 mm with the VBF (left) and the ggF Higgs production mode.

Table F.23: Prefit and postfit yields for background-only and signal-plus-background hypotheses of analysis for 55 GeV 10 mm.

	Prefit yield	Postfit yield	
Sample		b only	s+b
Signal	2.192 ± 3.844	0.000 ± 0.000	0.000 ± 0.014
QCD pred	13095.727 ± 1159.697	10981.017 ± 147.720	10981.061 ± 146.795
$t\bar{t}$	114.981 ± 95.185	108.103 ± 73.611	108.108 ± 67.974
SM Higgs	2.780 ± 2.642	2.627 ± 2.320	2.627 ± 2.211
Others	63.145 ± 73.746	49.626 ± 50.376	49.627 ± 50.611
Data	11121.000	11121.000	11121.000
total signal	2.192 ± 3.844	0.000 ± 0.000	0.000 ± 0.014
total background	13276.632 ± 1164.745	11141.372 ± 128.024	11141.423 ± 135.312
total	13278.823 ± 1164.939	11141.372 ± 128.024	11141.423 ± 135.313

Table F.24: Prefit and postfit yields for background-only and signal-plus-background hypotheses of analysis for 55 GeV 10 mm with ggF Higgs production mode.

	Prefit yield	Postfit yield	
Sample		b only	s+b
Signal	3.003 ± 5.146	0.000 ± 0.000	0.000 ± 0.006
QCD pred	13095.727 ± 1159.697	10981.017 ± 147.710	10981.040 ± 146.790
$t\bar{t}$	114.981 ± 95.185	108.103 ± 73.599	108.108 ± 67.998
SM Higgs	2.780 ± 2.642	2.627 ± 2.319	2.627 ± 2.212
Others	63.145 ± 73.746	49.626 ± 50.368	49.623 ± 50.614
Data	11121.000	11121.000	11121.000
total signal	3.003 ± 5.146	0.000 ± 0.000	0.000 ± 0.006
total background	13276.632 ± 1164.745	11141.372 ± 128.017	11141.397 ± 135.317
total	13279.635 ± 1164.973	11141.372 ± 128.017	11141.397 ± 135.317

List of Figures

List of Figures

List of Tables

List of Tables

Acronyms

ALICE A Large Ion Collider Experiment

ATLAS A Toroidal LHC ApparatuS

AUC area under the curve

BEH Brout-Englert-Higgs

BSM beyond the standard model

CERN European Organization for Nuclear Research

CKM Cabbibo-Kobayashi-Maskawa

CHS charged hadron subtraction

CL confidence level

CMS Compact Muon Solenoid

CR control region

CSC cathode strip chambers

DNN deep neural network

DT drift tubes

ECAL electromagnetic calorimeter

FCN fully connected network

ggF gluon-gluon fusion

HEP high-energy physics

HERA Hadron-Electron Ring Accelerator

HCAL hadronic calorimeter

HLT high-level trigger

IP impact parameter

IVF Inclusive Vertex Finder

JEC jet energy correction

JER jet energy resolution

L1 level-1 trigger

LHC Large Hadron Collider

LHCb Large Hadron Collider beauty

LLP long-lived particle

LSTM long short-term memory

MC Monte-Carlo

ML machine learning

NI nuclear interaction

NN neural network

PDFs parton distribution functions

PF Particle-Flow

PU pileup

PUPPI pileup per particle identification

pp proton-proton

QCD quantum chromodynamics

QED quantum electrodynamics

QFT quantum field theory

PV primary vertex

RNN recurrent neural network

ROC receiver operating characteristic

RPC resistive plate chambers

SR signal region

SM standard model

SUSY Supersymmetry

SV secondary vertex

UE underlying events

VBF vector-boson fusion

Danksagung

An dieser Stelle möchte ich mich gerne bei allen bedanken, die mich in den letzten Jahren begleitet und während der Promotion unterstützt haben.
Als erstes danke ich Gregor Kasieczka, der mir ermöglicht hat in seiner Arbeitsgruppe zu promovieren. Du hast dir jederzeit für Treffen Zeit genommen und mich in vielerlei Hinsicht unterstützt. So konnte ich bei den letzte Datennahmen 2018 dabei sein und im CMS Kontrollraum Trigger Schichten machen. Des Weiteren konnte ich sehr früh in meiner Zeit als Doktorandin eine Stelle als b tag Kontaktperson für die CMS "Exotica" Gruppe antreten und diese bis fast zum Schluss ausführen. Du hast mir außerdem ermöglicht zahlreiche Dienstreisen zu Sommerschulen, sowie zu Konferenzen zu machen, die mir viel neues Wissen und Einblicke gegeben haben. Zusätzlich bekam ich auch deine Unterstützung für verschiedene Gleichstellungsprojekte, wie die Physik-Projekt-Tage und die Physikerinnentagung 2020.
Außerdem möchte ich mich auch bei Peter Schleper, meinem Zweitgutachter, bedanken, mit dem man immer gut ein Schwätzchen halten konnte, wenn wir zusammen auf Teewasser gewartet haben (zumindest vor der Home-Office Zeit). Der Dank geht außerdem auch an die restliche Prüfungskommission.
Ein riesiger Dank geht an Anna Benecke, die mich nicht nur im Privaten, sondern auch für die Analyse immer wieder mit Rat und Tat zur Seite gestanden hat. Mit dir ist auch die Organisation von den Physik-Projekt-Tagen oder der Physikerinnentagung 2020 mit 350 Teilnehmenden ein Leichtes. Die gemeinsame Zeit mit dir, sei es nun Hochzeitstorte backen, virtueller Sport oder die vielen Konferenzen (mit sehr wenig Schlaf) haben mir viel Freude bereitet und ich hoffe es folgen noch viele weitere gemeinsame Aktivitäten. Durch dich bin ich mehr und mehr zur Gleichstellung gekommen und ich konnte immer auf dich Zählen, besonders in den letzten beiden Jahren hast du mir viel Mut und Kraft gegeben!
Ein weiterer sehr großer Dank geht an Karim El Morabit. Du arbeitest zwar "erst" seit einem dreiviertel Jahr mit an der Analyse, aber gemeinsam haben wir viel erreicht! Ich danke dir für die gemeinsame Strukturierung der Analyse und den tausenden

von spontanen Zoom Meetings, in denen wir uns immer wieder die Köpfe zerbrochen haben, um mehr zu verstehen. Deine Motivation, die vielen hilfreichen Kommentare und Ratschläge haben vieles einfacher gemacht. Die Auflockerungen durch Geschichten über Eichhörnchen kamen dabei immer zur richtigen Zeit... Grammatikfehler viele du korrigiert hast, entschuldigen ich mich muss! ;)
Des Weiteren danke ich Jörg Schindler, unsere gemeinsame Zeit im Büro, die Kochabende und auch die virtuellen Kaffeepausen mit deiner Ehrlichkeit und realistischen Einschätzungen haben mir immer gut getan. Tobias Quadfasel, die Zeit im Büro und auch die virtuellen Kaffeepausen hast du mit deiner offenen und fröhlichen Art immer aufgelockert. Alexandra Tews, es hat viel Spaß gemacht mit dir eine Konferenz zu organisieren und sich über alles mögliche auszutauschen. Zudem geht ein Dank an das "Team Long-Lived" und den weiteren Personen aus unserer Arbeitsgruppe, dem Institut und der CMS Kollaboration. Insbesondere: Erik Buhmann, Sascha Diefenbacher, Mary Hadley, Joscha Knolle, Roman Kogler, Tobias Kramer und vielen weiteren.
Philipp Eich danke ich für die große Unterstützung bei allem, was ich mir so in den Kopf gesetzt hab, ohne dich wäre vieles nicht denkbar. Du warst mir auch in den letzten beiden Jahren ein toller Büro Nachbar, eine große Stütze und ich hab die viele Zeit mit dir sehr genossen. Meiner Mutter danke ich, die immer für mich da ist und mir immer zur Seite steht. Ein großer Dank geht auch an meine Schwester, mit der ich letztes Jahr viel überstanden hab und ebenfalls immer da ist. Auf euch, sowie auch auf die restliche Familie, kann ich immer zählen. Danke!